3rd Conference on
**Sustainability in Process Industry**
**SPI-2016**

19-20th October, 2016

# CONFERENCE PROCEEDINGS

**Department of Chemical Engineering**
**University of Engineering and Technology, Peshawar**

# PROCEEDINGS

## of the

## 3rd CONFERENCE ON SUSTAINABILITY IN PROCESS INDUSTRY

### OCTOBER 19-20th, 2016

## DEPARTMENT OF CHEMICAL ENGINEERING

## UNIVERSITY OF ENGINEERING AND TECHNOLOGY, PESHAWAR

# EDITORIAL BOARD

## ORGANIZING COMMITTEE

### Patron-in-Chief

Prof. Dr. Iftikhar Hussain

Vice Chancellor, UET Peshawar

### Conference Advisor

Prof. Dr. Noor Muhammad Khan

Dean, Faculty of Engineering, UET Peshawar

### Conference Chair

Dr. Mohammad Younas

Chairman, Department of Chemical Engineering

### Conference Co-Chair

Dr. Saeed Gul

Director ORIC/Associate Professor, Department of Chemical Engineering

### Conference Secretary

Engr. Amir Muhammad

Lecturer, Department of Chemical Engineering

### Protocol and Registration Committee

Dr. Nehar Ullah

Engr. Unsia Habib

Engr. Abdul Hai

Engr. Amjad Ali

Engr. Qazi Sohaib

## Media and Publications Committee

Dr. Muhammad Imran Ahmad

Dr. Asmat Ullah

Dr. Naseer Ahmed Khan

Engr. Qazi Sohaib

Engr. Amir Muhammad

## Boarding and Lodging Committee

Engr. Imran Khan Swati

Engr. Amad Ullah Khan

Engr. Wajid Ali

## Food and Entertainment Committee

Engr. Imran Khan Swati

Engr. Wajid Ali

Engr. Amir Naveed

Engr. Aimal Khan

Engr. Arshad Hussain

Engr. Syed Zakria Bacha

## Conference Hall and Stage Committee

Dr. Muddasar Habib

Engr. Amad Ullah Khan

Engr. Murtaza Khan

## SCIENTIFIC EXPERTS COMMITTEE

Prof. Dr. Naveed Ramzan (UET Lahore)

Prof. Dr. Zafar Noon (UET Lahore)

Prof. Dr. Mehmood Saleem (ICET PU Lahore)

Prof. Dr. Muhammad Tayyeb Javed (PIEAS Islamabad)

Prof. Dr. Shahid Raza Malik (NFC IEFR Faisalabad)

Prof. Dr. Sohail A Soomro (MUET Jamshoro)

Prof. Dr. Arshad Hussain (NUST Islamabad)

Prof. Dr. Suleman Tahir (University of Gujrat)

Dr. Asim Laeeq Khan (COMSATS CIIT Lahore)

Dr. Waqar Ali Khan (NFC IEFR Faisalabad)

Prof. Dr. Rizwan A. Gul (PCAS-E UET Peshawar)

Prof. Dr. Sahar Noor (UET Peshawar)

Prof. Dr. Siraj Ul Islam (UET Peshawar)

Prof. Dr. Daulat Khan (UET Peshawar)

Dr. Saeed Gul (UET Peshawar)

Dr. Afzal Khan (UET Peshawar)

Dr. Gul Muhammad Khan (UET Peshawar)

Dr. Mohammad Younas (UET Peshawar)

Dr. Farid Ullah (UET Peshawar)

# PREFACE

Sustainability means "to maintain or endure." According to the work of the UN Brundtl and Commission, sustainability in the context of development is to "meet the needs of the present without compromising the ability of future generations to meet their own needs". Sustainability in process industries is globally known since last few decades. Sustainable development contains social, cultural, environmental and economic aspects.

Pakistan is facing various problems and energy is one of the main issues today. There are many reasons behind energy crisis in Pakistan, inefficient processes are one of the major factors amongst them. It is high time to address sustainability, link it to the process industries, and to contribute to sustainable development in order to overcome the energy crisis in Pakistan.

The Chemical Engineering Department of University of Engineering and Technology, Peshawar plays a vital role in research areas of national interest. Our faculty is actively involved in applied research at both national and international level.

The 1st conference on **"Sustainability in Process Industries (SPI-2012)**, held at UET, Peshawar on March 28, 2012, attracted prominent researchers from all over Pakistan which created a linkage and presented approaches for the application of sustainability in the process industry.

The Department of Chemical Engineering had again taken initiative to hold a 2nd conference on **"Sustainability in Process Industry(SPI-2014)"**, on May 22, 2014 in collaboration with PASTIC and NAYS. Continuing this tradition, the 3rd conference in this series, i.e. **"Sustainability in Process Industry (SPI 2016)"** October 19-20, 2016 is organized with the support of Higher Education Commission (HEC) in collaboration with PASTIC.

The mission of this conference is to identify new directions for research and development on **"Sustainability in Process Industry"** and share success stories regarding applied research and industrial case studies on R&D.

We hope that you will find this 3rd conference on **"Sustainability in Process Industry (SPI 2016)"** interesting and that the conference will provide you with a valuable opportunity to share ideas with other researchers and industrial practitioners.

Dr. Mohammad Younas
*Conference Chair*

Engr. Amir Muhammad
*Conference Secretary*

# ACKNOWLEDGEMENT

We first thank the authors for providing the content of the program in the form of oral and poster presentations and all other participants. We are also grateful to the keynote speakers from academia and various industries. These valuable talks can and will guide us to a better understanding of "Sustainability in Process Industry".

We also thank the host organization, UET, Peshawar, and our generous sponsors HEC, PASTIC, NAYS, Technology Links (Pvt) Ltd, Rizvi and Co. (Pvt) Ltd, and Meditron (Pvt) Ltd, without their support it would not be possible to hold this conference.

We are grateful to all organizers, who worked hard in order to make this conference successful.

# SPONSORS PROFILE

## ABOUT PASTIC

Pakistan Scientific and Technological Information Centre (PASTIC) formerly known as Pakistan National Scientific and Technical Documentation Centre (PANSDOC) was established under auspices of Pakistan Council of Scientific and Industrial Research (PCSIR) with the technical assistance of UNESCO. PANSDOC was later transferred to Pakistan Science Foundation, an autonomous organization of Ministry of Science & Technology and was renamed as Pakistan Scientific and Technological Information Centre (PASTIC). At present PASTIC is functioning under administrative control of Pakistan Science Foundation, Ministry of Science and Technology. PASTIC is the premier organization in the field of scientific and technological information dissemination serving thousand of researchers and R&D workers in the country. PASTIC mission to serve as a Gateway for S&T information for research and development community by catering to their information needs through its anticipatory and responsive scientific information services. PASTIC collects information from within the country as well as from abroad, processes and organizes the same and disseminate to its users. Major users of PASTIC services are S&T and R&D organizations, educational institutions, medical professionals, Govt departments and industry. PASTIC National Centre is housed in its own building at Quaid-i-Azam University Campus, Islamabad and its six Sub Centres are located at, Karachi, Lahore, Peshawar, Faisalabad, Quetta and Muzaffarabad (AJ&K). PASTIC is functioning under following aims and objectives.

- Acquisition, processing and dissemination of scientific & technological information to the researchers, scientists, academicians, R&D workers, industrialists, entrepreneurs etc.
- Provision of S&T documents and literature searching facilities, both On-line & Off-line.
- Development of inter-library cooperation and resource sharing at national level.
- Interaction and collaboration with regional and international information agencies / networks.
- Provision of trainings in contemporary techniques and methods of information handling & dissemination.

Compilation and publishing of reference information publications, such as Abstracting and Indexing Journals, Union Catalogue, Directories etc.

The information services and activities of PASTIC to meet the aims and objectives includes

Document Supply Service (Copies of full text articles)
Bibliographic Information Service/Literature Search
Technology/Patent Information Service
Abstracting and Indexing Service/Reference Information Publications
Reprographic Service

Trainings / Workshops
Information Dissemination through Media (TV)

PASTIC is striving for information support of S&T and R&D community of the country and playing its indirect role in the socio economic development of the country.

# ABOUT NAYS

-Faith, Knowledge, Dedication-
National Academy of Young Scientists (NAYS) Pakistan is a registered organization with Government of Pakistan under Societies Registration Act XXI, 1860. It was established in 2009 with the basic objective to promote and popularize science in Pakistan through collaborative effort of young researchers under the guidance of senior scientists.

Young researchers are always keen to play their role for development of the country but unfortunately no big platform was present for them at that time and for this we laid the foundation of NAYS® on 14 August 2009, presently we have more than 3500 registered member of NAYS. Among them, more than 200 young researchers are working as volunteer officials of NAYS,

Several projects have been started to promote science and help young scientists including include e-bulletin, e-newsletter, NAYS e-magazine, NAYS lecture series, Science for Youth, Community Education and Awareness Program, NAYS international Office, Mobility and Migration, Public Health Services, NAYS-Survey, Scientific Workshop series etc.

NAYS® is 5th in NYAs (National Young Academies) all over the world and now 19 have been established in a similar way. NAYS have organized number of workshops, trainings & Seminars for young researchers in various cities of Pakistan. NAYS®-Pakistan is trying to play its role by providing a platform and a place for networking among youth.

## Reference:
www.nays.com.pk
https://www.facebook.com/nayspakistan
http://www.linkedin.com/groups/National-Academy-Young-Scientists-Pakistan

**MEDITRON**
Trading Corporation
Sales Service & Training

SUPPLIER & DISTRIBUTORS OF MEDICINE &
ELECTRO MEDICAL EQUIPMENT

*Established in 1992, Meditron are the Supplier/Distributor of Electro Medical Equipment*
*Head Office*
*8, Al Syed Plaza, University Road, Peshawar, KP, Pakistan*
*Tel: 92-91-5841986; Fax: 92-91-5702951*
*Email: meditron@meditron-inst.com*

**TECHNOLOGY LINKS (PVT) LTD.**

*The company specializes in the supply, installation and maintenance of equipment in the fields of Education, Training, Research, Quality Control, Laboratory, Health, Environment & Pollution Control, and Material Testing.*

*Head Office (Karachi)*
*Technology Links (Pvt) Limited, 4-10/11, Rimpa Plaza, M. A. Jinnah Road, Karachi-Pakistan*
*Phone: +92-21-32734260- 61; Fax: +92-21-32730728*
*Email:* info@technologylinks.com.pk

# RIZVI & Company

*Head Office*
*B-24, Block-9, Gulshan-e-Iqbal*
*P. O. Box No. 17514,KARACHI-75300*
*Ph. (021) 34827124 – 34821116*
*Fax: (92-21) 34968626 – 34993570*
*E-mail: sales@rizviandco.com.pk*

# TABLE OF CONTENTS

# Electromagnetic based energy harvesting from gas flow in pipelines

*Farid Ullah Khan[1*], Shahzad Ahmad[1]*
*[1]Institute of Mechatronics Engineering, University of Engineering & Technology Peshawar*
*Email: dr_farid_khan@uetpeshawar.edu.pk*

## Abstract

In oil and gas producing countries where piping system is considered the most important infrastructure to transport oil and gas from one part of country to another. To protect these pipelines is one of the most important issues in safe transportation of these resources. Normally, to monitor these pipelines, wireless sensor nodes (WSNs) are employed over the whole length of the pipeline. However, using WSN has one serious problem of battery's life cycle which actually reduces the importance of WSNs in this application. This paper describes the fabrication and characterization of an electromagnetic flow energy harvester that is capable of producing power from the flowing gases in the pipeline. The reported harvested is composed of a tube in which a wound coil is produced. A spherical magnet which is placed freely in the tube actually levitates and rotates because of flowing gas in the harvester's tube, this relative motion between the magnet and coil resulted in the production of voltage in the device. The developed prototype is tested inside lab on different flow rates of air ranging from 0.70 lit/s to 1.03 lit/s. During experimentation the energy harvester showed the capability of generating a maximum power of 1456 µW and maximum rms voltage of 650 mV when connected to optimum load resistance of 290 ohms.

**Keywords**: Electromagnetic, Energy harvester, Gas flow, Pipeline monitoring, Random output, Wireless sensor nodes.

## 1    Introduction

Technology has wide and paramount role in industry and in our daily life. With the emergence of micro and nano fabrication techniques efficient, compact and cost-effective sensing and monitoring technology is developed and has been successfully utilized in applications, like, industrial process control and monitoring, health monitoring of buildings and bridges, monitoring of enemy movements, health care, weather forecasting, home automations and specially in sensing and monitoring of piping systems of oil and gas. Due to the rapid development the demand for energy has drastically increased. The world economy is now greatly dependent on the fossils fuel. The fossil fuel, specially petroleum and natural gas resources

and facilities are the most important assets of the world. For the economic progress of countries, the safety of these resources and facilities are very essential.

As piping system is one of the most important ways to safely and efficiently transport oil and natural gas from one place to another place. These pipelines are considered to be the important infrastructures of the oil and gas producing countries. The safety of these pipelines is regarded as the main concern as it directly affects the economic and development of these countries. To ensure the safe operation of the pipelines, the parameters of the flowing fluid, such as, pressure, temperature and flow rate of the fluid need to be continuously monitored throughout the length of the piping system.

There are a number of technologies used for pipeline sensing and monitoring, however, the utilization of wireless sensor nodes (WSNs) technology for the monitoring purposes is more preferred. The WSNs can consistently send the information about pipe status by quantifying inside or outside these pipelines. Inside measurement can be pressure, flow rate, concentration and temperature; however, the outside measurements are pipeline surrounding monitoring, weather status, pipe leakage and fire detection. The architecture for WSN mounted on pipeline is shown in figure 1.
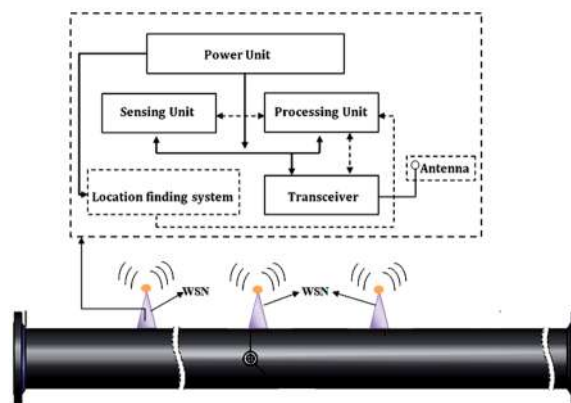


**Fig.1:** Architecture of wireless sensor nodes mounted for pipeline monitoring.

In figure 1, WSN composed of a sensing unit (sensor), processing unit, built-in memory, transmission unit and power unit. In WSN the power unit empowers all the onboard units; however, the sensing unit converts the physical parameters such as pressure, temperature or flow rate into electrical signals. The processing unit conditioned the electrical signals which are then transmitted by transceiver to the control room. The location finding unit tells the exact position of sensor that help in finding the exact location where the fault need to

**Table.1:** Commercial sensors utilized for pipeline monitoring.

| Sensor | Sensing type | Company | Model | Voltage (V) | Current (mA) | Power (mW) |
|---|---|---|---|---|---|---|
| **Pressure** | Electromagnetic | TECSIS | P3297 | 5 | 4 | 20 |
| | Piezoresistance | OMRON | 2smpp-02 | .002 | .1 | 0.0002 |
| | Capacitive | SENSATA | 70CP | 6 | 4 | 24 |
| | Infrared | MELIXIS | MLX90614Axx | 4.5 | 1 | 4.5 |
| **Temperature** | Thermopile | TEXAS instruments | tmp006 | 2.2 | 0.24 | 0.528 |
| | Digital | NXP | PCT2202 | 1.8 | 0.03 | 0.054 |
| | Electromagnetic | ONICON | F3500 | 20 | 250 | $5 \times 10^{-3}$ |
| **Flow** | Optical | PHOTONIC | FOCUS 2.0 | 24 | 150 | $3.6 \times 10^{-3}$ |
| | Thermal mass flow sensing | MEMSIC | MFA1100R | 2.7 | 0.07 | 0.189 |

be cured. Table 1 shows the list of low power commercially available pressure, temperature and flow sensors along with its voltage and power requirements. In the table 1, the power and current requirements of the sensors lies in the range of $3.6 \times 10^{-3}$ mW to 20 mW and 250 mA to 0.07 mA respectively. Due to small power requirement of these sensors the energy harvester has the capability to power these sensors or continuously charge their batteries to improve their lifecycle. Usually, the WSNs used for pipeline monitoring utilize battery as a power unit. Due to limited lifecycle of a battery, WSNs normally require maintenance in the form of battery recharging or replacement. However, the large number of WSNs which are mounted over a huge length of the pipe, this battery's recharging and replacement is not feasible. For the operation of WSNs a long lasting, alternative power source is actually the necessity. Energy harvesters are quite capable to be used as the alternative power units in WSNs. These energy harvesters can provide an alternative solution for energy source and the

most promising advantage being that these harvesters will continuously convert ambient available energies, such as, heat, vibration, solar, acoustic and thermal energy into useful electrical energy.

In order to produce energy from vibration or motion (mechanical energy), three transduction methods are piezoelectric method, electrostatic method and electromagnetic method. In piezoelectric transduction method electrical energy is produced by applying and releasing pressure or strain on piezoelectric material, whereas, through electrostatic method energy is produced due to the change in capacitance of a variable plate capacitor. However, with electromagnetic transduction method, energy is extracted by relatively moving a coil or a magnet or both with respect to each other. The relative motion between the coil and magnet causes change in magnetic flux over a coil and thus voltage is generated according to Faraday's law of electromagnetism. To produce power for the operation of WSNs mounted on a pipeline a considerable amount of research work has already been performed. Wang et

al. [1] developed a energy harvester having flexible diaphragm to which a permanent magnet was attached. When there is a flow across the diaphragm, it vibrates, resulted in the oscillation of magnet over a coil due to which voltage is generated across the coil's terminals. When the developed prototype is subjected to pressure amplitude of 0.3 kPa, a peak–to-peak voltage of 20 mV and power of 1.77 µW at 62 Hz frequency are reported. A piezoelectric type energy harvester for extracting the energy from the flowing fluids is developed in [2]. The produced prototype has the capability to generate the energy from the flowing water which continuously oscillates the piezoelectric material. The reported energy harvester generated an open circuit peak to peak voltage of 120 mV and an output power of 0.7 nW in response to a pressure amplitude of 0.3 kPa and frequency of 52 Hz. An energy harvester based on electromagnetic transduction method is reported by [3]. The harvester produced the electrical energy from fluid flow. The fabricated device consisted of a flow channel made from acrylic, flexible diaphragm (100 µm) to which a permanent magnet was attached and a coil. The developed device harvested an output peak to peak voltage of 20 mV when excited by pressure of 254 Pascal and a frequency of 30 Hz. Moreover, a power of 0.4 µW is also reported for the harvester under same conditions. An micro energy harvester [4] is developed for high pressure environment, normally greater than 200 kpa. The reported harvester is comprised of two flexible chambers. Which are interconnected by multiple channels on which different coils are wounded and train of magnet separated by spacer are free to move in these channels. As a result of an input pressure and displacement of 200kPa and 5mm respectively, the energy harvester generated an output power of 268.96 µW. A piezoelectric type flow energy harvester [5] is produced to generate power from flowing water. In the developed device a piezoelectric film is glowed to an acrylic flow channel. The reported harvester showed the capability of producing a peak to peak voltage of 72 mV and power of 0.45 nW when subjected to 20.8 kPa pressure and 45 Hz frequency.. An energy harvester is developed to produce energy from gas flow in pipelines [6]. The fabricated harvester has a piezoelectric material which converts gas flow energy into electrical energy. An output power generation of 20 mW is reported for the developed harvester. A turbine type energy harvester having size of 2 cm in diameter is developed in [7]. Developed prototype was fabricated using the traditional machining method, rapid prototyping and printed circuit board technique. When the developed harvester is tested at a wind speed of 10 m/s, it produced a maximum power of 4.3 mW.

In this work an electromagnetic energy harvester is developed to produce energy from the gas flow. Most of the previously reported flow energy harvesters need pulsating flow condition for working; however, the fabricated energy harvester does not require the pulsating flow for its operation. The working mechanism of the developed energy harvester is very simple and its power generation is dependent on the flow rate of gas through the pipeline. In the harvester the permanent magnet is not supported by any suspension structure (beams), rather the levitation and rotation of the magnet is utilized to generate the voltage in the coil of the harvester.

## 2   DEVICE ARCHETECTURE, WORKING PRINCIPLE AND FABRICATION

The developed energy harvester is composed of a spherical shaped permanent magnet and a wound coil as shown in figure 3. The architecture and working principle of the developed prototype is based on levitation and rotation of a spherical magnet in response to gas flow in a pipeline. The developed prototype has an inlet and outlet through which gas enter from main pipeline into the harvester and then returned to the main pipeline (through outlet). When there is a flow across the harvester it lifts and rotates a spherical shape permanent magnet (5 mm diameter) placed freely inside a cylindrical cavity made from polypropylene plastic. However, the wound coil of energy harvester is made through manual winding machine with a copper wire of 80 µm and properly insulated through epoxy resin. The photograph of the developed prototype is shown in figure 4. Due to rotation of magnet change in magnetic flux occurs inside wound coil made from a copper wire (80 µm diameter). The rate of change of magnetic flux at the coil induces a voltage according to Faraday's law of electromagnetism. In the device, the voltage generation depends on the orientation of the rotating magnet. Different orientation of the magnet with respect to a coil on which maximum, minimum or no voltage will be produced is shown in the figure 2. In the harvester, when the axis of the spherical magnet is perpendicular to the axis of the wound coil then maximum voltage will be produced, figure 2(a). However, moderate voltage generation is expected when the magnet's axis is partially inclined to the coil's axis, figure 2(b). The

harvester will produce absolutely no voltage when the magnet's axis is aligned to the coil's axis, figure 2(c)



**(a) Maximum Voltage**

**(b) Minimum Voltage**
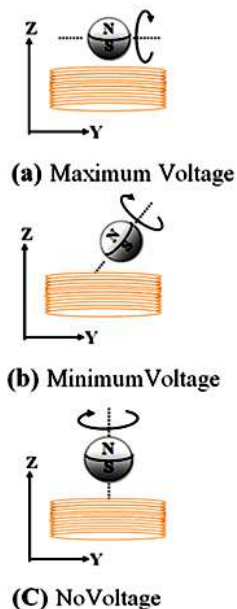
**(C) No Voltage**

**Fig.2:** Voltage output with respect to different orientation of magnet: (a) Maximum voltage generation, (b) moderate voltage generation, (c) No voltage generation.
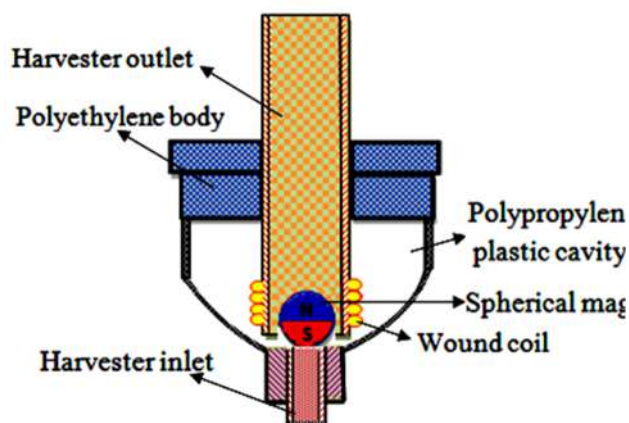


**Fig.3:** Cross section view of the developed energy harvester.
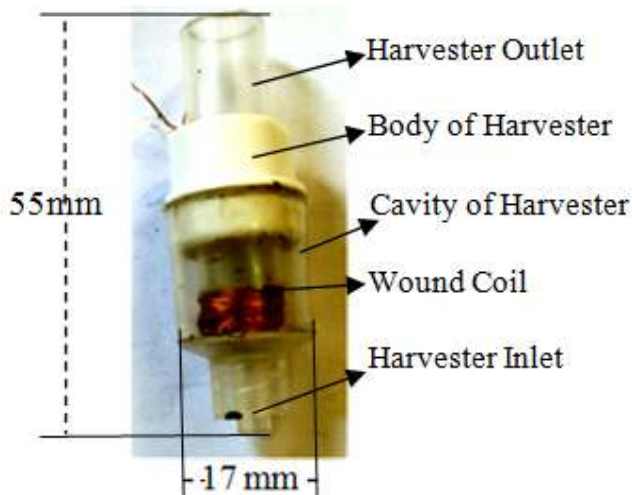


**Fig.4:** Assembled flow energy harvester

## 3  EXPERIMENTAL SETUP AND RESULTS

The block diagram of the setup used for the experimentation of the developed prototype is shown in figure 5; however, figure 6 shows the photograph of the devised experimental setup. The developed experimental setup is comprised of air blower, flow control valve, pipe, multi-meter and anemometer. The energy harvester is mounted in the by-pass air line. During experimentation the flow control valve is used to regulate the air flow inside the main pipe in order to perform experiments under different air flow rates, while, flow velocity of air is measured through anemometer. In order to monitor the output of the energy harvester, the developed prototype is connected to multi-meter.
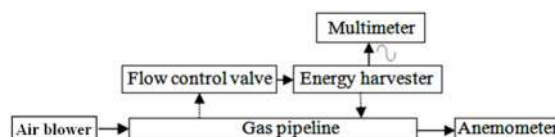


**Fig.5:** Block diagram of the experimental setup.
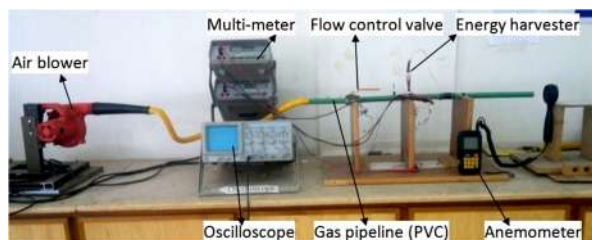
**Fig.6:** Photograph of the devised experimental setup.

Figure 7 shows the output load voltage produced by the energy harvester; however, the average load power of the energy harvester is shown in figure 8. From figure 7 it can be seen that increasing the load resistance led to increase the output voltage. During experimentation it was found that the device can generate a maximum load voltage and load power of 650 mV and 1420 µW respectively under a maximum air flow rate of 1.03 lit/s and an optimum load resistance of 290 Ω.
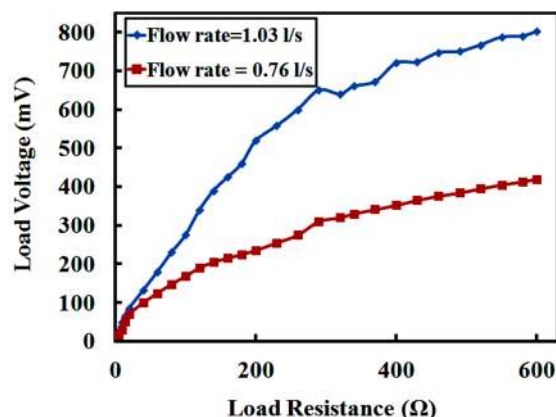


**Fig.7:** Load voltage produced as a function of load resistance at different air flow rates.

Figure 9 shows the electrical current generation as a function of load resistance. As seen in the figure by increasing the load resistance the output current from the device starts decreasing which is due to more resistance offered to the current.
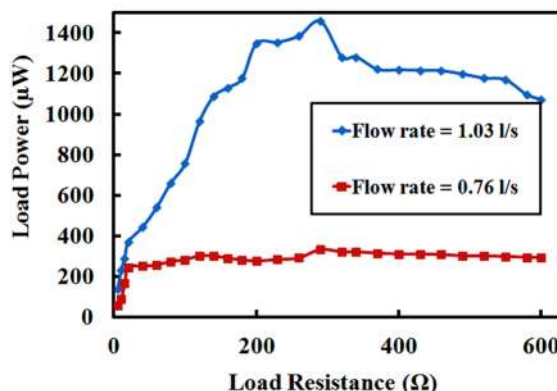


**Fig.8:** Load power as a function of load resistance at different air flow rates.
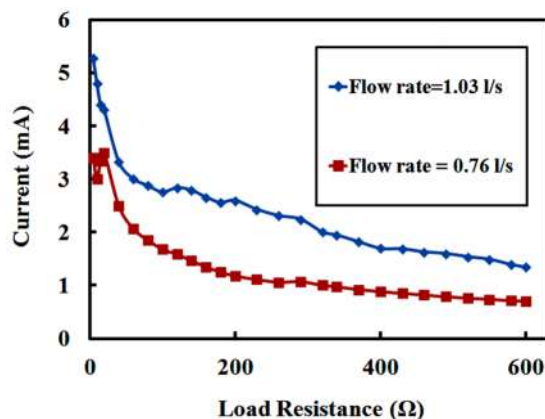


**Fig.9:** Load resistant Vs Current of device.

Figure 10 represents the randomness of the output of the developed energy harvester. To check the dependence of the harvester's output on the magnet's orientation, the device is subjected to air flow and instantly the open circuit voltage of the harvester is recorded. The data of 110 such experiments is plotted in figure 10 for a flow rate of 1.03 l/s. On most of the occasions the voltage generation is above 150 mV and a maximum of 1200 mV is produced only once. From the experimentation it is quite clear that the energy harvester is capable of generating an average voltage of about 600 mV.

Figure 11 shows that the output of the harvester is normally distributed with mean (average value) of 572.9 and standard deviation of 234.95. In figure 11, the horizontal line represent the open circuit voltage obtained during each experiment, however, while vertical line shows the normal distribution of the data,

The standard deviation of the normal distribution can be obtained with equation 1.

$$\sigma = \sqrt{\frac{1}{N}\sum_{i=1}^{N}(x_i - \mu)^2}$$

(1)

Where, $N$ is the total number of experiments, $x_i$ and $\mu$ represent the individual data and mean respectively.
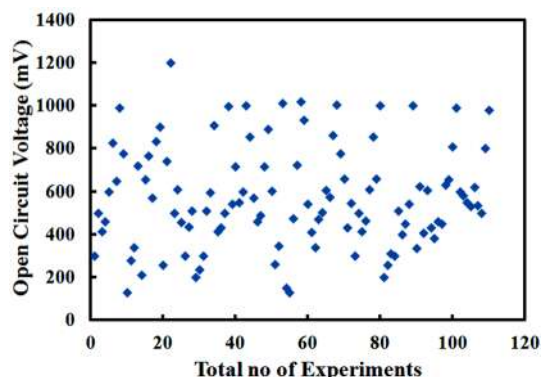


**Fig.10:** Instantaneous (random) voltage output of the harvester.
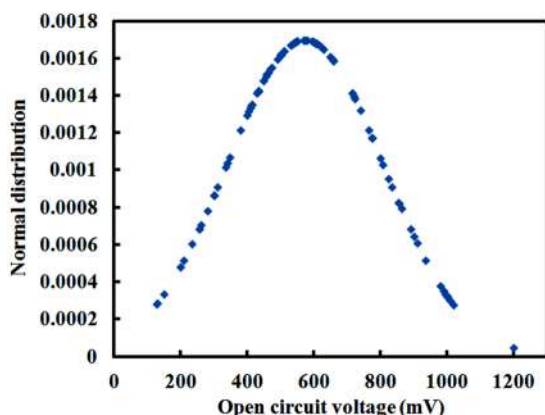


**Fig.11:** Normal distribution curve for the random output of the harvester.
**Table.2:** Comparison table of power and voltage of other energy harvesters.

| Pressure (Kpa) | Voltage (mV$_{pp}$) | Load.Power .(µW) | Ref. |
|---|---|---|---|
| 0.3 | 20 | 1.77 | [1] |
| 0.3 | 120 | 0.0007 | [2] |
| 200 | - | 268.96 | [4] |
| 0.254 | 20 | 0.4 | [3] |
| 0.070 | 14 | 0.00059 | [13] |
| 20.8 | 72 | 0.00045 | [5] |

Table 2 shows the voltage and power produced by the reported flow energy harvesters. The voltage and power of these harvesters lie in the range of 14 mV to120 mV and 0.45 nW to 268.96 µW. The harvester reported in this work showed the capability of producing 650 mV voltage and 1420 µW power, which comparatively to large than the voltage and power generation of the developed flow harvesters listed in table 2.

**Conclusion**

An electromagnetic gas flow energy harvester is reported for wireless sensor node (WSNs) application. The investigations on the developed harvester found that the device has the capability of producing an open circuit voltage of 1 V rms, moreover, when the harvester was tested for a mass flow rate of 1.03 l/s it generated a maximum output power 1456 µW and maximum load voltage of 650 mV when connected to 290 ohms load. Comparatively, the developed energy harvester is producing more voltage and power from the previously reported flow energy harvester and its out power are quite sufficient to operate the WSNs mounted on the pipelines for sensing and condition monitoring.

**References**

[1] D.A Wang, Chun-Yuan Chiu, Huy-Tuan Pham, Electromagnetic energy harvesting from vibrations induced by Karman Vortex Street, journal of intelligence mechatronics, (2012) 746-756.

[2] D-A Wang, Wang, D. A., Pham, H. T., Chao, C. W, & Chen, J. M. , A Piezoelectric Energy Harvester Based on Pressure Fluctuations in Karman Vortex Street, World renewable energy congress-Sweden (2011).

[3] D.-A. Wang and K.-H. Chang, "Electromagnetic energy harvesting from flow induced vibration," Microelectronics Journal, vol. 41, pp. 356-364, 2010.

[4] A. Bramhanand and H. Kim, "Micro Fluidic Energy harvesting system for high force and large deflection accommodation," Power MEMS 2011 Proc.—Seoul, 2011.

[5] D.-A. Wang and N.-Z. Liu, "A shear mode piezoelectric energy harvester based on a pressurized water flow," Sensors and Actuators A: Physical, vol. 167, pp. 449-458, 2011.

[6] H.J.Lee, S.Sherrit, L.P.Tosi, P.Walkemeyer, and T.Colonius,"Piezoelectric Energy Harvesting in Internal Fluid Flow,"Sensors, vol. 15, pp.26039-26062,2015.

[7] A. Bansal, D. Howey, and A. Holmes, "Cm-scale air turbine and generator for energy harvesting from low-speed flows," in Solid-State Sensors, Actuators and Microsystems Conference, 2009. TRANSDUCERS 2009. International, 2009, pp. 529-532.D.

[8] J.M.D.Coey.,"Permanent Magnet Applications"Journal of Magnetism and Magnetic Materials,Vol.248 pp. 441-456,2002.

[9] E.M.Purcell,Electricity and magnetism, 2nd EDITION, McGraw-Hill, Boston, US, 2004.

[10] "The World Factbook ". Retrieved 12/7/2016, 2016, from https://www.cia.gov/library/publications/the-world-factbook/fields/2117.html.

[11] C.C Federspiel, j. Chen,"Air powered sensors", in Proc.   IEEE Sensors 2033, Toronto, Canada, 22-24, Oct.2003, vol.1, pp.22-25.

[12] Xie, j; Hu, Y; Chen, X.A piezoelectric energy harvester based on flow-induced flexural vibration of circular cylinder. J. Intell. Master. Syst.Struct.2011.23.135-139.

[13] H.-D. T. Nguyen, H.-T. Pham, and D.-A. Wang, "A miniature pneumatic energy generator using Kármán vortex street," Journal of Wind Engineering and Industrial Aerodynamics, vol.116, pp.40-48, 2013.

# Comparing structural design of infilled frames with bare frame for Seismic Zone 2B.

*Fayyazur Rahman[1*], Qaisar Ali[1]*

[1]*Department of Civil Engineering, University of Engineering & Technology, Peshawar 25000, 1st Floor Earthquake*

*Engineering Centre*

[1*]*Corresponding author*

*Email: enginrfayyaz@gmail.com*

## Abstract

This paper presents an analytical work to study the effects of infill wall modeling on the design parameters i.e. fundamental time period, design base shear, maximum story drift and design reinforcement of a reinforced concrete building. Seven 3-D models of a nine story regular reinforced concrete frame, with different arrangements of infill walls, were analyzed and designed for Seismic Zone 2B in finite element software ETABS 2015 in accordance with UBC-97. Infill walls were modeled using single strut approach. The results showed that the fundamental time period of the building decreases with increase in the number of infill walls in a given direction and vice versa for the design base shear. Infill walls reduce the maximum story drift in all cases of infilled frames. Modeling infill walls reduce the flexure reinforcement in all cases of regular and irregular infilled frames, analyzed and designed through static lateral force procedure or response spectrum procedure and the reduction is proportional to the number of infill walls. It was also observed that bare frame analysis significantly underestimates the design reinforcement of soft story columns. Based on these observations, it is concluded that modeling infill walls is mandatory from the view point of both safety and economy.

**Keywords:** Time period, Base Shear,Drift, Reinforcement.

## Introduction

Reinforced concrete buildings with unreinforced masonry infill walls are commonly found in many regions around the world. It is customary to analyze and design these buildings without modeling infill walls. In reality, Infill walls contribute to the lateral strength and stiffness of the constituted buildings [1] and therefore must be considered in modeling. Two types of modeling techniques are currently used to represent infill walls in the analysis of infilled frame buildings. These are: (1) micro-modeling where bricks, bed joints, head joints and frame-infill interface are modeled discretely by using plane finite elements and (2) macro-modeling where infill panel is replaced by equivalent strut. Micro-models can simulate the behavior in great detail; however, they can't be used in the analysis and design of large structures due to the requirement of computational effort [2]. Macro-models like single strut, double strut and triple strut are computationally simple. Single strut model, though neglecting some aspects of infill-frame interaction, represent the global response of the infilled frames with reasonable accuracy [3].

Based on experimental tests on infilled steel frames, Holmes [4] proposed replacing infill panel by equivalent strut having width equal to one-third of the diagonal length. Subsequently, Stafford smith [5] proposed a relation for calculating the width of strut based on the stiffness of infill relative to the surrounding frame. To this end, Mainstone [6], Liaw and Kwan [7], Decanini and Fantin [8], Paulay and Priestley [9], Durrani and Luo [10], Cavaleri and Papia [11] presented alternative proposals. However, the relation proposed by Paulay and Priestley is simple and conservative useful for design applications.

Seven 3-D models of a nine story regular reinforced concrete frame, with different arrangements of infill walls, were analyzed and designed in finite element software ETABS 2015 in accordance with UBC-97. Infill walls are modeled using single strut proposed by Paulay and Priestley. The objective is to find the effects of infill wall modeling on the design parameters i.e. fundamental time period, design base shear, maximum story drift and design reinforcement of a reinforced concrete building.

**Method**

**Equivalent Strut Model of Infill Walls**

For analysis and design of large structures the most suitable numerical model to represent infill walls is single strut model as it is simple and predicts the global response of large buildings with reasonable accuracy [3]. The thickness of strut is taken equal to thickness of infill wall. There are many expressions given in the literature to determine the width of strut. However the simplest relation proposed by Paulay and Priestlay [9] have been used in this study, according to which the width of strut is equal to one-fourth of the diagonal length.
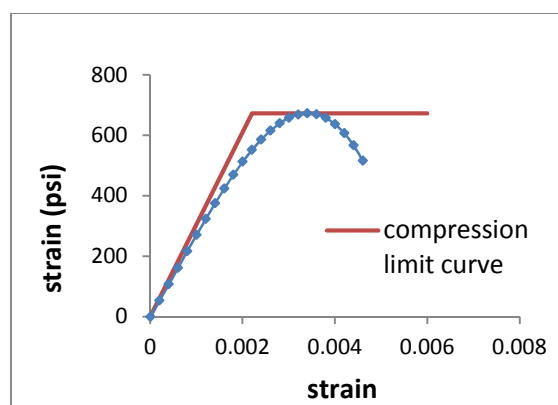


*Figure 1: compression limit model in FE software Etabs*

However, it is highly recommended that for design purposes, the typical properties of local masonry given in local codes and /or databases be used. Therefore the following material properties are used.

$f_m$ = 600 psi (Qaisar Ali, 2004)

$E_m$= 400x fm = 240 ksi (Qaisar Ali, 2004)

The material non linearity of strut is modeled usingtension/compression limit option in ETABS. The compressive force corresponding to the compressive strength of masonry is assigned to masonry strut as compression limit. A value of zero for tension limit is assigned to masonry strut as the strut resists only compressive forces. Once the compression limit in a strut is reached, the strut loss the ability to take increasing loads as shown in Figure 1.

**Analysis and Design by Means of Etabs Software**

ETABS is a sophisticated, yet easy to use, special purpose analysis and design software developed specifically for building systems. ETABS 2015 used in this study has several advantages over the previous versions including fast non linear analysis.

Two types of analysis are carried out as given in UBC-97 section 1630.2 and 1631.5 respectively which are Static lateral force procedure and Response spectrum analysis. Bare frame is analyzed using static lateral force procedure. Infilled frames are checked for vertical and horizontal irregularity according to UBC-97 Tables 16-L and 16-M, respectively. Irregular infilled frames are analyzed through response spectrum as well as static lateral force procedure. Regular infilled frame is analyzed through static lateral force procedure. Linear analysis is carried out on bare frame while non- linear analysis is performed on infilled frames. The bare frame and corresponding infilled frames are analyzed and designed for Zone 2B. The design output parameters i.e. base shear, time period, maximum story drift and reinforcement of infilled frames are compared with bare frame. The design input parameters and modelling techniques used in the software are tabulated below.

*Table 1: Material properties*

| | | | |
|---|---|---|---|
| **Material Properties** | **Concrete** | Compressive Strength (Psi) | 3000, 4500 |
| | | Elastic Modulus (Ksi) | 3122, 3800 |
| | **Masonry Infill** | Compressive Strength (Psi) | 600 |
| | | Elastic Modulus (Ksi) | 240 |
| | **Reinforcing Bar** | Yield Strength(Psi) | 60,000 |
| | | Elastic Modulus (Ksi) | 29,000 |

*Table 2: Earthquake **load parameters***

| | |
|---|---|
| Seismic Zone Factor | 0.2 |
| UBC-97 Soil Type | Type-D |
| Importance Factor | 1 |
| Response Modification Factor, R | 8.5 |
| Mass Source | Self-Weight +Super Imposed Dead Loads |

*Table 3: gravity loads*

| Super imposed Live load | 40 psf |
|---|---|
| Super imposed Dead load | 100 psf including weight of infill walls |
| Dead load | self weight of the structural members calculated automatically by the software |

*Table 4: Modeling elements*

| Beam and column | Line element (linear elastic) |
|---|---|
| Slab | Shell element (linear elastic) |
| Infill strut | Line element (Non linear) |

## Presentation of the Case Study

A nine storey reinforced concrete building having three bays, regular in plan and elevation, is considered for the case studies. The storey height and the bay length are 12ft and 20ft respectively. The building is analyzed and designed as bare frame without modeling infill walls. The sizes of structural members with given material properties, are selected as the minimum sizes which fulfill all the design requirements. Infill walls are then added only at the perimeter of the same building with different arrangements. Fully infilled frame contain infill walls in all storeys, infilled frame 1 has no infill walls in bottom storey, and infilled frame 2 has no infill walls in storey 4 and story 5. Infilled frame 3 has no infill walls in storey 4 and story 5 along X direction, however, it has no infill walls in grid A frame and fully infilled at grid D frame to incorporate horizontal irregularity along Y direction. As the design of slab is governed by gravity loads only, the design reinforcement of slab is same for bare frame and infilled frames. Similarly the shear reinforcement in beams and columns is provided according to the SMRF requirement which is also same for both infilled frame and bare frame buildings. Therefore, the flexure reinforcement in beams and columns of infilled frames has been compared with corresponding bare frame.

## Results

### Time period

As the infill struts increase the lateral stiffness of the building therefore the time period in all cases of infilled frames is lower than the corresponding bare frame.

Additionally, the time period is inversely proportional to the number of infill walls as can be seen in Figure 2, therefore, the time period of fully infilled frame is smaller than all the partially infilled frames.
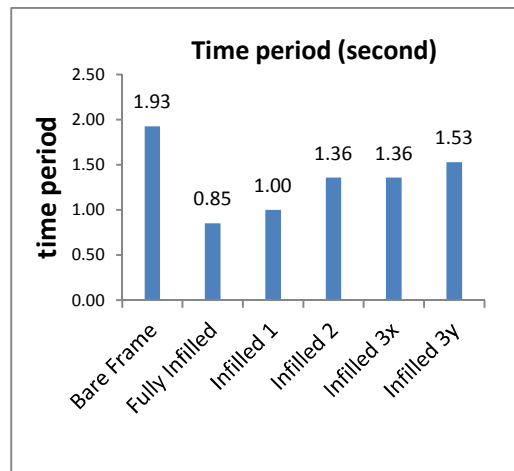


*Figure 2: Time period comparison*

### Base shear

Since the base shear is inversely proportional to the time period as given in UBC-97 1630.2.2, therefore, the base shear of fully infilled frame, for which the time period is the smallest, is larger than all the other frames. Though the fundamental time period of the bare frame is smaller than infilled 3 in Y direction, the base shear is same for both of the frames as illustrated in Figure 3. It is because the fundamental time period of both frames exceeds 40 percent of the time period calculated by method-A. Hence the design time period calculated by software is 1.4 times the time period calculated by method-A which is same for both frames.
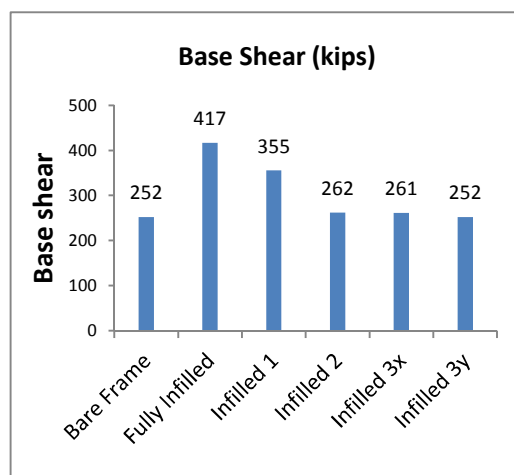


*Figure 3: Base shear comparison*

**Maximum story drift**

Story drift is significantly reduced in case of fully infilled frame due to the increased lateral stiffness by infill walls. Since the drift ratio of a story depends on its stiffness relative to the storey above and below; therefore, ignoring infill walls in the design may underestimate the maximum story drift of a building. This is illustrated in Figure 4 for Infilled 2 and Infilled 3x cases.
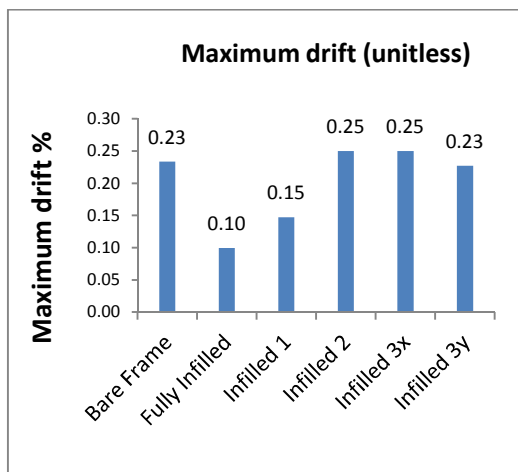


*Figure 4: Maximum story drift comparison*

**Beam flexure reinforcement**

Modeling infill walls reduce the beam flexure reinforcement in all cases of regular and irregular infilled frames, analyzed and designed through static lateral force procedure or response spectrum method as clear from Figure 5. The reason is that infill walls reduce the story drifts, which reduce the negative bending moments at ends of beams, resulting in smaller values of negative reinforcement. Since negative reinforcement is usually the maximum reinforcement in a beam of moment resisting frame, therefore, smaller values of negative reinforcement in turn reduce bottom flexure reinforcement at ends of beams and top flexure reinforcement at mid span of beams owing to SMRF requirements. **Column flexure reinforcement**

Figure 6 shows that the column flexure reinforcement depends highly on severity of irregularity as well as type of analysis used for the design i.e. static lateral force method or response spectrum method as can be observed for infilled 2 and infilled 3 cases. The reason is that irregular arrangement of infill walls may excite higher modes which can't be captured well in static lateral force procedure. Although the column flexure reinforcement

in bare frame and infilled 3-RS is almost the same as shown in Figure 3, however, considering infill walls in the model and analyzing it through response spectrum method will ensure the reinforcement to be placed in columns where it is required.

**Total flexure reinforcement**

It is clear from Figure 7 that total flexure reinforcement in beams and columns of infilled frames is less than the corresponding bare frame. Also the total flexure reinforcement in the infilled frames increases with decrease in number of infill walls. Additionally, infilled frame 2 and infilled frame 3 analyzed through response spectrum procedure are having higher values of reinforcement than the same analyzed through static lateral procedure.
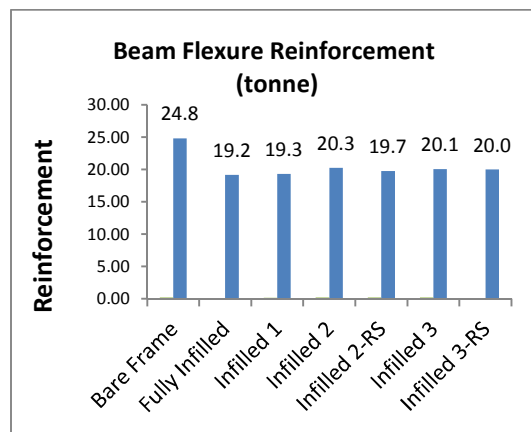


*Figure 5: flexure reinforcement in beams*
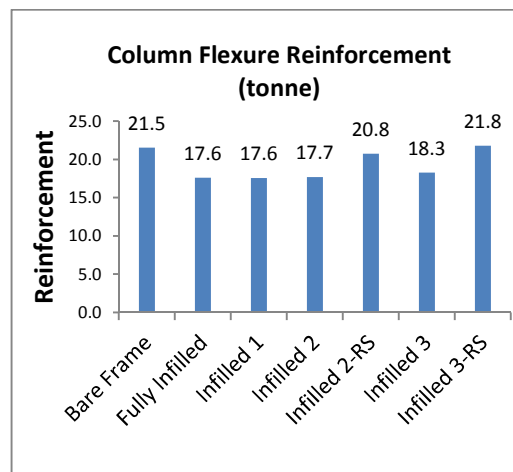


*Figure 6: flexure reinforcement in columns*
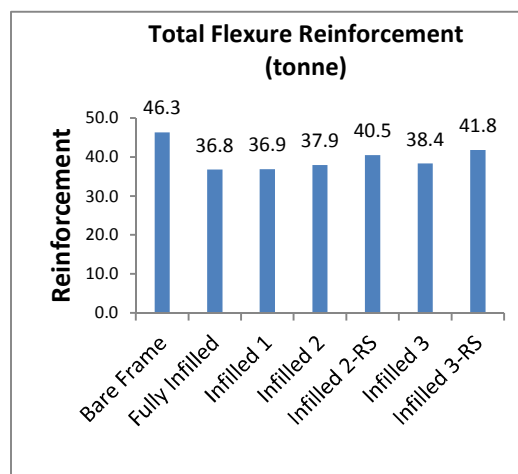
*Figure 7: Total flexure reinforcement in beams*

## Conclusions

Infill walls increase the lateral stiffness of the infilled frames, thus reducing the fundamental time period, decreasing the story drifts and increasing the base shear. However, higher values of story drifts may result in soft storeys.

Modeling infill walls economize the overall reinforcement irrespective of irregular arrangement. Additionally it will make sure the reinforcement to be placed in columns where it is required as bare frame analysis underestimates the reinforcement of soft story columns.

Irregular frames analyzed through response spectrum procedure results in higher values of reinforcement than corresponding frames analyzed through static lateral force procedure.

Based on the above results it is concluded that modeling infill is necessary from the viewpoint of both safety and economy.

## References

[1] Liaw TC, Kwan KH. Nonlinear behavior of non-integral infilled frames. Comput. Struct. 18, 551-560, 1984.

[2] Kaushik HB, Rai D, Jain SK. A Rational Approach to Analytical Modeling of Masonry Infills in Reinforced Concrete Frame Buildings. Proceedings of the 14th World Conference on Earthquake Engineering, Beijing, China, 2007.

[3] Asteris PG. Finite Element Micro-Modeling of Infilled frames. Electronic Journal of Structural Engineering, 2008

[4] Holmes M. Steel frames with brickwork and concrete infilling. Proceedings of the Institution of Civil Engineers 19, 1961.

[5] Stafford Smith B. Behaviour of Square Infilled Frames. Proceedings of the American Society of Civil Engineers, Journal of Structural Division, 92, no STI, 381-403, 1966.

[6] Mainstone RJ. On the Stiffness and strength of infilled frames. Proc. Supplement, Trans. of Instn. Of Civil Engrs, State Univ. of New York, 1974.

[7] Liaw TC, Kwan KH. Non-linear analysis of multistory infilled frames. Proceedings of the Institution of Civil Engineers, Vol 73(2), pp 441-454, 1982.

[8] Decanini LD, Fantin GE. Modelos simplificados de la mamposteria incluida en porticos. Caracteristicas de rigidez y resistencia lateral en estado limite. Jornadas Argentinas de Ingenieria Estructural, Buenos Aires, Argentina, Vol.2, pp.817-836, 1986.

[9] Paulay T, Priestley MJN. Seismic Design of Reinforced Concrete and Masonry Buildings. John Wiley & Sons, New York, 1992.

[10] Durrani AJ, Luo YH. Seismic Retrofit of Flat-slab Buildings with Masonry Infills. NCEER workshop on seismic response in Masonry Infills, 1994.

[11] Cavaleri L, Papia M. A new dynamic identification technique: application to the evaluation of the equivalent strut for infilled frames. Engineering Structures 25, 889-901, 2003 http://www.sciencedirect.

# Experimental Study of Separation of Carbon Dioxide from Natural Gas Using Hollow Fiber Membrane Contactor

**Aimal Khan\*, Amir Muhammad, Mohammad Younas, Imran Khan Swati**

*Department of Chemical Engineering, University of Engineering and Technology, Peshawar, P.O. Box 814, University Campus, Peshawar 25120, Pakistan*

\*Corresponding author: engr_aimalkhan@uetpeshawar.edu.pk

## ABSTRACT

In present research a mini module of hollow fiber membrane contactor (HFMC) made of polypropylene has been used to remove $CO_2$ from $CH_4$ with alkanolamine solutions (MEA, DEA) and water. Gas mixture was allowed to flow in the shell side of contactor while liquid absorbents flown in tube side. Experiments revealed that MEA was more efficient in $CO_2$ removal. Concentration of absorbent solutions was also studied and it was found that increasing concentration increases the removal efficiency. From the results we found that removal efficiency exceeded 87 % for 0.6 molar MEA. However, it was observed that a higher concentration may lead to the unwanted membrane wetting which greatly reduces the mass transfer across membrane. Experiments were also performed to check the effects of feed and absorbent flowrates on absorption. Efficiency was reduced with increasing feed flowrate while absorbent flowrate was found to have an opposite effect. Pilot plant tests revealed that the HFMC has a great potential in the area of $CO_2$ separation from natural gas when absorbent's concentration and trans-membrane pressure are selected carefully.

**Keywords:** Natural gas; membrane gas separation; hollow fiber membrane contactors.

## 1. INTRODUCTION

Natural gas, the fossil fuel widely used both for domestic and industrial application is contaminated with $CO_2$ and other impurities during exploration. The presence of $CO_2$ in natural gas significantly reduces its heating value. It also causes the corrosion of gas transportation pipelines.Thus the amount of $CO_2$ must be lowered to less than 2% before using natural gas. The percentage of $CO_2$ in environment is also increased after burning of natural gas. Carbondiaoxide, the major component of greenhouse gases has greatly affected the global temperature andis considered as a big threat to planet.

Conventionally absorption column were used for natural gas purification [1]. These units suffer from common problems like flooding, channelling & unloading and high capital and operating costs. Membrane technology in the form dense polymeric membrane has been tested for gas separation [2-4]. However, permeability-selectivity trade off makes its commercial application difficult and costly. A new hybrid membrane gas absorption technology has attracted the attention of researchers in recent decades. This technology combines the advantages of conventional chemical absorption and membrane separation. This technique uses hollow fiber membrane contactor (HFMCs), devices that achieve the gas liquid absorption without the phase dispersion. The most common advantages of HFMCs are, there is no occurrence of flooding, channelling and unloading, the interfacial area between phases remains the same during operation, several times higher mass transfer area and less capital and operating costs as compared to conventional chemical absorption systems. Because of these advantage HFMCs have attracted a number of researchers towards itself for the removal of gas solutes [5-7]. HFMCs modules configuration resembles to shell and tube heat exchanger where hollow fibres are installed in a shell. Gas is normally allowed to pass through shell side while the liquid is passed through tube side of the membrane contactor. For achieving better mass transfer both streams flow counter-currently [8].

In the current research work removal of $CO_2$ from natural gas is investigated through HFMCs. The gaseous mixture is composed of 90% natural gas and 10% $CO_2$. Different absorbents like MEA, DEA, with various concentrations are used for the absorption of $CO_2$. The concentration of absorbents were carefully monitored as increasing absorbents concentration causes membrane wetting, which leads to a lower separating efficiency. The parameters investigated in current research work are the effects of liquid absorbent flowrate, absorbent concentration and gaseous mixture flowrate on contactor efficiency. The efficiency of absorbents was also compared under same conditions.

## 2. MATERIALS & METHODS

The experimental setup is shown in Figure 1. The gases from the two gas cylinders of $CH_4$ and $CO_2$ were allowed to mix for the preparation of gaseous mixture (90% of $CH_4$ and 10 % of $CO_2$). Mixture composition was controlled through gasflowmeters. After mixing the gaseous mixture was passed though tube side of the HFMCs. While from the opposite side the liquid absorbent was pumped into the shell side. The liquid flowrate was controlled through liquid flowmeter. A slightly higher pressure was applied to tube side in order to prevent the dispersion of liquid absorbent in gaseous phase. The two streams thus contacted through the pores of membrane where $CO_2$ was transferred from the gaseous stream to the liquid absorbent. The rich absorbent was then collected in the absorbent tank while the treated sampleswere collected and analysed for $CO_2$ using Gas Chromatography.

Sets of experiments were performed to study the effect of different parameters on $CO_2$ removal

The following parameterswere studied in current research work were;

- Concentration of absorbents
- Gaseous mixture flowrate
- Absorbent flowrate

These parameters were varied for each type of absorbent and removal efficiency was evaluated.
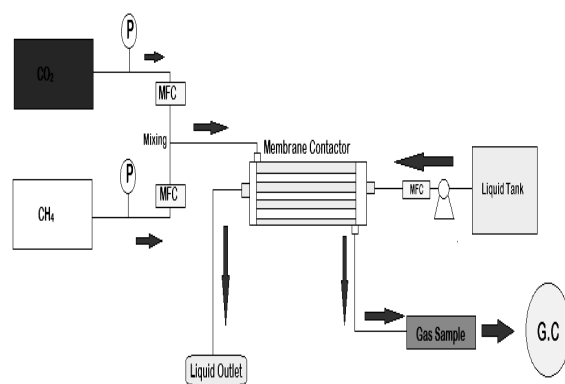


Figure 1. Schematic for removal of $CO_2$ from natural gas in HFMCs

## 3. RESULTS & DISCUSSIONS

### 3.1 Effect of absorbent flowrate on $CO_2$ removal efficiency

The effect of the absorbent flowrate is shown in the Figure 2. While studying this effectthe concentration of absorbents was kept 0.4M for MEA and NaOH. Absorbents used were MEA, NaOH and distilledwater. The flowrate of gaseous mixture was constant at 100ml/min, while that of absorbent was varied up to 800 ml/min. As shown in Figure, $CO_2$ removal efficiency was increased with increase in liquid flowrate. Maximum efficiency was achieved in case of MEA where it has reached to 81% for a flowrate of 800 ml/min. In case of distilledwater the maximum efficiency achievedwas 43%. In fact increasing the liquid flowrate rapidly provide the fresh surfaces by removing already extracted $CO_2$. Thus concentration gradient increases which results in transfer of more and more $CO_2$ from gas to absorbent side.
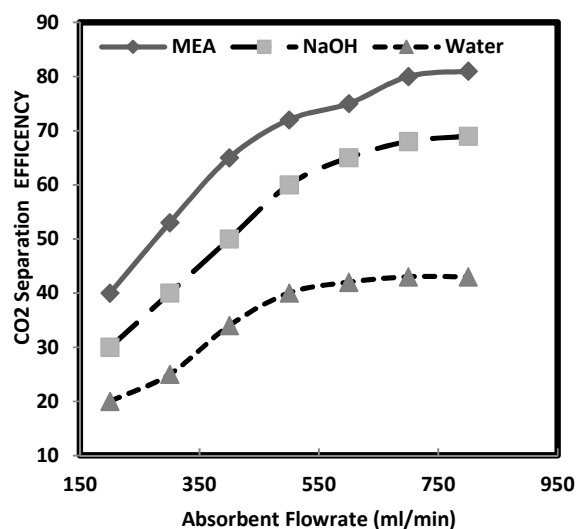


Figure 2. Effect of absorbent flowrate on $CO_2$ removal efficiency

The $CO_2$ removal efficiency was calculated using following equation.

$$\eta = (Q_{in} * C_{in}) - (Q_{out} * C_{out}) / (Q_{in} * C_{in})$$
$$(1)$$

here $\eta$ denotes the separating efficiency, $Q_{in}$ (ml/min) & $Q_{out}$ (ml/min) denote the gas inlet & outlet

flowrates respectively and $C_{in}$, $C_{out}$ denote the inlet and outlet $CO_2$ concentration.

### 3.2 Effect of gaseous mixture flowrate on $CO_2$ removal efficiency

The influence of the gaseous flowrate on $CO_2$ removal efficiency is shown in Figure 3. The concentration and flowrate of absorbent were kept constant at 0.4M and 400ml.min respectively. The gaseous mixture flowrate was varied between 50 ml/min and160ml/min. High flowrate decreased the removal efficiency. This is because of the fact increasing the gaseous mixture flowrate decreases the residence time of $CO_2$ in the membrane contactor which results in less $CO_2$ removal. The removal efficiency in case of water is very low as compared to MEA and NaOH which is because of it comparatively less affinity for $CO_2$.
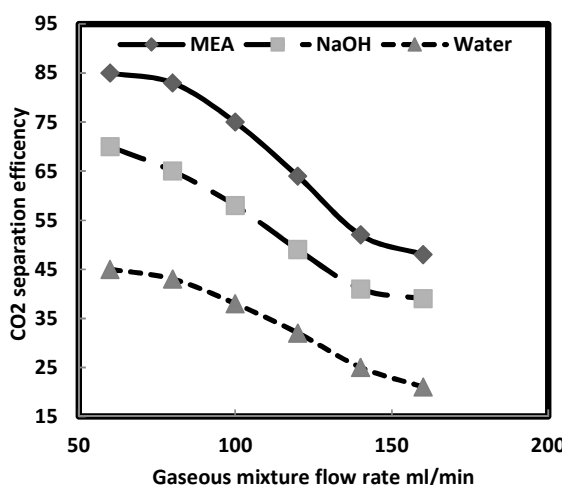


Figure 3. Effect of gas flowrate on removal efficiency

### 3.3 Effect of solvent concentration on $CO_2$ removal efficiency

Theeffect of absorbents concentration on the $CO_2$ removal efficiency is given in figure 4. The concentration of MEA &NaOH was varied from 0.1mol/L to 1mol/L. absorbent concentration showed an irregular effect towards separation efficiency, first the separation efficiency increased with increasing concentration and after reaching a certain limit i.e. 0.6M in case of MEA and 0.7M for NaOH, the separation efficiency decreased. This decrease is because of the surface tension of absorbent concentration which according to Laplace equation decreases with increase in absorbent concentration. The absorption efficiency of MEA

was greater than that of NaOH and this is because of the high reacting rate of MEA with $CO_2$. One point must be kept in mind that for membrane contactors the absorbent concentration must be carefully selected as increasing the concentration leads to membrane wetting which significantly reduces the separating efficiency. Therefor a trade-off should be developed between the absorbent concentration and membrane wetting for better removal of $CO_2$ solute.
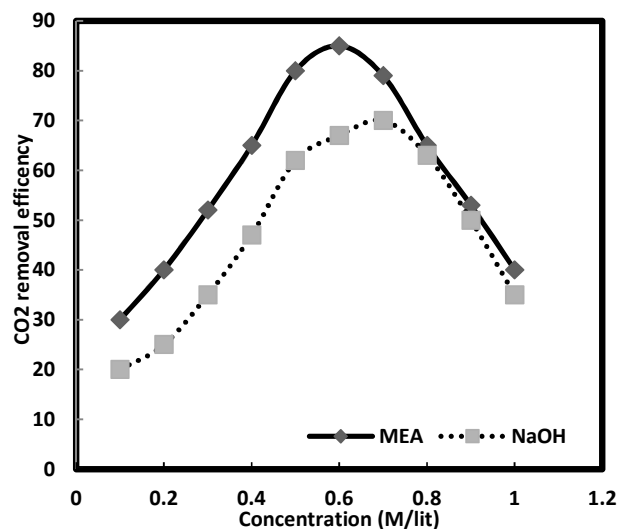


Figure 4. Effect of solvent concentration on $CO_2$ removal efficiency

### 4. Conclusion

The experiments in this research work were performed through hollow fiber membrane contactor made of polypropylene. While the absorbent used for $CO_2$ removal were MEA, NaOH& water. Different set of experiments were performed for studying the effect of different parameters on absorption. These include absorbent concentration, gaseous mixture and absorbent flowrates. The results showed that the $CO_2$ removal efficiency was increased with increasing the solvent concentration & absorbent flowrate while decreased with increasing gaseous mixture flowrate. Although solvent concentration increasethe removal efficiency however, it must not cross a certain limit as it will then cause membrane wetting.

### 5. Acknowledgement

**6. References:**

[1] Gabelman, A., Hwang, S., (1999) 'Hollow Fiber Membrane Contactors' *J. Membr. Sci.* Vol. **159**, 61-106.

**[2]** Husain, S., Koros, W.J, (2007) 'Mixed matrix HFM made with modified HSSZ-13 zeolite PEI polymer matrix for gas separation' *J. Membr. Sci*. Vol. **288,** 195-207.

[3] Li, K., Teo, W.K. (1998) 'Use of permeation & absorption method for $CO_2$ removal in hollow fiber membrane modules' *Sep. Puri. Technol*. Vol. **13**, 79-88.

[4] Park, H. B., Han, S. H., Jung, C. H., Lee, Y. M. & Hill, A. J. Thermally rearranged (TR) polymer membranes for $CO_2$ separation. *J. Memb. Sci.* 359, 11–24 (2010).

**[5]** <u>Powell</u>, C.E., Qiao, G.G., (2006) 'Polymeric $CO_2/N_2$ gas separation membranes for the capture of carbon dioxide from power plant flue gases' *J. Membr. Sci.*, Vol. **279,** 1-49.

[6] Robeson, L.M., (2008) 'The upper bound revisited' *J. Membr. Sci*., Vol. 320, 390-400.

[7] Sun, X., Meng, F., Yang, F., (2008) 'Application of seawater to enhance $SO_2$ removal from simulated flue gas through hollow fiber membrane contactor' *J. Memb. Sci.* Vol. **312**,6-14.

[8] Yeh, J.T, Pennline, H.W. (2001) 'Study of $CO_2$ absorption and desorption in a packed column' J. *Energy Fuels*, Vol. **15**(2), 274-278.

# Numerical Simulation of Co₂ Removal from Natural Gas in Hollow Fiber Membrane Contactor

*Amjad Ali [1,*], Amir Muhammad [1], Mohammad Younas [1]*

[1] *Department of Chemical Engineering, University of Engineering and Technology, Peshawar, Pakistan*

[*]*Corresponding author*

*Email: amjadali393@gmail.com*

## Abstract

CO₂ is a main unwanted component in raw natural gas decreasing its heat value, increasing gas transportation cost and also corrode the process equipment. CO₂ separation from raw natural gas is needed before its use as a fuel or for any other purpose i.e. as a raw material in some process industry. The separation techniques available for the purpose are absorption, adsorption and separation using membrane technology. Dispersive separation of gaseous mixture through traditional separation equipment like spray towers, packed columns etc., cause several problems like emulsion, unloading, entrainment etc. These problems may be eliminated by utilization of hollow fiber membrane contactors (HFMC) by keeping a non-dispersive contact (NDC) between gaseous and liquid phases and also make available a higher interfacial between two phases. The modeling and simulation for mass transfer in such types of NDC contacting devices provide understanding of the process and linear scaling up of such separators in a simple and cheap way comparing to experimentation in a laboratory. In the work presented in this paper, a 2-D comprehensive mathematical model has been developed for CO₂ absorption in distilled water utilizing HFMC as a separating device. A set containing mathematical equations has been developed by considering a steady state mass transfer by convection-diffusion in tube of HFMC, diffusion in membrane and convection-diffusion in flow cell of HFMC by taking the gas and liquid flowing in opposite direction to each other. The developed model has been simulated by COMSOL Multiphysics computer software through CFD techniques. The concentration profile in all sections of HFMC i.e. tube, membrane and shell, velocity profile, separating efficiency, structure parameters regarding HFMC like porosity-tortuosity with operation regarding parameters i.e. temperature have been studied for the purpose of finding the effects of these parameters over separation in a comprehensive way. The results obtained showed that the separation process through non-dispersive HFMC is an easy and cheap way for CO₂ separation from raw natural gas.

**Key words**: CO₂ removal, CFD, Natural gas up gradation, Hollow fiber membrane contactors, Mathematical Modeling, Simulation.

## 1. Introduction

Industrial activities have caused an increase in the amount of greenhouse gases in atmosphere which is one of the major reasons for environment regarding problems like global warming [1]. Using fossil fuels as a heat source like coal, CH₄, furnace oil etc. in industrial sector contributes to CO₂ emission by 50% and then CO₂ amount in atmosphere contributes to greenhouse gases by 80% [2]. CO₂ is a major impurity in natural gas and reduces its energy efficiency by lowering its heat value, increases the compression and transportation cost. Because of all these problems, CO₂ removal from natural gas is very important, necessary and a need of the day. Using it, as a fuel causes an increase in greenhouse gases amount in atmosphere which causes environmental issues [3]. Some conventional separation towers and columns are used for gas/liquid absorption purposes but the main challenge in designing of such columns is to provide the maximum interfacial contact area between gas and liquid phases. A lot of problems are also faced during the operation of such traditional separation towers including unloading, entrainment, emulsion etc.

A novel technique has been introduced by researchers in order to overcome these issues. This novel technique is to provide the non-dispersive gas-liquid contact through non-selective membrane. Membrane has no selectivity for the component to be separated and this just a physical barrier between the phases. The membrane in this process may be hydrophobic or hydrophilic. In case of hydrophobic membrane, the

membrane openings filled of gas and the $CO_2$ transfer occurs due to diffusion across the membrane pores. This approach has many advantages over the conventional absorbers. As the contact is non-dispersive, so both the fluids may be controlled independently and no loading or unloading of the unit occurs during operation of the unit. The interfacial area is much larger than conventional techniques and fluids of same density can be separated. The scale up of the plant is linear and it can be operated on higher or lower production capacities by adding or removing the modules.

The novel technological approach of using hollow fiber membrane contactor as a separator for gaseous mixtures have attracted the researchers more as compared to old traditional technologies [3,4]. HFMC device consists of two parts of tube and shell. Both phases flow in parallel or anti-parallel direction to each other and form a liquid-gas interface on the absorbent side as the membrane pores have been filled by gas phase [5]. The membrane material has no selectivity for the component to be separated and a better efficiency is obtained as the equilibrium limits are eliminated [6]. The partition coefficient has been affected by mass transfer occurring through diffusion [7]. Concentration gradient is the only responsible deriving force for mass transport and pressure gradient has no role in mass transport but a little bit pressure gradients is needed for a stagnant gas-liquid interface at the pore mouth on the absorbent side. A lot of hydrophobic membranes are applied for CO2 separation i.e. polytetrafluoroethylene and polypropylene with the most suitable alkanolamines. Several researchers have applied the CFD techniques to the CO2 removal through HFMC.

Al-Marzouqi et al. [8] worked on simulation of carbon dioxide separation in HFMC using CFD methods considering water as an absorbent for CH4-CO2 mixture. A 2-D model basing upon non-wetting mode for $CO_2$ transport in HFMC has been established. Model was simulated by COMSOL Multiphysics. They indicated that a change in concentration in cross section of tube and membrane is small and a fast decline is observed in flow-cell due to less resistance to diffusion of $CO_2$ in gas media in lumen and membrane pores. It was shown that with increase of gas flow rate, separation rate decreases due to less residence time but absorbent flow rate has direct relation with removal efficiency due to fresh absorbent

availability. Model has been validated literature available. Shirazian et al. [9] carried out research work upon $CO_2$ separation from CH4 by absorbing in water through development of mathematical model and investigated that with increase in absorbent flow rate; separation rate increases and has a reverse effect with gaseous phase flow rate. Rezakazemi et al. [10] published a study based upon experimentation and theory regarding $CO_2$ and hydrogen sulphide separation from natural gas by HFMC device using MDEA absorbent and conducted simulation of a model. Module has been found very efficient as 96% of hydrogen sulphide separation was gained.

All CFD research gives a detail of the HFMC for $CO_2$ absorption in absorbent. Operational parameter i.e. flow rate, temperature and pressure can be determined. The work presented in this paper regards model developing based upon equations of conservation for $CO_2$ separation from $CO_2/CH_4$ gaseous mixture followed by simulating the model through COMSOL, by the powerful tools of CFD methods. The model may be used considering high flow rates of fluids as the only purpose of a technology is to be applied commercially.

## 2. Model development

Material balance was carried out for sub domains of the module as given in Figure 1.

### 2.1 Shell side

Applying steady state material balance on tube, assuming tube of cylindrical shape, following relation is derived for transport of CO2 in tube.

$$D_{CO2-tube} \left[ \frac{\partial^2 C_{CO2-tube}}{\partial r^2} + \frac{1}{r} \frac{\partial C_{CO2-tube}}{\partial r} + \frac{\partial^2 C_{CO2-tube}}{\partial z^2} \right] = u_{z-tube} \frac{\partial C_{CO2-tube}}{\partial z} \quad (1)$$
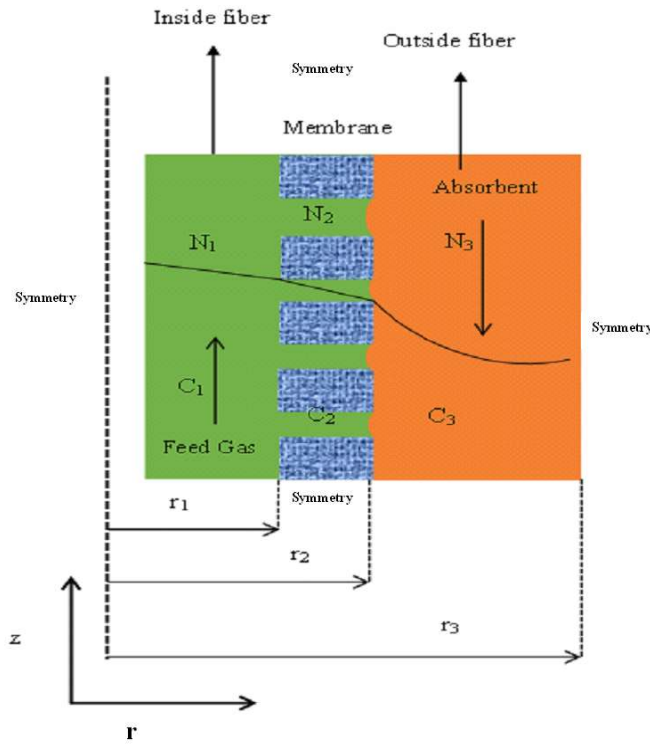
Figure 1: Mass transfer mechanism through all sections of HFMC

Laminar, fully developed and parabolic velocity profile was considered in the tube side so the tube side velocity is given by

$$u_{z-tube} = 2u\left[1 - \left(\frac{r}{r_1}\right)^2\right] \qquad (2)$$

As $u$ is the average velocity in tube side.

Following boundary conditions were employed tube subdomain

@ $z = 0$,     $C_{CO2-tube} = C_{CO2-initial} = C_0$

@ $r = 0$,     axial symmetry

@ $r = r_1$,   $C_{CO2-ube} = C_{CO2-membrane}$

@ $z = L$,     Convective flux

CO$_2$ transport through membrane

Assuming steady state for cylindrical coordinates, the CO$_2$ transfer in membrane is given by

$$D_{CO2,membrane}\left[\frac{\partial^2 C_{CO2-membrane}}{\partial r^2} + \frac{1}{r}\frac{\partial C_{CO2-membrane}}{\partial r} + \frac{\partial^2 C_{CO2-membrane}}{\partial z^2}\right] = 0$$
(3)

Boundary conditions for membrane side are given as

@ $z = 0$                Symmetry

@ $r = r_1$                $C_{CO2-membrane} = C_{CO2-tube}$

@ $r = r_2$                $C_{CO2-membrane} = C_{CO2-fc}/m$

@ $z = L$                Symmetry

Where m indicates solubility of CO$_2$

 CO$_2$ transfer in shell side of the contactor (Flow Cell)

CO$_2$ transfer in shell side of the HFMC occurs due to convection and diffusion and is given by the following equation when a steady state material balance is applied over the flow cell

$$D_{CO2-fc}\left[\frac{\partial^2 C_{CO2-fc}}{\partial r^2} + \frac{1}{r}\frac{\partial C_{CO2-fc}}{\partial r} + \frac{\partial^2 C_{CO2-fc}}{\partial z^2}\right] = u_{z-fc}\frac{\partial C_{CO2-fc}}{\partial z} \qquad (4)$$

$C_{CO2-fc}$ is concentration of CO$_2$ in flow-cell side of membrane contactor.

Navier-Stokes equation for incompressible liquid in laminar steady state flow,

$$\rho\frac{\partial u}{\partial t} - \nabla.\mu(\nabla u + (\nabla u)^T + \nabla p = F$$
(5)

$$\nabla u = 0 \qquad (6)$$

Where $\rho$ , $U, \mu, p, F$ are Density, velocity vector, viscosity of absorbent, Pressure and Body force respectively.

Boundary conditions

@ $z = L$     $C_{CO2-fc} = C_{CO2-initial} = 0$

@ $r = r_2$        $C_{CO2-fc} = m * C_{CO2-membrane}$

@ $r = r_3$        $\frac{\partial C_{CO2-fc}}{\partial r} = 0$ (Symmetry)

@ $z = 0$ Convective flux

Boundary conditions for momentum balance (Navier-Stokes equation)

@ $z = L$     Inlet, $u = u_0$

While $u_0$ is inflow velocity.

**3. Numerical simulation**

Model equations set with defined boundary condition was simulated using COMSOL software using CFD techniques. In COMSOL software, method of finite volume has been applied to the numerical simulation of equations combining with error and meshing controlling by UMFPACK solver for the process of diffusion and convection-diffusion phenomena. Due to lot of difference in radial and axial domain dimensions, a scaling factor of 100 has been introduced to eliminate additional nodes. The geometry is scaled back by the COMSOL after meshing. The elements are 463872 in number and mesh points are 232721.

Model navigator window was opened and the parameters given in Table 1 and Table 2 were put in the list of constant. Geometry was specified by putting the dimensions of membrane for all subdomains i-e tube, membrane and shell of the flow cell. Settings of sub domains were carried out and then appropriate boundary condition was introduced. After performing all the above steps, geometry meshing was performed. For a better accuracy refining of meshing was performed too for the purpose to gain the results of higher accuracy. At the last, solver was set and model simulation was started and successfully completed. The time of simulation was noted to be 8 minutes and 50 seconds by a CORE i3 Laptop of Haier brand. After successful run post processing was performed for the purpose to obtain desired results.

Table: 1 Membrane structural parameters

| Parameters | Values |
|---|---|
| Gaseous diffusion coefficient ($D_{gas}$) | 1.85e-5 m$^2$/s |
| Liquid diffusion coefficient ($D_{liq}$) | 1.92e-9 m$^2$/s |
| Membrane diffusion coefficient ($D_m$) | $D_{gas}$ ($\varepsilon/\tau$) m$^2$/s |
| Initial $CO_2$ concentration ($C_0$) | 4.475 mol/m$^3$ |
| Absorbent | Distilled Water |
| Scale factor for axial direction | 100 |

Table: 2 Simulation parameters

| Membrane Structural Parameter | Values |
|---|---|
| Internal Radius of tube ($r_1$) | 1.1e-4 m |
| Outside Radius of tube ($r_2$) | 1.5e-4 m |
| Shell radius ($r_3$) | 3.15e-4 m |
| Length (L) of module | $2.00 \times 10^{-3}$ (m) |
| Porosity ($\varepsilon$) | 0.4 |
| Tortuosity ($\tau$) | 1/ $\varepsilon$ |
| No. of fibers | 10202 |

## 4. Results and discussion

After model solving, post processing has been performed to obtain the results.

### 4.1 Axial-Radial 2-D Concentration Profiles

Concentration profile of $C/C_0$ is given in the Figure 2. The feed gas entered in tube side of the flow cell at Z = 0 with a initial $CO_2$ of 4.475 mol/m$^3$ in gaseous mixture. The distilled water is fed to flow cell of HFMC in to opposite i.e. at Z = L in counter current direction to that of the feed gas. A constant trans-membrane pressure is given to the feed gaseous mixture to avoid diffusion of distilled water in pores in order to create a gas-liquid interfacial area and to protect the membrane from wetting phenomenon as the membrane is hydrophobic. It shows no selectivity for separating component and the only driving force is the concentration gradient. The concentration profile shown in Figure 2 presents that $CO_2$ concentration of feed gas reduces as it travels from Z = 0 to Z = L in axial direction. It is may also be seen from Figure 3 that concentration of absorbent increases as it moves from Z = L to Z = 0 in axial direction.
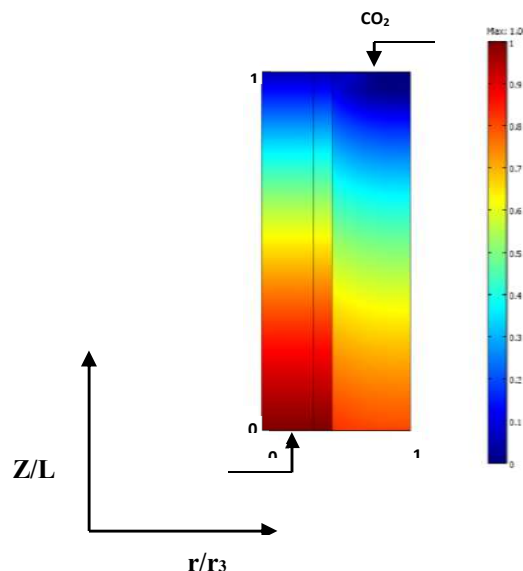


Figure 2: Concentration profile in module

Figure 3 indicates Radial concentration profiles in membrane module.
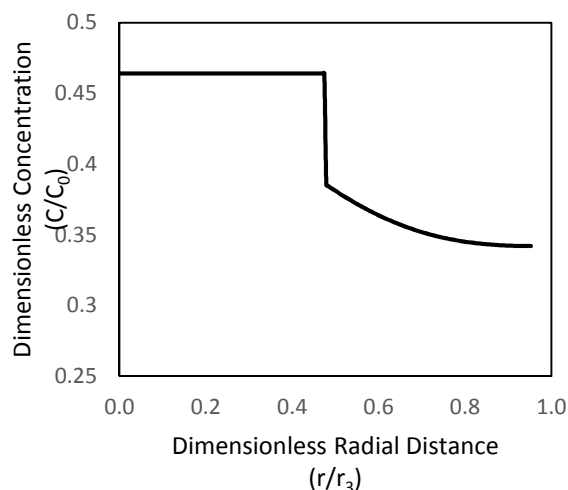


Figure 3: Cross sectional concentration profile in membrane module

### 4.2 Model Validation

Validation of the presented 2-D model has been carried out with experimentation of previous work in literature [8]. Comparison in experimental results and of model is presented in Figure 5. It is shown that there is a good agreement in experimentation data and results gained by model simulation.
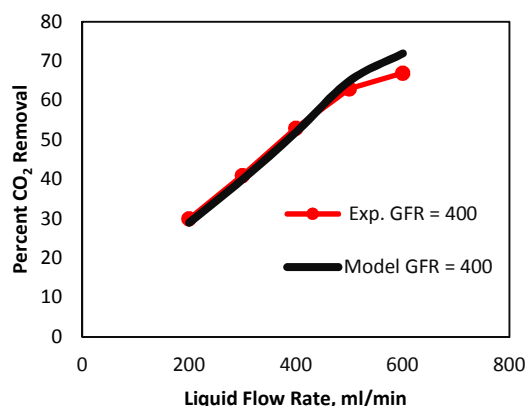


Figure 5: Comparison of model results with experimental data (Gas flow rate (FGR) = 400 ml/min)

### 5. Conclusion

A 2-D comprehensive mass transfer mathematical model was developed for the separation of $CO_2$ from natural gas through distilled water using hollow fiber membrane contactors devices. A set of mathematical equations was developed by assuming a steady state mode of mass transfer through convection and diffusion in tube side, diffusion in membrane and convection and diffusion in shell side of flow cell of HFMC by assuming the gas and liquid flowing counter currently. The model was then simulated through COMSOL Multiphysics software using CFD techniques. The axial and radial concentration profiles were investigated. The shell side velocity profile was obtained and it was found that the absorbent flow in shell side of the flow cell is not fully developed at the entrance at Z=L and becomes fully developed after a small length of fiber. Total flux, convective flux and diffusive flux were also determined. It was found that diffusion is dominant in axial direction as convective flux is dominant in axial direction. The $CO_2$ transfer occurs through gaseous phase on behalf of convection and diffusion. The effects of feed gas and absorbent flow rates were studied and it was found that by increasing the absorbent flow rate, the removal efficiency of $CO_2$ increases. This is because of the concentration gradient increase due to the instantaneous availability of fresh absorbent. It was also found that by increasing the feed gas flow rate, the removal efficiency decreases due to less contact time. It was also found that by increasing the $CO_2$ absorbent temperature, the $CO_2$ removal efficiency decrease due to the decrease in solubility of $CO_2$ in the absorbent. The effect of porosity to tortuosity was also investigated and its effect on concentration and $CO_2$ removal efficiency studied. It was found that with the increase in porosity to tortuosity ratio, the separation efficiency increases due to an increase in diffusion mass transfer coefficient across the membrane due to greater porosity.

### References

[1] Herzog, H., Eliasson, B., Kaarstad, O. Capturing greenhouse gases. Sci. Am J, 182 (2000) 72–79.

[2] Desideri, U., Paolucci, A. Performance modeling of a carbon dioxide removal system for power plants. Energy Convers. Manage J, 40 (1999) 1899–1915.

[3] Faiz, R., Al-Marzouqi, M. Mathematical modeling for the simultaneous absorption of $CO_2$ and $H_2S$ using MEA in hollow fiber membrane contactors. J. Membrane Science, 342 (2009) 269–278.

[4] Gabelman, A., Hwang, S.T. Hollow fiber membrane contactors. J. Membrane Science, 159 (1999) 61–106.

[5] Vajda, M., Havalda, I., Macek, R. Membrane-based solvent extraction and stripping of zinc in a hollow-fibre contactor operating in a circulating mode. Desalination 163 (2004) 19-26.

[6] Younas, M., Druon-Bocquet, S., Sanchez, J. Kinetic and Dynamic Study of Liquid-Liquid Extraction of Copper in a HFMC: Experimentation, Modeling, and Simulation. AIChE J, 56 (2010) 1469–1480.

[7] Cussler, E.L., Crespo, J.G., BoÈddeker, K.W., Membrane Processes in Separation and Purification. Kluwer Academic Publishers, Netherlands, 1994, pp. 375-394.

[8] Al-Marzouqi, M.H., El-Naas, M.H., Marzouk, S.A.M., Al-Zarooni, M.A., Nadia, A., Faiz, R. Modeling of $CO_2$ absorption in membrane contactors. J. Separation and purification technology 59 (2008) 286-293.

[9] Shirazian, S., Moghadassi, A., Moradi, S. Numerical simulation of mass transfer in gas–liquid hollow fiber membrane contactors for laminar flow conditions. J. Simulation Modelling Practice and Theory 17 (2009) 708–718.

[10] Rezakazemi, M., Niazi, Z., Mirfendereski, M., Shirazian, S., Mohammadi, T., Afshin. CFD simulation of natural gas sweetening in a gas-liquid hollow-fiber membrane contactor. J.Chemical engineering 168 (2011) 1217-1226.

# Converging, non-converging slotted pores membranes and oil drops deformation

*Waseem Qadar[1], Saad Ullah khan[1], Asmat Ullah[1\*]*

[1]*Department of Chemical Engineering,*

*University of Engineering & Technology Peshawar, Pakistan*

[1\*]A.Ullah@uetpeshawar.edu.pk

## ABSTRACT

For oil droplet deformation by a converging slotted pore membrane, a mathematical model is presented in earlier work. In the assumption of previous work the droplets of oil deforms to a prolate spheroid shape from a spherical shape when passes by a converging slot. While in the present work the assumption is the oil droplet deformation to oblate spheroid shape when passes over a non-converging slot and also a mathematical model is developed for this work. The static and drag force concept is drawn-out and in findings static force for non-converging slotted pore membrane is higher than the static force of converging pore membrane. Due to greater static force the drops deforms in non-converging slotted pore membrane. In current work, oil drops in two systems of different interfacial tensions i-e 4 & 9 mN/M have been used and it was evaluated that for drops with high interfacial tension a greater rejection is attained at different permeate velocities.

**Key Words:** Oil drops Passage and deformation, non-converging and converging slotted pore membrane, membrane based separation.

## 1. INTRODUCTION

Waste water (oil in water or water in oil) in vast volume are produced from different process industries like transportation, petroleum etc [1]. Which contain large numbers of oil particles. These waters are then disposed into streams, sea, rivers etc. Content of oil in water is unsafe for marine life. Therefore, an efficient process is required to remove the oil content from water to meet the internal environmental regulatory standards. Different locations have different concentration of oil in water. It ranges from 100 to 1000ppm or more [2]. International environmental authority set the standard for oil to be disposed into streams, rivers, or sea should be in range of 10-15mg/l or less [3]. There are different techniques which are used for removal of water from oil but its removal efficiency is limited is oil drop size of 10 μm. such as coalescence or hydro-cyclones are used [4-6]. Membrane technology is proved to be efficient separation technology due to higher separation efficiency as compared to conventional technology, due to which it become main focus for scientist and researcher [7]. Different membranes processes have been tried for separation of oil from water but it was not economical due to high trans membrane pressure, and too low permeate flux such as reverse osmosis, nano filtration and ultra-filtration process. These processes were more attractive for waste produced from offshore platforms [8-10]. Microfiltration membrane process, having low trans membrane pressure, with high permeate flux for the separation of oil- water, proved to be more economical then other membrane separation process [11]. Two different techniques of microfiltration, depth microfiltration and surface filtration are used for separation of oil water. The membrane used for the depth micro filtration fouled extensively and needed to be replaced due to its cleaning difficulties. Surface micro filtration found effective the depth microfiltration as the membrane fouled less and drop were more successfully separated [12-15]. In recent years, slotted pore membrane proved more efficient then circular pore membrane because of the separation of deforming oil drops. Higher permeate flux are also produced by Slotted pore membrane then circular pore membrane [16-19]. Current work describes the passage of oil drop through a slotted pore membrane with non- converging slots and its objective were investigated.

## 2. Theory

The current study described mathematical model which is developed for oil drops passing through non-

converging slots. Oil drop deformation is presumed passing through a non-converging slot due the drag force also referred as force of deformation created by the flow of fluid around the drop. Drag force and static force are schematically exhaustive in Fig.1.
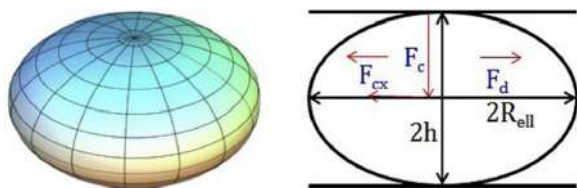


**Fig 1**. Drops when passes through a non-converging slot changes its shape into an oblate spheroid.

Oil drop is hugged and bends into an oblate spheroid when the diameter of the drop is bigger than the slot width. The force tries to keep the drop spherical and comes from the interfacial tension between the continuous and dispersed phases is known as static force [16].

$$Fcx = 2\pi\partial[\frac{3R_{sp}^2}{h} + \frac{1}{R_{sp}}\frac{h^2}{1-\frac{h^3}{R_{sp}^3}}[\frac{3}{2} - \tanh^{-1}[1 -$$

$$\sqrt{1 - \frac{h^3}{R_{sp}^3}}\frac{3h^3}{2R_{sp}^3\sqrt{1-\frac{h^3}{R_{sp}}}}] - 4R_{sp}]] \qquad (1)$$

The last form for the static force when drops passing through a non-converging slot is Eq (1) [20]. The drag force over the drops in channels is always higher than the drag force over the drops without channels [17]. The drag force without channels is equal to drag force in channels increased by a correction factor that referred as wall correction factor [21].

$$F_d = k_w 12\pi\mu R_{sp}U \qquad (2)$$

Here, (U) is the in-pore velocity or interstitial velocity and ($\mu$) is viscosity of the fluid [20]. Both Eqs. (1) and (2) can be used for 100% cut-off of drops through a non-converging slotted pore membrane. By supposition that drops will be 100% cut-off or rejected by membranes when both Eqs. (1) and (2) balances each other. When (Fcx) becomes equal to (Fd) the droplet will be under steady state conditions and will stay on the surface of the membrane. When (Fd > Fcx) the drop will bend, and will pass through the membrane and when ($F_d < F_{cx}$) it will be excluded by the membrane [20].
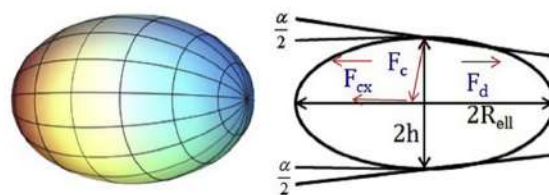


**Fig 2**. Drop when passes through a converging slot changes its shape into prolate spheroid.

## 3. Experimental set-up

### 3.1 Material and method

Oil micro droplets were produced with food blender (1-15 μm). Created oil drops in both Tween 20 and PVA broke up waters are gone through a 4 μm converging slotted pore membrane (see Fig. 3).
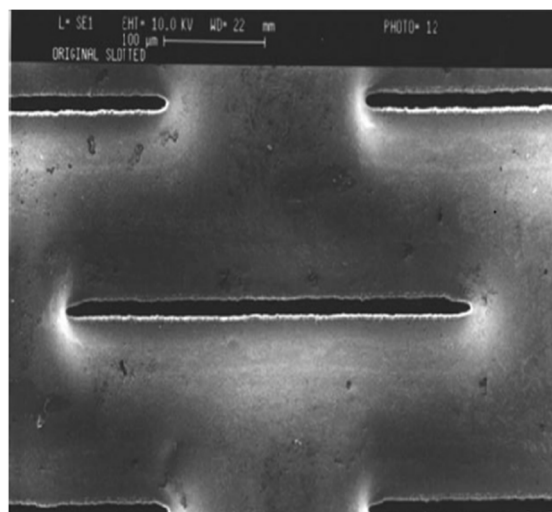


**Fig.3** Slotted pore membrane surface image [16-19].

Experimental details (set-up, method) for converging slotted pore membrane is point by point in Fig. 3 of [16].

## 4. Result and discussion

This study presents that the expected drops change into oblate spheroid in place of prolate spheroid when going through a non-converging opening and scientific model is formed (Eq. (1)).

The expression for static force for drops going through a converging opening is final which is describe in the following [17].

$$Fcx = -[2\pi\partial \left[ \frac{2h}{R_{sp}} + \frac{[-3\left[\frac{h}{R_{sp}}\right]^3 - arc\cos\left[\frac{h}{R_{sp}}\right]^3 \frac{1}{2}\frac{1}{\sqrt{1-\left[\frac{h}{R_{sp}}\right]^6}}\left[-8\left[\frac{h}{R_{sp}}\right]^6 + 2\right]]}{\left[\frac{h}{R_{sp}}\sqrt{1-\left[\frac{h}{R_{sp}}\right]}\right]^2} \right] \sin\frac{\alpha}{2} \quad (3)$$

Various interfacial oil droplets tension is assumed to go through converging and non-converging slotted pore membranes and their outcomes for the static force are looked at for the same drag force ($F_d$) at equal interval.

Examination between the static force for non-converging openings and the static power for converging openings at numerous in-pore filtration velocities for oil drop in Tween 20 dissolved is demonstrated in Fig.4, When the drop size is greater than the opening width, the drop misshapes and the droplets drive through with size beneath the opening width without misshaping through the membrane openings.
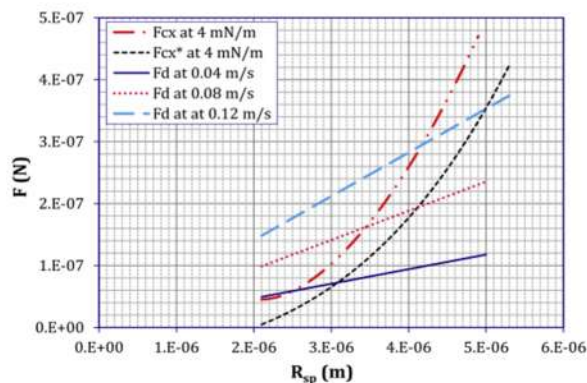


**Fig 4**. Comparison between static force for non-converging slots and static force for converging slots at different in pore filtration velocities (0.04, 0.08 and 0.12 m/s) with oil/water system of 4 mN/m.

The reactionary force is the static force, when the drops twist from the round shape to spheroid shape static force get to be dynamic and it acts in inverse manner to the drag force and dependably tries to reestablish the circular state of a drop. A greater static force for non-converging openings is achieved than the static force for converging openings at different filtration velocities. The droplets turn from circular to prolate spheroid step by step when going through the opening on account of converging slots. The droplets again change all of a sudden from circular to oblate spheroid when going through a non-converging opening and that would be the reason of a higher static force for non-converging opening than the static force for converging openings.

A co-relation between the static forces for converging and non-converging openings for oil and PVA dissolved water system that transported an interfacial pressure of 9 mN/m is expresses in Fig.5. At 0.04 m/s in-pore filtration velocity. The static force for non-converging openings is higher than the drag force for each single of the drops greater than the openings width, and for each single of the drops greater than the openings width would be rejected by the membrane without changing its shape. At the same in-pore filtration velocity (0.04m/s) the static force equalizations the drag force at drop span of 2.4 µm which implies that each drop at 2.4 µm or more are 100% rejected by the membrane. Drops from circular to an oblate spheroid is distorted to begins by utilizing non-converging slotted pore membranes at 0.08 m/s filtration velocity for oil/water arrangement of 9 mN/m.
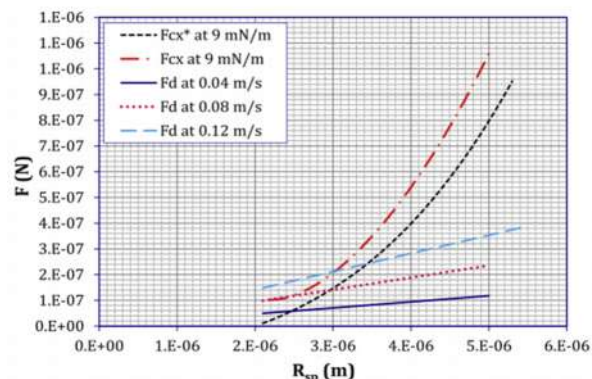


**Fig 5.** Comparison between static force for non-converging slots and static force for converging slots at different in pore filtration velocities (0.04, 0.08 and 0.12 m/s) with oil/water system of 9 mN/m.

100% cut-off points for oil drops in Tween 20 dissolved water shows in Fig.6, which is obtained from Fig.4. When the static force for the converging and the non-converging slotted pore membranes become equal to the drag force is referred is 100% cut-off point. The static force for no converging slots is developed than the static force for converging slots at the same drag force. A linear function of the in-pore

filtration velocity is drag force and due to this 100% cut-off point linearly increased with the in-pore filtration velocity. Similarly, Fig.7 shows 100% cut-off points for oil drops in PVA dissolved water which is obtained from Fig.5. In this case, the static force balanced the drag force at lower drop size due to which lower 100% cut-off point are achieved.
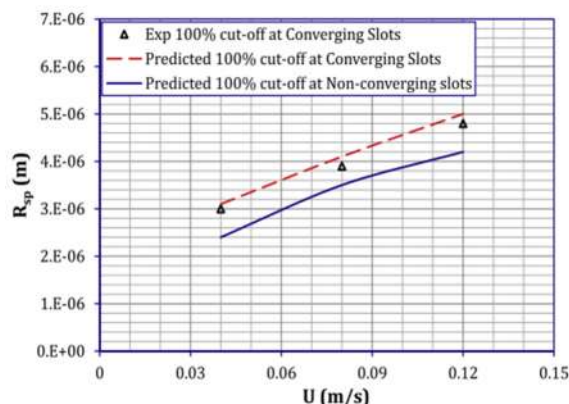


**Fig 6**.100% cut-off points of oil drops in Tween 20 dissolved water with an interfacial tension of 4 mN/m.
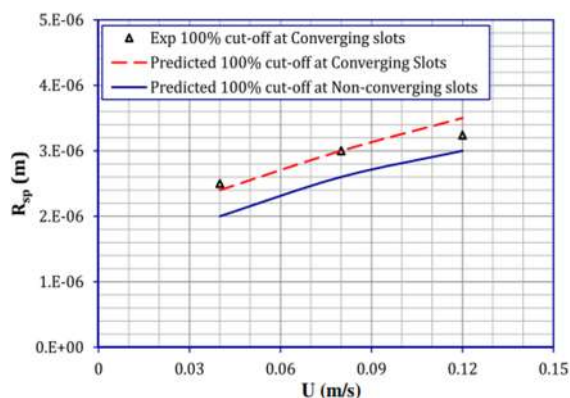


**Fig 7.** 100% cut-off points of oil drops in PVA dissolved water with an interfacial tension of 9 mN/m.

This model can also be used for more other purposes i-e bendy materials like yeast through non-converging slotted pore membrane. The above model can be strained out for the prediction of size distribution of scarring drops of different sorts in the saturate utilizing non-converging slotted pore membrane.

## 5. Conclusion

A scientific model for the passage and deformation of twisting oil drops through non-converging slotted pore membrane has been created; expecting that drops changing from round to an oblate spheroid when going

through the non-converging openings. Looking at the static force ($F_{cx}$) for non-converging openings with the static force ($F*_{cx}$) for converging openings, it has been examined that a higher static force for non-converging openings/slots has been accomplished than the static force for converging openings at different in-pore filtration velocities. Drops disfigure quickly and all of a sudden in the converging openings, while the twisting of drops is progressive in the converging openings that may the outcome of a higher static for non-converging openings. The study can equally be allied for other deforming drops like immature microorganisms and yeast division through non-converging slotted pore membrane. Saturate size circulation of twisting drops through non-converging opened pore can be anticipated by utilizing the applied model that would give a thought whether the concentration of oil in the saturate is underneath the standard set by worldwide international environmental authorities for the oil concentration in the permeate.

## Nomenclature:

$E_{ca}$:    capillary energy (n m)

$F_{cx}$:    static force for non-converging slots (n)

$F*_{cx}$:    static force for converging slots (n)

$F_d$:    drag force inside the slot (n)

$S_{sp}$:    surface area of sphere (m2)

$F_o$:    drag force without channel (n)

$R_{sp}$:    spherical drops radius (m)

$R_{ell}$:    ellipsoid (spheroid) radius (m)

$S_{ell}$:    surface area of ellipsoid (m2)

$\mu$:    viscosity (pa s)

$\Sigma$:    interfacial tension (n/m)

$\alpha$:    angle at which the slot converges towards inside.

$K_w$:    wall correction factor

## References:

[1] M. Abbasi, A. Salahi, M. Mirfendereski, T. Mohammadi, A. Pak, Dimensional analysis of permeation flux for microfiltration of oily wastewaters using mullite ceramic membranes, Desalination 252 (2010) 113–119.

[2] B. Chakrabarty, A.K. Ghoshal, M.K. Purkait, Ultrafiltration of stable oil-in-water emulsion by

polysulfone membrane, J. Membr. Sci. 325 (2008) 427–437.

[3] A. Bevis, The treatment of oily water by coalescing, Filtr. Sep. 29 (4) (1992) 295–298.

[4] D.A. Colman, M.T. Thew, Correlation of separation results from light dispersion hydrocyclones, Chem. Eng. Res. Des. 61 (A) (1983) 233–240.

[5] J.H. Hargreaves, R.S. Silvester, Computational fluid dynamics applied to the analysis of deoiling hydrocyclone performance, Trans. I. Chem. E. 68 (1990) 365–383.

[6] D. Wolbert, B.F. Ma, Y. Aurelle, J. Seureau, Efficiency estimation of liquid–liquid hydrocyclones using trajectory analysis, AIChE J. 41 (6) (1995) 1395–1401.

[7] J. Kong, K. Li, Oil removal from oil-in-water emulsions using PVDF membranes, Sep. Purif. Technol. 16 (1) (1999) 83–93.

[8] T. Mohammadi, M. Kazemimoghadam, M. Saadabadi, Modeling of membrane fouling and flux decline in reverse osmosis during separation of oil in water emulsions, Desalination 157 (2003) 369–375.

[9] H. Peng, K. Volchek, M. MacKinnon, W.P. Wong, C.E. Brown, Application of nanofiltration to water management options for oil sands operations, Desalination 170 (2004) 137–150.

[10] W. Chen, J. Peng, Y. Su, L. Zheng, L. Wang, Z. Jiang, Separation of oil/water emulsion using Pluronic F127 modified polyethersulfone ultrafiltration membranes, Sep. Purif. Technol. 66 (2009) 591–597.

[11] J. Mueller, Y. Cen, R.H. Davis, Crossflow microfiltration of oily water, J. Membr. Sci. 129 (1997) 221–235.

[12] T. Tanaka, T. Nishimoto, K. Tsukamoto, M. Yoshida, T. Kouya, M. Taniguchi, D.R. Lloyd, Formation of depth filter microfiltration membranes of poly (l-lactic acid) via phase separation, J. Membr. Sci. 396 (2012) 101–109.

[13] J.M. Frey, P. Schmitz, Particle transport and capture at the membrane surface in cross-flow microfiltration, Chem. Eng. Sci. 55 (2000) 4053–4065.

[14] I.W. Cumming, R.G. Holdich, I.D. Smith, The rejection of oil by microfiltration of a stabilised kerosene/water emulsion, J. Membr. Sci. 169 (2000) 147–155.

[15] P. Schmitz, B. Wandelt, D. Houi, M. Hildenbrand, Particle aggregation at the membrane surface in cross-flow microfiltration, J. Membr. Sci. 84 (1993) 171– 183.

[16] A. Ullah, R.G. Holdich, M. Naeem, V.M. Starov, Stability and deformation of oil droplets during microfiltration on a slotted pore membrane, J. Membr. Sci. 401–402 (2012) 118–124.

[17] A. Ullah, M. Naeem, R.G. Holdich, V.M. Starov, S. Semenov, Microfiltration of deforming droplets, Prog. Colloid Polym. Sci. 139 (2012) 107–110.

[18] A. Ullah, R.G. Holdich, M. Naeem, V.M. Starov, Shear enhanced microfiltration and rejection of crude oil drops through a slotted pore membrane including migration velocities, J. Membr. Sci. 421–422 (2012) 69–74.

[19] A. Ullah, V.M. Starov, N. Naeem, R.G. Holdich, Microfiltration of deforming oil droplets on a slotted pore membrane and sustainable flux rates, J. Membr. Sci. 382 (2011) 271–277.

[20] A. Ullah , S.W. Khan , A. Shakoor , V.M. Starov, Passage and deformation of oil drops through non-converging and converging micro-sized slotted pore membranes, Separation and Purification Technology 119 (2013) 7–13

[21] H.J. Keh, Y.C. Po, Slow motion of a droplet between two parallel walls, Chem.Eng. Sci. 56 (2001) 6863–6871.

# Mineralogical characterization and evaluation of phosphate ore from Garhi Habib Ullah, District Mansehra, Khyber Pakhtunkwa, Pakistan

Naseer Muhammad Khan[1*], Ishaq Ahmad[1]

[1]Department of Mining Engineering, University of Engineering and Technology, Peshawar

*Corresponding author

E-mail: engrnaseer1@gmail.com

## Abstract

Geological survey of Pakistan (GSP) conducted a detailed investigation in 1969 on the Dolola area of the Garhi Habib Ullah and reported the presence of about 0.9 million tons of phosphate ore. The content in the ore of $P_2O_5$ more ore equal to 30% are consider as marketable. In order to evaluate and upgrade the phosphate ore, GHU, different mineralogical, chemical studies and beneficiation studies were carried out. In the first step mineralogical studies included the petrography, scanning electron microscope (SEM), X-Ray fluorescence (XRF), X-ray diffraction (XRD) to study phosphate ore. In the second step on the basis of mineralogy shaking table were used for the beneficiation of phosphate ore. It is concluded from mineralogy study that the apatite mineral is present with association of gangue mineral such as calcite, quartz and hematite. .petrography show that the phosphate rock are of dolomitized formation. SEM result show that the apatite mineral are locked between calcite and quartz, need optimum liberation. XRF result show that the apatite mineral were 22.85 %.XRD also show that the major gangue with ore mineral are quartz, calcite and hematite. Beneficiation techniques were used such as shaking table, which up-grade the phosphate ore mineral upto marketable grade 30.22% with average 58% recovery. It was proposed that the phosphate recovery could be

increased if the shaking table tailings could be reprocessed using froth flotation and magnetic separation technique.

**Keyword:** Apatite, beneficiation, Garhi Habib Ullah, , grade, recovery, shaking table

## 1. Introduction

Generally phosphate rock is a rock which contain high concentration of phosphate mineral. The phosphate mineral such as chemical formula $Ca_5(PO_4CO_3)_3(F,OH,Cl)$ [1] is known as apatite . The total phosphate 90% were used for fertilizer industry. The phosphate mineral concentrate less 30% are consider as uneconomical and are not used in fertilizer ,therefor for fertilizer industry the rock must be contain at least 30% phosphate mineral for industrial

used. Phosphate mineral required to industry were fill full through mining and mineral processing [2].Pakistan import large quantity of phosphate from Morocco, Tunisia and Jordan to fill the required demand of the fertilizer [3].Dolola deposits occur between 34´´25´ N and 73´´21´ to 73´´23´.This area is the small part of GHU and are structurally complicated.

There are three phosphorite zones [4]were identified in the hazra formation silty bed. The first bed were 1692 m long and its terminate by thrust fault at north of Dawlat mar. Its dip steep at $41^0$-$71^0$ to the west and thick 13 m to south and 3m to north. Second bed start at Begla Gali about 152 m to north-east (N-E) and are continues for a distance of 819m in the strike length. Deposits are in the lenticular shape, having thickness 23 m and dips $40^0$ -$65^0$.The third zone and the second zone are parallel to each other and having length of 303 m to west and extend for a distance 1799 m in the strike length. The total deposits are 0.9 million tones estimated by geological survey of Pakistan in 1979 with an average grade 22-25% $P_2O_5$ which are low grade and directly not used in the industry. Before going to beneficiation first step is to find the mineralogical investigation and on the basis of its beneficiation technique were decide.

Optical microscopy is the most robust and potential instrument used for mineralogical examination [7, 8].Whereas technologically its power of magnification were enhance by electron microscope [5]. XRD is use to identify the ore mineral and rock mineral. SEM is the most adaptable instrument used all over the world for the investigation of microstructure property of the mineral [6]. EDX with SEM were used to determine the element in the specimen. This study evaluate and determine the characterizations of GHU phosphate rock. The aim of this research was to carry out mineralogical studies on the basis of it beneficiation of the specimen of the GHU district Manshera, KP, to make it economical usable in industry.

## 2. Material and methods

The samples were collected from Dawlat Maar (Dolola) randomly having 34°19'3.91"N, 73°21'23.69"E coordinate of area of GHU. Samples were mixed, crushed and grind upto size -250μm. Using coning and quartering methods for

Figure 1.Chert embedded in dolomitized lime mud matrix.
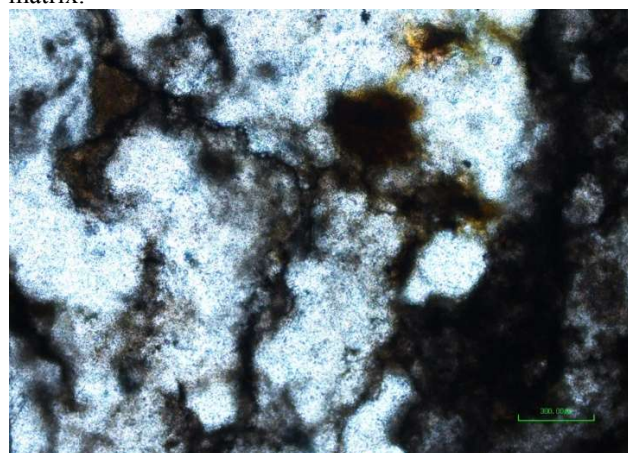


Figure 2. Disseminated chert in the ore mineral
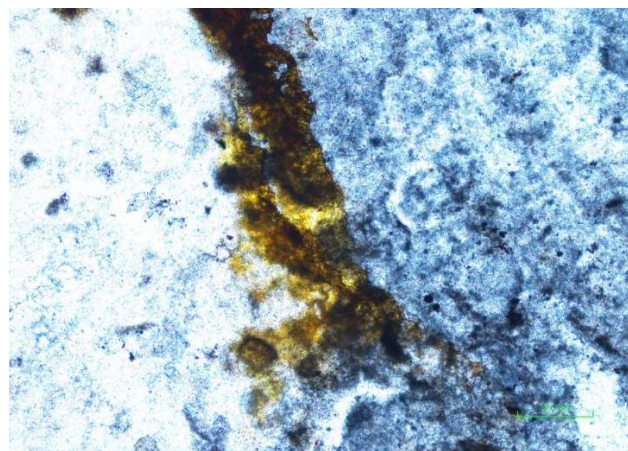


Figure 3. High interference of quartz in fracture

representative sample. Representative sample split into two parts; one grind up to 200 μm and second one used for thin sections (petrographic study). XRD and chemical analysis carried out on powder material. Mineralogical characterization have been carried out

on various instruments like SEM, XRD, EDX, polarizing microscope and sieve analysis, and the results obtained from all these techniques were compared. After complete mineralogical analysis beneficiation methods such as shaking table were used for the up-gradation of phosphate mineral and to produce high content phosphate mineral concentrate.

## 2.1 Experimental

### 2.1.1 Minerological study

Reflected microscope (Nikon Microphoto-FXA, type 118) were used for the thin section studies of samples .Different mineral were identified on the basis of color property. Thin section study are shown in the **Figs.1-3.**

## 2.1.2 X-ray Diffraction

XRD analysis were identified and show ore minerals presence in the phosphate rock. The results is shown in **Fig. 4** show four main minerals in the ore are; calcite, flourapatite, quartz and hematite. The rock samples were run through XRD, which unit is Cu.K and wavelength 1.540598 Å of the radiation. The peaks appear at different point having different intensities and 2 theta value .The intensity Value were converted into lattice space (d in Å units) with help of conversion charts and different mineral were identified.

## 2.1.3 Scanning Electron Microscopy

SEM is type of electron microscope which scan the sample with focus beam of electron and produce image which give information about surface and composition. Thin section was prepared for SEM in the Geology department, University of Peshawar. Samples of phosphate rock were investigate and analyze under SEM, 6380 (LA) with the energy range of 0-20 keV as shown in **Fig .5.** The SEM and EDX were used to determine the elemental composition of the phosphate ore as shown the **Fig. 6.**

## 2.2 Shaking Table

The efficiency of shaking table are affect by the factor such as particle size, density of particle of different mineral ,shape, riffle design ,deck shape and slope ,dressing water flow rate ,feeding flow rate and shaking table movement and speed. Mineralogical the phosphate ore contain dolomite, quartz, flourapatite and hematite having specific gravity; 2.84, 2.65, 3.20 and 5.1 g/cm³ respectively.

The basic Selection criterion for the gravity separation of shaking table is considering degree of liberation. The liberation size were vary and other parameter were investigate such as deck angle, feed flow rate,

dressing flow rate were optimized, for this purpose several experiment were carry out as such that the optimum grade and maximum recovery achieved.

## 3. Results

Mineralogical Dolola phosphate rock are dolomitized formation in deep environment with association of mud stone .The rock are highly fracture as show in **Figs.1-3** .Fracture are filled with ferruginous and stylolite and the quartz give high interference in the fracture area. XRD analysis conform the apatite mineral as ore mineral and gangue mineral are calcite, hematite and quartz as shown in the **Fig.4**.SEM analysis show that the phosphate are interlocked between calcite and quartz so carful liberation take
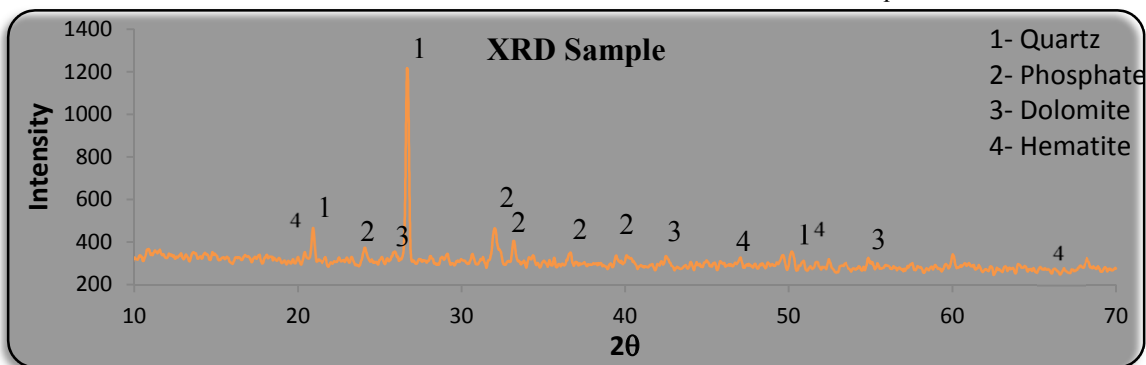


**Figure 4. X-ray diffraction analysis of phosphate rock.**

place to avoid overgrinding and undergrinding .EDX also conformed the Phosphate ,calcium and Hematite elemental presence in the ore as shown in the **Fig. 5** .On the basis of that mineralogy for the beneficiation shaking table were used with different liberation size and with varying parameter to get the optimum recovery and grade. Different experiment were perform by investigate the different parameter to achieve the high recovery and grade. The overall result of shaking table are shown in **Table 1**.

Experimentally it was concluded that the optimal deck slop was $5^0$ degree, feed flow rate was 4 L/min and dressing flow rate was 7 L/min.
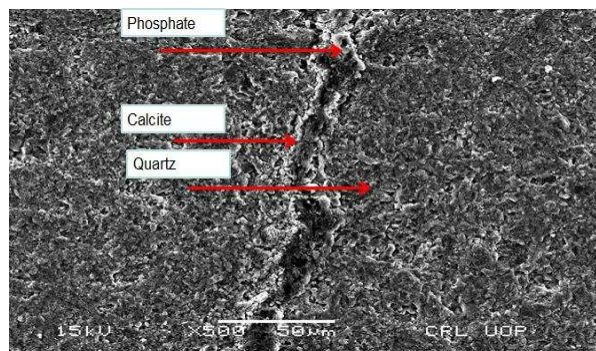


**Figure 5.SEM mineralogical analysis of phosphate rock**
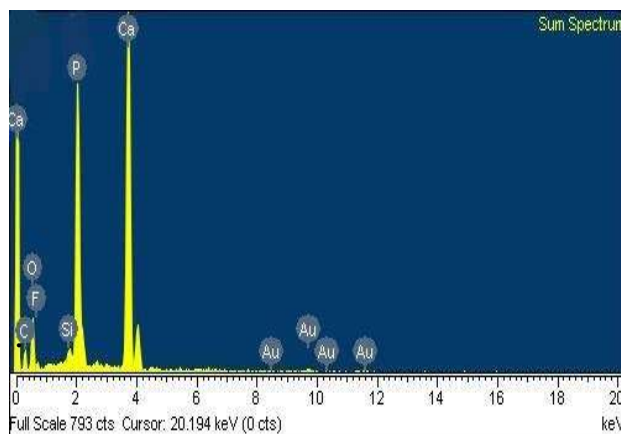


**Figure 6. SEM with EDX analysis to determine the elemental composition of phosphate rock**

**Table 1**

| Sample | Particle size (μm) | Weight (gram) | Weight (%) | P₂O₅ (%) | Recovery (%) |
|---|---|---|---|---|---|
| Concentrate | 300-450 | 243 | 24.3 | 34 | 36.15 |
| Middling | 300-450 | 390 | 39 | 20.3 | 34.65 |
| Tailing | 300-450 | 367 | 36.7 | 18 | 28.91 |
| Feed | 300-450 | 1000 | 100 | 22.85 | 100 |
| Concentrate | 150-200 | 340 | 34 | 28 | 41.66 |
| Middling | 150-200 | 310 | 31 | 21.3 | 28.90 |
| Tailing | 150-200 | 350 | 35 | 19 | 29.10 |
| Feed | 150-200 | 1000 | 100 | 22.85 | 100 |
| Concentrate | 53-150 | 440 | 44 | 30.3 | 58.34 |
| Middling | 53-150 | 230 | 23 | 19 | 19.12 |
| Tailing | 53-150 | 330 | 33 | 15.5 | 22.38 |
| Feed | 53-150 | 1000 | 100 | 22.85 | 100 |

**4. Conclusion**

The Characterization of the GHARI Habib Ullah show that the ore contain quartz in the form of clay and it was removed through shaking table at optimum size of liberation 53-150 μm to achieved 30.2 grade of phosphate with recovery of 58-59% range. The optimum parameter for shaking table for optimum grade and recovery achievement.

**5. Recommendation**

The tail of the shaking table contains 17-18 % $P_2O_5$ and high content of $Fe_2O_3$ were up-grade through high intensity magnetic separator and flotation.

## References

[1] M. Ashraf, Artist, *Reaction kinetics and mass transfer studies.* [Art]. Bahauddin Zakariya University ,Mulatan, 2010.

[2] S. jasinski, ". "Phosphate Rock"," U.S. Geological Survey, Reston, VA, USA, 2014.

[3] F. trude, "Federal bureau of statistics ,statistic division," Government of Pakistan, Islamabad , 1989.

[4] R. P. S. D. F. D. A. J. G. Notholt, Phosphate rock deposite and resource, UK: Camberage University press, 1989.

[5] J. Stephens, "Microprobe Applications in Mineral Exploration and Development programs," *Miner.Sci.Engg,* vol. 4, no. 1, pp. 26-37, 1971.

[6] W. A. Barry, Mineral Processing Technology, Oxford UK: Elsevier, 1992.

[7] R. Hagni, "Ore microscopy Applied to Beneficiation," *Min. Eng. (N.Y.),* vol. 30, no. 10, pp. 1437-1447, 1978.

[8] E. N. Cameron, Ore Microscopy, New york: John Willey & Sons, 1662.

# Process Design for Bio-Ethanol fermentation from potato peels waste Simultaneous Saccharification and Fermentation of Starch by Very High Gravity process

Micaiah Cyril Das[1*], Sidratel Muntaha[1], Uzair Tariq[1], Sarfaraz Khan[1], Sundus Khusnood[1], Noor ul Ain Tahir[1], Yayha Gul[1], Saeed Gul[1]

[1]Department of Chemical Engineering, University of Engineering and Technology, Peshawar 25000, University Road

*Corresponding author

Email: micaiahcyrildas@hotmail.com,

## Abstract

Bio-Ethanol, a type of bio-fuel, has great value as a prospect fuel due to its high efficiency and low environmental impact. From the different types of feed source available, potato peel waste available from land cultivation and food processing industries has been selected as a feed for yeast cells, for fermentation, due to being a less valuable feedstock. Peels are a high source of nutrients but in itself they have a low starch content. The primary concern is to use a raw material that is inedible and causes disposal problems.

The process starts with pretreating the peels mainly washing to prevent any dirt and grit to enter the liquefaction and Saccharification process. Liquefaction around 65°C causes starch to come out to the surface making it easily reachable for the microorganisms to complete the conversion to glucose and finally to Bio-Ethanol. This study employs Simultaneous Saccharification and Fermentation for its economic feasibility. Also use of Talaromyces Cellulolyticus as the source for pectin, alpha amylase and Cellulase proven economically beneficial to the production process, is employed to promise higher yields. The research focuses on developing a working process flowsheet for the SSF of Potato Peels.

**Keywords:** Plant Design, Control methods, Feasibility, Simulation.

## 1. Introduction

Reducing dependence on fossil and non-renewable sources of fuel is a great step in order to protect the environment as well as suppling our energy needs. Therefore, Bio-ethanol, a biological energy source, is a prospective alternative to fossil fuels. It has the capacity to be modified for meeting increasing demand as energy for various capital ventures [1]. In 1819, the French chemist, Henri Braconnot, hydrolyzed cellulose to sugar by sulfuric acid, hence the first to employ acid hydrolyzation [2].

Cellulose, acid hydrolysis was first employed in a commercial plant in Germany in 1898. The last two decades have seen a fleeting advancement in enzyme technologies, hence replacing the acid hydrolysis with enzymatic hydrolysis. For effective conversion to sugars using enzymatic hydrolysis, a pretreatment process is required for removal of contamination.

Recent statistics show an increase in fuel consumption [3]. Economic issues put aside, fossil fuels contribute the most when it comes to environmental degradation. Hence, burning of fossil fuels release various oxides, prominent among them are oxides of nitrogen, Sulphur and carbon. Carbon dioxide is responsible for raising the temperature of Earth by forming an invisible layer in the stratosphere and reflects back the irradiation from the earth's surface. These oxides wouldn't have posed much of a threat and could very easily be controlled if it hadn't been for the various metallic additives embedded in the fuel to increase its burning efficiency. Tetra Ethyl Lead or TEL is an organic compound of lead vastly used as an anti-knocking agent, Lead vapors from the engines exhaust are dispersed into the air and have the potential to cause acute lead poisoning. Another problem is that even low level of lead pollution are highly precarious to health. Apart from lead additives, Tertiary amyl methyl ether (TAME) and Methyl tert-butyl ether (MTBE), are also poisonous and injurious to health. If leaked into nearby water source they will render that water useless for any purpose.

With above arguments, attention was shifted to renewable energy source such as solar, wind, hydel, Geothermal, etc., who by the way have gained popularity in some areas, while in others, unpredictable climate, makes it a nuisance to have an operable setup. Cost is also a major factor that limits the use of these renewable energies since a large group of people cannot afford such costly setups. Therefore, Bio-energy started to gain awareness globally. Bio-ethanol among other sources of bio-energy, has a huge potential of serving, the rising energy demand by

being inexpensive, clean and renewable. Worldwide production of ethanol has escalated since the last decade [4, 5]. 73% of the fermented ethanol was utilized as fuel while the rest was employed for use in beverages. Apart from being used directly as fuel, it also found its way as an additive by replacing MTBE and TAME. It has higher octane boosting abilities than either MTBE or TAME [6]. On top of providing lower carbon dioxide emission, higher octane number, lower dust emission, biodegradable, and renewable, it can either be used purely as fuel or blended with other fuel [7].

The energy demand of the world has been increasing due to an increasing population. Bio-energy being an alternative source for power in its many forms one of which is Bio-Ethanol, has gained popularity globally and production has started all over the world [4,5]. **Figure 1** shows annual production in gallons over the last 8 years.

### Literature Survey

Ethanol, a pure alcohol, commonly known as ethyl alcohol, is a flammable, volatile, and colorless, liquid with a pungent smell. It has a melting point of − 114.1°C, and boils at around 78.5°C. Low freezing point of ethanol, makes it a suitable antifreeze agent for automobile radiators [8] and a temperature sensor. Ethanol properties are given as, in **table 1**. Being ecofriendly it doesn't pose a threat when leaked into water sources. When compared, ethanol's octane boosting properties by far exceed that of either MTBE or TAME. Transportation in various countries including Brazil, have seen a rise in automobiles recruiting pure ethanol or gasoline blended ethanol as a fuel alternative for their engines [9].

### Global Ethanol Production by Country/Region and Year
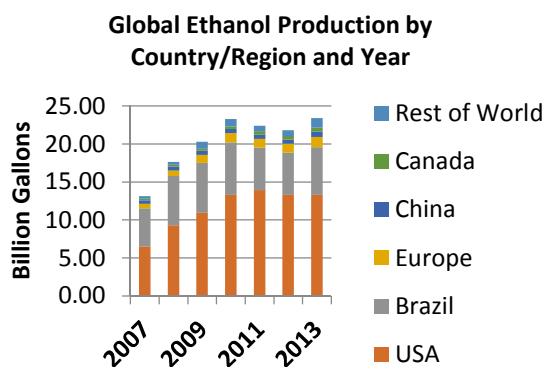


**FIGURE 1: WORLD ETHANOL PRODUCTION**

Although it has partially replaced petroleum derived fuels some of the properties like water solubility, low density and flame luminosity among others, put bio-ethanol at a disadvantage [9]. Potato is a very starchy tuberous crop of the Solanaceae family. Roughly

potato peel waste consists of 58% of dry weight as starch [10] while a potato is composed of 18% starch [11]. Pakistan cultivated about 3,491,800 Tons of potatoes in the year 2011[12]. Approximately 5-20 percentage of the produce is likely to be wasted during potato cultivation while 18 percent of the potato waste is available in the form of peels from potato processing industries [10].

Disposal of potato peels is a major issue of the food industry since normal dumping won't solve the issue and because of the wetness of the peel due to processing, the peels are susceptible to rapid microbial spoilage [13]. Hence the utilization of this waste will result in pollution control, and a valuable energy source leading to reduced environmental pollution due to fossil fuels and such. This also means that bio-ethanol production from inedible raw material will save edible raw materials from being utilized. Apart from fermentation, potato waste can be utilized as animal feed after going through a drying process. But since it is an energy demanding process hence they are utilized for fermentation without having the need to be dried [14].

**Table 1: Properties of Ethanol [8]**

| Molecular Formula | $C_2H_6O$ |
|---|---|
| Density | 0.789 g/cm3 (at 20°C) |
| Melting Point | 159 K |
| Boiling Point | 351.52 K |
| Flash Point | 13–14 °C |
| Auto Ignition Temperature | 363 °C |
| Lethal Dose-50 (LD50) | 5628 mg kg−1 |
| Calorific value (MJ/kg) | 26.9 |
| Stoichiometric air/fuel ratio (kg air/kg fuel) | 9 |
| Lower flammability | 2.06 |
| Higher flammability | 0.3 |
| Motor octane number /research octane number | 89/107 |
| Cetane number | 8 |
| Flame temperature (K) | 2235 |

## 2. Process Selection

There are various processes employed for ethanol fermentation. These include:

### 2.1. *Separate Hydrolysis and Fermentation, SHF*

The SHF is a process capable of producing high yields of ethanol with higher concentration. It is limited by

expensive equipment's, possible chance of contamination, lower yield rates, conversion and concentration than SSF and possible inhibition of glucose.

## 2.2. Simultaneous Saccharification and Fermentation, SSF

After liquefaction of raw material to gelatinized form Saccharification and fermentation are carried side by side in a single tank. Enzymes are added in the tank wherein Saccharification occurs and as soon as glucose is produced it is converted to ethanol and carbon dioxide. This process is characterized by high yield, conversion rate, concentration and purity of the fermented ethanol. The only drawback is that it needs optimized conditions of Saccharification and fermentation to be carried out simultaneously, which is not impossible but difficult to achieve.

Co-fermentation can also be employed to increase ethanol yield by coupling two or more microorganisms. One of the two microorganisms, convert the substrate to glucose and the second one converts it to Ethanol. Apart from microorganism culturing being a problem, the reduction in substrate inhibition/retention time favors SSF over SHF.

## 2.3. Direct Microbial Conversion, DMC

The DMC combines enzyme production, hydrolysis and fermentation, all in a single vessel. Bacteria are employed to breakdown cellulose into hemicellulose and hemicellulose into ethanol. Unfortunately, the bacteria also produce a number of products in addition to ethanol and yields are lower than both SSF and SHF [14].

## 2.4. Continuous Process

Continuous process, which is also known as chemo stat, continuous-flow, or stirred-tank fermentation, employs a fresh sterile media fed into a reactor continuously. In addition to feeding the reactor with fresh nutrients, the effluent is removed from the reactor constantly as to keep the volume of the reactor, constant. The rates of feeding and removing are also equal. To avoid wash-out, which means taking away all the enzyme cells from the reactor, growth rate of the microorganism is chosen as a function of the cell removal rate [14].

Advantages of continuous process over batch fermentation are low construction costs of bioreactors, lower maintenance and operational requirements, higher yield, and a better control of the process [9]. Stability of culture, however, is an issue for continuous fermentation. Even small changes in any of parameters, such as: temperature, dilution rate, substrate concentration of feed, etc., can decrease yield.

With the above arguments in mind, continuous SSF process is selected for maximum conversion of glucose into ethanol using Talaromyces Cellulolyticus as producer micro-organism, and employing very high gravity conditions (VHG conditions). VHG conditions involve the preparation and fermentation of mash containing high dissolved solids (>300 g/L) to yield a high ethanol concentration [15,16]. This is desirable for production of fuel grade ethanol because of its potential to increase throughput of the fermenting tank, and reduce processing costs [16]. Potato peels waste is chosen as the raw material due to being inedible, difficult for industries to properly dispose of and relatively of low cost. Table 2 shows a typical composition of potato peel waste obtained from industries. Amount of raw material was calculated using amount of bio-ethanol required, as basis. Performing back calculations on stoichiometric reactions are used to calculate the material requirement for a 100% efficiency after which the actual amount of materials required are calculated using the actual yield of the process, as described by Shinichi Yano in his paper [17]. **Table 3** gives a general description of the used microorganisms. Using Acremonium Cellulase obtained from Talaromyces Cellulolyticus has advantage over the other microorganism as it directly converts starch to monosaccharides and also reduces the inhibition time of monosaccharides, which results in an increase in ethanol yield.

**Table 4** presents a couple of reactions involved in the process.

**Table 2: Typical composition of Potato Peels [18]**

| Parameters | % dry weight |
|---|---|
| Moisture | 85.06 |
| Nitrogen | 1.3 |
| Protein | 8.0 |
| Total Soluble Sugars | 1.0 |
| Total Carbohydrates | 58.7 |
| Reducing Sugars | 0.61 |
| Fat | 2.6 |
| Ash | 6.34 |

**Table 3: Properties of Microorganisms used [13]**

| Component | Characteristic | Volume |
|---|---|---|
| Acremonium Cellulase | Powder form and retains the characteristics of water | The same volume as would be occupied by Water having the same mass as the enzyme. |
| Baker's Yeast, Saccharomyces Cerevisiae | Solid form | Volume based on density of the micro-organism |

**Table 4: Reactions and Conditions involved**

| Process | Reaction | Conditions |
|---|---|---|
| **Saccharification** | $C_{12}H_{22}O_{11} + H_2O ---\rightarrow 2\ C_6H_{12}O_6$ | Temperature: $37^0 C$<br>Pressure: Atmospheric pressure<br>Retention time: 23 hrs.<br>Enzyme: Acremonium Cellulase<br>Microorganism: Talaromyces Cellulolyticus |
| **Fermentation** | $2\ C_6H_{12}O_6 ---\rightarrow 4\ C_2H_5OH + 4\ CO_2$ | Temperature: $37^0 C$<br>Pressure: Atmospheric pressure<br>Retention time: 4 Days<br>Enzyme: Zymase<br>Microorganism: Saccharomyces cerevisiae |

## 4. Process Description

The process taking place can be placed in 5 steps as follows:

1) Pre-treatment
2) Simultaneous Saccharification and Fermentation
3) Centrifugation
4) Distillation
5) Per-vaporation

### 4.1. Pre-treatment

Raw material containing starch based feedstock has to be treated prior to the fermentation process. Potato peels or potato tuber waste as used and required are to be washed prior to fermentation to remove dirt and gravel from the raw material. However, a mashing unit is also to be considered if potato tuber waste is used as raw material. Mashing is carried out to increase surface area of the tuber for ease of fermentation. After the necessary pretreatment is carried out, the pretreated raw material is sent to the SSF reactor for the actual process to begin.

### 4.2. Simultaneous Saccharification and Fermentation

Potato waste enters the reactor along with water. There are two steps taking place inside the reactor:

A) *Gelatinization:* Raw material will be treated, with water at a temperature of 65° C, for 23 hours.

Water vapors at 65°C and atmospheric pressure will rise and condense on the surface of the raw material. Gelatinization occurs as starch molecules are broken down into low molecular weight dextrins. After 23 hours the process is stopped the temperature is dropped to SSF temperature by means of cool air.

B) *SSF*: After gelatinization Acremonium Cellulase and Baker's Yeast are added inside the reactor to start the fermentation process. This is the main step of the process and requires a lot of monitoring. Monitoring include controlling variables like temperature, pH, pressure, foaming etc. Cellulase breaks down the dextrins in the mash into low weight mono-sugars which are then simultaneously converted to ethanol by the action of Saccharomyces Cerevisiae, a yeast strain. Conversion takes place at a temperature of 37° Celsius for maximum Ethanol yield. Also it is necessary to maintain a pH of 5.5 inside the reactor for maximum growth of yeast cells. The SSF process is carried out for a time period of 4 days. The process is batch and unaerated.

### 4.3. Centrifugation

After fermentation period is over, the product mixture containing unhydrolyzed material, ethanol product, enzyme solution, yeast cells and under 1% of by-product, undergo centrifugation. Unconverted solid

potato waste is removed and starch and yeast get converted into pellet form and passed along with Ethanol, enzyme solution and unconverted liquid glucose for distillation.

**Table 5** shows the raw material amount for stoichiometric and actual calculations for the process.

**Table 5: Stoichiometric, Basis Calculations for 100% process efficiency, Basis Calculations for Actual Yield, and Enzyme Calculations.**

| Components | 100% conversion | % Actual conversion | 100% conversion | Actual Conversion | Unreacted |
|---|---|---|---|---|---|
| | Stoichiometric Requirement | | Basis requirement | Basis requirement | |
| Starch | 324 | 68.7 | 176.0869565 | 256.3128916 | 80.225935 |
| Total Water | 36 | - | 19.56521739 | 28.47921018 | 8.9139928 |
| Glucose | 360 | 90 | 195.6521739 | 217.3913043 | 21.73913 |
| Carbon Dioxide | 174 | - | 94.56521739 | 94.56521739 | - |
| Ethanol | 184 | - | 100 | 100 | - |
| Potato peels | 551.9591141 | - | 299.9777794 | 436.6488783 | - |
| ***Basis: 100 Kg Ethanol*** | | | | | |
| **Enzyme** | 14.55496261 | | Standard Dosage of Cellulase is 10 FPU/g of biomass | | |
| **Yeast** | 8.732977567 | | 1 g of Cellulase equals 300 FPU | | |

### 4.4. Distillation

Distillation can either be continuous or batch depending on the scale of production. A batch distillation can be used where annual ethanol production is less than 100000 Liters'. In batch system the product from centrifuge, is fed to a large vessel, which is then heated. Vapor formation takes place and are passed into the distillation column. Ethanol in the product is obtainable up to 95% pure after which it forms an azeotropic mixture in water.

### 4.5. Per-vaporation

Fuel grade Ethanol requires high purity content, hence it is required that ethanol have a purity of as high as 99% and not a percent lower. This is where membrane technology comes in handy. Ethanol water azeotrope is charged into the pervaporation module for a membrane based separation. The product is a 99% pure ethanol ready to be used as a bio-fuel.

**Figure 2** shows a proposed process flow sheet for the selected process. The sheet is designed keeping in mind the process constraints.
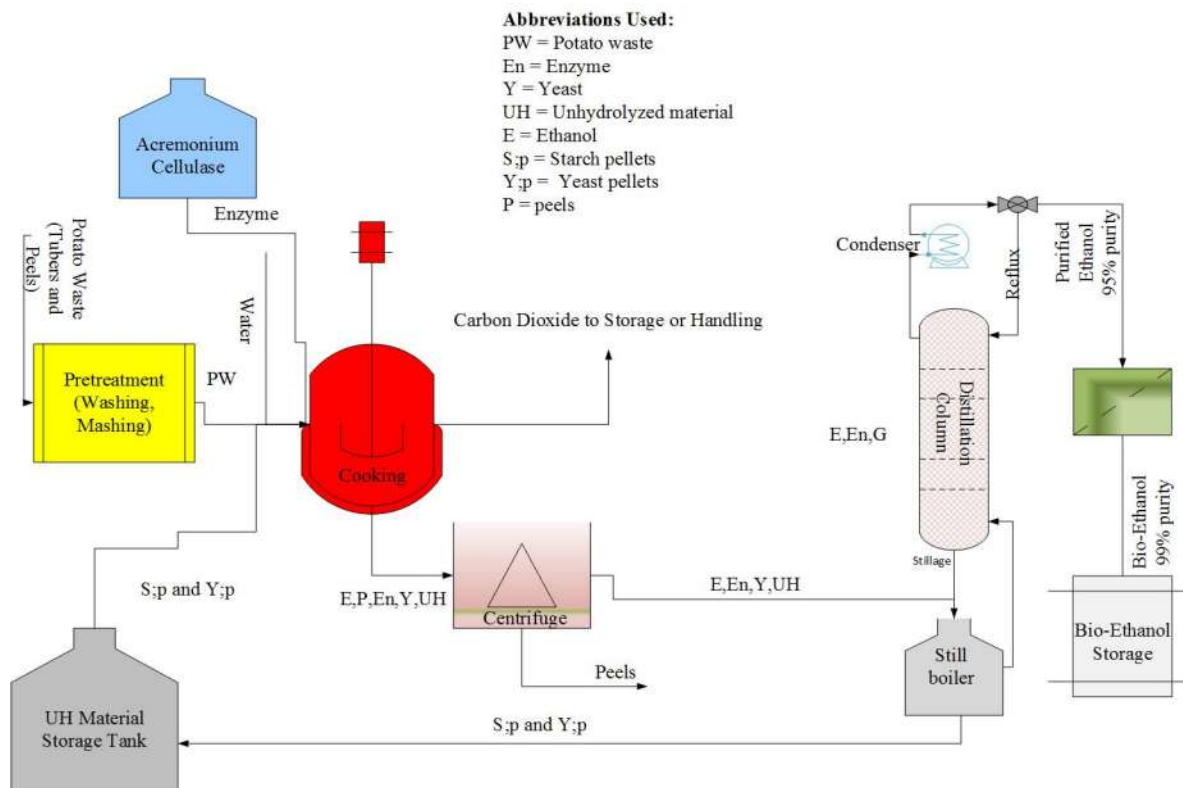
**Figure 2: Proposed Process Flow Sheet generated using Visio**

## 5. Conclusions

The main aim of the research is to establish a Process design, for the production of Bio-Ethanol. Potato peels are available as feed material, in large quantities across the world, can be used starting of course with a small scale unit in Pakistan. The research focuses on proposing an entire Bio-Ethanol manufacturing process for a small scale production.

Future works on the research can focus on giving a theoretical design using knowledge of Plant design and Simulation. Future recommendations might include:

i. using an external nitrogen source to boost ethanol yield by increasing yeast production in the fermenter.

ii. Performing a Hazop and Economic analysis based on the plant design, to calculate economic feasibility of the plant.

iii. Trying to adopt a continuous process, by employing a membrane bioreactor, by reducing the factors that prevents its employment for Bio-Ethanol manufacturing.

## References:

[1]    Balat, M.; Balat, H.; Oz, C. Progress in bioethanol processing. *Prog. Energ. Combust.* **2008**, *34*, 551–573.

[2]    Braconnot, H. Annalen der Physik. 1819, 63, 348.

[3]    Pakistan Exports, Imports and Trade, 29th March 2010, The Nation. Available at www.economywatch.com/world_economy/pakistan/export-import. Accessed on 19th October 2014.

[4]    F.O.Lichts World Ethanol and Biofuels. Available at: www.worldethanolandbiofuel.com/. Accessed on 19th October 2014

[5]    Woodson, M. and and C. J. Jablonowski. 2008. An economic assessment of traditional and cellulosic ethanol technologies. *Energy Sources, Part B* 3:372–383, 2008.

[6]    Reimelt, S., F. Winkler, K. Mogel, and M. Kirchhof. 2002. Bioethanol technology of Lurgi Life Sciences. *Zuckerindustrie. Sugar Industry* 127(10): 770-781.

[7]    Pakistan Exports, Imports and Trade, 29th March 2010, The Nation. Available at: www.economywatch.com/world_economy/pakistan/export-import. Accessed on 19th October 2014

[8]    Shakhashiri, B.Z. 2009. Chemical of the week: Ethanol. Available at:

scifun.chem.wisc.edu/CHEMWEEK/PDF/Ethanol.pdf Accessed on 15th November 2014.

[9]  Sanchez O.J. and Carlos A. Cardona. 2008. Trends in biotechnological production of fuel ethanol from different feedstock. *Bioresource Technology* 99(13) : 5270-5295

[10] C. Israilides, A. G. Vlyssides, D. Arapoglou, R. Marchant, and A.A.Vlysides, "Integrated Management Of Potato Starch Wastes," September 2008, pp. 16–17.

[11] Ushikubo, A. Present state of food wastes and countermeasures for Food Recycling Act. Available at: mie.lin.go.jp/summary/recycle/recycle. (in Japanese). Accessed on 22nd November 2014.

[12] Potato Statistical Yearbook. Available at: nationalpotatocouncil.org/2014-potato-statistical-yearbook. Accessed on 20th October 2014.

[13] Frank R. C., Sergio V. B., Harry R., Industrial Uses of Biomass Energy: The Example of Brazil, 13th Sept 2000, Science, pp. 233-234

[14] S. Andreas, Marleny D. A. S. , Potato Peels: A source of Nutritionally and Pharmacologically Interesting Compounds-A Review, Global Science Books, pp. 1-3.

[15] Thomas KC, Hynes SH, Jones AM, Ingledew WM. Production of fuel alcohol from wheat by VHG technology: effect of sugar concentration and fermentation temperature. Appl Biochem Biotechnol 1993;43:211–26.

[16] Thomas KC, Hynes SJ, Ingledew WM. Practical and theoretical considerations in the production of high concentrations of alcohol by fermentation. Process Biochem 1996;31:321–31

[17] Shinichi Yano et al. Production of ethanol from potato pulp: Investigation of the role of the enzyme from Acremonium Cellulolyticus in conversion of potato pulp into ethanol. Process Biochemistry 47 (2012) 2110–2115

[18] Ushikubo, A., Present state of food wastes and countermeasures for Food Recycling Act. Available at mie.lin.go.jp/summary/recycle/recycle. (in Japanese). Accessed on 22nd November 2014

# Exploring Energy Output Using Bioelectrochemical Cell

## Madiha Qayyum[1]*, Dr. Naeem Arbab[2]

[1]United States Pakistan Centre for Advanced Study in Energy, University of Engineering & Technology Peshawar, Pakistan
[2]Department of Electrical Engineering University of Engineering & Technology Peshawar, Pakistan
[1]*Corresponding Author.
Email: madiha_qayum@yahoo.com

## ABSTRACT

It is new and novel approach that blends interdisciplinary research work. There is worldwide shortage of energy. Energy Demand exceeds energy consumption and resources are depleting rapidly. Extracting energy by conventional means has already been saturated. The foresaid research is a way to reduce electricity costs by making efficient on site hybrid electricity production unit. It imparts excellent way to combine solar technology with natural plants material to yield electricity. A Bio electrochemical cell was assembled and tested in both laboratory and field setup using simple approach that can be duplicated by the people everywhere. The technical knowledge opted in this paper is the applied concept that plants absorb light, and yield excited electrons as a by-product during photosynthesis, which in succession produces voltage across the anode and cathode of the cell. The chlorophyll regains its lost electron with reversible redox reaction. This work utilized three different light sources: red and blue fluorescent lamps and the sunlight; each having different wavelengths in visible spectrum range. The voltages and currents measured from each specie were individually reported. The photo electrochemical parameter for solar cell by using the said material depicted maximum open circuit voltage (Voc) of 1.01 V. Cells made from local flora were discretely experimented on, and results depicted that all such species carry potential to yield reasonable quantity of electrons. This is because their energy band requirement is minimum enabling the maximum release of electrons when illuminated. The photosynthetic bio cell is very appealing because the materials needed are not only readily available but also cheap. In this laboratory work, efficiency evaluation observed was very good for the said cell.

**Key Words:** *Bioelectrochemical cell, Photosynthesis, spinacia oleracea, voltage, chlorophyll.*

## 1 INTRODUCTION

The foresaid research is a way to reduce electricity costs by making efficient on site hybrid electricity production unit. It imparts excellent way to combine solar technology with natural plants material to yield electricity.

Like silicon cells use solar energy, similarly photosynthetic organisms use sunlight to make their food. Simultaneously an electron is emitted as a byproduct from chlorophyll (a green pigment found in plants, responsible for an electron emission[1] This emitted electron can be captured by different techniques to be made available as electricity in the form of bio cell or battery.[2] A plug in gadget equipped with on site electron extraction can be attached to photosynthetic material anytime, anywhere to get electricity. The prime objective of the research is to make prototype of bio cell with comprehension of photosynthesis phenomenon. The reduction of nano electrodes[3] to macro sized electrodes has also to be achieved along with quest for efficient electrode material in this study.The proposed research is about designing of Photosynthetic bio electrochemical cells with certain desirable features[4]. As opposed to a normal battery, photosynthetic electrochemical cells use renewable form of energy and do not need to be recharged. In addition to this, they can operate well in mild conditions, varying temperatures from 20 °C to 40 °C and

also at variable range of pH. Its working mechanism is as follows.

## 1.1 PHOTOSYNTHESIS:

"Photosynthesis is the process by which plants convert sunlight to chemical energy". This chemical energy is prime focus of our research to be coverted to electrical energy. Chlorophyll found in green plants and chromoplast in fruits absorbs sunlight and turn carbon dioxide (from air) and water (from roots) into glucose and oxygen inside plants.[5]

There are many ways to convert this energy from Natural photosynthesis phenomenon to electricity, such as when photosynthetic organisms/plants consume a substance for e.g. glucose in presence of oxygen, they produce carbon dioxide and water. However, in absence of oxygen, they produce CO2, protons, and electrons, as described by equation [1] where "*e*"stands for electrons.

$$C_6H_{12}O_6 + H_2O + CO_2 = O_2 + H_2O + e^- \qquad (1)$$
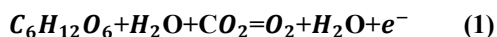
The solar energy, now converted to chemical energy, is stored in the bonds of sugars and polysaccharides that plants use for food. This process takes place in chloroplasts; the chloroplasts are also called power houses for energy [6] .Here water is broken down into oxygen and electrons. Sunlight gets absorbed in the chloroplast and raises the electrons to a high energy level, and a protein captures them to more higher energy level. These electrons are passed down a series of proteins (thykoloids), which successively capture more and more of the electrons' energy to synthesize sugars until all the electrons' energy is spent[7]. But instead of giving electron's energy to those proteins, we can divert its path and can make electrons available for our usage as electricity. Final version of this resembles single chamber Salt battery or electrochemical (galvanic) cell without proton exchange membrane with two different electrodes and photosynthetic material as electrolyte.

### 1.1.1 LITERATURE REVIEW:

The other existing technologies employs inorganic mediating agents (catalysts) to get inside electron transport chain of cells fastly and make paths for electrons produced[8]. The mediating agent crosses bacterial outer membrane; then it makes electrons free from electron transport chain which finally are taken up by oxygen .Then this reduced mediating with electrons is transferred to an electrode where it deposits electrons so this electrode becomes the negatively charged electrode. This cycle is repeated and mediating agent goes back to chlorophyll. It can happen only in presence of oxygen; if oxygen is present, it will attract and recombine with all the electrons, because it is more electronegative than mediating agents. This is the main theme or principle behind generating electrons flow from photosynthetic organisms. To turn this process into usable supply of electricity, it is recommended to accommodate this assembly into normal salt battery like structure and complete the circuitry by connecting external wire between electrodes.[9].This novel approach blends interdisciplinary research work of electrical engineering, biology and electrochemistry and also solar energy [10]. A rough comparison of current solar cell cost and efficiency of current technologies is summarised in the graph below.



**Graph1: Comparison of solar cell price (Rough estimate).**

Photosynthetic bio e-cell has a promising future but certain improvements are needed to make it practical for long term performance like replacement of expensive gold nano electrodes[11,12] with cost effective macro sized electrode

and search of photosynthetic material that do not die out within an hour and produces high energy yields to make it economically viable solution[13,14] and also quest for alternative techniques at hand thus rejecting dependency on foreign technology. These features have been researched out here extensively and rigorously to lower the per unit price. Such cells have variety of potential uses. The most readily apparent is tranducing electricity for use as a free energy source. The use of bio-electrochemical cell is appealing for applications that require only low power but where replacing batteries may be time-consuming and expensive such as wireless sensor networks. Virtually any photosynthetic material whether eukaryote or prokaryote can be used to feed such solar cell.[15].It means we can virtually make electricity while travelling by roads and trees coupled with ease and lowest possible cost.

Efficiency enhancing techniques like absorption of certain wavelengths of sunlight to increase photosynthesis rate thus enhancing electricity are quite useful in multiplying electrical energy output.This is the first step towards the final launch of the sustainable product, which is to be covered in the future work.

The hypothesis is addressed in this research paper is question that if electrons are emitted during photosynthesis, can they be indigenously utilized in practical situations with economical setup. If yes then how to overcome potential obstacles such as expensive gold nano size electrodes to macro size structure as used in previous work by others [16] and reduction of high internal resistance. Future work demands a good trade off between efficiency and high cost.

## 2 Materials & Method

### 2.1 Materials

Keithley 2410 Source meter, Digital Voltmeter,Any photosynthetic material like grass, Spinacia oleracea, Allium Cepa, Allium Sativum . Malus domestica, Capsicum, Lycopersicon Esculentum ,living plants,and distilled water.

Blue and Red electric lamps. Conducting wires, Metallic Nails,Different Alloyed Electrodes, Glass Tubes or small containers.

### 2.2 Preparation of a Spinach Extract

One-half bag *of spinacia oleracea* (supermarket spinach leaves) was placed in a commercial blender with about 50 mL of distilled water and grounded thoroughly for 5-10 minutes until all of the leaves were blended. The result was dark green paste containing large amount of chlorophyll.
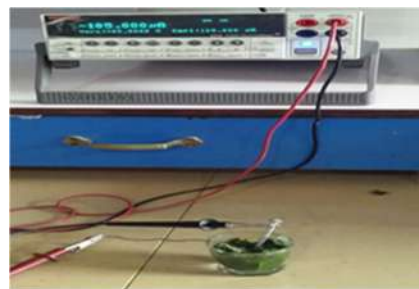


**Figure 1. Amperage of Spinacea Oleracia using Ketheley Source Meter**

### 2.3 Fabrication of Photosynthetic solar cell

There are two modes of its construction.

### 2.3.1 Solid Mode:

Take one specie for example living tree or citrus limon and insert two different electrodes in it. Tie conducting wires to the electrodes and measure voltage in parallel and current in series using digital meter .Alternatively one electrode wire(red) and ground probe(black) of voltmeter can be inserted into green leaves ,flowers, fruits or shoots of living pot plant or garden plant as shown in Fig.2



**Figure 2. Reasonable Voltage from Living Plant.**

## 2.3.2. Semi liquid Mode:

This green paste made earlier was then placed in glass tube upto three fourth part to avoid any leakage of the mixture. Alternatively this material could be placed in container of virtually any size and material. Two ordinary conducting wires (electrodes) of different metals (iron nail and zinc copper nickel alloy/copper) were dipped in the dark green photosynthetic mixture. This is basic and the most simple design of Bio cell and can be functional even with 2cm cubic amount of the photosynthetic electrolyte paste each on both electrodes. More than this amount of electrolytic area just depicts the same results however inter electrode position and distance do matter and varying results can be seen. Open circuit voltage was measured directly between these two electrode terminals using digital multimeter as shown below.



**Figure 3: Bio E-Cell in Cascade Setup**

## 3 Results & Discussions

### 3.1 I-V Curve

Unlike typical solar cell ,its voltage versus current graph using ketheley source meter depicted linear straight line from -10 to +10 voltage source with 0.5 compliance range. This means that the photosynthetic material is internally shorted and behaves as pure resistance. Some noise was also obsereved in the IV curve
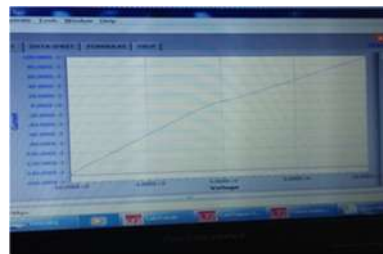


**Figure 4. IV Curve**

### 3.2 Measurements using Digital Multimeter

Single cell of spinacia oleracea paste depicted maximum of 0.68 volts of open circuit voltage and 498 micro amperes of short circuit current in cascade setup under ambient temperature and pressure condition and normal day light. Almost same results were obtained from other photosynthetic materials in light and dark. Good results depend on numbers of factors like plant health, electrode material and size, amount of time period passed , amount of light irradiance and wavelength of light. Greater the electrode surface, higher the voltage. Also longer the wire length, lesser will be the current.

Electrode material affects the results for instance Aurum is more conductive than copper consequently it would have lesser voltage drops in wire consequently output will be high . Chlorophyll absorbs blue and red light [17] and the cell efficiency was raised when photosynthetic electrolyte exposed to such wavelengths in natural setup[18]. More over connecting Bio electrochemical cell in series with different electrode material enhances the voltage output to double ,triple, quadruple and so on while joining them in parallel increases electric current from micro ampere to milli ampere and above ranges so it can be optimized and utilized in practical small scale application as per need and demand.

**Table 1: Output Comparison of Different Species using Cu and CuZnNi Alloy Electrodes**

| Photosynthetic Material | Max.Short circuit current (μA) | Open circuit voltage (Max) |
|---|---|---|
| Grass | 68 | 0.49 |
| Spinacia oleracea | 498 | 0.68 |
| Capsicum | 60 | 0.95 |
| SolanumTuberosum | 164 | 0.94 |
| Allium Sativum | 125 | 0.92 |
| Zingibir officinale | 50 | 0.86 |
| Rotten Musa | 302 | 0.8 V |
| Malus domestica | 89 | 1.01 |
| Allium cepa | 192 | 0.95 |
| Living plant | 69 | 0.88 V |

## 4 Conclusions

Green energy from renewable natural sources like fully grown solid parts of eukaryotic plants ( such as fresh or rotten green leaves, shoots, grass, fruits, vegetables and leftover peel of them after being cut from tree) and grinded paste of such photosynthetic parts is capable of producing electricity(Fig. 4). Similarly a living indoor or outdoor plant can lighten up LEDs and other low amperage devices like calculator, clock and sensors up to minimum of 76 hours and maximum up to whole plant life under ambient conditions by utilizing series and parallel combinations of Bio electrochemical cells as per need without hampering the plant growth. This acts as free energy source as well as producing oxygen and fruits(if any) as by products under light and dark conditions. Floral or vegetative waste parts which are left unused can also be used as whole or grinded. Although there is need to make this setup more sustainable in future endeavours ,at present, growing plants on domestic or large scale as raw material for Bioelectrochemical cell, creating such awareness and its commercialisation by stepping up the dc voltage via buck boost converters is recommended in order to extract on site electricity production at homes and offices. It would not only reduce electricity bills but also transmission and distribution costs from generating stations would be minimum.

## References

[1] Y. Houman, Bio-Photoelectrochemical Solar Cells Incorporating Reaction Center and ReactionCenter Plus Light Harvesting Complexes:Graduate thesis and dissertations, 9( 2015), *5803-6115.*

[2] L. Peter, Lindberg, O.Pia, S. Paulo, H. Karin , Design, engineering, and construction of photosynthetic microbial cell factories for renewable solar fuel production:Ambio,41(2012), 163-168

[3] G. Iwona , M. John, I. Chris, Self-sustainable electricity production from algae grown in a microbial fuel cell system: Biomass and Bioenergy, 82(2015), 87-93

[4] S. Keise , H. Shota, K. Yasuyukii, S.Yuki , M. Osamui, O. Makoto, Improvement of a direct electron transfer-type fructose/dioxygen biofuel cell with a substrate-modified biocathode: PCCP,16(2014), 4823-4829.

[5] D. S, H.Terlouv, H. Hamelers, C. J N, Renewable sustainable biocatalyzed electricity production in a photosynthetic algal microbial fuel cell (PAMFC): Applied Microbiology and Biotechnology, 81(2008) , 659-668

[6] **C.**Gonzalez , P.Araceli, C.Jose , R.Pablo, F.Manuel , J.Francisco, Characterization of light/dark cycle and long-term performance test in a photosynthetic ,microbial fuel cell,FUEL,140(2015) , 209-216.

[7] L, B.Kien , C.Eric , L.Mu, A MEMS photosynthetic electrochemical cell powered by subcellular plant photosystems : Journal of Microelectromechanical Systems,15(2006), 1243-1250.

[8] L.Washington , Bioelectricity generation from fruits and vegetables waste by using single chamber microbial fuel cells with high Andean soils : EnergyProcedia ICAE 75(2015), 2009-2014.

[9] Y. Cetinkaya, O.Bestami , T.Ergin, K.Dogan C.Mehmet ,The production of electricity from dual-chambered microbial fuel cell fueled by old age leachate: Energy Sources, Part A: Recovery, Utilization, and Environmental Effects, 38(2016), 1544-1552

[10] M.Rosenbaum, H.Zhen, A.Largus, Light energy to bioelectricity- photosynthetic microbial fuel cells: Current Opinion in Biotechnology,21(2010), 259-264.

[11] M. Shahparnia, Mehdi ,Polymer Micro Photosynthetic Power Cell: Design, Fabrication, Parametric Study and Testing : Masters Thesis, 7(2011), 1-589

[12] M.Thirumal , M. Shobhan , M.Abhishek , Study and Analysis of Dye Sensitized Solar Cells: International Journal of Modern Engineering Research (IJMER), 5( 2012) .3597-3601

[13] ] R. Syafinara*, N. Gomesha, M. Irwantoa, M. Fareqa, Y.M. Irwana, Chlorophyll Pigments as Nature Based Dye forDye-Sensitized Solar Cell (DSSC) : Energy Procedia 79( 2015) ,109-119.

[14] B.Aakash , A.Ali , Y.Sachin , R. Pratibha , SPINACH AND BEETROOT EXTRACTS AS SENSITIZERS FOR ZnO BASED DSSC: International Journal OF Engineering Sciences & Management Research ,5(2015), 897-908.

[15] K. Ishara , J.Bharat , G.John , K.. Lakshmi , Elucidating the design principles of photosynthetic electron-transferproteins by site-directed spin labeling EPR spectroscopy :Biochimica et Biophysica Acta, 1857 (2016) 548–556.

[16] YC.Dennis, Wu.Leung, M.K.H.Xuan Wu, A review on biodiesel production using catalyzed transesterification: Applied Energy 87(2010) 1083–10.

[17] Y. Hubenova, M. Mitov, Conversion of solar energy into electricity by using duckweed in Direct Photosynthetic Plant Fuel Cell :Bioelectrochemistry, 87(2012),185-191.

[18] Lam, B .Kien , A. EriC ,L. Liwei, A bio-solar cell powered by sub-cellular plant photosystems: IEEE, 15(2004) ,1243-1250.

# Upgradation of Mianwalli Coal using Froth Flotation and Hydrochloric Acid Leaching

*Zahid Ghulam Rasool, Fatima Sajid Khurram Shahzad\*, Javaid Akhtar, Shahid Munir*
*Center for Coal Technology, University of the Punjab*
*\*Khurram Shahzad*
*Email: khurram.cct@pu.edu.pk*

**Abstract:** Mianwalli coal was upgraded using flotation process followed by acid leaching. For flotation test, test conditions such as pH (7, 8, 9, 10, 11), impeller speed (1000, 1100, 1200, 1300, 1400 rpm), solids in pulp (15, 20, 25, 30, 35 %) and particle size {(-105, +127 μm) (-127, +149 μm) (-149, +199 μm) (-199, +250 μm)} were used to optimize the results. By flotation the total carbon content increased from 44.32 to 68.3% (54.1 % increases), ash content reduced from 35.2 to 25% (28.9% reduction) and sulfur content reduced from 6.3 to 4.2% (33.4% reduction). Leaching tests on flotation concentrate were carried out to further improve the grade of coal. Test conditions for leaching were: acid concentration v/v (10, 15, 20, 25, 30 %), leaching time (30, 45, 60, 75, 90 minutes), stirring rate (0,250, 500, 750, 1000 rpm) and temperature (30, 45, 60, 75,90ºC). Under optimum leaching conditions further reduction of59.76 % in sulfur content and 39.2 % in ash content was speculated by hydrochloric acid leaching. The overall reduction in sulfur and ash contents was 57.6 % and 42.6 %. The clean coal thus obtained, contains 20.2% ash content and 2.65% total sulfur content and the coal is suitable as fuel for cement industry and power plants for electricity production.

**Key words**: Coal Desulfurization, Combination

Technology, Demineralization of Coal, froth flotation

and  Acid Leaching.

## 1      Introduction

Due to growing concerns for energy security and day to day fluctuation in oil prices, coal has attained special significance. World trade of coal is expected to increase about 40%, from 800 million tons in 2007 to 1122 million tons in 2030[1].Coal as an indigenously available resource and world's fastest emerging fuel has a strategic importance. Many countries in the world, recognizing importance of coal have switched over to coal to encounter their energy needs. India, Indonesia, Germany, USA, Australia and UK are among those countries that have embarked upon new coal based power plants[2].

Coal usually contains significant amount of different impurities such as sulfur, silicates, and carbonates. These undesirable components cause harmful effects on humans, animals, agricultural products and global environment. Therefore, it is essential to reduce sulfur and mineral matter from coal prior to usage in many applications[3]. The removal of sulfur from coal is complicated due to the complex occurrence of sulfur as sulfates, inorganic sulfides, and a wide range of organic compounds, and in some cases even as elemental sulfur. Demineralization and desulfurization of coal may be achieved by both physical and chemical methods. Physical methods are cost effective but not effective in separation of finely dispersed minerals and those bound to coal structure chemically[4]. Up to 50% of inorganic sulfur can be removed by froth flotation process. Leaching is one of the most common methods employed for coal desulfurization[5]. [6]  Worked out on the desulfurization of Mequinenza coal by leaching alone with nitric acid. Results showed the removal of inorganic sulfur was significant.[7] Investigated the flotation of coal which was followed by leaching of flotation concentrate with potassium hydroxide and methanol. Total sulfur and ash from its original value was reduced 82.50% and 82.34 % respectively by the use of combination technique. [8] Studied the combination technique of flotation and leaching on Tubas mezino coal with nitric acid. Its total sulfur and ash contents from its original value were reduced approximately to 75.4 and 53.2 % respectively. [9]Investigated the effect of flotation followed by leaching with sodium hydroxide on Hazro, Turkey coal. Using combination technique, total sulfur, ash and volatile matter contents from its original value were reduced to 88.06%, 63.13% and 77.32%, respectively. It is obvious that a combination of two different desulfurization processes can give better cleaning results than a single type of desulfurization process. Combination technique can give the synergistic effect in which the product quality is much higher than with either process alone. This is possible because the types of sulfur bearing particle that cannot be affected by one process can be readily removed by the another process This is particularly true of combination of processes based on physical properties (froth flotation) with processes based on chemical

properties (chemical leaching)[10]. Objective of this study is to achieve maximum reduction in sulfur and ash with the froth flotation followed by HCL leaching. This is achieved by simultaneously exploiting physical and chemical properties of Mianwalli coal to be used in the local power plants and other industries.

## 2        Materials and Methodology

Bulk coal sample from Mianwalli mine, Punjab Pakistan was crushed and ground up to 250 micron. Then sieve analysis, quartering and coning process of bulk sample was done according to ASTM standard procedure to obtain a representative sample. Proximate analysis as per ASTM D 3173-75, determination of total carbon, sulfur as per ASTM D5016 and GCV as per ASTM D5865 were carried out. Results are reported in Table 1. Froth flotation was carried out as per ASTM D5114[11] using oleic acid as collector [5 drops (500mg/kg coal)] and pine oil as frother [2-3 drops (250mg/kg coal)][12]. Different conditions of pH (7, 8, 9, 10, 11), Rotor speed (1000, 1100, 1200, 1300, 1400) rpm, Solid in pulp (15, 20, 25, 30, 35) % and Particle size {(-105, +127 μm) (-127, +149 μm) (-149, +199 μm) (-199, +250 μm)} were used to optimize the results. Then at optimum parameters, coal sample of (-149, +199 μm) was subjected to flotation process at ph. 7, agitation 1200 rpm and solid in pulp 20 %. The flotation machine consist of a separate container (or cell which carries flotation pulp) and an impeller fitted with electric motor to rotate impeller it controls the speed of impeller. The impeller has two parts, rotor which rotates in pulp and a stator which does not rotate but protects the turbulent action of rotor. At the middle air inlet is present through which the air is introduced in the pulp. Flotation concentrate was then dried, weighed and analyzed. Results are reported in Table2. Nitric acid was used to leach the floated coal for ultimate removal of ash and sulfur content of coal. Effect of acid concentration (10, 15, 20, 25, 30 %), leaching time (30, 45, 60, 75, 90 minutes), stirring rate (0, 250, 500, 750, 1000 rpm) and temperature (30, 45, 60, 75, 90oC) were studied as major parameters. For single experiment of leaching, 5g of coal concentrate was taken in three neck flask in which 250ml of nitric acid was added as leachant. The reaction temperature was constantly monitored. Agitation in flask was done by magnetic stirrer. After leaching process the leached coal (obtained from the optimum parameters i.e.,30% acid concentration, 90 minutes leaching time, 1000rpm stirring rate and 90oC temperature) was

dried, weighed and analyzed. Results are reported in Table3. The findings of this investigation indicated that acid concentration with a high contribution had the most dominant effect on desulfurization process followed by temperature, stirring speed and time

**TABLE 1:** PROXIMATE & TOTAL CARBON/SULFUR

ANALYSIS (AS RECEIVED BASIS)

| Total Moisture % | Volatile Matter % | Ash % | Fixed Carbon % | Total Sulfur % | Total Carbon % |
|---|---|---|---|---|---|
| 8.8 | 30 | 35.2 | 26 | 6.3 | 44.32 |

## 2        Results and Discussion

### 2.1        *Optimization of Froth Flotation Parameters*
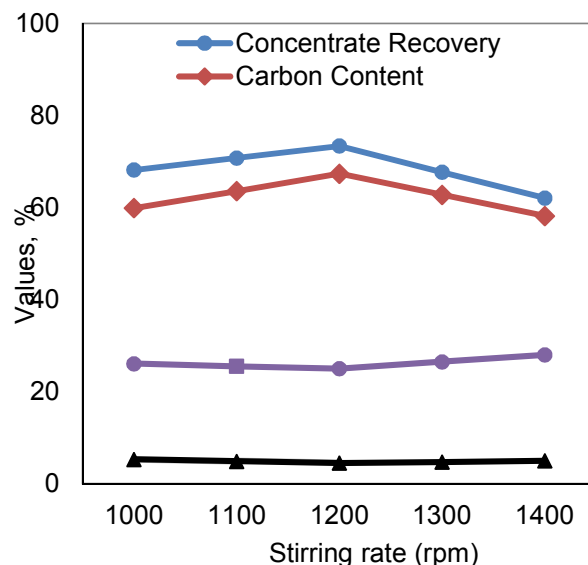


**FIGURE 1:** EFFECT OF STIRRING RATE ON PERCENTAGE RECOVERY, CARBON, ASH AND SULFUR

Figure 1 shows the effect of stirring rate on percentage recovery, carbon sulfur and ash while keeping other parameters fixed such as 7 pH , -149, +199 μm particle size  and 20% solids in pulp. It was evident from the results that for 1000,1100, 1200, 1300  and 1400 rpm stirring rate percentage recovery of flotation varied from 68.2, 70.8, 73.4, 67.7 and 62.1 %, carbon varied from 59.9, 63.6, 67.4, 62.8 and 58.2 %, ash varied

from 26.1, 25.5, 25, 26.5 and 28 % and sulfur varied from 5.3, 4.9, 4.5, 4.7 and 5 % respectively. Percentage of Sulfur and ash was minimum at 1200 rpm whereas recovery and carbon was found to be maximum. The lower values of % recovery, %carbon and higher values of %ash and %sulfur at lower rpm could be due to less agitation resulting ineffective separation of minerals and coal particles. Whereas at higher rpm shear agitation has been observed in the flotation cell yielding air bubbles bursting out causing a decrease in flotation recovery and increase in % ash and % sulfur was an indication of an entrainment of mineral particles due to higher agitation speed at higher rpm. For the parameters, under investigation, 1200 rpm was found to be the optimum.
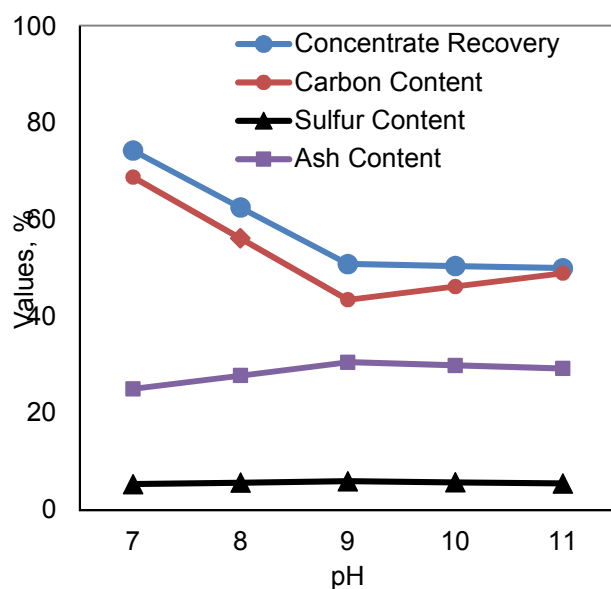


**FIGURE 2:** EFFECT OF pH ON PERCENTAGE RECOVERY, CARBON, ASH AND SULFUR

Figure 2 shows the effect of pH on percentage recovery, carbon, sulfur and ash contents while keeping other parameters fixed such as 1200 stirring rate , -149, +199 µm particle size  and 20% solids in pulp. It was evident from the figure that for pH 7, 8, 9, 10 and 11, percentage recovery of flotation varied from74.3, 62.5, 50.83, 50.4 And 49.97 %, carbon varied from 68.8, 56.12, 43.44, 46.19and 48.94 %, ash varied from 25, 27.75, 30.5, 29.86 and 29.23 % and sulfur varied from 5.3, 5.6, 5.9, 5.66 and 5.42% respectively. Percentage of Sulfur and ash was minimum at 7 pH whereas recovery and carbon was found to be maximum. A pH below 7 was not selected for the study due to the fact that pyrite may become floatable, because under acidic conditions the iron sulfate dissolves, leaving only the hydrophobic

elemental sulfur on the surface. It was found from experimental results that at pH 7, % sulfur reduced from 6.3% (table 1) to 5.3% and % recovery was also found to be decreased. For the set of experiments performed in the study, a pH 7 was found to be optimum.
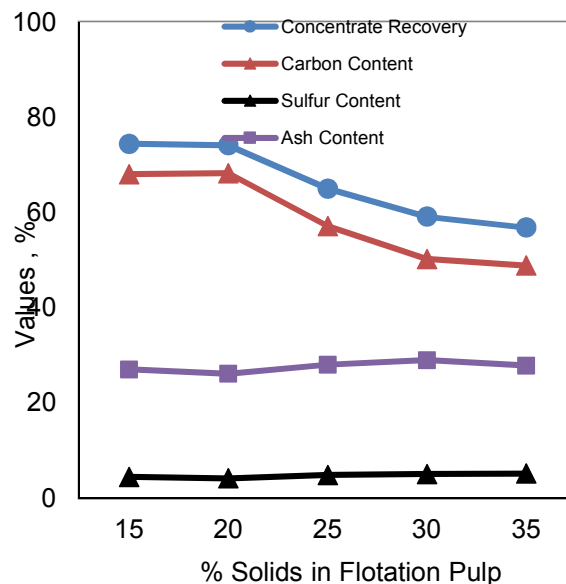


**FIGURE 3:** EFFECT OF SOLID IN PULP ON PERCENTAGE RECOVERY OF CONCENTRATE, CARBON, ASH AND SULFUR

Figure 3 shows the effect of solids in pulp on percentage recovery, carbon, sulfur and ash while keeping other parameters fixed such as 1200 rpm stirring rate, -149, +199 µm particle size and 7 pH. was evident from results that for 15, 20, 25, 30 and 35 % solids in pulp, percentage recovery of flotation varied from 74.5, 74.2, 65.1, 59.2 and 56.9%, carbon varied from 68.1, 68.3, 57.2, 50.29 and 48.9 %, ash varied from 27.1, 26.2, 28.1, 29.04 and 27.9% and sulfur varied from 4.5, 4.2, 4.9, 5.1 and 5.2 %. Percentage of sulfur and ash was found to be minimum at 20 % solids in pulp whereas % recovery and carbon was found to be maximum. For the parameters, under investigation, 20% solids in pulp was found to be optimum.
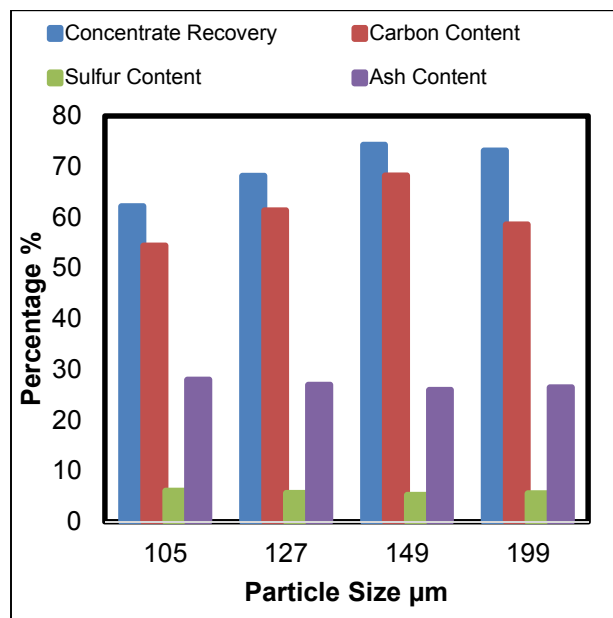
**FIGURE 4:** EFFECT OF PARTICLE SIZE ON PERCENTAGE RECOVERY, CARBON, ASH AND SULFUR

| Volatile Matter % | Ash % | Fixed Carbon % | Total Sulfur % | Total Carbon % |
|---|---|---|---|---|
| 38 | 25 | 32.7 | 4.2 | 68.3 |

## 2.2 Leaching of Flotation Concentrate with Hydrochloric Acid
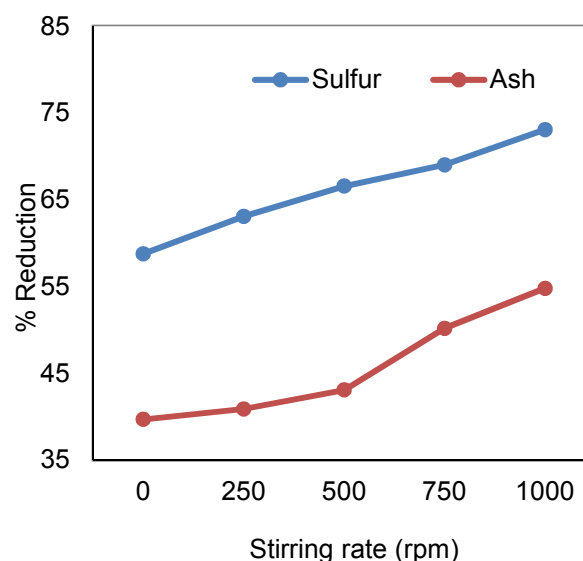


**FIGURE 5:** EFFECT OF STIRRING RATE ON PERCENTAGE REDUCTION OF ASH AND SULFUR

Figure 4 shows the effect of particle size on percentage recovery, sulfur, ash and carbon while keeping other parameters fixed such as 1200 rpm stirring rate, 7 pH and 20% solids in pulp. It was evident from the results that for(-105, +127 μm) (-127,+149 μm) (-149,+199 μm) (-199,+250 μm) particle size percentage recovery of flotation varied from 62.23, 68.2, 74.3, 73.2 and 72.29 %, carbon varied from 54.47, 61.38, 68.29, 58.61 and 48.94%, ash varied from 28, 27, 26, 26.5, and 29.23% and sulfur varied from 6.1, 5.7, 5.3, 5.6 and 5.9 % respectively. Percentage of sulfur and ash was found to be minimum at (-149, +199μm) particle size whereas recovery and carbon was found to be maximum. From the experimental results it was found that a decrease in the coal particle size improves its surface characteristics and increases its adherence to air bubble by increasing its hydrophobicity. An increase in % ash and % sulfur could be due to the fact that at smaller particle size the physical weight of particles compensates the surface characteristics, for which the dirtier coal particles tend to rise along with bubbles and accumulate in the froth on the surface resulting an increase in ash content. For the parameters under investigation, (149, +199μm) particle size was found to be the optimum.

**TABLE 2:** PROXIMATE & TOTAL CARBON/SULFUR ANALYSIS OF FLOTATION CONCENTRATE

Figure 5 shows the effect of stirring rate on percentage reduction of sulfur and ash. It was evident from results that for 0, 250, 500, 750 and 1000 rpm stirring rate percentage reduction of ash varied from 32.9, 34.94, 38.9, 40.6 and 42.6 % and sulfur varied from38.3, 44.4, 52.06, 56.3 and 57.7% respectively. Since acid leaching of coal is a chemical process and as long as the coal particles are fully suspended in the acid, the rate of stirring will have little influence on sulfur removal rate. From the experimental results it was observed that at higher stirring rate there was comparatively more sulfur and ash removal than without stirring[13]. This may be due to the presence of uniform temperature and even distribution of acid in the solution. Percentage reduction of sulfur and ash was found to be maximum at 1000 rpm [8]. For the set of experiments performed in this study a stirring rate of 1000 rpm was found to be optimum.

.
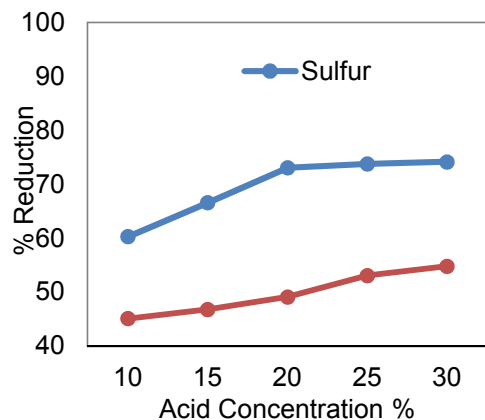


**FIGURE 6: EFFECT OF ACID CONCENTRATION ON PERCENTAGE REDUCTION OF SULFUR AND ASH**

Figure 6 shows the effect of Acid Concentrations on percentage reduction of sulfur and ash. It is evident from results that for 10, 15, 20, 25 and 30 % acid concentration, % reduction of ash varied from 35.7, 39.4, 40.6, 41.1 and 42.3 % and sulfur varied from 40.4, 43.01, 52.06, 53.17 and 57.61% respectively. From the experimental results, acid concentration was found to be a very important parameter for desulfurization process[14]. The froth concentrate possesses sulfur content of 4.2% and at an acid concentration of 30%, sulfur content reduced to 2.67% that is a 63.5% reduction. This significant reduction in sulfur % could be due to the reaction occurring between hydrochloric acid and pyrite resulted in sulfur removal, therefore, the acid concentration showed a direct influence on the reaction rate[8].From the experimental results it is evident that an increase in acid concentration, increases sulfur and ash removal %. Percentage of sulfur and ash reduction was found to be maximum at 30 % acid concentration. For the parameters, under investigation, a 30 % acid concentration was found to be the optimum.
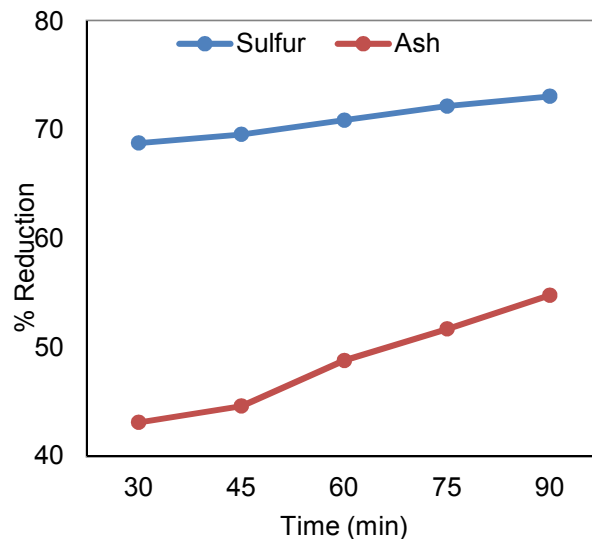


**FIGURE 7:** EFFECT OF RESIDENCE TIME ON PERCENTAGE REDUCTION OF SULFUR AND ASH

Figure 7 shows the effect of time on percentage reduction of sulfur and ash. It was evident from results that for 30, 45, 60, 75 and 90 minutes leaching time % reduction of ash varied from 35.7, 38.9, 40.6, 41.4 and 42.04 % and sulfur varied from 42.06, 47.7, 51.7, 54.2 and 57.9 % respectively that means a reduction of 27.39% in an hour. From the experimental results, leaching time was found to be another parameter of significance. However, desulfurization is a slow process therefore it requires more reaction time for complete removal of sulfur and ash. This was in agreement with the findings of M. Abdollahy et al[7]. Percentage reduction of sulfur and ash was found to be maximum at 90 min. From figure 7, it can be concluded that there is a direct relationship between residence time and sulfur and ash removal. For the parameters, under investigation a 90 minute reaction time was found to be the optimum.

Figure 8 shows the effect of temperature on percentage reduction of sulfur and ash. . It was evident from results that for 30, 45, 60, 75 and 90º C temperature, % reduction of ash varied from 34.6, 36.3, 39.4, 40.4 and 42.6 % and sulfur varied from 45.2, 50.4, 54.1, 56.3 and 57.3 % respectively. From the experimental results it is obvious that an increase in the temperature increases the reaction rate and simultaneously rate of sulfur removal also increases. As it is well established phenomenon in literature that temperature has a great impact on the reaction rate. According to Octave Leven spiel[15], a 10 ºC increase in temperature may double the reaction rate. At temperature above 90 ºC hydrochloric acid can rapidly be destroyed. Due to this

phenomenon, sulfur removal decreases above this temperature. This was in agreement with the findings of Alam H.G., et al[8]. Percentage reduction of sulfur and ash was found to be maximum at 90$^0$C. For the parameters, under investigation a 90 $^0$C temperature was found to be the optimum temperature.
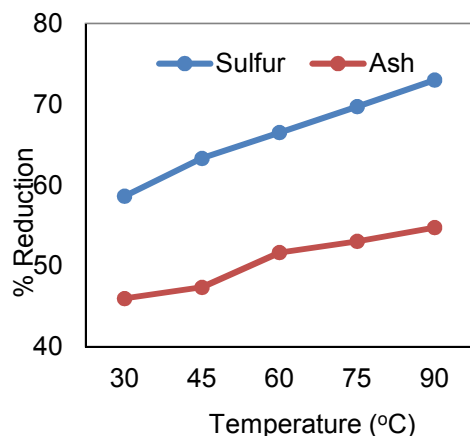


**FIGURE 8:** EFFECT OF TEMPERATURE ON PERCENTAGE REDUCTION OF SULFUR AND ASH

**TABLE 3:** PROXIMATE & TOTAL CARBON/SULFUR ANALYSIS OF FLOTATION CONCENTRATE AFTER NITRIC ACID LEACHING

| Volatile Matter % | Ash % | Fixed Carbon % | Total Sulfur % | Total Carbon % |
|---|---|---|---|---|
| 39 | 20.2 | 37.6 | 2.65 | 62.6 |

## 3. Conclusions

Combination technology was employed on coal sample of Mianwalli to upgrade it to an extent that it could be suitable as a fuel for cement industry and power plants. For cleaning of coal, the coal sample was first subjected to froth flotation using oleic acid as collector and pine oil as frother followed by leaching with HCL. Optimum parameters for recovery of flotation concentrate of better grade were pH, 7, rotor speed 1200rpm, solids in flotation pulp 20% and particle size -149, +105μm. By froth flotation the total carbon content increased to 54.1%. Ash and total sulfur content was reduced to 25% and 4.2% respectively. The flotation concentrate was then subjected to leaching for its further cleaning of coal. The following parameters were found to be optimum in leaching:

- Acid concentration: 30%

- Temperature: 90 $^o$C

- Time: 90 min.

- Stirring rate: 1000 rpm

The overall reduction in sulfur and ash contents was 57.6 % and 42.6 % respectively. The clean coal thus obtained, contains 20.2% ash and 2.65% (table#3) total sulfur which is quit suitable for the power plants for electricity production.

**References**

1. ZhiDong, L., *An econometric study on China's economy, energy and environment to the year 2030.* Energy Policy, 2003. **31**(11): p. 1137-1150.
2. Yu, Z. and X. Zheng, *Coal market outlook in China.* International journal of global energy issues, 2005. **24**(3/4): p. 211 - 227.
3. Cebeci, Y., U. Ulusoy, and S. Şimşek, *Investigation of the effect of agglomeration time, pH and various salts on the cleaning of Zonguldak bituminous coal by oil agglomeration.* Fuel, 2002. **81**(9): p. 1131–1137.
4. Usman, R., et al., *Cleaning of Dukki (Baluchistan) coal by oil agglomeration process.* International Journal of Oil, Gas and Coal Technology, 2015. **9**(1): p. 79-88.
5. Aktas, Z., *Some factors affecting spherical oil agglomeration performance of coal fines.* International Journal of Mineral Processing, 2002. **65**(3–4): p. 177–190.
6. Rodríguez, R.Á., C.C. Jul, and D. Gómez-Limón, *Evolution of the organic sulfur and other components during nitric acid leaching of Mequinenza coal.* Fuel, 1997. **76**(14–15): p. 1445-1450.
7. Abdollahy, M., A.Z. Moghaddam, and K. Rami, *Desulfurization of mezino coal using combination of 'flotation' and 'leaching with potassium hydroxide/methanol'.* Fuel, 2006. **85**(7–8): p. 1117-1124.
8. Alam, H.G., A.Z. Moghaddam, and M.R. Omidkhah, *The influence of process parameters on desulfurization of Mezino coal by HNO3/HCl leaching.* Fuel Processing Technology, 2009. **90**(1): p. 1-7.
9. Saydut, A.T., et al., *Desulphurization of Hazro, Turkey coal using combination of flotation and leaching with sodium hydro*

*oxide.* Energy Exploration & Exploitation, 2007. **26**(2): p. 133-142.

10. S. Komar, K. and E. Timothy C., *Coal Desulfurization, High Efficiency Preparation Methods*. 2001, Taylor & Francis. p. 360.

11. American Society for Testing and Materials, *Standard Test Method of Froth Flotation ASTM D-5114*. 2008: p. 525-532.

12. S. Komar Kawatra and Timothy C. Eisele, *Coal Desulfurization, High Efficiency Preparation Methods*. 2001: p. 41-42.

13. Coulson and Richardson, *Chemical Engineering: Particle Technology and Separation Processes*. 2002. p. 503.

14. Ahn, S., G. Choi, and D. Kim, *The effect of wood biomass blending with pulverized coal on combustion characteristics under oxy-fuel condition*. Biomass and Bioenergy, 2014. **71**: p. 144-154.

15. Octave Leven Spiel, *Chemical Reaction Engineering*. 1999. 3rd Edition, Wiley Publisher.

# Assessment of different industrial ceramic wastes and their potential for possible applications: A pilot scale renewable materials investigation

*M. Sohail[1*], M. Saleem Khan[2], Noor Saeed[2], Majid Khan[2], M. Arif[2],*
[1]*Shaheed Benazir Bhutto University Sheringal Dir (Upper)*
[2]*National Center of Excellence in Physical chemistry, University of Peshawar, KP, Pakistan*
[1*]*Corresponding author*
*Email: msohail2000@gmail.com*

## Abstract

In Pakistan, ceramic industry has been recognized to yield large quantities of wastes that have become an environmental alarm due to their misplace disposal. Solutions to reuse and incorporate industrial ceramic wastes can be rewarding regarding environmental, economic and technical aspects. In the present study, three ceramic wastes collected from the sites of ceramic factories located in Hayatabad industrial zone, Peshawar, KP, Pakistan were investigated via different physicochemical techniques. Ceramic wastes were found to be the mixture of various metal oxides. TGA confirmed that the materials are thermally stable up to 700°C. General dielectric properties such as dielectric constant, dielectric loss, capacitance and conductivity in the frequency range from 1 MHz - 3 GHz at room temperature showed that ceramic wastes will be best substitutes for application in embedded capacitors. Rheology studies revealed that the wastes are mechanically rigid and stiff drawing attention to the reusability of these wastes in mechanically tough composites.

**Key words**: Please list 3-6 key words in alphabetical order separated by commas. Please avoid to use same words that have already appeared in title.

## 1 Introduction

Ceramic industries produce large quantities of wastes which are discarded without any further treatment that lead to severe environmental pollution and significant land occupation (Mohammad et al., 2014). Waste materials produced are approximately one third of the total ceramic production. The ability to handle these wastes depends on sector and geographic location of the industry, company size, resource availability and strategic attitude. Natural resources are facing a drop with time due to uncontrolled uses. It is worth noticing that improvement in concrete technology might be a useful way to decrease the use of natural resources by recycling the ceramic wastes coming out from the industries (Chen et al., 2003). Reuse and recycling of waste materials suggest energy saving, possibly superior products, cost reduction and less or no hazards to the surrounding environment.

It has been observed that ceramic wastes are hard, durable, extremely resistant to chemical, physical and biological degradations and highly thermally stable (Pacheco-Torgal and Jalali, 2010). Due to an increase in heaping up ceramic wastes, there is a pressure on the producers for their valuable disposal. Different countries in the world are trying to reduce the load of solid wastes by exploiting them in a better way. In Pakistan, there are seven ceramic industries which manufacture ceramic products like tiles, porcelain/pottery, stoneware, and bricks (Kaisar and Akbar, 2011)]. During quarrying and processing procedures, large quantities of ceramic wastes are produced in the form pellets, powders and cakes. The most common destination of these wastes is landfill disposal, although, notified vicinities have been identified for the disposal of wastes near the industrial units, however, most of them discard away the wastes into the adjacent ditches or open spaces. Subsequently, severe environmental effects occurred due to misplace dumping whereas accommodating a vast land area. It is a fact that by recycling wastes, landfilling is reduced while more natural resources are protected (Kelestemure et al., 2014). In Pakistan, most of the ceramic producing units are small and medium enterprises and there is deficiency of considering environmental influences ascending from this industry. The immense impacts of these wastes are increasing day by day which alternatively damages the environment and hence public health. The present research work is dedicated to find an appropriate solution for the clearance of these wastes. The present study focuses on the reusability and proper discarding of the ceramic wastes collected from the surroundings of three different industries. Thermal, dielectric and viscoelastic characteristics of the collected wastes were determined. Reusing ceramic wastes in different areas such as ceramic heaters, capacitors and tough composites could be a win-win approach. That is on one hand by resolving the problem of wastes generating by the ceramic industries and at the same time their reutilizing in places where natural resources face degeneration.

## 2 Method

Waste samples were collected from three different ceramic producing industries (1. Fort Ceramics, 2. Marble Complex and 3. Rehman Marbles) located in the North-West region (KP, Peshawar) of Pakistan. Three wastes samples consisting of pellets, powder, tiles and stones were collected form the premises of three mentioned companies along with information about ceramic wastes management. In addition, tape as well as double distilled water was used for washing purposes. The wastes samples were first washed with tap water for removing the obvious dust and soil particles. After drying, the samples were ground properly to obtain homogenous powder. Moreover, the samples were washed two times with double distilled water so as to eliminate the contaminants like adsorbed dust particles and organic matters. All the three samples were then kept for 12 hours in an electric oven at 60 °C. After cooling, the dried samples were then crushed properly in an agate mortar. Consequently, the powder samples were then passed through 200, 220 and 240μ mesh in order to get powder's particles in the same micro proportions. Lastly, the samples were named with CW-F, CW-M and CW-R for Fort Ceramics, Marble Complex and Rehman Marbles respectively.

Energy dispersive X-ray spectroscopy (EDX) was used to analyze the chemical compositions of the ceramic wastes. Thermo-gravimetric analysis (TGA) was done in the range from 30-800 °C under $N_2$ atmosphere. RF Impedance material analyzer was used to examine the dielectric properties of the materials. Pellets of samples with 5-10 nm diameters were prepared by a hydraulic press machine under 5 tons hydraulic pressure. Before subjecting between the electrodes, all the pellets were sintered at 300°C for 5 hours. Rheological properties were determined by Anton Paar Rheometer, Physica MCR 301. About 5 mg of each sample was applied between the plates under internally controlled thermal conditions.

## 3 Results

### a. Chemical Composition of Wastes

EDX examination showed the chemical composition of CW-F, CW-M and CW-R ceramic wastes as summarized in Table 1. It is seen that the major elements present in CW-F are Si, Al, K, Ca, Fe, Ti and Mg in their corresponding oxidized forms (Faria and Holanda, 2012). EDX spectrum for CW-M shows peaks for Ca, Mg, Si and C. It is assumed that these metals are present in their respective oxide and carbonated forms such as $MgCO_3$, $CaCO_3$ and $SiO_2$ (Lavat et al., 2009). CW-R is composed of only Ca and C that shows $CaCO_3$ and CaO compounds.

### b. Thermal Properties

TGA curves for CW-F, CW-M and CW-R are given in Figure 1. During the experiment, all the samples were subjected to a temperature range from 30 °C to 800 °C at the interval of 10 °C per minute. The wastes are thermally stable in the temperature range from 600°C to 700°C. It is accredited to the strong inter-ionic interactions between the metal ions present in these ceramics. At the initial stage (80-100°C), no weight loss was observed due to the presence of water/moisture contents. It is due to the thermal activation of the wastes before subjecting to TG analysis. An insignificant degeneration above 660°C in CW-F with about 10% weight loss, at 670°C in CW-M with 7% mass loss and at 697°C in CW-R with 15% weight loss is due to the complete de-intercalation of residual water and other additives. The remains of all the three wastes at 800°C represent the dispersed form where the grain boundaries of the constituents in the ceramics are dispersed away (Li et al., 2015). Thermal stability of ceramic wastes up to 700°C suggest these materials as better substitutes for application in thermal protective coatings (TPC). Automotive, aerospace industries and oil exploration use electronic components which can work at temperature > 200 °C. In this connection, the ceramic wastes understudy may be a best option for these industries.

**Table 1.** Chemical composition of the collected ceramic wastes.

| Waste Sample | Elemental composition Weight% | | | | | | | | | |
|---|---|---|---|---|---|---|---|---|---|---|
| Codes | Si | Al | K | Ca | Fe | Ti | Mg | Na | C | O |
| CW-F | 23.65 | 8.64 | 1.36 | 4.46 | 3.55 | 0.40 | 2.46 | 0.35 | --- | 55.14 |
| CW-M | 0.31 | --- | --- | 36.63 | --- | --- | 0.30 | --- | 10.80 | 51.69 |
| CW-R | --- | --- | --- | 37.94 | --- | --- | --- | --- | 10.15 | 51.92 |
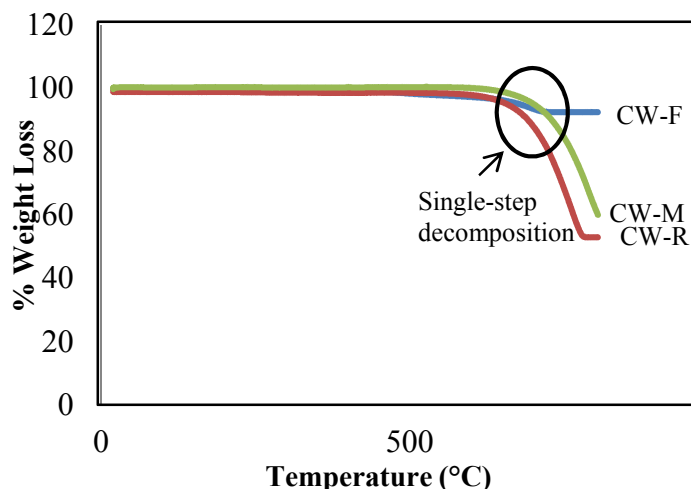
**Figure 1.** Thermo-grams for collected ceramic wastes.

### c. Dielectric Properties

Dielectric properties are related with the storage and dissipation of electrical energy in a material. Frequency dependence dielectric parameters such as dielectric constant ($\varepsilon'$), dielectric loss ($\varepsilon''$) and loss tangent (tan$\delta$) were investigated in the frequency range from 1MHz to 3 GHz at 300K while using the following equations (Javed et al., 2010).

$$\varepsilon' = Cd/A\varepsilon_0 \qquad (1)$$

$$tan\delta = 1/2\pi f R_p C_p \qquad (2)$$

$$\varepsilon'' = \varepsilon' tan\delta \qquad (3)$$

where C is the capacitance, d is the thickness of the pellets, A is the cross-sectional area, $\varepsilon_0$ is the constant of permittivity, $f$ is the applied field frequency, $C_p$ is the equivalent parallel capacitance and $R_p$ is the equivalent parallel resistance. Figure 3a, b and c show the variation of $\varepsilon'$, $\varepsilon''$ and tan$\delta$ as a function of frequency for CW-F, CW-M and CW-R respectively. It is observed that all the samples exhibit frequency dependent phenomena that is the values of dielectric parameters decrease with increasing applied field frequency and become constant at certain specific frequency ($1.6 \times 10^8$-$1.8 \times 10^9$ Hz). This can be defined on the bases of space charge polarization due to electron dislocation. According to Maxwell/Wagner model (Ashiq et al., 2009), space charge polarization appears due to the presence of inhomogeneity in the dielectric structure of the material where the strong conducting grains are disconnected by poor thin conducting borders. This is due to the well-up polarization of the dipoles in low frequency regions thus enhancing dielectric properties of the materials. In our case, the collected ceramic wastes are composed of inhomogeneous grains and species as confirmed by the EDX studies and hence show high values for dielectric parameters at low frequency. At low frequency, high $\varepsilon'$ value reflects the presence of dislocations, voids and other defects in the ceramic wastes. For all samples, $\varepsilon'$, $\varepsilon''$ and tan$\delta$ show decrease in their values at high frequency. This is due to the decrease in space charge polarization with increasing frequency. It has been reported in literature (Ashiq et al., 2009; Bos et al., 2012; Malana et al., 2016), that in a dielectric material, space charge carriers require finite time to line up themselves parallel to an applied electric field and if the electric field frequency is increased, a point reaches where the space charge carriers cannot adjust with the alternating field hence resulting in the decrease of $\varepsilon'$, $\varepsilon''$ and tan$\delta$. This indicates that at high frequency space charge carriers add no contribution in the polarization of the materials. Normally, dielectric losses represent conductivity measurements i.e. materials with high losses show high conductivity and vice-versa. The appearance of extra peaks in $\varepsilon'$, $\varepsilon''$ and tan$\delta$ curves at about 2 GHz is ascribed to the fact that electron hopping frequency becomes equal to the applied field frequency which results in a resonance type performance by the materials in high frequency regions. The dispersion depth of electromagnetic waves is decreased due to high $\varepsilon'$ via increasing skin effect. So the low $\varepsilon'$ value (5.50-5.51) obtained for ceramic wastes allows their application at high frequencies. Frequency dependence tan$\delta$ is an vital parameter and it must be as low as possible in an ideal capacitor. In this regard, the ceramic wastes will be suitable candidates for applications in capacitors due to their low tan$\delta$ magnitudes as shown in Table 2. Relative to other two samples, high $\varepsilon'$ value for CW-F signifies the presence of $Fe^{+2}$ and $Ti^{+3}$-site vacancies which help in improving $\varepsilon'$.

Figure 3 shows the variation of capacitance with increasing frequency at ambient temperature for CW-F, CW-M and CW-R. It is seen that CW-F has highest capacitance (4.45 pF) at I MHz relative to CW-M (3.07 pF) and CW-R (2.19 pF). High value of capacitance at low frequency is ascribed to the decrease in space charge regions at electrodes surfaces. At about 2.14 GHz, an immediate fall is seen in the capacitance of all samples which is due to the occurrence of partially blocked charge carriers near

the electrodes. The highest values of capacitance for each material are listed in Table 2.
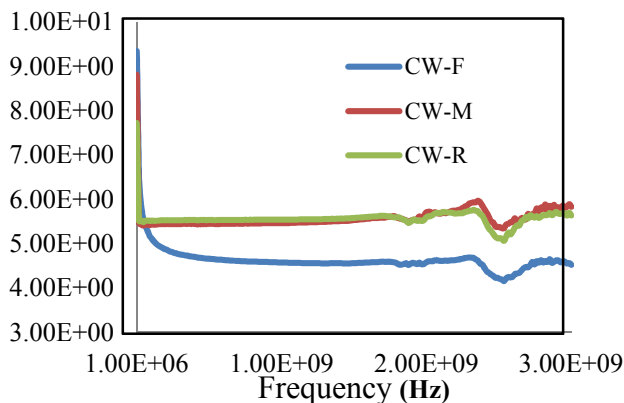


**(Figure 2a)**
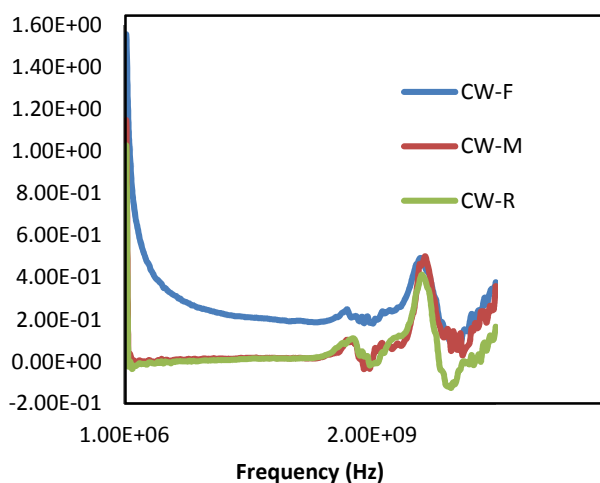


**(Figure 2b)**
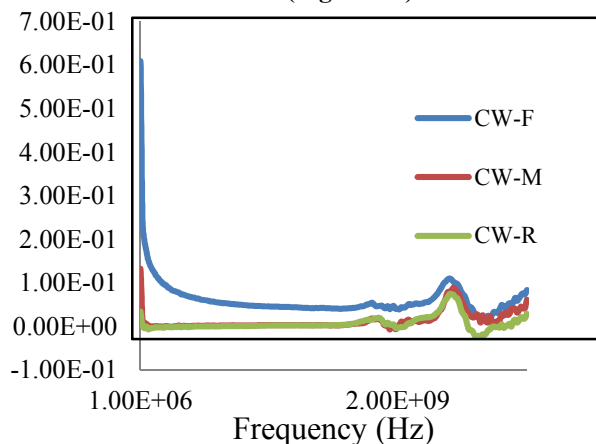


**(Figure 2c)**

**Figure 2. (a)** Dielectric constant **(b)** Dielectric los **(c)** Tan Loss
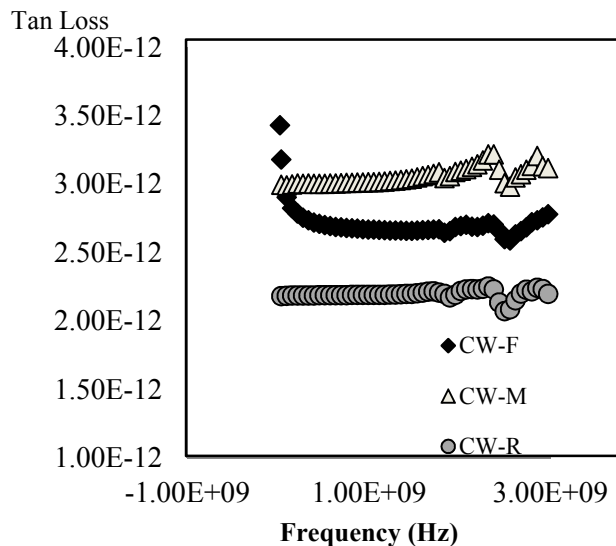


**Figure 3.** Capacitance versus frequency plot.

Frequency dependence AC conductivity ($\sigma_{ac}$) of all the samples was calculated by using the following equation;

$$\sigma_{ac} = \omega \varepsilon_0 \varepsilon' \tan \delta$$

(4)

where $\omega = 2\pi f$ and $\varepsilon_0$ is the permittivity of free space. The statistics obtained was plotted against applied field frequency as shown in Figure 4. It is seen that conductivity of all the three materials is increasing linearly with frequency. The samples exhibit highest value of conductivity at about 2.45 GHz. The increase in AC conductivity is usually due to tunneling and hopping of electrons between the localized     states. In the present case, the conductivity improvement is especially due the translational hopping of electrons in conductivity dispersion regions as reported earlier (Shi et al., 2016). Due the presence of oxygen vacancies present in these samples, a decline in conductivity of the samples occurs beyond 2.43 GHz which is attributed to the loss in hopping of electrons (Naceur et al., 2013). A further boost in conductivity at high frequency for all samples may be due the reorientation of electrons hooping that are well-localized. The highest conductivity achieved by each material in high frequency region is shown in Table 2. The dielectric properties and AC conductivity values of the samples make them useful in miniaturizing microwave devices.
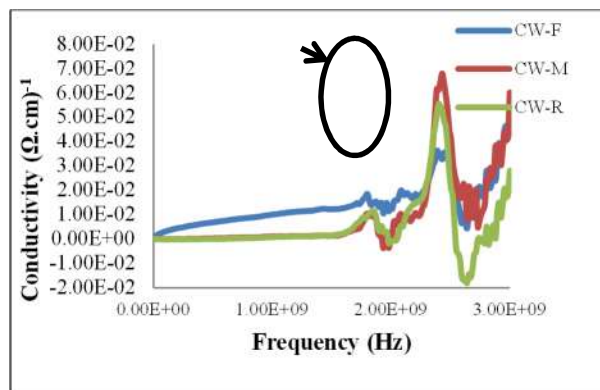
**Figure 4.** AC conductivity of the samples.

### d. Rheological Characteristics

Rheological properties such as viscosity, storage modulus and loss modulus of the ceramic wastes were checked in order to find their durability in different areas. Flow curves which represent shear rate versus viscosity plots for CW-F, CW-M and CW-R are shown in Fig. 4a, b and c. The data was recorded at three different temperatures i.e. 30, 40 and 50°C. It is seen that viscosity of all the samples is decreasing with increasing shear rate indicating shear thinning or non-Newtonian behavior. This suggests the presence of an aggregated structures in the materials (Tanurdijaja et al., 2011). Weak dipolar and strong metallic interactions are responsible for holding together the particles of ceramic wastes, while with increasing shear rate, interactions among the particles become weak which results in the decrease in resistance to flow and hence decrease in viscosity.
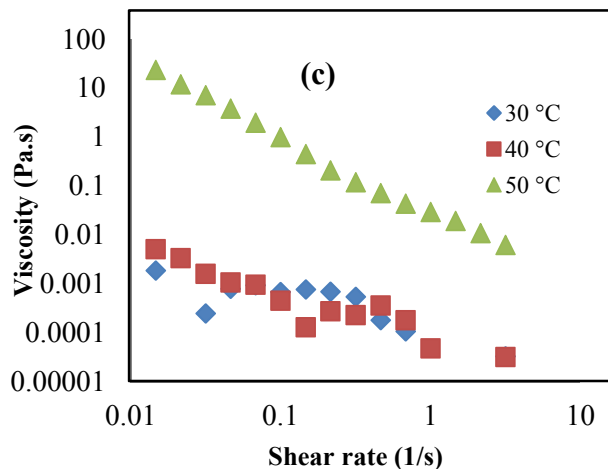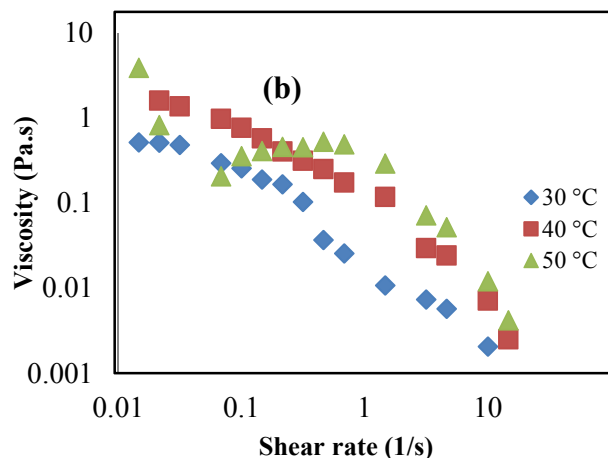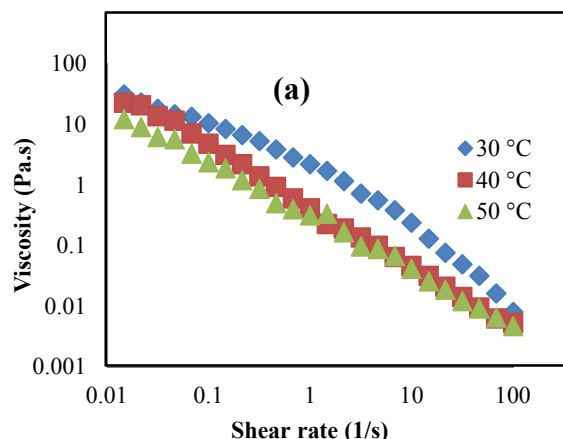




**Figure 4.** Viscosity versus Shear rate plots.



Angular frequency dependent storage modulus (G′) and loss modulus (G″) plots for all the three samples are shown in Fig 5a, b and c. It is obvious that with increasing frequency, both G′ and G″ increased which is due to the shear thinning behavior of these materials as revealed in the flow curves. This also labels the rigidity of the all the three samples due to which these materials display high thermal stability. It was found that CW-F achieved highest G′ value of 6.49 x $10^3$ Pa relative to CW-M (5.51 x $10^3$ Pa) and CW-R (5.50 x $10^3$ Pa. This shows that CW-F is mechanically more rigid material than the other two. G″ is comparable for all the samples recorded at one definite temperature. This indicates the stiffness of the ceramic wastes which is very useful for the implementation of these materials in polymer based tough membrane composites (Ferry, 1980). Different viscoelastic properties of the materials are listed in Table 2.
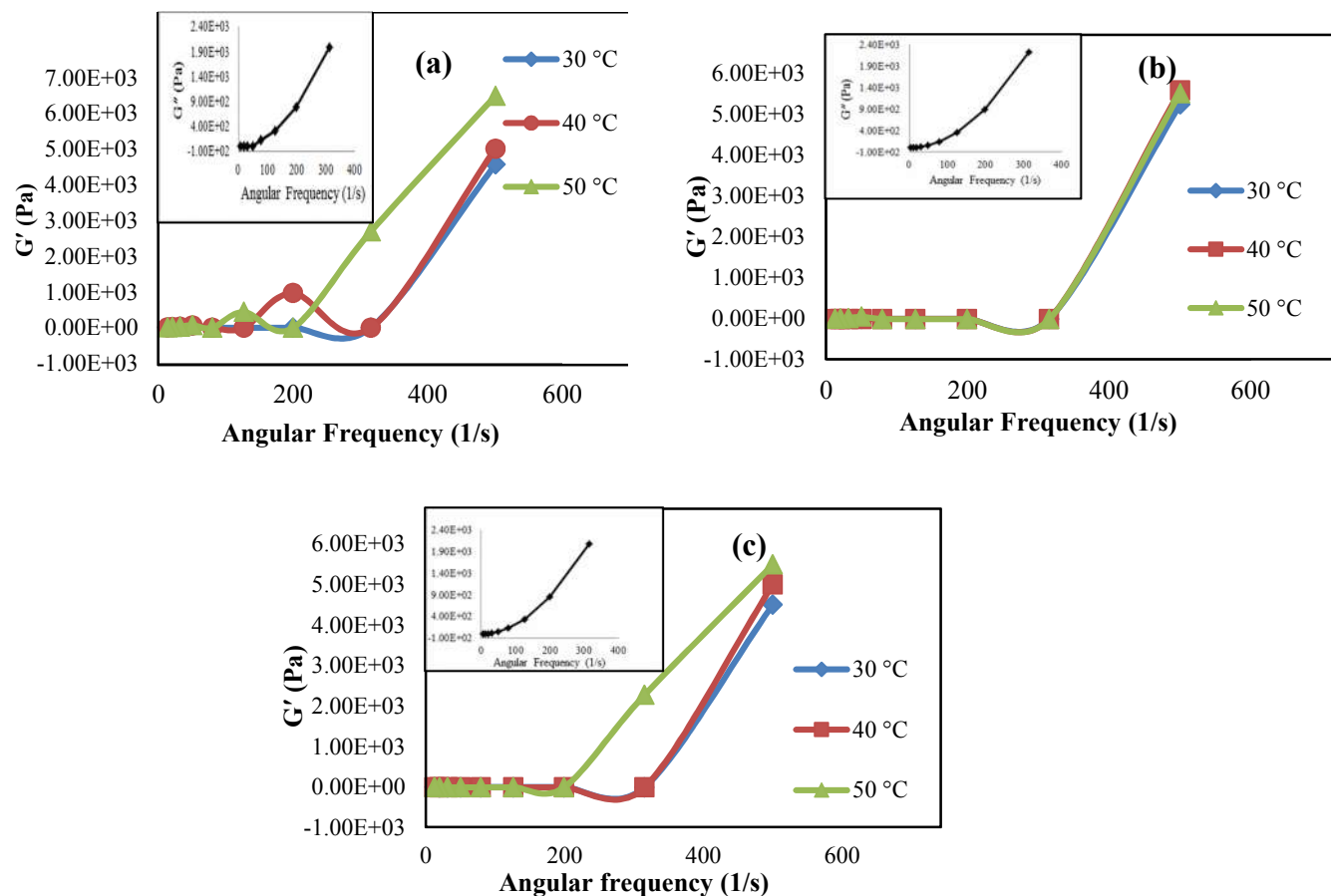
**Figure 5.** Storage and loss moduli for the collected samples

**Table 2.** The values of different parameters measured for CW-F, CW-M and CW-R samples.

| Samples | $\varepsilon'$ | $\varepsilon''$ | tan$\delta$ | Cp (pF) | $\sigma$ ($\Omega$.cm)$^{-1}$ | $\eta$ (Pa.s) | G' (Pa) | G'' (Pa) |
|---------|------|------|-------|---------|----------------|----------|-----------|-----------|
| CW-F | 9.35 | 1.56 | 0.609 | 4.45 | 0.034 | 31.1 | $6.49 \times 10^3$ | $2.0 \times 10^3$ |
| CW-M | 8.81 | 1.15 | 0.133 | 3.07 | 0.068 | 03.8 | $5.51 \times 10^3$ | $2.2 \times 10^3$ |
| CW-R | 7.72 | 1.03 | 0.034 | 2.19 | 0.050 | 28.9 | $5.50 \times 10^3$ | $2.1 \times 10^3$ |

**Conclusions**

Ceramic wastes obtained from three different local ceramic producing industries were investigated and characterized by different physicochemical techniques. The chemical compositions showed that the ceramic wastes are composed of normal and some transition metal oxides. The materials were found to have thermal stability up to 700°C with least weight loss ~15%. Wastes exhibited dielectric properties with highest value of $\varepsilon'$ = 9.35 and lowest tan$\delta$ = 0.034 which refer the materials for possible application in

capacitors. Rheological characteristics revealed their worthy elastic nature with G' = 6.49 x 10$^3$ (Pa) and G'' = 2.2 x 10$^3$ (Pa). On the basis of these properties, ceramic wastes studied are suggested to be possibly used in protective coatings, high temperature sensors, embedded capacitors and tough membranes.

## References

[1] K.R. Mohamed, S.M. Mousa, G.T. El-Bassyouni, Fabrication of nano structural biphasic materials from phosphogypsum waste and their in vitro applications, Material Research Bulletin 50 (2014) 432-439.

[2] H-J. Chen, T. Yen, K-H. Chen, Use of building rubbles as recycled aggregates, Cement and Concrete Research 33 (2003) 125-132.

[3] F. Pacheco-Torgal, S. Jalali, Reusing ceramic wastes in concrete, Construction and Building Materials 24 (2010) 832-838.

[4] H.R. Kaiser, Z.K. Akbar, Other Non- Metalic Products - Glass & Ceramics (2011) 1-15.

[5] O. Kelestemur, S. Yildiz, B. Gökçer, E. Arici, Statistical analysis for freeze–thaw resistance of cement mortars containing marble dust and glass fiber. Material Design 60 (2014) 548-555.

[6] K. Faria, J. Holanda, Using SEM/EDS for characterization of clay ceramic bearing sugarcane bagasse ash waste, Current Microscopy: Contribution in Advance Science and Technology (2012) 1085-1092.

[7] A.E. Lavat, M.A. Trezza, M. Poggi,. Characterization of ceramic roof tile wastes as pozzolanic admixture, Waste Management 29 (2009) 1666-1674.

[8] Y. Li, Y. Shi, F. Cai, J. Xue, F. Chen, Q. Fu,. Graphene sheets segregated by barium titanate for polyvinylidene fluoride composites with high dielectric constant and ultralow loss tangent, Composites Part A- Applied Science Manufacturing 78 (2015) 318-326.

[9] M.N. Ashiq, M.J. Iqbal, I.H. Gul,. Structural, magnetic and dielectric properties of Zr–Cd substituted strontium hexaferrite ($SrFe_{12}O_{19}$) nanoparticles, Journal of Alloys and Compounds 487 (2009) 341-345.

[10] S. Bose, A.K.. Mishra, T. Kuila, N.H. Kim, O-K.. Park, J.H. Lee, Tunable electrical conductivity and dielectric properties of triglycine sulfate-polypyrrole composite, Chemical Engineering Journal 187 (2012) 334-340.

[11] M.A. Malana, R.B. Qureshi, M.N. Ashiq, M.F. Ehsan, Synthesis, structural, magnetic and dielectric characterizations of molybdenum doped calcium strontium M-type hexaferrites, Ceramics International 42 (2016) 2686-2692.

[12] Y. Shi, W. Hao, H. Wu, L. Sun, E. Cao, Y. Zhang, High dielectric-permittivity properties of NaCu3Ti3Sb0.5Nb0.5O12 ceramics, Ceramics International 42 (2016) 116-121.

[13] H. Naceur, A. Megriche, M.E. Maaoui,. Frequency-dependant Dielectric Characteristics and Conductivity Behavior of Sr1-x(Na0.5Bi0.5)xBi2Nb2O9 (x = 0.0, 0.2, 0.5, 0.8 and 1.0) Ceramics, Oriental Journal of Chemistry 29 (2013) 937-944.

[14] S. Tanurdjaja, C. Tallon, P.J. Scales, G.V. Franks, Influence of dispersant size on rheology of non-aqueous ceramic particle suspensions, Advance Powder Technology 22 (2011) 476-481.

[15] J.D. Ferry, Viscoelastic properties of polymers, John Wiley & Sons, 1980

# Effect of operating parameters on the performance of membrane reactor for Biodiesel Production

*Syed Zakria\*, Amir Naveed, Saeed Gul*
*Department of Chemical Engineering,*
*University of Engineering & Technology Peshawar, Pakistan*
*\**Corresponding author.
Email: engrzakria@uetpeshawar.edu.pk

**ABSTRACT**

With the increasing population, high demand of fossil fuels and the reduction of petroleum assets have forced the world to embrace biodiesel (FAME) as a substitute energy source. Biodiesel as a renewable and nonpolluting fuel has received extensive consideration. Biodiesel market is amongst the fastest evolving renewable energy markets. However, the conventional methods for the production of biodiesel have some serious limitations and inefficiencies like limited mass transfer due to immiscible reactants, unwanted by-products, multiple downstream processing steps, low quality and high production cost that obstructing its commercialization. In this since using membrane reactors can achieve high quality and easy separation of products by means of reaction equilibrium shifting to the product side. In the present work, membrane reactor has been used for the FAME production from waste cooking oil (WCO) feedstock and alcohol (methanol). The outcome of different operating parameters like pressure, temperature and catalyst concentration has been examined. For this purpose, a lab scale membrane reactor system has been designed and fabricated with use of ceramic membrane having pore size of 0.1-0.2µm and active surface area 0.08494 m². In this research work, transesterification process initiated by a base-catalyst (NaOH) was used for the FAME (biodiesel) production. Experiments were carried out at 55, 60, 65, 70 and 75 °C, at different pressure and catalyst concentrations in the membrane reactor. Experimental results showed that variation in pressure, catalyst concentration and temperature have significant effect on the conversion of Tri-glycerides (TG) to FAME. Reaction products (biodiesel/glycerol) were effectively separated through membrane reactor.

**Key Words:** *Biodiesel, Membrane Reactor, Reaction Equilibrium, Waste Cooking oil.*

## 1 INTRODUCTION

Biodiesel also known as FAME is an unpolluted fuel which does not have aromatic hydrocarbons, sulphur, and crude oil residues [1]. Biodiesel is more beneficial over other petroleum based fuels because of renewability, biodegradability and very low gaseous emission which make it environment friendly fuel [2]. Biodiesel, which is composed of FAME (fatty acid methyl ester), is a combination of long-chain fatty acids of monoalkyl esters commonly resulting from the vegetable oil and fats of animals through esterification and transesterification. Subject to the local soil circumstances, climate and accessibility, numerous bio lipids have been used in different countries as feedstock for the biodiesel production [3].

To produce biodiesel the most common process used is called transesterification. In this technique, in the existence of acid or base catalyst feedstock that is tri-glyceride reacts with an alcohol to produce FAME and glycerine as a byproduct [4].
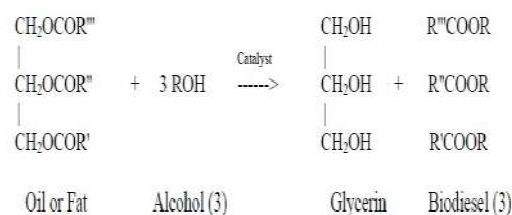


**Figure 1: Reaction mechanism of triglyceride to FAME conversion**

High energy demand because of industrialization, population rise, environmental issues and the diminution of petroleum based fuels are the principal causes that lead to create additional attention in the area of renewable fuel research. But the biodiesel cost production from numerous feedstocks is considerably greater compare to petroleum based diesel. The price of feedstock, purification of biodiesel, and the assessment of by products are quiet main problems [5]. In all these issues the cost of feedstock and purification of biodiesel are the significant aspects that essential to be taken into interpretation. Consequently employing competent and integrated production approaches to aid the economics of the process is essential [6].

Mass transfer and mixing between oil and methanol during biodiesel production are the main issues. For the purpose to overcome these problems various Novel reactors have been used to advance mass transfer and

mixing between oil and methanol during biodiesel production. A micro channel reactor was used which delivered good reaction rate due to high mass transfer rate and high volume/surface ratio. Restrictions of this reactor include low production and high cost [7]. The oscillatory flow reactor which works as plug flow reactor can provide good mass and heat transfer with keeping plug flow. It also advances biodiesel production economy [8]. Another type of reactor used is spinning tube reactor having large interfacial contact area which enhances the reaction rate [9]. A microwave reactor is another kind of reactor used for biodiesel production which uses its irradiation to transfer energy to reactants which increases transesterification reaction rate. Related to other conventional reactors a microwave reactor attains similar conversion with small reaction time in a more energy effective way [10].

Many Novel reactors have been used for biodiesel production comprising reactors mentioned above. However none of these reactors are able to overcome chemical equilibrium limitations of transesterification except membrane reactor. IUPAC has defined membrane reactor as a device which integrates separation and reaction in one unit [11]. Researchers have stated membrane as a favorable technology for the biodiesel production. FAME production with the use of membrane reactors is a growing concept. Membrane uses a selective barrier to adjust the transport of substances and mass transfer rates [12]. Membrane plays a significant role in biodiesel production together through eliminating glycerol and FAME from product or retaining unreacted triglycerides in membrane. Membrane separation technology for biodiesel production is based on two basic principles; Separation by catalytic membrane and separation by oil droplet size [13].

As it results with a fatty acid methyl ester (FAME)-rich phase hence membrane reactor has clear advantages over conventional processes, a precise contact of unsuited reactants, and removal of undesired side reactions. In the membrane reaction and separation occurs in a single process, therefore decreasing cost of separation and recycle necessities, and an improvement of thermodynamically restricted or product inhibited reactions that end in advanced conversions [14].

In this work, we focused on the biodiesel production with two-phase ceramic membrane reactor by using base as a catalyst through transesterification of waste cooking oil. Ceramic membranes are of specific benefits as they can resist chemical attack and can withstand at high temperatures.

## 2 Materials & Method

### 2.1 Materials

For this research work the raw materials used were:

- Waste cooking oil (WCO)
- Catalyst (NaOH)
- Alcohol (methanol).

Waste cooking oil is collected from different hotels and bakery shops while NaOH and methanol were purchased from HAQ Chemicals.

### 2.2 Experimental Methodology

Figure 2A and 2B shows the Experimental setup and VISIO schematic of membrane reactor lab scale unit. Ceramic membrane of pore size 0.1 to 0.2µm and active surface area of 0.08494 m² is used for the membrane reactor setup. Pump is used to feed the reactants and provide the circulation across the loop with two inlet valves one for methanol and the other for oil and feed recycling/oil. A heating element is used in the reaction setup to heat the reactants to the desired temperature. A temperature panel was used to monitor the temperature of the system.



**Figure 2A: Experimental Setup of Lab scale Membrane Reactor**

Alcohol and catalyst is heated to 40 °C and mixed. Waste cooking oil is charged to the reactor system. Semi continuous or continuous feeding of alcohol/catalyst and/or waste cooking to membrane reactor loop at a certain ratio with a trans-membrane pressure creating the permeation of FAME/alcohol/glycerol/catalyst and does not allow lipid feedstock to pass through membrane which is collected as Retentate. Product obtained is collected in

permeate tank and then separated with the use of centrifuge. The biodiesel (FAME) yield obtained is calculated using the following equation.
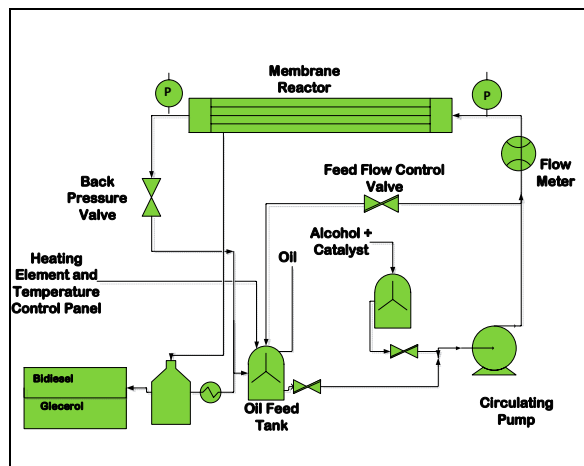


Figure 2B: VISIO Schematic of lab scale Membrane Reactor setup

$$Biodiesel\ Yield(\%) = \frac{mass\ of\ biodiesel\ in\ product\ vessel}{initial\ mass\ of\ WCO\ oil\ in\ the\ mixing\ vessel} \times 100$$
[15]

## 3 Results & Discussions
### 3.1 Temperature effect on permeate

With increase in temperature up to a certain limit the permeate flux increases as the reaction goes forward. In our experiments, five different reaction temperatures 55, 60, 65, 70 and 75 $^{O}$C were selected. It was observed that there is a considerable increase in permeate flux with the temperature. Figure 3 shows the relation of temperature and permeate flux for the biodiesel production by membrane reactor.
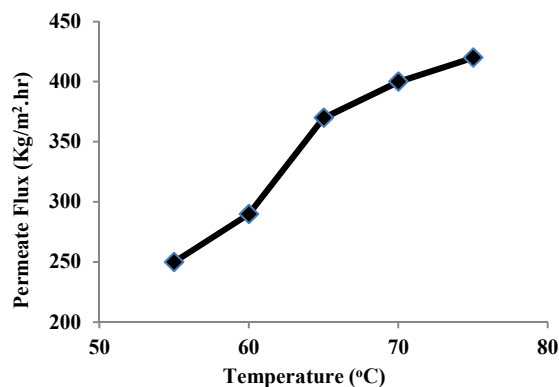


Figure 3: Temperature effect on permeate

### 3.2 Effect of catalyst concentration

On the conversion of waste cooking oil to FAME, catalyst concentration was found to have significant outcome on the conversion. The transesterification of

waste cooking oil with alcohol i.e. methanol was examined at different concentration of catalyst and residence times (RT) in a membrane reactor. Experiments were carried out at 0.03, 0.05, 0.5, and 1 wt. % catalyst on the basis of oil. It was concluded that a base catalyst concentration above 0.05 wt. % for one-hour retention time (RT) resulted in the steady-state biodiesel production via the membrane reactor. Such catalyst quantities are much lesser compare to those used in the production of FAME on industrial scale. Figure 4 shows the catalyst effect on biodiesel in membrane reactor.
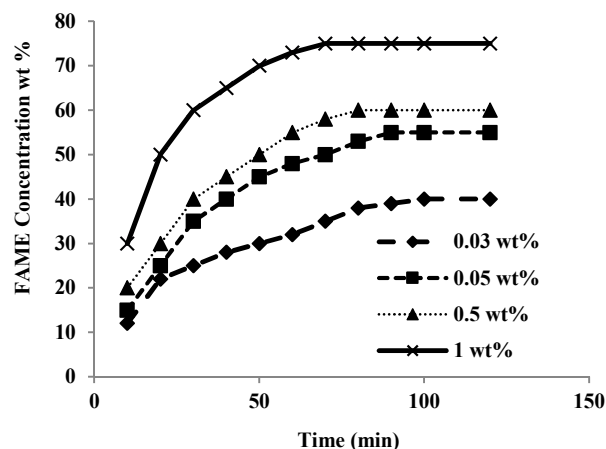


Figure 4: Effect of catalyst concentration

### 3.3 Effect of pressure on permeate Flux

In biodiesel production via membrane reactor the effect of pressure on the permeate flux was noticed in our experiment throughout. Figure 5 shows the relation of pressure and permeate flux in membrane reactor.
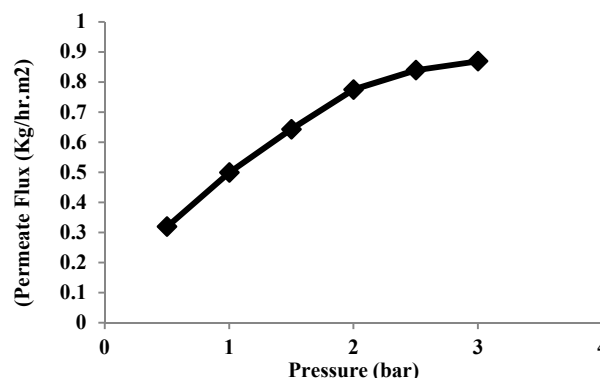


Figure 5: Effect of pressure on permeate flux

Suspension formed in circulating loop of membrane reactor due to immiscibility of lipid feed stock and alcohol. Large lipid droplets forms, which stops

---

permeation of lipid through membrane pores. As FAME, alcohol and catalyst is miscible so they pass through membrane pores. Low quality feedstock WCO reacted with base catalyst in membrane reactor. Soaps is formed which appeared to be retained in membrane reactor and results in straight forward purification of FAME in permeate. Membrane also retained particulate and Unreactable matter, thus eliminating presence of stable emulsion phase on washing biodiesel. Permeate easily DE-phased at room temperature thus giving high quality biodiesel.

## 4 Conclusions

Membrane reactor ability to produce biodiesel from high FFA lipid feedstock has been carried out. Membrane reactor offers an essential change in quality. This effort has confirmed that a membrane reactor can be used to ease several problems in biodiesel production and effectively complete the transesterification of triglycerides to biodiesel. At first, permeate was moderately concentrated then as the reaction persistent, the concentration of permeate is reduced. In most procedures, as the reaction moves forward, the made biodiesel will ultimately act as a joint solvent for the Tri-glyceride and that of alcohol phases. These findings indicate excellent potential for the commercial use of membrane reactor for the production of biodiesel.

## 5 References

[1] M. Dubé, A. Tremblay, J. Liu, Biodiesel production using a membrane reactor: Bioresource Technology 98 (2007), 639-647.

[2] A. Phan, A. Harvey, M. Rawcliffe, Continuous screening of base-catalysed biodiesel production using new designs of mesoscale oscillatory baffled reactors: Fuel Processing Technology 92 (2011), 1560-1567.

[3] S. Baroutian, M. Aroua, A. Raman, N. Sulaiman, Methanol recovery during transesterification of palmoil in a TiO2/Al2O3 membrane reactor: Experimental study and neural network modeling: Separation and Purification Technology 76(2010), 58-63.

[4] M. Vares. Reza, Sarmasti, M. Emami, K. Tahvildari, A Novel Membrane Reactor for Production of High- Purity Biodiesel: European Online Journal of Natural and Social Sciences 03(2014), 421-426.

[5] S.Shuit, Y.Ong, K.Lee, B.Subhash, S.Tan, Membrane technology as a promising alternative in biodiesel production: A review. Biotechnology Advances 30(2012), 1364-1380.

[6] L.Cheng, Y.Cheng., S.Yen, J.Chen, Ultrafiltration of triglyceride from biodiesel using the phase diagram of oil–FAME– MeOH: Journal of Membrane Science 330(2009), 156-165.

[7] I.Atadashi, M.Aroua, A.Aziz, Biodiesel separation and purification, A review: Renewable Energy 36(2012), 437-443.

[8] N.Dizge, C.Aydiner, D.Imer, M.Bayramoglu, A.Tanriseven, B.Keskinler, Biodiesel production from sunflower, soybean, and waste cooking oils by transesterification using lipase immobilized onto a novel microporous polymer: Bioresource Technology 100(2009), 1983-1 991.

[9] J.CARO, Catalysis in Micro-structured membrane Reactors with Nano-designed Membranes: Chinese Journal of Catalysis 29(2008), 1169-1177.

[10] T.Barnard, N.Leadbeater, M.Boucher, L.Stencel., B.Wilhite, Continuous-Flow Preparation of Biodiesel Using Microwave Heating: Energy & Fuels 21(2007), 1777-1781

[11] P.Cao, M.Dubé, A.Tremblay, High-purity fatty acid methyl ester production from canola, soybean, palm, and yellow grease lipids by means of a membrane reactor: Biomass and Bioenergy 32(2008a), 1028-1036.

[12] Z.Qiu, L.Zhao, L.Weatherley, Process intensification technologies in continuous biodiesel production: Chemical Engineering and Processing: Process Intensification 49(2010), 323-330.

[13] KW.Böddeker, Liquid separations with membranes: Springer-Verlag Berlin Heidelberg 39(2008), 34-42.

[14] P.Cao, M.Dubé, Tremblay. A, Methanol recycling in the production of biodiesel in a membrane reactor: Fuel 87(2008b), 825-833.

[15] A.N.Phan, T.M.Phan, Biodiesel production from waste cooking oils. Fuel 87(2008), 3490-3496.

[16] YC.Dennis, Wu.Leung, M.K.H.Xuan Wu, A review on biodiesel production using catalyzed transesterification: Applied Energy 87(2010) 1083–10.

# Beneficiation Study on Teerah Barite

**Mohammad Imran Ahmad** , **Zia Ur Rehman***

1Department of Chemical Engineering, University of Engineering & Technology Peshawar Pakistan

1*Corresponding author

Email: ziakhattak77@gmail.com

**Abstract**

The aim of this research work is to increase the concentration of low grade barite ore, using chemical treatment method. The concentrated barite ore assaying more than 90% barium sulphate can be used by for various industrial applications especially for oil and gas well drilling purposes. Several physical and chemical processes such as, shacking table, magnetic separation, jigging, leaching, flotation and/or combination of these processes may be used for the beneficiation of barite. Three samples of comparatively low, intermediate, and high quality barite ore from Teerah Valley (34° 44' 42" North, 71° 36' 28" East) of Khyber Agency (Pakistan) were investigated for the possible upgradation. The samples were treated with 25% HCL solution in different feed to solution ratio. The elemental analysis of the samples (feed and product) was carried out using EDX (Energy Dispersive X-rays Spectroscopy). Results show that barite ores assaying 93.50%, 78.80%, and 58.77% barium sulphate can easily be concentrated up to 96.00%, 94.00%, and 88.56% barium sulphate. The concentrated barite ores with more than 90% barium sulphate can be used by various barite utilizing industries.

.**Key words**: Barite, Size Reduction, HCL Treatment, EDX Analysis

## 1    Introduction

"The present study is about the upgradation of barite ore from Teerah Valley of Khyber Agency, so that it may be used by various barite utilizing industries in order to produce high quality products.

Barite", the mineralogical name of barium sulfate consists of about 65.7% barium oxide (BaO) and 34.3% Sulphur Trioxide (SO3). It is has a gravity specific gravity (4.2 - 4.5 $g/cm^3$).    [1-3] Barite is the most important and fundamental  source of barium and its compounds that are used in automotive paints, stabilizers for plastics, case hardening steels, bricks, tiles, lubricating oils, and jet fuel as well as in various types of pesticides. [4-7]

General specifications of barite ore for various commercial applications are given in table- 1.1.

Barite is a common industrial mineral and its deposits are found all around the world. According to U.S. Geological Survey (USGS) China, India, Morocco, and the United States are the four top barite-producing countries in the world. In Europe the most important sources of barite occur in Germany, France, Italy, UK, Belgium and Spain. In Americas significant deposits are found in USA, Canada, Mexico, Brazil and Argentina. In Africa, Morocco is the most important. In middle and Far East the barite producing countries are India, Iran, Turkey, Indonesia, North Korea, Thailand, Pakistan, Malaysia, Japan and Australia. China is the largest producer of barite and produces $1.5 \times 10^6$ tons/annum of barite. [1]

Barite deposits in Pakistan are found in Baluchistan and Khyber Pukhtoonkhwa Provinces. About eleven metrics millions tones barite exist at Gunga (Baluchistan). [2, 8, 9]

The most important and high grade barite deposits are found in Hazara division of Khyber Pukhtunkhwa (KPK). The largest barite deposit of Hazara is in Kohala and is quit pure. The estimated reserves are about 25,000 to 30,000 short tonnes with 3-10 tonnes production per day. Small barite deposits are also found in Sawabi, Swat, Salt Range and Teerah Valley. [8, 10-12].

## 1    Method

### a.    Material

Three samples of comparatively high (A), intermediate (B), and low (C), quality barite ore from Teerah Valley (34° 44' 42" North, 71° 36' 28" East) of Khyber Agency (Pakistan) were investigated for the possible upgradation. Sample A and B are whitish in color and contain a minute amount of foreign particles. Sample C is yellowish in color and is highly contaminated by unwanted particles. HCL was used as a fluidizing agent.

### b.    Methodology

All the three samples were successively crushed and ground within a size range of about 45-250 μ using jaw crusher and gyratory crusher. The percentage composition of barium Sulphate ($BaSO_4$), Silica ($SiO_2$), Aluminum Oxide ($Al_2O_3$), Calcium Oxide (CaO), Magnesium Oxide (MgO), Strontium Oxide (SrO), Iron Oxide ($Fe_2O_3$), Sulphur Trioxide ($SO_3$), and Zinc Oxide was determined using EDX. Moisture contents and loss on ignition (LOI) were determined through the standard method of chemical analysis. [18]

All the three samples were washed 3-4 times with tape water and were treated with 25% HCL solution in different feed to solution ratio, i.e. 1:1(50gm of $BaSO_4$ in 50 ml HCL solution), 1:2(50gm of $BaSO_4$ in 100 ml

HCL solution), 1:3(50gm of BaSO4 in 150 ml HCL solution), 2:1(100gm of BaSO4 in 50 ml HCL solution), and 3:1 (150gm of BaSO4 in 50 ml HCL solution). The mixture was stirred in 500 ml beaker for 25 minutes at a constant stirring speed of 260 rpm. All the samples were washed (3-4 time) again with tape water and were dried at $115^0C$ for one hour. The elemental analysis of the dried samples was carried out again. The chemical composition of the samples (Feed and Product) is given in table 1.The specific gravity of all the samples was determined using a pycnometer.

$$MgCO_3 + 2HCL \longrightarrow MgCl_2 + CO_2 + H_2O$$
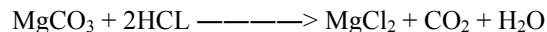
With decreasing feed to solution ratio in case of all the three samples, the concentration of $BaSO_4$ in the final product increases as most of the gangue material react with HCL during HCL treatment. With a feed to solution ratio of 1:3, the concentration of $BaSO_4$ increases from 93.50% to 98.02% for (Sample A), from 78.80% to 95.50% for (Sample B), and from 59.00% to 82.00% for (Sample C). Similarly at the same feed to solution ratio, the concentration of oxides decreases from 3.86% to 0.76% in case of Sample (A), from 16.40% to 0.00% in case of Sample (B), and from 17.80% to 1.06% in case

Table:- 1.1  General Specification of Barite for Commercial Application [13-17]

| Property | As a Wetting Agent | Filler Applications | Glass Grade Barite | Barium Chemicals Manufacturing | Paint Grade Barite |
|---|---|---|---|---|---|
| Sp. Gravity (gm/cm$^3$) | 4.2 | --- | --- | --- | --- |
| BaSO$_4$ | 92% min | 95% min | 95% min | 92-96% min | 95% min |
| SiO$_2$ | --- | --- | 1.5%max | --- | --- |
| Fe$_2$O$_3$ | --- | --- | 0.15% max | 1% max | 0.05% max |
| Al$_2$O$_3$ | --- | --- | 0.15% | --- | --- |
| Color | --- | near white | White | --- | White |
| Particle Size | 95% (45 μm) | 95% (45 μm) | 100% (8.5 μm) | gravel size | 37 μm |

## 3  Results

Alkali and alkaline earth metal such as Ca, Mg, K, and Sr present within the ore react with HCL and form water soluble chloride that can easily be washed out with distilled/tap water. Following chemical reaction take place during HCL treatment.

$$CaCO_3 + 2HCL \longrightarrow CaCl_2 + CO_2 + H_2O$$
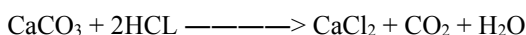
of Sample (C) and the specific gravity of sample "A" increases from 4.2 to 4.41gm/cm$^3$, sample "B" increases from 3.8 to 4.21 gm/cm$^3$, and sample "C" increases from 3.2 to 3.91 gm/cm$^3$. The initial and final concentration of $BaSO_4$ and oxides of all the three samples i.e. Sample (A), Sample (B), and Sample(C) is shown in figure table 3.1, table 3.2, table 3.3, and 3.4.

Table 3.1 Chemical Composition of Barite in its Crude form (wt %)

| Sample | BaO | SO$_3$ | SiO$_2$ | Oxides | LOI | Moisture Content | BaSO$_4$ | Total | Sp. gr g/cm$^3$ | Recovery |
|---|---|---|---|---|---|---|---|---|---|---|
| A | 65.53 | 28.00 | 0.00 | 3.86 | 1.56 | 0.16 | 93.50 | 99.50 | 4.20 | ---- |
| B | 58.00 | 22.60 | 1.83 | 16.40 | 2.69 | 0.21 | 78.80 | 99.93 | 3.80 | ---- |
| C | 42.00 | 17.00 | 20.27 | 17.80 | 3.65 | 0.27 | 59.00 | 100.16 | 3.20 | ---- |

Table 3.2 Chemical Composition of Sample A (wt %) with different Feed to Solution ratio

| Feed/Sol (gm/ml) | BaO | $SO_3$ | $SiO_2$ | Oxides | LOI | Moisture Content | $BaSO_4$ | Total | Sp. gr g/cm$^3$ | %Recovery |
|---|---|---|---|---|---|---|---|---|---|---|
| 1:1 | 66.20 | 30.10 | 0.00 | 1.25 | 1.48 | 0.17 | 96.00 | 99.20 | 4.32 | 90.76 |
| 1:2 | 66.64 | 30.40 | 0.00 | 1.06 | 1.18 | 0.15 | 97.04 | 99.50 | 4.347 | 91.89 |
| 1:3 | 66.73 | 31.29 | 0.00 | 0.75 | 1.07 | 0.16 | 98.02 | 99.91 | 4.41 | 94.16 |
| 2:1 | 65.30 | 29.6 | 0.00 | 1.50 | 2.30 | 0.25 | 94.90 | 98.95 | 4.27 | 90.33 |
| 3:1 | 64.60 | 28.4 | 0.00 | 1.7 | 3.20 | 0.30 | 93.00 | 98.20 | 4.21 | 89.51 |

Table 3.3 Chemical Composition of Sample B (wt %) with different Feed to Solution ratio

| Feed/Sol (gm/ml) | BaO | $SO_3$ | $SiO_2$ | Oxides | LOI | Moisture Content | $BaSO_4$ | Total | Sp. gr g/cm$^3$ | %Recovery |
|---|---|---|---|---|---|---|---|---|---|---|
| 1:1 | 67.01 | 27.12 | 1.41 | 0.56 | 3.5 | 0.2 | 94.13 | 99.71 | 4.201 | 90.78 |
| 1:2 | 65.92 | 28.7 | 1.4 | 0.47 | 2.38 | 0.19 | 94.62 | 99.62 | 4.217 | 91.53 |
| 1:3 | 66.87 | 28.63 | 1.15 | 0 | 3.11 | 0.21 | 95.50 | 99.87 | 4.219 | 95.51 |
| 2:1 | 65.17 | 28 | 1.7 | 2.3 | 2.6 | 0.2 | 93.17 | 99.99 | 4.14 | 92.22 |
| 3:1 | 64.5 | 26 | 2.56 | 4.61 | 2.18 | 0.24 | 90.51 | 100 | 4.09 | 91.88 |

Table 3.4 Chemical Composition of Sample C (wt %) with different Feed to Solution ratio

| Feed/Sol (gm/ml) | BaO | $SO_3$ | $SiO_2$ | Oxides | LOI | Moisture Content | $BaSO_4$ | Total | Sp. gr g/cm$^3$ | Recovery |
|---|---|---|---|---|---|---|---|---|---|---|
| 1:1 | 52.00 | 26.00 | 10.28 | 1.25 | 3.4 | 0.27 | 78.00 | 99.74 | 3.71 | 92.54 |
| 1:2 | 54.50 | 25.10 | 10.23 | 1.16 | 3.9 | 0.26 | 79.6 | 95.12 | 3.80 | 93.09 |
| 1:3 | 56.60 | 25.4 | 10.20 | 1.06 | 6.00 | 0.29 | 82.00 | 99.61 | 3.91 | 94.25 |
| 2:1 | 52.00 | 25.00 | 11.80 | 4.88 | 6.01 | 0.30 | 77.00 | 99.99 | 3.69 | 91.35 |
| 3:1 | 48.71 | 21.30 | 16.00 | 7.3 | 6.20 | 0.31 | 70.00 | 99.81 | 3.61 | 95.31 |

## 4 Conclusions

A significant change in the concentration of $BaSO_4$ from 93.50% to 98.02% in case of Sample (A), 78.80% to 95.50% in case of Sample (B), and 59.00% to 82.00% in case of Sample (C), makes the process more reliable and feasible for the beneficiation of barite. The concentrated barite samples, i.e. Sample (A) and (B) contains more than 90% barium sulphate and may be used in the manufacturing of barium chemicals, oil and gas well drilling process as well as in paint and glass industry.

Since Sample (C) contains more impurities, so it may be concentrated by further decreasing feed to solution ratio or by the combination of some other physical and chemical processes.

## 5 References

[1] Wayne S. Moen, Barite in Washington, Bulletin No. 51, (1963)

[2] A.Khan, F. Kanwal and M. Aurangzaib, Study on the Beneficiation of Gunga Barite with different concentration of Hydrochloric Acid, P.C.S.I.R Laboratory, *Jour.Chem.Soc.Pak*. Vol. 25, No. 1, (2003)

[3] S. A. Khan and H.Khan, Enrichment of Barite Deposits of NWPF for Commercial Utilization, *Jour.Chem.Soc.Pak.* Vol.24, No.3, (2002)

[4] H. Crookshank and A.M Heron, *Geological Survey Pak,* Records 7 (Part 2) (1954)

[5] Z. Ahmad. Geological Survey Pak, Records 15 part (2)

55 (1969

[6] J. Griffith "Barite non drilling applications" Industrial Minerals, U.K 21(1984)

[7] L. Walter, *Geol.Jb.A*, **127**, .299 (1991)

[8] F.L. Klinger U.S. Geological Survey and R.L. Richards, U.S. Bureau of Mines, "BARITE IN PAKISTAN" PROJECT REPORT Pakistan Investigations, (IR) PK- 31, (1973)

[9] F.L. Klinger and M.I Ahmad, *Geol. Surv. Pak.* 21(1967)

[10] Sajjad Ali, Yaseen Iqbal and Rick Ubic, Phase and Microstructural Characterization of Hazara Barite, Pakistan. JPMS Conference Issue Material (2011)

[11] R. A. Shah and I. A. Khan, Reduction of Barite with sui gas, a Preliminary Report, pp. 165, (1963)

[12] S. M. Ali and S. Aziz, *Pak. Jr. Sci. Ind. R*es. 8, 136 (1965)

[13] V. Hussain, H Khan, K. M Qureshi, N. Ahmad, and Ali, *Pak.Jr.Sci.Ind. R*es. 34, (2-3). (1991)

[14] Andrew Scogings, Drilling grade barite: the global outlook, December (2014)

[15] Kevin A Bonel, British Geological Survey, Mineral Profile, Barytes, September (2005)

[16] P.R.A. Andrews and R.K. Coolings, 'Barite in Canada" Industrial Minerals 46-57 (1990)

[17] Michael J. Harris, Barite Flotation, New Mexico Bureau of Mines and Mineral Resources, Open File Report #336, (1988)

[18] W. W. Scott and N H. Furman "Standard Method of Chemical Analysis" 16th Edition; (1962)

# Effect of Soluble and Neat cutting oils on machining Alloy steel

**Sohail Aamer[1],***, **Iftikhar Hussain[1]**

[1]Departmen of Industrial Engineering, University of Engineering and Technology, Peshawar
***Email**: sohailaamar95@gmail.com*

**Abstract**

In todays era of industrialisation, quality throughput and low production cost are keys ingredients to survival in competitive global market. These aspects are further pronounced while dealing machining processes. Hitherto, Metal cutting fluids occupy a nucleus position in industry and a play a sheet anchor role in drooping cutting area temperature and provision of requisite lubrication. Numerous factors affect work piece surface quality and tool life while machining, major being the type of cutting fluid vis a vis tool type and cutting conditions. In this paper,effect of 2 x cutting fluids ( 1 x neat cutting oil & 1 x soluble cutting oil with 8% concentration being used in local industry ) on surface quality and tool life have been examined while turning AISI4140 alloy steel, at specific cutting conditions / parameters i.e spindle speed, feed rate, depth of cut using carbide inserts. During experimentation it was revealed that type of cutting fluid bears significance while studying surface quality of AISI 4140 & carbide insert life. Moreover, it was concluded that soluble cutting oils are fruitful to be employed as cutting media as compared to neat cutting oil considering surface finish / tool life as output responses while machining AISI4140.

**Key words**: Spindle speed, depth of cut, feed rate, lubricant, tool life and surface finish.

## 2    Introduction

The usage of cutting fluids in metal working dates back to 1894 when F. Taylor found out an average increment in speed to 33 % whilst cutting fluid is applied and tool life is not compromised [1]. Cutting fluid enhances efficacy of an industrial system while providing lubrication and low temperatures at cutting zones. [2]. Better surface quality and better facet precision are attained by using cutting fluids. Major properties of metal cutting fluid include:-

- To present a lubricant layer between metal and tool, to   decrease friction.
- Act as a coolant to decrease accumulation of heat during machinig.
- Blushing away the produced metallic chips.
- Acquire requisite work piece surface finish.

The impulsion these days is to achieve maximized production rate in fewer possible time with better tool life / surface finish. [3]. Lawal et al. [4] carried out turning on  AISI 4340 alloy steel using carbide inserts. Water based mineral oil and a synthetic fluid was used as cutting fluid. It was found out that nature of cutting fluid accounted for approx 50 % effect on surface quality. Moreover depth of cut and spindle speed bore approximate 33% & 65% on surface quality respectively. Belluco and De Chiffre [7] carried out experiments to gauge effect of vegetable oils in drilling AISI 316L steel using cobalt based high speed steel tools. Cutting forces, tool wear and chip making ware studied by utilizing said lubricants. Relative increment in tool life coupled with certain decrease in cutting forces was observed during said experiment. In addition it was found out that vegetable oils displayed better than mineral ones. Khan et al. [5]carried out turning on AISI 9310 alloy steel to investigate effect of minimum quality lubrication (MQL) technique utilizing vegetable oil cutting fluid in comparison with dry / flood machining. Surface quality, tool life, interfacial temperature / chip formation were validated using carbide tools at certain given cutting conditions i.e speed (483, 348, 246, 223, m/min), depth of cut (1.0 mm), feed rate (0.10, 0.13, 0.16 and 0.18 mm/rev). An increase in cutting speed / feed rate enhanced tool / chip temperature under minimum quantity lubricant technique. This happened due to changing cutting parameters and energy increment. Surface quality decreased much under flooding in comparison to dry turning due to electro chemical reaction between workpiece and carbide insert. Moreover, principal flank wear appeared to enhance as well underf all conditions. Finally MQL was presumed to be better a option in exhibiting better surface finish. Krishna et al. [6] studied the turning operation on AISI 1040 alloy steel using SAE-40 / coconut oil with cemented carbide tool. Following cutting conditions were enforced while machinig;

Spindle speed (60, 80 and 100 m/min), depth of cut as1.0 mm and feed rate (0.14, 0.16, 0.2 mm/rev. The measurement of temperature done using embedded thermocouple placed at tool insert bottom. The surface quality reduced with corresponding increment in spindle speed / feed rate. Moreover, coconut based oil displayed significantly better performance as compared to SAE-40 oil in terms of average flank tool wear / cutting temperature / tool wear.

## 3    Conduct of Experiment

The experiments were conducted on TC-20 Johan ford CNC machine.Coated carbide tool VNMG 160408V company KYOCERA, made in Japan were employed. Moreover, tool holder, PCLNR2020O-12 N7Y1 was

used.Work piece used was AISI 4140. The composition of work piece is as under:-

Table 1: Composition of AISI 4140

| Elements | | | | | | |
|---|---|---|---|---|---|---|
| C | Si | Mn | P | S | Cr | Mo |
| 0.42 | 0.28 | 0.86 | 0.015 | 0.034 | 0.95 | 0.15 |



Fig 1: TC-20 Johan ford CNC machine / Tool holder PCLNR2020O-12 N7Y1

Table 2: Details of cutting parameters

| Spindle speed (rpm) | Feed rate (mm/rev) | Depth of Cut (mm) |
|---|---|---|
| 1200 | 0.10 | |
| 1600 | 0.15 | 0.5 |
| 2000 | 0.20 | |

Turning operations for above mentioned parameters were performed for 3 x cutting mediums namely **dry, commercial neat cutting oil and commercial soluble cutting fluid (8%concentration).** The experiments were performed in a local industry. Aim of experiment is to determine the optimal cutting fluid that bears better surface quality and tool wear while turning AISI 4140. Mitutoyo Sj series was used to determine the surface roughness and tool wear of work piece. The procedure

adopted to measure surface roughness and tool wear is appended below:-

- **Surface Roughness**. 12 x measurements were taken after turning 150mm work piece @cutting conditons given in table 2 using 3 x different cutting mediums.The Mitutoyo Sj series gauge was employed each time for measuring surface roughness i.e **Ra values (µm).**

- **Tool Wear**. The tool wear has been measured in terms of tool life i.e minutes.The workpiece was machined till it reached surface roughness value of 1.6µm using Mitutoyo Sj series gauge else insert met premature failure. Simultaneously, time spent in meeting aforesaid condition was noted,thus bearing tool life.

**4    Results / Analysis**

Various measurements of surface roughness and tool life achieved during carrying out above mentioned experiment @ 0.5mm ( depth of cut ) are given in table below:-

Table 3: Surface roughness values @ 3 x Cutting media

| Spindle speed (rpm) | Feed rate (mm/rev) | Medium | Surface Roughness (µm) | Tool life (mins) |
|---|---|---|---|---|
| 1600 | 0.10 | Dry | 0.43 | 10.6 |
| 2000 | 0.10 | Dry | 0.45 | 6 |
| 1600 | 0.15 | Dry | 0.44 | 8.5 |
| 2000 | 0.15 | Dry | 0.48 | 4 |
| 1600 | 0.10 | **Neat oil** | 0.40 | 21 |
| 2000 | 0.10 | **Neat oil** | 0.41 | 16.6 |
| 1600 | 0.15 | **Neat oil** | 0.39 | 15 |
| 2000 | 0.15 | **Neat oil** | 0.42 | 9.7 |
| 1600 | 0.10 | *Soluble(8%)* | 0.37 | 22 |
| 2000 | 0.10 | *Soluble(8%)* | 0.39 | 18 |
| 1600 | 0.15 | *Soluble(8%)* | 0.38 | 16.5 |
| 2000 | 0.15 | *Soluble(8%)* | 0.40 | 11 |

## 3.1 Surface Roughness

A line graph has been plotted for various surface roughness values against combination of 4 x cutting conditions at 3 x different cutting media i.e dry, neat oil, soluble oil with 8% concentration. Following can be implied keeping in view obtained surface roughness values:-
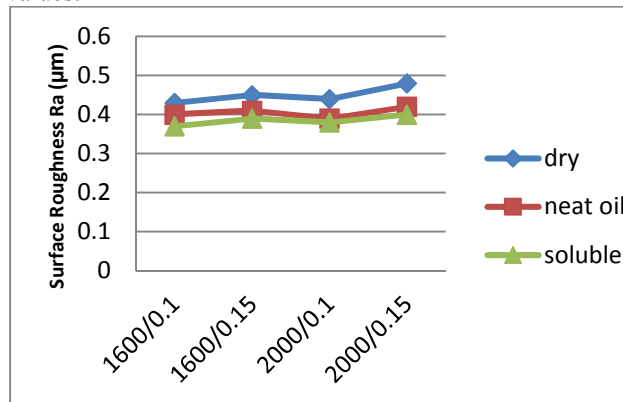


Fig 2. Surface roughness @ 4 x cutting conditions

(i)    Highest surface roughness value (0.48μm) was observed while machining at 2000rpm and 0.15mm/rev, feed rate.
(ii)   Lowest surface roughness value (0.37μm) was observed while machining at 1600rpm and 0.10mm/rev, feed rate.
(iii)  The soluble oil (8% concentration) exhibited least surface roughness values as compared to other competing media i.e dry/neat oil cutting.
(iv)   At low cutting speeds/feed rates, the surface quality tends to enhance.
(v)    At higher cutting speeds/ feed rates, the surface roughness values enhance profoundly owing to increasing temperature at cutting zone.

*The relationship between various cutting conditions / media in terms of percentage effect on obtained Ra(μm) values is represented in following graphs vis a vis explained in ensuing paras:-*
(i)    Keeping in view Ra value attained during machining at **dry cutting** medium and parameters (**1600 rpm/0.10mm/rev feed rate**) as reference, surface quality increased by 6.97% and 13.95% using neat oil and soluble oil(8% concentration) respectively.
(ii)   Keeping in view Ra value attained during machining at **neat oil cutting** medium and parameters (**1600 rpm/0.10mm/rev feed rate**) as reference, surface quality increased by 7.5% using soluble oil(8% concentration).
(iii)  Keeping in view Ra value attained during machining at **dry cutting** medium and parameters (**1600 rpm/0.15mm/rev feed rate**) as reference,

surface quality increased by 8.88% and 13.33% using neat oil and soluble oil(8% concentration).
(iv)   Keeping in view Ra value attained during machining at **neat oil cutting** medium and parameters (**1600 rpm/0.15mm/rev feed rate**) as reference, surface quality increased by 4.87% using soluble oil(8% concentration).
(v)    Keeping in view Ra value attained during machining at **dry cutting** medium and parameters (**2000 rpm/0.10mm/rev feed rate**) as reference, surface quality increased by 11.36% and 13.63% using neat oil and soluble oil(8% concentration).
(vi)   Keeping in view Ra value attained during machining at **neat oil cutting** medium and parameters (**2000 rpm/0.10mm/rev feed rate**) as reference, surface quality increased by 2.56% using soluble oil(8% concentration).
(vii)  Keeping in view Ra value attained during machining at **dry cutting** medium and parameters (**2000 rpm/0.15mm/rev feed rate**) as reference, surface quality increased by 12.5% and 16.66% using neat oil and soluble oil(8% concentration).

(viii) Keeping in view Ra value attained during machining at **neat oil cutting** medium and parameters (**2000 rpm/0.15mm/rev feed rate**) as reference, surface quality increased by 4.76% using soluble oil(8% concentration).
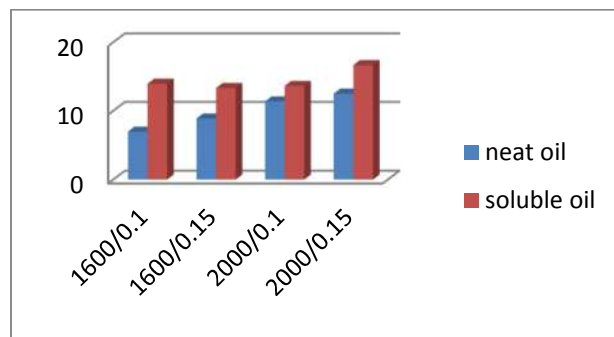


Fig 3. Percent change in Ra values(μm) using dry cutting    medium in relation to neat/soluble oil @ 4 x cutting conditions

## 3.2 Tool Life

A line graph has been plotted for different tool life values obtained against combination of 4 x cutting conditions at 3 x different cutting media i.e dry, neat cutting oil, soluble oil   (8% concentration). Following can be deduced keeping in view obtained results:

(i)    Highest tool life (**22 mins**) was achieved using soluble oil (8% concentration) at cutting parameters (1600rpm, 0.10mm/rev feed rate).

(ii) Least tool life while turning AISI 4140 was obtained at dry cutting medium i.e **4 mins** with cutting parameters (2000rpm, 0.15mm/rev).
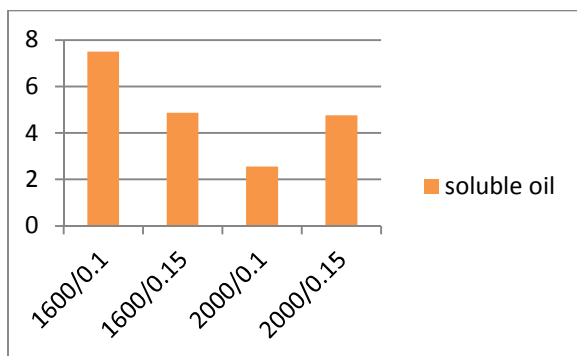


Fig 4. Percent change in Ra values(μm) using soluble oil as cutting medium in relation to neat oil @ 4 x cutting conditions
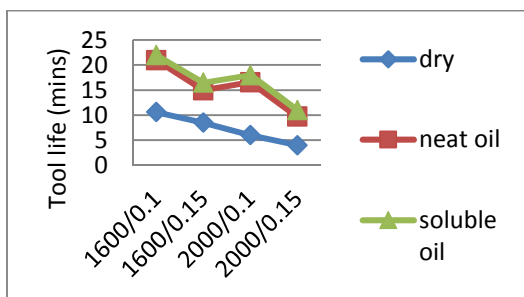


Fig 5. Tool life @ 4 x cutting conditions

(iii) At low cutting speeds / feed rates, the tool life tends to enhance.

*(iv)* At higher cutting speeds and feed rates, the tool life reduces.

*The relationship between various cutting conditions / media in terms of percentage effect on obtained tool life (mins) values is represented in following graphs vis a vis explained in ensuing paras:-*

(i) Considering tool life value attained while machining at **dry cutting** medium and parameters (**1600 rpm/0.10mm/rev feed rate**) as reference, tool life increased by 98% and 107.54% using neat oil and soluble oil(8% concentration) respectively.

(ii) Considering tool life value attained while machining at **neat oil cutting** medium and parameters (**1600 rpm/0.10mm/rev feed rate**) as reference, tool life increased by 4.76% using soluble oil(8% concentration).

(iii) Considering tool life value attained while machining at **dry cutting** medium and parameters (**1600 rpm/0.15mm/rev feed rate**) as reference, tool life increased by 76.47% and 94.12% using neat oil and soluble oil(8% concentration) respectively.

(iv) Considering tool life value attained while machining at **neat oil cutting** medium and parameters (**1600 rpm/0.15mm/rev feed rate**) as reference, tool life increased by10% using soluble oil(8% concentration).

(v) Considering tool life value attained while machining at **dry cutting** medium and parameters (**2000 rpm/0.10mm/rev feed rate**) as reference, tool life increased by 177.66% and 200% using neat oil and soluble oil(8% concentration) respectively.

(vi) Considering tool life value attained while machining at **neat oil cutting** medium and parameters (**2000 rpm/0.10mm/rev feed rate**) as reference, tool life increased by 8.4% using soluble oil(8% concentration).

(vii) Considering tool life value attained while machining at **dry cutting** medium and parameters (**2000 rpm/0.15mm/rev feed rate**) as reference, tool life increased by 142.5% and 175% using neat oil and soluble oil(8% concentration) respectively.

(viii) Considering tool life value attained while machining at **neat oil cutting** medium and parameters (**2000 rpm/0.15mm/rev feed rate**) as reference, tool life increased by 13.40% using soluble oil(8% concentration).
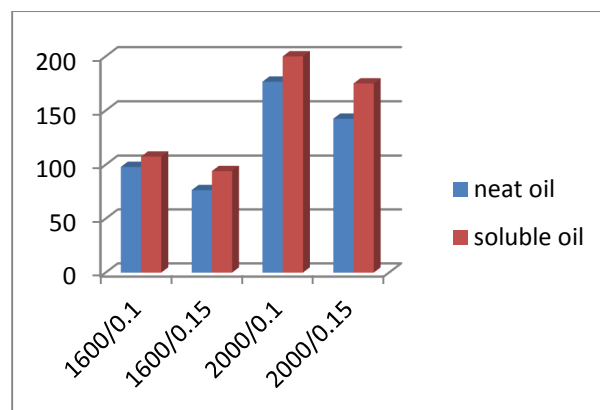


Fig 6. Percent change in Tool life using neat / soluble oils in relation to dry cutting @ 4 x cutting conditions
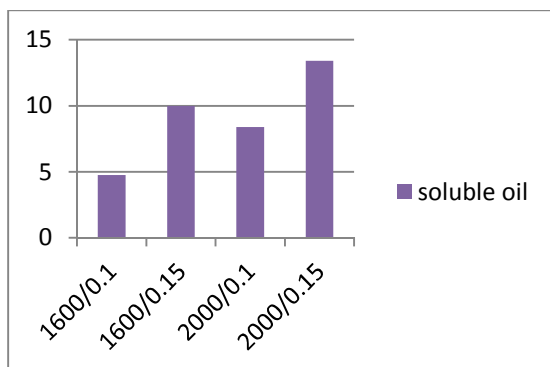
Fig 7. Percent change in Tool life using neat oil as cutting medium in relation to soluble oil @ 4 x cutting conditions

## 5     Conclusion

Extensive experiments were carried out in turning AISI 4140 alloy steel to obtain desired surface quality and tool life at different sets of cutting parameters using 3 x different cutting media namely dry, neat oil, Soluble oil (8% concentration).Finally it can be inferred that soluble oils are better to use as cutting fluids as compared to neat cutting oils / dry cutting i.e providing high surface integrity / quality and enhanced tool life

## 6     Acknowledgments

The author is highly indebted to **DAUD&SONS**, kohat road, Peshawar for the valuable / extensive help extended in carrying out research work at their factory premises.

## 7     References

[1]   R. F. Ávila, A. M. Abrão, "The effect of cutting fluids on the machining of          hardened AISI 4340 steel," Journal of Materials Processing Technology 2001;119-124.

[2]   D. U. Braga, A. E. Diniz, G. W. A. Miranda, N. L. Coppini, "Using a minimum   quantity of lubricant (MQL) and a diamond coated tool in the drilling of aluminum- silicon alloys," Journal of Materials Processing Technology 2012;122:127-138.

[3] J.S. McCoy, "Introduction: Tracing the historical development of metal working fluids," in: J.P. Byers (Ed.) (2010) 611–616.

 [4]   S.A. Lawal, I.A. Choudhury, Y. Nukman, "Evaluation of vegetable and mineral           oil-in-water emulsion cutting fluids in turning AISI 4340 steel with coated carbide          tools, " J. Clean. Prod. 66 (2014) 610–618.

[5] M.M.A. Khan, M.A.H. Mithu, N.R. Dhar, "Effects of minimum quantity           lubrication on turning AISI 9310 alloy steel using vegetable oil-based cutting fluid,"         J. Mater. Process. Technol.209 (2009) 5573–5583.

[6] P.V. Krishna, R.R. Srikant, D.N. Rao, "Experimental investigation on the performance of nanoboric acid suspensions in SAE-40 and coconut oil during  turning of AISI 1040 steel," Int. J.Mach. Tool Manuf. 50 (2010) 911–916.

[7] W. Belluco, L. De Chiffre, "Performance evaluation of vegetable – based oils in drilling austenitic stainless steel," J. Mater 50 (2014) 31–56.

# Experimental Analysis of Pressure Retarded Osmosis from Salinity Gradients using Hollow Fiber Membrane Contactor

**Arshad Hussain[1*], Wajid Ali[1], Mohammad Younas[2]**
Department of Chemical Engineering, University
of Engineering & Technology Peshawar Pakistan
*Corresponding author[*]*
*Email: engr_arshadhussain@uetpeshawar.edu.pk*

**Abstract**
Pressure retarded osmosis (PRO) is a proficient membrane technique that gets energy from salt solution without negative effects on the atmosphere. PRO setup works between fresh water (river water) through membrane into pressurized high salinity draw water (sea water). Through the using of many membrane technique, hollow fiber membrane contactors (HFMC) are well suited for its use in PRO process due to its self-mechanical supportive capability and without the use of any spacer. In the current research work, PRO lab scale setup was designed and fabricated. Power density, reverse salt flux and water flux were the important performance parameters that were analyzed during the study. Effect of applied pressure and process temperature were investigated on the PRO performance. Outcomes show that water flux and power density increases significantly by increasing temperature. 0.19 W/m² power was attained at optimum applied pressure and temperature. Tube side of HFMC fronting saline solution also improves process performance.
**Key words**: Pressure Retarded Osmosis, Hollow Fiber Membrane Contactor, Salinity Gradients, Power Density

## 1 Introduction

The membrane separation methods are very common these days. This is very popular and has increased admiration in many applications like water treatment, metal extraction, wastewater treatment and several other industrial techniques. There is also a very much attention in osmotic processes like reverse osmosis (RO), PRO and forward osmosis for water and energy bids due to their potential for energy productions [1]. Numerous methods have been invented for this task containing reverse electrodialysis; PRO, hydrogel swelling and capacitive mixing [2]. Those procedures which are available nowadays, pressure retarded osmosis have gained the most attention.

PRO is a favorable membrane separation technique that makes power through the usage of salinity gradients without causing the surroundings [3]. Pressure retarded osmosis power production setup works on salinity gradient between a fresh water feed solution (river water) through membrane into pressurized high salinity draw solution (sea water),

through the help of the difference in osmotic pressure across the membrane. A part of the high salinity water is passing through a generator for power generation [4]. PRO is a naturally friendly technology use for energy generation and RO brine recycles [5].

She et al. [6] describes the key terminologies related to PRO, in which efficiency was enhanced by lowering the concentration of feed solution, increasing the draw solution concentration and temperature, and adjusting the membrane with tube side facing saline solution. RO and marketablly obtainable membranes were tried by loeb et al. [7]. They were found that these membranes did not function correctly in PRO due to higher salt flux. Achilli et al was also hired FO membrane in PRO [8] and experimentally found that the FO membrane was bent under high pressures. FO membranes were also leading to severe salt leakage through the membrane due to which considerably reduces the power density and lowers the optimum pressure in PRO. Furthermore, the shadow effect prepared by the spacer in the feed side channel was start to decrease the total water flux and power density of the FO membrane investigated by Kim et al. [9].

By using numerous membranes for this process, HFMC are best suitable for its use in PRO techniques due to its own mechanical caring ability, high packing density and without the use of any spacer [10]. Membrane contactors (MCs) depends on difference in concentration crossways the membrane to allows for separating components of solute from gaseous and liquid mixture. By increasing quantity mass transfer and reduce the center and functioning rate exertions have been complete to advance different designs of MCs. Hollow fiber membrane contactor module is found to be utmost efficient owing to its cheap module and high packing densities as its practical applications are also more common. Parts of the contactors are huge quantity of fibers fixed with compact epoxy at membrane shell sides. This procedure indications properly as shell and tube heat exchanger [11].In the present research work, a new lab scale pressure retarded osmosis design is proposed to analyze experimentally the various process and operating parameters by using Hollow fiber membrane contactor.

## 2 Materials and Methods

A lab scale PRO setup and visio schematic as shown in figure.1 and 2. It consist of tanks, water baths, pumps, valves and a HFMC.
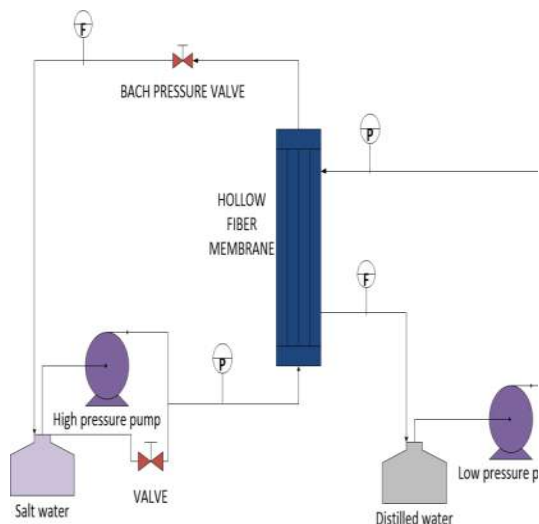


**Figure 1: VISIO Schematic of PRO**



**Figure 2: Experimental Setup of PRO**

## 2.1 PRO Experiments Lab Scale System

Critical ranking sodium chloride (NaCl) was used throughout the experiments to make saline solutions.

Fresh water was used as feed solution saline water enter into the tube side of HFMC and this solution was pressurizing by high pressure diaphragm pump. Applied pressure was control by pressure release valve and flow rate was monitor with the help of needle valve. Fresh water enter into the shell side of HFMC using low pressure pump. Pressure was observed by using pressure transmitters. Flow rate of both solutions were observed by flow meters. Water baths were used in the trials for temperature measurement. Both solution Salinity was measured by using conductivity meter.

## 2.2 ANALYSIS AND CALCULATION

By using the data of pressure and change in feed water for each run. Water flux and power density was calculated according to the relationships.

$$J_w = \frac{\Delta V}{A \Delta t} \quad \text{.........................(1)}$$

$$W = \Delta P \bullet Jw \quad \text{.....................(2)}$$

Where;

    Jw is water flux

    $\Delta V$ is change in feed water

    A is membrane area

    $\Delta t$ is change in time

    W is power density

    $\Delta P$ is change in applied hydraulics pressure

Water Flux through the HFMC was calculated founded on the change of weight of water in the distilled water tank.

## 3 RESULTS AND DISCUSSION

### 3.1 Effect of Pressure on Water Flux

Water flux was determined by the equation (1). PRO performance was investigated for different set of pressure. Feed and draw water flow rate were kept constant at 400 ml/min. Concentration of saline water is 30 g/l for all experiments. It was detected that by increasing pressure water flux considerably decreases as shown in figure.3.1.

### 3.2 Effect of Temperature on Water Flux

Each experiments were performed for 50 minutes to optimize the effect of temperature with same conditions but different temperature of 25, 30 and 35 °C. Figure 3.2 shows that water flux increases by increasing temperature. 35°C is optimum temperature for PRO process.

### 3.3 Effect of Pressure on Power Density

Pressure is one of the key parameter for PRO performance. Power was determined by the product of

applied pressure and water flux as showed in equation (2). Figure 3.3 displays the influence of pressure on power production. It was noted that by increasing pressure from 1" to 5", more power was generated
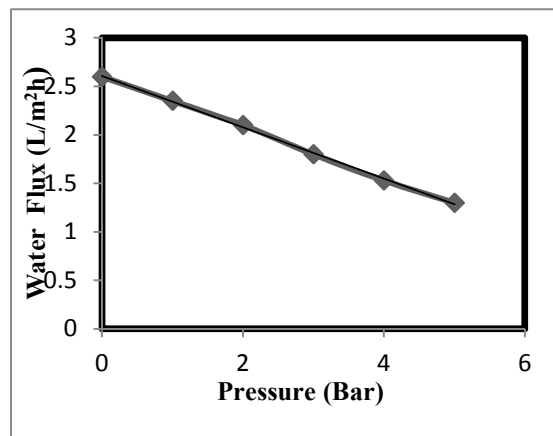


**Figure 3.1: Water Flux by Varying Applied Pressure**
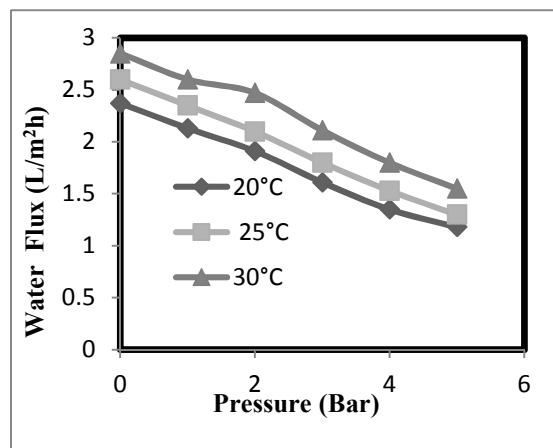


**Figure 3.2: Water Flux by Varying Operating Temperature**

(Flow rate of both solutions: 400 ml/min , salt water concentration: 30 g/l, Temperature 20 ºC, 25 ºC, 30 ºC)

**3.4 Effect of Temperature on Power Density**

Effect of temperature on PRO power density was calculated for three temperatures i.e 20ºC, 25 ºC and 30 ºC. Power density data was calculating for different temperature and pressure. Figure 3.4 mentions the connection of pressure with power density for diverse temperature. By experimentation it was determined that power density of 1.10W/m² was attained at a temperature of 35 ºC.
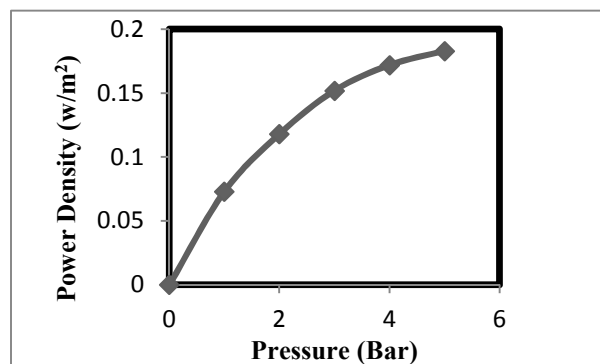


**Fig.3.3. power density by varying applied pressure**

(Flow rate of both solutions: 400 ml/min , salt water concentration: 30 g/l, Temperature 25 ºC)
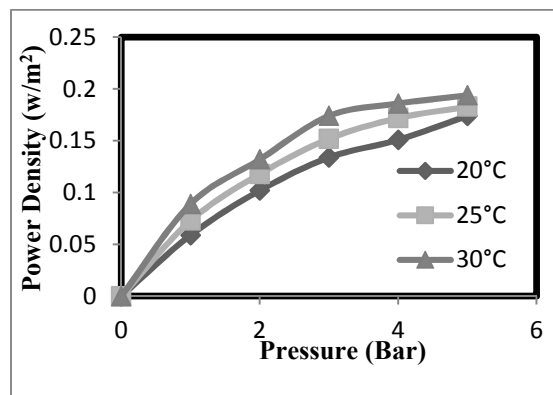


**Figure.3.4: Power density by varying temperature and pressure**

(Flow rate of both solutions: 400 ml/min , salt water concentration: 30 g/l, Temperature 20 ºC, 25 ºC, 30 ºC)

**3.3 Optimization of Pressure and Temperature**

From figure 3.4, it is evident that pressure and temperature has a significant effect on water flux and power density. In order to find out the optimum conditions, average energy generated for a time period of 1 hours at various pressure and temperatures were determined and it was observed that 5 bar pressure and 30 ºC operating temperature are the best operating conditions for this kind of PRO setup.

**4 Conclusions**

The current work estimations the performance of pressure retarded osmosis for Power density at numerous optimum pressure and temperature. 0.193 W/m² power is attained at a pressure of 5 bar and temperature 30 ºC. Furthermore, it was also found that salt flux occurs in feed water by increasing pressure and temperature from optimum condition which

decrease water flux. HFMC cleaning is a dynamic step for usage of membrane capably as it decreases the growth of microbes and membrane fouling. The study illustrate that PRO can be used for osmotic energy generation.

**Acknowledgement**

**Nomenclature**

PRO   : Pressure Retarded osmosis

HFMC   : Hollow Fiber Membrane Contactor

FO    : Forward Osmosis

RO    : Reverse Osmosis

NaCl    : Sodium Chloride

**References**

[1] Xu. Y. Peng, X.Y. Tang, C.Y. Fu QSA, S. Z. Nie, Effect of draw solution concentration and operating conditions on forward osmosis and pressure retarded osmosis performance in a spiral wound module, J Membr Sci 348 (2010) 298–309.

[2] X. Zhu, W. Yang, M.C. Hatzell, B.E. Logan, Pressure retarded osmosis for power generation from salinity gradients: is it viable?, J Environ Sci 48 (2014)7157–7163.

[3] S.Chou, R.Wang, L. She, Q. She, C. Tang, A.G. Fane, Thin film composite hollow fiber membranes for pressure retarded osmosis (PRO) process with high power density. J Membrane Sci 389 (2012) 25–33.

[4] I.L. Alsvik, M.B. Hägg, Pressure retarded osmosis and forward osmosis membranes: materials and methods, J Polymers Sci 5 (2013) 303–327.

[5] G. Han, S. Zhang, X. Li, T. Chung, High performance thin film composite pressure retarded osmosis membranes for renewable salinity gradient energy generation, J Membrane Sci 440 (2013) 108–121.

[6] Q. She, X. Jin, C.Y. Tang, Osmotic power production from salinity gradient resource by pressure retarded osmosis: effects of operating conditions and reverse solute diffusion, J Membrane Sci 402 (2012) 262–273.

[7] S. Loeb, T. Honda, M. Reali, Comparative mechanical efficiency of several plant configurations using a pressure retarded osmosis energy converter, J Membrane Sci 51 (1990) 323–335.

[8] A. Achilli, T.Y. Cath, A.E. Childress, Power generation with pressure retarded osmosis: an experimental and theoretical investigation, J Membrane Sci 343 (2009) 42–52.

[9] Y.C. Kim, M. Elimelech, Adverse impact of feed channel spacers on the performance of pressure retarded osmosis, J Environ Sci 46 (2012) 4673–4681.

[10] S.Chou, R.Wang, A.G.Fane, Robust and high performance hollow fiber membranes for energy harvesting from salinity gradients by pressure retarded osmosis, J Membr Sci 448 (2013) 44–54.

[11] A. Gabelman, S.T. Hwang, Hollow fiber membrane contactors, J Membrane Sci 159 (1999) 61-106.

# Sedimentation, Eustasy and Tectonic Constraints of the Eocene to lower Miocene Hydrocarbon Systems of the Gulf of Gabes Basin (GGB) in Tunisia

*Fatma TAKTAK*

*National School of Engineers of Sfax, Lab.-3E, BP, 3038 Sfax, Tunisia*
*Faculty of Sciences, University El Manar, Lab.-URGAMM, Tunis, Tunisia*
*College of Business, University of Modern Sciences, Dubai, United Arab Emirates*
*Corresponding author:*
*f.taktak@ums.ae and fatimtak@gmail.com*

## Abstract

The objectives of this work is to demonstrate the close time palogeographic relationships and geodynamic configurations of the Eocene to Langhian series considered two major and superposed petroleum systems in the **GGB** covering a time span from the Eocene to the Lower-Middle Langhian times. 66The major constraints on the lithotectonic evolution, differentiation of sedimentary deposits and basin geometry are also examined in the light of sismostratigraphical and sismotectonic interpretations. The modeling approach helps to contribute of the economic potential of the carbonate platform of Eocene to Langhian series in the **GGB**. The main results Mesozoic era dominated by distension / transtension in relation to global Tethyan and geodynamic events, a period of transpressional initiated in the Santonian-Campanian, are formed in larger bending radii folds, with a recovery during the Eocene (Pyrenean phase). Basin platform transition towards **SW-NE**, appears clearly controlled by tectonic transverse steering dominant **NW-SE**, Nature of the sliding tectonic cross resulted in flowers fault structures, elevated structures, platforms deposits seats carbonate and blocks collapses half grabens in the presence of significant vertical component of rejection on oblique sliding cross accidents. In this work, we identified a very similar scenario occurs again during the Oligocene transition with the same polarity direction, platform facies of the Kétatna formation, and pelagic facies of Salammbô formation. The benthic El Garia and Ketatna Formations and the corresponding coeval but pelagic Boudabbous and Salammbô Formations extend in a broad area covering the gulf of Hammamet, Pelagian Block and gulf of Gabes in the Southeast Tunisia. A similar geodynamic fact generates the same structures and paleogeography results. The reconstruction of petroleum system series in the **GGB** help decipher a stratigraphical scenario of repetitive benthic carbonate platforms stacked in the sequence of stratigraphic ages, fitting laterally and upwards into pelagic counterparts. The Eocene El Garia reservoir passes laterally to into the Boudabbous source rock Formation. This complex is sealed by Cherahil Formation, which in turn is transgressed over by a repetitive benthic but moderately to highly thick limestone packages in the Ketatna Formation and fits laterally into its pelagic counterpart the Salammbô Formation.

**Key words:** Petroleum Industry, Seismic 2D/3D Reflection, Hydrocarbon petroleum system, superposed carbonate platforms, Eocene to the Lower-Middle Langhian times.

## 1 Introduction

In the Gulf of Gabes Basin (GGB), limestones in the El Garia (Ypresian) and Ketatna (Rupelian-Burdigalien) formations are gas and oil prone (Fournié, 1978; Ben Ferjani and al., 1990; Beavington Penney and al., 2008; Taktak and al., 2010; Taktak and al., 2011). They are comprised of carbonate platforms on which sedimentation, eustasy, tectonics and inter-related subsidence have exerted important controls. They were deposited in a lithotectonic setting dominated by two major orogenic phases, the Pyrenean and the Alpine. The former enabled collision of the North African plate margin against its Apulian counterpart (Dewey ans al., 1989; Er Raioui, 1994; Rabhi, 1999 ; Tlig and al., 2010), the initiation of the Tethys closure, the erection of the so-called box-folds and subsequent emersion of the Saharan Atlas (Castany, 1951, 1952).

The benthic El Garia and Ketatna Formations and the respectively coeval but pelagic Boudabbous and Salammbô Formations extend in a broad area covering the gulf of Hammamet, gulf of Gabes and Pelagian Block in the Southeast Tunisia (Fournié, 1978; Bishop and al., 1988; Ben Ferjani and al., 1990; Taktak and al., 2011). Detailed petrographic and petrophysical studies of the limestones building the El Garia Formation have shown these series form commercial reservoir in the Ashtart, Cercina, Chergui, … oilfields.

Furthermore, the study of petroleum system series in the GGB help decipher a stratigraphical scenario of repetitive benthic carbonate platforms stacked in the sequence of stratigraphic ages, fitting laterally and upwards into pelagic counterparts. The Eocene El Garia reservoir settled in a broad area in the southwest of the

GGB in continuity with the NW-SE directed Nummulitic ridge, passes laterally to the northwest into the Boudabbous Formation, a source rock dominated by marly limestones and black shales highly enriched in marine kerogen. This complex is sealed by a thick shaly Cherahil Formation, which in turn is transgressed over by a repetitive benthic but moderately to highly thick limestone packages in the Ketatna Formation. The latter broadly covers the proximal areas in the GGB, Pelagian Block and gulf of Hammamet, and fits laterally into its pelagic counterpart the Salammbô Formation which consists of rather marly deposits interceded with limestone beds. Moreover it is likely that increasing tectonic subsidence which might have dominated in the study area during the Lower Miocene has caused the marls and black shale deposits in the Salammbô Formation prograde over and seal the Ketatna limestone reservoirs.

Based on recent fieldwork, stratigraphic data, well results and wireline log details, and seismic data, the main aim of this study is to demonstrate the close time/palogeographic relationships and configurations of these two major and superposed petroleum systems in the GGB covering a time span from the Eocene to the Lower-Middle Langhian times. The major constraints on the lithotectonic evolution, differentiation of sedimentary deposits and basin geometry are also examined in the light of sismostratigraphical and sismotectonic interpretations. The modeling approach help decipher benthic carbonate platform- and pelagic depositions, paleoeustatic changes in sealevel, tectonics and inter-related subsidence, and as a consequence reservoir quality and source rock formation and maturation in the study time interval. This help us better contribute to the knowledge of the economic potential of the Eocene to Langhian series in the GGB.

## 2    Materials and Methods:

The reconstruction of basin framework is based on the biostratigraphy, sequence stratigraphy and seismotectonics of the Paleocene to Lower Miocene series in the study area. Wellbore core and cuttings data were compared to sonic and gamma ray wireline logs and migrated 2D-seismic profiles. The wellbores with total depths ranging from 2800 to 3500m, were performed in the main concessions and oilfields in the Gulf of Gabes basin and onshore in the coastal Gabès-Sfax and southeastern Jeffara areas (**Fig. 01**). The biostratigraphic and lithostratigraphic details obtained for the wells were compared to those outcrop lithologies described by previous authors for the Paleogene and Early Neogene series in the Central Tunisia, Sahel and Cap Bon areas.

The 2D-seismic reflection profiles covering the study area were acquired by the CGG (Compagnie Générale de Géophysique) in the period 1978–1995. The seismic sections were calibrated to the main lithologic successions and biostratigraphic data, as well as Gamma Ray and acoustic wireline log details registered for the wells (**Fig. 01**). This helps depict seismic horizons and sequence boundaries with local gaps and tectonic discontinuities, delineate sequence organizations and correlate the subsurface depositional systems. The reconstruction of basin framework is based on the main seismic facies and seismotectonic features with clear offsets but also on the detailed petrology of cores and well-cuttings and the varying geometries of depositional systems including clear tectonic and sedimentary gaps.
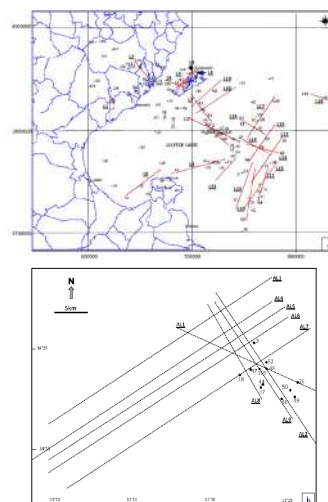


**Fig - 01.-** Location of the Oil wells survey in the Gulf of Gabes and the near continent. **a.**: L$_x$ Profiles located in the Gulf of Gabes (L$_x$); **b.**:Profiles AL$_x$ intersecting with Ashtart field.

## 3    Results and discussion:

According to previous works, the Atlassic domain (Burollet, 1956; Boukadi, 1994; Henchiri, 2009) and Sahel area (Haller, 1983; Touati, 1985; Boussiga, 2008), as well as the entire study area (Bishop, 1988; Taktak and al, 2010) were subjected to a dominant transpressive tectonic period beginning in the Santonian and ending in the early Paleogene with local East-verging reverse faulting identified in Santonian series of the Sahel area (Boussiga, 2008). During this period, transpressional move southeastwards exerted on transverse regional faults (E-W, S-N and NW-SE), has created rhomb-shaped and rotating blocks (Bédir and al., 1992) with dominant lowstand followes by a transgressive (TST) benthic carbonate sedimentation deposited in peritidal to infratidal milieu as indicated by frequent hummocky cross stratifications. These series have formed during the entire Senonian and have covered broad anticline structures and fault-bend folds. However, the latter were rimmed by depressions and remarkably subsiding tectonic troughs which have been infilled by the Upper

Maastrichtian-Paleocene marls of the El Haria Formation.

The Ypresian to Lower Lutetian was a period of intense tectonic activity with dominant transpression directed NW-SE. In the Atlassic domain and Sahel area, tectonic deformation caused local uplift and erosion, continental/lacustrine sedimentation on emerged blocks and has initiated the Atlassic box and salt-cored folds directed majorly NE-SW (Castany, 1952; Burollet, 1956; Bishop, 1988). In contrast, no clear folding features have been observed in the study area. Instead, the tectonic framework includes a dominant tilted morphology with ramp-shaped and uplifted blocks surimposed to a network of normal faults directed majorly NW-SE and faced NE, but conjugated with additional regional sutures, S-N and particularly E-W in strike. This paleogeograpic style has closely controlled the Lower Eocene sedimentation. Indeed, during the Ypresian and Lower Lutetian, the ramp-shaped blocks were the sites of benthic carbonate deposition and enrichments in coarsened foraminifered tests(**Fig.02**).
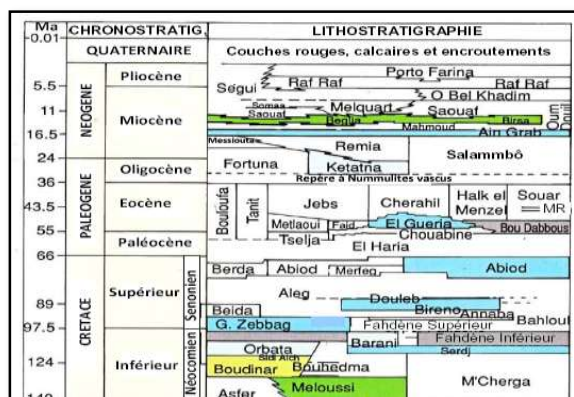


**Fig. 02.-** Lithostratigraphic Chart of study area in Central eastern part of Tunisia (based on the work of Burollet, (1956), Biély et al. (1972), Comte et Dufore (1973), Fournié (1978), Vernet (1981), Bismuth et Bonnefous (1981), Blondel (1991), Bonnefous et Bismuth (1982), Bismuth (1984), Bishop (1985, 1988) et Ben Ferjani et al. (1990)).

The Ypresian to Lower Lutetian platforms include carbonate sequences deposited in a Transgressive Systems Tract during a period of sealevel rise. These deposits may rest disconformably over the older El Haria and Abiod Fms sequences. Towards the Jeffara mole, the Eocene Group (Chouabine and El Garia Fms) fits laterally into the Tanit Formation which comprises shales and dolomites deposited in a shallow, presumably lagoonal environment, whereas, to the northeast, in the deeper basin parts, this Group passes laterally to thick pelagic series of bituminous black shales and lime mudstones enriched in Globigerinids in the Boudabbous Fm.

The Ypresian to Lower Lutetian transpression was followed by a period of dominant subsidence and basinfill by remarkably thick, shaly and carbonate series

of the Cherahil Fm which may rest disconformably over older deposits of the El Garia, El Haria and Abiod Fms. The Cherahil Fm are shales and siliciclastics poor in faunal content, interceded by mollusk bearing limestones. In field outcrops, these are forth to fifth order sequences with dominant shaly strata at the base shallowing upward into Bryozan, Mollusk and Ostrea-rich limestones. The Cherahil/Souar shaly series provide seals for the oil prone El Garia Fm reservoirs and subdivide into three main Members: the so-called lower Cheral/Souar A and Upper Cherahil.Souar B separated by the middle Reineche Member formed by lime mud to wackestone containing mainly Nummulites. The latter horizon, picked in seismic limes, could represent a Lutetian TST even if tectonic transpression, folding and uplift would be accompanied by bottom elevation and subsequent carbonate deposition in the photic zone. Indeed, tectonics is thought to have intervened and enabled the Cherahil Fm present local gaps and rest disconformably over the Maastrichtian Abiod, El Garia and EL Haria Fms.

During the Rupelian to Burdigalian period, carbonates and marls prevailed with a clear disparity between platform and basin deposits. In the carbonate platforms, a basal Rupelian Horizon, 2 to 20m thick is easily picked in seismic lines in the Sahel, Pelagian Block and study area and is described as the lime wacke/packstones enriched in *Nummulites vascus*. It retraces a retrograding TST during the Early Oligocene, and passes upward to a highly thick carbonate series the stratotype of which was described by Fournié in the Ketatna well. The series include lime mudstones and wacke/packstones enriched in coarse grained foraminifered tests, Nummulites, Bryozoans, Echinoids, Mollusks and Corals, dolomite beds and clay intervals. At the Jebel Abderrahman, Lower Oligocene limestone packages appear stratified, admit marl intercalations and display a similar faunal content (Chine Dehman, 1986; Taktak et al., 2012). In study area, the Ketatna Fm deposited to the west on a broad platform rimming a local basin centered on the gulf of Gabes.

The geometry of the Rupelian-Burdigalian deposits was dictated by deep-seated and reactivating shear faults directed NW-SE, S-N and SW-NE, with antithetic branches. Due to prevalently transtensional move of these flower-faults almost NW-SE in azimuth and with dominant vertical offsets, polygonal blocks organized in stacked ramps have formed, among which the most uplifted were the sites for benthic carbonate facies of the Ketatna Fm with clear shallowing up features on paleohighs. In contrast, subsiding blocks have formed graben and half graben basins always infilled by pelagic shales, marls and embedded lime mudstones of the Salammbô Fm. The latter may disconformably overlie the Boudabbous, the Abiod and the Douled Formations.

Also, in the Oil wells, the Ketatna Fm transgresses the El Garia and Douleb Fms respectively.

Thus, the basin framework during the Rupelian-Burdigalian times, responds to those continuously reactivating shear zones inter-related with the older Upper Cretaceous-Lower Paleocene and Upper Eocene tectonic phases. This is clearly evidenced by the lateral variations in facies and total thicknesses of the Ketatna and Salammbô Fms, but also by the facies inversions and interpenetrations thus forming a transition zone between these formations. The transitional lithofacies are dominated by an admixture of marls and carbonate deposits as observed in wells and in seismic lines cutting across the Ashtart oilfield, with flower faults and discontinuous hummocky cross-stratified seismic facies. The seismic facies reconstruction and extension of the platforms of El Garia and Ketatna are complex. In the internal ramp area of the two platforms of El Garia and Ketatna, seismic reflections are continuous, high amplitude and concordant; this can be explained by stacking carbonate seismic reflectors; however, the frequency is often low, so that reflections are sub-parallel configurations resulting spatiotemporal continuity of carbonate sedimentation. The seismic facies of the middle ramp variables are generally characterized by discontinuous reflections are strong amplitudes and sometimes clearly arranged in parallel or sometimes chaotic. The external ramp is cut by seismic reflections that offer high amplitude, discontinuous, sometimes heckled with an oblique configuration or hummocky (**Fig. 03**).
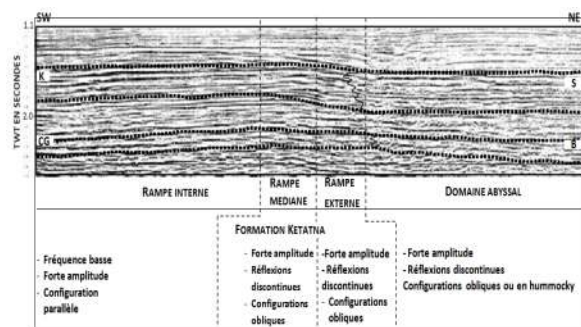


**Fig. 03.-** Seismic zoning reconstitution of areas of carbonate rimmed shelf to Basin for the complex Kétatna formation – Salammbô formation. Formations: CG (Chouabine and El Garia), B: Boudabbous, K: Ketatna, S: Salammbô.

The findings of the study based on the well to well correlations enhanced by logging analyzes, information obtained from the 3D seismic picking of seismic horizons and conversion in depth from Oil well data, stratigraphically well defined, and delineation of facies by discontinuities and sequences hiatus, gives Fms El Garia and Ketatna form of carbonate platforms. The respective periods of lithofaicies genesis, these platforms have recognized regional extension and were dislocated by regional dominant accidents NW-SE direction which was originally transpressive paleostress movements

especially during the Maastrichtian, the Late Eocene, middle Miocene and Miocene-upper.

These carbonate platforms seem to have been built in favorable photic conditions. The sedimentary floor may be relatively steady incline imposed on blocks cut by branched flowers faults that appear in the seismic profiles. Trends in bioaccumulations large foraminifera, including the Eocene and richness of carbonate productivity are indicatives of dominance of an environment beaten by the currents, well ventilated and oxygenated with absence of turbidity and away from detrital input. This type of environment supports Nummulites accumulations installed on the platform depth sloping shaped carbonate ramp built during the lower Eocene, then later repeated with the same intensity of productivity carbonates and explosion biological diversity in marine shallow during the Oligocene-Miocene.

Successive sedimentation periods, was also conditioned by two factors: tectonics and eustasy. The tectonic factor contributes to the fragmentation of the blocks, their tilt; and in the distal area, subsidence basin with a marked change in the sedimentation represented by the micrite and pelagic deposits nature. Thus, by collapse of blocks of El Garia Formation is relayed by the facies of the Boudabbous Formation, and Formation Ketatna by pelagic deposits Salammbo Formation. Similarly, the above figures show that it is practically the same rooted accidents that have structured the Eocene sedimentary floor and controlled spatial and temporal distribution of deposits, by replaying the Oligocene- lower Miocene to impose similar palaeogeographical limits and almost at the same place of transition between Fm Ketatna and Salammbo Formation.

Tracking facies described using cuttings and cores from boreholes clarifies the facies distribution and to recognize the characteristics of three distinct environments facies usually described for carbonate platforms ramp shaped (Read, 1982, 1985; Bosence, 2005): internal ramp facies (inner ramp), the middle ramp facies low bathymetry (mid-ramp) and outer ramp facies (outer-ramp) depth seaward up the talus (Wilson, 1975; Read, 1982, 1985; Burchette and Wright, 1992; Collins et al., 2006).

Finally, eustatisme also involved in instaurations of retrograde transgressive deposits like those of Reinèche, Ain Ghrab and Melqart marking a remarkable extension of carbonate platforms in response to accelerated in the average level of sea rising.

In the major parts of the basin of GGB faulting and subsidence controls on sedimentation. We found the deep effects of tectonics in the heightening blocks, deformation and sealing unconformably. The most common events were those Maastrichtian-Paleocene transition with the creation of bald areas in the NW part

of the field of study and particularly in the Sahel of Sfax (Touati, 1985). Dynamic events largely affected the series were also identified through the well data to higher-Priabonian Eocene to Langhian-Serravallian, then the passage of the Group Oum Douil Fm Somaa preceding the transgression of the limestone Fm Melqart and continentalization corresponding to laguno-lacustrine deposits Fm Oued Belkhédim.

Carbonated systems associated with the development of a carbonate sedimentation on rhombic blocks which can be controlled by the eustatisme; but such carbonate sedimentation with an environmental dimming internal platform type to external platform environments. The deposits are thick and have lateral facies transitions with equivalent formations formed in the pelagic environment in abyssal conditions.

We also noted the repetition over time of this type of sedimentation especially the yprésienne time (Fms El Garia / Boudabbous) and later during the Oligocene-Burdigalian (Fms-Ketatna Salammbo). When comparing the zonal distribution of one and the other of these formations, and taking into consideration the well data and literature information, we realize in the study area, it is the same tectonic lineaments that have worked at successive periods to score quite deeply lithology series along paléogéographique transition lines passing between paleogeographic areas kind of training and different environment.

The results of the seismic analysis enhanced by well logging allowed to recognize the architecture of the sedimentary cover at different times and to establish the relationship between lithostratigraphic formations (lateral facies passages), but also amongst tectonics and sedimentation.

The major tectonic style is the continuity amongst a deep tectonic affecting the basement, which witnesses have been described by the authors in Medenine and Jeffara area (Burollet 1991; Bouaziz et al., 2002). We demonstrate that old tectonic dating to the Paleozoic and early Mesozoic is transmitted into the sediment cover. These manifestations are ramified to flowers faults that reactivated at different epoch. The major trending faults NW-SE to NS most often play slideably with escarpments often looks NE, dislocated and raised of blocks and basins in grabens and half-grabens, very similar of what is commonly described by the authors on the continent in Central of Tunisia and in the chain of Chotts.

The research of the discontinuities amongst sequences linked to the main geodynamic events that have controlled the basin sedimentation helps to clarify the geometry and the Seismic-sequences cutting series. Thus, it is possible to correlate the seismic supersequences to what is known in regions in central Tunisia as sedimentary megacycles identified by the authors regionally.

In previous work (Taktak et al., 2008. Taktak et al, 2009), we found a great similarity in the distribution of deposits platforms and those pelagic equivalent, but at different ages as the Ypresian and Oligocene-Miocene epoch. We also showed the precise controls of eustatisme, reactivation of tectonic deep accidents, and morphology of the basins (platform, abyssal areas, shoals, emerged edges of blocks, ...) in the differentiation of carbonate sedimentary environments.

Thus, it clearly shows by geophysical profiles in Ashtart province, on the vast field of the Pelagian block, the range of platforms (internal, intermediate and external shelf) and transitions to pelagic abyssal domains (basins) at the Ypresian (Formations Jebs, Metlaoui, El Garia, Boudabbous) and Miocene-Oligocene (Formations Messiouta / Fortuna, Ketatna Salammbo) are controlled by the same tectonic lineaments reactivated by ramified faults (flower structure) and sliding at different epochs.

Cutting blocks, the heightening local, also the subsidence allows the installation of carbonates platforms ramps environments in which carbonates productivity is provided by large foraminifera as Nummulites the Operculines the Discocyclines for Ypresian strata but also by Nummulites, the Amphistégines lepidocyclines and in the case of deposits of Oligocene-Miocene. These carbonate platforms ramps often isolated because of dislocated tectonic blocks. These ramps are distally deepened (distally steepened) and rarely bordered (rimmed shelves) (**Fig. 04**).



**Fig. 04.-** proposed sedimentation models for the Ypresian and Oligocene carbonate platformes (A). Oligocene complex: 1. Deposits rubified Fm Messiouta; 2. Fm. Fortuna; 3. Clay; 4. Nummulites and other Foram. ; 5. bryozoans and algae; 6. bioclastes; 7. pelagic Wildlife; 8. Limestone and dolomite; 10.Faults Mvts; 11. Limestone; (B) Complex Ypresian: 1. Nummulites type B; 2. Nummulites type A. 3. Bivalva; 4. gastropods; 5. Crinoids; 6. Faults; 7. Globigerinidae; 8. Nummulitoclastes; 9 Stromatolites and

algal laminae; 10. Clay; 11. Gypsum; 12. Limestone and dolomite; 13. fault movements direction.

## Conclusions

As we mentioned in the case of the Permian, this architecture division of the Southeast margin of Tunisia during the Permian, Triassic, Jurassic, Cretaceous and as demonstrated in this work for the Cenozoic, is controlled by ancient tectonic directions affecting the basement (Bouaziz et al, 2002), has always supported the development of carbonate platforms and bioconstructions. It is therefore the same environmental control factors and sedimentation at different periods, produce the same effects. However, more NE and north, block subsidence allows the establishment of a frank pelagic sedimentation, where the lateral transitions in bathymetry conditions contrast between El Garia Fms / Boudabbous and Ketatna / Salammbô.

The interest and petroleum implications of these formations is the tectonic dynamic controlled the genesis of carbonate facies platforms ramp, but also their subsequent deformation: the El Garia Fm was distorted by tectonqiues Pyrenean deep reactivated movements during the Lutétien -to Priabonian, and Fm Kétatna by Alpine movements dating from Langhian-Serravallian.

The deformation of the blocks and their emersion promotes the effects of the diagenesis dolomitisante enhances the porosity and permeability of such reservoirs; while the tectonic enhances fracture porosity and permeability. Moreover, reservoirs in contact with older source rocks (Bahloul, Fahdène, Aleg, El Haria, Tselja, Chouabine), but also with contemporary source rocks (Fms Boudabbous / El Garia and Salammbo / Ketatna) and the existence of thick clay layers forming impermeable seal against of oils migration (Fms Souar, Fm higher Salammbo; Oum DOUIL Group), offer a real opportunity for improving national reserves on hydrocarbons.

## Acknowledgments

## References

**Beavington-Penney,S.J., Nadin,P., Wright , V.P.,  Clarke, E., McQuilken, J., Bailey, H.W., 2008.** Reservoir quality variation on an Eocene carbonate ramp, El Garia Formation, offshore Tunisia: Structural control of burial corrosion and dolomitisation. Sedimentary Geology, 209 :  42–57

**Bédir M., Zargouni F., Tlig S. et Bobier C., 1992.** Subsurface geodynamics and petroleum geology of transform margin basins in the Sahel of Mahdia and El Jem (Eastern Tunisia), American Association of Petroleum Geologists, v.76, n° 9, pp. 1417-1442.

**Ben Ferjani, A., Burollet, P.f., Mejri, F., 1990.** Petroleum Geology of Tunisia.ETAP, 194p.

**Biely, A., Rakus, M., Robinson, P., Salaj, J., 1972.** Essai de corrélation des formations miocènes au Sud de la dorsale tunisienne. Note du Service Géologique de Tunisie. Tunis, vol. 38, pp. 73–92.

**Bishop, W. F., 1985.** Eocene and Upper Cretaceous reservoirs in East central Tunisia. Oil Gas J.1, p 137-142.

**Bishop, W. F., 1988.** Petroleum Geology of East- Central Tunisia. American Association of Petroleum Geologists Bulletin, V. 72, n°9, pp. 1033-1058

**Bismuth, H., et Bonnefous, J., 1981.** The biostratigraphy of carbonate deposits of the Middle and Upper Eocene in northeastern offshore Tunisia, Palaeogeogr. Palaeoclimat. Palaeoecol. 36 191–211.

**Bismuth, H., Hooyberghs, H.J.F., 1994.** Foraminifères planctoniques et biostratigraphie de l'Oligocène et du Néogène dans le sondage de Korba-1 (Cap Bon, Tunisie nord-orientale). Bull.Centr. Rech. Explor. Prod. Elf-Aquitaine 18 (2), pp. 489–528.

**Blondel, T., 1991.** Les séries à tendance régressive marine du Miocène inférieur à moyen en Tunisie centrale. Thèse ès-Sciences Géologiques. Université de Genève, Suisse, 487 p.

**Bonnefous, J., Bismuth. H., 1982.** Les faciès carbonatés de plate forme de l'éocène moyen et supérieur dans l'offshore tunisien nord-oriental et en mer pélagienne : implications paléogéographiques et analyse micropaléontologique.- Bull. Centre de Rech. Explor. Prod. Elf Aquitaine- Pau 6, 2, pp. 337-403.

**Bosence, D., 2005.** A genetic classification of carbonate platforms based on their basinal and tectonic settings in the Cenozoïc. Sedimentary Geology, 175: 49-72.

**Bouaziz, S., Barrier, E., Soussi, M., Turki, M.M., Zouari, H., 2002.** Tectonic evolution of the northern African margin in Tunisia from paleostress data and sedimentary record, Tectonophysics, 357, 227– 253.

**Boukadi, N., 1994.** Structuration de l'Atlas de Tunisie : signification géodynamique et cinématique des noeuds et des zones d'interférences structurales au contact de grands  couloirs tectoniques. Thèse Doc. Es Sciences, Univ. Tunis II, 252p.

**Boussiga, H., 2008.**  Géophysique appliquée aux séries paléogènes du Sahel de Tunisie. Tectonique de socle, halocinèse et implications pétrolières. Thèse en Sciences Géologiques, Université Tunis El Manar. 159p.

**Boussiga, H., 2008.** Géophysique appliquée aux séries mésocénozïques du Sahel : sismostratigraphie, sismotectonique et implications pétrolières. Thèse Sciences Géologiques, Université Tunis El Manar, 1605p.

**Burchette, T.P. et Wright, V.P., 1992.** Carbonate ramp depositional systems. Sedimentary Geology, 79: pp 3-5

**Burollet, P.F., 1956.** Contribution à l'étude stratigraphique de la Tunisie Centrale : Ann. Min. Géol., Tunis, 18, 350p.

**Burollet, P. F., 1991.** Structures and tectonics of Tunisia. Tectonophysics, 195. pp 359 - 369.

**Castany, G., 1951.** Etude géologique de l'Atlas tunisien oriental. Thèse Sci., Annales Mines Géol., Tunis, 8, 632p.

**Castany, 1952.** Paléogéographie, tectonique et orogenèse de la Tunisie. XIXth international Geological Congress, Alger, "Monographies Régionales", 2, (1), 63p.

**Chine-Dehman, N., 1986.** Les calcaires néritiques de l'Oligocène au Miocène moyen en Tunisie orientale. Stratigraphie et Sédimentologie. Dipl. Etudes Approfond., Faculté des Sciences de Tunisie, 113p.

**Collins, L.B., Read J.F, Hogarth, J.W., J.W. Coffey, B.P., 2006.** Facies, outcrop gamma ray and C–O isotopic signature of exposed Miocene subtropical continental shelf carbonates, North West Cape, Western Australia. Sedimentary Geology, 185, 1-19.

**Comte, D., Dufaure, P., 1973.** Quelques précisions sur la paléogéographie tertiaire en Tunisie centrale et centro-orientale, du cap Bon à Mezzouna, Ann. Mines Géol., Tunis 26 (1973) 241–256.

**Dewey, J.F., Helman M.L., Knott S.D., Turco E. et Hutton D.H.W., 1989.** Kinematics of the western Mediterranean, Geological Society, London, Special publications, v. 45, pp. 265-283.

**Erraoui, L., 1994.** Environnements sédimentaires et géochimie des séries de l'Eocène du Nord-Est de la Tunisie. Thèse de Doctorat de Spécialité, Université Tunis II, 244p.

**Fournié, D., 1978.** Nomenclature lithostratigraphique des séries du Crétacé supérieur au Tertiaire de Tunisie. Bull. Cent. Rech. Expl. Prod. Elf. Aquitaine, V. 2, n° 1, p. 79-148.

**Haller, P , 1983.** Structure profonde du Sahel tunisien. Interprétation géodynamique, thèse de 3ème cycle, Université de Besançon, 163 p.

**Henchiri, M., 2009.** Les faciès siliceux éocènes dans le bassin de Gafsa, Tunisie 695 méridionale: Sédimentologie, Minéralogie et transformations diagénétiques. 696 Thèse Sciences Géologiques, Université Tunis-El Manar, 130 pp.

**Rabhi, M., 1999.** Contribution a` l'étude stratigraphique et analyse de l'évolution géodynamique de l'axe Nord-Sud et des structures avoisinantes, Thèse Sciences, Université Tunis II, 217p

**Read, J. F., 1982.** Carbonate platforms of passive (extensional) continental margins-types, characteristics and evolution. Tectonophysics, 81, 195-212.

**Read, J.F., 1985.** Carbonate platform facies models. Amer. Assoc. Pet. Geol. Bulletin, 69, 1 –21.

**Taktak, F., Bouaziz, S., Rigane, A. et Kharbachi, S., 2008.** Contexte tectono-sédimentaire dans le golfe de Gabès au cours de l'Yprésien (Tunisie Centre-Est). 22ème Colloque de Géologie Africaine, Hammamet, 4-6 novembre, p. 142.

**Taktak, F., Bouaziz, S., Rigane, A. Boufarès, T. et Kharbachi, S., 2008.** Dépouillement des réponses diagraphiques des séries oligocènes : caractérisation lithostratigraphique et interprétation tectono-sédimentaire d'un gisement de l'off-shore tunisien (golfe de Gabès, Tunisie Centre-Est), 22ème Colloque de Géologie Africaine, Hammamet, 4-6 nov., p. 141.

**Taktak, F., Rigane, A., Bouaziz, S. et Kharbachi, S., 2008.** Contexte tectono -sédimentaire de la région de Sfax au cours de l'Yprésien (Tunisie centre – Est – Golfe de Gabès). 3èmes Journées Tunisiennes de la Géologie Appliquée(JTGA) – Sousse, 21-23 mars, Tunisie.

**Taktak, F., Rigane, A., Bouaziz, S., 2009.** Modélisation de bassins et systèmes pétroligènes : exemple de l'Eocène du golfe de Gabès en Tunisie centro-orientale. 4ème Congrès Maghrébin de Géophysique Appliquée. Hammamet (Tunisie) : 26-27 mars. Livre résumés , p. 178

**Taktak, F., Kharbachi, S., Bouaziz, S., Tlig, S., 2010.** Basin Dynamics and
708 Petroleum Potential of the Eocene Series in the Gulf of Gabes, Tunisia. Journal 709 of Petroleum Science and Engineering 75, 114–128.

**Taktak, F., Rigane, A., Boufarès, T., Kharbachi, S., Bouaziz, S., 2011.** Modelling 711 approaches for the estimation of irreducible water saturation and heterogeneities 712 of the commercial Ashtart reservoir from the Gulf of Gabes, Tunisia. J. Pet. Sci. 713 Eng. 78, 376–383.

**Taktak, F., S. Bouaziz; S.Tlig (2012) -** Depositional and tectonic constraints for

715 hydrocarbon targets of the Lutetian–Langhian sequences from the Gulf of Gabes 716 — Tunisia - Journal of Petroleum Science and Engineering, 82-83.

**Tlig, S., Sahli, H., Er-Raioui, L., Alouani, R., Mzoughi, M., 2010.** Depositional 718 environment controls on petroleum potential of the Eocene in the North of 719 Tunisia. Journal of Petroleum Science and Engineering 71, 91–105.

**Touati, M. A., 1985.** Etude géologique et géophysique de la concession de Sidi El Itayem en Tunisie orientale. Sahel de Sfax. Histoire géologique du bassin et évolution de la fracturation et des structures du Crétacé au Plioquaternaire. Thèse Doct. Univ. P. et M. Curie, Paris VI.

**Vernet, J.P., 1981.** Esquisses paléogéographiques de la Tunisie Durant l'Oligocène et le Miocène inférieur. Actes du Premier Congre`s National des Sciences de la Terre (Tunis, Septembre 1981), pp. 231–244.

**Wilson, J.L., 1975.** Carbonate facies in geological history. Springer Verlag, New York, 471p.

# Application of Monte Carlo Simulation for Cement Raw Material Blending Optimization

Kausar Sultan Shah[*1], Safi Ur Rehman[1]

*[1]Dept. of Mining Engineering, University of Engineering and Technology, Peshawar-25120, Pakistan*
*\*Corresponding author*

***Email***: kausarsultanshah@gmail.com

## Abstract

One of the most significant processes in cement manufacturing is raw mix preparation for the kiln. Multiple raw materials are blended in appropriate proportions to produce a raw mix. Raw mix design requires a balance of different oxides for good burn ability and to produce a quality product. One of the challenges relating raw mix design and cement quarry operations is the uncertainty in chemical composition of raw material mined from the quarry and purchased from the market. These uncertainties affect the mining activities and raw mix design. In this research, Monte Carlo simulation was used to cope with the challenges associated with uncertainties in raw material composition. Drill hole samples data was used to generate statistical models and identify the statistical distribution of the quality parameters of raw material. Monte Carlo simulation and linear programming optimization model was developed in MS Excel and was tested, using data from Kohat Cement Quarry, located in Khyber Pakhtunkhwa, Pakistan, as a case study. The results of this case study revealed that the variation in chemical composition of raw material which affects the cement plant operations, can be handled using simulation and optimization techniques.

**Keywords:** Uncertainties, burn ability, Quarry, Statistics and probability distribution.

## 1    Introduction

Cement manufacturing is a mineral based process industry. It consist four basic steps including [1],

1. Providing raw material from quarry.
2. Raw mix preparation from raw material and additives.
3. Raw mix processing (burning) in cement kiln to produce clinker and
4. Clinker grinding to achieve final product as cement.

Calcareous and argillaceous minerals are major ingredient of cement. Mostly, these raw materials are mined through quarry operations. These raw materials are blended in appropriate proportion to meet the stoichiometric needs i.e. required quality and quantity of major and minor oxides.

In order to produce the final product i.e. cement, required quantity and quality of various oxides (Calcium ($CaO$), Iron ($Fe_2O_3$), Silica ($SiO_2$) and Alumina ($Al_2O_3$)) is required is [2]. To achieve the balance of these oxides following indices needs to be within a specified range given in equation 1, 2 and 3:

$$LSF = \frac{CaO}{2.80SiO_2 + 1.18Al_2O_3 + 0.65Fe_2O_3}$$

*Range (0.845 – 0.9)*       (1)

$$SR = \frac{SiO_2}{Al_2O_3 + Fe_2O_3}$$

*Range (2.6-2.9)*       (2)

$$AM = \frac{Al_2O_3}{Fe_2O_3}$$

*Range (1.5-2.0)*       (3)

Where LSF stand for Lime saturation factor (LSF), SR for Silica ratio and AM for Alumina ratio.

Similarly, the individual major oxides must be kept within limit i.e. CaO (40-42%), $SiO_2$ (14-15%), $Al_2O_3$ (2.7-3.4%) and $Fe_2O_3$ (1.65-2.17%). If the raw material containing small amount of some harmful constituents, it may produce adverse effect either on the quality of the final product cement/clinker or to the processing of the clinker. During selecting the raw materials, following constituents should be kept below this range i.e. free silica (<3%), magnesia (<5%), alkalies (sodium and potassium <0.60%), chlorine (<0.05%). If free silica is present in the raw material in excessive amount cause wear in the mill and crusher [4]. Therefore raw material mined from quarry or purchased from the market must meet the quality/raw mixing constraints i.e. provide required percent content of major oxides and minimize the cost of overall raw material preparation.

Monte Carlo is a well-known stochastic simulation technique mostly used to find data uncertainty. It is used in three main field i.e. optimization, numerical integration and probability distribution. It is also used in weather forecasting and providing help in future decisions for business. Monte Carlo simulation primarily use random number to solve problems which might be deterministic in nature [10]. Bruni et al. (2011) incorporate the uncertainty importance of resources as a constraint to scheduling of a project. Cantoni et al. (2000) use genetic algorithms (GAs) with Monte Carlo simulation to find optimal designs for many plant design alternatives. They apply this approach to solve issue related to economic and safety conflicts.

Most of the researcher has focused on the control blending at the mill but to provide the required quality of raw material for blending process is not a trivial task due to fluctuation in their chemical composition e.g. if the material is mined from different quarries [3]. One of the challenges relating raw mix design and cement quarry operations is the uncertainty in chemical composition of raw material mined from the quarry and purchased from the market. These uncertainties affects the mining activities and raw mix.

For cement raw material blending various researcher contribute to some extent i.e. *Kizilaslan et al. (2003)* carried out a comparative study of cement industry's raw material blending process modelling using conventional and intelligent techniques. Their work is based on modeling intelligent techniques i.e. Neural Networks and Adaptive Nero-Fuzzy Inference System (ANFIS), for raw material blending and compare it with classical system identification method (ARX model). Neural Networks and ANFIS techniques performed better in approximating actual plant, data due to non- linear structures. Although, this work is based on control design of raw material blending at plant but this approach can be used for raw material blending control from quarry.

Banyasz et al (2003) described an adoptive control system for raw material blending in cement industry. The control system was based on new generic optimal controller structure. The control system is focus on important phase of proportioning, burning and grinding operation preceding by estimate the raw material composition. However this work focus on control system of raw material blending at mill but it can be improve by considering the variation of chemical composition at quarry.

Asad (2010) presented an approach to raw material blending optimization model based on linear programming for short range production planning. The objective of this linear programming formulation was to develop a raw mix stockpile by using raw material from three sources i.e., benches, stockpiles of material from quarry and additives from market. This model was successfully implemented through a case study and found significant benefits in cost saving, continuous supply of raw material and saving employee time in scheduling. While this work is based on linear programming model but this method can be used with Monte Carlo simulation for the variation in chemical composition to achieve better results.

Vinicius de Oilveira et al. (2011) addresses a model to control the raw material blending process in cement

industry by Robust gain Schedule. A linear parameter varying model was developed with some set points as scheduling parameters. The uncertainty in raw material chemical composition fluctuation was represented as a polytopic multi model uncertainty. The control process was simulated and compare it with the prepare model. Although this work contribute the fluctuation in the chemical composition and control of raw material at plant but it can better by using at quarry.

Xianhong Li et al. (2012) proposed a nonlinear time varying (G-NLTV) model for raw material blending process while considering the variation of chemical composition in feed flow, production constraints and various craft. Various objective functions are introduced to obtain optimum ingredient ratios related to various production requirements. Raw material ratio optimization problem is transform from linear to nonlinear constraint optimization problem. A framework of grid interior point technique is introduce to resolve nonlinear ingredient ratio optimization problem. To study ingredient ratio optimization problem some numerical examples are solved. Beside this work is focus on time variation in raw material blending, it can be helpful to achieve better result in case of incorporating fluctuation in chemical composition of ingredient from quarry.

## 2. Method

### 2.1 Application implementation

The objective of this paper is to present the application of Monte Carlo simulation to the raw material blending for short range production planning. In this paper two objective are considered i.e. the percent contents of ingredient in limestone samples and percent content of major oxides in additives from the market. The percent contents of major oxides of limestone were found from quarry drill hole samples through chemical analysis. Drill hole sample data was used to generate statistical models and identify the statistical distribution of the quality parameters of raw material. LP formulation were used to find the

optimum blending. The data of percent contents of major oxides found by chemical analysis from drill hole samples were used as input for Monte Carlo simulation. Random numbers were generated and the input data were simulated for 500 simulation. Various statistics and probability distributions of randomly generated data were find and compare it with the statistics and distribution followed by the actual data taken from drill hole samples.

For raw material blending optimization, averages of randomly generated major oxides were used as input and compare the optimum result with optimum result taken from the data of drill hole samples. For optimization LP model formulated by Asad (2010) were used. Excel were used as an analytical tool for all the calculations. The framework of this application is shown in figure 1.

## 3 Results

### 3.1 Application Example

To validate the method, application was applied to data taken from Kohat cement quarry which is located in Khyber Pakhtunkhwa, Pakistan. Kohat cement has five quarries in which currently four are in quarrying operation. These quarries provide not only limestone but also shale up to some extent. Limestone of these quarries varies from low to high grade in each quarry. The average percent content of limestone chemical Compositions in these quarry is following CaO (47.21%), $SiO_2$ (3.766%), $Fe_2O_3$ (1.04%), $Al_2O_3$ (1.533%), MgO (1.833%) $K_2O$ (0.3%) and $Na_2O$ (0.08%). For cement production at least 12000 tons of raw material is provided from cement quarries to the plant. In this research firstly, for raw material blending the drill hole data was used. To find the optimum cost and balances of major oxide the formulas of LSF (lime saturation factor), SR (silica ratio), AM (Alumina ratio), $C_3A$, $C_3S$, $C_2S$ and $C_4AF$ was used. Excel spread sheet were used trial and error base to achieve the objective function of raw material blending optimization. From the calculation it was found, that at optimum cost of blending, balances of major oxides

were near to their range. Various statistics for chemical compositions of raw material were found shown in table 1. OXMATRIX were used to draw the frequency distributions and distribution analyzer were used to find the distributions followed by the data taken from core drill samples, shown in graph 1.
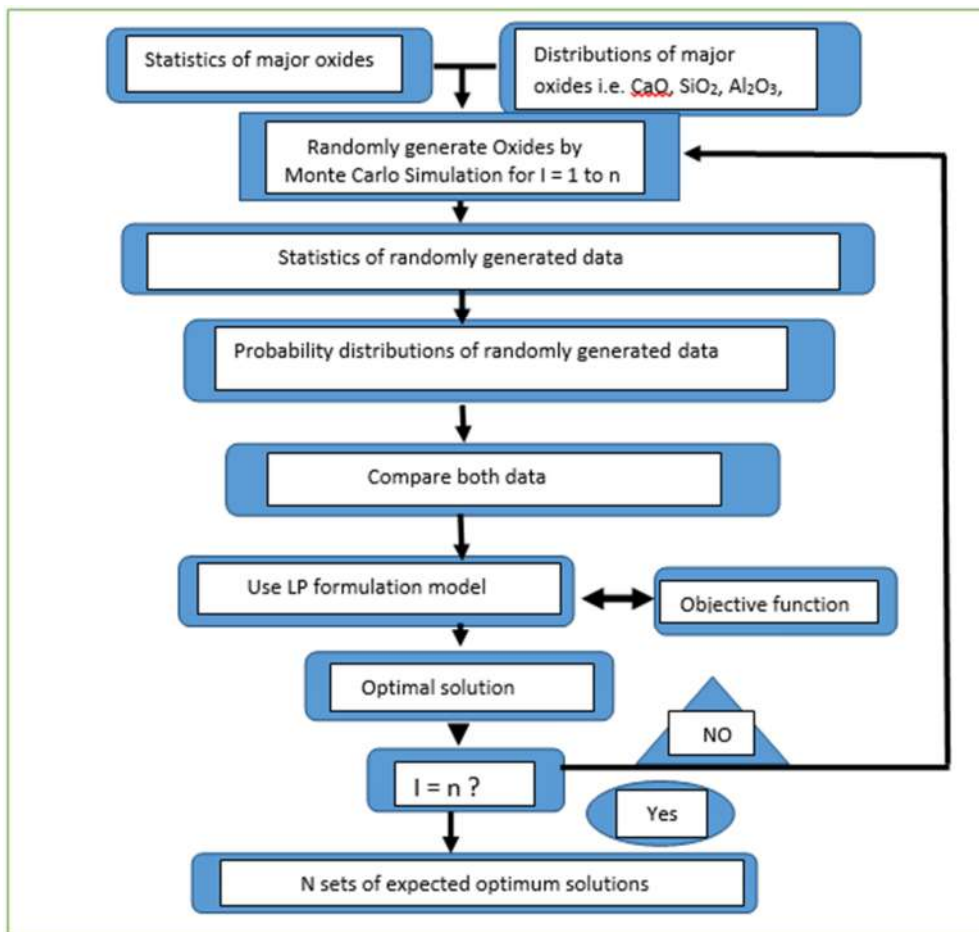


Figure 1: Framework for the Application

**Table 1: Summary Statistics of chemical composition from drill core samples**

| Summary statistic | $SiO_2$ | $Al_2O_3$ | CaO | $Fe_2O_3$ | MgO | $K_2O$ | LOI |
|---|---|---|---|---|---|---|---|
| Mean | 8.76 | 1.90 | 47.23 | 1.23 | 1.34 | 0.26 | 38.59 |
| S.D | 3.27 | 1.05 | 3.31 | 0.64 | 0.24 | 0.14 | 2.46 |
| Median | 8.45 | 1.99 | 47.11 | 1.21 | 1.26 | 0.27 | 38.36 |
| Mode | 11.02 | 1.21 | 51.94 | 1.2 | 1.24 | 0.29 | 42.25 |
| Sample Variance | 10.6 | 1.10 | 10.98 | 0.41 | 0.06 | 0.02 | 6.04 |
| Kurtosis | -0.62 | -0.77 | -0.81 | 1.88 | 2.96 | -1.00 | -0.92 |
| Skewness | 0.26 | 0.12 | -0.23 | 0.38 | 1.50 | 0.03 | -0.06 |
| Confidence level | 0.10 | 0.03 | 0.10 | 0.02 | 0.01 | 0.00 | 0.08 |

By using distribution analyzer it was found that various distributions are followed by the data taken from drill hole samples i.e. CaO (Johnson family), $SiO_2$ (Beta), $Al_2O_3$ (uniform), $Fe_2O_3$ (loglogistic family), LOI (Johnson family), MgO (Beta), $Na_2O$ (Beta) and $K_2O$ (Johnson family). A new data of 500 counts were randomly generated by using Monte Carlo simulation from the chemical composition of drill hole samples data. For raw material blending optimization their averages were calculated and the above discussed formulas in equation 1,2 and 3 were used in excel to find out optimum blending result. Statistics of randomly generated data were found shown in table 2. By the above used software the distributions of data were generated and also found what type of distributions followed by the data i.e. CaO (Johnson family), $SiO_2$ (Pearson family), $Al_2O_3$ (Beta), $Fe_2O_3$ (Jonson) family), MgO (Beta), $Na_2O$ (Pearson family), $K_2O$ (Uniform) and LOI (Johnson family).

**Table 2: Summary statistics of simulated chemical composition**

| Summary statistic | $SiO_2$ | $Al_2O_3$ | $Fe_2O_3$ | CaO | MgO | $K_2O$ | LOI | $Na_2O$ |
|---|---|---|---|---|---|---|---|---|
| Mean | 3.7 | 1.634 | 1.18 | 47.4 | 2.3 | 0.3 | 44.35 | 0.245 |
| S.D | 1.77 | 0.42 | 0.24 | 2.09 | 0.75 | 0.046 | 2.94 | 0.18 |
| Median | 3.25 | 1.83 | 1.18 | 47.89 | 2.64 | 0.31 | 44 | 0.3 |
| Mode | 2.5 | 1.96 | 1.24 | 48.82 | 2.64 | 0.31 | 44.37 | 0.34 |
| Sample variance | 3.14 | 0.18 | 0.056 | 4.4 | 0.56 | 0.0021 | 8.66 | 0.33 |
| Kurtosis | 2.56 | -1.40 | 1.95 | 0.29 | -1.34 | -1.26 | 2.85 | -1.63 |
| Skewness | 1.58 | -0.08 | -1.21 | -0.94 | -0.18 | -0.05 | -0.07 | 0.26 |
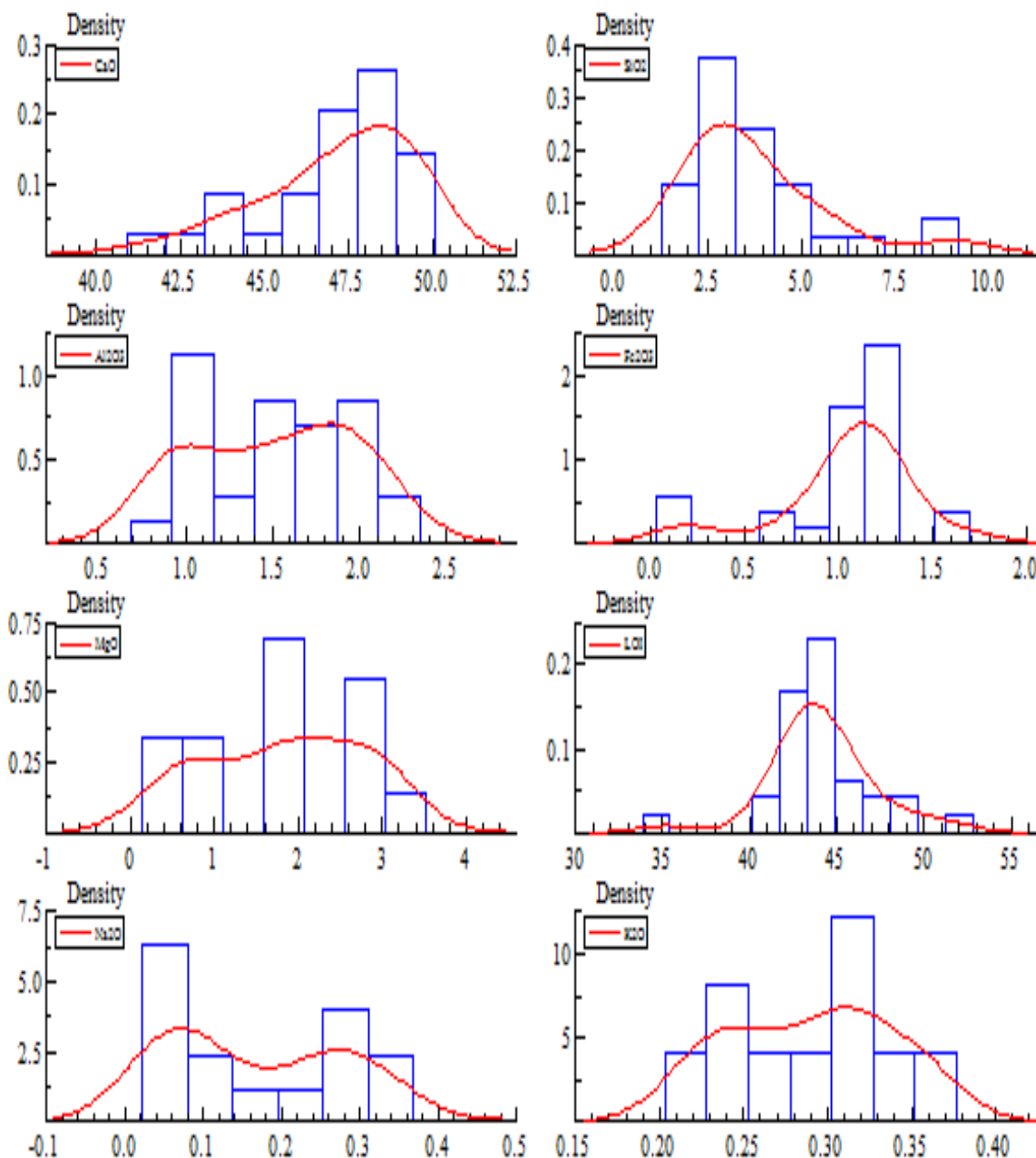
**Graph 1: Frequency distribution of chemical composition of limestone**
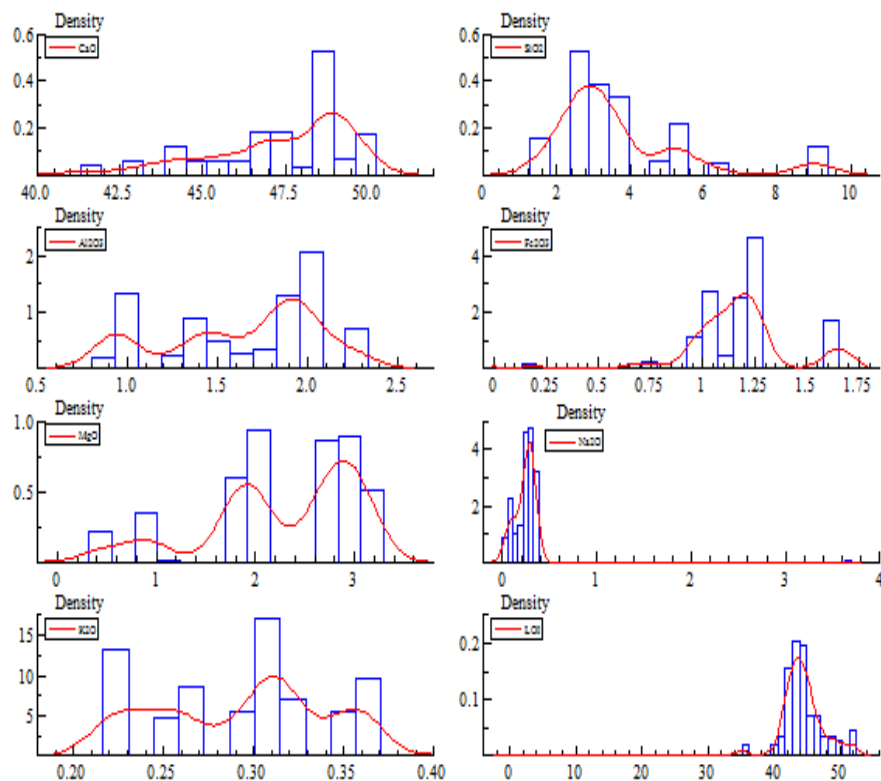
**Graph 2: Frequency distribution of simulated chemical composition of limestone**

#### 4    Conclusions

Appropriate production planning of raw material extraction from different quarry sites, has key role to optimize the raw material blending. There is lot of variation in chemical composition, if the raw material is mined from different quarries. The uncertainties in chemical composition of raw material affects the mining activities and raw mix design. In this research, Monte Carlo simulation was used to cope with the challenges associated with uncertainties in raw material composition. By generating statistical models it is found that there is small variations in the statistics of both drill hole samples and randomly generated data by Monte Carlo simulation, while from the statistical distributions it is examine that the trend of chemical compositions of quality parameters is completely change by comparing both the cases.

Raw material blending calculation for drill hole samples gives result near to balances required for proper blending with in optimum cost. But in case of randomly generated data with same cost it gives more efficient result then the preceding one. During production planning for raw material blending there is great role of chemical composition variation in raw material. The results of a case study revealed that the variation in chemical composition of raw material which affects the cement plant operations can be handled using simulation and optimization techniques.

Currently all the models and controller design for raw material blending does not consider the variation in limestone chemical composition from quarry during production planning. This consideration may need inclusion of Monte Carlo simulation in their models and designs. To improve these model and designs this is the future possible area of research.

## 5    References

[1] G. T. Austin, *Shreve's Chemical Process Industries*, 5th Edition, McGraw Hill Book Company, New York (1984).

[2] M. W. A. Asad, "Implementing a blending optimization model for short-range production planning of cement quarry operation" Journal of Mining Science, 2010.

[3] V. De Oliveira, M. Amrhein, A. Karimi, "Robust gain-scheduled blending control of raw-mix quality in cement industries," 50th IEEE Conference on Decision and Control and European Control Conference (CDC-ECC), E. Chong, Ed., IEEE, Orlando, USA 2011, p. 4189

[4] Abdul Majid "Handbook for cement engineers" June 2002.

[5] K. Kizilaslan, S. Ertugrul, A. Kural, and C. Ozsoy, "A comparative study on modeling of a raw material blending process in cement industry using conventional and intelligent techniques," in Proceedings of the IEEE Conference on Control Applications, pp. 736–741, June 2003.

[6] Xianhong li, Haibin yu and Mingzhe yuan, "Modeling and optimization of cement raw materials blending process," Journal of mathematical problems in Engineering, Volume 2012.

[7] V. De Oliveira, M. Amrhein, A. Karimi, "Robust gain-scheduled blending control of raw-mix quality in cement industries," 50th IEEE Conference on Decision and Control and European Control Conference (CDC-ECC), E. Chong, Ed., IEEE, Orlando, USA 2011, p. 4189.

[8] Cs. Banyasz, L.Keviczky and Istvan vajk, "A novel adaptive control system for raw material blending" IEEE control systems magazine 2003.

[9] Peeray Inyin and Yimin Zhu, "Application of Monte Carlo simulation and optimization to multi-objective analysis to sustainable building designs" Computing in civil and building engineering 2004.

[10] Monte Carlo Simulation, https://en.wikipedia.org/Wiki//MCS, ( accessed 12,08,2016)

[11] Bruni, M. E., Beraldi, P., Guerriero, F., and Pinto, E. (2011). "A heuristic approach for resource constrained project scheduling with uncertain activity durations." *Comput. Oper. Res.*, 38(9), 1305-1318.

[12] Cantoni. M, Marseguerra, M, and Zio, F, "Genetic algorithms and Monte Carlo simulation for optimal plant design". Reliab. Eng.Syst. Saf., 68(1), 29-38

# Video Streaming data estimation and management for efficient bandwidth utilization using Probabilistic Models

*Nadia Masood Khan*, Gul Muhammad Khan*
*Center for Intelligent Systems and Networks Research*
*University of Engineering and Technology Peshawar, Pakistan.*
**Email: nadiamasoodkhan@gmail.com*

**Abstract:** Proficient bandwidth usage demonstrated for Moving Picture Expert Group (MPEG-4) traffic by using estimation and scheduling algorithm in various traffic scenarios. For multiuser MPEG-4 Variable Bit Rate (VBR) traffic, both linear regression and probabilistic methodologies are entertained to discover the most ideal combination of estimation and scheduling. The future VBR traffic is calculated using ARMA (Auto Regressive Moving Average) and MACD (Moving Average Convergence Divergence). The VBR traffic estimation proves to perform better than present statistical models. The estimation is followed by four unique algorithms: SRPT (Shortest Remaining Processing Time), Fixed, Probabilistic, and Priority based scheduling. Different traffic scenarios in various numbers of users are entertained for all these networks and results are arranged. The outcomes shows challenging results with estimation of as high as 98% and efficient use of bandwidth up to 50% with no packet drop.

**Key words**: Auto Regressive Moving Average, Bandwidth Estimation, Moving Average Convergence Divergence, Moving Picture Expert Group Scheduling, Shortest Remaining Process Time.

## 1    Introduction:

The phenomenal growth in video applications in the past few years demands an algorithm for effective video streaming over packet switched networks. Continuous real-time streams transmission over the network is needed for multimedia applications which can have high data rate and variable bandwidth. There is a huge demand of high speed Internet for downloading and streaming videos because of increase in number of computers and mobile users. When the traffic is properly estimated and scheduled, the limited resources can be used to handle dynamic traffic. Most of the traffic on the internet is because of MPEG-4 VBR video streaming and transmission having huge bandwidth requirement. Implementing a method for successful estimation and allocation of bandwidth is a prerequisite for such immense bandwidth demand. The optimization of VBR traffic resources with no compromise on video quality that can result due to packet loss is a big challenge in today's modern web era. When the VBR traffic is estimated prior to the arrival of actual frame so there will be enough processing time for allocation and management of bandwidth. Many bandwidth allocation algorithms are presented in past, one such algorithm is Shortest Reaming Processing Time (SRPT) [1]. SRPT works on reaming processing time of requests which is the request size. In most web servers request size is already known so all users get a fair share of bandwidth.

A lot of traffic is experienced by web servers because it is serving hundreds of users at same time. The web server is not a single resource system so at time it is overloaded due to scheduling of huge amount of users. Rene sitters [2] examined minimizing average completion in machine scheduling. In his work SRPT proved to be competitive with other contemporary methods introduced having lesser average completion time because of assigning weights to jobs in SRPT. Web server is loaded because of all processing done at runtime in most of the methodologies. We propose to estimate bandwidth necessity ahead of time for each individual associated with the server and assigns the transmission capacity before the actual arrival of frame, in this way taking much lesser handling time. There is enough time for decision regarding bandwidth distribution because the frame is not arrived yet and web server know the bandwidth requirement of every user. In this way, waiting time is reduced for every user because all the users get the bandwidth according to their demand and there is no wastage of bandwidth. Hence the bandwidth is used smartly. The linear regression models used for estimation of VBR traffic have comparatively low computational cost.

## 2    Literature Review:

The handling of VBR traffic in various distributed system to have congestion control of Transmission

Control Protocol (TCP) of an Internet path is a milestone for researchers in the video streaming applications Fixed data rate traffic is easy to schedule but variable bit rate traffic scheduling might give rise to issues that is non-trivial in nature[3]. Dynamically changing data rate for the flow of VBR traffic requires a good scheduling scheme that can deal with these issues. Multimedia flows take a large share of available bandwidth and hence giving rise to situation in which bandwidth falls short of the amount actually required by the user. There is a immense need of proficient scheduling technique that can set a rational and useful dispersal of the available bandwidth within numerous individuals of the network to expedite them in adeptly supporting their specific multimedia flows. When a user is to be provisioned with less bandwidth than the link they have is physically capable of, this limitation will typically be implemented at the data link layer, with some mechanism at the data link layer delaying or discarding 2 frames so as to enforce the maximum allocated bandwidth. Our proposed algorithm deals with the issues that arise in Open Systems Interconnection (OSI) layer 2. There is a high demand of lossless video streaming applications because of internet videos, video teleconferencing, video sharing services such as Youtube, Video On Demand (VoD), home video. These digital videos go through different processing stages before it reach the end user of a video. Some stages in this processing degrade the video quality and some attempt to improve. Evaluating the video quality play a vital role to maintain Quality of Service (QoS). Video quality assessment (VQA) is the only reliable method to assess the video quality perceived by a human observer by asking them for their opinion. A subjective study is done by [4] to examine the effects of present generation video compression and communication technologies on the perceptual quality of digital video

Remaining processing time is used to schedule the requests in SRPT at web servers. SRPT scheduling mechanism proves to minimize mean response time and mean slowdown time. The request having lesser processing time are given service first while the requests having larger processing time is put in the queue to be served later. Meanwhile, if a web server receives a request having comparatively lesser processing time then the new request will be served [5]. Sometimes the requests are scheduled independent of their size and

every request receives a fair share of bandwidth. [6] Have given priority to shortest remaining time requests in accordance with SRPT. For maximum utilization of wireless resources and maintaining QoS, broadband multimedia wireless network systems uses priority based scheduling [7].

One probabilistic predication based joint packet scheduling approach is proposed by [8] for maintaining QoS to delay sensitive traffic. They have classified the arriving traffic into three categories (1) highest priority i.e. emergency traffic (2) medium priority i.e. constant rate traffic (3) low priority i.e. normal traffic and are stored in different queues. The required bandwidth for each service class is calculated based on increase/decrease in high priority average queue length. They have used probabilistic approach for measuring the increased traffic from the previous time slots and allocate the bandwidth to each service. Their approach is different because it works on time of requests while our proposed approach takes into account the frame size in bytes. Various mechanisms utilized to enhance the efficiency of multimedia traffic are discussed above. We have proposed the mechanism of estimating multimedia traffic and then using that estimation to efficiently manage the bandwidth of network.

### 3    Proposed Algorithm

The proposed algorithm involves two steps. In first step bandwidth is estimated using linear regression models, in second step using the estimated packet size data, bandwidth is allocated. The first subsection discusses the estimation algorithms, the estimators' experimental setups and their results & analysis, and the second subsection detail the bandwidth allocator simulation and experimental setups followed by result & analysis.

TABLE I
ESTIMATION RESULT OF ARMA AND MACD IN TERMS OF MAPE WITH
THE CORRESPONDING SD ON EIGHT DIFFERENT MOVIES

| Movie | ARMA | MACD | Standard Deviation(SD) |
|---|---|---|---|
| Alladin | 2.4 | 2.3 | **0.05** |
| JurassicPark | 5.1 | 4.8 | 0.12 |
| Robinhood | 5.3 | 4.9 | 0.10 |
| Simpsons | **6.5** | **6.1** | 0.14 |
| The firm | 5.3 | 4.8 | 0.14 |
| Startrek | 3.8 | 2.7 | 0.14 |
| Starwars | 3.5 | 3.1 | 0.11 |
| Southpark | 5.0 | 4.3 | 0.10 |

### 3.1. Linear Regression Models
Linear regression is used to develop an extrapolative model for stock exchange. For the first time we used it

for Internet traffic estimation. In this work, we have explored two efficient linear regression models.

### 3.1.1. Autoregressive Moving Average (ARMA):

ARMA model is tailored by least squares regression to identity parameters that minimize the error term. It provides depiction of stochastic process for auto-regressive and moving average [9]. It is used to estimate forthcoming values of a time series Xt. Here we have used Autoregressive moving-average model with exogenous inputs (ARMAX) model having expression:

$$X_t = \xi_o + \eta_t + \sum_{i=1}^{p} \xi_i \, X_{t-i} + \sum_{i=1}^{q} \omega_i \eta_{t-i} + \sum_{i=1}^{b} \varphi_i \, d_{t-i}$$

Where $X_t$ is dependent variable at time t, $X_{t-1}$- - -$X_{t-p}$ are lagged dependent variables, $\xi_0$- - - $\xi_p$ regressions coefficients, $\eta_t$ residual terms and $\omega_1$- - - $\omega_q$ weights and $\varphi_1$- - -$\varphi_b$ are the parameters of exogenous input $d_t$

### 3.1.2. Moving Average Convergence Divergence (MACD):

MACD is a technical analysis trading indicator introduced by Gerald Appel in the late 1970s for stock prices [10]. The main tenacity of this is to estimate alterations in the strength, direction, momentum, and duration of trends in stock's prices. MACD comprises of two moving average series M1;t and M2;t having different lengths and estimation is decided such that, "if the short-term moving average(SMA) intersects the long-term moving average(LMA) from below a long position is taken. Conversely, if the long-term moving average is intersected from above a short position is taken."

### 3.2. Bandwidth Estimation Simulation Setup:

Here we have used ARMA and MACD models to estimate upcoming frame sizes. The estimated Frame size then helps in bandwidth allocation. Preceding ten frames values are used to estimate the eleventh frame size using MACD and ARMA. Table I shows the list of movies being tested using these setups. The training is performed on mpeg-4 data of one movie and testing on eight diverse movies. Performance of the estimating algorithms is presented in terms of Mean Absolute Percentage Error (MAPE) [11].

### 3.3. Results and Analysis Bandwidth Estimation:

The proposed models ARMA and MACD estimate the required bandwidth for efficient frame transmission. The estimation model ARMA and MACD calculates the future VBR traffic for lossless video transmission.

TABLE II

ESTIMATION RESULTS OF MACD WITH DIVERSE CONTENTION WINDOW SIZES

| Movie | MACD (10:30) | MACD (30:90) | MACD (12:26) |
|-------|--------------|--------------|--------------|
| Alladin | 2.4 | 2.8 | **2.3** |
| JurassicPark | 5.0 | 6.4 | 4.8 |
| Robinhood | 5.1 | 6.2 | 4.9 |
| Simpsons | 6.2 | 7.5 | 6.0 |
| The firm | 5.0 | 7.0 | 4.8 |

TABLE III

FRAME PREDICTION COMPARISON WITH OTHER LINEAR REGRESSION MODELS

| S.No | Technique | % Prediction Error |
|------|-----------|--------------------|
| 1 | Least Mean Square(LMS) [13] | 10.7 |
| 2 | Adaptive Least Mean Square(ALMS) [15] | 7.4 |
| 3 | $\rho$- domain rate model [14] | 5.2 |
| 4 | PuP (estimation algorithm using PDF) [16] | 3.6 |
| **5** | **Proposed Scheme MACD** | **2.34** |

The estimated data is sent to Scheduling model which allocates bandwidth based on these estimations. The testing results of both ARMA and MACD for eight different movies with 20,000 frames each is shown in Table I, with conforming Standard deviations. Table I indicate the best MAPE being achieved for Alladin movie, with 2.4% for ARMA, and 2.3% for MACD because of lesser fluctuations evident from lesser standard deviation value. Table I also shows that MACD perform better on average in comparison to ARMA. Diverse mixtures of contention window sizes: (10:30), (30:90) and (12:26) were explored on five different movies data (as shown in Table II) to assess MACD model obtaining optimum contention window being 12:26 [12]. A comparison of MACD with previous linear regression approaches for estimation is tabulated in Table III showing the competitiveness of the proposed algorithm. The next subsections provide details on various probabilistic models used to allocate bandwidth based on the estimated data.

### 3.4. Bandwidth Allocation Algorithms

To compare bandwidth allocation efficiency as a consequence of frame size estimation by MACD model, different simulation scenarios have been taken under

consideration for various numbers of users streaming the MPEG-4 data in diverse bandwidth availability scenarios. In this work four types of bandwidth allocation setups has been explored.

**3.4.1 Probability Based Scheduling:** In this setup, every user is assigned a range based on its percentage contribution in the overall bandwidth based on their estimated values. A pseudo random number is then generated, if that falls within the range of a particular user. The frame of that user is dropped. When bandwidth requirement is still high, then th users pass through the same process again and new ranges are assigned to them. The process continues until the required and available bandwidth is equal. Figure 1 shows the various blocks of probability based scheduling highlighting different steps involved.

**3.4.2 Priority Based Scheduling**: The second setup involves the priority based bandwidth allocation scenario in which we have given priority to some users for data streaming such that, in case of 5 users, first user is given priority, in case of 15 users first 5, in case of 25 first 10, and finally first 20 users are given priority in case of 50 users respectively. These will always be allocated with bandwidth and the rest will be shared among other users using probability based bandwidth allocator

**3.4.3 Fixed Data Rate**: Fixed data rate algorithm fixes the data rate of some users and then separates the users streaming fixed data rate and variable data rate. The fixed data rate users are served first and the remaining users go through probability based scheduling.

**3.4.4 Shortest Remaining Process Time (SRPT):** The SRPT gives priority to the requests having shortest remaining processing time so the request having largest processing time is dropped. Frames are dropped until all the request can be served in the available bandwidth.

**a.   Bandwidth Allocation Simulation Setup:**
After the successful estimation of bandwidth, the allocator works on the estimated data. Both Markovian and non- Markovian cases are considered, in first case the dropped frame is added to the next queue considering

a buffer of enough memory, whereas it is dropped in second case.

**3.6. Results and Analysis for Bandwidth Allocation**
The bandwidth distribution efficacy is premeditated by percentage frame dropped for diverse number of users in allotted bandwidth. Table IV shows results for Markovian and Non- Markovian cases
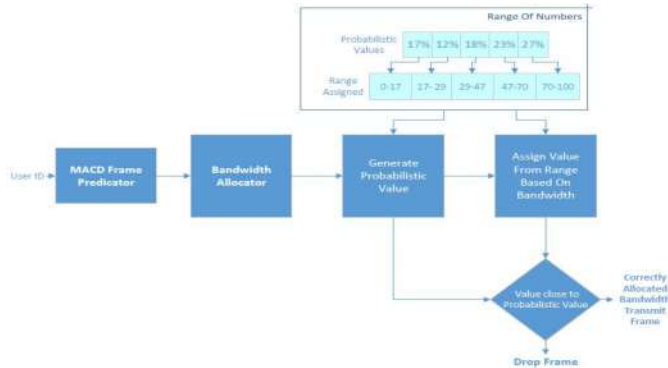


**Fig.1.** Probability Based Bandwidth Allocator

The overall bandwidth constraint is obtained by adding maximum frame size of all users. This provides us the preferred bandwidth for consistent video streaming. The maximum requirement of individual user doesn't occur at the same point, thus providing us an ability to save bandwidth by efficient estimation and management. A reduced bandwidth of 50% and 75% of the maximum required bandwidth is allocated to examine the frame dropped in various probabilistic cases with almost no frame dropped in both cases as revealed in table IV.
Table IV shows better result for Markovian case in comparison to non-Markovian, though it requires extra computational cost. The results also show that the performance of both estimated and actual data is almost similar with estimation. Thus providing us the upcoming bandwidth information in advance and thus making the system independent of computational delay. SRPT perform better when the number of users are lesser, and probability when the numbers of users are more, with no frame dropped even at 50% as evident from the table IV.

TABLE IV
AVERAGE FRAME DROPPED-FOR MARKOVIAN AND
NON-MARKOVIAN SETUPS

| | | %Bandwidth Allocation | | | | | | | |
|---|---|---|---|---|---|---|---|---|---|
| | | Extra Frame Dropped | | | | % Extra Frame Added | | | |
| | | 50% | | 75% | | 50% | | 75% | |
| Users | Scenarios | Act(%) | Est(%) | Act(%) | Est(%) | Act(%) | Est(%) | Act(%) | Est(%) |
| 5 | SRPT | 0.14 | 8.42 | 0.00 | 0.00 | 0.00 | 0.00 | 0.00 | 0.00 |
| | Fixed | 0.40 | 8.76 | 0.00 | 0.00 | 0.00 | 3.98 | 0.00 | 0.00 |
| | Probability | 0.24 | 5.22 | 0.00 | 0.00 | 0.80 | 3.40 | 0.00 | 0.00 |
| | Priority | 0.20 | 5.14 | 0.00 | 0.00 | 0.09 | 2.96 | 0.00 | 0.00 |
| 10 | SRPT | 0.03 | 4.21 | 0.00 | 0.00 | 0.00 | 0.00 | 0.00 | 0.00 |
| | Fixed | 0.04 | 6.58 | 0.00 | 0.00 | 0.00 | 2.27 | 0.00 | 0.00 |
| | Probability | 0.02 | 3.26 | 0.00 | 0.00 | 0.04 | 0.50 | 0.00 | 0.00 |
| | Priority | 0.02 | 3.32 | 0.00 | 0.00 | 0.00 | 1.45 | 0.00 | 0.00 |
| 15 | SRPT | 0.08 | 2.04 | 0.00 | 0.00 | 0.00 | 0.00 | 0.00 | 0.00 |
| | Fixed | 0.00 | 3.07 | 0.00 | 0.00 | 0.00 | 0.00 | 0.00 | 0.00 |
| | Probability | 0.00 | 1.58 | 0.00 | 0.00 | 0.00 | 0.14 | 0.00 | 0.00 |
| | Priority | 0.00 | 1.51 | 0.00 | 0.00 | 0.00 | 0.64 | 0.00 | 0.00 |
| 25 | SRPT | 0.00 | 0.96 | 0.00 | 0.00 | 0.00 | 0.00 | 0.00 | 0.00 |
| | Fixed | 0.00 | 1.22 | 0.00 | 0.00 | 0.00 | 0.00 | 0.00 | 0.00 |
| | Probability | 0.00 | 0.67 | 0.00 | 0.00 | 0.00 | 0.00 | 0.00 | 0.00 |
| | Priority | 0.00 | 0.56 | 0.00 | 0.00 | 0.00 | 0.00 | 0.00 | 0.00 |
| 50 | SRPT | 0.00 | 0.00 | 0.00 | 0.00 | 0.00 | 0.00 | 0.00 | 0.00 |
| | Fixed | 0.00 | 0.00 | 0.00 | 0.00 | 0.00 | 0.00 | 0.00 | 0.00 |
| | Probability | 0.00 | 0.00 | 0.00 | 0.00 | 0.00 | 0.00 | 0.00 | 0.00 |
| | Priority | 0.00 | 0.00 | 0.00 | 0.00 | 0.00 | 0.00 | 0.00 | 0.00 |

## 4 Conclusions

Frame size estimator and bandwidth allocator is explored in this work using linear regression and probabilistic models. The essential bandwidth for VBR MPEG-4 video streaming is premeditated through MACD model, and then scheduled at server using SRPT and probabilistic model with fixed, priority and normal circumstances. Through estimations, the best utilization of bandwidth is achieved independent of processing delay. Results prove the proficiency of model by achieving a bandwidth efficiency of up to 50%. The same method can be applied in other similar scenarios.

## 5 References

[1] Fujiwara, Hiroshi, and Yoshiyuki Sekiguchi, "An improved analysis of SRPT scheduling algorithm on the basis of functional optimization",
Information Processing Letters, 112(23),911-915,2012.
 [2] Sitters, Ren, "Efficient algorithms for average completion time scheduling", Integer Programming and Combinatorial Optimization, Springer Berlin Heidelberg, 411-423,2010.
[3] Y.-H. Tseng, E. H.-K. Wu, G.-H.Chen, "Scene-change aware dynamic bandwidth allocation for real-time VBR video transmission over IEEE 802.15.3 wireless home networks", IEEE Transactions on Multimedia, 9, 642–654,2007.

[4] K. Seshadrinathan, R. Soundararajan, A. Bovik, L. Cormack, "Study of subjective and objective quality assessment of video", IEEE Transactions on Image Processing, 19, 1427-1441,2010.
[5] Ahmad, F. ; Mahmud, S.A. ; Khan, G.M. ; Yousaf, F.Z., "Shortest remaining processing time based schedulers for reduction of traffic congestion.", Connected Vehicles and Expo (ICCVE) Int. Conf. on. ,271 - 276, 2013.
[6] Bansal, Nikhil, MorHarchol-Balter, and Bianca Schroeder., "Implementation of SRPT Scheduling in Web Servers.",2000.
[7] Babu, Thimma VJ., "Performance analysis of broadband multimedia wireless communication networks." Diss.Concordia University, 2001.
[8] Sharma, Reema, et al. "Probabilistic Prediction based Scheduling for Delay Sensitive Traffic in Internet of Things." Procedia Computer Science 52 (2015): 90-97.
[9] George, E. P. (1970). Time series analysis: Forecasting and control.Holden-D
[10] Gerald Appel, E.D. 2008. Understanding MACD (Moving Average Convergence Divergence). Traders Press, Inc
[11] J. Armstrong and F. Collopy, "Error measures for generalizing about forecasting methods: Empirical comparisons", International Journal of Forecasting, 8(1), 6980, 1992.
[12] Rosillo, R., D. De la Fuente, and J. A. L. Brugos., "Technical analysis and the Spanish stock exchange: testing the RSI, MACD, momentum and stochastic rules using Spanish market companies.", Applied Economics, 45(12), 1541-1550,2013.
[13] Adas, A., "Supporting real time VBR video using dynamic reservation based on linear estimation",INFOCOM '96. Proc. IEEE,1996,3,1476 - 1483.
[14] Lee, Chu-Chuan and Chang, Pao-Chi, "A novel long-span traffic estimator for real-time VBR videos via _-domain rate model",Communications Letters, IEEE,9(3),279–281,2005.
[15] Yoo, Sang-Jo,"Efficient traffic estimation scheme for real-time VBR MPEG video transmission over high-speed networks", Broadcasting, IEEE Transactions on, 48(1),10–18,2002.
[16] Lee, Kang Yong, et al. "Accurate estimation of real-time MPEG-4 variable bit rate video traffic." ETRI journal 29(6), 823-825,2000

# Non-Linear Time History Analysis of Reinforced Concrete Special Moment Resisting Frames for Loss Estimation

## Muhammad Rashid[1,*], Naveed Ahmad[2]

[1]Department of Civil Engineering, University of Engineering & Technology, Peshawar 25000, 2nd Floor Earthquake Engineering Centre
[2]Earthquake Engineering Centre, University of Engineering & Technology, Peshawar 25000, 2nd Floor Earthquake Engineering Centre
[1*]Corresponding author
Email: ce.rashid@gmail.com

## Abstract

This study presents the seismic performance assessment of reinforced concrete frame structures designed to modern buildings codes, for quantifying the economic losses due to earthquake-induced structural damages. The structures investigated in the present research considered four (3,5,8,10 storey) prototype special moment resisting frame (SMRF) structures designed to Uniform Building Code–97, also adopted in the Building Code of Pakistan. Quasi-static cyclic tests carried out on special moment resisting beams were used for the development of damage scale and beam reparability cost ratio. The considered structures were analyzed using incremental dynamic analysis procedure using a set of seven natural and design spectrum compatible ground motion records. Damage to structural components was identified for each intensity level and integrated over the whole structure, with the required repair cost, to calculate the structure repair cost ratio (RCR). The structure RCR is correlated with the seismic intensity to develop seismic vulnerability curves, which can be used for the economic loss estimation of SMRF structures given the seismic intensity. This can help guide the designers to quantify the economic losses of code-designed structures for design level earthquakes, which should be communicated to the owners, during the initial planning and design phase, in order to facilitate them in taking measures regarding the future expected losses.

**Keywords:** RC SMRFs, Incremental Dynamic Analysis, Structural Damage, Repair Cost Ratio, Economic Losses

## Introduction

Earthquakes bring about extensive economic losses, massive casualties, and occupancy & business interruption, not only in the developing parts of the world but also in the developed and scientifically well-established (particularly in Earthquake Engineering) parts of the world. Recent and past observations have shown that earthquakes happen to be one of the costliest natural disasters in the history of human kind (Guin and Saxena 2001). The 2011 Tohoku, Japan and Christchurch, New Zealand earthquakes are the recent examples of the potential of earthquakes to cause huge economic losses, which are regarded as some of the highest economic losses to insurance industry (Chang *et al.*, 2013, Nanto *et al.*, 2011).

Pakistan is a region with a high seismic risk, due to the prevailing earthquake hazard (moderate to severe) and high seismic vulnerability of structures and infrastructures (Ahmad *et al.*, 2014, Ali *et al.*, 2011). The seismic vulnerability of the reinforced concrete building stock of Pakistan was visible in the recent 2005 Kashmir earthquake due to the lack of seismic design nature of structures and poor quality of construction (Bothara and Hicyilmas 2008, Naseer *et al.*, 2010, Rossetto and Peiris 2009). It is worth mentioning that this region is capable of triggering one or more future large earthquakes up to or even greater than magnitude 8 and this was manifested in the 2015 Nepal earthquake, which shares the same Himalayan belt (Avouac *et al.*, 2006, Bilham 2004).

Reinforced concrete special moment resisting frame (SMRF) is the most prevalent structural system in the modern building stock of Pakistan. These structures are primarily designed to the Uniform Building Code-97 (UBC-97), which is adopted in the Building Code of Pakistan–seismic provisions (BCP-2007). With the development and modernization of major cities of Pakistan such as Karachi, Islamabad, Lahore and Peshawar, the construction of multi-story reinforced concrete moment resisting frames is showing a rampant growth. Modern seismic design codes (ACI-318, NZS 3101:2006, EC-8) design buildings with the objective to protect occupants and control damage in design level earthquakes and avoid collapse in very rare earthquakes. The satisfactory or acceptable level of performance of a building designed to modern seismic design codes is only defined qualitatively and the performance of the building in a future earthquake can only be qualitatively described. Assuming that these buildings perform as intended by the building code: saves lives, avoids collapse and sustains damage in a design level earthquake, the unaware client has to bear repercussions like repair costs, building closure and in the worst case, the building might not even be repairable and must be

demolished, which is a state of absolute loss for the owner as experienced in the recent earthquakes 2010 Chile and 2011 Christchurch (Kam W. Y., et al. 2011, Westenenk B. et al. 2012). This points to the importance of vulnerability assessment of code-designed structures to quantify the structural risk and losses that can help guide the decision makers on seismic risk mitigation.

The advent of Performance Based Earthquake Engineering (PBEE) has made possible the performance-based assessment of buildings for future expected earthquakes in a probabilistic manner (Hamburger et al., 2000, Moehle et al., 2004). It is a comprehensive methodology for seismic performance assessment of structures, which encompasses hazard analysis for seismic hazard characterization, structural analysis for response evaluation, damage analysis of components for the expected demand and loss estimation for the incurred damages (and the required repairability) in components and structure. The current generation of PBEE allows assessing the seismic performance of structures, quantifying it in reliable measures relevant to the needs of stakeholders e.g. damageability, repair cost, casualties, business downtime, etc. (FEMA P-58).

The present research adopts the PBEE methodology for seismic performance assessment and direct economic loss estimation of SMRF structures (3,5,8,10 storeys) designed to UBC-97/BCP-2007 for structural damageability and the subsequent repairability cost. The considered structures are analyzed using incremental dynamic nonlinear time history analysis for a suite of seven natural accelerograms compatible to the design spectrum extracted from the PEER NGA database. The economic losses due to direct structural damages are calculated and correlated with the seismic intensity to derive seismic vulnerability curves.

## Description of Analytical Models

Four reinforced concrete SMRF structures of different heights, representing low to medium to high-rise buildings, have been considered for seismic performance analysis and subsequent economic losses. The selected frames have been designed for seismic Zone 2B of BCP-2007 for a soil type $S_D$ (as per NEHRP soil classification). The specifications of ACI-318 (ACI-318, 2008) have been used for the design and detailing of structural beam-column members and joints. The selected frames used for analysis are 2D frames are extracted from recently designed real moment resisting frames, as shown in Figure 1.
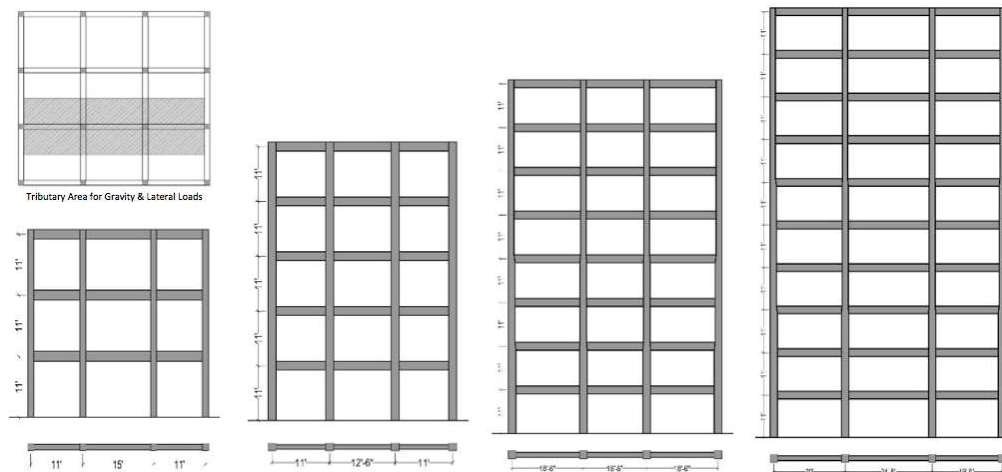


**FIGURE 7: 2D PORTAL FRAMES, EXTRACTED FROM THE REAL BUILDINGS, CONSIDERED FOR SEISMIC PERFORMANCE ASSESSMENT**

Numerical models were prepared in finite element based software SeismoStruct (SeismoStruct, 2015) for the considered frames to in accordance with standard modeling procedures in literature (Jeon, 2013). The inelastic behavior of beam-column members was modeled using force-based plastic hinge elements. Fiber-based elements can simulate the spread of flexure inelasticity along the plastic hinge length of the structural member and can also account for member axial force and moment interaction. Shear behavior of members is not considered, due to the fact that SMRF members respond primarily in flexure and shear response of these members is essentially elastic. Bar slip of beam longitudinal bars was modeled using moment-rotation spring at the beam-joint interface. The joints are modeled using elastic beam-column frame elements, due to the fact that these primarily respond elastically when detailed as per the code specifications.
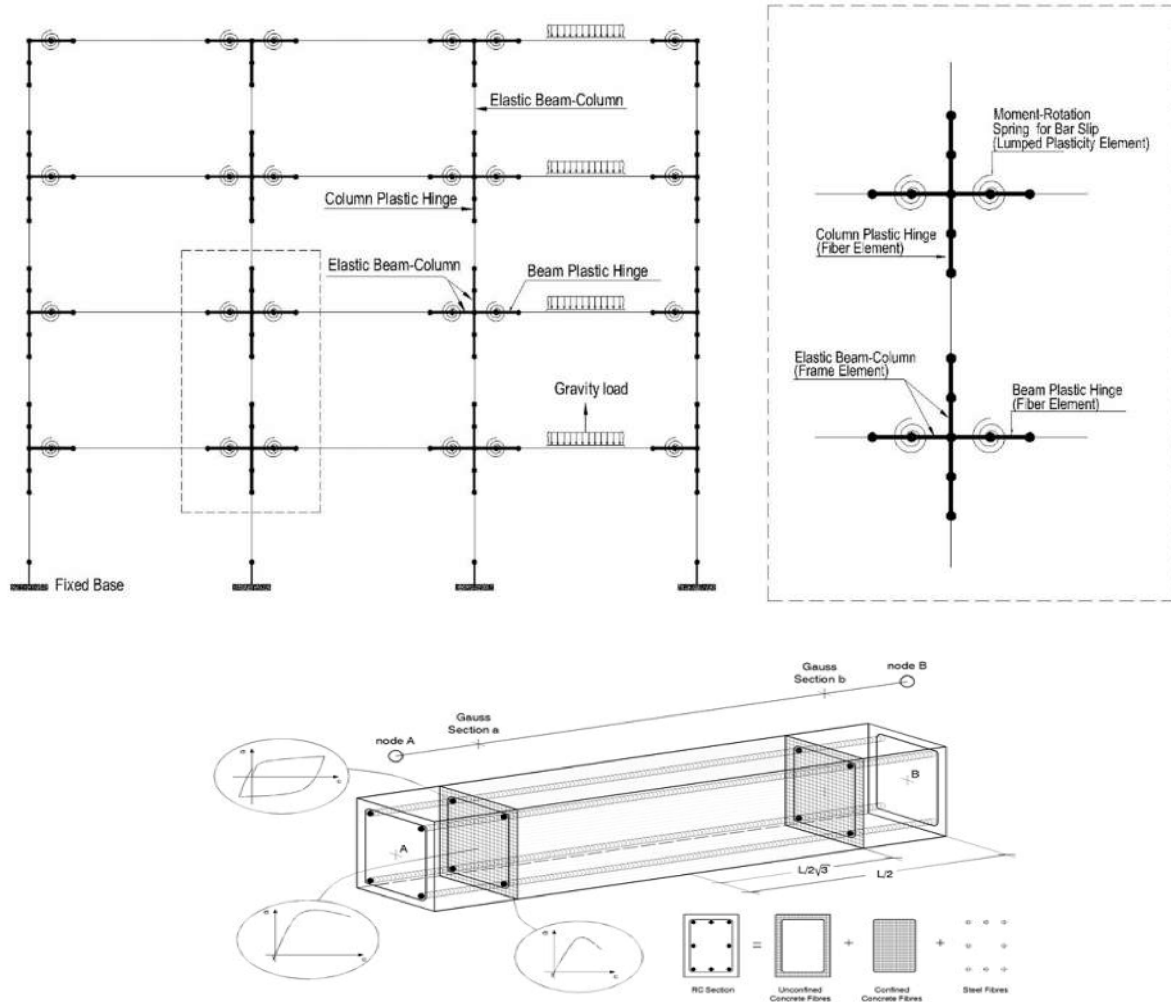
**FIGURE 8: NUMERICAL MODELING OF REINFORCED SMRF STRUCTURES**

All the column and beam sections have been divided into unconfined and confined concrete. Mander et al. (1988) model was used to model the behavior of confined concrete. The effects of confinement on the enhancement of strength and ductility are automatically accounted for by the analysis software SeismoStruct. The cyclic behavior of longitudinal steel was simulated using the reinforced steel model of Giuffre-Menegotto-Pinto (1983). The considered forced-based element has end plastic hinge zones with a middle elastic portion. The plastic hinge length $L_p$ was assumed to be equal to half of the member depth for beams and full depth for columns (Rashid, 2016). The lumped plasticity moment-rotation springs, used for the bar-slip modeling, were assigned with bilinear moment-rotation constitutive relationship, developed based on the experimental quasi-static cyclic tests carried out on full scale SMRF beams at the Earthquake Engineering Center of UET Peshawar (Rashid, 2016).
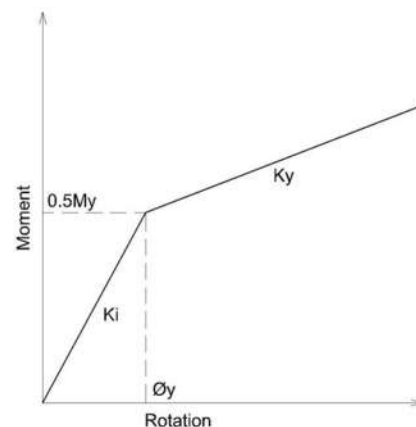


**FIGURE 9: MOMENT-ROTATION CONSTITUTIVE RELATIONSHIP FOR BAR-SLIP MODELING, DEVELOPED BASED ON QUASI-STATIC CYCLIC TESTS ON FULL SCALE BEAMS (RASHID, 2016)**

**Selection of Ground Motions for Time History Analysis**

Seven ground motion records were extracted from the PEER NGA strong ground motions database. A magnitude of $M_W$ 6 to $M_W$ 7.5, source-to-site distance of 10 km to 30 km, $V_{S30}$ 180 m/sec to 360 m/sec were used in the search engine to obtain ground motions compatible with the site seismic hazard. The final ground motions included records taking into account regional and earthquake-to-earthquake variability (Figure 4). The ground motions were scaled and matched, using wavelet based approach in SeismoMatch (SeismoSoft, 2015, Abrahamson, Hancook), to the design spectrum corresponding to seismic Zone 2B and soil type $S_D$, for a period range of 0.2T to 3T as suggested by Haselton (2010), where T corresponds to the first mode vibration period.
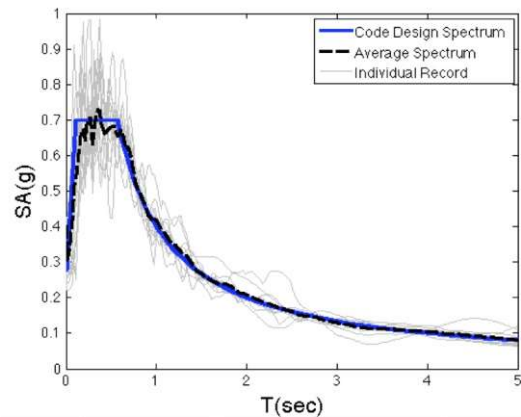


| Record No. | Event Name | Year | Station/Component | $M_W$ | PGA(g) |
|---|---|---|---|---|---|
| 1 | Kobe, Japan | 1995 | Abeno | 6.90 | 0.327 |
| 2 | San Fernando, USA | 1971 | LA – Hollywood Sto FF | 6.61 | 0.346 |
| 3 | Tabas, Iran | 1978 | Boshrooyeh | 7.35 | 0.252 |
| 4 | Duzce, Turkey | 1999 | Bolu | 7.14 | 0.418 |
| 5 | Victoria, Mexico | 1980 | Chihuahua | 6.33 | 0.235 |
| 6 | Spitak, Armenia | 1988 | Gukasian | 6.77 | 0.300 |
| 7 | L'Aquilla, Italy | 1983 | Avezzano | 6.30 | 0.256 |

**FIGURE 10: DETAILS OF GROUND MOTION RECORDS USED FOR NONLINEAR TIME HISTORY ANALYSIS.**

**Procedure for Economic Loss Estimation**

The economic losses for the considered structures were calculated using the PBEE framework for seismic performance assessment. The structures are first analyzed using incremental dynamic analysis in which the matched accelerograms were scaled to various levels of seismic intensity for structural response analysis. The PGA of ground motion records is used as an intensity measure with target levels 0.028g, 0.112g, 0.196g, 0.28g, 0.364g, 0.448g, 0.532g, 0.616g, 0.700g, 0.784, 0.840g, 0.980g, 1.120g. Beam-column chord rotation demand was used as the engineering demand parameter (EDP), to identify the damage state of members and the required repair cost.

A damage scale was established for beam members based on the quasi-static cyclic tests performed on full-scale SMRF beams (Rashid, 2016), which has been linked to the EDP for damage measure (DM) assessment i.e. identification of beam damage states during non-linear time history analysis for a given seismic intensity. Although, the columns in code designed SMRF structures primarily respond elastically, the damage scale developed by Bearman (2012) for columns was adopted herein. Furthermore, the study carried out on the repair of damaged full-scale SMRF beams for various damage states, using epoxy injection and concrete patching (Rashid, 2016), were considered and analyzed to derive the beam repair cost ratio (RCR); the ratio of repair cost to specimen construction cost. The same repair cost ratio was also used for column members with similar damage levels. Table 1 shows the beam-column members damage scale used in the present study.

**TABLE 5: DAMAGE SCALE AND REPAIR COST RATIO USED BEAM-COLUMN MEMBERS**

| Description | Chord Rotation (%) | | | Confined Concrete Crushing Strain |
|---|---|---|---|---|
| | Initial cracking | Moderate Cracking | Severe Cracking + Spalling | Collapse |
| Beam | 0.78 | 2.6 | 4.7 | as per Mander Model (1988) |
| Column | 0.3 | 1 | 1.5 | as per Mander Model (1988) |
| Repair Cost Ratio (%) | Epoxy Injection | Epoxy Injection | Epoxy Injection + Concrete Patching | Replacement |
| | 0.3 | 0.56 | 0.87 | 1 |

The considered structures were analyzed for the PGA-based target seismic intensity levels. The analyzed structures were investigated; for each scale factor, and the number of beams and columns in a particular damage state were identified to calculate the required repair costs, as per Table 1, and then integrated over the whole structure to compute the total structure repair cost. It is normalized by the total super structure cost to calculate the structure repair cost ratio (RCR):

$$RCR_{|IM} = \frac{\sum_j^n \sum_i^m (Beam\, DS_i \times RCR_i + Column\, DS_j \times RCR_j)}{Total\, Cost\, of\, Super\, Structure}$$
**(EQ. 1)**

Where DS is the attained damage state of the structural member and RCR is the corresponding required repair cost ratio for the damage. The structural RCR is correlated with the intensity measure, PGA, to develop the vulnerability curves.

Figure 5 shows the derived vulnerability curves for the considered structures based on each of the individual ground motion record and the median curves.
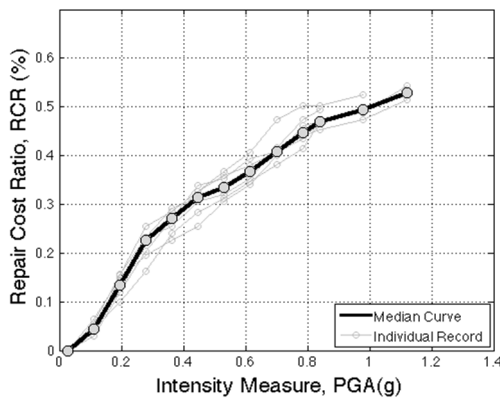


**(3 STOREY SMRF FRAME STRUCTURE)**
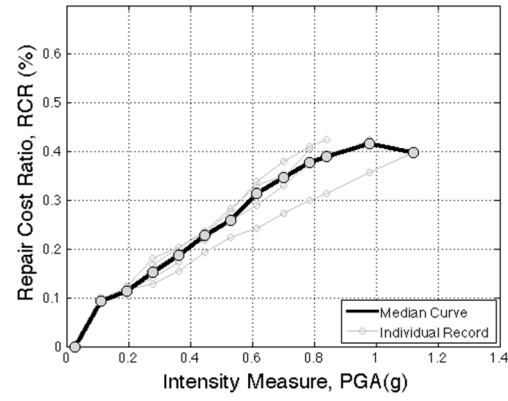


**(8 STOREY SMRF FRAME STRUCTURE)**
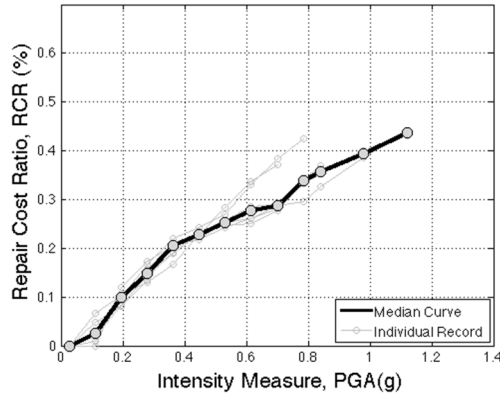


**(5 STOREY SMRF FRAME STRUCTURE)**
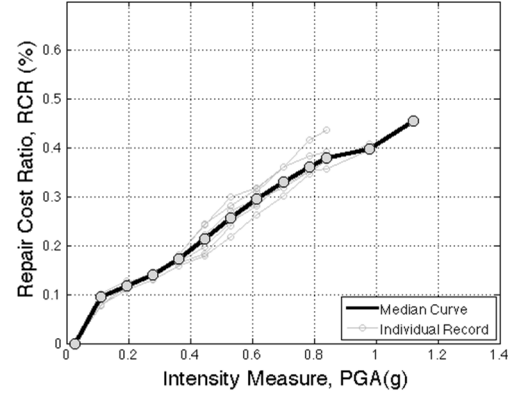
**FIGURE 11: VULNERABILITY CURVES DERIVED USING IDA/NLTHA AND THE PBEE FRAMEWORK.**

Furthermore, the mathematical functional form of fragility proposed by Kircher at al. (1997) is used for fitting to the derived vulnerability curves to facilitate future usability.

$$RCR|IM(PGA > pga) = \Phi\left(\frac{1}{\beta} Ln \frac{PGA}{\overline{PGA}}\right)$$
**(EQ. 2)**

where $\Phi$ is the standard normal cumulative distribution function, RCR|IM is the structural repair cost ratio given the intensity measure IM (PGA), $\overline{PGA}$ is the threshold intensity measure that has 50th percentile probability, $\beta$ is the logarithmic standard deviation.. The above equation is fitted to the derived vulnerability curves for the considered structures. Figure 6 shows the median vulnerability curves and fitting through the Equation (2).
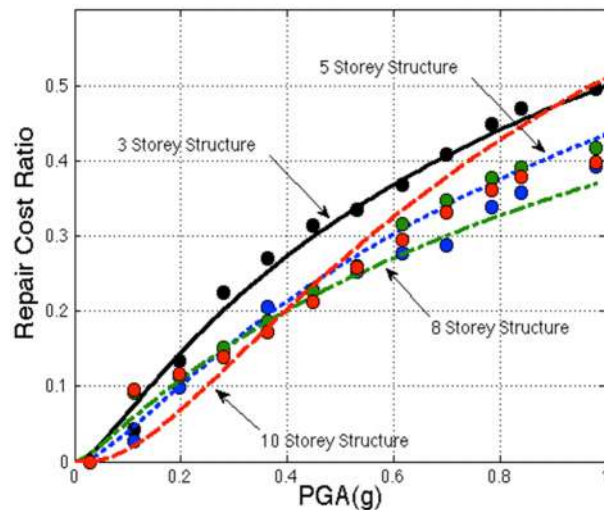
**FIGURE 12: MEDIAN VULNERABILITY CURVES AND FITTING USING THE LOGNORMAL FUNCTION.**

The derived vulnerability curves are analyzed to obtain the economic losses of the considered structures for the design-basis earthquake ground motions. RCR of 22.50% for 3 storey, 14.80% for 5 storey, 13.77% for 8 storey and 13.60% for 10 storey structures are obtained. The losses in actual buildings can be even more than this, as the indicated values of RCR represent the direct losses due to structural damage only. In a real scenario, these structural losses will be accompanied by losses due to non-structural damage as well and the subsequent closure of building (business downtime) during repair.

## Conclusions

Seismic performance assessment of the considered SMRF structures have shown that buildings designed to modern codes may have considerable cost implications upon being subjected to design level earthquakes, due to the resulting damage and subsequent repairability (i.e. epoxy injection and concrete patching, as normally practiced). The repair cost ratio of structures with low height are relatively more than the medium and high-rise structures (but does not differ very significantly), since the initial cost of medium and high-rise structures are more, the cost implications in medium and high-rise structures will be higher. The resulting losses are significant, which are generally not known to the designers, and may surprise the owner following the design level earthquake, who is considering his building to be earthquake-proof. The owner may not regard the code-designed building as an earthquake-resistant and may blame the designer for consequences.

This points to the fact that there is a strong need to incorporate performance-based earthquake engineering in structural design practices to provide structural design with various performance objectives i.e. achieving earthquake resistant design with reduced implications of cost and casualties, and the same can be communicated to the owner in the design and planning phase of structures to arrive at a mutually agreed design.

## Acknowledgement

## References

ACI-318 (2008) Building Code Requirements for Structural Concrete, American Concrete Institute (ACI).

Ahmad N. and Rashid, M. (2016) "Quasi-static cyclic tests on full-scale reinforced concrete SMRF beams – Part 2: Damage scale, cyclic response, repairability and cost", Earthquake Engineering Center, UET Peshawar, KP Pakistan.

Ahmad N., Ali Q., Crowley H., Pinho R. (2014) "Earthquake loss estimation of residential buildings in Pakistan", Natural Hazards, Vol. 73 (3), pp. 1889-1955.

Ali, S.M., Khan, A.N., Rahman, S., Reinhorn, A.M. (2011) "A survey of damages to bridges in Pakistan after the major earthquake of 8 October 2005", Earthquake Spectra, Vol. 27 (4), pp. 947-970.

Avouac, J., Ayoub, F., Leprince, S., Konca, O., and Helmberger, D.V. (2006) "The 2005 Mw 7.6 Kashmir earthquake: Sub–pixel correlation of ASTER images and seismic waveforms analysis", Earth and Planetary Science Letters, Vol. 249(3-4), pp. 514-528.

Bearman, C.F. (2012) Post-earthquake assessment of reinforced concrete frames. M.S. Thesis, Department of Civil and Environmental Engineering, University of Washington, Seattle, WA.

Bilham, R. (2004) "Earthquakes in India and in the Himalaya: tectonic, geodesy, and history", Annals of Geophysics, Vol. 47(2/3), pp. 839-858.

Bothara, J.K. and Hicyilmas, K.M.O. (2008) "General observations of building behavior during the 8th October 2005 Pakistan earthquake", Bulletin of the New Zealand Society for Earthquake Engineering, Vol. 41 (4), pp. 209-233.

BCP-07 (2007) "Building Code of Pakistan – Seismic Provisions", Ministry of Housing & Works, Islamabad, Pakistan.

Chang, A. et al., (2013). Organizational resilience to natural disasters: New Zealand's Experience. China Policy Review, Volume 10- 2013, pp 117-119.

EC8(2004) Eurocode 8: Design of structures for earthquake resistance", CEN, Brussels.

FEMA-P58 (2012) "Next-generation methodology for seismic performance assessment of buildings", Federal Emergency Management Agency (FEMA), Washington, D.C., USA.

Guin, J. and Saxena, V. (2002) "Extreme losses from natural disasters – earthquakes, tropical cyclone and extratropical cyclones", Technical Report, Air WorldWide, Boston, MA, USA.

Hamburger, R. O., and Moehle, J.P., (2000). State of performance based-engineering in the united state", Proceedings of the second US-Japan workshop on performance-based design methodology for reinforced concrete building structures. Sapporo, Japan.

Jeon, J. S. (2013). Aftershock vulnerability assessment of damaged reinforced concrete buildings in California, PhD. Thesis, School of Civil and Environmental Engineering, Georgia Institute of Technology.

Kam, W. Y., Pampanin, S., Dhakal, R. P., Gavin, H., and Roeder, C. W. (2010). Seismic performance of reinforced concrete buildings in the September 2010 Darfield (Canterbury) earthquakes" Bulletin of New Zealand Society of Earthquake Eng., Vol. 43(4), pp. 340-350.

Kam, W. Y., Pampanin, S., and Elwood, K. (2011) "Seismic performance of reinforced concrete buildings in the 22 February 2011 Christchurch (Lyttelton) earthquake" Bulletin of New Zealand Society of Earthquake Eng., Vol. 43(4), pp. 239-278.

Kircher CA, Nassar AA, Kustu O, Holmes WT. (1997) "Development of building damage functions for earthquake loss estimation", Earthquake Spectra, Vol. 13 (4), pp. 663-682

Rashid, M. (2016). Earthquake induced damaged in modern reinforced concrete special moment resisting frames: repair-ability and cost implications", MSc Thesis, Department of Civil Engineering, University of Engineering & Technology, Peshawar, KP Pakistan.

Moehle, J.P., and Deierlein, G.G., (2004) "A framework methodology for performance-based earthquake engineering", Proceedings of the 13th World Conference on Earthquake Engineering. Vancouver, B.C., Canada, Paper No. 679.

Haselton C. B., and Deierlein G., (2007). Assessing seismic collapse safety of modern reinforced concrete frame buildings", PEER Report 2007/08, Pacific Engineering Research Center, University of California, Berkeley, California.

Naeim F., (2011-12). Performance of tall buildings during the 2/27/2010 Chile earthquake.

Nanto, D. et al., (2011) "Japan's 2011 earthquake and tsunami: economic effects and implications for the United States", Congressional Research Service Report for Congress.

Naseer, A., Naeem, A., Hussain, Z. and Ali, Q. (2010) "Observed seismic behavior of buildings in northern Pakistan during the 2005 Kashmir earthquake", Earthquake Spectra, Vol. 26(2), pp. 425-449.

NZS 3101:2006 Concrete structures standard, Standards New Zealand, Wellington, NZ.

Park, Y. J. and Ang, A. H.-S. (1985). Mechanistic seismic damage model for reinforced concrete, Journal of Structural Engineering, ASCE, Vol. 111(4), pp. 722-739.

Rossetto, T. and Peiris, N. (2009) "Observations of damage due to the Kashmir earthquake of October 8, 2005 and study of current seismic provisions for buildings in Pakistan", Bulletin of Earthquake Engineering, Vol. 7(3), pp. 681-699.

UBC (1997) "Uniform Building Code – 97", International Conference of Building Officials, Whittier, California, USA.

Vamvatsikos D, and Cornell CA., (2002). Incremental dynamic analysis", Earthquake Engineering and Structural Dynamics, Vol. 31, pp. 491–514.

B. Westenenk, J.C. de la Llera, R. Jünemann, M. Hube & J.J. Besa. (2012). Seismic response of reinforced concrete buildings in Concepcion during the 2010, Maule earthquake. 15th World Conference on Earthquake Engineering.

# Modified Strawberry Algorithms for Global Optimization Problems

Abd Ullah[1,*], Ishtiaq Ahmad[1],W.K.Mashwani[1], M.A. Jan[1], M.Asim[1], M. Asad[2]

*1Kohat University of Science and Technology, KPK, Pakistan*

*2Bacha Khan University Charsada, KPK, Pakistan*

*\*Email:abdullah123maths@gmail.com*

**Abstract***:* Evolutionary optimization has become a blistering area of research due it wide application in different fields of Sciences and Engineering. Since its inception, several natures inspired based EAs are developed in the field of evolutionary computation (EC) for dealing with diverse test suite of optimizations problems. Among them, Strawberry Algorithm (SBA) is recently novel developed algorithm as like differential evolution (DE) algorithm. In this paper, DE has been used as search operator in SBA framework and as resultant its modified version of SBA denoted by MSBA is developed. We have examined the performance of the modified version of SBA by using benchmark functions of single objective optimization. The experimental results show the MSBA has obtained better experimental results for most used test problems.

**Keywords**: Optimization Problems, Evolutionary Computation, Evolutionary Algorithms, Modified Strawberry Algorithm

## 1. Introduction

Optimization is the mathematical discipline which is concerned with finding the optimal solution of functions, possibly subject to constraints. In general, optimization problems can be categorized into constrained and unconstrained optimization problems. In general unconstrained optimization problem can be expressed as a minimization (without loss of generality) problem as follows:

$$Minimize\ f(x)\ ; \qquad x_l \le x \le x_u \qquad (1)$$

Where $f: R^m \longrightarrow R$ isthe m-variable objectives (cost) function to be minimized, x $\epsilon$ $R^m$ is the solution vector to be determined, and $x_l, x_u \epsilon R^m$ are the vectors representing lower and upper bounds of the variables.

Naturally the process of evolution is completed in two-steps namely random variation and selection. Mathematically, it could be modeled as $x[t + 1] = s(v(x[t]))$, where $x[t]$ and $x[t + 1]$ are the previous and current populations obtained at a times t and t+1 respectively, through the performance of selection (s) and variation (v) operators. These processes of evolution develop an algorithm is called evolutionary algorithm (EA). Evolutionary algorithms (EAs)are stochastic optimization techniques based on natural evolution and survival of the fittest plan establish in biological processes. EAs are successfully used to solve the complex optimization problems in the field of business [1, 2], engineering [3, 4], and science [5, 6].

EAs generate randomly a set of initial solutions based on the seed and population size. Later on it will be go through evolution process such as crossover and mutation before evaluated by the cost function. EAs are randomly initialized population algorithms and the population evolves under many generations. In the last many decades EAs are used to solve different types of unconstrained/constrained optimization problems [7, 8]. EAs create different results at every run, due to random search process. They have strong ability of handling different types of optimization and real world problems.

In this paper, we have utilized different mutation strategies of DE to enhance SBA and developed its modified version called MSBA. The suggested MSBA has been examined over some well-known test problems.

The rest of the paper is arranged as under. Section 2 presents basic information about the strawberry algorithm. Section 3 provides modified strawberry algorithm, evolutionary algorithm and four differential evolution mutation strategies. Section 4 devoted to the numerical results used some well-known functions. Section 5 explain the conclusion this paper with some future work plan.

## 2. Strawberry Algorithm

Strawberry algorithm (SBA) was first introduced by F. Merrikh-Bayat [9]. Mathematical models of SBA describe how to migrate strawberry plant from one place to another and how the number of runners and roots are produce. Strawberry plant presents a sort of optimization due to roots and runners. Such plant at the same time carries out both the roots and runners for global and local searches, respectively, to discover the resources like minerals and water. In strawberry plants runners and roots are generated randomly, but when a root or a runner

emerge at a place, where a large amount of water resources are available , then the corresponding daughter plant generates more roots and runners at that place, which affects upon growth of the whole plant as well.

In order to come at the stage, where the numerical optimization algorithm inspired by strawberry plant is created. Then such algorithm is called strawberry algorithm (SBA).

The behavior of strawberry plant can be developed due to the following three facts:

- Each strawberry plant produces roots and root hairs for local search while runners for global search randomly.
- Every strawberry plant is transmitting through the runners (global search).
- Strawberry daughter plants approaches to more affluent resources grow faster and create more roots and runners. While the strawberry daughter plants approaches to inadequate resources are more credible to die.

In the proposed SBA first we defined certain number of computational agents in the domain of problem randomly, each of such agents are imagine as a strawberry mother plant. All the mother plants (strawberry plants) create one root and one runner (daughter plant) at each iteration. In SBA roots and runners are moves with small and large random steps in the domain of problem, respectively. After that the objective function is measured at the points mention by roots and runners, and half of these points are chosen by roulette wheel or elite selection for considering as a mother plant for next iteration while the remaining half are goes to death. This procedure is continuous until a fixed termination condition is hold. The pseudo code of the original SBA is outlined in the Algorithm1.

### 1. Modified Strawberry Algorithm (MSBA)

In proposed algorithm, SBA has been inserted with different mutation strategies of differential evolution (DE) abbreviated by (MSBA). A simple strategy of mutation such as DE/rand/1 has been utilized in the original framework of SBA for the purpose of improving their search progression upon the different well-known test problems. The pseudo code of modified version of SBA with DE Injection is hereby outlined in the Algorithm 2.

```
Algorithm 1 Strawberry Algorithm
 1: N, m, Kmax, ul = -600, uh = 600, drunner = 400, droot = 10, a = 0;
 2: r1 = ul + (uh - ul). * rand(m, N) ← Initialize-Parents plant;
 3: fbest = 1e6 ← Arbitary initial value for fbest;
 4: f = zeros(1, 2 * N) ← generate space for i-th column of f;
 5: xbest = ones(m, 1); ← xbest contains the best solution obtained so far
 6: for k ← 1 : kmax do
 7:    r2 = [r1 + drunner * (rand(m, N) - .5)r1 + droot * (rand(m, N) - .5)] ←
       r2 contains the locations of runners and roots;
 8:    for i ← 1 : m do
 9:       for j ← 1 : N * 2 do
10:          if r2(i, j) > uh then
11:             r2(i, j) = uh;
12:          else
13:             if r2(i, j) < ul then
14:                r2(i, j) = ul;
15:             end if
16:          end if
17:       end forj
18:    end fori
19:    f ← Evaluate function values
20:    fsorted = sort(f, ascend) ← Sort function values;
21:    for j ← 1 : N/2 do
22:       r1(:, j) = r2(:, find(f = fsorted(j), 1));
23:    end forj
24:    for j ← 1 : 2 * N do
25:       if f(j) > 0 then
26:          weights(j) = 1/(a + f(j));
27:       else
28:          weights(j) = a + abs(f(j));
29:       end if
30:    end forj
31:    for j ← N/2 + 1 : N do
32:       chosenindex = fortunewheel(weights);
33:       r1(:, j) = r2(:, chosenindex);
34:    end forj
35:    if min(f) < fbest then
36:       fbest = min(f) ← Save the best results;
37:    end if
38: end fork
```

### 3.1 Differential Evolution

Differential Evolution (DE) is one of the well-known EA, which was first introduced by Rainer Storn and Kenneth Price in 1997[10]. DE appears with the concept of using vector differences for disturbing the vector population [11]. To improve the convergence of DE over complicated constrained and nonlinear (unconstrained) optimization problems mathematician introduce the adaptation schemes in the framework of DE [12]. The important operators of DE are mutation, crossover and selection to generate and select solutions for its next generation of population evolution. While the parameters of DE are $NP$ (Population size), $F_m$ (mutation factor) and $Cr$ (crossover ratio). The process to maintain genetic diversity from one generation to the other is called mutation. For each generation g of DE, $V_{i,g}$ is the mutant vector of the current

population,$x_{i,g,i=1,2,...,NP}$ is designed by using one of the following strategies.

1.  DE/rand/1

    $$V_{i,g}=x_{r1,g} + F_m(x_{r2,g} - x_{r3,g})$$

2.  DE/best/1:

    $$V_{i,g}=x_{best,g} + F_m(x_{r2,g} - x_{r3,g})$$

3.  DE/rand-to-best/1:

    $$V_{i,g}=x_{r1,g} + x_{best,g} + F_m(x_{r2,g} - x_{r3,g})+F_m(x_{best,g} - x_{r3,g})+$$

4.  DE/current-to-best/1:
    $$V_{i,g}=x_{r1,g} + x_{best,g} + F_m(x_{r2,g} - x_{r3,g})+F_m(x_{best,g} - x_{i,g})+$$

Where$x_{r2,g} - x_{r3,g}$is a difference variation vector with respect to corresponding to the current best and i[th] individual$x_{i,g}$, $x_{best,g}$ of the current generation and $F_m \in (0,+1)$ is the scaling factor.

## 4  Tested Functions

Due to the flurry of EAs recently developed, their performance is mainly measured on different test suites. In the last few years, several test suites of unconstrained (i.e. bound constrained) and constrained problems have been designed and presented in special sessions of IEEE Conference of Evolutionary Computation (IEEE-CEC).In study of this paper, we have used 20 different unconstrained test functions as formulated in the Table below.

```
Algorithm 2 Framework of Modified Strawberry Algorithm
1:  N, m, Kmax, ul = -600, uh = 600, drunner = 400, droot = 10, a = 0;
2:  r1 = ul + (uh - ul) * rand(m, N) ← Initialize-Parents plant;
3:  fbest = 1e6 ← Arbirtary initial value for fbest;
4:  f = zeros(1, 2 * N) ← generate space for i-th column of f;
5:  xbest = ones(m, 1); ← xbest contains the best solution obtained so far
6:  for k ← 1 : kmax do
7:      if mod(k, 2) == 0 then
8:          F = 0.5;
9:          I1 = randperm(50);
10:         I2 = randperm(50);
11:         I3 = randperm(50);
12:         r2 = [r1 + drunner * (rand(m, N) - .5)r1(:, I1) + F * (r1(:, I2) - r1(:
            , I3))] ← Apply Differential Evaluation(DE) strategy ;
13:     else
14:         r2 = [r1 + drunner*(rand(m, N) - .5)r1 + droot*(rand(m, N) - .5)] ←
            r2 contains the locations of runners and roots;
15:     end if
16:     for i ← 1 : m do
17:         for j ← 1 : N * 2 do
18:             if r2(i, j) > uh then
19:                 r2(i, j) = uh;
20:             else
21:                 if r2(i, j) < ul then
22:                     r2(i, j) = ul;
23:                 end if
24:             end if
25:         end forj
26:     end fori
27:     f ← Evaluate function values
28:     fsorted = sort(f, ascend) ← Sort function values;
29:     for j ← 1 : N/2 do
30:         r1(:, j) = r2(:, find(f = fsorted(j), 1));
31:     end forj
32:     for j ← 1 : 2 * N do
33:         if f(j) > 0 then
34:             weights(j) = 1/(a + f(j));
35:         else
36:             weights(j) = a + abs(f(j));
37:         end if
38:     end forj
39:     for j ← N/2 + 1 : N do
40:         chosenindex = fortunewheel(weights);
41:         r1(:, j) = r2(:, chosenindex);
42:     end forj
43:     if min(f) < fbest then
44:         fbest = min(f) ← Save the best results;
45:     end if
46: end fork
```

**Table 1: Numerical Results for the 20 problems with r=0.5**

| S.No | Functions names | Formulations | Dimensions |
|---|---|---|---|
| 1 | Himmelblau | $f=(x_1^2+x_2-11)^2+(x_1+x_2-7)^2$ | 2-D |
| 2 | Rastrigin | $f=20 + x_1^2 -10*\cos(2*pi*x_1)+x_2^2-10*\cos(2*pi*x_2)$ | 2-D |
| 3 | Rastrigin | $f=20 + x_1^2 -10*\cos(2*pi*x_1)+x_2^2-10*\cos(2*pi*x_2)+ x_3^2-10*\cos(2*pi*x_3)+x_4^2-10*\cos(2*pi*x_4)$ | 4-D |
| 4 | Rosenbrock | $f = (1-x_1)\hat{}2+100*(x_2-x_1\hat{}2)\hat{}2$ | 2-D |
| 5 | Griewank | $f = 1+(x_1\hat{}2+x_2\hat{}2)/4000- \cos(x_1)*\cos(x_2)/\text{sqrt}(2)$ | 2-D |
| 6 | Schaffer1 | $f =0.5 + (\sin(x_1\hat{}2 + x_2\hat{}2)\hat{}2 - 0.5)/ (1+0.001*x_1\hat{}2 + x_2\hat{}2))\hat{}2$ | 2-D |
| 7 | Schaffer3 | $f= 0.5 + (\sin(\cos(\text{abs}(x_1\hat{}2 - x_2\hat{}2))).\hat{}2 - 0.5)/ (1+0.001*(x_1\hat{}2 + x_2\hat{}2)).\hat{}2$ | 2-D |
| 8 | Sine-Valley | $f=100*(x_2-\sin(x_1)).\hat{}2+0.25*x_1\hat{}2$ | 2-D |
| 9 | Powell | $f=(x_1+10*x_2)\hat{}2+5*(x_3-x_4)\hat{}2+(x_2- 2*x_3)\hat{}4+10*(x_1-x_4)\hat{}4$ | 4-D |
| 10 | Sphere | $f = x_1\hat{}2 + x_2\hat{}2;$ | 2-D |
| 11 | Haupt F1 | $f = \text{abs}(x_1) + \cos(x_1)$ | 1-D |
| 12 | Haupt F2 | $f = \text{abs}(x_1) + \sin(x_1)$ | 1-D |
| 13 | Bukin4 | $f=100*x_2\hat{}2 + 0.01*\text{abs}(x_1 + 10)$ | 2-D |
| 14 | Beale's | $f=(1.5 - x_1 + x_1.*x_2)\hat{}2 + (2.25 -x_1 + x_1*x_2.\hat{}2)\hat{}2 + (2.625 - x_1 + x_1*x_2\hat{}3)\hat{}2$ | 2-D |
| 15 | Booth's | $f =(x_1 + 2*x_2 - 7)\hat{}2 + (2*x_1 + x_2-5)\hat{}2$ | 2-D |
| 16 | Helical Valley | $f= 100*(x_3- 10*\tan2(x_2+ x_1)/2/pi)\hat{}2 + (\text{sqrt}(x_1\hat{}2 + x_2\hat{}2) - 1)\hat{}2) + x_3\hat{}2$ | 2-D |
| 17 | Three Hump Camel | $f=2*x_1\hat{}2 - 1.05*x_1\hat{}4 + x_1\hat{}6/6 + x_1*x_2 + x_2\hat{}2;$ | 1-D |
| 18 | Levi13 | $f=\sin(3*pi*x_1)\hat{}2 + (x_1-1)\hat{}2*(1 + \sin(3*pi*x_2)\hat{}2) + (x_2-1)\hat{}2*(1 +\sin(2*pi*x_2))\hat{}2);$ | 2-D |
| 19 | Sum of Difference | $f=\text{abs}(x_1+1)+\text{abs}(x_2+1)+\text{abs}(x_3+1);$ | 3-D |
| 20 | matyas | $f=0.26*(x_1)\hat{}2+(x_2).\hat{}2-0.48*(x_1*x_2)$ | 2-D |

## 4.1 Discussion Regarding the Numerical Results

The experiments have been carried out by using above formulated test functions and the following computing platform:

- Operating system: Windows XP Professional;
- Programming language of the algorithms: Matlab;
- CPU: Core 2 Quad $2.4$ GHz;
- RAM: 4 GB DDR2 1066 MHz;
- Execution: 25 times each algorithm with different random seeds.

To examine, the algorithmic performance of the proposed MSBA, we have used the above formulated test functions and summarized their numerical results in terms of Best, worst, Mean, standard deviation and time (s) in the Table 1-2-3, respectively.

These experimental results are obtained with setting r=0.5, 0.4 and0.3 which are used in the suggested MSWA. Table 1 obtained with r=0.5, Table 2 with r=0.4 and Table 3 with r=0.3 by solving each test problem. Figure 1 and 2 represent the convergence graphs of twenty two (22). The results offered by proposed algorithm in both numerical and graphical form display the capability and creditability of the MSWA in term of promity.

**Table 2: Numerical Results for the 20 problems with r=0.4**

| Problems | best | mean | median | st. dev. | worst | Time (s) |
|---|---|---|---|---|---|---|
| f01 | 0.013254 | 0.041984 | 0.039113 | 0.007179 | 0.053923 | 18.311345 |
| f02 | 0.000448 | 0.005825 | 0.009081 | 0.008410 | 0.026555 | 15.381166 |
| f03 | 0.003707 | 0.171438 | 0.277801 | 0.277623 | 0.789577 | 15.057570 |
| f04 | 4.976185 | 8.237157 | 8.071841 | 2.085814 | 10.895955 | 14.703899 |
| f05 | 0.001144 | 0.008526 | 0.008720 | 0.005560 | 0.017633 | 20.099213 |
| f06 | 0.000559 | 0.007431 | 0.006355 | 0.003821 | 0.010712 | 18.122986 |
| f07 | 24.306000 | 0.011741 | 0.015245 | 0.011040 | 0.039680 | 17.482208 |
| f08 | 0.001617 | 0.007713 | 0.007316 | 0.003233 | 0.013210 | 17.658623 |
| f09 | 0.000044 | 0.003459 | 0.004043 | 0.003588 | 0.008907 | 17.706780 |
| f10 | 0.480470 | 1.758164 | 1.758649 | 0.000000 | 2.892772 | 19.973529 |
| f11 | 0.000027 | 0.000361 | 0.000568 | 0.000617 | 0.002054 | 17.523526 |
| f12 | 1.000010 | 1.000131 | 1.000219 | 0.000234 | 1.000833 | 17.316274 |
| f13 | 0.000233 | 0.005502 | 0.005836 | 0.003769 | 0.011231 | 18.309198 |
| f14 | 0.000313 | 0.001267 | 0.001429 | 0.000804 | 0.002911 | 16.590836 |
| f15 | 0.000249 | 0.002441 | 0.002130 | 0.001090 | 0.003800 | 15.984303 |
| f16 | 0.198596 | 0.823828 | 0.986613 | 0.626809 | 2.053012 | 17.825071 |
| f17 | 0.000230 | 0.000835 | 0.000957 | 0.000654 | 0.001874 | 16.593335 |
| f18 | 0.000573 | 0.003824 | 0.005325 | 0.004837 | 0.015998 | 16.389606 |
| f19 | 0.099552 | 0.289528 | 0.246384 | 0.109321 | 0.400482 | 15.385896 |
| f20 | 0.100253 | 0.326194 | 0.338526 | 0.206109 | 0.752910 | 12.433991 |

**Table 3: Numerical Results for the 20 problems with r=0.3**

| Problems | best | mean | median | st. dev. | worst | Time (s) |
|---|---|---|---|---|---|---|
| f01 | 1.957371 | 3.164092 | 3.235599 | 0.740330 | 4.595424 | 18.117524 |
| f02 | 0.001044 | 0.003249 | 0.006297 | 0.000000 | 0.031003 | 14.692612 |
| f03 | 0.014202 | 0.263798 | 0.307297 | 0.294556 | 1.022828 | 18.396995 |
| f04 | 2.042091 | 7.852659 | 8.102214 | 2.014103 | 13.160968 | 16.319974 |
| f05 | 0.000683 | 0.005653 | 0.007191 | 0.005255 | 0.019328 | 17.508011 |
| f06 | 0.001205 | 0.002744 | 0.003734 | 0.002494 | 0.007877 | 17.589653 |
| f07 | 24.306000 | 0.013923 | 0.012541 | 0.005741 | 0.019952 | 17.383195 |
| f08 | 0.001641 | 0.007359 | 0.009289 | 0.007788 | 0.027508 | 17.636765 |
| f09 | 0.000132 | 0.001648 | 0.002000 | 0.001483 | 0.005185 | 17.623641 |
| f10 | 0.570350 | 2.519990 | 3.366124 | 2.734523 | 8.007998 | 16.407395 |
| f11 | 0.000022 | 0.001016 | 0.000876 | 0.000523 | 0.001705 | 15.567878 |
| f12 | 1.000003 | 1.000084 | 1.000215 | 0.000287 | 1.000894 | 15.826348 |
| f13 | 0.000350 | 0.005066 | 0.006795 | 0.005234 | 0.015327 | 17.738399 |
| f14 | 0.000311 | 0.001813 | 0.002595 | 0.002437 | 0.008078 | 17.139471 |
| f15 | 0.000089 | 0.000978 | 0.001219 | 0.001280 | 0.004465 | 22.439831 |
| f16 | 0.055241 | 0.544932 | 0.530986 | 0.302211 | 0.894170 | 14.583631 |
| f17 | 0.000143 | 0.000773 | 0.000880 | 0.000664 | 0.002126 | 14.748386 |
| f18 | 0.000249 | 0.004808 | 0.006880 | 0.006422 | 0.023489 | 14.474610 |
| f19 | 0.082985 | 0.278843 | 0.283016 | 0.098232 | 0.493294 | 14.598457 |
| f20 | 0.143550 | 0.373909 | 0.410282 | 0.216382 | 0.704464 | 21.077804 |
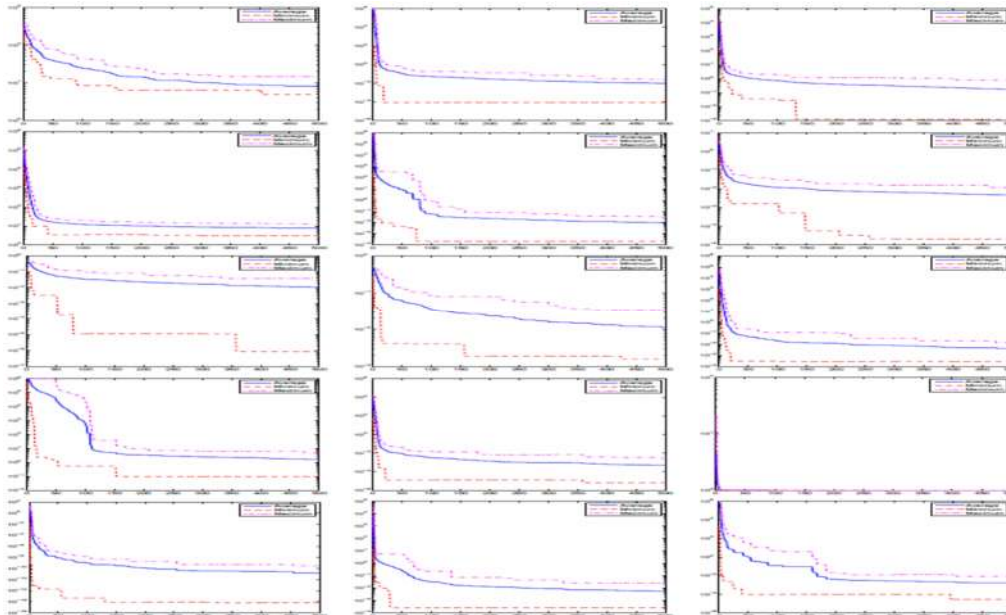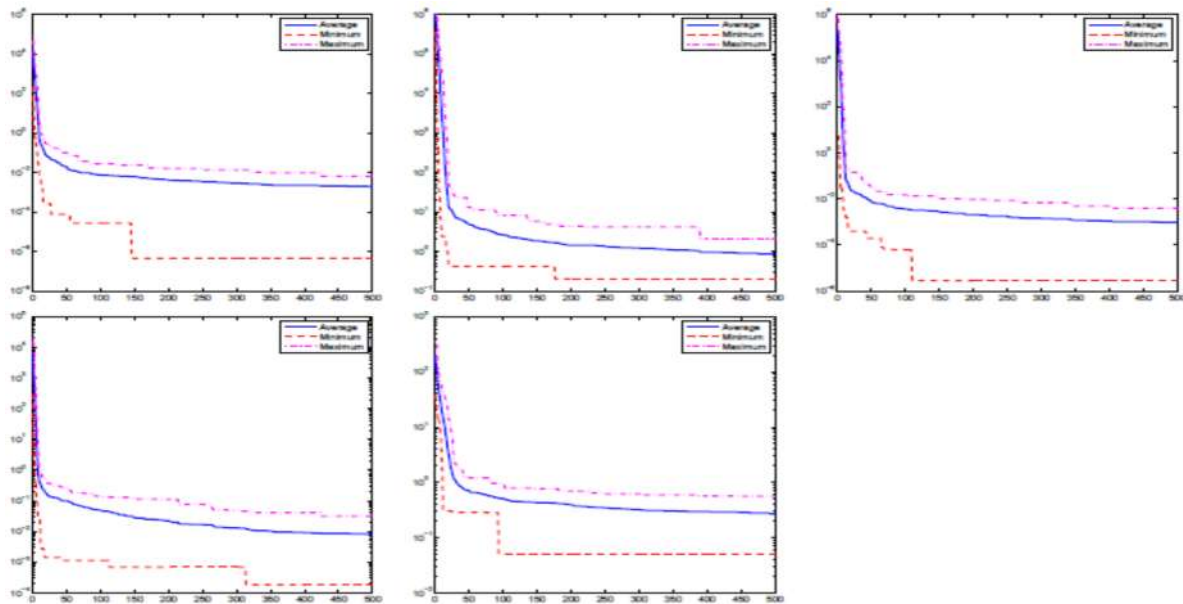
Figure 1: **Convergence Graphs of Average Mean Values against generations of Functions 1-20 with r=0.5.**
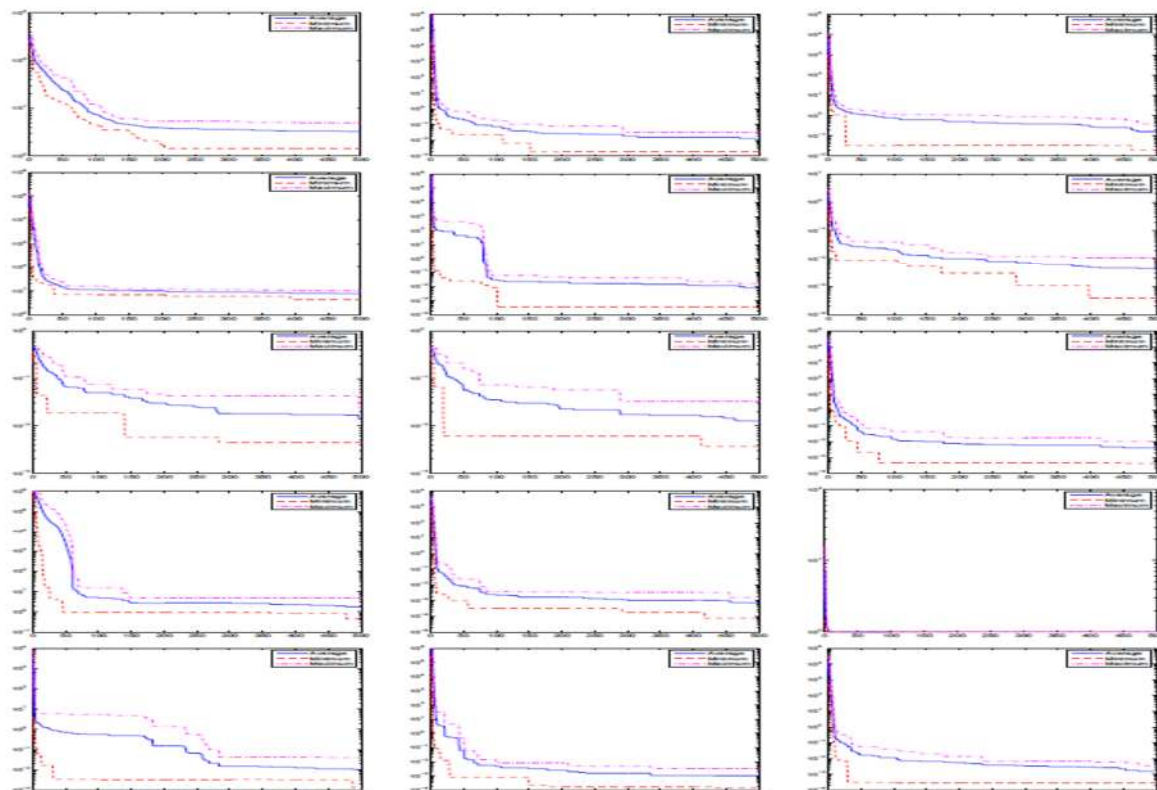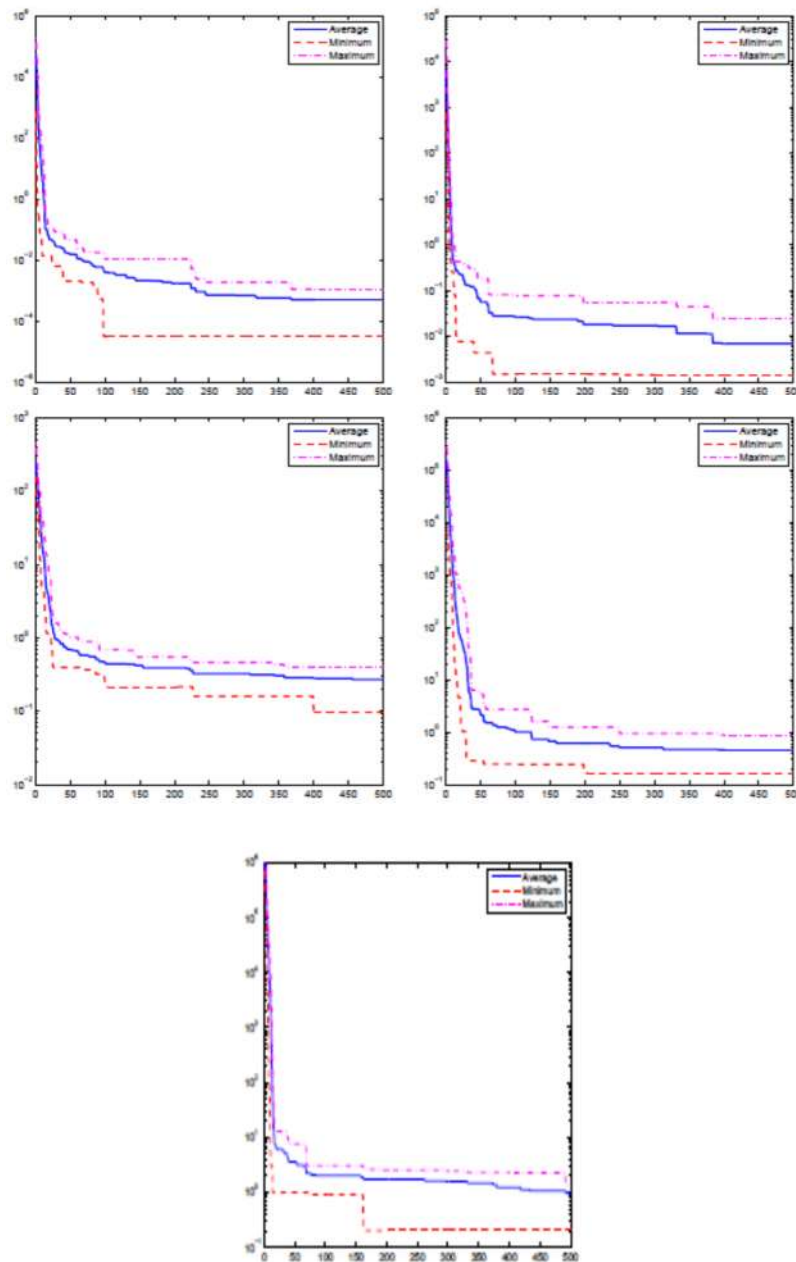
Figure 2: **Convergence Graphs of Average Mean Values against generations of Functions 1-20 with r=0.4**

## 5 Conclusions

In this paper, modified version of SBA in which DE has been applied as search technique aiming at to improve the search ability of the original SBA algorithm while solving global optimization problems. We have introduced different mutation strategies of DE in SBA framework and developed its modified version called MSBA. In this paper, we have tried DE/rand/1 mutation strategy of DE is a search operator for population evolution while SBA has been used as a global search algorithm. The experimental results clearly indicate that suggested MSBA have tackled most of the used test problems. In future, we intend to analysis the performance of the suggested proposal to apply upon some latest test

functions for the sake of satisfaction to better judge its ability and credibility in scientific way.

## References

[1] C.T. Su, C.L. Chiang, An incorporated algorithm for combined heat and power economic dispatch. *Electric Power Systems Research.* 69 (2004) 187-195.

[2] J. Y. Wu, Computational Intelligence-Based Intelligent Business Intelligence System: Concept and Framework. In Proceedings of the Second International Conference on Computer and Network Technology, (2010) 57-89.

[3] A. Carlos, C. Coello, Use of a self-adaptive penalty approach for engineering optimization problems. *Computers in Industry*, 41 (2000) 113-127.

[4] M. Falconer, G. Greenwood, K. Morgan, et al., Using evolutionary algorithms for signal integrity assessment. of high-speed data buses. *Journal of Electronic Testing: Theory and Applications.* 26 (2010) 297-305

[5] S. Rahnamayan, H.R. Tizhoosh, M.M.A. Salama, A novel population initialization method for accelerating evolutionary algorithms. *Computers and Mathematics with Application* 53 (2007) 1605-1614.

[6] A. Nobakhti, on natural based optimization. *Cognitive Computation*. 2 (2010) 97-119.

[7] D. V. Arnold, "Noisy Optimization with Evolution Strategies." Norwell, MA: Kluwer, (2002).

[8] C. A. C. Coello, D. A. Van Veldhuizen, and G. B. Lamont, "Evolutionary Algorithms for Solving Multi-Objective Problems", Norwell, MA: Kluwer, (2002).

[9] F. Merrikh-Bayat, "A Numerical Optimization Algorithm Inspired by the Strawberry Plan$t^1$", PP: 10-36.

[10] R. Storn and K. Price, ''Differential evolution: A simple and efficient adaptive scheme for global optimization over continuous spaces", Journal of Global Optimization. 4(1997) 341-359.

[11] R. Storn and K. Price, "Differential Evolution, A Simple and efficient Adaptive Scheme for Global Optimization over Continuous Spaces", ''International Computer Science Institute", Berkeley, (1995), Tech. Rep. TR-95-012.

[12] Wali Khan Mashwani, Enhanced versions of Differential Evolution: State-of-the-art Survey", International Journal Computing Sciences and Mathematics (IJCSM), 5(2), PP: 107-126, 2014.

# Numerical evaluation of three-dimensional integrals over planar domain using multi-resolution cubature rules

*Habib Nawaz khan[1], Siraj-ul-Islam[1*], Sakhi Zaman[1]*
*[1]Department of Basic Sciences and Islamiat,*
*University of Engineering and Technology Peshawar, Pakistan*
*[*]Email: siraj-ul-islam@nwfpuet.edu.pk*

**Abstract**

In this paper we have evaluated triple integrals over planar domain regions having finite limits of integration. The domain regions consist of cuboid and tetrahedron. Haar wavelets and hybrid functions based cubature rules are used to evaluate the integrals. Some test problems are included to justify accuracy and efficiency of the new methods. Numerical results of the proposed methods are compared with the methods reported in the literature as well.

**Key words**: Triple integrals over planer domain, Cubature rules, Hybrid and Haar functions.

## 1 Introduction

Triple integrals over planer and non-planer regions have many applications in science and engineering, such as mechanics, heat mass transfer, electro-magnetic field theory and finite element method etc.[7]. This type of integrals cannot be solved analytically due to the simplex domain. Numerical approximation is the only tool for evaluating these integrals. The general form of the integrals is given by,

$$I[f] = \int_\Omega f(\mathbf{x})d\mathbf{x} \quad , \quad \mathbf{x} \in \mathbb{R}^3, \tag{1}$$

where $\Omega = \{(x,y,z)\,|\, a \le x \le b, \ c(x) \le y \le d(x), \ e(x,y) \le z \le t(x,y)\}$.

If c(x), d(x), e(x, y) and t(x, y) are linear functions, then $\Omega$ is either a 4-face, a 5-face or a 6-face region like a tetrahedron, cube, cuboid, prism or pyramid etc.. Each face or boundary of these regions will be either triangular or in trapezium shape. Some such regions are shown in Figure (1).

Many researchers have contributed in evaluating one dimensional integrals [4, 9, 17]. Integrals over two dimensional domain such as triangular and quadrilateral regions are computed in the literature [11, 13, 14]. Numerical evaluation of three dimensional integrals by cubature rules is the part of the papers [5, 6, 8, 10, 12, 16]. Recently, in [7], the authors have transformed the domain of integration into a zero-one cube. According to this transformation they have transformed cuboid, tetrahedron, prism, pyramid and some other regions

having planar and non-planar faces. Generalized Gaussian quadrature rule is used to evaluate these integrals.

In the proposed work, we have used multi-resolution cubature rules like hybrid functions of order m=8 (HF8), hybrid functions of order m=6 ($HF6$) and Haar wavelets ($H_rW$) [2, 3]. Comparison of the proposed cubature rules with generalized Gaussian quadrature (GGQ) [7] is also performed.

The rest of the paper is organized as follows. In section (2) the multi-resolution cubature are discussed along with error bounds. In section (3), some test problems are also included. At the end the paper contain some conclusion as well.

### 1.1 Planar Domain

In [7], the author has used generalized Gaussian quadrature for numerical solution of triple integral over a cuboid with zero-one cube and is defined as: $\Omega = \{(x,y,z) \mid 0 \le x \le 1, 0 \le y \le 1, 0 \le z \le 1\}$. Similarly, the author also evaluated the integrals over tetrahedron type domain defined by:
$$\Omega = \{(x,y,z)|0 \le x \le 1, 0 \le y \le 1-x, 0 \le z \le 1-x-y\}.$$
In this paper, we have considered the triple integrals $I_1[f]$, $I_2[f]$ and $I_3[f]$ over cuboid domain and $I_4[f]$ and $I_5[f]$ are defined over tetrahedron type domain. The geometrical shapes of these domain regions are shown in Fig. 1.
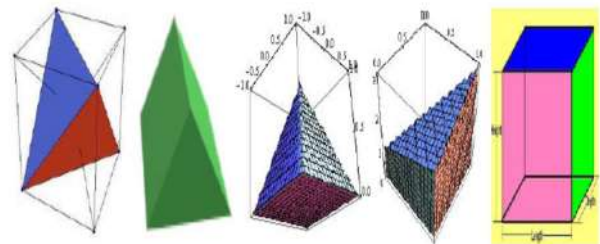


Figure: 1 Three dimensional figures with planar regions.

## 2    Cubature Rules and Error Bounds

An accurate cubature methods are used for numerical solution of triple integrals with planar domain. Both constant and variable limits of integration of the triple integrals are included. The detail description is given below:

### 2.1   Hybrid functions based cubature

The detailed description and proof of the formulae for Hybrid functions of order $m = 1,2,\ldots,10$ is given in [2, 3].

In this paper, we have used hybrid functions based cubature of order $m = 6$ and $m = 8$ in context of triple integrals over planar region like cuboid and tetrahedron. The formula for HF of order m=6 for computing triple integral $\int_a^b \int_{c(x)}^{d(x)} \int_{e(x,y)}^{t(x,y)} F(x,y,z)dzdydx$ is given by

$$HF6 = \frac{6h}{1280} \sum_{i=1}^{n} \left[ 247\, H\left(a + \frac{h}{2}(12i - 11)\right) \right.$$
$$+ 139\, H\left(a + \frac{h}{2}(12i - 9)\right)$$
$$+ 254\, H\left(a + \frac{h}{2}(12i - 7)\right)$$
$$+ 254\, H\left(a + \frac{h}{2}(12i - 5)\right)$$
$$+ 139\, H\left(a + \frac{h}{2}(12i - 3)\right)$$
$$\left. + 247\, H\left(a + \frac{h}{2}(12i - 1)\right) \right],$$

where

$$H(x) = \frac{6k}{1280} \sum_{i=1}^{n} \left[ 247\, G\left(c(x) + \frac{h}{2}(12i - 11), x\right) \right.$$
$$+ 139\, G\left(c(x) + \frac{h}{2}(12i - 9), x\right)$$
$$+ 254\, G\left(c(x) + \frac{h}{2}(12i - 7), x\right)$$
$$+ 254\, G\left(c(x) + \frac{h}{2}(12i - 5), x\right)$$
$$+ 139\, G\left(c(x) + \frac{h}{2}(12i - 3), x\right)$$
$$\left. + 247\, G\left(c(x) + \frac{h}{2}(12i - 1), x\right) \right],$$

and

$$G(x,y) = \frac{6l}{1280} \sum_{i=1}^{n} \left[ 247\, F\left(e(x,y) + \frac{l}{2}(12i - 11), x, y\right) \right.$$
$$+ 139\, F\left(e(x,y) + \frac{l}{2}(12i - 9), x, y\right)$$
$$+ 254\, F\left(e(x,y) + \frac{l}{2}(12i - 7), x, y\right)$$
$$+ 254\, F\left(e(x,y) + \frac{l}{2}(12i - 5), x, y\right)$$
$$+ 139\, F\left(e(x,y) + \frac{l}{2}(12i - 3), x, y\right)$$
$$+ 247\, F\left(e(x,y) + \frac{l}{2}(12i - 1), x, y\right) \right], \qquad (4)$$

where   $h = \frac{b-a}{6n}$,  $k = \frac{d(x)-c(x)}{6n}$  and  $l = \frac{t(x,y)-e(x,y)}{6n}$.

Similarly, the HF8 for computing the triple integral $\int_a^b \int_{c(x)}^{d(x)} \int_{e(x,y)}^{t(x,y)} F(x,y,z)dzdydx$ over planar domain is given by

$$HF8 = \frac{8h}{1935360} \sum_{i=1}^{n} \left[ 295627 \, H\left(a + \frac{h}{2}(16i - 15)\right) \right.$$

$$+ 71329 \, H\left(a + \frac{h}{2}(16i - 13)\right)$$

$$+ 471771 \, H\left(a + \frac{h}{2}(16i - 11)\right)$$

$$+ 128953 \, H\left(a + \frac{h}{2}(16i - 9)\right)$$

$$+ 128953 \, H\left(a + \frac{h}{2}(16i - 7)\right)$$

$$+ 471771 \, H\left(a + \frac{h}{2}(16i - 5)\right)$$

$$+ 71329 \, H\left(a + \frac{h}{2}(16i - 3)\right)$$

$$\left. + 295627 \, H\left(a + \frac{h}{2}(16i - 1)\right) \right],$$

where

$$H(x) = \frac{8k}{1935360} \sum_{i=1}^{n} \left[ 295627 \, G\left(c(x) \right. \right.$$

$$+ \frac{k}{2}(16i - 15), x\right)$$

$$+ 71329 \, G\left(c(x) + \frac{k}{2}(16i - 13), x\right)$$

$$+ 471771 \, G\left(c(x) \right.$$

$$+ \frac{k}{2}(16i - 11), x\right)$$

$$+ 128953 \, G\left(c(x) + \frac{k}{2}(16i - 9), x\right)$$

$$+ 128953 \, G\left(c(x) + \frac{k}{2}(16i - 7), x\right)$$

$$+ 471771 \, G\left(c(x) + \frac{k}{2}(16i - 5), x\right)$$

$$+ 71329 \, G\left(c(x) + \frac{h}{2}(16i - 3), x\right)$$

$$+ 295627 \, G\left(c(x) \right.$$

$$\left. \left. + \frac{h}{2}(16i - 1), x\right) \right],$$

and

$$G(x, y) = \frac{8l}{1935360} \sum_{i=1}^{n} \left[ 295627 \, F\left(e(x, y) \right. \right.$$

$$+ \frac{l}{2}(16i - 15), x, y\right)$$

$$+ 71329 \, F\left(e(x, y) \right.$$

$$+ \frac{l}{2}(16i - 13), x, y\right)$$

$$+ 471771 \, F\left(e(x, y) \right.$$

$$+ \frac{l}{2}(16i - 11), x, y\right)$$

$$+ 128953 \, F\left(e(x, y) \right.$$

$$+ \frac{l}{2}(16i - 9), x, y\right)$$

$$+ 128953 \, F\left(e(x, y) \right.$$

$$+ \frac{l}{2}(16i - 7), x, y\right)$$

$$+ 471771 \, F\left(e(x, y) \right.$$

$$+ \frac{l}{2}(16i - 5), x, y\right)$$

$$+ 71329 \, F\left(e(x, y) \right.$$

$$+ \frac{h}{2}(16i - 3), x, y\right)$$

$$+ 295627 \, F\left(e(x, y) \right.$$

$$\left. \left. + \frac{h}{2}(16i - 1), x, y\right) \right], \quad (5)$$

where $h = \frac{b-a}{8n}$, $k = \frac{d(x)-c(x)}{8n}$ and $l = \frac{t(x,y)-e(x,y)}{8n}$.

If $a = c = e = 0, n = 4$ and $l = \frac{(b-a)(d-c)(t-e)}{9n}$, then the truncation error for computing integral (1) by HF8 is given by

$$E = |I[f] - HF8|$$
$$= \frac{(a - b)^9 (d - c)^9 (t - e)^9}{4.54 \times n^8} f^{(8)}(\xi_1, \, \xi_2, \xi_3),$$

where $(\xi_1, \xi_2, \xi_3) \in (a, b) \times (c, d) \times (e, t)$.

## 3 Haar wavelets based cubature

We have used the $H_r W$ [1, 15] for numerical evaluation of the integral $\int_a^b \int_{c(x)}^{d(x)} \int_{e(x,y)}^{t(x,y)} F(x, y, z) \, dz \, dy \, dx$. The detail derivation of the methods can be found in [1, 15]. The formula for $H_r W$ is given by

$$\int_a^b \int_{c(x)}^{d(x)} \int_{e(x,y)}^{t(x,y)} F(x,y,z)\,dzdydx$$

$$\approx h \sum_{j=1}^{2p} H\big(a + h(j - 0.5)\big),$$

where

$$H(x) = k \sum_{j=1}^{2N} G(c(x) + k(j - 0.5), x),$$

and

$$G(x,y) = l \sum_{j=1}^{2M} F(e(x,y) + l(j - 0.5), x, y),$$

where $h = \frac{b-a}{2P}$, $\quad k = \frac{d(x)-c(x)}{2N}$ $\quad$ and $\quad l = \frac{t(x,y)-e(x,y)}{2M}$.

## 4 Numerical results and discussion

Some numerical test problems [7] are included in this section to justify the accuracy of the new proposed methods. Exact values of the some test integrals are obtained by MAPLE 15 and some are taken from the paper [16]. Absolute errors Labs are obtained in each test problem.

Test problem 1. We have considered numerical evaluation of the integrals [7].

$$I_1[f] = \int_0^1 \int_0^1 \int_0^1 8(1 + 2(x + y + z))^{-1}\,dzdydx$$

$$I_2[f] = \int_1^2 \int_3^4 \int_5^6 \sqrt{x + y + z}\,dzdydx$$

$$I_3[f] = \int_0^\pi \int_0^\pi \int_0^{\pi/2} \cos(x + y + z)\,dzdydx,$$

by the new methods HF8, HF6 and $H_r W$. The results in terms of absolute error are shown in table (1). From the table, it clear that the HF8 gives a high order accuracy than all the other methods. The results of the new quadrature rules are compared with the results of generalized Gaussian quadrature [7] at the same nodal points.

The CPU time (in seconds) comparison of all the proposed methods is shown in table (2). It is shown in the table that the proposed methods are efficient.

**Table 1**: Test problem 1 $L_{abs}$ of $HF8$, $HF6$ and $H_r W$ and their comparison with the result of [7].

| | | $HF8$ | $HF6$ | $H_r W$ | GGQ[7] |
|---|---|---|---|---|---|
| $I_1[f]$ | N=5 | 7.86e-11 | 1.43e-08 | 2.10e-03 | 4.99e-07 |
| | N=10 | 3.62e-13 | 2.40e-10 | 5.16e-04 | 7.15e-13 |
| | N=20 | 8.43e-15 | 3.83e-12 | 1.29e-04 | 1.06e-13 |
| $I_2[f]$ | N=5 | 4.44e-16 | 8.88e-16 | 9.22e-06 | 4.64e-12 |
| | N=10 | 00 | 4.44e-16 | 2.30e-06 | 8.97e-14 |
| | N=20 | 00 | 4.44e-16 | 5.76e-07 | 7.40e-13 |
| $I_3[f]$ | N=5 | 8.09e-11 | 1.11e-07 | 3.72e-02 | 2.65e-04 |
| | N=10 | 3.33e-13 | 1.72e-09 | 9.30e-03 | 1.95e-11 |
| | N=20 | 2.13e-14 | 2.68e-11 | 2.30e-03 | 1.10e-13 |

**Table: 2** CPU time comparison (in seconds) of $HF8$ and $HF6$.

| Integral | Nodes | HF6 | HF8 |
|---|---|---|---|
| $I_1[f]$ | N=5 | 3.0090e-01 | 6.8463e-1 |
| | N=10 | 2.2723e-0 | 5.3065e-0 |
| | N=20 | 1.78289e1 | 4.182463e-1 |
| $I_2[f]$ | N=5 | 4.1846e-01 | 9.56658e-1 |
| | N=10 | 3.1630e-0 | 7.4273e-0 |
| | N=20 | 2.48990e1 | 5.86579e-1 |
| $I_3[f]$ | N=5 | 2.9876e-01 | 6.9745e-01 |
| | N=10 | 2.2711e-0 | 5.2858e-0 |
| | N=20 | 1.76128e-1 | 4.15978e-1 |

**Test Problem 2**. Consider the following integrals [7]

$$I_4[f] = \int_0^1 \int_0^{1-x} \int_0^{1-x-y} \sqrt{x + y + z}\,dzdydx$$

$$I_5[f] = \int_0^1 \int_0^{1-x} \int_0^{1-x-y} \frac{1}{\sqrt{x+y+z}}\,dzdydx.$$

Both the integrals are defined over the planar domain regions of tetrahedron type. The integrals are evaluated by the new methods HF8, HF6 and $H_r W$. The results are shown in table 3. It is clear from the table that all the three methods improve the accuracy on finer grids. The results of the proposed methods are compared with the results of [7] at the same nodal points. It is also shown in the table that the results of HF8 are comparable with the results of generalize Gaussian quadrature (GGQ) [7] at the same nodal points.

**Table: 3** $L_{abs}$ of $HF8, HF6$ and $H_r W$ and their comparison with the results of [7].

| | | $HF6$ | $HF8$ | $H_r W$ | GGQ [7] |
|---|---|---|---|---|---|
| $I_4[f]$ | N=5 N=10 N=15 N=20 | 4.80e-08 4.46e-09 1.10e-09 4.06e-10 | 1.02e-08 9.32e-10 2.28e-10 8.37e-11 | 1.91e-04 4.72e-05 2.09e-05 1.17e-05 | 2.64e-08 4.50e-12 ---- ---- - |
| $I_5[f]$ | N=5 N=10 N=15 N=20 | 5.75e-06 1.04e-06 3.84e-07 1.88e-07 | 2.07e-06 3.74e-07 1.36e-07 6.68e-08 | 1.10e-03 2.89e-04 1.32e-04 7.57e-05 | 2.75e-07 2.40e-09 ---- - ---- - |

**Conclusion:**

In this paper, multi-resolution quadrature like Haar wavelets and Hybrid functions are used for numerical evaluation of triple integrals with constant and variable limits. Triple integrals over planner regions like cuboid and tetrahedron are solved. Theoretical error bounds of the proposed quadrature rules are found by using Maple 15. Numerical tests verified the accuracy and efficiency of the proposed methods.

**References:**

[1] I. Aziz, Siraj-ul-Islam, and W. Khan, *Quadrature rules for numerical integration based on Haar wavelets and hybrid functions*, Applied Mathematics and Computation.61 (2011), 27702781.

[2] Imran Aziz, Fazal Haq, et al., *A comparative study of numerical integration based on Haar wavelets and hybrid functions*, Applied Mathematics and Computation.59 (2010), 2026–2036.

[3] Imran Aziz, Wajid Khan, et al., *Quadrature rules for numerical integration based on Haar wavelets and hybrid functions*, , Applied Mathematics and Computation. 61 (2011), 2770–2781.

[4] Klaus-J¨urgen Bathe, *Finite element procedures*, Klaus-Jurgen Bathe, 2006.

[5] Michael G Duffy, *Quadrature over a pyramid or cube of integrands with a singularity at a vertex*, SIAM journal on Numerical Analysis 19 (1982), 1260–1262.

[6] Sarada Jayan and KV Nagaraja, *Numerical integration over n-dimensional cubes using generalized Gaussian quadrature*, Proc. Jangjeon Math. Soc, vol. 17, 2014, pp. 63–69.

[7] *A general and effective numerical integration method to evaluate triple integrals using generalized Gaussian quadrature*, Procedia Engineering 127 (2015), 1041–1047.

[8] Ethan J Kubatko, Benjamin A Yeager, and Ashley L Maggi, *New computationally efficient quadrature formulas for pyramidal elements*, Finite Elements in Analysis and Design 65 (2013), 63–75.

[9] J Ma, V Rokhlin, and Stephen Wandzura, *Generalized Gaussian quadrature rules for systems of arbitrary functions*, SIAM Journal on Numerical Analysis 33 (1996), 971–996.

[10] S.E. Mousavi and N Sukumar, *Generalized Gaussian quadrature rules for discontinuities and crack singularities in the extended finite element method* Computer Mathematics and Applied. Mechanics and Engineering 199 (2010), 3237–3249.

[11] KV Nagaraja and Sarada Jayan, *Generalized Gaussian quadrature rules over regions with parabolic edges*, International Journal of Computer Mathematics 89 (2012), 1631–1640.

[12] HT Rathod, KV Nagaraja, and B Venkatesudu, *Numerical integration of some functions over an arbitrary linear tetrahedra in euclidean three-dimensional space*, Applied Mathematics and Computation 191 (2007), 397–409.

[13] HT Rathod, KV Nagaraja, B Venkatesudu, and NL Ramesh, *Gauss-Legendre quadrature over a triangle*, Journal of the Indian Institute of Science 84 (2013), 183.

[14] Jayan Sarada and KV Nagaraja, *Generalized Gaussian quadrature rules over two-dimensional regions with linear sides*, Applied Mathematics and Computation 217 (2011), 5612–5621.

[15] Siraj-ul-Islam, I. Aziz, and Fazal-e-Haq, *A comparative study of numerical integration based on Haar wavelets and hybrid functions*, Computer Mathematics with Application. 59(6) (2010), 2026–2036.

[16] Paul Van Dooren and Luc de Ridder, *An adaptive*

algorithm for numerical integration over an n-dimensional cube, Journal of Computational and Applied Mathematics 2 (1976), 207–217.

[17] Olgierd Cecil Zienkiewicz, Robert Leroy Taylor, Olgierd Cecil Zienkiewicz, and Robert Lee Taylor, *The finite element method*, vol. 3, McGraw-hill London, 1977.

# Segmentation of Texture Images via L0 Norm Smoothing

*Hassan Shah[1,*], Noor Badshah[1], Fahim ullah[1]*

[1] *Department of Basic Science and Islamiat, UET Peshawar, Peshawar*

*\*Corresponding author*

*Email*: hassanshah1122@yahoo.com

**Abstract**

Segmentation of images is a great challenge in the field of computer vision. Many variational models have been developed for this task such as Mumford Shah (MS) model and Chan Vese (CV) model. As CV-model is not convex, so it may stuck at local minima. To overcome this problem Bresson et al. proposed a fast global minimization of the active contour model (FGM). Although these segmentation models work well in synthetic and real images, yet these models fail to segment texture images accurately. Xu et al. proposed the L0 Gradient minimization (LGM) model for image smoothing. The LGM model has a strong smoothing ability. It can remove minor details and enhance salient edges in the image.

In this paper, we propose a new method that is based on both LGM model and FGM. This method works in the following way: initially, we use the LGM model to smooth texture image and then FGM model is used to segment the smoothed image. We compare the results of our proposed model with CV-model and FGM-model.

**Keywords:** Texture Images, Minimization, Smoothing and Segmentation.

## 1 Introduction

One of the most important and ubiquitous tasks in the field of image analysis is segmentation. The main aim of image segmentation is to partition an image into a set of distinct regions, which are more meaningful and easier to analyze. For example, if we want to segment tumors from healthy brain tissue in an MRI image, segmenting written or typset characters on a page, etc.

Up to now many types of methods have been developed and used for segmentation of images. Active contour approach is employed mostly in many segmentation models. Generally, active contour segmentation models are categorized into two groups, the edge-based active contour models [3, 15, 16] and region-based active contour models [7, 8, 13]. Edge-based active

contour models look only for discontinuities [7], whereas region-based active contour models analyze homogeneous regions [13]. However, the edge-based models produces problems of segmenting weak object boundaries in the image. Region-based models aim to identify each interested region by the ability of capturing region intensity information [13, 16].

MS-model [18], is the well-known region-based active contour model that has been utilized in many research papers for image segmentation [12, 20, 25, 26]. Chan and Vese [7] proposed a segmentation model for gray images and is based on MS-model [17]. The model can globally segment synthetic homogeneous images, and divide them into two parts, one part show the foreground and the other part show the background.
CV-model is not convex, so it may stuck at local minima. To solve this problem Bresson et al. [2] proposed a FGM-model. FGM-model is the convex formulation of the CV-model. In this model a fast numerical scheme based on the Chambolle algorithm is used. Although MS-model, CV-model and FGM-model work well in synthetic and real images, yet these models fail to segment texture images accurately.

In order to overcome the problem of texture image segmentation, it is very important to add image features as an extra term in the segmentation models. Up to now, there are many approaches to deal with the extraction of texture image feature. Such approaches are: bilatering [24], the weighted least square optimization [9], the robust anisotropic diffusion model [1], the Gabor representation [14, 32], the wavelet transforms [21], the structure tensor model based diffusion [27, 31], the local structure tensor [31], the manifold model based diffusion [23], and modified Perona-Malik model [29] etc.

The TV model is mostly used for image smoothing in many papers [4, 5, 10, 11, 28, 33]. However TV model has a drawback as well, that this model suffers from stair-casing effect. Xu et al. [34]

proposed LGM-model for image smoothing. In this model, L1 norm of the $\nabla I$, in the TV model is replaced with the L0 norm [34].

In this study, a new method based on both LGM and FGM models is developed. This method works in the following way: initially, we use the LGM model to smooth texture image and then FGM model is used on the smoothed image to segment it.

The remaining sections of the paper are explained in the following way: In section (2), we briefly review the LGM- model, CV-model and FGM-model respectively. Our proposed method, experimental results of the proposed model with CV-model and FGM-model on the synthetic and real texture images are presented in section (3). Some conclusion is included in section (4).

## 2    Related Variational models:

A brief overview of some image smoothing and segmentation models are presented in this section.

### a.    LGM Model

Xu et al. proposed the LGM model for image smoothing [34]. In this model, $\nabla L0$ is used instead of $L1$ norm for gradient [22]. The model is defined as:

$$min_S \{E(S) = \sum_p |Sq - Iq|^2 + \lambda\, G(S) \},$$ 
(1)

$L0$ norm of $\nabla S$, is defined as:

$$G(S) = \{q / |\frac{\partial Sq}{\partial x}| + |\frac{\partial Sq}{\partial y}| \neq 0\},$$ 
(2)

where $q$ is the number of those pixels where the sum of gradient norms along x and y directions is not equal to zero. As the optimization of regularization term $G(S)$ is difficult because $G(S)$ give constant value. Therefore, it is non-convex and it has zero derivative. Two auxiliary variables $uq$ and $wq$ are incorporated in the model to replace $\frac{\partial Sq}{\partial x}$ and $\frac{\partial Sq}{\partial y}$ respectively by using the alternating minimization (AM) algorithm [30]. Then the model (1) becomes the form:

$$min_{S,u,w} \{\Sigma_q |S_q - Iq|^2 + \beta\left(|\frac{\partial Sq}{\partial x} - u_q|^2 + |\frac{\partial Sq}{\partial y} - w_q|^2\right) + \lambda G(S)\},$$ 
(3)

where $\lambda$ is the smoothing parameter and $\beta$ measure the discrepancy between variables $(uq, wq)$ and their corresponding gradients $\frac{\partial Sq}{\partial x}$ and $\frac{\partial Sq}{\partial y}$ respectively.

### i.    AM Algorithm

AM algorithm [30] is used to solve equation (3) for (u, w) and S respectively. Keeping S fixed minimizing equation (3) for $(uq, wq)$ we get:

$$min_{u,w} \{\Sigma_q\left(|\frac{\partial Sq}{\partial x} - u_q|^2 + |\frac{\partial Sq}{\partial y} - w_q|^2\right) + \frac{\lambda}{\beta} G(S)\}.$$ 
(4)

Equation (4) is accordingly decomposed to:

$$\sum_p min_{u,w} \{\left(|\frac{\partial Sq}{\partial x} - u_q|^2 + |\frac{\partial Sq}{\partial y} - w_q|^2\right) + \frac{\lambda}{\beta} H(|u_q| + |w_q|)\}.$$ 
(5)

$H(|u_q| + |w_q|)$ is the binary function returning 1 if $|u_q| + |w_q|$ is not equal to zero and zero otherwise. Solving equation (5) we get:

$$E_q = \{\left(|\frac{\partial Sq}{\partial x} - u_q|^2 + |\frac{\partial Sq}{\partial y} - w_q|^2\right) +$$
$$\frac{\lambda}{\beta} H(|u_q| + |w_q|)\}, (6)$$

Equation (5) give its minimum value:

$$(u_q, w_q) = \begin{cases} (0,0), & \left(\frac{\partial q}{\partial x}\right)^2 + \left(\frac{\partial S_q}{\partial y}\right)^2 < \frac{\lambda}{\beta} \\ \left(\frac{\partial S_q}{\partial x}, \frac{\partial S_q}{\partial y}\right), & otherwise. \end{cases}$$
(7)

Keeping (u, w) fixed, minimizing equation (3) for S.

$$min_S \{\{\Sigma_q |Sq - Iq|^2 + \beta\left(|\frac{\partial Sq}{\partial x} - u_q|^2 + |\frac{\partial Sq}{\partial y} - w_q|^2\right)\}\}.$$
(8)

Equation (8) is quadratic in S and thus a global minimum is achieved. Alternatively, we diagonalize derivative operators $\partial x, \partial y, \partial x^T, \partial y^T$ respectively after applying Fast Fourier Transform (FFT). Thus S is obtained:

$$S = \mathcal{F}^{-1}\left\{\frac{\mathcal{F}(I) + \beta\left(\mathcal{F}(\partial x^T * u) + \mathcal{F}(\partial y^T * w)\right)}{\mathcal{F}(1) + \beta\left(F(\partial x^T) * \mathcal{F}(\partial x) + \mathcal{F}(\partial y^T) * \mathcal{F}(\partial y)\right)}\right\},$$
(9)

where $\mathcal{F}$ and $\mathcal{F}^{-1}$ are the is the FFT and inverse FFT operators respectively. This model has a strong ability to remove minor details and preserve and enhance sharp edges.

### b.    CV Model

Chan et al. proposed a region based active contour model for segmentation of gray images [7]. This model is the piecewise constant case of the MS model [18]. The energy functional of the CV model is given by:

$$E^{CV} = \mu.length(\acute{C}) + \int_{in(\acute{C})} |I - \acute{c}_1|^2 dx\, dy +$$
$$\int_{out(\acute{C})} |I - \acute{c}_2|^2 dx\, dy,$$ 
(10)

Where, parameters $\acute{c}_1$ and $\acute{c}_2$ are the average intensities value inside and outside of the counter ($\acute{C}$). In the level set method [19], $\acute{C} \subset \Omega$, is defined by:

$$\begin{cases} \acute{C} = \partial\omega = \{(x,y) \in \Omega : \phi = 0\} \\ in(\acute{C}) = \omega = \{(x,y) \in \Omega : \phi > 0\} \\ out(\acute{C}) = \Omega\backslash\overline{\omega} = \{(x,y) \in \Omega : \phi < 0\} \end{cases},$$ 
(11)

Thus equation (10) takes the form:

$$E^{CV} = \mu. \int_\Omega \delta_\varepsilon(\phi)|\nabla\phi| dxdy + \int_\Omega |I - \acute{c}_1|^2 dx\, dy + \int_\Omega |I - \acute{c}_2|^2 dx\, dy,$$
(12)

Where $H_\varepsilon(\phi)$ and $\delta_\varepsilon(\phi)$ are the regularized form of Heaviside and Dirac Delta functions, respectively.

$$H_\varepsilon(\phi) = \frac{1}{2}\left(1 + \frac{2}{\pi}\arctan\left(\frac{\phi}{\varepsilon}\right)\right) ,$$
(13)

and

$$\delta_\varepsilon(\phi) = \frac{1}{2}\left(\frac{\varepsilon}{\varepsilon^2 + \phi^2}\right),$$
(14)

Keeping $c_1, c_2$ fixed, minimizing equation (12) for $\phi$ we get:

$$\frac{\partial\phi}{\partial t} = \delta_\varepsilon(\phi)\left[\mu\nabla.\left(\frac{\nabla\phi}{|\nabla\phi|}\right) - |I - \acute{c}_1|^2 + |I - \acute{c}_2|^2\right],$$
(15)

This model is used for segmenting gray scale images. The final segmentation result obtained from this model can divide the image into two parts; one part shows the background and the other part show the foreground.

### 2.2.3 FGM Model

Bresson et al. proposed a fast global minimization of the CV model [2]. In this model, first they made CV model convex and then used dual formulation for minimization. As the CV model (10) is non-convex, so local minima exist and therefore, a smooth approximation of the Heaviside function is selected in this model. Thus the steady state solution of the equqtion (15) is same as:

$$\frac{\partial\phi}{\partial t} = \left[\mu\nabla.\left(\frac{\nabla\phi}{|\nabla\phi|}\right) - |I - \acute{c}_1|^2 + |I - \acute{c}_2|^2\right],$$
(16)

And equation (16) is the partial differential equation obtained from the given energy $E$:

$$E = \int_\Omega |\nabla\phi| + \int_\Omega |I - \acute{c}_1|^2 + |I - \acute{c}_2|^2 \phi dx.$$
(17)

Due to the incorporation of edge indicator function $g$ in the length term of above model, the new model takes the form:

$$E = \int_\Omega g(x)|\nabla\phi| + \int_\Omega |I - \acute{c}_1|^2 + |I - \acute{c}_2|^2 \phi dx.$$
(18)

This energy $E$; will provide us a global minima. It is homogeneous of degree 1 in $\phi$ and therefore, it has no stationary solution. To get the optimal solution, some constrained must be imposed on $\phi$. Then the problem can be written as follows:

$$\min_{0\leq\phi\leq1} E(\phi) \quad \text{where}$$

$$E = \int_\Omega g(x)|\nabla\phi| + \int_\Omega |I - \acute{c}_1|^2 + |I - \acute{c}_2|^2 \phi dx$$
(19)                The unconstrained form using [6] of above minimization problem is:

$$\min_\phi\left\{E = \int_\Omega g(x)|\nabla\phi| + \int_\Omega \{[|I - \acute{c}_1|^2 + |I - \acute{c}_2|^2]\phi + \alpha v(\phi)\} dx\right\},$$
(20)

where

$$v(\phi) = max\left\{0, 2\left|\phi - \frac{1}{2}\right| - 1\right\},$$
(21)

is an exact penalty function provided that the constant $\alpha$ is chosen a large number :

$$\alpha > \frac{1}{2}||(I - \acute{c}_1)^2 + (I - \acute{c}_1)^2||_{L^\infty} ,$$
(22)

Using dual formulation, the variational problem (20) is regularized as:

$$\min_{\phi,\phi_1}\left\{E = \int_\Omega g(x)|\nabla\phi| + \frac{1}{2\theta}||\phi - \phi_1||^2 + \int_\Omega \{[|I - \acute{c}_1|^2 + |I - c_2|^2]\phi_1 + \alpha v(\phi_1)\} dx\right\},$$
(23)

Keeping $\phi_1$, fixed minimizing equation (23) for $\phi$,

$$\min_\phi\left\{\int_\Omega g(x)|\nabla\phi| + \frac{1}{2\theta}||\phi - \phi_1||^2\right\},$$
(24)

Keeping $\phi$, fixed minimizing equation (23) for $\phi_1$,

$$\min_{\phi_1}\left\{\frac{1}{2\theta}||\phi - \phi_1||^2 + \int_\Omega \{[|I - \acute{c}_1|^2 + |I - \acute{c}_2|^2]\phi_1 + \alpha v(\phi_1)\} dx\right\}.$$
(25)

Solution of equation (24) is:

$$\phi = \phi_1 - \theta\nabla.\left(\frac{\nabla\phi}{|\nabla\phi|}\right),$$
(26)

Where $\frac{\nabla\phi}{|\nabla\phi|}$, is obtained as,

$$g(x)\nabla\left(\phi_1 - \theta\nabla.\left(\frac{\nabla\phi}{|\nabla\phi|}\right)\right) - |\nabla\left(\phi_1 - \theta\nabla.\left(\frac{\nabla\phi}{|\nabla\phi|}\right)\right)|\frac{\nabla\phi}{|\nabla\phi|}$$
(27)

Using fixed point method on the above equation we obtained

$$p^{n+1} = \frac{p^n + \delta t\nabla\left(\nabla.p^n - \frac{\theta_1}{\theta}\right)}{1 + \delta t/_{g(x)}|\nabla\left(\nabla.p^n - \frac{\theta_1}{\theta}\right)|},$$
(28)

Where $p = \frac{\nabla\phi}{|\nabla\phi|}$.

$\phi_1$, is obtained by minimizing equation (25).

$$\phi_1 = min\{max[\phi - \theta\lambda\{|I - \acute{c}_1|^2 + |I - \acute{c}_2|^2\}, 0], 1\}.$$
(29)

This model improved the performance of the CV-model when there is a very little intensity change in the object to be detected and the background.

### 3  Proposed model

In this model we use LGM model [34] and FGM model [2] alternatively. We first use LGM model to smooth texture in the image and then apply the FGM model for segmentation. Smoothing of texture is done

by model (2) and then using FGM-model for smoothed image S. Using fast global minimization based on the Chambolle algorithm, equation (23) takes the form:

$$min_{\phi,\phi_1}\left\{E = \int_\Omega g(x)|\nabla\phi| + \frac{1}{2\theta}||\phi - \phi_1||^2 + \int_\Omega\{[|S - c_1|^2 + |S - c_2|^2]\phi_1 + \alpha v(\phi_1)\}dx\right\}.$$

(30)

Keeping $\phi_1$ fixed, minimizing equation (30) for $\phi$,

$$min_\phi\left\{\int_\Omega g(x)|\nabla\phi| + \frac{1}{2\theta}||\phi - \phi_1||^2\right\}.$$

(31)

Keeping $\phi$, fixed minimizing equation (30) for $\phi_1$,

$$min_{\phi_1}\left\{\frac{1}{2\theta}||\phi - \phi_1||^2 + \int_\Omega [|S - c_1|^2 + |S - c_2|^2]\phi_1 + \alpha v(\phi_1)\right\}.$$

(32)

Solving equation (31) we get:

$$\phi = \phi_1 - \theta\,\nabla.p.$$  (33)

Solving equation (32) we get:

$$\phi_1 = min\{max[\phi - \theta\lambda\{|S - c_1|^2 + |S - c_2|^2\}, 0], 1\}.$$  (34)

**3.1        Experimental results**

Experimental results of the three image segmentation models are presented here. We compare the proposed model with CV-model [7] and FGM-model [2] respectively. We tested some synthetic and natural gray-scale texture images of size 256 ×256.



(a) Original image



(b) CV model



(c) F
GM model
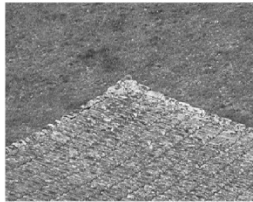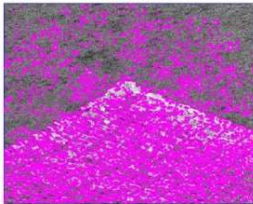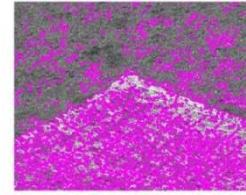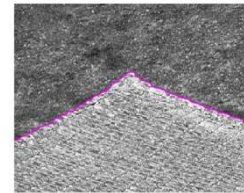


(d) Proposed method

Figure (1). The parameter values for (b) $\mu = 0.1 \times 255^2/100$. (c) $\theta = 1/500000000$ (d) $\lambda = 0.06$, $\theta = 1/500000000$.



(a)  Original image
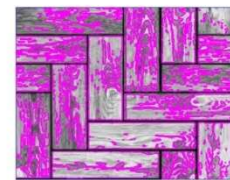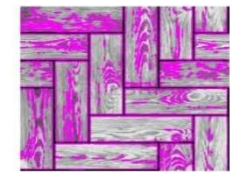


(b) CV model
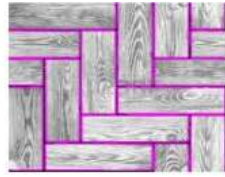


(c)  FGM model

(d) Proposed method

Figure(2). The parameter values for (b) $\mu = 0.1 \times 255^2/100$. (c) $\theta = 1/3000$ . (d) $\lambda = 0.037$, $\theta = 1/3000$.
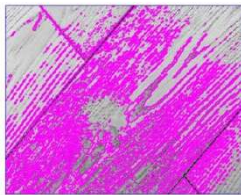


(a) Original Image   (b) CV model
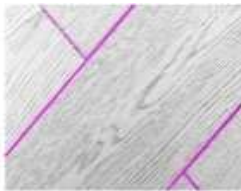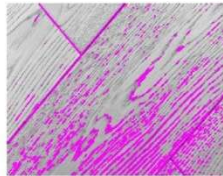


(c) FGM model  (d) Proposed method

Figure(3) The parameter values for (b) $\mu = 0.1 \times 255^2/100$. (c) $\theta = 1/5500000$ (d) is $\lambda = 0.024$, $\theta = 1/500000000$

## 4   Conclusion

A new method which is based on LGM-model and FGM-model is proposed in this paper. In this method, first an L0 norm is used for smoothing texture in the image and then FGM-model is employed on the smoothed image for segmentation. By using LGM-model, an alternating minimization algorithm is used to solve the optimization problem. In this algorithm, a fast Fourier transform is used after diagonalizing the derivative operators for speedup. The FGM-model is used for segmentation on the smoothed image which is obtained from the LGM-model.

Finally, experimental results showed that the performance of the proposed method is more efficient as compared to CV-model and FGM-model respectively.

## 5   References

[1] M. J. Black, G. Sapiro, D. H. Marimont, D. Heeger,
   Robust anisotropic diffusion, IEEE trans. Image Processing
   7 (1998) 421-432.
[2] X. Bresson, S. Xavier, P. Esedoglu. Fast global
   minimization of the active contour/snake model, J.
   Math. Imaging and Vision 28 (2007) 151-167.
[3] V. Caselles, R. Kimmel, G. Sapiro, Geodesic active
    Contours, Int. J. Comput. Vision 22 (1997) 61-79.
[4] A. Chambolle, An algorithm for total variation minimization
   and applications, J. Math. Imaging and Vision 20 (2004) 89-
    97.
[5] A. Chambolle, P. L. Lions, Image recovery via total
    variation minimization and related problems, Numerical
    Mathematics 76 (1997) 167-188.
[6] T. F. Chan, S. Esedoglu, M. Nikolova, Algorithms for
    finding global minimizers of image segmentation and
    denoising models, SIAM J. on app. Mathematics 66 (2004)
    1632-1648.
[7] T. F. Chan, L. A. Vese, Active contours without edges,
    IEEE Trans. on Image Processing 10 (2001) 266-277.
[8] D. Cremers, M. Rousson, R. Deriche, A
   review of statistical approaches to level set
   segmentation: integrating color, texture, motion
   and shape, Int. J. Comput. Vision 72 (2007) 195-215.
[9] Z. Farbman, R. Fattal, Edge preserving
   decompositions for multi-scale tone and detail

manipulation, ACM Trans. Graphics 27 (2008) 67-67 .

[10] S. Fu, C. Zhang, Adaptive non-convex total variation regularisation for image restoration, IEE Electronics Letters 46 (2010) 907-908).

[11] S. Fu, C. Zhang, Fringe pattern denoising via image decomposition, Optics Letters 37 (2012) 422-424.

[12] S. Gao, T. D. Bui, Image segmentation and selective smoothing by using mumford shah model, IEEE Trans. Image Processing 14 (2005) 1537-1549.

[13] L. He, Z. Peng, B. Everding. A comparative study of deformable contour methods on medical image segmentation, Image and Vision computing 26 (2008) 141-163.

[14] M. Kass, J. Solomon, Smoothed local histogram filters, ACM Trans. on Graphics 29 (2010) 100.

[15] M. Kass, A. Witkin, D. Terzopoulos, Snakes: active contour models, Int. J. Comput. Vision 1 (1988) 321-331.

[16] R. Kimmel, A. Amir, A. Bruckstein, Finding shortest paths on surfaces using level set propagation, IEEE Trans. Pattern Anal. Mach. Intellegence 17 (1995) 635-640.

[17] J. M. Morel, S. Solimini, Segmentation of images by variational methodes: A constructive approach. Revista Matematica Universidad Complutense de Madrid 1 (1988) 169-182.

[18] D. Mumford and J. Shah, Optimal approximation by piecewise smooth functions and associated variational problems, Communications on Pure and Appl. Mathematics 42 (1989) 577-685.

[19] S. Osher, J. A. Sethian, Fronts propagating with curvature dependent speed: Algorithms based on hamilton jacobi formulations. J. Comput. Physics 79 (1988) 12-49.

[20] N. Paragios, R. Deriche, Geodesic active regions and level set methods for supervised texture segmentation, Int. J. Comput. Vision 46 (2002) 223-247.

[21] P. Perona, J. Malik. Scale-space and edge detection using anisotropic diffusion, IEEE trans. Pattern Analy. and Machine Intelligence 12 (1990) 629-639.

[22] L. I. Rudin, S. Osher, E. Fatemi, Nonlinear total variation based noise removal algorithms, Physica D: Nonlinear Phenomena 60 (1992) 259-268.

[23] N. Sochen, R. Kimmel, R. Malladi, A general frame work for low level vision, IEEE trans. Image Processing 7 (1998) 310-318.

[24] C. Tomasi, R. Manduchi, Bilateral filtering for gray and color images, ICCV (1998) 839-846.

[25] A. Tsai, A. Yezzi, A. S. Willsky, Curve evolution implementation of the mumford shah functional for image segmentation, denoising, interpolation, and magnification, IEEE Trans. Image Process 10 (2001) 1169-1186.

[26] L. A. Vese T. F. Chan, A multiphase level set framework for image segmentation using the mumford and shah model, Int. J. Comput. Vision 50 (2002) 271-293.

[27] X. Wang, D. Huang, H. Xu, An efficient local Chan Vese model for image segmentation, Pattern Recognition 43 (2010) 603-618.

[28] Y. Wang, W. Chen, S. Zhou, T. Yu, Y. Zhang. MTV: modified total variation model for image noise removal, IET Elect. Letters 47 (2011) 592-594.

[29] Y. Wang, J. Guo, WF. Chen, W. Zhang, Image denoising using modified Perona-malik model based on directional laplacian, Signal Processing 93 (2013) 2548-2558.

[30] Y. Wang, J. Yang, W. Yin, A new alternating minimization algorithm for total variation image reconstruction, SIAM J. Imaging Sciences 1 (2008) 248-272.

[31] J. Weickert, Coherence-enhancing diffusion of color images, Image and Vis. Computing 17 (1999) 201-212.

[32] B. Weiss. Fast median bilateral filtering, ACM Trans. on Graphics 25 (2006) 519-526.

[33] C. L. Wu, X. C. Tai, Augmented lagrangian method, dual methods and split bregman iteration for ROF, vectorial total variation and high order models. SIAM Journal on Image Sciences 3 (2010) 300-339.

[34] L. Xu, C. Lu, Y. Xu, Image smoothing via L0 gradient minimization. ACM Trans. on Graphic30(2015)1-11

# Numerical solution of Fisher's Equation by using Meshless method of lines

*Hina Mujahid$^{1*}$, Mehnaz$^1$*

$^1$*Department of Mathematics, Shaheed Benazir Bhutto Women University, Peshawar 25000.*

*\*Corresponding author*
***Email**: hinamujahid12@gmail.com*

## Abstract

Many problems in science and engineering field are modeled by Partial Differential equations (PDEs). Non-linear, reaction diffusion equation, Fisher's equation, models different problems in ecology, biology and mass and heat transfer. This paper concern with the development of meshless method of lines (MOL) for solving Fisher's equation. This method is applied in two steps. In the first step, Space derivatives are approximated by different radial basis functions. It results in conversion of PDE to system of ordinary differential equations (ODEs) which are then solved by Runge Kutta method of order 4 (RK4) in the second step. Finally $L_2$, $L_\infty$ and root mean square (RMS) error norms are hired to check the behavior of the method. Our method is compared with some other methods in literature.

**Key words**: Multi Quadric (MQ), inverse Multi Quadric (IMQ), Gaussian (GA), inverse Quadric (IQ), Runge Kutta method of order 4 (RK4) .

## Introduction

In applied mathematics and physics, nonlinear phenomena plays an essential role. For PDEs field of nonlinear control problems are the most mathematically challenging in the association of distributed parameter systems. Fisher's equation was first introduced by Fisher to model the advance of freak gene in an infinite domain and is nonlinear evolution equation [1]. Furthermore, Fisher's equation has been used as a basis to model the spatial spread of gene in chemical wave propagation, branching Brownian motion process, flame propagation, nuclear reactor theory [2, 3, 4, 5], spread of invasive [6], bacteria [7], epidemics [8], and many other disciplines.

The Fisher's equation is defined by

$$\frac{\partial u}{\partial t} = D\frac{\partial^2 u}{\partial x^2} + \alpha u(1-u),$$

(1.1)

where $t$ shows the time and $x \in (-\infty, \infty)$ shows the position. A reactive coefficient $\alpha$ and diffusion coefficient $D$ parameterized the reactive and diffusion process.

In this paper we have considered the following form of Fisher's equation,

$$u_t - u_{xx} - \alpha u(1-u) = 0.$$

(1.2)

Where $\alpha$ is an arbitrary constant.

The exact solution of Eq. (1.2) is given in [2],

$$u(x,t) = \frac{1}{\left[1 + e^{(\sqrt{\frac{\alpha}{6}})x - \frac{5\alpha.t}{6}}\right]^2}$$

(1.3)

Many properties of Fisher's equation as a typical nonlinear reaction diffusion system, have been studied by many authors, including the singular property and the traveling wave behaviour [9, 10, 11, 12, 2]. Excellence summaries of Fisher's equation are provided by Kawahara et al. [13], Baraznik et al. [14] and Larson [15]. The analytical study of Fisher's equation by using Adomian decomposition method are discussed by Wazwaz et al. [2]. For the generalized Fisher's equation, the exact and explicit solitary wave solution has presented by Wang [16]. Till 1947s, the numerical solutions of Fisher equation were not present in the literature. First time Gazdag et al. [17], presented the numerical solution of Fisher's equation with a pseudo-spectral approach. After that Fisher's equation has been solved numerically by a lot of researchers. To discuss the numerical solution of

Fisher equation, the implicit and explicit finite differences algorithms were presented by Twizell et al. [18] and Parekh et al. [19]. Carey et al. [20] used a least-squares finite element method. Comparison of nodal integral and non-standard finite schemes by Rizwan-Uddin [21] and Galerkin finite element method is proposed by Tang et al. [22]. By using centered finite difference algorithm, the asymptotic boundary conditions are developed by Hagstrom et al. [23]. A best finite-difference scheme for Fisher's equation proposed by Mickens [24], a pseudo spectral method was proposed by Olmos et al. [25], a moving mesh method is used by Qiu et al. [26]. Also by applying wavelet Galerkin method, Fisher's equation is studied by Mittal et al. [27].

MOL is an efficient technique to find the numerical solution of PDEs. The main theme of this method is to discretize the space derivatives and the time derivatives remain continuous. The German mathematician Erich Rothe introduced MOL in 1930 [28]. He applied it to parabolic type equations, but it can be used in broad sense. MOL is considered as special case of FDM but it is more effective than FDM due to its accuracy and less computational cost.

We first discretize the given PDE in space variable by approximating the spatial derivatives by RBF/FDM and then solve the system of ODEs by any ODE solver. In recent years, different PDEs are solved by MOL, including, burger's type equation [29], generalized Kuramoto-Sivashinsky equation [30], KdV equation [31]. KdV equation for small time [32]. For stability and convergence of MOL see [33, 34, 35].

**Formulation of Method of Lines**

In this section we will find the numerical solution of Eq. (1.2) by applying MOL. By using RBF, the problem domain will be discretized in space variable which will convert the given PDE into system of ODEs, which will be easily solved by using any appropriate ODE solver. In this work we will use RK4 method.

**RBF collocation**

This section is concerned with MOL-RBF interpolation. By using RBF we will interpolate the approximate solution to the problem.

Let $\widetilde{u}$ be the RBF approximation to $u$, which denote solution of the given PDE. Let us divide the problem

domain in $n$ nodes, $x_1, x_2, \cdots, x_n$, in $\Omega \cup \partial\Omega$ where $\Omega$ represents the interior and $\partial\Omega$ is the boundary of the domain. Also $x_1, x_n \in \partial\Omega$, while $x_2, x_3, \cdots, x_{n-1} \in \Omega$.

The RBF approximation of $u(x)$ is given by,

$$\widetilde{u}(x) = \sum_{j=1}^{n} k_i \phi_j = k_1\phi_1 + k_2\phi_2 + \cdots + k_n\phi_n,$$

$$\Rightarrow \widetilde{u}(x) = \Phi^T(x)\boldsymbol{k}$$

(2.1.1)

Where $\Phi(x) = [\phi_1(x), \phi_2(x), \cdots, \phi_n(x)]^T$ and $\boldsymbol{k} = [k_1, k_2, \cdots, k_n]^T$.

Here $\phi_j$ denotes the RBFs and $k_j$ are the unknown constants.

Let we denote approximate solution is at $j^{th}$ node by $u_j$ i.e. $\widetilde{u}(x_j) = u_j$ Then from Eq. (2.1.1),

$$u_1 = \Phi^T(x_1)\boldsymbol{k},$$
$$u_2 = \Phi^T(x_2)\boldsymbol{k},$$
$$\vdots = \vdots,$$
$$u_n = \Phi^T(x_n)\boldsymbol{k},$$

which can be written in the matrix form as,

$$\mathbf{B}\boldsymbol{k} = \mathbf{u},$$

(2.1.2)

where $\mathbf{B} = \begin{bmatrix} \phi_1(x_1) & \phi_2(x_1) & \cdots & \phi_n(x_1) \\ \phi_1(x_2) & \phi_2(x_2) & \cdots & \phi_n(x_2) \\ \vdots & \vdots & \ddots & \vdots \\ \phi_1(x_n) & \phi_2(x_n) & \cdots & \phi_n(x_n) \end{bmatrix},$

$$k = \begin{bmatrix} k_1 \\ k_2 \\ \vdots \\ k_n \end{bmatrix} \text{ and } \mathbf{u} = \begin{bmatrix} u_1 \\ u_2 \\ \vdots \\ u_n \end{bmatrix}.$$

In above equation matrix $\mathbf{B}$ is called the interpolation (or collocation) matrix and it consist of RBFs at nodes.

From Eq. (2.1.2), we have,

$$k = \mathbf{B}^{-1}\mathbf{u}$$

Putting this value in Eq. (2.1.1), we get

$$\tilde{u}(x) = \Phi^T(x)\mathbf{B}^{-1}\mathbf{u},$$

$$\Rightarrow \tilde{u}(x) = \mathbf{P}(x)\mathbf{u},$$

(2.1.4)

Here $\Phi(x) = [\phi_1(x), \phi_2(x), \cdots, \phi_n(x)]^T$,

$\mathbf{u} = [u_1, u_2 \cdots; u_n]$ and $\mathbf{P}(x) = \Phi^T(x)\mathbf{B}^{-1}$,

The singularity of collocation matrix $\mathbf{B}$ depends on the choice of RBF. For this purpose, choose the value of shape parameter $c$ as large as possible to get large difference between atleast two columns of $\mathbf{B}$. However this produces less accuracy to contrast with that of small values of $c$. But small value of $c$ causes ill-conditioning of collocation matrix. So the shape parameter has great effect on condition number [36]. The determination of best value of $c$ is still problem. There are many methods to find the best value of $c$. The most easy and popular is the brute force method in which Max-error is plotted for different values of $c$. The value of $c$ on which the least Max-error is appeared is considered as best value of shape parameter on. This technique is applied to find the optimum value of $c$ by the authors in [30] and [31]. Different methods of finding optimal value of $c$, are given in [37, 38, 39, 40, 41].

Application of MOL-RBF to Fisher's Equation Using RBF

In this section, we will approximate the unknown solution $u(x)$ as a linear combination of $n$ RBFs to find the numerical solution of Fisher's equation by applying MOL. We consider Fisher's equation,

$$u_t - u_{xx} - \alpha u(1-u) = 0$$

(2.2.1)

where $\alpha$ is arbitrary constant,

the initial condition is taken as,

$$u(x,0) = \psi(x) \qquad\qquad a \le x \le b,$$

(2.2.2)

and the boundary conditions are,

$$u(a,t) = \xi(t), \qquad\qquad u(b,t) = \eta(t).$$

(2.2.3)

Using Eq. (2.1.4) to Eq. (2.2.1), we get the following collocated form of Eq. (2.2.1)

$$\frac{du_j}{dt} - \mathbf{P}_{xx}(x_j)u - \alpha u_j(1-u_j) = 0,$$

$$j = 1, 2, \cdots, n, \quad (2.2.4)$$

where $u_j(t) = u_j$ , and

$$\mathbf{P}_{xx}(x_j) = \begin{bmatrix} P_{1xx}(x_j) & P_{2xx}(x_j) & \cdots & P_{nxx}(x_j) \end{bmatrix},$$

with $P_{kxx}(x_j) = \dfrac{\partial^2}{\partial x^2} P_k(x_j).$

To write the system of (2.2.4) as a column vector, let

$$U = \begin{bmatrix} u_1 & u_2 & \cdots & u_n \end{bmatrix}^T,$$

$$P_{xx} = \begin{bmatrix} P_{kxx}(x_j) \end{bmatrix}_{n \times n}.$$

Then Eq. (2.2.4) can be written as,

$$\frac{dU}{dt} - P_{xx}U - \alpha U(1-U) = 0,$$

(2.2.5)

we can write Eq. (2.2.5) in compact form as,

$$\frac{dU}{dt} = F(U),$$

(2.2.6)

where

$$F(U) = P_{xx}U + \alpha U(1-U).$$

(2.2.7)

The initial condition can also be written as,

$$U(t_0) = U_0 = \begin{bmatrix} u^0(x_1) & u^0(x_2) & \cdots & u^0(x_n) \end{bmatrix}^T.$$

(2.2.8)

From the boundary conditions,

$$u_1(t) = \xi(t), \qquad u_n(t) = \eta(t).$$

(2.2.9)

Now we will solve resulting system of ODEs (2.2.6) with initial conditions (2.2.8) by using RK4 method.

The RK4 algorithm for Eq. (2.2.6) is

$$U^{m+1} = U^m + \frac{\Delta t}{6}(K_1 + 2K_2 + 2K_3 + K_4).$$

(2.2.10)

Here $K_1 = F(U^m),$

$$K_2 = F(U^m + \frac{\Delta t}{2}K_1),$$

$$K_3 = F(U^m + \frac{\Delta t}{2}K_2),$$

$$K_4 = F(U^m + \Delta t K_3).$$

Here $U^m$ is the approximate solution at $m^{th}$ time level, $\Delta t$ is the time step.

Results

In this section we will give numerical example to show the accuracy of our method. We will compare our method with DQM.

**Test Problem 1**

We consider the Fisher's equation,

$$u_t - u_{xx} - \alpha u(1-u) = 0$$

(3.1)

where $\alpha$ is an arbitrary constant.

The exact solution of Eq. (3.1) is given by,

$$u(x,t) = \frac{1}{\left[1 + e^{(\sqrt{\frac{\alpha}{6}})x - \frac{5\alpha.t}{6}}\right]^2},$$

The initial condition and boundary conditions are,

$$u(x,0) = \frac{1}{\left[1 + e^{\left(\sqrt{\frac{\alpha}{6}}\right)x}\right]^2},$$

$$u(a,t) = \frac{1}{\left[1 + e^{\left(\sqrt{\frac{\alpha}{6}}\right)a - \frac{5\alpha.t}{6}}\right]^2},$$

$$u(b,t) = \frac{1}{\left[1 + e^{\left(\sqrt{\frac{\alpha}{6}}\right)b - \frac{5\alpha.t}{6}}\right]^2}.$$

Numerical calculation is performed over the interval $[0,1] \times [0,1]$ with step size $h = 0.1$ and time step $\Delta t = 0.001$, with $\alpha = 6$. Different types of RBFs are used such as MQ, IMQ, GA and IQ. Table 2.1 is concerned with the error norms to assess the behavior of MOL, which are define as follows,

$$L_\infty = \max |u^* - u|,$$

(3.3)

$$L_2 = \sqrt{h \sum_{i=1}^{n} (u^* - u)^2},$$

(3.4)

$$L_{rms} = \sqrt{\frac{\sum_{i=1}^{n} (u^* - u)^2}{n}}.$$

(3.4)

Where $u^*$ and $u$ are exact and numerical solutions respectively. From Table 2.1 it can be easily observed

that MQ, IMQ, and GA has more accurate results than IQ. We have taken the values of $c = 1, 1.4, 2.2$ and $0.34$ for MQ, IMQ, GA and IQ respectively. In Table 2.2 there is comparison of MOL and DQM and it shows that MQ, IMQ and GA results are more accurate than that of DQM whereas IQ has less accuracy than DQM.

In this work we have applied brute-force technique to find the best value of $c$. From Fig. 3.1 we can see that the least Max-error for MQ is at $c = 1.1$, Fig. 3.2 shows that least Max-error for IMQ is at $c = 1.4$. Similarly in Fig. 3.3 one can see that least Max-error for GA occurs at $c = 2.2$ and the Fig. 3.4 represents that Max-error for IQ attains its minimum value at $c = 0.34$.

Now we highlight the figures of comparison of numerical and exact solution. In Fig. 3.5 graph of numerical solution falls nearly to that of exact solution. And same as the result for the graph of IMQ and GA, In Fig. 3.6 and 3.7 respectively, but the graph of IQ in Fig. 3.8 is slightly different from others.

Table 3.1: $L_\infty$, $L_2$ and $L_{rms}$ for different RBFs

| t | RBF | $L_\infty$ | $L_2$ | $L_{rms}$ |
|---|---|---|---|---|
| 0.1 | MQ | 2.6452E-07 | 1.3234E-07 | 1.3234E-07 |
| | IMQ | 3.5363E-07 | 2.1788E-07 | 2.1788E-07 |
| | GA | 7.5121E-07 | 2.8072E-07 | 2.8072E-07 |
| | IQ | 5.5756E-03 | 2.9324E-03 | 2.9324E-03 |
| 0.2 | MQ | 4.7441E-07 | 2.9961E-07 | 2.9961E-07 |
| | IMQ | 4.0007E-07 | 2.5327E-07 | 2.5327E-07 |
| | GA | 8.7103E-07 | 3.3578E-07 | 3.3578E-07 |
| | IQ | 2.2767E-02 | 1.1850E-02 | 1.1850E-02 |

| t | RBF | $L_\infty$ | $L_2$ | $L_{rms}$ |
|---|---|---|---|---|
| 0.3 | MQ | 7.3297E-07 | 4.9349E-07 | 4.9349E-07 |
| | IMQ | 4.6189E-07 | 2.4497E-07 | 2.4497E-07 |
| | GA | 9.3713E-07 | 3.6373E-07 | 3.6373E-07 |
| | IQ | 5.3162E-02 | 3.4769E-02 | 3.4769E-02 |
| 0.4 | MQ | 9.9249E-07 | 6.6783E-07 | 6.6783E-07 |
| | IMQ | 5.2276E-07 | 2.4321E-07 | 2.4321E-07 |
| | GA | 9.9070E-07 | 3.9942E-07 | 3.9942E-07 |
| | IQ | 8.8148E-02 | 6.0523E-02 | 6.0523E-02 |
| 0.5 | MQ | 1.1806E-06 | 7.9318E-07 | 7.9318E-07 |
| | IMQ | 6.1118E-07 | 2.6904E-07 | 2.6904E-07 |
| | GA | 1.0535E-06 | 4.4895E-07 | 4.4895E-07 |
| | IQ | 1.1332E-01 | 7.8289E-01 | 7.8289E-01 |
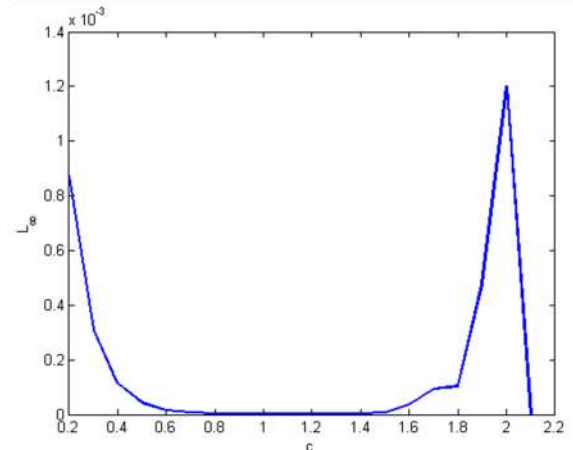


Figure 3.1: $L_\infty$ error norm for different values of $c$ using MQ
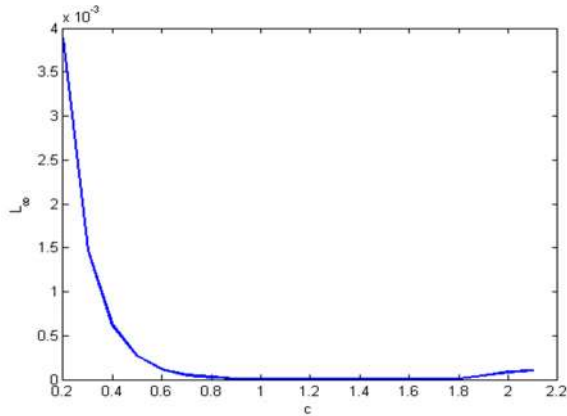
Figure 3.2: $L_\infty$ error norm for different values of *c* using IMQ
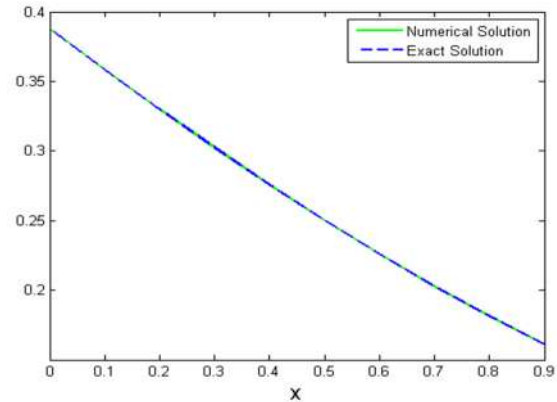


Figure 3.5: Comparison of numerical and exact solution using MQ
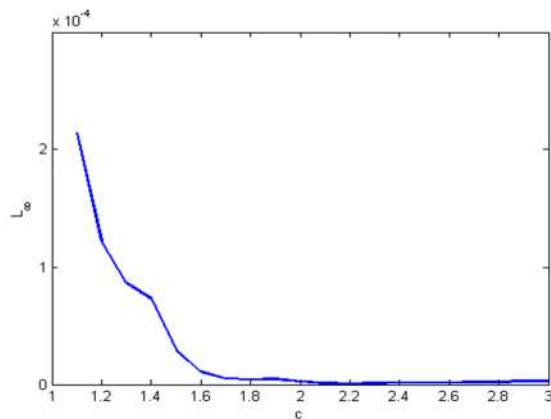


Figure 3.3: $L_\infty$ error norm for different values of *c* using GA
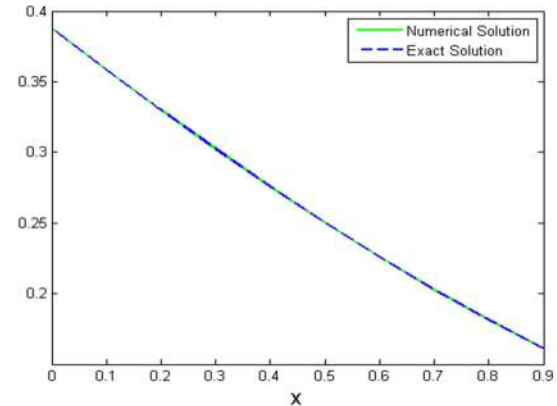


Figure 3.6: Comparison of numerical and exact solution using IMQ
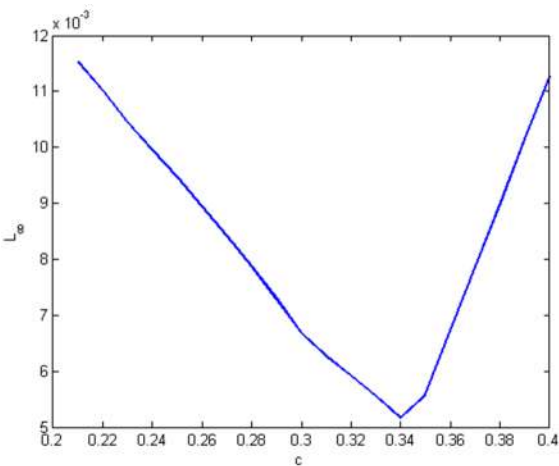


Figure 3.4: $L_\infty$ error norm for different values of *c* using IQ
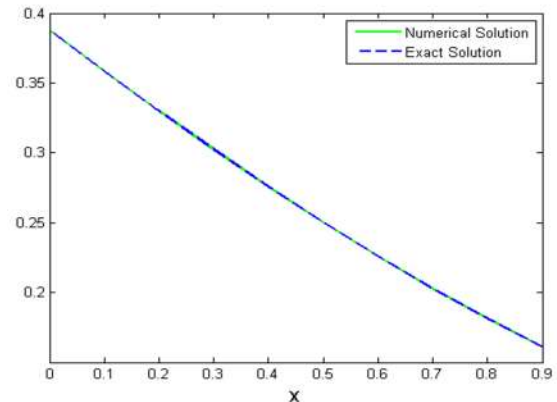


Figure 3.7: Comparison of numerical and exact solution using GA
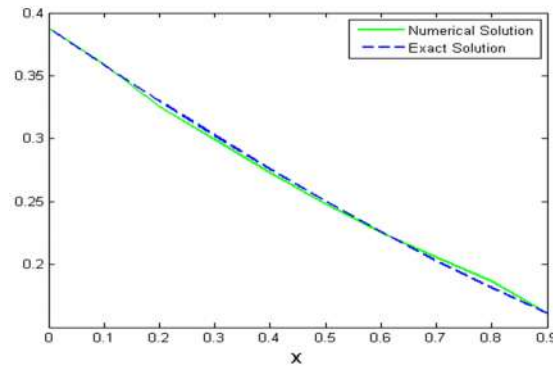
Figure 3.8: Comparison of numerical and exact solution using IQ

Table 3.2: Comparison of MOL RBF and DQM

| x | t | MQ c=0.8 | IMQ c=01 | GA c=4.5 | IQ c=0.01 | Exact Solution | DQM [42] |
|---|---|---|---|---|---|---|---|
| 0.25 | 0.5 | 0.818389 | 0.818393 | 0.818399 | 0.826779 | 0.818393 | 0.81843 |
| | 1.0 | 0.982915 | 0.982919 | 0.982926 | 0.999993 | 0.982919 | 0.98292 |
| | 2.0 | 0.999881 | 0.999883 | 0.999889 | 1.000312 | 0.999883 | 0.99988 |
| | 5.0 | 0.999999 | 0.999999 | 1.000004 | 1.000338 | 1.000000 | 1.00000 |
| 0.50 | 0.5 | 0.775800 | 0.775803 | 0.775811 | 0.769864 | 0.775803 | 0.77585 |
| | 1.0 | 0.978144 | 0.978147 | 0.978155 | 0.985615 | 0.978147 | 0.97815 |
| | 2.0 | 0.999849 | 0.999850 | 0.999857 | 1.000253 | 0.999850 | 0.99985 |
| | 5.0 | 0.999999 | 0.999999 | 1.000002 | 1.000290 | 1.000000 | 1.00000 |
| 0.75 | 0.5 | 0.725819 | 0.725823 | 0.725832 | 0.697997 | 0.725824 | 0.72588 |
| | 1.0 | 0.972068 | 0.972071 | 0.972080 | 0.979299 | 0.972071 | 0.92208 |
| | 2.0 | 0.999806 | 0.999808 | 0.999815 | 1.000333 | 0.999808 | 0.99981 |
| | 5.0 | 1.000000 | 0.999999 | 1.000000 | 1.000386 | 1.000000 | 1.00000 |

**Conclusions**

In this paper we implemented MOL over Fisher's equation. Different types of RBFs are used to approximate the solution of the governing equation. Results shows the impressive behavior of our method. We have compared our method with DQM and obtain more accurate results than DQM.

**References**

1. Fisher, R. A. The wave of advance of advantageous genes Annals of Eugenics, 7 (1937) 355-369.

2. Abdul-Majid Wazwaz, Alice Gorguis, An analytic study of Fisher's equation by using Adomian decomposition method, Applied Mathematics and Computation, 154(2004) 609-620.

3. N. F. Britton, Reaction-Diffusion Equation and their applications to biology, Academic press, 1986.

4. L. Debthnath, Nonlinear Partial Differential Equation for Scientist and Engineers, Birkhanser, Boston, 1997.

5. J. D. Murray, Mathematics Biology, Springer-Verlag, 1993.

6. Michael G. Nenbert, Ingrid M. Parker, Projecting rates of spread for invasive species, Risk Anal. 24(4) (2004) 817-831.

7. V. M. Kerke, Results from varients of the fisher equation in the study of epidemics and bacteria, Physica A 342(2004) 242-248.

8. Tridip Sardar, Sourav Rana, Joydev Chattopadhyay, A mathematical model of dengue transmation with memory, Commun, Nonlinear Sci. Numer. Simul. 22(1-2) (2015) 511-525.

9. Z. S. Feng, Traveling wave behavior for a generalized Fisher's equation, Chaos Solitons Fractals, 38(2008) 481-488.

10. B.Guo. Z. Chen, Analytic Solutions of the Fisher's equation, J. Phys. A: Math. Gen, 24(1991) 645-650.

11. N. A. Kudryashor, Exact solitary waves of the Fisher's equation, Phys. Lett, A 342(2005) 99-106.

12. A. M. Wazwaz, The tanh method for traveling waves solutions of nonlinear equations, Appl. Math. Comput, 154(2004) 713-723.

13. Kawahara, T. and Tanaka, M., Interactions of travelling fronts : an exact solution of a nonlinear diffusion equation, Phys, Lett. A. 97(8) (1983), 311-314.

14. Barazhnik, P. and Tyson, On traveling wave solution of fisher equation in two spatial dimensions, SIAM J. Appl. Math. 60(2) (1999) 371-391.

15. Lorson, D. A., Transient bounds and time-asymptotic behavior of solution to nonlinear equation to Fisher's type, SIAM J.Appl. Math. 34(1978) 93-103.

16. Wang, X. Y., Exact and explicit solitary for the generalized Fisher's equation, Phys. Lett. A, 131(4/5) (1988) 277-279.

17. Gazdag, J. and Canosa, J., Numerical solution of Fisher equation, J. Appl. Probab., 11(1974) 445-457.

18. Twizell, E. H., Wang, Y. and Price, W. G., Chaos free numerical solution of reaction-diffusion equations, Proc. Roy. Soc. London Sci. A., 430(1990) 541-576.

19. Parekh, N. and Puri S., A new numerical scheme for the Fisher's equation, J. Phys. A, 60(7) (1990) L1085-L1091.

20. Carey, G. F. and Shen, Y., Least-squares finite element approximation of Fisher's reaction-diffusion equation, Numer. Methods in partial differential equation, 11(1937) 175-186.

21. Rizwan-Uddin, Comparison of the nodal integral method and non standard finite-difference scheme for the Fisher's equation, SIAM J. Sci. Comput., 22(2001) 1926-1942.

22. Tang, S. and Weber, R. O., Numerical study of Fisher's equation by a Petrov-Galerkin finite element method, J. Austral. Math. Soc. Sci. B, 33(1991) 27-38.

23. Hagstrom, T. and Keller, H. B., The numerical solution of travelling wave solution of nonlinear parabolic equations, SIAM J. Sci. Statist. Comput., 7(1986) 978-988.

24. Mickens, R. E., A best finite-difference scheme for Fisher's equation, Numer. Meth. Part. Diff.Eqns, 10(1994) 581-585.

25. Daniel, Olmas, Bernie. D. and Shizgal, A pseudospactral method of solution of Fisher's equation, J. Comput. Appl. Maths, 193(2006) 219-242.

26. Qiu, Y. and Sloan, D. M., Numerical solution of Fisher's equation using a moving mesh method, J. Comput. Phys., 146(1998) 726-746.

27. Mittal, R. C. and Sumit, Kumar. Numerical study of Fisher's equation by wavelet Galerkin method, Int. J. Computer Math., 83(2006) 287-298.

28. E. Rothe, Zweidimensionale parabolische randwertaufgaben als grenzfall eindimensionaler randwertaufgaben. Math. Anna. 102(1930) 650-670.

29. A. Ali, F. Haq, I. Hussain, A numerical meshless technique for the solution of some burger's type equations, World Appl. Sci.J. 14(2011) 1792-1798.

30. S. Haq, N. Bibi, S. I. A. Tirmizi, M. Usman, Meshless method of lines for the numerical solution of generalized kuramoto-sivashinsky equation, Appl. Math. Comput, 217(2010) 2404-2413.

31. Q.Shen, A mashless method of lines for the numerical solution of KdV equation using radial basis function, Eng. Anal. Bound. Elem, 33(2009) 1171-1180.

32. A. ozdes, E. N. Aksan, The method of lines solution of the korteweg-de vries equation for small times, Int. J. Contemp. Math. Sciences, 1(2006) 639-650.

33. Z. M. Wu, Radial basis function scattered data interpolation and the meshless method of numerical solution of PDEs, Chinese J. Eng. Math, 19(2002) 1-12.

34. Z. M. Wu, R. Schaback, Local error estimates for radial basis function interpolation of scattered data, IMA J. Numer. Anal, 13(1992) 13-27.

35. S. C. Reddy, L. N. Trefethen, Stability of the method of lines, Numer. Math, 62(1992) 235-267.

36. G. R. Liu, Y. T. Gu, A point interpolation method for two-dimensional solids, Int. J. Numer. Meth. Engng, 50(2001) 937-951.

37. M. R. Dubal, Contruction of three-dimensional black-hole initial data multiquadrics, Phys. Rev. D., 45(1992) 1178-1187.

38. S. Rippa, An algorithm for selecting a good value for the parameter $c$ in radial basis function interpolation, Adv. Comput. Math., 11(1999) 193-210.

39. C. S. Huang, C. F. Lee, A. H. D. Cheng, Error estimate, optimal shape factor, and high precision computation of multiquadric collocation method, Eng. Anal. Bound. Elem., 31(2007) 614-623.

40. J. G. Wang, G. R. Liu, On the optimal shape parameters of radial basis function used for 2-D meshless methods, Comput. Meth. Appl. Mech. Eng., 191(2002) 2611-2630.

41. J. Yoon, Spectral approximation orders of radial basis function interpolation on the sobolov space, SIAM J. Math. Anal., 33(2001) 946-958.

42. R. C. Mittal, Ram Jiwari, Numerical solution of Fisher's equation by using differential quadrature method, International Journal of information and system sciences, 5(1) (2009) 143-160.

# Impact of Waste Marble Dust on the Sustainability of Cement Sand Mortar

*Muhammad Bilal Israr[1*], Khan Shahzada [2], Sajjad Wali Khan[2]*

[1] *National Institute of Urban Infrastructure and Planning, University of Engineering and Technology, Peshawar*
[2] *Department of Civil Engineering, University of Engineering and Technology, Peshawar*
[1*]*Corresponding author*
*Email: bilalisrar@yahoo.com*

## Abstract

The cement manufacturing practice is a key donor to greenhouse gas emissions and reduction of natural assets. Waste Marble Dust (WMD) on the other side is a cheap and environmental demeaning form of marble processing units, which if used in civil works will create Sustainable Structures (SS) and will save our environment from degradation with positive impact on our country's Gross Domestic Product (GDP). This paper states the sustainability of cement sand mortar integrated with WMD. The outcome of WMD on the mechanical properties of cement sand mortar has been studied using five samples incorporated with varying magnitude of WMD (upto 20%) and evaluated for Compressive Strength, Tensile Strength, Permeability, Flow, Bulk Density and Air Content mechanism. Results obtained show that 10% substitution of cement by WMD provided competent results.

**Key words**: Limestone, Marble Powder, Mortar, Sustainable Structures.

## 1 Introduction

Cement is the hub and elite component of civil structures which is used in profusion in civil engineering works and the universal demand for cement based materials has increased and suppositions are that it will be broadly used in construction industry during the early 21st century. Economic and environmental deliberation had a vital role in the supplementary cementing material usage as well as better engineering and performance properties [1, 2].

In current era many researches demonstrated that mineral admixtures can be successfully and cheaply utilized in mortar, asphalt, concrete and other binding materials to improve some properties of theses structural materials.

Marble is very essential component that is used in buildings since earliest period, especially for ornamental works. However its waste powder has unenthusiastic effects on our green environment, water, fertility of soil, aquatic and human health. Waste Marble Dust (WMD) is generated from these processing plants when huge irregular blocks of marble is sawed and polished and is converted into

different sizes as per market requirements. About 25% of the developed marble is turned into dust or powder form called Waste Marble Dust [3, 4].

A study exposed that by processing of marble quarries produce marble dust, which floats in the air and may then be inhaled in by the workers there. Epidemiological investigation shows that workers open to the elements of marble dust are exposed to the risk of suffering from asthma symptoms, chronic bronchitis, nasal inflammation and injury of the lungs function [5].

Utilization of waste marble dust in the mortar has not set up tolerable concern. Classification of waste marble dust mixed with mortar and concrete were comprehensively investigated. With high percentage of waste marble dust in mortar, the longer setting time and lower strength characteristics for varying curing time were noted [6].

The impact of waste marble dust on different properties of cement pastes was studied. The effects of using natural pozzolana and marble powder on the fresh and hardened properties of mortar and self compacting concrete were examined [7, 8, 9, 10, and 11].

In an extensive studies by some researchers confirmed to some extent of substituting the cement with industrial wastes such as silica fume, waste marble dust, fly ash, rice husk ash, wood dust, blast furnace slag and pond ash etc. They stated that by utilizing waste materials in place of virgin materials results in widespread energy savings by reducing the number of manufacturing techniques necessary for the built-up of the out items [12].

The effect of practically utilizing Waste Marble Dust (WMD) in mortar, cement, tiles, self compacting concrete, agglomerate marble, pavements, embankment, glues and paints with fruitful outcomes were demonstrated [13].

The results of substitution of 10% of sand by waste marble powder was investigated and observed that it gives maximum compressive strength at the no changeable workability and have no effect on cement

paste's setting time. The industries that dumps this marble powder matter consists of very fine powder; today forms one of the environmental problems around the globe [14].

In a work carried out ended with results that the compressive strength of mortar decreases with the substitution of percentage of cement by waste marble powder [15].

The use of waste marble dust, silica fume, fly ash and slag as replacement of cement on the compressive strength and cost effectiveness of low water cement (w/c) ratio super plasticized portland cement mortars was evaluated. Cement mortars (1:3 and 1:6) integrated with a variety of magnitude of industrial wastes was designed to have a flow of 110 ± 5%. The compressive strength of mortars with and without super plasticizer was investigated at 1, 3, 7, 28 and 180 days was studied and their cost efficiency was evaluated [16].

The use of waste supplies from dissimilar mechanized activities in the preparation of mortar and concrete were studied. The use of waste marble dust was anticipated in partial substitution of cement, for the manufacturing of mortar and concrete mixes. Tests were carried out on the mortars and concrete mixes cured for varying times in order to evaluate their workability, flexural as well as compressive strength. Partial substitution of cement by waste marble powder reveals that high waste marble powder (WMP) ratio results in increased workability and compressive strengths of the mortar and concrete [17].

The result of Marble Slurry Wastes (MSW) produced by marble processing units was studied in 1:2:4 concrete where the cement was partially substituted with MSW from 0 to 100%. The results illustrated that cement in concrete can be replaced by MSW up to 7%. The compressive strength and splitting tensile strength of concrete was greater than before by 15% and 6% by the substitution of 10% MSW. Strength was increased by adding the 20% of MSW to the 1:2:4 concrete. On the other hand, by the addition of MSW in concrete, its workability is found to be abridged [18].

By utilizing Waste Marble Dust as a partial replacement of cement will save this natural source (cement) and hence energy will be saved and also the $CO_2$ release from these cement manufacturing companies will be minimized upto certain extent. Also the valuable powder is wasted from marble industries causing financial loss to the Pakistan Gross Domestic Product (GDP), as well as playing active role in environmental pollution. Thus the waste marble dust

needs to be utilized as alternative material in preparation of cement sand mortar which will be used in the construction of sustainable structures, which in turn will help in minimizing this raw product and hence our environment will be saved from pollution.

## 2 Methodology
The methodology adopted for carrying out this research work has been subdivided into the subsequent extensive categories as discussed below.

### a. Material Used
The materials used in this research were Portland cement, waste marble dust, sand and water.

#### i. Sand
The sand incorporated in this research work was collected from Nizampur quarry. The mine was selected because of the enhanced values of Fineness Modulus (FM) of 2.44 of the sand samples.

#### ii. Cement
Kohat factory cement, conforming to the ASTM Type-I cement was purchased for casting of mortar cubes, briquettes and other specimens.

#### iii. Waste Marble Dust
The waste generated from the waste marble processing units during the processing was brought down in dry form from Mulla Gori of Warsak Road. It was free from organic matters and dust particles.

#### iv. Water
The water used in this research was local and free from suspended particles with white mirror color.

### b. Mixture Proportioning
The tests were carried out on a wide range of water cement (W/C) ratio ranging from 0.38 to 0.52 trials on a mix of cement sand mortar, with one part of cement and three parts of sand (1:3) as per the ASTM standards and BS standards. A total of five different mixes of cement sand mortar incorporated with varying ratio of waste marble dust were prepared (controlled specimen, 5% WMD specimen, 10% WMD specimen, 15% WMD specimen and 20% WMD specimen). Details of mortar mix are shown in **Table 1**.

### c. Casting
The mortar specimens casted from varying percentages of waste marble dust were grouped on the basis of the varying percentages of WMD. And for this different group of specimens ranging from 3 to 6 numbers were casted for each day interval calculations in order to get more precise results. Materials were casted in different standard moulds as per the test

requirements and were removed from the respective moulds after 24 hours of casting period.

**Table 1: Mortar Mix (1:3) when Cement was replaced with WMD**

| Cement (gm) | Replacement Level (%) | Sand (gm) | WMD (gm) | Water (ml) | W/C ratio |
|---|---|---|---|---|---|
| 1100 | 0 | 3300 | 0 | 505 | 0.45 |
| 1045 | 5 | 3300 | 55 | 505 | 0.48 |
| 940 | 10 | 3300 | 104 | 505 | 0.53 |
| 799 | 15 | 3300 | 141 | 505 | 0.63 |
| 639 | 20 | 3300 | 160 | 505 | 0.79 |

d.    **Curing**

The samples were then marked with proper ID's for their identification and were kept in water tub for a curing period of 3 days, 7 days, 14 days, 28 days and 54 days.

e.    **Experimental Procedure**

The main tests carried out on cement sand mortar incorporated with varying percentages of waste marble dust are Compressive Strength, Tensile Strength, Permeability, Flow, Bulk Density and Air Content test. These are discussed briefly as.

i.    **Compressive Strength Test**

The compressive strength of cement sand mortar was carried out in accordance with the **ASTM C-109** requirement, in order to establish the capability of mortar mix under the compressive loadings. For gaining the oriented results, standard cubes of 2" x 2" x 2" were made using the procedure illustrated in the ASTM standard and were tested after 3 days, 7 days, 14 days, 28 days and 54 days of curing under the Universal Testing Machine (UTM). The relation used for calculating the compressive strength is;

$$\text{Compressive Strenght (fm)} = \frac{p}{A}$$

Where,

f$_m$ = Compressive Strength (psi or MPa)

P = Total Maximum Load (lbf or N)

A = Area of Loaded Surface (in$^2$ or mm$^2$)

**Figure 1** shows view of the Compressive strength testing apparatus.



**Figure 1: Compressive Strength Test of mortar Cube in UTM**

ii.    **Tensile Strength Test**

The tensile strength of cement mortar was carried out in accordance with the **ASTM C-307** requirement, in order to establish the capability of mortar mix under the tensile loadings. Standard briquettes were made using the procedure illustrated in the ASTM standard and were tested after 3 days, 7 days, 14 days, 28 days and 54 days of curing under the Briquette Testing Machine. The relation used for calculating the tensile strength is;

$$\text{Tensile Strenght (S)} = \frac{P}{bd}$$

Where,

S = Stress of the specimen at a waist (psi or MPa)

P = Load at Moment of Break (lbf or N)

b = Width of the waist of briquette (mm)

d = Depth of Briquette tested (mm)

**Figure 2** shows view of the Briquette Testing apparatus.

**Figure 2: Tensile Strength Test of Briquette**



**Figure 3: Permeability Test Apparatus**

**iii.        Permeability Test**

The water permeability test of the cement mortar was carried out in compliance with the **EN 12390-B-2000** requirement, in order to set up the system of hardened mortar mix for its water permeability deliberation. The permeability apparatus is entirely automatic device and is deliberated to take out the water permeability test of the cubes or cylinders of mortar as well as concrete. For gaining the oriented results, standard mortar cylinders having 5.875"Φ x 6"h were made using the procedure illustrated in the ASTM standard and were tested after 28 days curing under the Permeability Testing Machine. Final results of permeability after the experiment performance were calculated using the relation of Darcy's co-efficient using relation;

$$\text{Permeability Coefficient (K)} = \frac{CC \text{ x } H}{A \text{ x } t \text{ x } P}$$

Where,

K= Permeability Coefficient (cm/sec)

Cc= Permeated Water ($cm^3$)

H= Height of Specimen (cm)

A= Area of Specimen ($cm^2$)

T= Time to Penetrate Water (sec)

P= Hydrostatic Pressure of Water Column (bars)

**Figure 3** shows view of the Permeability Testing apparatus.

**iv.        Flow Table Test**

The flow of cement mortar was carried out in accordance with the **ASTM C-1437** requirement, in order to establish the capability of mortar mix flow. The testing program is called the **"Flow Table Test"**. Mortar using ASTM standards were made and were tested in a fresh state with varying water cement ratios under the Flow Table Testing Apparatus. The relation used for calculating the flow of the cement sand mortar is;

$$\text{Mortar Flow (F)} = \frac{(Df - Di)}{Di} * 100$$

Where;

F= Flow of Mortar (%)

$D_f$= Final flow traces of Mortar samples (in)

$D_i$= Initial flow traces of Mortar sample (in)

**Figure 4** shows view of the flow of mortar on Flow Table Testing apparatus.



**Figure 4: Flow of Mortar Specimen on Base of Flow Table**

### v.    Bulk Density Test

The bulk density of the cement mortar was carried out in compliance with the **BS EN 1015-6** requirement, in order to set up the system of fresh mortar mix for its bulk density deliberation. For gaining the oriented results, the sample of fresh hydraulic cement sand mortar with varying waste marble dust and water ratio were filled in a container of calculated volume and by using mathematical relations the final result in form of Bulk Density were determined. The bulk density of cement sand mortar can be traced out by using the following relation;

$$\text{Bulk Density } (\rho m) = \frac{m_2 - m_1}{Vv}$$

Where;

$\rho_m$= Bulk Density (kg/m$^3$)

$m_1$ = mass of empty container

$m_2$ = mass of container plus mortar

$V_v$ = volume of container

### vi.    Air Content Test

The air content of the cement mortar was approved in compliance with the **BS EN 1015-7** requirements. For ease and availability of the instrument, the method used so far is called the **"Alcohol Test"**. This method involves filling a cylinder with 200 ml of fresh mortar of a know batch and then a solution of 60% Ethyl Alcohol and 40% distilled water is added to the mortar so that it can attain a total height of 500 ml in the graduated cylinder. A cork is introduced at the top of the cylinder for stopping down the evaporation and the beaker is inverted 20 times in a minute. The final results can be traced out by using the following relation;

$$\text{Air Content } (L) = \frac{(500 - Vmf)}{Vml}$$

Where;

L= Air Content of Mortar (%)

$V_{ml}$= Actual Volume of 200 ml Mortar sample (ml)

$V_{mf}$= New Volume after Alcohol has been Added (ml)

### 3    Results and Analysis

The schematic results regarding the tests are displayed briefly in the following sections.

### a.    Compressive Strength Test

The results of compressive strength obtained after 3 days, 7 days, 14 days, 28 days and 54 days are given in **Figure 5.** It is clear from the figure that with the addition of waste marble dust, the compressive strength of cement sand mortar cubes decreased from **1.41% to 9.83%** when cement is replaced with WMD.
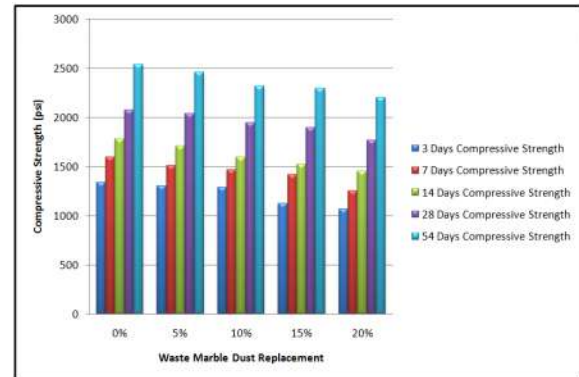


**Figure 5: Overall Compressive Strength Results with Various Percentages of WMD**

It is clear from the results that with the addition of waste marble dust, the compressive strength of cement sand mortar reduces at a certain level when cement is replaced with waste marble dust. The reduction in compressive strength is due the factor that by utilizing waste marble dust in mortar reduces clinker content of the cement and hence the compressive bonding forces formed will be weak and the amount of cementitious gel formed from pozzolanic will also be decreased.

### b.    Tensile Strength Test

The results of tensile strength obtained after 3 days, 7 days, 14 days, 28 days and 54 days are given in **Figure 6.** It is clear from the figure that with the addition of waste marble dust, the tensile strength of cement sand mortar briquettes decreased from **1.56% to 7.42%** when cement is replaced with WMD.
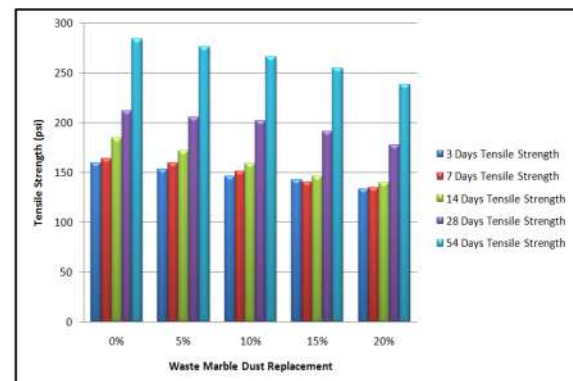


**Figure 6: Overall Tensile Strength Results with Various Percentages of WMD**

It is clear from these results that with the addition of waste marble dust, the tensile strength of cement sand mortar reduces. The reduction in tensile strength is due

the factor that if cement is replaced with waste marble dust, the percentage of clinker will be reduced in the paste of mortar, which will lead to weak tensile forces and also the bonding capabilities will be decreased.

### c. Permeability Test

The results of permeability test obtained after 28 days of curing are given in **Figure 7**. It is clear from the figure that with the addition of waste marble dust, the permeability of cement sand mortar increased from **2.17% to 8.92%** with the increase in WMD.
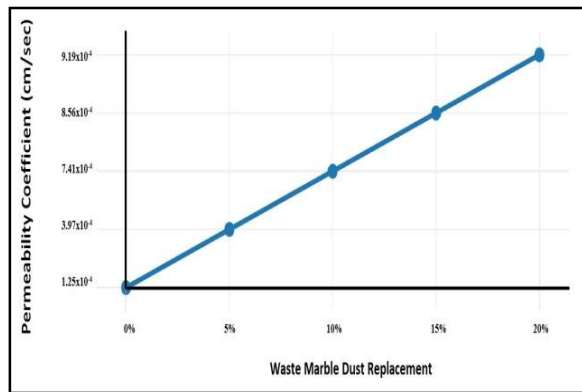


**Figure 7: Permeability Test Results**

It is clear from the results that with the addition of waste marble dust, the permeability of cement sand mortar increases. This rate of increase in the permeability of the specimen is due the factor of decrease in clinker in the mortar paste and also the bonding capabilities (weak bonding) of the waste marble dust with the cement and sand in mortar.

### d. Flow Table Test

The results of flow test of a fresh hydraulic cement sand mortar are tabulated in **Figure 8**. It is clear from the figure that with the addition of waste marble dust, the flow or workability of mortar paste decreased from **1.79% to 11.42%** when cement is replaced with WMD.
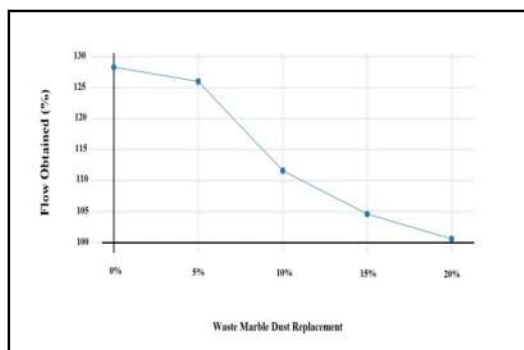


**Figure 4.8: Flow Table Test Results**

It is clear from these results that with the addition of waste marble dust, the flow of cement sand mortar decreased and is due the factor of decrease in the pores space between the relative molecules of the waste marble dust, cement and sand. Hence the particles of the specimen will show that they are tightly packed.

### e. Bulk Density Test

The results of bulk density test of a fresh hydraulic cement sand mortar are tabulated in **Figure 9**. It is clear from the figure that with the addition of waste marble dust, the bulk density of cement sand mortar decreased from **0.27% to 0.61%** as we increase the percentage of WMD.
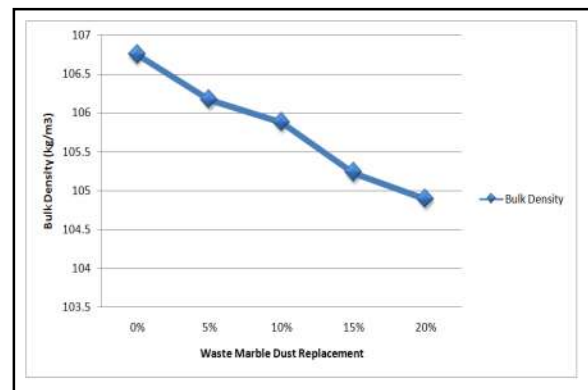


**Figure 9: Bulk Density Test Results**

It is clear from the results that with the addition of waste marble dust, the consumption of cement is reduced and the number of fine particles in the known volume of cylinder is increased. Hence larger number of fine particles fills the space of the cylinder which leads to a decrease of the bulk density.

### f. Air Content Test

The results of air content test of a fresh hydraulic cement sand mortar are tabulated in **Figure 10**. It is clear from the figure that with the addition of waste marble dust, the air content of cement sand mortar paste decreased from **3.17% to 16%** when waste marble dust is replaced with cement.

It is clear from the results that with the addition of waste marble dust, the air content of cement sand mortar decreases. This rate of decrease is due the factor of decrease in the pores space between the relative molecules of the waste marble dust, sand and cement, as there will be less chance of entrapped air because of the dense packing of marble particles and aggregates of mortar.
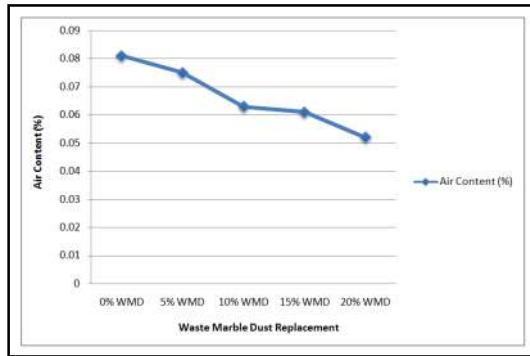
**Figure 10: Air Content Test Results**

## 4. Conclusions

The following conclusions were drawn from this research work.

1. Engineering utilization of waste marble dust rather than dumping in landfills is the best policy to deal with waste marble dust.
2. Waste marble dust can be used as a cement substitution upto certain level in mortar for best results, which saves environment from pollution and save the GDP of country by construction of sustainable structures.
3. Compressive strength of the cement sand mortar decreased from 1.41% to 9.83% as the percentage of Waste Marble Dust increases.
4. Tensile strength of the cement sand mortar decreased from 1.56% to 7.42% as the percentage of Waste Marble Dust increases.
5. Air content of the mortar decreases from 3.17% to 16% as the percentage of Waste Marble Dust increases.
6. Workability or Flow of the cement sand mortar decreased from 1.79% to 11.42% as the percentage of Waste Marble Dust increases.
7. Permeability of the cement sand mortar increased from 2.17% to 8.92% as we kept on increasing the percentage of Waste Marble Dust.
8. The bulk density of the cement sand mortar decreased from 0.27% to 0.61% as we increase the percentage of Waste Marble Dust.
9. Results obtained show that 10% of substitution of sand by waste marble dust provides competent results.

**References:**

[1] E.Badogiannis, V.G. Papadakis, E. Chaniotakis, S. Tsivilis. (2004), "Exploitation of poor Greekkaolins: strength development of metakaolin concrete and evaluation by means of k- value", *Cement and Concrete Research*, vol.34, p.1035–1041, 2004.

[2] A.A, Ramezanianpour, V.M Malhotra. (1995), "Effect of curing on the compressive strength, resistance to chloride ion penetration and porosity of concretes incorporating slag, fly ash, or silica fume", *Cement Concrete Composite*, vol.17, p.125–133, 1995.

[3] Celik MY and Sabah E. (2008), "Marble Deposits and the Impact of Marble Waste on Environmental Pollution Geological and technical characterization of Iscehisar (Afyon–Turkey)", *J Environ Manage* 87: p.106–116, 2008.

[4] Alyamac KE and Ince R. (2009), "A preliminary concrete mix design for SCC with marble powders". Construction and Building Materials 23, p.1201–1210, 2009.

[5] Leikin E, Zickel-Shalom K, Balabir-Gurman A, Goralnik L, and Valdovsky E. (2009), "Caplan's Syndrome in Marble Workers as Occupational Disease". Harefuah 148, p.524–526, 2009.

[6] Corinaldesi V, Giacomo M and Naik TR. (2010), "Characterization of marble powder for its use in mortar and concrete", *Construction and Building Materials* 24, p.113–117, 2010.

[7] Topcu IB, Bilir T and Uygunoḡlu T. (2009), "Effect of waste marble dust content as filler on properties of self-compacting concrete". *Construction and Building Materials* 23, p.1947–1953, 2009.

[8] Mehmet Gesoḡlu, Erhan Guneyisi, Mustafa E. Kocabag, Veysel Bayram and Kasım Mermerdas. (2012), "Fresh and hardened characteristics of self-compacting concretes and mortar made with combined use of marble powder, limestone filler, and fly ash". *Construction and Building Materials* 37, p.160–170, 2007.

[9] Guneyisi E, Gesoḡlu M and Ozbay E. (2009): Effect of marble powder and slag on the properties of self-compacting mortars. Mater Struct 42, p.813–826, 2009.

[10] A.S.E. Belaidi a, L. Azzouz b, E. Kadri c and S. Kenai. (2012), "Effect of natural pozzolana and marble powder on the properties of self-compacting concrete". *Construction and Building Materials* 31, p.251–257, 2012.

[11] Aruntas HY, Dayı M, Te in I, Birgul R and S_ims_e O. (2007), "Effects of marble powder on the properties of self-compacting concretes. In:

*Proceeding of second national symposium on chemical admixtures use in structures*, Ankara, p.161–172, 2007.

**[12]** Sallehan Ismail, Mahyuddin Ramli. (2013), "Engineering properties of treated recycled concrete aggregate (RCA) for structural applications", Construction and Building Materials 44, p.464–476, 2013.

**[13]** Elham Khalilzadeh Shirazi. (2011), "Reusing of stone waste in various industrial activities", 2nd International Conference on Environmental Science and Development IPCBEE vol.4, p.217-219, 2011.

**[14]** Valeria Corinaldesi, Giacomo Moriconi, Tarun R. Naik. (2010), "Characterization of marble powder for its use in mortar and concrete", Construction and Building Materials, Volume 24, Issue 1, p.113–117, 2010.

**[15]** Valeria Corinaldesi. (2009), "Characterization of Marble Powder for Use in Mortar and Concrete", Scientific Research and Essay Vol. 1 (2), p.128-133, 2009.

**[16]** S.K. Agarwal, Deepali Gulati. (2006), "Utilization of industrial wastes and unprocessed micro-fillers for making cost effective mortars", Volume 20, Issue 10, p.999-1004, 2006.

**[17]** **Er. Tanpreet Singh** and **Er. Anil Kumar Nanda. (2012), "**Influence of Marble Powder on Mechanical Properties of Mortar and Concrete Mix", p.193-203, 2012.

**[18]** Arshad A, Shahid I, Anwar U. H. C, Baig M N, Khan S and Shakir K. (2014), "The Wastes Utility in Concrete", Int. J. Environ. Res., 8(4):1323-1328, Autumn 2014.

# Solving the non-linear Harry Dym equation by Kansa's method

Naureen[1,*], Mehnaz[1]

[1]Department of Mathematics, Shaheed Benazir Bhutto women university, Peshawar 25000.

*Corresponding author

Email: nmscmaths@gmail.com

## Abstract

The Harry Dym (HD) equation plays a significant role in physical systems. HD equation is used to represent the system in which dispersion and non-linearity are coupled together. The distinguish aspect of HD equation is its completely integrable nature. Moreover it comply with an infinite number of conversion laws. HD equation is related to Kortwege-de Vries (KdV) equation. In this paper Kansa's approach is used to find the numerical solution of HD equation. This approach uses the combination of collocation method and first order accurate forward difference scheme. Radial basis functions (RBFs) are used for collocation. It reduces HD equation to system of linear equations which is solved by direct solver. $L_2$, $L_\infty$ and $L_{rms}$ error norms are used to assess the method. Relationship between numerical and exact solution is shown with the help of figures. Our method is compared with some other methods in the literature. Results shows the accuracy of our method over other methods.

Keywords: MultiQuadric (MQ), inverse MultiQuadric (IMQ), Gaussian (GA), inverse Quadric (IQ), $\theta$-weighted scheme, Crank-Nicolson scheme.

## Introduction

Consider the HD equation

$$u_t = u^3 u_{xxx},$$

where $u = u(x,t), u_{xxx} = \dfrac{\partial^3 u}{\partial x^3}$ , is one of the most interesting and an central dynamical equation. It has applications in several physical systems. It was discovered by Harry Dym in 1973, in an unpublished paper. Kruskal and have given name to this equation [1] and this name is used from that time. The distinguish factor of HD equation is that it is completely integrable nonlinear equation and for detailed discussion about its properties see [2]. The HD equation has strong connection to Kdv equations. HD equation is interesting because it has a bi–Hamiltonian structure, an infinite number of conversation laws and symmetries [3]. However it does not possess the Painleve property.

Recently, many researchers studied the existence of solutions of HD equation. Its exact solution was studied by Mokhtari [4]. The invariance of the (1+1)-dimentional HD equation under a reciprocal transformation was studied in 1984 by Rogers et al. [5], the algebraic by geometric solution of the HD equation Novikov [6], the solitons solutions of the (2+1)-dimemsional HD equation by Halim [7], and the multi–soliton solutions of (2+1) dimensional HD equation by Dmitrieva et al. [8].

The meshless methods are widely used to find the approximate solutions of many types of ordinary differential equations (ODEs) and partial differential equations (PDEs). The use of meshless method, known as, Kansa collocation radial basis functions (RBFs) method, for the numerical solutions of PDEs gained the attention of many researches in different fields of engineering and science. Kansa method is recently extended to solve ODEs and PDEs including free boundary problems, one-dimensional nonlinear Burger's equation with shock waves, heat transfer problems, and shallow water equations [9-13]. Later on Fasshauer [14] modified this approach to a Hermite-type collocating method for solvability of the resulting collocating matrix. In 1971it was introduced by Hardy [15] as a multi-dimensional scattered collocation method. He introduced it in modeling of the Earth's gravitational fields. In 1990 Kansa [16, 17] gave an idea of a meshfree method by directly using the RBFs, particularly the multiquardatic (MQ) to collocate the solution and for solving various types of PDEs. Micchelli [18], Madych [19] Frank and Schaback [20] studied the uniqueness, existence and the convergence of the Kansa method. Tawater [21] found in his numerical experiment that the magnitude of shape parameter c has great influence on the accuracy of the method.

## Meshless Collocation Technique

This section is focused to discuss a meshless collocation method based on $\theta$ weighted scheme. Crank-Nicolson scheme ($\theta = \frac{1}{2}$) will be applied to given PDE and then

will be solved in terms of solution at $(n+1)^{th}$ time step from which the unknown solution can be found by solving system of linear equations.

**Formulation of the proposed Method**

Consider the governing equation,

$$u_t = u^3 u_{xxx,} \qquad (1)$$

with initial condition and boundary conditions defined by,

$$u(x,0) = g(x), \quad x \in [a,b], \qquad (2)$$

$$u(a,t) = f_1(t), \qquad u(b,t) = f_2(t). \qquad (3)$$

First take $\theta$-weighted scheme to Eq. (1), we get,

$$\frac{u^{n+1} - u^n}{\delta t} = \theta \left[ (u^3 u_{xxx})^{n+1} \right] + (1-\theta) \left[ (u^3 u_{xxx})^n \right],$$

Putting $\theta = \dfrac{1}{2}$, to get Crank-Nicolson scheme,

$$\frac{u^{n+1} - u^n}{\delta t} = \frac{1}{2} \left[ (u^3 u_{xxx})^{n+1} \right] + \frac{1}{2} \left[ (u^3 u_{xxx})^n \right] \qquad (4)$$

where $u^{n+1}$ is the solution at $(n+1)^{th}$ time step, and $t^{n+1} = t^n + \delta t$, where $\Delta t$ is the time step.

There is nonlinear term $u^3 u_{xxx}$ in Eq. (4). To linearize this nonlinear term we use the following procedure:

$$\frac{d}{dt}(uv) = u\frac{d}{dt}v + v\frac{d}{dt}u,$$

$$\frac{(uv)^{n+1} - (uv)^n}{\delta t} = u^n \frac{(v^{n+1} - v^n)}{\delta t} + v^n \frac{(u^{n+1} - u^n)}{\delta t} ,$$

Simplifying, we get,

$$(uv)^{n+1} = u^n v^{n+1} + v^n u^{n+1} - v^n u^n. \qquad (5)$$

Proceeding in the same way, we have,

$$(u^2 v)^{n+1} = (u^n)^2 v^{n+1} + v^n (u.u)^{n+1} - v^n (u^n)^2,$$

By using Eq. (5) in above equation, we obtain

$$(u^2 v)^{n+1} = (u^n)^2 v^{n+1} + 2 u^n u^n u^{n+1} v^n - 2(u^n)^2 v^n. \qquad (6)$$

Similarly

$$(u^3 v)^{n+1} = (u^n)^3 v^{n+1} + v^n (u.u^2)^{n+1} - v^n (u^n)^3,$$

Using Eq. (5) in above equation, it take forms,

$$(u^3 v)^{n+1} = (u^n)^3 v^{n+1} + u^{n+1}(u^n)^2 + u^n (u.u)^{n+1} v^n - u^n (u^n)^2 v^n - v^n (u^n)^3,$$

again using Eq. (5) in above in above equation, we get

$$(u^3 v)^{n+1} = (u^n)^3 v^{n+1} + 3u^{n+1}(u^n)^2 v^n - 3(u^n)^3 v^n. \qquad (7)$$

Taking $u = u$ and $v = u_x$ Eq. (5), Eq. (6) and Eq. (7) becomes,

$$(u u_x)^{n+1} = u^n u_x^{n+1} + u^{n+1} u_x^n - u^n u_x^n. \qquad (8)$$

$$(u^2 u_x)^{n+1} = (u^n)^2 u_x^{n+1} + 2u^n u^{n+1} u_x^n - 2(u^n)^2 u_x^n. \qquad (9)$$

$$(u^3 u_x)^{n+1} = (u^n)^3 u_x^{n+1} + 3u^{n+1}(u^n)^2 u_x^n - 3(u^n)^3 u_x^n. \qquad (10)$$

After linearizing the nonlinear term, Eq. (4) becomes

$$\frac{u^{n+1} - u^n}{\delta t} = \frac{1}{2} \left[ 3u^{n+1}(u^n)^2 u_{xxx}^n - 3(u^n)^3 u_{xxx}^n + (u^n)^3 u_{xxx}^{n+1} \right] + \frac{1}{2} \left[ (u^n)^3 u_{xxx}^n \right] \qquad (11)$$

$$u^{n+1} - u^n = \frac{\delta t}{2} \left[ 3u^{n+1}(u^n)^2 u_{xxx}^n + (u^n)^3 u_{xxx}^{n+1} \right] + \frac{\delta t}{2} \left[ -3(u^n)^3 u_{xxx}^n + (u^n)^3 u_{xxx}^n \right],$$

(12)

0r

$$u^{n+1} - \frac{\delta t}{2} \left[ 3u^{n+1}(u^n)^2 u_{xxx}^n + (u^n)^3 u_{xxx}^{n+1} \right] = u^n - \delta t (u^n)^3 u_{xxx}^n \qquad (13)$$

Let $u^n$ represents the approximate solution at $n^{th}$ iteration. Let us approximate solution of Eq. (1) by,

$$u^n(x) = \sum_{J=1}^{M} a_j{}^n \phi_j,$$

where $a_j$ are the constants and $\phi : R^n \to R$, is the RBF, which depends only on the radial distance or distance from the central point (or also in some cases on shape parameter). Collocating the approximate solution at $i^{th}$ node and denoting it by $u^n(x_i)$, we have

$$u^n(x_i) = \sum_{j=1}^{M} a_j{}^n \phi_{ij}, \qquad (14)$$

Where $i = 1,2,...,M$

Substituting Eq. (14) in Eq. (13), we get

$$\sum_{j=1}^{M} a_j{}^{n+1} \phi_{ij} - \frac{\delta t}{2}\left[ 3\sum_{j=1}^{M} a_j{}^{n+1}\phi_{ij}\left(\sum_{j=1}^{M}a_j{}^n\phi_{ij}\right)^2 \sum_{j=1}^{M}a_j{}^n\phi_{ij}'''\right.$$

$$\left. + \left(\sum_{j=1}^{M}a_j{}^n\phi_{ij}\right)^3 \sum_{j=1}^{M}a_j{}^{n+1}\phi_{ij}'''\right]$$

$$= \sum_{j=1}^{M}a_j{}^n\phi_{ij} - \delta t\left(\sum_{j=1}^{M}a_j{}^n\phi_{ij}\right)^3 \sum_{j=1}^{M}a_j{}^n\phi_{ij}''' \qquad (15)$$

The difference equation (15) can be solved to obtain the unknown solution.

The boundary conditions will take the form,

$$\sum_{j=1}^{M} a_j{}^{n+1} \phi_{0j} = f_1(t), \qquad (16)$$

$$\sum_{j=1}^{M} a_j{}^{n+1} \phi_{Mj} = f_2(t). \qquad (17)$$

Eqs. (15) – (17) forms system of linear equations. We can use by direct solver like LU–factorization method or Gauss elimination method to solve it.

### Numerical Results

This section is focused to give numerical example in order to show the impressive behaviour of our method with the help of error norms and figures.

### Test Problem

Consider the governing equation,

$$u_t = u^3 u_{xxx}, \qquad (18)$$

Consider the solitary wave solution of Eq. (18),

$$u(x,t) = \left(\alpha - 3\frac{\sqrt{\beta}}{2}(x + \beta t)\right)^{\frac{2}{3}} \qquad (19)$$

The initial condition obtained from Eq. (9) is,

$$u(x,0) = \left(\alpha - 3\frac{\sqrt{\beta}}{2}x\right)^{\frac{2}{3}},$$

Similarly the boundary conditions are,

$$u(a,t) = \left(\alpha - 3\frac{\sqrt{\beta}}{2}(a1 + \beta t)\right)^{\frac{2}{3}},$$

$$u(b,t) = \left(\alpha - 3\frac{\sqrt{\beta}}{2}(b1 + \beta t)\right)^{\frac{2}{3}}.$$

Here we take $\alpha = 4$ and $\beta = 1$. Numerical computations are performed over the interval $[0,1] \times [0, 0.005]$. Here we have considered the value of step size $h = 0.1$ and time step $\delta t = 0.001$. We have taken MQ, IMQ, GA and IQ RBFs. Table 3.1 is devoted to error norms to assess the behavior of MMCN, which are defined by,

$$L_\infty = \max\left|u^{exact} - u^{app}\right|, \qquad (20)$$

$$L_2 = \sqrt{h\sum_{i=1}^{M}\left(u^{exact} - u^{app}\right)^2}, \qquad (21)$$

$$L_{RMS} = \sqrt{\frac{\sum_{i=1}^{M}\left(u^{exact} - u^{app}\right)^2}{M}}. \qquad (22)$$

From Table .1 it can be seen that GA has more accurate results than MQ, IMQ and IQ. Here we have taken c=135, 1760, 1760 and 115 for MQ, IMQ, GA and IQ respectively.

Form Fig.1 it can be see that, the Max-error for MQ attains its maximum value at $c = 180$ while its minimum value occurs at $c = 135$ and in Fig. 2 the Max-error for IMQ increases for the value of $c = 1700$

**TABLE 1: ERROR NORMS FOR MQ, IMQ, GA AND IQ**

| t | RBF | $L_\infty$ | $L_2$ | $L_{RMS}$ |
|---|---|---|---|---|
| 0.001 | MQ | 4.1182E-4 | 1.8917E-4 | 1.8037E-4 |
| | IMQ | 4.3190E-4 | 2.4570E-4 | 2.3426E-4 |
| | GA | 2.6184E-4 | 1.4952E-4 | 1.4257E-4 |
| | IQ | 2.0337E-4 | 1.2950E-4 | 1.2347E-4 |
| 0.002 | MQ | 1.9000E-3 | 8.7384E-4 | 8.3283E-4 |
| | IMQ | 2.6000E-3 | 1.6000E-3 | 1.5000E-3 |
| | GA | 9.8233E-4 | 6.8928E-4 | 6.5721E-4 |
| | IQ | 1.7000E-3 | 1.2000E-3 | 1.1000E-3 |
| 0.003 | MQ | 4.000E-3 | 2.5000E-3 | 2.4000E-3 |
| | IMQ | 3.1000E-3 | 1.8000E-3 | 1.7000E-3 |
| | GA | 1.7000E-3 | 1.3000E-3 | 1.3000E-3 |
| | IQ | 1.8000E-3 | 1.2000E-3 | 1.2000E-3 |
| 0.004 | MQ | 2.7000E-3 | 1.6000E-3 | 1.5000E-3 |
| | IMQ | 6.2000E-3 | 3.5000E-3 | 3.3000E-3 |
| | GA | 2.4000E-3 | 2.0000E-3 | 1.9000E-3 |
| | IQ | 4.5000E-3 | 3.0000E-3 | 2.9000E-3 |
| 0.005 | MQ | 5.7000E-3 | 2.5000E-3 | 2.4000E-3 |
| | IMQ | 6.7000E-3 | 4.0000E-3 | 3.8000E-3 |
| | GA | 3.1000E-3 | 2.6000E-3 | 2.5000E-3 |
| | IQ | 5.3000E-3 | 3.7000E-3 | 3.5000E-3 |
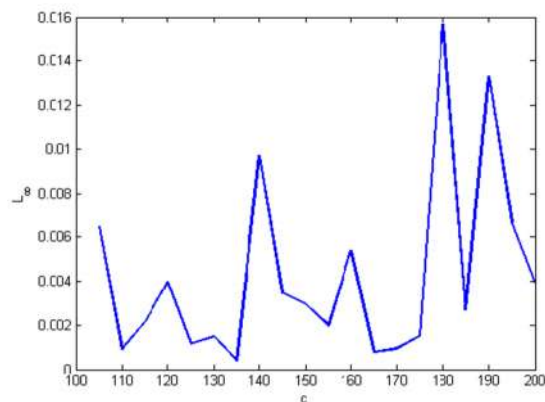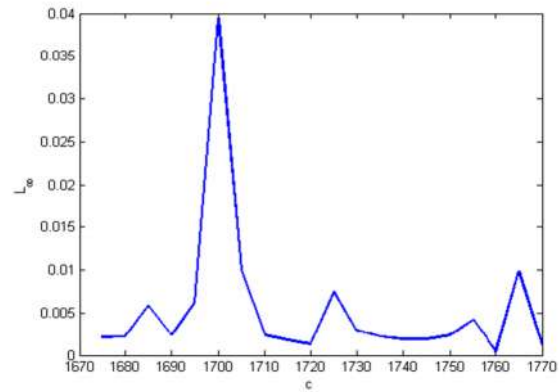


**FIGURE 2: MAX-ERROR FOR VALUES OF C USING IMQ**
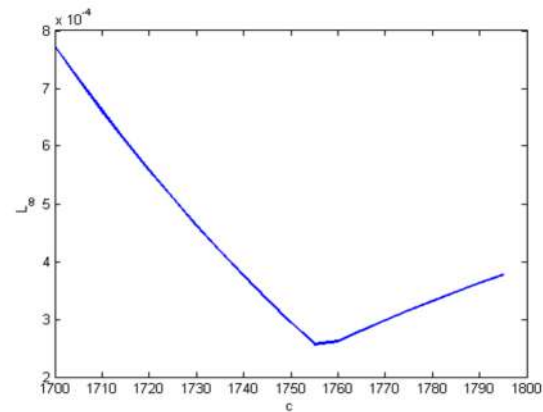


**FIGURE 3: MAX-ERROR FOR VALUES OF C USING GA**



**FIGURE 4: MAX-ERROR FOR VALUES OF C USING IQ**
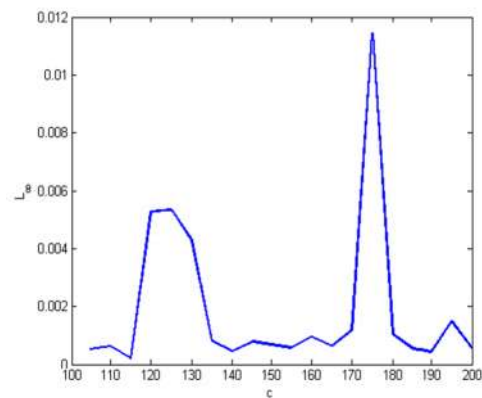


**FIGURE 1: MAX-ERROR FOR VALUES OF C USING MQ**
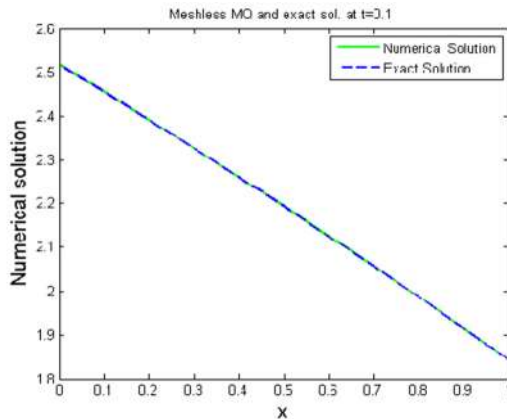
**FIGURE 5: RELATIONSHIP BETWEEN EXACT AND MQ SOLUTION**
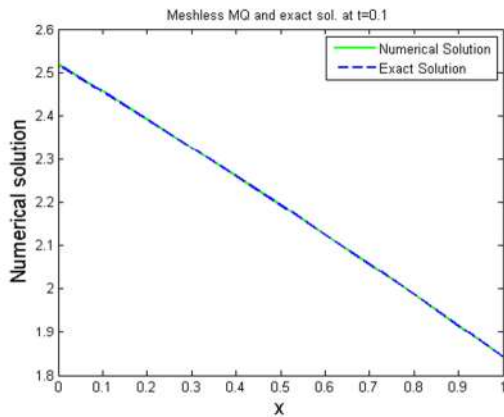


**FIGURE 6: RELATIONSHIP BETWEEN EXACT AND IMQ SOLUTION**
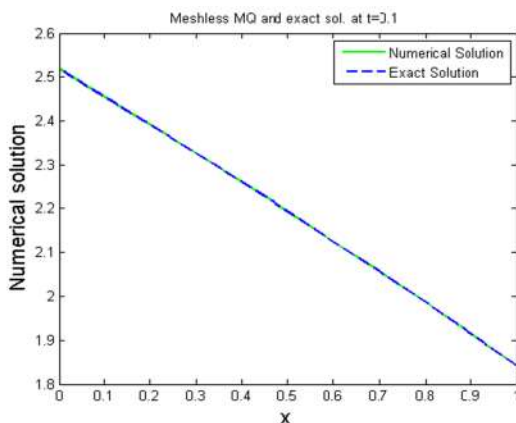


**FIGURE 7: RELATIONSHIP BETWEEN EXACT AND GA SOLUTION**
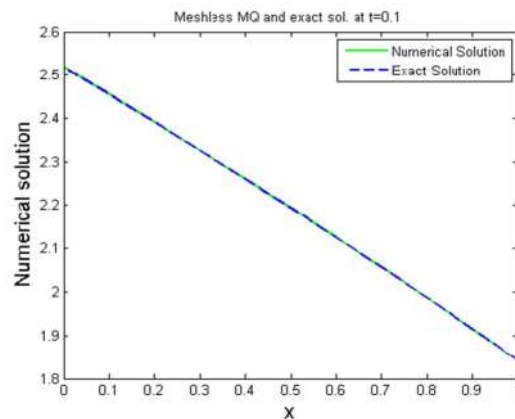


**FIGURE 8: RELATIONSHIP BETWEEN EXACT AND IQ SOLUTION**

## Conclusions

The main purpose of this paper was to propose a meshless scheme to solve HD equation. Kansa' method has an edge over other methods due to its meshless nature. We have considered MQ, IMQ, GA and IQ RBFs. Numerical examples are given to demonstrate the accuracy of the method.

## References

[1] Kruskal MD, Moser j. Dynamical systems, theory and applications, lecturer notes physics. Berlin: Sringer; 1975, 310.

[2] W. Hereman, p. p. Banerjee, M.R. Chatterjee, On the nonlocal charges associated with the Harry Dym hierarchy kortewege-de vries equation, J.phys. A22(1989).

[3] J.C.Bruneli, G. da costa, On the nonlocal equations and nonlocal charges associated with the Harry-Dym hierarchy, J. Math. Phys. 43(2002) 6116-6128

[4] Mokhtari R. Exact solutions of the Harry Dym equation. Commun.Theor.Phys.55 (2011) 204-208

[5] C. Rogers and P. Wong, On reciprocal Bbklund transformations of inverse scattering schemes. Phys. Scripta 30(1989)10-14.

[6] Novikov DP. Algebraic geometric solution of the Harry Dym equation. Siberian Math. J., 40 (1999)136-140.

[7] Halim AA. Solitons solutions of the (2+1)-dimensional Harry Dym equation via Darboux transformation. Chaos Solitons Fract., 36(2008)646-53.

[8] Dmitrieva L, Khlabystova M. Multi-Solitons solutions of (2+1)-dimensional Harry Dym equation. Phys. Lett.-A, 237(1998) 369-80.

[9] Hon YC, Mao XZ. An efficient numerical scheme for Burgers equation. Appl. Math. Comput., 95(1998)37–50.

[10] Hon YC, Cheung KF, Mao XZ, Kansa EJ. Multiquadric solution for shallow water equations. ASCE J Hydraul. Eng., 125(1999)524–33.

[11] Hon YC, Mao XZ. A radial basis function method for solving options pricing model. Financial Eng.,8(1999)31–49.

[12] Marcozzi M, Choi S, Chen CS. On the use of boundary conditions for variational formulations arising in financial mathematics. Appl. Math. Comput., 124(2001)197–214.

[13] Zerroukat M, Power H, Chen CS. A numerical method for heat transfer problem using collocation and radial basis functions. Int. J. Numer. Math. Eng., 42(1998)1263–1278.

[14] Fasshauer GE. Solving partial differential equations by collocation with radial basis functions. In: Le Me´haute´ A, Rabut C, Schumaker LL, editors. Surface Fitting and Multiresolution Methods. Nashville, TN: Vanderbilt University Press; 1997, 131–138.

[15] Hardy RL. Multiquadric equations of topography and other

irregular surfaces. J Geo-phys. Res., 176 (1971) 1905–1915.

[16] Kansa EJ. Multiquadrics—a scattered data approximation scheme with applications to computational fluid dynamics—I. Comput. Math. Appl., 19(1990)127–145.

[17] Kansa EJ, Hon YC. Circumventing the ill-conditioning problem with multiquadric radial basis functions applications to elliptic partial differential equations. Comput. Math. Appl., 39 (2000) 123–37.

[18] Micchelli CA. Interpolation of scattered data: distance matrix and conditionally positive definite functions. Constr. Approx., 2(1986) 11–22.

[19] Madych WR, Nelson SA. Multivariate interpolation and conditionally positive definite functions II. Math. Comput., 54 (1990)211–230.

[20] Franke C, Schaback R. Convergence order estimates of meshless collocation methods using radial basis functions. Adv. Comput. Math., 8(1998) 381–399.

[21] Tarwater AE. A parameter study of Hardy's multiquadric method for scattereddata interpolation. Technical Report UCRL-54670, Lawrence Livermore National Laboratory, 1985.

# Numerical solution of Harry Dym equation by meshless technique

*Hifza Sheraz[1*], Mehnaz [1]*

*[1]Department of Mathematics, Shaheed Benazir Bhutto Woman University, Peshawar 25000*
*[1*]Corresponding author*
*Email: Hifza.shiraz2016@gmail.com*

**Abstract**

The Harry Dym (HD) is an important non-linear partial differential equation (PDE). It has applications in physical systems. Different system in which dispersion and non-linearity are coupled together are represented by HD equation. It is completely integrable and also it obey san infinite number of conversion laws. A meshless technique, named, Method of lines (MOL) is proposed to solve non-linear HD equation. This method has an edge over traditional methods due to its meshless nature. Different types of Radial basis functions are used to discretize the problem domain in space variable which reduces PDE to system of ordinary differential equations (ODEs). RK4 is used to solve system of ODEs. Numerical results are given to show the accuracy of the method. For this purpose $L_2$, $L_\infty$ and $L_{RMS}$ error norms are used. Figures are used to show exact and numerical solution. Our method is compared with some other methods in the literature. Results shows the accuracy of our method over other methods.

**Key words**: Multi Quadric (MQ), inverse Multi Quadric (IMQ), Gaussian (GA), inverse Quadric (IQ), Runge Kutta method of order 4 (RK4) .

**Introduction**

The Herry Dym (HD) equation is,

$$u_t = u^3 u_{xxx}$$

Where,

$$u = u(t, x), u_x = \frac{\partial u}{\partial x}, u_{xx} = \frac{\partial u^2}{\partial x^2}, u_{xxx} = \frac{\partial u^3}{\partial x^3}$$ is one of the exotic and most interesting soliton equations. Harry Dym discovered it in an unpublished paper in 1973 and it appeared in a more general form in [1] within the classical string problem. The relationship between HD and classical string problem, with elastic parameter, was pointed out again by Sabatier [2]. Kruskal [3] named this equation as HD equation. HD equation is completely integrable and its properties are discussed in detail in [4]. HD equation is an important dynamical equation which is integrable and finds applications in several physical systems [5]. Applications of HD equation were found to

the problems of hydrodynamics [6]. Reciprocal transformation can be used to connect HD equation to KdV equation [7]. HD equation is rediscovered in more general form in [8]. Two dimentional HD equation possesses many properties, typical for soliton equations [9, 10]. Moreover, S. Kumar, M.P. et al. [11], obtained approximate solution to the fractional HD equation.

MOL is an efficient numerical technique to find numerical solution of PDEs. It was first purposed by the German mathematician Erich Rothe in 1930 [12]. He applied this technique to the parabolic type equations, but it can be used in more broad sense. The main idea behind MOL is to descritize the domain problem by substitution of algebraic approximations for the derivatives and retention of derivatives with respect to remaining variables. By applying MOL, the given PDE changes into a system ODEs and then system of ODEs can be solved by integration algorithm. We have used RK4 method in this work as ODE solver. MOL has been recently applied to different PDEs such as KdV equation for small time [13], KdV equation [14], generalized kuramoto-Sivashinsky[15], CH- $\gamma$ equation [16]. Stability and convergence of MOL are discussed in [17, 18, 19].

**Method**

The main aim of this section is to solve HD equation numerically by MOL. In MOL semi discretization is done in space variable while the time variable remain uninfluenced. This semi discretization results in conversion of PDE to system of $M$ ODEs, which can be solved by using any appropriate ODE solver. In this work we will use ODE solver RK4.

**RBF interpolation**

This section is concern with MOL-RBF interpolation. With RBF the approximate solution to the problem will be approximated, that will semi discretize the problem domain in space variable.

Let $u^k(x)$ be the RBF approximation to $u$, which represents solution of the given PDE. Let us divide the problem domain in $M$ nodes $x_l, l = 1, 2, \cdots, M \in \Lambda \cup \partial\Lambda$ where $\Lambda$ is the interior

and $\partial \Lambda$ is the boundary of the domain. Also $x_1$ and $x_M$ are the boundary points, while $x_l: \quad l = 2,3,\cdots M-1$ are interior points.

RBF approximation of $u(x)$ is given by,

$$u^k(x) = \sum_{l=1}^{M} B_l \phi_l = B_1 \phi_1 + B_2 \phi_2 + ... + B_M \phi_M,$$

$$\Rightarrow u^k(x) = \Phi^T(x)\mathbf{B},$$

$$\Phi(x) = [\phi_1(x), \phi_2(x), \phi_3(x),...,\phi_M(x)]^T$$

(1)

And $\mathbf{B} = [B_1, B_2, B_3,...,B_M]^T$. Here $\phi_l$ are the RBFs and $B_l$ are the unknown constants.

Let us denote the approximate solution at $l^{th}$ node by $u_l$ i.e. $u^k(x_l) = u_l$. Then from Eq. (1)

$$u_1 = \Phi^T(x_1)\mathbf{B},$$

$$u_2 = \Phi^T(x_2)\mathbf{B},$$

$$\vdots = \vdots$$

$$u_M = \Phi^T(x_M)\mathbf{B}.$$

Which can be written in the form of matrix as,

$$\mathbf{HB} = \mathbf{u}$$

(2)

Where $\mathbf{H} = \begin{bmatrix} \phi_1(x_1) & \phi_2(x_1) & \cdots & \phi_M(x_1) \\ \phi_1(x_2) & \phi_2(x_2) & \cdots & \phi_M(x_2) \\ \vdots & \vdots & \ddots & \vdots \\ \phi_1(x_M) & \phi_2(x_M) & \cdots & \phi_M(x_M) \end{bmatrix}$,

$$\mathbf{B} = \begin{bmatrix} \\ \vdots \\ \\ \end{bmatrix} \begin{bmatrix} B_1 \\ B_2 \\ \vdots \\ B_M \end{bmatrix}$$

and $\mathbf{u} = \begin{bmatrix} \\ \vdots \\ \\ \end{bmatrix} \begin{bmatrix} u_1 \\ u_2 \\ \vdots \\ u_M \end{bmatrix}$.

Matrix $\mathbf{H}$ given in Eq.2.12 is known as interpolation matrix and it **consist** of RBFs at nodal points. From Eq. (2)

So we have,

$$\mathbf{B} = \mathbf{H}^{-1}\mathbf{u}$$

(3)

Putting this value in Eq. (1) we get,

$$u^k(x) = \Phi^T \mathbf{H}^{-1}\mathbf{u},$$

$$\Rightarrow u^k(x) = \mathbf{W}(x)\mathbf{u},$$

(4)

Where $\mathbf{W}(x) = \Phi^T(x)\mathbf{H}^{-1}$

Collocation matrix $\mathbf{H}$ must be nonsingular to guarantee the invertibility of matrix $\mathbf{H}$. The singularity of matrix $\mathbf{H}$ depends on position of mesh points and on selection of RBF. Matrix $\mathbf{H}$ is invertible if we select distinct mesh points. One should take the value of shape parameter as large as possible, which will produce large differences between columns of, $\mathbf{H}$ to avoid singularity of $\mathbf{H}$

**Meshless MOL for Herry Dym Equation using RBF**

To find numerical solution of HD equation we will apply MOL in this section. We consider our problem and apply RBF interpolation on it. For this consider HD equation,

$$u_t - u^3 u_{xxx} = 0$$

(5)

With initial condition,

$$u(x,0) = h(x) \qquad a \le x \le b,$$

(6)

and boundary conditions,

$$u(a,t) = f_1(t), \qquad\qquad u(b,t) = f_2(t) \quad .$$

(7)

Applying Eq. (4) to Eq. (5) and collocating at each node $x_l$, we get

$$\frac{du_l}{dt} - u_l^3 (W_{xxx}u), l=1,2,...,M.$$

(8)

Where $u_l(t)=u_l$

In same way,

$$W_{xxx}(x_l)=[W_{1xxx}(x_1)W_{2xxx}(x_2)..W_{MXXX}(x_l)],$$

And $W_{kxxx}(x_l)=\dfrac{\partial^3}{\partial x^3}W_k(x_l).$

$$U=[u_1u_2...u_M]^T,$$

$$W_{xxx}=[W_{kxxx}(x_l)]_{M \times M}$$

**THIS EQ. (8) CAN BE WRITTEN AS,**

$$\frac{dU}{dt}-U^3*(W_{xxx}U)=0,$$

(9)

We write this above Eq. (9) in compact form as,

$$\frac{dU}{dt}=E(U)\text{ Where}$$

(10)

$$E=U^3*(W_{xxx}U)$$

(11)

Initial condition can be rewritten as

$$U(t_0)=[u^0(x_1)u^0(x_2)..u^0(x_M)]^T$$

(12)

from boundary conditions,

$$u_1(t)=f(t),u_M(t)=f_2(t)$$

(13)

With RBF interpolation this was first step of MOL coupled.

**Runge-Kutta method of order 4**

To solve equations (10) to (13) we will apply RK4 method. This method is suitable to the computer because it needs no special starting and this method is numerically stable due to its single step nature. For Eq. (10) the RK4 algorithm is

$$W(i)=U(i)+\frac{\Delta t}{6}(K_1+2K_2+2K_3+K_4),\text{ where}$$

$$K_1=E(U^i),$$

$$K_2=E\left(U^i+\frac{\Delta t}{2}K_1\right),$$

$$K_3=E\left(U^i+\frac{\Delta t}{2}K_2\right),$$

$$K_4=E(U^i+\Delta tK_3).$$

Here $\Delta t$ is the time step.

**Results**

In this section we will give some numerical examples to show accuracy of our method as compared to other methods.

Consider our desired equation,

$$u_t-u^3u_{xxx}=0$$

(15)

With initial condition,

$$u(x,0)=\left(\alpha-3\frac{\sqrt{\beta}}{2}x\right)^{\frac{2}{3}},$$

And boundary conditions, obtained from exact solution,

$$u(a_1,t)=\left(\alpha-3\frac{\sqrt{\beta}}{2}(a_1+\beta t)\right)^{\frac{2}{3}},$$

$$u(b_1,t)=\left(\alpha-3\frac{\sqrt{\beta}}{2}(b_1+\beta t)\right)^{\frac{2}{3}}.$$

The solitary wave solution of (15) given by,

$$u(x,t)=\left(\alpha-3\frac{\sqrt{\beta}}{2}(x+\beta t)\right)^{\frac{2}{3}}.$$

(16)

Here $\alpha=4$ and $\beta=1$.

Numerical simulations is carried out on the interval $[0,0.5]\times[0,0.002]$ with step size $h=0.1$ and time step $\Delta t=0.001$ by using different type of RBFs namely MQ, IMQ, GA and IQ. Table 1 is devoted to error norms to assess the behavior of MOL, which are defined by,

$$L_\infty = \max \left| u^{exact} - u^{app} \right|,$$

$$L_2 = \sqrt{h \sum_{i=1}^{M} \left( u^{exact} - u^{app} \right)^2},$$

$$L_{rms} = \sqrt{\frac{\sum_{i=1}^{M} \left( u^{exact} - u^{app} \right)^2}{M}}.$$

From Table 1 it is clear that MQ, IMQ and GA has more accurate results than IQ at t=0.004,0.006 and 0.008. Here we have the values of c=2600, c=63, c=1840 and c=70 for MQ, IMQ, GA and IQ respectively. In Table 2 the comparison is considered between FRDTM and MOL

and it is clear that our method produces accurate results than FRDTM. As we have discussed already in section 2.1 that the accuracy of RBF interpolation depends on shape parameter c. There are so many methods to find the optimal value of c which have discussed earlier, while in this work we have applied brute-force technique and figures are given in Fig. 1-4. From Fig. 1 we can easily see that, the least Max-error for MQ can be obtain for c=2600. In Fig. 2 the least Max-error for IMQ is at c=63. Also Fig. 3 and Fig. 4 shows that the minimum value of Max-error attains at c=1840 and c=70 for GA and IQ respectively.

**TABLE 1:** $L_\infty$, $L_2$ AND $L_{rms}$ FOR DIFFERENT TYPES OF RBFS

| t | RBFs | $L_\infty$ | $L_2$ | $L_{rms}$ |
|---|---|---|---|---|
| 0.002 | MQ | 1.4000E-03 | 1.3000E-03 | 1.2000E-03 |
| | IMQ | 1.1000E-04 | 6.2333E-04 | 5.9433E-04 |
| | GA | 4.9572E-04 | 3.0287E-04 | 2.8878E-04 |
| | IQ | 1.3000E-03 | 6.6377E-04 | 6.3288E-04 |
| 0.004 | MQ | 2.9000E-03 | 2.6000E-03 | 2.5000E-03 |
| | IMQ | 2.4000E-03 | 1.4000E-03 | 1.4000E-03 |
| | GA | 9.9670E-04 | 6.0612E-04 | 5.7791E-04 |
| | IQ | 7.1000E-03 | 3.6000E-03 | 3.4000E-03 |
| 0.006 | MQ | 4.3000E-03 | 3.9000E-03 | 3.7000E-03 |
| | IMQ | 4.1000E-03 | 2.5000E-03 | 2.4000E-03 |
| | GA | 1.5000E-03 | 9.0975E-04 | 8.6741E-04 |
| | IQ | 3.1300E-02 | 1.5500E-02 | 1.4800E-02 |
| 0.008 | MQ | 5.8000E-03 | 5.1000E-03 | 4.9000E-03 |
| | IMQ | 6.4000E-03 | 4.0000E-03 | 3.8090E-03 |
| | GA | 2.0000E-03 | 2.1000E-03 | 2.1000E-03 |
| | IQ | 1.1990E-01 | 6.0100E-02 | 5.7300E-02 |

**TABLE 2 COMPARISON OF MOL RBF WITH FRDTM**

| x | t | Numerical | MQ | IMQ | GA | IQ | FRDTM |
|---|---|---|---|---|---|---|---|
| 0 | 0.002 | 2.51858 | 2.51858 | 2.51858 | 2.51858 | 2.51858 | 2.51858 |
| | 0.004 | 2.51732 | 2.51732 | 2.51732 | 2.51732 | 2.51732 | 2.51732 |
| | 0.006 | 2.51606 | 2.51606 | 2.51606 | 2.51606 | 2.51606 | 2.51606 |
| | 0.008 | 2.5148 | 2.5148 | 2.5148 | 2.5148 | 2.5148 | 2.5148 |
| 0.3 | 0.002 | 2.32581 | 2.32581 | 2.32581 | 2.32581 | 2.32581 | 2.32581 |
| | 0.004 | 2.3245 | 2.3245 | 2.3245 | 2.3245 | 2.3245 | 2.3245 |
| | 0.006 | 2.32319 | 2.32319 | 2.32319 | 2.32319 | 2.32319 | 2.32319 |
| | 0.008 | 2.32187 | 2.32187 | 2.32187 | 2.32187 | 2.32187 | 2.32187 |
| 0.6 | 0.002 | 2.12468 | 2.12468 | 2.12468 | 2.12468 | 2.12468 | 2.12468 |
| | 0.004 | 2.12331 | 2.12331 | 2.12331 | 2.12331 | 2.12331 | 2.12331 |
| | 0.006 | 2.12194 | 2.12194 | 2.12194 | 2.12194 | 2.12194 | 2.12194 |
| | 0.008 | 2.12056 | 2.12056 | 2.12056 | 2.12056 | 2.12056 | 2.12056 |
| 1 | 0.002 | 1.84054 | 1.84054 | 1.84054 | 1.84054 | 1.84054 | 1.84054 |
| | 0.004 | 1.83907 | 1.83907 | 1.83907 | 1.83907 | 1.83907 | 1.83907 |
| | 0.006 | 1.83759 | 1.83759 | 1.83759 | 1.83759 | 1.83759 | 1.83759 |
| | 0.008 | 1.83612 | 1.83612 | 1.83612 | 1.83612 | 1.83612 | 1.83612 |
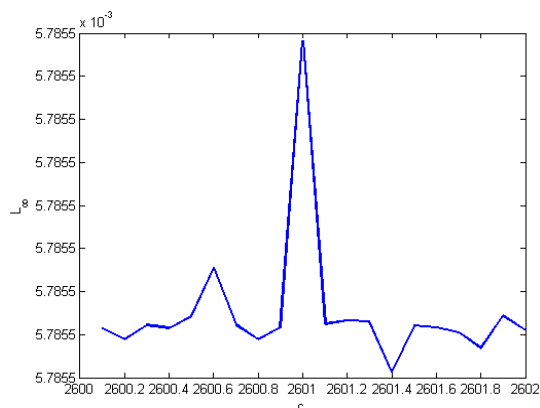
**FIGURE 1  L∞ ERROR NORM FOR DIFFERENT VALUES OF C USING MQ**



**FIGURE 2  L∞ ERROR NORM FOR DIFFERENT VALUES OF C USING IMQ**
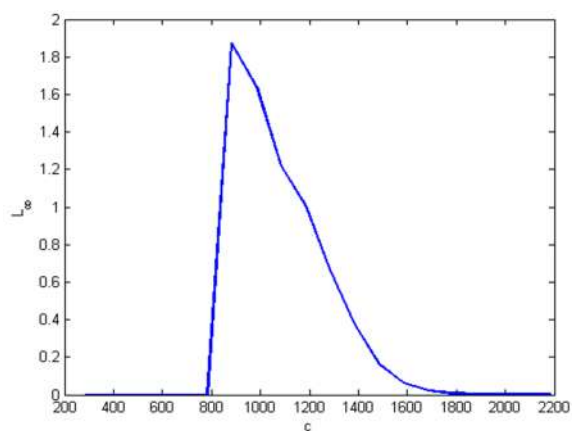


**FIGURE 3 L∞ ERROR NORM FOR DIFFERENT VALUES OF C USING GA**



**FIGURE 4  L∞ ERROR NORM FOR DIFFERENT VALUES OF C USING IQ**



**FIGURE 5 EXACT AND NUMERICAL SOLUTION FOR MQ**
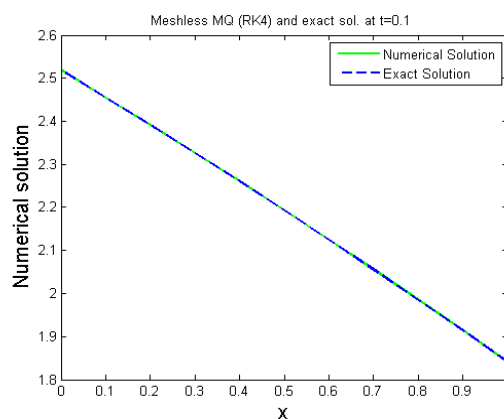


**FIGURE 6 EXACT AND NUMERICAL SOLUTION FOR IMQ**
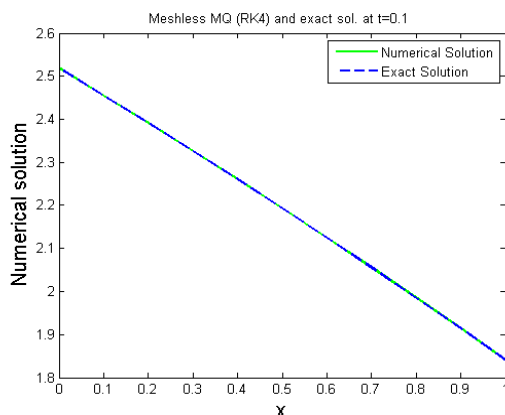
**FIGURE 7 EXACT AND NUMERICAL SOLUTION FOR GA**
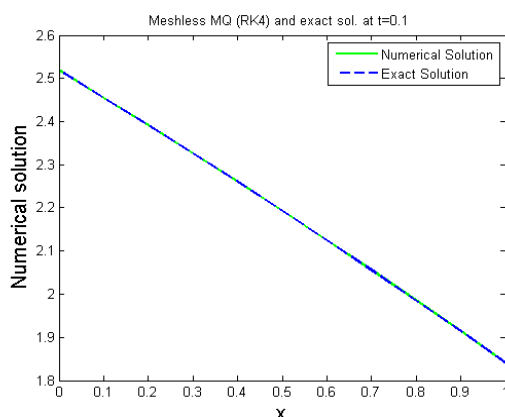


**FIGURE 8 EXACT AND NUMERICAL SOLUTION FOR IQ**

## Conclusions

In this work we presented MOL RBF for the approximate solution of Herry Dym equation. In MOL, problem does not depend on mesh points. We have approximated derivatives by RBFs. RK4 method is used as time integrator. We have given examples and assess the accuracy of method with the help of different norms. Our method is compared with FRDTM which results in superiorty of MOL. MQ, IMQ, GA and IQ are used.

## References

[1]. P.C. Sabatier, On some spectral problems and isospectral evolutions connected with the classical string problem. I. Constants of motion, Lett. Nuovo Cimento 26:477–482, 1979.

[2]. Sabatier P C 1979 On some spectral problems and isospectral evoluations connected with the classical string problem 1 lett. Nouro Cimento 26:477-82

[3]. M.D. Kruskal, J. Moster, Dynamical Systems: Theory and Applications, in: Lecture Notes in Physics, Springer, Berlin, 1975.

[4]. W. Hereman, P.P. Banerjee, M.R. Chatterjee, On the nonlocal equations and nonlocal charges associated with the Harry-Dym hierarchy Korteweg–deVries equation, J. Phys. A 22: 241–25, 1998.

[5]. S. Kumar, M.P. Tripathi, O.P. Singh, A fractional model of Harry Dym equation and its approximate solution, Ain Shams Engineering Journal. 4,(2013), 111–115.

[6]. Vosconcelos. GL, kaclanoff L.P, Stationary solution for the saffman Taylor problem with surface tension. Phys Rev A 44:6490-5, 1991.

[7]. W. Hereman, P.P. Banerjee, M.R. Chatterjee, On the nonlocal equations and nonlocal charges associated with the Harry-Dym hierarchy Korteweg–deVries equation, J. Phys. A 22: 241–25, 1998.

[8]. P.C. Sabatier, lett. Nuovo Cimanto, 26:477-483, 1979. Lecture Notes in physics, Vol. 120 eds M.Boiti, I. pempinelli and G. soliani p. 85.
[9]. F. Calogero and A.Degasperis, spectral Transform and solitons(North-Holland, Amsterdam, 1982).

[10]. W. Hereman, P.P. Benerjee and M.R. Chatterjee, J.phys A. 22(1989)249.

[11] S. Kumar, M.P. Tripathi, O.P. Singh, A fractional model of Harry Dym equation and its approximate solution, Ain Shams Engineering Journal. 4,(2013), 111–115.

[12]. E. Rothe. Zweidimensional parabolische randwertaufgaben als grenzfall eindimensionaler randwertaufgaben. Math. Anna. , 102:650-670, 1930

[13]. A. ozdes, E. N. Aksan. The method of lines solution of the korteweg-de vries equation for small times. Int. J. Contemp. Math. Sciences, 1:639-650, 2006.

[14]. Quan Shen. A meshless method of lines for the numerical solution of kdv equation using radial basis functions. Eng. Anal. Bound. Elem. , 33:11711180, 2009.

[15]. Sirajul Haq, Marjan Uddin . Rbfs approximation method for kawahara equation Eng. Comput, 217:2404-2413, 2010.

[16]. M. Garshasbi, M. Khakzad, the RBF collocation method of lines for the numerical solution of the CH-$\gamma$ equation, Advance research in Dynamical and control systems, Vol. 7:65-83, 2015.

[17]. Zong-min Wu. Radial basis function scattered data interpolation and the meshless method of numerical solution of pdes. J. Eng. Math. , 19:1-12, 2002.

[18]. Zong-min Wu, Robert Schaback. Local error estimates for radial basis function interpolation of scattered data. IMA J. Numer. Anal. , 13:13-27, 1992.

[19]. Satish C. Reddy, Lloyd N. Trefethen. Stability of the method of lines. Numer. Math. , 62:235-267, 1992.

# Crushing Circuit Design for Processing of North Waziristan Copper Ore

Sajid Khan[1]*, Ishaq Ahmad[1]

*[1]Dept. of Mining Engineering, University of Engineering and Technology, Peshawar-25120, Pakistan*
*\*Corresponding author*

*Email*: engrsajid0604@gmail.com

## Abstract

The material parameters required for the design of a crusher for mineral processing operations are type of ore, its strength, abrasiveness, density, moisture and clay contents. The characteristics of North Waziristan (NW) copper ore were studied to select suitable crusher type and to design the crushing plant flowsheet. Crusher types usually classified are primary, secondary and tertiary which is normally selected on the basis of material parameters. However, the size of the crusher is identified by the plant throughput, its feed and product size. A detailed discussion on the design parameters of crushers have been given. The moisture and clay contents of the NW copper ore are negligible. Therefore, there is no need of the addition of drying or washing units for the ore before crushing. The ore can be classified as soft in nature on the basis of its strength characteristics. The run-of-mine size of NW copper ore determined was 500 mm and the feed size required for the tumbling mill i.e. grinding operation in average is 12.5 mm. The reduction ratio of one crushing stage is usually 3 to 6. Therefore, 2 to 3 crushing stages are required to obtain the desired feed size for tumbling mills. On the basis of material properties jaw or gyratory crushers could be used for primary operations whereas roll or cone crushers are recommended for secondary and tertiary operations.

**Keywords:** Material parameters, design, ore, strength, North Waziristan copper, plant through put.

## 1. Introduction

There are a number of copper bearing minerals available in nature but only a few of them are viable sources to metal. The most important copper ores are chalcopyrite ($CuFeS_2$), Chalcocite ($Cu_2S$), Malachite [$CuCO_3.Cu(OH)_2$], Bornite ($Cu_5FeS_4$), Covellite (CuS) and important associated gangue minerals are quartz, rock matrix, dolomite, calcite, rhodochrosite, siderite, barite and zeolite. In general, copper sulphide ores are found in association with intrusives of quartz, monazite and related rocks less commonly with mafic intrusives. However, the mineral content and associations depend on the types of ore deposit found in varying geologic conditions. Generally types of copper ore along with associated impurities determines the method of treatment. Oxidized ores are usually leached or directly smelted. Acid leaching or specific solvent solutions is used for carbonate ore [1].

Huge resources of copper ore are available in North Waziristan (NW) agency at places like Degan and Shinkai which is situated in Federally Administrated Tribal Area (FATA) of Pakistan. The FATA Development Authority has confirmed a minimum of 122 million tons of inferred reserves of Cu in NW area [2, 3]. The NW copper ore contains chalcopyrite as the ore mineral having copper grade varying from 0.386% to as high as 2% [2-5] while pyrite ($FeS_2$), pitchlimonite ($Fe_2O_3.$ $H_2O$), bronchanitite [$Cu_4SO_4(OH)_6$], chamosite [$(Mg,Fe)_3Fe_3(Al,Si_3)O_{10}(OH)_8$], nimite [$(Mg, Ni, Al)SiO_2 (OH)$] and quartz ($SiO_2$) are gange minerals.

Crushing is the first stage in the process of comminution to reduce the run-of-mine ore to a size suitable for downstream operation followed by grinding to liberate valuable mineral from the gangue. The crusher can be divided into primary, secondary and tertiary depending upon the size of the feed, product and throughput required. Primary crusher can handle run-of-mine ore up to 1.52 m and these are

reduced to 10-20 cm sizes in primary crushing stage [6]. The opening feed of any crushing operating in the world is 1.83m Traylor crusher [7]. Primary crusher is design to operate 75% of the available time because of the mechanical delays or insufficient supply of the material [8].The primary crusher has a maximum capacity of 12000 mtph. It is operated in open circuit. The reduction ratio of primary crusher is about 8 to 1. Product size material should be removed by installing scalping screen before primary crusher to increase the overall capacity [7]. A secondary stage is included to crush the primary product material and to produce the final product. The feed to the secondary crusher is normally less than 15cm [6]. However if the ore is slippery and tough then the tertiary crushing stage may be replaced by Coarse grinding in Rod Mills. In order to optimize the operation vibrating screens are placed ahead of the secondary crusher to remove product size material, or scalp the feed and by this process capacity of the secondary crusher is increased. For non steaky ore there is no need of including a washing stage. For secondary crushing application the standard cone crusher is traditionally selected in crushing plant flowsheet. Secondary crusher product is feed to the tertiary crusher to produce the final product. The average size of the feed to the tertiary crusher is about 37 mm and the product size is about 12mm [9]. In order to maximize the operation crusher is operated in close circuit with vibrating screens. Product of the secondary and tertiary crusher is collected and transported to the screen through conveyer belt. Undersized of the screen is send to the fine ore storage and oversize is send back to tertiary crusher.

A lot of experimental work has been done on laboratory scale and on pilot scale on the upgradation of NW chalcopyrite and determination of flotation parameters in the Department of Mining Engineering, University of Engineering and Technology (UET), Peshawar, Pakistan [10 - 13]. However, the efforts have not been made to design a process plant Flowsheet for industrial applications. The designing

of a crusher circuit is the first stage to have a complete process plant Flowsheet. The objectives of the current research work is to determine various parameters necessary for the design of a crushing plant and propose a scheme for the selection of most suitable crushing circuit for the crushing of NW copper ore.

Method

Samples of copper ore were collected from North Waziristan Degan copper deposit having coordinates 32° 57' North, 69° 52' East. These sample were brought to the Mining Department, UET Peshawar. Strength, density, moisture content and clay content were determined. On the basis of these parameters suitable crusher is selected and on the basis of feed size, product size and and throughput size of the crusher is selected.

Crusher Selection Parameters:

Effect of Strength on Crusher Selection:

Strength is the one of the most important parameters which effect the selection of crushers. From the strength of the material one can determine which crusher is suitable for primary crushing. Table 1 shows that the Gyratory crusher, DT Jaw crusher can handle a material having strength upto 600 Mpa. ST jaw, low speed sizer, impactor, hammermill and feeder breaker has a compressive strength of 200 Mpa. While double roll has the lowest strength of 100 Mpa.

In order to determine the compressive strength of the ore, core were taken from the samples using Core drilling machine these samples were then shaped and cut with the help of core cutting machine and five samples were prepared having dimensions of 10 cm × 5 cm (length × diameter ). Each core sample were placed in the Uniaxial compressive Testing machine to determine unconfined compressive strength (UCS) of core sample using the formula.

$$UCS = F/A \qquad (1)$$

In eq. 1, $F$ is applied load in KN and $A$ is the cross sectional area in m$^2$ of the core sample

### 1.1.1. Effect of Clay Content on Crusher Selection

Material like clay or sticky clay causes difficulty for almost every type of crusher. The crushing action of gyratory, jaw and double Roll crushers is by compression. These crusher will pack if the feed contain significant amount of clay. In gyratory and jaw crusher the material flow through by the action of gravity. When the clay packs in the chamber of crusher the throughput of the crusher is reduced and sometimes completely stopped. Double rolls crusher stop crushing in severe cases when the clay is packed between the teeth. For clay bearing material impactor and hammermills cannot be used as the chamber will pack quickly with the clay and stop impact crushing from taking place.

Single toggle jaw and feeder breakers represent a fair to good alternatives. The only machine that can handle clay easily is the low speed sizer as there is no impact that will cause the material to pack in the chamber.

For determination of clay content in the ore X-Ray Diffraction (XRD) analysis were carried out. Five samples of copper ore were passed through a 300 mesh (53um) British Standard Sieve (BSS). These sample were then run through X-ray diffraction unit Cu.K$\infty$ .radiation. The peaks appeared at $30^0$ values and onwards. The values at varying intensities were converted into lattice space (d in $A^0$ units) with the help of conversion charts mineral were identified. The result of XRD confirmed that chamosite, Nimite, quartz and chalcopyrite as major minerals. Other miner mineral were also confirmed but there is no clay content found in the result.

### 1.1.2. Effect of Mining Method on Crusher Selection

In addition to selection criteria the crusher for underground services must be design to handle blocky

and hard material. Steel in the form of roof bolts and drill steel and typically will be able to operate in an area of limited head room.

Gyratory crusher are mainly used for surface plant operation. But a few of them are used underground. Can handle steel but the bottom of the crusher incorporates arms that become a resting-place for steel. Table 1 shows that The DT and ST jaw crushers provide very large feed opening for crushing block cave materials. The jaw crusher can easily be sectionalized for underground installation. These machine can handle the steel quite well. The feeder breaker is design to operate underground efficiently. Due to its low reduction ratio these machine can give coarse product when crushing blocky material. The low speed sizer can provide distinct advantages in underground services and has the lowest headroom design available. The machine can handle clay quite well and is not adversely affected by water. The machine will handle large blocky ore.

### 1.1.3. Effect of Abrasiveness on Crusher Selection

The abrasiveness of a material has an important influence on the selection of the crusher. Hard ores are generally more abrasive than soft ores. But exceptions occur when the ore contain certain silica minerals or rich of mica. Rocks containing quartz, feldspar show high wear rates. Table 1 show that gyratory and DT jaw crusher can be used for material having high abrasion index upto 35000(Burbank). ST Jaw and Low Speed Sizer can be used for material having abrasion index upto 800(Burbank). Hammermill, Feeder Breaker and Double Roll can handle abrasiveness of a material upto 400(Burbank). While Impactor can handle the abrasiveness of a material upto 300(Burbank).

**Table 1. CRUSHER SELECTION PARAMETERS [9]**

| Crusher type | Compressive Strength (Mpa) | High Clay material | Underground Service | Abrasion Index (Burbank) |
|---|---|---|---|---|
| **Gyratory** | 0-600 | Poor | Good | 0-35000 |
| **DT Jaw** | 0-600 | Poor | Good | 0-35000 |
| **ST Jaw** | 0-200 | Fair | Good | 0-800 |
| **Double Roll** | 0-100 | Poor | Fair | 0-400 |
| **Low Speed Sizer** | 0-200 | Excellent | Excellent | 0-800 |
| **Impactor** | 0-200 | Poor | N/A | 0-300 |
| **Hammermill** | 0-200 | Poor | N/A | 0-400 |
| **Feeder Breaker** | 0-200 | Fair | Excellent | 0-400 |

### 1.1.4. Effect of Ore Density

Ore density has an important effect on specific throughput of the crusher. Material having high density results in higher specific throughput rates. In order to determine the average density of the sample. The weight of the sample was 10g, 20g and 30 g. Initial volume of the water was noted for all the 3 samples then after dipping the samples the final volume is noted. Using density formula average density of the sample were determined.

### 1.1.5. Effect of Moisture

High moisture content fines causing plugging of the equipment and lead to higher equipment downtime. Small amount of moisture do not effect wear. The wear rates mostly depend on the amount of moisture in the feed it also depend on the mineralogical composition of the material. Excess amount of moisture reduces throughput and causes problem with smooth rolls, reducing friction on the rolls and in the bed particles can cause slippage. Copper ore can be treated with up to 3 to 5 % moisture. However there is a critical level of moisture that should not be exceed [14]. For determination of moisture content fresh sample were taken. These sample were crushed in the Rolls Crusher and then it was grind in the disc crusher. Three samples of 1 g each were placed in the Muffle furnace at 1050 for 1 hour.

### Crusher Size Parameters

The feed size to the crusher depend on different mining methods and different ores. The crusher selected must be sized for the largest pieces that is expected from the mine and also for the throughput. A balance is often needed to ensure that size of the crusher and plant capacity are matched. Smaller the size of the feed ore smaller the dimension of the crusher.

Table 2 shows that the maximum feed size for the gyratory, DT jaw, ST jaw, double roll, impactor, feeder breaker is in the range of 1500 mm. The maximum feed size for the low speed sizer is in the range of 2000 mm. While for hammermill it is 2500 mm.

The end product size of copper ore will determine the number of crushing stages and type of crusher to be used. The gyratory crusher and low speed sizer can give the product size in the range of 150-300 mm. For DT jaw, ST jaw, impactor, hammermill has the same product sizes in the range of 100-300 mm. Feeder breaker can give the largest product size in the size range of 250-400 mm.

Capacities up to 10,000 Mtph can be achieved in gyratory crusher. DT and ST crusher can handle capacities up to 1000 Mtph. Double roll has a capacity up to 3000 Mtph. Low speed sizer has the highest

capacity in the range of 12000 Mtph. Impact or and hammermill has capacities of 2500 Mtph, while feeder breaker has capacity up to 2000 Mtph.

**Table 2. PRIMARY CRUSHER SIZE PARAMETERS: [9]**

| Crusher | Max Feed Size (mm) | Product Size (mm) | Max Capacity (Mtph) |
|---------|--------------------|--------------------|---------------------|
| **Gyratory** | 1500 | 150-300 | 10,000 |
| **DT Jaw** | 1500 | 100-300 | 1000 |
| **ST Jaw** | 1500 | 100-300 | 1000 |
| **Double Roll** | 1500 | N/A | 3000 |
| **Low Speed Sizer** | 2000 | 150-300 | 12000 |
| **Impactor** | 1500 | 100-300 | 2500 |
| **Hammermill** | 2500 | 100-300 | 2500 |
| **Feeder Breaker** | 1500 | 250-400 | 2000 |

**Results and Discussions**

The test results of the strength and other characteristics of the NW copper ore are given in table 3.

Table 3: NW copper ore characteristics.

| Parameter | Value |
|-----------|-------|
| Maximum Feed Size | 500 mm |
| Moisture content | 0% |
| Average density | 2.82 g/cm3 |
| Hardness | 3.3-3.8 |
| Compressive Strength | 43 Mpa (6234 Psi) |
| Abrasion index | 550-600 (Burbank) |
| Clay | 0 % |

Table 3 shows that the NW copper ore is soft in nature and has low strength of only 43 MPa. Therefore, in comparison to the compressive strength of table 1, any crusher type can be selected for the primary crushing of NW copper ore. Table 3 shows that the moisture content is negligible and the ore is non sticky and therefore, moisture content of the ore does not cause any problem e.g. by choking the machine or reduce throughput. It is clear from the table 3 that the clay content is negligible so there is no need of addition of any washing and drying unit before crushing. As the copper ore contain silica in the form of quartz which increase the abrasiveness of the material. The abrasion index of the NW copper ore is between 550 - 600 (Burbank) which imposes limits on the selection of a crusher having abrasion index of less than 600 (Burbank).

Therefore, a as per limitation of the abrasion index of NW copper ore, the only crusher that can be used for crushing is Gyratory, DT Jaw, ST Jaw and Low Speed Sizer. The density of the ore is determined to be 2.82 g/cm3 which is not too high to effect the throughput of the plant.

Climate condition also effects the selection of a crushing plant flowsheet. In a dry warm climate condition the crushing plant can be designed for an

outside installation while in wet condition it may be installed inside for operator accessibility and equipment protection. Very cold climate condition will favor that the plant should be enclosed for operator accessibility which will in turn increase the capital and operating cost. In a poor climate condition installation of a semi-autogeneous grinding (SAG) mill grinding circuit requiring only a single stage of primary crushing to prepare the ore feed size will be better than three crushing stages. Operating cost for both circuit may be similar but with the elimination of crusher building and ancillary equipment will reduce capital cost significantly favoring the selection of SAG mill.

Jaw crusher is recommended for primary crushing if t/h is less than 161.7 (gape in meter)2 for both surface and underground operation but if it is more than 161.7 (gape in meter)$^2$ then use gyratory crusher in open circuit. The required daily production is about 2000 tons/day and working hours is 16 hours/day. The crushing plant need to have a capacity around 125 t/h to meet the daily requirement of 2000 tons/day. These condition favor to use a jaw crusher for primary crushing.

The maximum fragment (feed size for primary crusher) size of the NW copper after blasting is 500 mm and the capacity is 125 t/h. The feed size and throughput will determine the size of the crusher to be selected. The end product size required for tumbling mill is around 12.5 mm which determines the number of crushing stages to be included.

Figure 1 and 2 show proposed flowsheets for the crushing plant of NW copper. These flowsheets have been developed in the mineral processing simulation tool ModSim student version [15]. Figure 1 shows that for a low tonnage average feed size of 12.5 mm to rod mill/ ball mill or single stage ball mill application will require two stage crushing circuit using a primary jaw crusher having dimension 2520× 1840 ×2303 with a reduction ratio 7:1 and a cone crusher having reduction ratio 6:1 with vibrating screen would be appropriate.

Figure 2 shows that for a similar, high tonnage operation will require a three crushing stage circuit using jaw crusher for primary crushing, standard cone crusher for secondary crushing and using shorthand cone crushers for tertiary crushing in closed circuit to produce the 12.5 mm product.

In order to increase the overall capacity of the plant, scalping screen have been added before primary crusher.
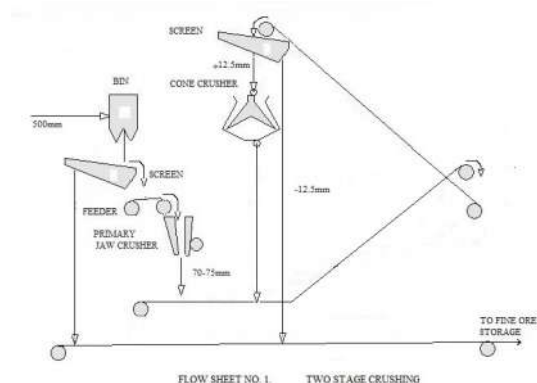


Figure 1 Two Stage Crushing circuit
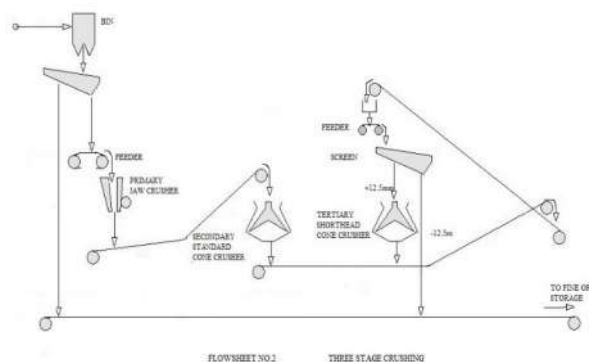


Figure 2 Three Stage Crushing Circuit

## 2. Conclusions

Crushers were selected and the flowsheets were proposed for the crushing operations of NW copper ore. On the basis of laboratory investigation, the comparison of results with various design parameters available in literature, keeping in view climate condition of the area and process economy Jaw Crusher is recommended for primary crushing operation having dimension 2520 × 1840 × 2303 for 500 mm feed size and at the rate of 125 t/h capacity. Two different flowsheets have been proposed for the crushing operations for low (upto 2000 t/d) and high (more than 2000 t/d) plant capacity. For coarser feed sizes (greater than 150 mm) and for poor climate conditions, it is recommended to use SAG mills in place of secondary and tertiary crushers.

## 3. References

[1] J. Meadl, J., and M.B. Alan, Economic Mineral Deposits, third ed (1981) 312-317.

[2] S.M Badshah, Development potential of Waziristan copper, Record of FATA Development Corporation, 11, 2 (1983).

[3] S.M Badshah, Development potential of Waziristan copper, Record of FATA Development Corporation, (1985)

[4] Z. Wang, Lecture on Distribution and Metallogenic Models of Large Copper Deposit of The World in North Waziristan Copper Ore, at UET Peshawar (1996).

[5] Khan et al, Flotation studies of North Waziristan copper ore, proceedings of Seminar on prospects and problems of mineral based industry in Pakistan, University of Engineering and Technology Peshawar (1984).

[6] B.A.Wills, N. Munn, Will's Mineral Processing Technology, seven ed. 2006.

[7] W. Ronald. Utley, Selection and Sizing of Primary Crushers, Mineral Processing Plant Design Practice and Control, Proceedings, volume 1.

[8] F.M. Lewis, J.L. Coburn, R.B. Bhappu, Comminution: A guide to size-reduction system design. Min.Engng, 28(sept.), 29. (1976).

[9] K. Major, Types and characteristics of crushing equipment and circuit flowsheets, Mineral Processing Plant Design Practice and Control, Proceedings, volume 1.

[10] M.K. Mansoor, M.R, E. Khan, Flotation of copper minerals from North Waziristan copper ore, On Pilot –Scale, Quartly science vision Vol.6(1) july-September, 2000.

[11] M.K. Mansoor, R. Mazhar, A. Siddique, Mineralogical examination and determination of optimium mesh of grind of north Waziristan copper ore (shinkai area), j. eng and appl. Sci. Vol. 18 No. 2 july-Dec.

[12] M. Rafiq, Pilot scale studies of North Waziristan copper ore, MSc Thesis, at UET Peshawar Mining Department (2001).

[13] I. Ahmad, Upgradation of chalcopyrite ore by hot flotation and using mixed collectors techniques, Msc Thesis, at UET Peshawar Mining Department (2004).

[14] R. Klymowsky, P. Norbert, K. johann, B. Egbert, 'Selection and sizing of high pressure grinding rolls', Mineral Processing Plant Design Practice and Control, Proceedings, volume 1.

[15] Modular Simulator for mineral processing plants, http:// www.mineraltech.com/MODSIM.

# Numerical approximation of rapidly oscillatory Bessel integral transforms

**Sakhi Zaman[1], Siraj-ul-Islam[1]**
*[1]Department of Basic Sciences & Islamiat,*
*University of Engineering & Technology Peshawar, Pakistan*
*Email: sakhizaman75@yahoo.com*

**Abstract**

We present a new procedure of Levin type that based on Gaussian radial basis function for evaluation of rapidly oscillating integrals that contains first kind of the Bessel function $J_v(\omega x)$. Multi-resolution quadrature rules like hybrid and Haar functions are used in the context of Bessel oscillatory integrals as well. Numerical test problems are solved to verify the accuracy and efficiency of the new methods.

**Key words**: Rapidly oscillatory integrand, Bessel Function of the first kind, Gaussian RBF, Hybrid and Haar functions.

## Introduction

Bessel oscillatory integrals have applications in many areas of science and engineering such as astronomy, optics, electromagnetics, seismology image processing etc. [2, 13]. In the present paper, we have evaluated the Bessel type of oscillatory integrals of the form:

$$I[g, \kappa]$$
$$= \int_c^d g(x) J_v(\omega x) dx, \qquad (1)$$

where g (x) is non-oscillatory smooth function and $J_v(\omega x)$ is the first kind of Bessel function with $v > 0$, order of the Bessel function.

Many accurate methods have been developed for numerical evaluation of the integrals of the form (1) such as Levin collocation method [7, 8, 11], generalized quadrature rule [4-6, 12], Homotopy perturbation method [2, 3] and some more.

Levin [7] proposed a new approach for numerical evaluation of Bessel type of oscillatory integrals of the form (1). In the same paper, he extended the method to the solution of integrals with Bessel-trigonometric and square of the Bessel oscillatory integrands. In the next paper [8], Levin calculated some theoretical error bounds for the method given in [7].

S. Xiang [11] investigated some new theoretical error bounds for the method reported in [7] with asymptotic order of convergence $O\left(\kappa^{-\frac{5}{2}}\right)$.

In this paper, we have used collocation with Gaussian RBF as basis function (GRBF) instead of monomials [7,

11]. The asymptotic order of convergent of the proposed method GRBF is $O\left(\kappa^{-\frac{7}{2}}\right)$. Multi-resolution quadrature rules like hybrid and Haar functions [1] are used for evaluation of the integrals (1) as well.

## Gaussian RBF based quadrature

According to this procedure, a new technique is proposed to evaluate a class of oscillatory integrals of the form:

$$\int_c^d \sum_{j=1}^n g(x) \Upsilon(\kappa, x) dx = \int_c^d G(x) . \Upsilon(\kappa, x) dx,$$
$$0 \le c \le x \le d, \qquad (2)$$

where G(x) and $\Upsilon(\kappa, x)$ are vectors of the non-oscillatory and the oscillatory functions respectively. The derivative of $\Upsilon(\kappa, x)$ is $\Upsilon'(\kappa, x) = B(\kappa, x) \ \Upsilon(\kappa, x)$, where $B(\kappa, x)$ is $n \times n$ matrix of non-oscillatory functions.

An approximate solution $\tilde{S}(x) = \sum_{i=1}^m w_i^{[j]} \varphi_i(x), i = 1, 2, \dots, n$ is supposed to satisfy the following ODE:

$$\pounds[S(x)] = G(x), \qquad 0 \le c \le x \le d, \qquad (3)$$

where

$$\pounds[S(x)] = S'(x) + B(\kappa, x) S(x).$$

Then the unknown coefficients $w_i^{[j]}$, $i = 1, 2, \dots, m, j = 1, 2, \dots, n$ can be determined by the interpolation condition:

$$\pounds[\tilde{S}(x_k)] = G(x_k), \qquad k = 1, 2, \dots, m. \qquad (4)$$

Thus integral (1) can be evaluated as:

$$GRBF = \int_c^d [\tilde{S}'(x) + B(\kappa, x) \tilde{S}(x)] . \Upsilon(\kappa, x) \ dx$$
$$= \int_c^d [\tilde{S}(x) . \Upsilon(\kappa, x)]' \ dx$$
$$= \tilde{S}(d) . \Upsilon(\kappa, d) - \tilde{S}(c) . \Upsilon(\kappa, c).$$

Particularly, to compute the integral $I[f, \kappa] = \int_c^d g(x) J_v(\omega x) dx$, we assume

$$B(\kappa, x) = \begin{pmatrix} \frac{v-1}{x} & -\kappa \\ \kappa & \frac{-v}{x} \end{pmatrix}, \quad \mathbf{Y}(\kappa, x) = \begin{pmatrix} J_{v-1}(x) \\ J_v(x) \end{pmatrix} \quad \text{and}$$

$$\mathbf{G}(x) = \begin{pmatrix} 0 \\ g(x) \end{pmatrix}.$$

In this case, the approximate solution $\tilde{S}(x) = \sum_{i=1}^m w_i^{[j]} \varphi_i(x), i = 1,2$ is supposed to satisfy the ODE (4) and then we can find the values of the unknown coefficients $w_i^{[j]}$, $j = 1,2$, $i = 1,2,...,m$.

On substituting the values of $B(\kappa, x)$, $S(x)$ and $\mathbf{G}(x)$ in (4), we obtain a system of coupled equations;

$$[\varphi'(x) + \frac{v-1}{x} \varphi(x)] w^{[1]} + \kappa \varphi(x) w^{[2]} = 0$$

$$-\kappa \varphi(x) w^{[1]} + [\varphi'(x) - \frac{v}{x} \varphi(x)] w^{[2]} = g(x). \quad (5)$$

The (5) can then be written in matrix form as:
$$A\beta = G,$$

where

$$\beta = \begin{pmatrix} w^{[1]} \\ w^{[2]} \end{pmatrix}, \qquad \mathbf{G}(x) = \begin{pmatrix} 0 \\ g(x) \end{pmatrix},$$

and $\mathbf{A}$ is a $2m \times 2m$ square matrix. $\beta$ and $\mathbf{G}(x)$ are the column matrices of order $2m \times 1$.

An accurate approximate solution of the ODE (3) is the aim of this paper. For this purpose, Gaussian RBF $\varphi(r, c)$ is used as basis function and is defined by;

$$\varphi(r, c) = e^{-\frac{r^2}{c^2}}, \quad (6)$$

and

$$\varphi'(r, c) = \frac{-2r}{c^2} e^{-\frac{r^2}{c^2}},$$

where c is the shape parameter of the Gaussian RBF and $r = \sqrt{(x - xc)^2}$, xc,s are the centers of Gaussian RBF. The accuracy as well as the condition number of the system (5) depend upon the value of c. Therefore, an optimal value of the shape parameter is still an open problem. In this paper, an algorithm [10] is used for an optimal value of c. In the algorithm [10], the value of c is changing with change in the nodal points as well as the frequency parameter $\kappa$. In this paper, we have used $c_L = 0$ and $c_U = 3$ for finding c in the algorithm.

Solving the system of equation (5) for the unknown coefficient matrix $\beta$ and fin d the approximate solution $\tilde{S}(x)$.

**Quadrature based on hybrid and Haar functions**

In this section, multi-resolution quadrature rules like hybrid functions (HFQ) and Haar wavelets (HWQ) are briefly described. The detail description and proofs of the formulae for HFQ and HWQ are given in [1, 9].

In this paper we have used hybrid function based quadrature of order m = 8 (HF Q8) for evaluating the integral of the form: $I[f] = \int_a^b f(x)dx$. Formula for the HFQ8 is given by

$$HFQ8 = \frac{8h}{1935360} \sum_{k=1}^N [295627 f\left(a + \frac{h}{2}(16k - 15)\right) + 71329 f\left(a + \frac{h}{2}(16k - 13)\right) + 471771 f\left(a + \frac{h}{2}(16k - 11)\right) + 128953 f\left(a + \frac{h}{2}(16k - 9)\right) + 128953 f\left(a + \frac{h}{2}(16k - 7)\right) + 471771 f\left(a + \frac{h}{2}(16k - 5)\right) + 71329 f\left(a + \frac{h}{2}(16k - 3)\right) + 295627 f\left(a + \frac{h}{2}(16k - 1)\right), \quad (7)$$

where $h = \frac{b-a}{8n}$.

Similarly, the formula of Haar wavelet based quadrature for computing the integral $I[f] = \int_a^b f(x)dx$ is given by $HWQ = h \sum_{k=1}^N f(x_k)$
$$= h \sum_{k=1}^N f(a + h(k - 0.5)), \quad (8)$$
where $h = \frac{b-a}{2M}$ and $N = 2M$.

**Note**: In case of Bessel type of oscillatory integrals, we take $f(x) = g(x) J_v(\omega x)$.

**Convergence**

Some theoretical results for convergence of the proposed methods are calculated. First, we consider the error bounds of the multi resolution methods HFQ and HWQ:

**Quadrature based on hybrid and Haar functions**

If a = 0, b = 1, n = 4 and $h = \frac{b-a}{8n}$, then the error bound of formula (7) is calculated as:

$$|Error| = \frac{h^9}{4.54} f^{(8)}(\xi), \quad (9)$$

where $\xi \in [a, b]$.

Similarly, for the integral $I[f] = \int_a^b f(x)dx$ and 2M = 4, then the error bound for the HWQ is defined as:

$$|Error| = \frac{h^3}{6} f''(\eta), \quad (10)$$

where $\eta \in [a, b]$.

## Gaussian RBF based quadrature

**Theorem 1.** Let $B(\kappa,x) = (\frac{1}{\kappa}A(\kappa,x))^{-1}$ exists and $G(x), A(\kappa,x), \Upsilon(\kappa,x) \in C^m[a,b]$ . Also $B(\kappa,x)$, $B^{-1}(\kappa,x)$ and their 2m derivatives are uniformly bounded on [a, b], then the error bound for computing the integral (1) by the Gaussian RBF based quadrature rule is given by

$$E(\kappa) = |I(g) - GRBF| = \mathrm{O}\left(\frac{h^{m-2}}{\kappa^{7/2}}\right).$$

## Numerical results

In this section, some test cases are considered to verify the accuracy and efficiency of the proposed methods. The real solution of the test problem is obtained from **MAPLE 15**. Results in terms of absolute errors (Error) are obtained.

**Test problem 1.** Consider the computation of the integral [2]

$$I_1[f,\kappa] = \int_1^2 \frac{1}{1+x^2} J_v(\omega x)dx,$$

by the Gaussian RBF based quadrature and multi-resolution quadrature rules like HFQ and HWQ. Numerical results related to the frequency parameter obtained from the three methods are shown in Fig.2. The proposed method GRBF improves the accuracy as the frequency $\kappa$ is increasing, while the multi-resolution methods HFQ and HWQ fail to retain the desired accuracy as shown in Fig. 2. The multi resolution methods give the desired accuracy at finer nodes which becomes computationally extensive as shown in Fig. 4. From both the figures, it is clear that the new method, GRBF retains the desired accuracy for high frequencies at coarser grid points.

It is clear from the Fig. 1 that the new method GRBF is accurate with asymptotic order of convergence $\mathrm{O}\left(\kappa^{-\frac{7}{2}}\right)$ at small nodes i.e. m = 10. The oscillatory behavior of the integrand is shown in Fig. 3 for $\kappa = 1000$. In last, the new method is tested for high frequency value. The results are shown in the table 1. It is shown in the table that the method GRBF is accurate and efficient at small number of nodal points.

| $\kappa$ | m = 10 | m = 20 | m = 30 |
|---|---|---|---|
| $10^2$ | $1.2418$ $e^{-11}$ (0.0209s) | $1:5043$ $e^{-011}$ (0:0981s) | $8:2876$ $e^{-012}$ (0:1539s) |
| $10^3$ | $3:5427$ $e^{-13}$ (0:0316s) | $3:2348\,e^{-012}$ (0:0917s) | $4:2022$ $e^{-014}$ (0:2088s) |
| $10^4$ | $1:1548$ $e^{-15}$ (0:0 267s) | $3:9864$ $e^{-016}$ (0:1022s) | $2:8363e^{-016}$ (0:1742s) |
| $10^6$ | $3:5506$ $e^{-19}$ (0:0 404s) | $7:3052$ $e^{-020}$ (0:0969s) | $2:8113$ $e^{-019}$ (0:1289s) |

**Table 1**: Absolute error and CPU time (in parenthesis) produced by the GRBF.

**Figure 1**: Absolute error scaled by $\kappa^{7/2}$ of GRBF
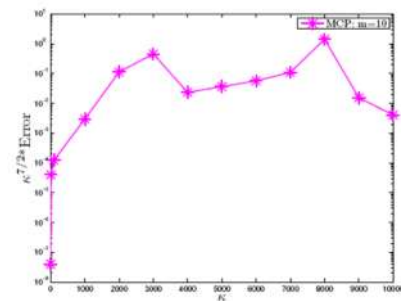


for m = 10.

**Figure 2**: Absolute error of HFQ, HWQ and GRBF
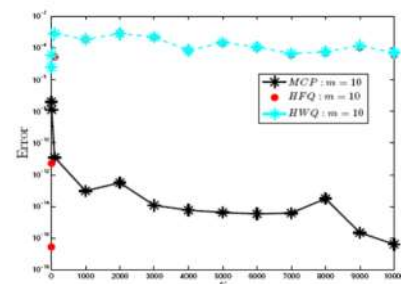


for m=10.

**Figure 3**: Oscillatory behaviors of the integrand for

$\kappa = 1000.$
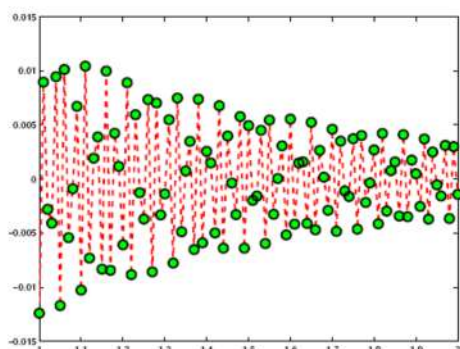


**Figure 4**: Absolute error of HFQ, HWQ and GRBF for $\kappa = 1000$ .
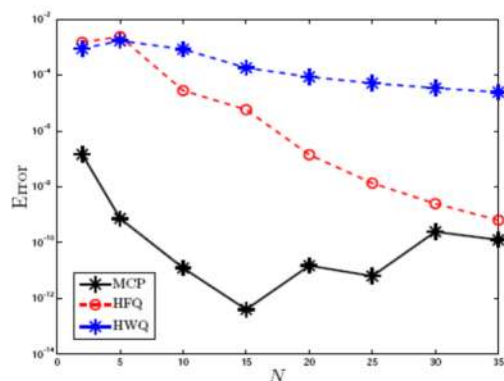


**Closing remarks**

In this paper, a collocation method based on Gaussian RBF and multi-resolution quadrature rules like HFQ and HWQ are used for numerical evaluation of Bessel type of oscillatory integrals. Some theoretical error bounds of the new methods are found. Test problem shows an improved results of the new methods.

**References**

[1] I. Aziz, Siraj-ul-Islam, and W. Khan. Quadrature rules for numerical integration based on Haar wavelets and hybrid functions. Comput. Math. Applic., 61:2770-2781, 2011.

[2] R. Chen. Numerical approximations to integrals with a highly oscillatory Bessel kernel. Appl. Numer. Math., 62(5):636-648, 2012.

[3] R. Chen and X. Liang. Asymptotic expansions of Bessel, anger and weber transformations. J. Math. Analy. Appl., 372(2):377-389, 2010.

[4] K..C. Chung, G.A. Evans, and J.R. Webster. A method to generate generalized quadrature rules foroscillatory integrals. Appl. Num. Math., 34(1):85-93, 2000.

[5] G. A. Evans and K.C. Chung. Some theoretical aspects of generalized quadrature methods. J. Complexity, 19(3):272-285, 2003.

[6] G.A. Evans and J.R. Webster. A high order, progressive method for the evaluation of irregular oscillatory integrals. Appl. Numer. Math., 23(2):205-218, 1997.

[7] D. Levin. Fast integration of rapidly oscillatory functions. J. Comput. Appl. Math., 67(1):95-101, 1996.

[8] D. Levin. Analysis of a collocation method for integrating rapidly oscillatory functions. J. Comput. Appl. Math., 78(1):131-138, 1997.

[9] Siraj-ul-Islam, I. Aziz, and F. Haq. A comparative study of numerical integration based on Haar wavelets and hybrid functions. Comput. Math. Appl., 59(6):2026-2036, 2010.

[10] Siraj-ul-Islam and S. Zaman. New quadrature rules for highly oscillatory integrals with stationary points. J. Comput. Appl. Math., 278:75-89, 2015.

[11] S. Xiang. Numerical analysis of a fast integration method for highly oscillatory functions. BIT Numer. Math., 47(2):469-482, 2007.

[12] S. Xiang and W. Gui. On generalized quadrature rules for fast oscillatory integrals. Appl. Math. Comput., 197(1):60-75, 2008.

[13] Z. Xu and S. Xiang. On the evaluation of highly oscillatory finite Hankel transform using special functions. Num. Algo., 72:1-20,

# Numerical Solution of Inverse Heat Problems

Samreen Ismail[1,*], Siraj-ul-Islam[1]

[1]*Department of Basic Sciences & Islamiat, University of Engineering & Technology Peshawar.*

***Email**: *samreen.rules@yahoo.com*

## ABSTRACT

Inverse heat problems are known to be ill-posed which make it difficult to solve. In this paper we develop a meshless method for numerical solution of an inverse heat problem. The numerical scheme is developed by using MQ radial basis function collocation method which can recover the time dependent heat source as well as right boundary condition. Example of inverse heat problem verifies the accuracy and efficiency of the method with mild to large noise.

**Keywords:** Meshless collocation method, Radial basis function, Inverse heat source problem.

## INTRODUCTION

In this paper we develop a numerical scheme by using meshless method based on MQ radial basis function for the solution of 1- dimensional time dependent inverse heat problems (IHP),

$$\frac{\partial w(y,t)}{\partial t} = \frac{\partial^2 w(y,t)}{\partial y^2} + F(t), \ (y,t) \in \Omega := \{0 < y < l, 0 < t \le t_f\}, \tag{1}$$

with initial and left boundary condition

$$w(y,0) = I(y),$$
$$w(0,t) = w_0(t),$$
$$w_y(0,t) = Q_0(t),$$

where $F(t)$, the heat source which depends on time only is unknown and the right boundary condition $w(l,t) = R(t)$, is also unknown. For the identification of these unknowns, an extra information is provided as $w_y(l,t) = Q_l(t)$, which is a measured data and so it must contains some noise.

Inverse heat problems are experienced in almost every branch of science and engineering. Specific applications can be found in mechanical, aerospace, chemical and nuclear engineerings. Engineers, mathematicians, astrophysicists and statisticians are all interested in this subject, each group with different applications in mind.

Difficulties experienced in solving IHP. Mathematically IHP are ill-posed that is there solution may become unstable due to measurements used in analysis. Although for the solution of such problems many work have been done with different numerical schemes. The difficulties in numerical computation of inverse heat problem (IHP) have not completely been overcome yet.

## SOLUTION PROCEDURE USING RADIAL BASIS FUNCTION (RBF)

RBF a function with real values is a meshless method. Its values are actually the distance from the origin $\varphi(x) = \varphi(\|x\|)$ or distance from center $\varphi(x,c) = \varphi(\|x-c\|)$ [4]. Any function with this property is a radial function. Some types of RBFs are: Multi quadric (MQ), Inverse multi quadric (IMQ), Inverse quadratic (IQ) and Gaussian (GS) [2]. We will solve our problem with MQ RBF. The MQ RBF is defined as, $\varphi(r,c) = \sqrt{r^2 + c^2}$, where $r = \|x - x_i\|$ and $c$ is a shape parameter, the shape parameter play a role of agent controlling shape of the RBFs.

RBF uses the approximation of the form

$$u(x) = \sum \alpha_i \varphi(r,c).$$

We use following substitution in Eq. (1) as used in [1, 3]

$$\mu = w_y$$

and derive

$$\frac{\partial \mu(y,t)}{\partial t} = \frac{\partial^2 \mu(y,t)}{\partial y^2}, \ (y,t) \in \Omega := \{0 < y < l, 0 < t \le t_f\}, \tag{2}$$

$$\mu(y,0) = I'(y),$$
$$\mu(0,t) = Q_0(t),$$
$$\mu(l,t) = Q_l(t),$$

we can then recovered $f(t)$ by

$$f(t) = \dot{w}(t) - \mu_y(0,t), \tag{3}$$

and the right boundary condition $w(l,t) = R(t)$, can be find by

$R(t) = w_0(t) + \int_0^l \mu(\gamma, t)d\gamma.$

(4)

Now we use MQ RBF for the solution of Eq. (2) to find $\mu(y,t)$, and then insert back in Eq. (3) to recover heat source $F(t)$ and in Eq. (4) to recover right boundary condition $R(t)$.

We imposed the noise on measured data by

$$\mu(l,t) = Q_l(t) = Q_l(t) + S\,rand(i),$$

where $S$ is the noise intensity and $rand(i)$ generate random numbers between $[-1,1]$.

## 3. RESULTS AND DISCUSSIONS

**Test Problem 1.**

The exact solution $w(y,t)$ and exact heat source $F(t)$ of (1) is given by

$$w(y,t) = y^2 + 2t + 3y^2t + \frac{y^4}{4} + \sin(2\pi t),$$

$$F(t) = 2\pi\cos(2\pi t) - 6t,$$

where $y$ lies in range $0 \le y \le 1$ and $t$ lies in $0 \le t \le 1$.

For the solution of $\mu(y,t)$, we take $n = 21$, the shape parameter $c = 0.3$ and we raised the noise intensity to $S = 0.2$.

The initial and boundary condition is obtained from the exact solution. For analyzing the accuracy of the method, we find the maximum error from the exact and numerical heat sources which is 0.0815 and is very accurate as shown in fig.1 and the maximum error in

the recovery of right boundary condition is 1.8891e-004 which is also very accurate to exact as in fig.2.
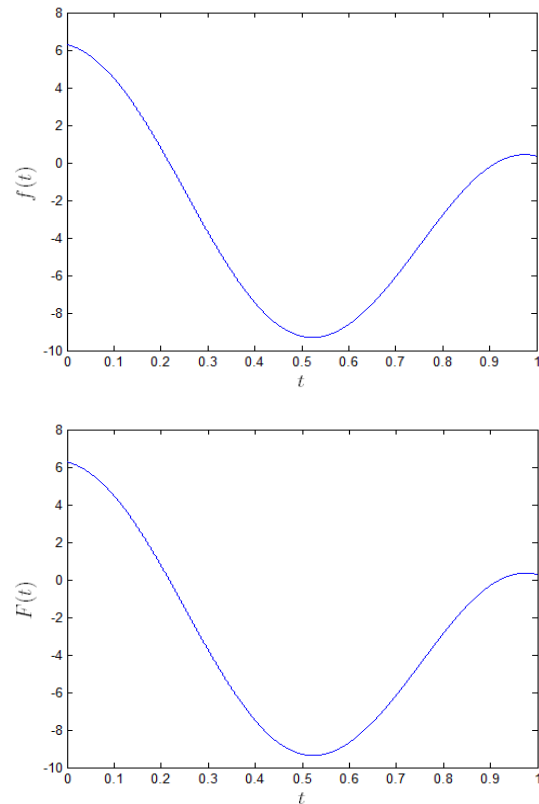


**Fig. 1**. For the inverse heat problem, the numerical heat source (left) and exact heat source (right) of Test Problem 1.
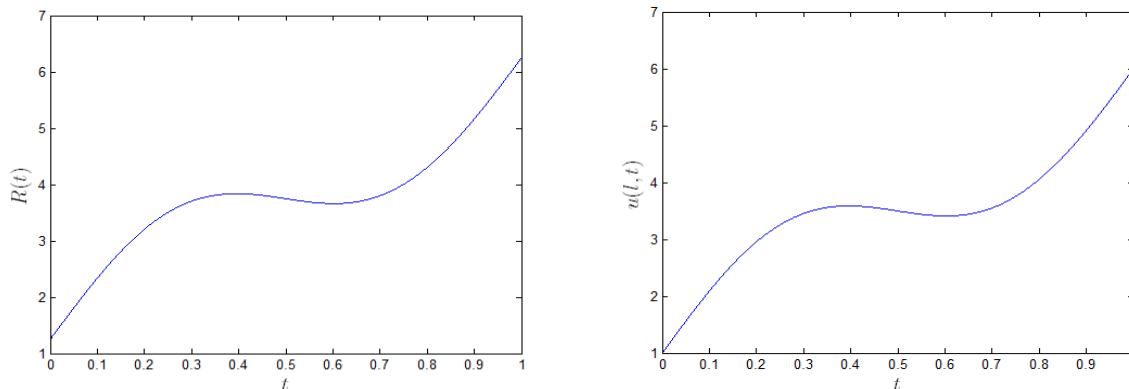


**Fig.2.** For the inverse heat problem, the numerical right boundary condition (left) and exact right boundary condition (right) of Test Problem 1.

## References

[1] C.-S. Liu, Lie-group differential algebraic equations method to recover heat source in a Cauchy problem with analytic continuation data, Int. J. Heat Mass Transfer 78 (2014) 538–547.

[2] D. Gottlieb and S.A. Orszag, Numerical analysis of spectral methods. Society for Industrial and Applied Mathematics. 2 (1997):7-19.

[3] Liu, Chein-Shan, Chung-Lun Kuo, and Wun-Sin Jhao. "The multiple-scale polynomial Trefftz method for solving inverse heat conduction problems."*International Journal of Heat and Mass Transfer* 95 (2016): 936-943.

[4] Sarra, Scott A., and Edward J. Kansa. "Multiquadric radial basis function approximation methods for the numerical solution of partial differential equations." *Advances in Computational Mechanics* 2.2 (2009).

# Efficient quadrature rules for numerical evaluation of singular and hyper singular integrals

**Shafiq Ahmad[1], Siraj-ul-Islam[1], Sakhi Zaman[1]**

*[1]Department of Basic Sciences & Islamiat,*

*University of Engineering & Technology Peshawar, Pakistan*

*Email:* shafiqahmad102@gmail.com

## Abstract

In this paper Newton-Cote type quadrature rule, Haar wavelets and hybrid functions based quadratures are used for numerical solution of singular and hyper singular integrals having singularity at the origin. These integrals include the Cauchy principle value and Hadamard finite part integrals. The proposed rules are tested numerically on some test problems to check the efficiency and accuracy of the new methods.

**Key words**: Cauchy principle value integrals, Hadamard finite part integrals, Haar wavelets and Hybrid functions.

## Introduction

Singular integrals have a wide range of application in science and engineering including aerodynamics, wave propagation or fluid and fracture mechanics [4, 7, 8, 12].

Generally, singular integrals can be written in the form:

$$I_\gamma(g, \tau) = \int_a^b \frac{g(x)}{(x-\tau)^{\gamma+1}} dx, \quad a < \tau < b, \qquad (1)$$

where, g(x) is a smooth function in [a, b]. Conventional quadrature rules like Simpson rule, Gaussian quadrature etc. fail to compute the integral (1) due to the pole of order $(\gamma+1)$ at $x = \tau \in [a,b]$. For $\gamma = 0$, equation (1) is known as Cauchy principle value (CPV) integral and can be expressed as:

$$I_c(g, \tau) = P \int_a^b \frac{g(x)}{x-\tau} = \lim_{v \to 0^+} \left[ \int_a^{\tau-v} \frac{g(x)}{x-\tau} dx \int_{\tau+v}^b \frac{g(x)}{x-\tau} dx \right], \quad (2)$$

provided that the limit exists.

For $\gamma = 1$, equation (1) is known as Hadamard finite part (HFP) integral and can be uniformly expressed as:

$$I_h(g, \tau) = H \int_a^b \frac{g(x)}{(x-\tau)^2} dx$$

$$= \lim_{v \to 0^+} \left[ \int_a^{\tau-v} \frac{g(x)}{(x-\tau)^2} dx \int_{\tau+v}^b \frac{g(x)}{(x-\tau)^2} dx \right]$$

$$= H \int_a^b \frac{g(x)}{(x-\tau)^2} dx \lim_{v \to 0^+} \frac{2g(\tau)}{v}. \qquad (3).$$

Many efficient methods have been developed for numerical evaluation of the singular integral [2, 5, 10, 11, 13, 20, 22]. E.Venturino [3] has divided the interval of integration into sub-domain and then evaluated HFP integral over these subintervals using low order Gaussian type quadrature. Criscuolo [2] has developed an algorithm for numerical evaluation of CPV and HFP integrals. Pawel Keller has used Adaptive quadrature rule for numerical solution of CPV integrals [12]. In [20], the authors have replaced the phase function f(x) of the CPV integral by Lagrange's interpolating polynomial with Chebyshev-Gauss-labatto nodes. In this method the integral is sub-divided into non-singular and singular integrals. The singular part is then calculated analytically. Recently, the authors [9] have developed a Newton cotes type quadrature rules for numerical evaluation of the CPV and the HFP.

In paper [6], the authors transformed the CPV integral problem into a non-singular and an oscillatory singular integral. The non-singular integral is evaluated by an improved Levin method after applying Taylor series expansion and the singular part is solved analytically. More recently, a

uniform approximation scheme is developed for numerical evaluation of HFP integrals [23].

In paper [15], a uniform Haar Wavelets and Hybrid Functions quadrature rules are developed for approximating a numerical solution of single, double and triple definite integrals with constant limits. In the next paper of the same authors [1], the Haar wavelets and the hybrid functions are extended to evaluate single, double and triple integrals with variable limits. Formulas for the hybrid functions of order m = 2,3,…,10 are derived to evaluate the definite integrals with variable limits. In [14], the authors have applied meshless procedure, hybrid and Haar based quadratures for numerical evaluation of one dimensional highly oscillatory integrals. In the next paper of the same authors, an algorithm is developed for solution of HOIs having stationary points [19].

In the present work, we have used the Newton cotes type quadrature rules [9], hybrid and Haar based quadrature rules [1, 14, 18] for the numerical solution of CPV and HFP integrals. The interesting thing to use these quadrature rules in the context of CPV and HFP integrals is that they remove the singularity of the integral at x = 0. The accuracy of the three methods increases on dense nodal points. The accuracy of the new methods in the context of CPV and HFP integrals are justifies on solving some test problems.

## 2 Newton cotes type quadrature

In this section we have proposed Newton-Cote type quadrature rule (NC) for numerical evaluation of CPV and HFP integrals.

### 2.1 CPV integral

In this section we derive (4m -1)-point Newton cote type quadrature rule for numerical evaluation of CPV integrals of the form:

$$I_c(g, \tau) = P \int_{-a}^{a} \frac{g(x)}{x - \tau} dx, \qquad (4)$$

where $a \in R^+$ and $\tau = 0$ is a unique singular point of the integral.

In this procedure, we subdivide the intervals [-a , a] into (4m-2)-points:

$$0, \pm \frac{a}{2m}, \pm \frac{2a}{2m}, \pm \frac{3a}{2m}, \dots, \pm \frac{(2m-1)a}{2m}.$$

The formula for (4m-1)-point Newton cotes type quadrature is given as:

$$NC = W_{m0}g(0) + \sum_{k=1}^{2m-1} W_{mk} \left[ g\left(\frac{ka}{2m}\right) - g\left(-\frac{ka}{2m}\right) \right].$$

In this formula, the weights $W_{m0}$ and $W_{mk}, k = 1, 2, \dots, (2m - 1)$ are calculated from the moment equation $AW = B$ at the given nodes. To avoid the singularity at $x = 0$. We take $g(0) = 0$ for all nodal points. The moment equation $AW = B$ in terms of matrix notation is given as:

$$\begin{bmatrix} 1 & 2 & \dots & (2m-1) \\ 1^3 & 2^3 & \dots & (2m-1)^3 \\ \vdots & \vdots & \vdots & \vdots \\ 1^{(2k-1)} & 2^{(2k-1)} & \dots & (2k-1)^{(2k-1)} \end{bmatrix} \begin{bmatrix} W_{m1} \\ W_{m2} \\ \vdots \\ W_{m(2m-1)} \end{bmatrix} = $$
$$\begin{bmatrix} \frac{2m}{1} \\ \frac{(2m)^3}{3} \\ \vdots \\ \frac{(2m)^{(2m-1)}}{(2m-1)} \end{bmatrix}.$$

Newton-cotes formulae for $m = 1,2,\dots,6$ are derived and are given as:

$$NC1 = 2 \left[ g\left(\frac{a}{2}\right) - g(-\frac{a}{2}) \right].$$

$$NC2 = (2.9778) \left[ g\left(\frac{a}{4}\right) - g\left(-\frac{a}{4}\right) \right]$$
$$- (0.9156) \left[ g\left(\frac{a}{2}\right) - g\left(-\frac{a}{2}\right) \right]$$
$$+ (0.9511) \left[ g\left(\frac{3a}{4}\right) \right.$$
$$\left. - g(-\frac{3a}{4}) \right].$$

$$NC3 = (8,4438) \left[ g\left(\frac{a}{6}\right) - g\left(-\frac{a}{6}\right) \right]$$
$$- (8.06231) \left[ g\left(\frac{a}{3}\right) - g\left(-\frac{a}{3}\right) \right]$$
$$+ (6.0322) \left[ g\left(\frac{a}{2}\right) - g\left(-\frac{a}{2}\right) \right]$$

$$-(2.0995)\left[g\left(\frac{2a}{3}\right)g\left(-\frac{2a}{3}\right)\right]$$

$$+ (0.7964)\left[g\left(\frac{5a}{2}\right)\right.$$

$$\left. - g\left(-\frac{5a}{2}\right)\right].$$

$$NC4 = (50.82)\left[g\left(\frac{a}{8}\right) - g\left(-\frac{a}{8}\right)\right] - (68.50)\left[g\left(\frac{a}{4}\right) - g\left(-\frac{a}{4}\right)\right]$$

$$+(6.0322)\left[g\left(\frac{3a}{8}\right) - g\left(-\frac{3a}{8}\right)\right]$$

$$- (2.0995)\left[g\left(\frac{a}{2}\right) - g\left(-\frac{a}{2}\right)\right]$$

$$+ (0.7964)\left[g\left(\frac{5a}{8}\right)\right.$$

$$\left. - g\left(-\frac{5a}{8}\right)\right]$$

$$- (31.4820)\left[g\left(\frac{3a}{4}\right)\right.$$

$$\left. - g\left(-\frac{3a}{4}\right)\right]$$

$$+ (3.1484)\left[g\left(\frac{7a}{8}\right)\right.$$

$$\left. - g\left(-\frac{7a}{8}\right)\right].$$

$$NC5 = (433.0835)\left[g\left(\frac{a}{10}\right) - g\left(-\frac{a}{10}\right)\right]$$

$$- (647.4785)\left[g\left(\frac{a}{5}\right) - g\left(-\frac{a}{5}\right)\right]$$

$$+ (599.76)\left[g\left(\frac{3a}{10}\right)\right.$$

$$\left. - g\left(-\frac{3a}{10}\right)\right]$$

$$- (400.9167)\left[g\left(\frac{2a}{5}\right)\right.$$

$$\left. - g\left(-\frac{2a}{5}\right)\right]$$

$$+ (202.0275)\left[g\left(\frac{a}{2}\right)\right.$$

$$\left. - g\left(-\frac{a}{2}\right)\right]$$

$$- (76.2869)\left[g\left(\frac{3a}{5}\right)\right.$$

$$\left. - g\left(-\frac{3a}{5}\right)\right]$$

$$+ (21.51)\left[g\left(\frac{7a}{10}\right)\right.$$

$$\left. - g\left(-\frac{7a}{10}\right)\right]$$

$$- (4.102)\left[g\left(\frac{4a}{5}\right) - g\left(-\frac{4a}{5}\right)\right]$$

$$+ (0.6752)\left[g\left(\frac{9a}{10}\right)\right.$$

$$\left. - g\left(-\frac{9a}{10}\right)\right].$$

$$NC6 = (4241.563)\left[g\left(\frac{a}{12}\right)\right.$$

$$\left. - g\left(-\frac{a}{12}\right)\right]$$

$$- (6665.610)\left[g\left(\frac{a}{6}\right) - g\left(-\frac{a}{6}\right)\right]$$

$$+ (6675.6\ 56)\left[g\left(\frac{a}{4}\right)\right.$$

$$\left. - g\left(-\frac{a}{4}\right)\right]$$

$$- (501.9547)\left[g\left(\frac{a}{3}\right) - g\left(-\frac{a}{3}\right)\right]$$

$$+ (2959.769)\left[g\left(\frac{5a}{12}\right)\right.$$

$$\left. - g\left(-\frac{5a}{12}\right)\right]$$

$$-(1386.985)\left[g\left(\frac{a}{2}\right) - g\left(-\frac{a}{2}\right)\right]$$

$$+ (514.534)\left[g\left(\frac{7a}{12}\right) - g\left(-\frac{7a}{12}\right)\right]$$

$$- (148.360)\left[g\left(\frac{2a}{3}\right) - g\left(-\frac{2a}{3}\right)\right]$$

$$+ (32.505)\left[g\left(\frac{3a}{4}\right) - g\left(-\frac{3a}{4}\right)\right]$$

$$- (4.998)\left[g\left(\frac{5a}{6}\right) - g\left(-\frac{5a}{6}\right)\right]$$

$$+ (0.6407)\left[g\left(\frac{11a}{12}\right) - g\left(-\frac{11a}{12}\right)\right].$$

All the formulae are open Newton cotes quadrature rules as the end points of the interval are not included.

## 2.2 HFP integrals

To compute the HFP integrals of the form:

$$I_h(g,\tau) = H\int_{-a}^{a} \frac{g(x)}{(x-\tau)^2}dx, \qquad (5)$$

we use the following procedure:

Assume that g (z) is the analytic continuation of

g(x) in the disc:

$$S = \{z \in \mathbb{C} : \; |z| \le r; r > a\},$$

such that

$$g(z) = g(x); \; \forall\, x \in [-a, a].$$

The integral $I_h(g,\tau)$ for $\tau = 0$, can be written as:

$$I_h(g,\tau) = \int_{-a}^{a} \frac{\left(\frac{g(x)-c_1}{x}\right)}{x}dx + \int_{-a}^{a} \frac{c_1}{x^2}dx \,,$$

where $\quad c_1 = res_{x=0}\left\{\frac{g(x)}{x}\right\}$

$$= \int_{-a}^{a} \frac{h(x)}{x}dx + c_1\int_{-a}^{a}\frac{1}{x^2}dx$$

$$= I_1 +$$

$I_2, \qquad\qquad\qquad (6)$

where $h(x) = \frac{g(x)-c_1}{x}$, $I_1$ is a CPV integral which can be solved using the rules NC1-NC6 and $I_2$ can be easily calculated using Fundamental Theorem of Calculus.

## 3 Multi-resolution quadrature rules

In this section, we briefly described multi-resolution quadrature rules like hybrid functions of order m=6 and m=8 and Haar wavelets based quadrature [1, 16]. The detail derivation of these quadrature rules is given in [1, 15].

### 3.1 Haar wavelets based quadrature

The definition and detail description of the Haar functions are given in the [15]. In this paper we have used Haar wavelets based quadrature [18] for numerical evaluation of CPV and HFP integrals, which is given by:

$$HW = \frac{(d-c)}{N}\sum_{l=1}^{N} g\left(c + \frac{(d-c)(l-\frac{1}{2})}{N}\right),$$

where N = 2m.

### 3.2 Hybrid functions based quadrature

In this section we briefly describe hybrid function based quadrature for numerical evaluation of singular integrals i.e. the CPV and the HFP integrals. The detail description and proofs of the formulae for hybrid functions of order $m = 1,2\ldots,10$ are reported in [1, 15].

In this work we use the hybrid functions based quadrature of order m = 6 and m = 8 to compute the integral of the form $\int_c^d g(x)dx$.

Formula for m = 6 is given by:

$$HY6 = \frac{d-c}{1280n}\sum_{l=1}^{n}\left[247g\left(c + \frac{(d-c)(12l-11)}{N}\right)\right.$$
$$+ 139g\left(c + \frac{(d-c)(12l-9)}{N}\right)$$
$$+ 254g\left(c + \frac{(d-c)(12l-7)}{N}\right)$$
$$+ 254g\left(c + \frac{(d-c)(12l-5)}{N}\right)$$
$$+ 139g\left(c + \frac{(d-c)(12l-3)}{N}\right)$$
$$+ 247g\left(c\right.$$
$$\left.\left. + \frac{(d-c)(12l-1)}{N}\right)\right],$$

where N = 12n.

Similarly, the formula for hybrid function based quadrature of order m = 8 is given by:

$$HY8 = \frac{d-c}{1935360n} \sum_{l=1}^{n} \left[ 295627g\left(c + \frac{(d-c)(16l-15)}{N}\right) \right.$$

$$+ 7139g\left(c + \frac{(d-c)(16l-13)}{N}\right)$$

$$+ 471771g\left(c + \frac{(d-c)(16l-11)}{N}\right)$$

$$+ 128953g\left(c + \frac{(d-c)(16l-9)}{N}\right)$$

$$+ 128953g\left(c + \frac{(d-c)(16l-7)}{N}\right)$$

$$+ 471771g\left(c + \frac{(d-c)(16l-5)}{N}\right)$$

$$+ 71329g\left(c + \frac{(d-c)(16l-3)}{N}\right)$$

$$+ 295627g\left(c + \left.\frac{(d-c)(16l-1)}{N}\right)\right],$$

where N = 16n.

## 4 Numerical results

Some test problems have solved to check the accuracy of the proposed methods. Two CPV and two HFP test integrals are included. The exact solution of the first and fourth test problems is taken from the [9], while the exact solution of second and third problems is found by using hybrid function of order m = 8 at higher nodal points. Absolute error $L_{ab}$ is calculated in all the test problems.

**Test Problem 1**. Consider the following CPV integral [9]:

$$I_c(e^x, \tau) = P \int_{-1}^{1} \frac{e^x}{x - \tau} dx .$$

The integrand has a singularity at $\tau = 0$ in the interval of integration. The traditional quadratures like Simpson rule etc. fail to compute this type of integrals due to the presence of singular point in the interval. The integral is computed by NC, HW, HY6 and HY8. The results in terms of absolute error are shown in the table 1. Also the results of the proposed methods are compared with the results of Newton cote formula [9]. From the table it is shown that the results of HW and NC are similar at the same nodal points while the results of HY6 and HY8 are better than the results [9].

The CPU time (in seconds) comparison of all the methods is given in Fig. 1. From the figure it is clear that all the methods are efficient. It is clear from the whole discussion that our proposed methods give better accuracy than the existing method [9].

**Table 1**: $L_{ab}$ of NC, HW, HY6 and HY8 for test problem 1.

| N | NC | HW | HY6 | HY8 | NC [9] |
|---|---|---|---|---|---|
| 3 | 3.01e- 02 | 1.91e -03 | 6.23e- 09 | 4.55e -12 | 3.00e -02 |
| 7 | 9.30e -06 | 7.48e -06 | 3.95e -11 | 5.40e -13 | 9.31e -06 |
| 11 | 2.59e -10 | 2.92e -08 | 3.13e -12 | 5.57e -13 | 2.60e -10 |
| 15 | 9.42e -13 | 1.14e -10 | 9.47e -13 | 5.37e -13 | MP |
| 19 | 5.53e -06 | 9.89e -13 | 6.42e -13 | 5.36e -13 | - |
| 23 | 4.88e -01 | 4.46e -13 | 5.75e -13 | 5.21e -13 | - |
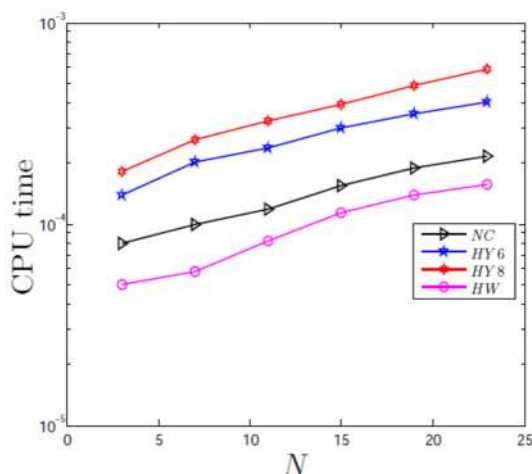
**Figure 1:** CPU time (in seconds) comparison of NC, HW,

HY6 and HY8 for $N = 3,7,...,23$ of test problem 1.

**Test Problem 2**. We consider the numerical computation of the CPV integral:

$$I_c(e^x(1+x^2), \tau) = P \int_{-1}^{1} \frac{e^x(1+x^2)}{x-\tau} dx.$$

The integral is evaluated by the proposed methods NC, HW, HY6 and HY8. $L_{ab}$ and CPU time (in seconds) comparison are shown in table 2 and Fig. 2 respectively. It is shown in the table that the proposed method HY8 gives an accuracy of order $O(10^{-14})$ while the rest of methods decreases the accuracy up $O(10^{-12})$ at small nodal points i.e. N = 23. The NC method oscillates the accuracy due to the instability of the method at higher nodal points. The HY6, HY8 and HW increase the accuracy on dense nodes. This means that Haar wavelets and hybrid functions based quadratures are stable at higher nodes.

It is shown in the Fig. 2 , that the three methods are efficient even for higher nodal points.

The integral has singularity at $\tau = 0$ of order 2 in the interval $[-2, 2]$. This type of integrals are difficult to evaluate by the quadrature rules like as Gaussian quadrature etc. due to the presence of second order singularity at $x = \tau$. The integral is evaluated by the proposed methods. The results in terms of $L_{ab}$ are shown in Tab. 3. It is shown in the table that all the

three methods give a high accuracy at coarse grid points.

**Table 2**: *Lab* of NC, HW, HY6 and HY8 for test problem 2.

| N | NC | HW | HY6 | HY8 |
|---|---|---|---|---|
| 3 | 2.44e -01 | 1.60e-02 | 2.89e-07 | 3.10e -10 |
| 7 | 4.07e -04 | 6.27e-05 | 1.82e-09 | 3.46e -13 |
| 11 | 2.89e -08 | 2.45e- 07 | 1.21e-10 | 1.90e -14 |
| 15 | 9.84e -12 | 9.58e-10 | 1.88e -11 | 8.43e -14 |
| 19 | 6.45e -06 | 3.79e-12 | 4.56e -12 | 1.15e -14 |
| 23 | 5.12e -01 | 1.42e-13 | 1.44e -12 | 2.39e -14 |
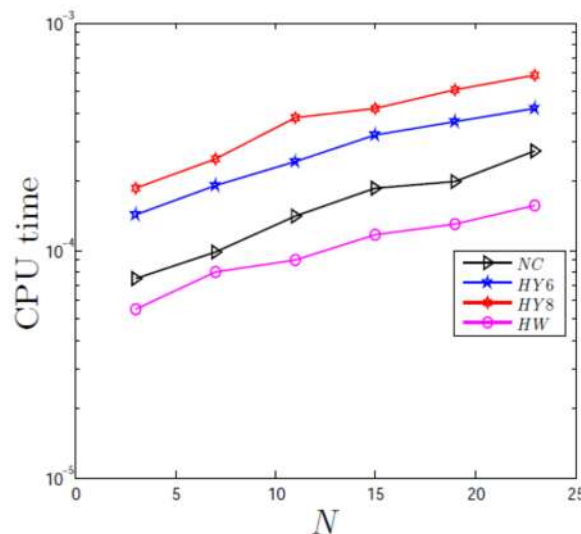


**Figure 2:** CPU time (in seconds) comparison of NC, HW,

HY6 and HY8 for $N = 3,7,...,23$ of test problem 2.

**Test Problem 3**. Consider the HFP integral:

$$I_h(1 - e^{2x}, \tau) = H \int_{-2}^{2} \frac{(1-e^{2x})}{(x-\tau)^2} dx.$$

The CPU time comparison of all the methods is given in the Fig. 3. From the figure it is clear that the computational time for computing HFP integrals is same to the computational time of CPV integrals. This shows that the efficiency and accuracy of the all

the proposed methods are not affected by the order of singularity.

**Table 3**: *Lab* of NC, HW, HY6 and HY8 for test problem 3.

| N | NC | HW | HY6 | HY8 | NC [9] |
|---|----|----|-----|-----|--------|
| 3 | 3.05e- 03 | 2.28e- 04 | 2.10e- 09 | 1.12e -11 | 3.00e -03 |
| 7 | 7.31e -07 | 9.02e -07 | 1.40e -11 | 4.79e -14 | 7.30e -07 |
| 11 | 3.67e -11 | 3.52e -09 | 9.72e -13 | 1.59e -14 | 3.70e -11 |
| 15 | 2.57e -14 | 1.37e -11 | 1.77e -13 | 3.55e -14 | M P |
| 19 | 5.38e -06 | 8.81e -14 | 6.70e -14 | 3.88e -14 | - |
| 23 | 4.84e -01 | 3.78e -13 | 4.26e -14 | 5.24e -14 | - |

**Table 4:** $L_{ab}$ of NC, HW, HY6 and HY8 for test problem 4.

| N | NC | HW | HY6 | HY8 |
|---|----|----|-----|-----|
| 3 | 2.05e -03 | 1.45e -01 | 7.56e -05 | 6.64e -07 |
| 7 | 6.34e -07 | 5.75e -04 | 5.29e -07 | 8.69e -10 |
| 11 | 4.65e -10 | 2.24e -06 | 3.57e -08 | 2.38e -11 |
| 15 | 3.52e -12 | 8.78e -09 | 5.58e -09 | 2.02e -12 |
| 19 | 1.37e -06 | 9.14e -11 | 1.35e -09 | 3.10e -13 |
| 23 | 7.94e -01 | 8.90e -12 | 4.31e -10 | 5.32e -14 |
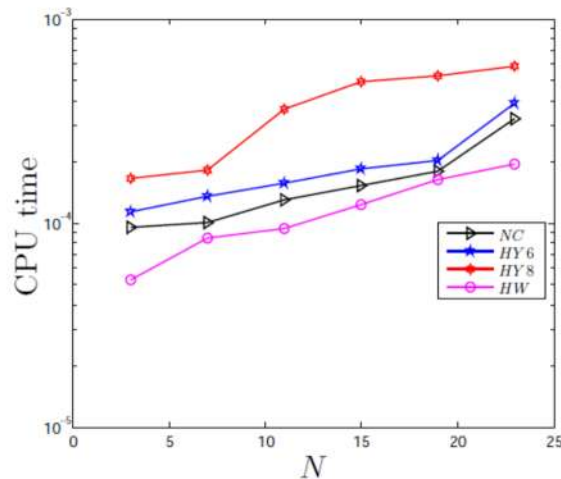


**Figure 3:** CPU time (in seconds) comparison of NC, HW, HY6 and HY8 for $N = 3, 7, \dots, 23$ of test problem 3.

**Test Problem 4.** We consider the computation of HFP integral [9]:

$$I_h(e^{-x} sinx , \tau) = H \int_{-1}^{1} \frac{(e^{-x} sinx)}{(x - \tau )^2} dx .$$

The integral is evaluated by the new methods NC, HW, HY6 and HY8. The absolute errors are obtained for $N = 3,7,...,23$ and are shown in table 4. The results of the new methods are compared with the NC [9]. It is shown in the table that the new methods give better accuracy than the method [9] at the same nodal points.

The CPU time comparison is shown in the Fig. 4. From the whole discussion it clear that the new methods are efficient and accurate than the existing literature.
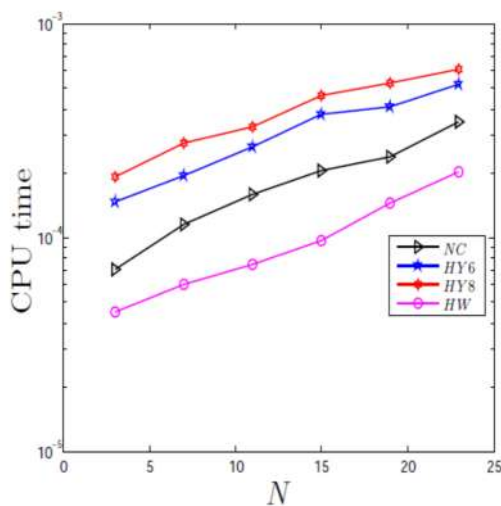


**Figure 4:** CPU time (in seconds) comparison of NC, HW, HY6 and HY8 for $N = 3,7,...,23$ of test problem 4.

### Conclusion

In this paper, Newton cote type quadrature, Haar and hybrid functions based quadrature are used for numerical evaluation of singular and hyper singular integrals. The proposed methods are applicable for evaluating CPV and HFP integrals having singularity at $\tau = 0$. Numerical tests show the accuracy and efficiency of the new methods.

### References

[1] I. Aziz, Sira-ul-Islam, and W. Khan. Quadrature rules for numerical integration based on Haar wavelets and hybrid functions. Comput. Math. Applic., 61:2770-2781, 2011.

[2] G. Criscuolo. A new algorithm for Cauchy principal value and Hadamard finite-part integrals. J. Comput. Appl. Math., 78:255-275, 1997.

[3] E.Venturino. On the numerical calculation of Hadamardfinite part integrals. Le.Math., 3:277-292, 1998.

[4] NI Ioakimidis. Application of finite part integrals to the singular integral equations of crack problems in plane and three-dimensional elasticity. Acta Mechanica, 45(1-2):31-47, 1982.

[5] X. Wang J. Li and T. Wang. Evaluation of Cauchy principal value integrals of oscillatory kind. Appl. Math. Comput., 217:2390-2396, 2010.

[6] X. Wang J. Li and T. Wang. Evaluation of Cauchy principal value integrals of oscillatory kind. Appl. Math. Comput., 217:2390-2396, 2010.

[7] A.Cemalettin Kaya and Fazil Erdogan. On the solution of integral equations with strongly singular kernels. Quar. Appl.Math., pages 105-122, 1987.

[8] C. Macaskill and E.O Tuck. Evaluation of the acoustic impedance of a screen. J.Aust.Math.Soc.Series B. App.Math., 20(01):46-61, 197.

[9] P. K. Mohanty. Quadrature rules for evaluation of hyper singular integrals. Appl. Math. Sci., 8:5839-5845, 2014.

[10] G. Criscuolo M.R. Capobianco. On quadrature for Cauchy principal value integrals of oscillatory functions. Comput. Appl. Math, 156:471-486, 2003.

[11] G.E. Okecha. Quadrature formulae for Cauchy principal value integrals of oscillatory kind. Math. Comput., 49(259-268), 1987.

[12] P.Keller. Roundo errors in the problem of computing Cauchy principal value integrals. Maths.NA, 2011.

[13] A.G. Ramm and A. Van der Sluis. Calculating singular integrals as an ill-posed problem, volume 57. 1990.

[14] Siraj-ul-Islam, A. S. Al-Fhaid, and S. Zaman. Meshless and wavelets based complex quadrature of highly oscillatory integrals and the integrals with stationary points. Engg. Analy. Bound. Elemt., 37:1136-1144, 2013.

[15] Siraj-ul-Islam, I. Aziz, and Fazal-e-Haq. A comparative study of numerical integration based on Haar wavelets and hybrid functions. Comput. Math. Applic., 59(6):2026-2036, 2010.

[16] Siraj-ul-Islam, I. Aziz, and W. Khan. Numerical integration of multi-dimensional highly oscillatory, gentle oscillatory and non-oscillatory integrands based on wavelets and radial basis functions. Engg. Analy. Bound. Elemt., 36:1284- 1295, 2012.

[17] Siraj-ul-Islam, I. Aziz, and B. Sarler. The numerical solution of second-order boundary-value problems by collocation method with the Haar wavelets. Math. Comput. Mod., 50:1577-1590, 2010.

[18] Siraj-ul-Islam, B. Sarler, I. Aziz, and F. Haq. The numerical solution of second-order boundary-value problems by collocation method with the Haar wavelets. I. J. Ther-mal Sc., 52:686-697, 2011.

[19] Siraj-ul-Islam and S. Zaman. New quadrature rules for highly oscillatory integrals with stationary points. J. Comput. Appl. Math., 278:75-89, 2015.

[20] H. Wang and S. Xiang. Uniform approximations to Cauchy principal value integrals of oscillatory functions. Appl. Math. Comput., 215:1886-1894, 2009.

[21] H. Wang and S. Xiang. Uniform approximations to Cauchy principal value integrals of oscillatory functions. Appl. Math. Comput., 215:1886-1894, 2009.

[22] H. Wang and S. Xiang. Uniform approximations to Cauchy principal value integrals of oscillatory functions. Appl. Math. Comput., 215(5):1886-1894, 2009.

[23] S. Xiang, C. Fang, and Z. Xu. On uniform approximations to hypersingular nite-part integrals .J. Math. Anal. Appl., 435(2):1210-1228, 2016.

# Numerical solution of Abel integral equation by Laplace transform and quadrature

**Shahid Khan[1*], Marjan Uddin [1]**

*[1*]Department Of Basic Sciences and Islamiat , University Of Engineering And Technology Peshawar.*
*[1*]Shahid Khan*
Email: *Shahidmathematics@gmail.com*

**Abstract**

Here a numerical method is used for approximation of the solution of Abel's integral representation of a physical phenomena. By using Laplace transform the integral equation reduces into algebraic equations then by inversion of Laplace transform it is represented as contour integral, evaluated with a quadrature. Complex Banach space is used for the discretization. Using the idea of conformal mapping, the corresponding contour has introduced. Various numerical examples have been investigated to check the accuracy and efficiency of the methodology.

To demonstrate the accuracy of the methodology, the results have been compared with the results of other method used.

**Key words**: Abel integral equation, Laplace Transform, Quadrature.

## 1 Introduction:

We investigate the importance and applicability of a numerical method proposed here and in [15], for the approximate solution of Abel's integral representation of a physical system which takes the form,

$$u(t) = f(t) + \int_0^t \frac{u(v)}{\sqrt{t-v}}\,dv,\ 0 \le t \le 1 \qquad (1.1)$$

.

N. Abel has been initiated the integral equations in 1823 in his studies [1, 2, 3, 4]. Many physical and engineering phenomena can be modeled accurately by Abel's integral equation e.g simultaneous dual relations [9], water wave [11], stellar winds [10], spectroscopic data[12]. Some important properties and types of the equation can be found in [2, 13]. R. K. Pandey, O. P. Sing and V. K. Sing in [5] have solved some important and different types of Abel's integral representation of some physical situations, Khan and Gondal [7], Yousefi [6], Li and Zhao [8], using different type of analytical and numerical methods. The purpose of the work is to investigate the methodology about the given contour. In the final section of the work, we consider the practical applications of the theoretical results. Particularly we consider the performance of existing methodology and compare them with the other methods for the solution of the Abel's integral representations. We consider, based on the results of the Numerical examples section, what the optimal choice of the length's step for a given method to find out more accurate results at minimum computations.

**1.1 Definition:** *If p is a real number such that p(> −1) then:*

$$\ell\{x^p\} = \frac{\Gamma(p+1)}{z^{p+1}},\ \ where\ \ \ R(z) > 0.$$

$$(1.1.1)$$

## 2 Method:

To start the procedure we choose a step size k>0 for the quadrature such that the accuracy at last should be best one. First of all we apply the Laplace transformation to equation (1.1) to reduce the given equation into algebraic equations as:

$$\ell(u(t)) = \ell(f(t)) + \ell(\int_0^t \frac{u(v)}{\sqrt{t-v}}\,dv), \qquad (2.1)$$

now with Laplace transform's convolution property , we find the following algebraic equations

$$\overline{u}(z) = (1 - \sqrt{\frac{\pi}{z}})^{-1}\overline{f}(z), \qquad (2.2)$$

where

$$\overline{u}(z) = \ell(u(t)),\ \ \overline{f}(z) = \ell(f(t)) \qquad (2.3)$$

Now inversion of Laplace transform leads to the result, as follows

$$u(t) = \ell^{-1}(\overline{u}(z))\frac{1}{2\pi i}\int_\Delta e^{zt}\overline{u(z)}dz,\ \ R(z) > 0. \qquad (2.4)$$

where ∆ is the integration contour with the restriction given as $S_r \supset \Delta$ and $z = z(\varsigma)$ as given in equation (2.2.1). Now substituting the value from equation (2.2.1) in equation (2.4), we get the integral representation in $\varsigma$ as

$$u(t) = \frac{1}{2\pi i}\int_\Delta e^{z(\varsigma)t}\overline{u(z(\varsigma))}z'(\varsigma)d\varsigma \qquad (2.5)$$

Finally using the step size k>0 discussed in the very first step for the quadrature to be applied on equation (2.5). Let setting for simplicity the expressions we set $z_j = z(\varsigma_j)$, $z'_j = z'(\varsigma_j)$ where $\varsigma_j$ = jk when j varies from -N to +N, we will get

$$u_N(t) = \frac{k}{2\pi i} \sum_{j=-N}^{N} e^{z_j t} \overline{u(z_j)} z'_j. \qquad (2.6)$$

We should solve the $2N+1$ algebraic equations given by (2.2), for finding the approximate solution $u_N$ when j varies from –N to +N.

**2.2 contour of integration:** The numerical solution $u_N$ given by equation (2.6) exist for all $t > 0$. The contour of integration is from [15] given as

$$S_r = \psi(\varsigma) = z = \omega + \lambda(1 - \sin(\delta - i\varsigma)), \qquad (2.2.1)$$

When $Im\ \varsigma = \eta$ and we write $z = x + iy$, the conformal transformation (2.2.1) in the complex plane reduces to the hyperbola,

$$\left(\frac{x-\omega-\lambda}{\lambda\sin(\delta+\eta)}\right) - \left(\frac{y}{\lambda\cos(\delta+\eta)}\right) = 1 \qquad (2.2.2)$$

Here the set with r>0 is $Y_r = \{\varsigma : r \geq Im\ \varsigma\}$ transformed into the hyperbola in (2.2.1) as $S_r = \{z : \varsigma \in Y_r\} \supset \Delta.$ Let

$$\sum_\phi = \{z \neq 0 : |\arg(z)| \leq \phi\} \cup \{0\}, \qquad \text{with}$$

$0 < \phi < \dfrac{(1-\alpha)\pi}{2}$, where $\alpha$ is a fractional number and let $\sum_{\beta^\omega} = \omega + \sum_\beta$ ,

$\Delta \subset S_r \subset \sum_{\beta^\omega}$ .

### 3 Results:

Practically some time we will be forced to solve such problems with a numerical method because the analytical solution will not be possible. The results here show us that the above methodology is the useful tool for the solution of such problems.

**Example 3.1**: Here we apply the present numerical method to the equation,

$$u(t) = \int_0^t \frac{x^n}{\sqrt{t-x}} dx. \qquad (3.3.1)$$

The exact solution is

$$u(t) = \frac{\sqrt{\pi} t^{\frac{1}{2}+n} \Gamma(n+1)}{\Gamma(n+\frac{3}{2})}.$$
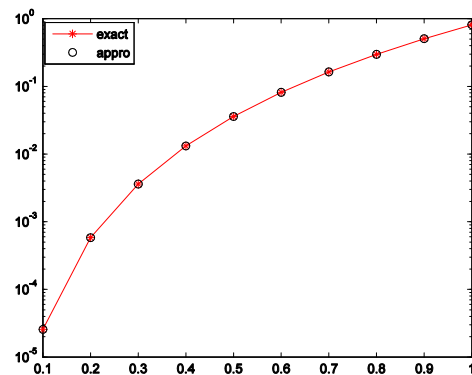


Figure 1. Comparison of approximate solution and the exact solution for example 3.1

**3.1.1 Discussion:** Here we can observe easily that the solution for example 3.1 is approximated better than that is approximated in [14]. The comparison can be shown graphically as Fig. 1 and fig. 2 in [14] and Figure. 1 here.

**Example 3.2:** . Here we apply the present numerical method to the equation,

$$u(t) + \int_0^t \frac{u(x)}{\sqrt{t-x}} dx = \frac{\pi t}{2} + \sqrt{t}, \quad 0 \leq t < 1. \quad (3.2.1)$$

With exact solution

$$u(t) = \sqrt{t}.$$

**3.2.1 Discussion:**
Also here in this example. 3.2, we have achieved better results than the results achieved in [14]. The comparison can be shown graphically as Fig. 3 in [14] and Figure. 2 here.

**Example 3.3:** Here we apply the present numerical method to the equation,

$$u(t) = 2\sqrt{t} - \int_0^t \frac{u(x)}{\sqrt{t-x}}\,dx, \quad 0 \le t < 1. \quad (3.1.1)$$

With exact solution

$$u(t) = 1 - e^{\pi t} erfc(\sqrt{\pi t}),$$

Where

$$erfc(x) = \frac{2}{\sqrt{\pi}} \int_x^\infty e^{-y^2}\,dy.$$
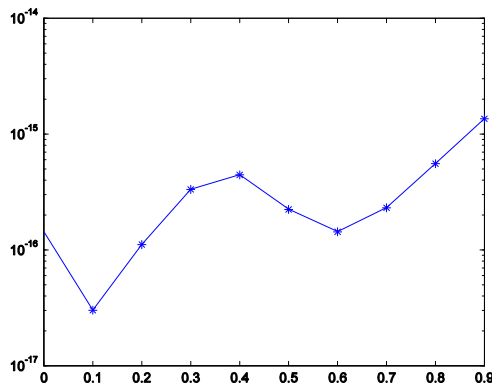


Figure 2. Absolute errors for example 3.2

Table 1: Numerical approximation: N=125, w=02, $\theta = 0.1$, r=0.3431, $\delta = 0.3812$, $[t_0, T]$=[0.1, 5].

| T | Absolute errors |
|---|---|
| 0.2 | 1.7701e-017 |
| 0.4 | 3.3313e-016 |
| 0.6 | 1.9905e-016 |
| 0.8 | 7.8099e-016 |
| 1.0 | 1.4439e-015 |
| [16] 3.81e-014 | (Standard base) |
| [16] 1.13e-014 | (Chebeshev base) |
| [16] 2.10e-014 | (Legendre base) |
| [16] 0 | (Legendre wavelet base) |

**3.3.1 Discussion:** . From table 1 we conclude that we have achieved better results than the results achieved in [16] for example 3.3.

## 4 Conclusions

From the results shown in the graphs and table 1, of the corresponding methodology we conclude that this methodology is very useful tool for the approximate solution of the Abel's integral representation for a physical phenomena. From comparison we have observed that the corresponding methodology is more efficient for the approximate solution of Abel's representation as integral equations than other methods. We conclude that by better selection of quadrature and parameters of the contour we can improve the corresponding methodology in the future also we can improve the corresponding methodology through selection of better contours. Finally we conclude that the corresponding methodology can be extended to the solution of many other problems in different branches of science and technology, engineering, applied sciences.

## 5 References

[1] A. M. Wazwaz, Linear and Nonlinear integral equations methods and applications, Springer, Heidelberge, Dordrecht, London, New york, (2011).
[2] A. M. Wazwaz, *A first course in integral equations*, World Scientific, New Jersy, (1997).
[3] R. Gorenflo and S. Vessella, abel integral equations, *springer, Berlin*, (1991).
[4] A. M. Wazwaz and M.S. Mehanna,The combined Laplace Adomian method for handling singular integral equation of heat transfer, *Int. J. Non- linear Sci*, **10** (2010), 248–252.
[5] R. K. Pandey, O.P. Sing and V.K. Sing, efficient algorithms to solve singular integral equations of Abel type, *Comput. Math. Appl.* **57** (2009), 664–676.
[6] S. A. Yousefi, Numerical solution of Abel's integral equation by using Legendre wavelets, *Appl. Math. comput.* **175** (2006), 574–580.
[7] M. Khan and M. A. gondal,A reliable treatment of Abel's second kind singular integral equation, *Appl. Math. lett* **25** (2012), 1666–1670.
[8] M. Li and W. Zhao, Solving Abel's type integral equation with Mikusinski's operator of fractional order, *Adv, Math. phy.*, (2013).
[9] J. Walton,,Systems of generalized Abel integral equations with applications to simultaneous dual relations, *SIAM J. Math. Anal.* **10** (1979), 808–822.
[10] O. Knill, R. Dgani and M. Vogel, A new approach to Abel integral operator and its application to stellar winds, *Astronom., Astrophys.* **274** (1993), 1002–1008.
[11] S. De, B. N. Mandal and A. Chakrabarti,Use of Abels integral equations in water wave scattering by two surface-piercing barriers, *Wave Motion* **47** (2010), 279–288.

[12] C. J. Cremers and R.C. Birkebak, Application of the Abel integral equation to spectroscopic data, *Appl. Opt.*, **5** (1966), 1057–1064.

[13] A. D. Polyanin and A.V. Manzhirov, Handbook of Integral Equations, *CRC Press, Boca Raton*, (1998).

[14] H. Song and M. Yi, Numerical Solution of the Arbitrary Order Weakly Singular Integral Equation Using Block Pulse Functions, *Proceedings of the World Congress on Engineering, London, UK*, **1** (2016).

[15] W. Mclean and V. Thomee, Numerical solution via Laplace transforms of a fractional order evolution equation, *journal of integral equations and applications*, **22** (2010), 57–94.

[16] R. Pourgholi, A. Tahmasebi and R. Azimi , Tau approximate solution of weakly singular Volterra integral equations with Legendre wavelet basis, *International Journal of Computer Mathematics*, (2016).

# On The Numerical Solution of Linear Multi-Term Fractional Order Differential Equations Using Laplace Transform and Quadrature

*Suleman Ahmad[1*], Marjan Uddin[1]*

[1] *Department of Basic Sciences and Islamiat, University of Engineering and Technology Peshawar, Peshawar, Pakistan,*

[1*]*Corresponding author*

*Email: sulemancare@gmail.com*

**Abstract**

In this work, we extended the work of [3] for the numerical solution of multi-term fractional order linear differential equations by an integral representation in the complex plane. The resultant integral is approximated to high order accuracy using quadrature. The accuracy of the method depends on the selection of optimal contour of integration. In the present work, linear multi-term fractional order differential equations are approximated for optimal contour of integration, and the results are compared with other methods available to demonstrate the accuracy and efficiency of the present numerical method.

**Key words**: Linear multi-term fractional order

differential equations, Laplace Transform, Quadrature.

## 1 Introduction

In this work, we want to investigate the applicability of the proposed numerical scheme for the solution of linear multi-term differential equations of fractional order whose general form to be discussed is,

$$D^{\beta_1} u(t) + \upsilon_1 D^{\beta_2} u(t) + \upsilon_2 D^{\beta_3} u(t) + \upsilon_3 u(t) = f(t)$$

(1.1)

Where $\upsilon_i$ ( i=1,2,3) and $0 < \beta_2 < \beta_3 < \beta_1$ are constants and the integer m is defined by $m \geq \beta_1 > m-1$, then one can specify suitable initial conditions,

$$u^i(0) = u_0^{\ i} \quad , i = 0,1,2,...,m-1$$

(1.2)

Where the Riemann-Liouville differential operators of

fractional order $\beta > 0$, is defined as:

$$D^\beta u(t) = \frac{1}{\Gamma(m-\beta)} \frac{d^m}{dt^m} \int_0^t \frac{u(x)}{(t-x)^{\beta-m+1}} dx$$

(1.3)

Where the integer m is defined by m ≥ β > m-1(see [1, 2]). It is the problem described in (1.1) and (1.2) that shall address in the present paper. It has been shown that this problem has a unique solution using Laplace transform methods under some strong conditions (in particular, the linearity of the differential equations) [1]. In the last section of the paper, we discuss how the theoretical results may be applied in practical cases. In particular we consider the performance of existing numerical methods for solving linear multi-term differential equations of fractional order when the equations to be solved depend upon parameters that must be estimated and are subject to errors. We are aware of applications, from material sciences, for example, in which the order of the equation is a parameter estimated only to certain degree of accuracy. We investigated how to optimize quadrature step size for the present method in order to gain maximum accuracy with less computational cost.

a. **Definition:** If a ( > -1) is a real number then:

$$L[t^a] = \frac{\Gamma(a+1)}{s^{a+1}}$$

(1.4)

Where R(s) > 0

b. **Lemma:**

For m − 1 < β ≤ m, m ∈ N, the Laplace transformation of differential operator of fractional order can be written as [5]:

$$L\left[\left(\frac{d^\beta f}{dt^\beta}\right)(t)\right] = \frac{s^m F(s) - s^{m-1} f(0) - s^{m-2} f'(0) - ... - f^{m-1}(0)}{s^{m-\beta}}$$

(1.5)

## 2 Method

We select a quadrature step k > 0 and an equal weight quadrature formula in our numerical computations. The procedure is follows as applying

Laplace Transformation to equation (1.1) for $\beta_1$ $\varepsilon$ (3, 4], $\beta_2$ $\varepsilon$ (0, 1] and $\beta_3$ $\varepsilon$ (1, 2], we get:

$$\hat{u}(s) = \left(s^{\beta_1} + v_1 s^{\beta_2} + v_2 s^{\beta_3} + v_3\right)^{-1} g(s)$$

(2.1)

Where

$$g(s) = s^{\beta_1-1} u_0 + s^{\beta_1-2} u_0' + s^{\beta_1-3} u_0'' + s^{\beta_1-4} u_0''' +$$
$$v_1 s^{\beta_2-1} u_0 + v_2 s^{\beta_3-1} u_0 + v_2 s^{\beta_3-2} u_0' + \hat{f}(s)$$

(2.2)

And

$$\hat{f}(s) = L(f(t))$$

(2.3)

Now using inverse Laplace transform to equation (2.1), we get

$$u(t) = \frac{1}{2\pi i} \int_\Gamma e^{st} \hat{u}(s) ds, R(s) \succ 0$$

(2.4)

Where $\Gamma$ is the integration contour such that $s_r \supset \Gamma$ and $s = s(v)$ given by equation (2.8). Now using equation (2.8) in equation (2.4), we get,

$$u(t) = \frac{1}{2\pi i} \int_\Gamma e^{s(v)t} \hat{u}(s(v)) s'(v) dv$$

(2.5)

Now for the quadrature rule we choose the step k > 0 and for simplicity we set $s_j = s(v_j)$, $s_j' = s'(v_j)$ where $v_j = kj$ for $N \geq j \geq -N$, we get

$$u_N(t) = \frac{k}{2\pi i} \sum_{j=-N}^{N} e^{s_j t} \hat{u}(s_j) s_j'$$

(2.6)

Now we solve the 2N+1 equations given in (2.7) for $N \geq j \geq -N$.

$$\hat{u}(s_j)\left(s_j^{\beta_1} + v_1 s_j^{\beta_2} + v_2 s_j^{\beta_3} + v_3\right) = g(s_j)$$

(2.7)

**a. Contour of integration**

We remarked that the numerical solution $\hat{u}(s_j)$ determined the approximate solution (2.6) for all 0 < t. However, in practice, the accuracy of approximate

solution depends on the selection of the contour $\Gamma$. A number of such contour available one such path is due to [4] given as

$$s = \omega + \lambda\left(1 - \sin\left(\delta - iv\right)\right)$$

(2.8)

In fact, when $\text{Im } v = \eta$ , then (2.8) reduces to the left branch of hyperbola,

$$\left(\frac{x - \lambda - \omega}{\lambda \sin(\eta + \delta)}\right)^2 - \left(\frac{y}{\lambda \cos(\eta + \delta)}\right)^2 = 1$$

(2.9)

Here the strip $Y_r = \{v : | \text{Im } v | \leq r\}$

with r > 0 transformed into the hyperbola

$$S_r = \{s : v \in Y_r\} \supset \Gamma$$

Let $\sum_\phi = 0 \cup \{s \neq 0 : | \arg s | \leq \phi\}$

With $\pi / 2(1 - \alpha) \succ \phi \succ 0$

And let $\sum_\beta^\omega = \omega + \sum_\beta$ , $\Gamma \subset S_r \subset \sum_\beta^\omega$ .

### 3 Numerical examples

We test the present method for taking a number of problems to validate our numerical method for accuracy and efficiency. By comparing the results of the present method with other methods, it is clear that the present method is very convenient and effective.

**a. Example No.1:**

Here we apply the present numerical method to the equation [6, 7],

$$D^{\beta_1} u(t) + v_1 D^{\beta_2} u(t) + v_2 D^{\beta_3} u(t) + v_3 u(t) = f(t)$$

(3.1)

$$u(0) = 0, u'(0) = -1, u''(0) = 2, u'''(0) = 0$$

Case1:

$$v_1 = v_2 = v_3 = 1,$$
$$\beta_1 = 3.91, \beta_2 = 0.77, \beta_3 = 1.44,$$
$$f(t) = \frac{2}{\Gamma(1.56)} t^{0.56} + \frac{2}{\Gamma(2.23)} t^{1.23} - \frac{1}{\Gamma(1.23)} t^{0.23} + t^2 - t$$

Case2:

$$\nu_1 = \nu_3 = 0.5, \nu_2 = 1,$$

$$\beta_1 = \sqrt{11}, \beta_2 = \frac{\sqrt{2}}{20}, \beta_3 = \sqrt{2},$$

$$f(t) = \frac{2}{\Gamma(1.59)} t^{0.59} + \frac{1}{\Gamma(2.93)} t^{1.93} - \frac{0.5}{\Gamma(1.93)} t^{0.93} +$$

$$0.5(t^2 - t)$$

In such cases $u(t) = t^2 - t$ is the exact solution.

Table 1: Numerical results: at t=0.1, ω=2, θ=0.1, r=0.3431, δ=0.3812, and [t₀,T] =[0.01,1] corresponding to case 1 of (3.1).

| N | Absolute error |
|---|---|
| 5 | 0.0773 |
| 15 | 7.2720 e$^{-005}$ |
| 30 | 1.8211 e$^{-007}$ |
| 50 | 3.3186 e$^{-010}$ |
| 70 | 7.9374 e$^{-013}$ |
| 90 | 2.3740 e$^{-015}$ |
| 100 | 1.8709 e$^{-016}$ |
| 120 | 5.6477 e$^{-017}$ |

Table 2: Numerical results: at t=0.1, ω=2, θ=0.1, r=0.3431, δ=0.3812, and [t₀, T] =[0.01,1] corresponding to case 2 of (3.1).

| N | Absolute error |
|---|---|
| 5 | 0.0773 |
| 15 | 7.2720 e$^{-005}$ |
| 30 | 1.8211 e$^{-007}$ |
| 50 | 3.3186 e$^{-010}$ |
| 70 | 7.9368e$^{-013}$ |
| 90 | 2.2772e$^{-015}$ |
| 110 | 1.3886e$^{-016}$ |
| 120 | 1.2541e$^{-016}$ |

Table (1) and (2) shows the numerical results of the present method for case 1 and case 2 of example 1 respectively. The maximum absolute

error for case 1 of example 1 obtained by [6] and [7] is 1.9e$^{-006}$ and 9.53e$^{-004}$ respectively, and the maximum absolute error for case 2 of example 1 obtained by [6] and [7] is 1.8e$^{-007}$ and 9.80e$^{-004}$ respectively. We have achieved better results than the results obtained by [6] and [7] of the same problem as shown in the table (1) and (2).

**b.     Example No.2:**

Consider the equation [6, 8],

$$D^2 u(t) + D^{\frac{3}{4}} u(t) + u(t) = t^3 + 6t + \frac{8.533333333}{\Gamma(0.25)} t^{2.25}$$

(3.2)

Where

$$u(0) = u'(0) = 0$$

In such case $u(t) = t^3$ is the exact solution.

Table 3: Numerical results: at t=0.1, ω=2, θ=0.1, r=0.3431, δ=0.3812, and [t₀,T] =[0.01,1] corresponding to (3.2).

| N | Absolute error |
|---|---|
| 5 | 0.1691 |
| 15 | 8.3417 e$^{-005}$ |
| 30 | 2.8584 e$^{-009}$ |
| 50 | 1.6338 e$^{-014}$ |
| 70 | 4.3748e$^{-016}$ |
| 90 | 1.8626e$^{-016}$ |
| 100 | 1.1279e$^{-016}$ |
| 120 | 4.1250e$^{-017}$ |
| 158 | 5.6722e$^{-019}$ |

Table (3) shows the numerical results of the present method for example 2. The maximum absolute error for example 2 obtained by [6] and [8] is 3.39e$^{-013}$ and 3.10e$^{-006}$ respectively. We have achieved better results than the results obtained by [6] and [8] of the same problem as shown in the table (3).

**4     Conclusions**

From the results in the tables we have observed that the corresponding methodology is more efficient for approximating the solution of linear multi term differential equations of fractional order than other various methods. Therefore we finally conclude that by better selection of quadrature and contour we can improve the corresponding methodology in the future.

## 5    References

[1] Kai Diethelm and N. J. Ford, Analysis of fractional differential equations, Journal of Mathematical Analysis and Applications 265 (2002), 229–248.

[2] K. B. Oldham and J. Spanier, The fractional calculus, Mathematics in Science and Engineering, Vol, 111, Academic Press, New York/London, 1974.

[3] D. Sheen, I. H. Sloan and V. Thomee, A parallel method for time discretization of parabolic equations based on Laplace transformations and quadrature, IMA J. Numerical. Anal. 23 (2003), 269–299.

[4] W. Mclean, V. Thomee, Numerical solution via Laplace transforms of a fractional order evolution equation, Journal of Integral Equations and Applications 22 (2010), 57–94.

[5] Saeed Kazem, Exact solution of some linear fractional differential equations by Laplace transform, International Journal of Nonlinear Science, 16 (1) (2013), 3–11.

[6] E.H. Doha, A.H. Bhrawy and S.S. Ezz-Eldien, Efficient Chebyshev spectral methods for solving multi-term fractional orders differential equations, Applied Mathematical Modelling, 35 (2011), 5662–5672.

[7] A.E.M. EL-Mesiry, A.M.A. EL-Sayed and H.A.A. EL-Saka, Numerical methods for multi-term fractional (arbitrary) orders differential equations, Applied Mathematics and Computation, 160 (2005), 683–699.

[8] N.J. Ford and J.A. Connolly, Systems-based decomposition schemes for the approximate solution of multi-term fractional differential equations, Computation and Applied Mathematics, 229 (2009), 382–391.

# A meshless collocation technique for the numerical solution of nonlinear Fisher Equation

Yusra Maheen[1,*], Mehnaz[1]

*[1]Department of Mathematics, Shaheed Benazir Bhutto women university, Peshawar 25000.*

*\*Corresponding author*

***Email**: yusramaheen111@gmail.com*

## Abstract

Fisher's equation is one dimensional, non-linear, reaction diffusion equation. It has interesting applications in many fields e.g. heat and mass transfer, ecology and biology. In this paper, we present a simple classical radial basis function (RBFs) collocation method (also known as kansa method) to find the numerical solution of the fisher equation. For this purpose different types of RBFs are used. Accuracy of the method highly depends on a constant called shape parameter. It is an open problem to discover the reasonable value of shape parameter. In this work Brute force technique is used to find the optimal value of shape parameter. Accuracy of the method is examined in terms of $L_2$, $L_\infty$ and root meansquare (RMS). Our method is compared with some other methods in literature.

**Key words**: Multi Quadratic (MQ), Inverse Multi Quadratic (IMQ), Gaussian (GA) Inverse Quadratic (IQ), $\theta$-weighted scheme, Crank-Nicolson scheme.

## 1 Introduction

Nonlinear phenomena play a vital role in many branches of physics and applied mathematics. Many problems inNonlinear control system are modeled by partial differential equations (PDEs). Fisher's equation is one of the nonlinear evolution equation. Fisher was the first to introduce it. The advance of a mutant gene in an infinite one-dimensionalhabitat can be modeled by Fisher's equation [1]. Furthermore, Fisher's equation iswidely used as a basisfor a variety of models for flame propagation,the spatial spread of gene in population,nuclear reactor theory, chemical wave propagation and branchingBrownian motion process [2–5].In recent years, many authors studied numerous properties of Fisher's equation, includingthe singularproperty andthe traveling wave behavior [6–10].Also,it is found that the initial valuessatisfying certain conditions lead to the occurrence of finite timesingularities [11]. In 1990, Kansa[13] proposeda meshless technique for solving PDEs. He used collocation method using RBFs.In Kansa's approach, the solution is approximated by RBFs, and then the unknown constants are the computed by the collocation method. multiquadric (MQ),inverse multiquadric(IMQ), Gaussians (GA), thin plate splines (TPS), and inverse quadric (IQ) are different types of RBFs. These RBFs are smooth and are commonly used for solvingPDEs. Micchelli [14], Madych et al.[15], Franke et al.[16] studied the existence, uniqueness and convergence of the Kansa method. Since the Kansa was the first one to apply the RBFs to solve PDEs, later on, this approach was hardened by Golberg et al. [17]. Hon[18] used RBFs for the numerical solutions of many ordinary differential equations (ODEs) and PDEs. These RBFs depends on shape parameter and by taking the appropriate value of the shape parameter one can getmost accurate results.

## 2 Kansa method

In this section we propose a meshless method based on $\theta$-weighted scheme. We applied a $\theta$-weighted scheme to given PDE and will be solved in terms of solution at $(n+1)^{th}$ time step through which the unknown solution found by solving system of linear equation.

### Construction of the Proposed Method

Consider the governing equation,

$$u_t = u_{xx} + \beta u(1 - u), \qquad (1)$$

with the initial condition,

$$u(x, 0) = k(x) x \in [a, b], \qquad (2)$$

and the boundary conditions,

$$u(a, t) = y(t), u(b, t) = g(t) \qquad (3)$$

Using θ-weighted scheme to Eq. (1), we get,

$$\frac{u^{n+1} - u^n}{\Delta t} = \theta[(u_{xx})^{n+1} + \beta u^{n+1} - \beta(u^2)^{n+1}] + (1 - \theta)[(u_{xx})^n + \beta u^n - \beta(u^2)^n]$$

Putting $\theta = \frac{1}{2}$, we obtain,

$$\frac{u^{n+1} - u^n}{\Delta t} = \frac{1}{2}[(u_{xx})^{n+1} + \beta u^{n+1} - \beta(u^2)^{n+1}] + \frac{1}{2}[(u_{xx})^n + \beta u^n - \beta(u^2)^n] \quad (4)$$

where $\Delta t$ is the time step and $u^{n+1}$ is the solution at $(n+1)^{th}$ time step.

Combining the same terms in Eq. (4), we get,

$$\left[\frac{u^{n+1} - u^n}{\Delta t}\right] = \left[\frac{(u_{xx})^{n+1} + (u_{xx})^n}{2}\right] + \left[\frac{\beta u^{n+1} + \beta u^n}{2}\right] - \left[\frac{\beta(u^2)^{n+1} + \beta(u^2)^n}{2}\right]. \quad (5)$$

$$u^{n+1} - \frac{\Delta t}{2}[(u_{xx})^{n+1} + \beta u^{n+1} - \beta(u^2)^{n+1}]$$
$$= u^n + \frac{\Delta t}{2}[(u_{xx})^n + \beta u^n - \beta(u^2)^n]. \quad (6)$$

Let the term $u^n$ represents the approximate solution at $n^{th}$ iteration. Now approximating the solution of Eq. (1) by,

$$u^n(x) = \sum_{j=1}^{M} a_j^n \emptyset_j,$$

where $\emptyset : R^n \to R$, is the RBF, and $a_j$ are the unknown constants. Let $u^n(x_i)$ represents the approximate solution at $i^{th}$ node. Then we have,

$$u^n(x_i) = \sum_{j=1}^{M} a_j^n \emptyset_{ij}, \quad (7)$$

where $i = 1,2,...,M$.

Substituting Eq. (7) in Eq. (6), we get

$$\sum_{j=1}^{M} a_j^{n+1} \theta_{ij} - \frac{\Delta t}{2}\left[\begin{array}{c}\sum_{j=1}^{M} a_j^{n+1} \theta_{ij}'' + \beta \sum_{j=1}^{M} a_j^{n+1} \theta_{ij} \\ -\beta\left(\sum_{j=1}^{M} a_j^{n+1} \theta_{ij}\right)^2\end{array}\right]$$
$$= \sum_{j=1}^{M} a_j^n \theta_{ij} + \frac{\Delta t}{2}\left[\begin{array}{c}\sum_{j=1}^{M} a_j^n \theta_{ij}'' + \beta \sum_{j=1}^{M} a_j^n \theta_{ij} \\ -\beta\left(\sum_{j=1}^{M} a_j^n \theta_{ij}\right)^2\end{array}\right].$$
(8)

From the difference equation (8) we can obtain the unknown solutions. So, the boundary conditions are given by,

$$\sum_{j=1}^{M} a_j^{n+1} \emptyset_{0j} = h(t), \quad (9)$$

$$\sum_{j=1}^{M} a_j^{n+1} \emptyset_{Mj} = k(t). \quad (10)$$

We can solve Equations (8)-(10) by direct solver like the LU-factorization method or Gauss elimination method.

**Numerical example**

In this section we have presented a numerical example which shows the accuracy of our method. we have compare our method with DQM.

The fisher equation is,

$$u_t = u_{xx} - \beta u(1-u) \quad (11)$$

where $\beta = 6$ is parameter.

With boundary conditions,

$$u(a,t) = \frac{1}{\left(1 + e^{\left(\sqrt{\frac{\beta}{6}}\right)a - \frac{5at}{6}}\right)^2}$$

$$u(b,t) = \frac{1}{\left(1 + e^{\left(\sqrt{\frac{\beta}{6}}\right)b - \frac{5at}{6}}\right)^2}$$

and initial conditions are given by,

$$u(x,0) = \frac{1}{\left(1 + e^{-\frac{5at}{6}}\right)^2}$$

and exact solution is

$$u(x,t) = \frac{1}{\left(1 + e^{\left(\sqrt{\frac{\beta}{6}}\right)x - \frac{5at}{6}}\right)^2}$$

In this example we have considered the interval $[0,1]\times[0,1]$ with time step $\Delta t = 0.0001$, and step size $h = 0.25$. Consider different types of RBFs including MQ, IMQ, GA and IQ and the results are matched with some other methods.

$$L_\infty = \max\left|v^{exact}-v^{app}\right|, \tag{12}$$

$$L_2 = \sqrt{h\sum_{i=1}^{M}\left(v^{exact}-v^{app}\right)^2}, \tag{13}$$

and

$$L_{rms}=\sqrt{\frac{\sum_{i=1}^{M}\left(v^{exact}-v^{app}\right)^2}{M}}. \tag{14}$$

**TABLE 1:** $L_\infty$, $L_2$ AND $L_{rms}$ USING DIFFERENT RBFs

| T | RBFs | $L_\infty$ | $L_2$ | $L_{rms}$ |
|---|---|---|---|---|
| 0.1 | MQ | 1.9E-02 | 1.60 E-02 | 1.43 E-02 |
| | IMQ | 1.83 E-02 | 1.25 E-02 | 1.12 E-02 |
| | GA | 1.240 E-02 | 9.32 E-02 | 8.34 E-02 |
| | IQ | 1.53 E-02 | 1.11 E-02 | 9.9 E-02 |
| 0.2 | MQ | 8.2 E-03 | 5.8 E-03 | 5.2 E-02 |
| | IMQ | 2.82 E-02 | 1.95 E-02 | 1.75 E-02 |
| | GA | 2.690 E-01 | 2.107 E-01 | 1.885 E-02 |
| | IQ | 5.2 E-03 | 3.9 E-03 | 3.5 E-02 |
| 0.3 | MQ | 9.3 E-03 | 5.7 E-03 | 5.1 E-02 |
| | IMQ | 3.05 E-02 | 1.90 E-02 | 1.70 E-02 |
| | GA | 4.116 E-02 | 3.358 E-01 | 3.004 E-01 |
| | IQ | 6.0 E-03 | 4.4 E-03 | 3.9 E-03 |
| 0.4 | MQ | 8.5 E-03 | 7.2 E-03 | 6.4 E-03 |
| | IMQ | 1.98 E-02 | 1.16 E-02 | 1.04 E-02 |
| | GA | 5.330 E-01 | 4.504 E-01 | 4.028 E-01 |
| | IQ | 1.27 E-02 | 9.2 E-03 | 8.2 E-03 |
| 0.5 | MQ | 1.02 E-02 | 7.0 E-03 | 6.2 E-03 |
| | IMQ | 4.3 E-02 | 2.9 E-03 | 2.6 E-03 |
| | GA | 6.336 E-01 | 5.430 E-01 | 4.856 E-01 |
| | IQ | 1.38 E-02 | 1.01 E-02 | 9.0 E-03 |

**TABLE 2: COMPARISON OF MMCN WITH DQM.**

| X | T | Exact | MQ | IMQ | GA | IQ | DQM[20] |
|---|---|---|---|---|---|---|---|
| 0.25 | 0.5 | 0.81839 | 0.81347 | 0.81836 | 0.90070 | 0.80829 | 0.81847 |
| | 1.0 | 0.98291860 | 0.98175049 | 1.04394531 | 1.14600191 | 0.98178265 | 0.98293 |
| | 2.0 | 0.99988342 | 1.00146484 | 1.06445313 | 1.17367452 | 1.00057450 | 0.99988 |
| | 5.0 | 1.00000000 | 1.00756836 | 1.06640625 | 1.17386639 | 1.00070431 | 1.00000 |
| 0.50 | 0.5 | 0.77580349 | 0.76562500 | 0.77148438 | 0.86742370 | 0.76196837 | 0.77590 |
| | 1.0 | 0.97814683 | 0.97857666 | 1.00000000 | 1.12646949 | 0.97642324 | 0.97816 |
| | 2.0 | 0.99985031 | 1.00244141 | 1.02539063 | 1.15587863 | 1.00077012 | 0.99985 |
| | 5.0 | 1.00000000 | 1.00488281 | 1.02539063 | 1.15608281 | 1.00093905 | 1.00000 |
| 0.75 | 0.5 | 0.72582358 | 0.71972656 | 0.72949219 | 0.81110273 | 1.10228315 | 0.72594 |
| | 1.0 | 0.97207053 | 0.97253418 | 0.95703125 | 0.81110273 | 0.97060472 | 0.97209 |

| 2.0 | 0.999807 80 | 1.00097 56 | 0.979492 19 | 1.102075 99 | 1.000496 27 | 0.9 998 1 |
|-----|-----|-----|-----|-----|-----|-----|
| 5.0 | 1.000000 00 | 0.999023 44 | 0.980468 75 | 1.102283 15 | 1.000704 24 | 1.0 000 0 |

In Table 1 it can be seen that IMQ , IQ and MQ has more accurate results than GA. We have taken the values of c = 41.80, 13.19, 1200 and 0.02 for IMQ, IQ, MQ and GA respectively. Also shows that IMQ,IQ and MQ has less error norms than GA. In Table 2 the comparison is made between MMCN and DQM.

The accuracy of RBF interpolation base on shape parameter c so it is a challenging task for researchers to find the best value of c and so many methods are there to find the optimal value of c. In this work brute-force technique is applied and we have plotted Max-error for different values of c and then we have find the possible optimal value of c.
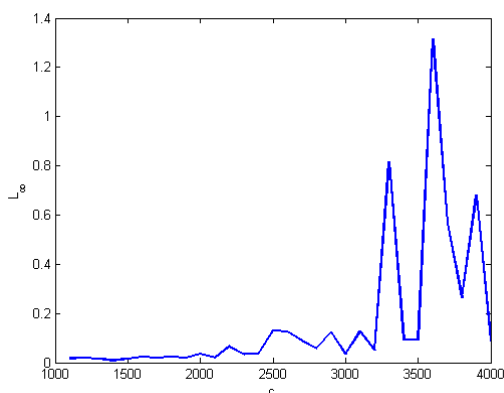


**FIGURE 2: MAX-ERROR FOR DIFFERENT VALUES OF C USING IMQ**
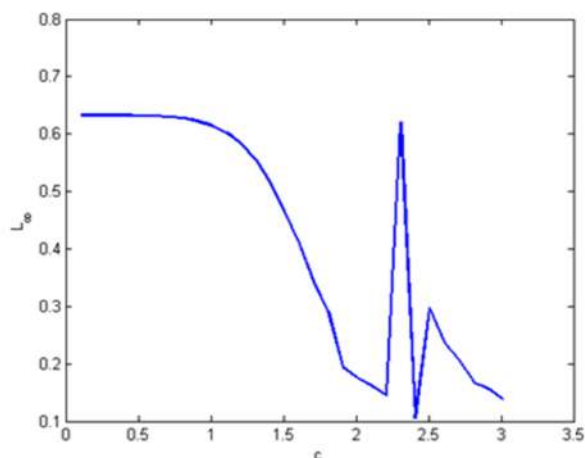


**FIGURE 1: MAX-ERROR FOR DIFFERENT VALUES OF C USING MQ**
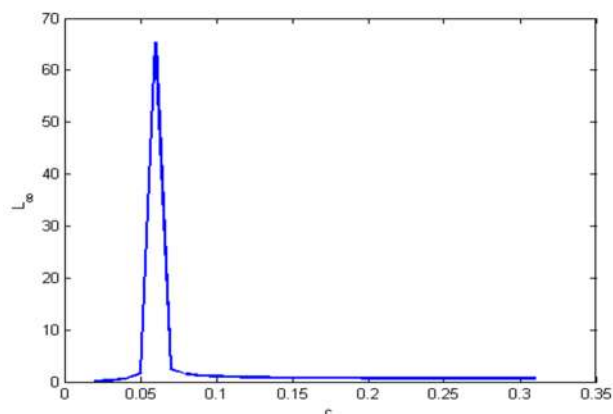


**FIGURE 3: MAX-ERROR FOR DIFFERENT VALUES OF C USING GA**

In Fig. 1 we can see that, Max error for MQ increases, if we use MMCN for the values of c between 3500 and 3700 while the least Max-error can be obtain for c=1500. Similarly in figure 2 for IMQ Max-error attains its minimum value at c= 2.4 while the maximum value of Max-error occurs at c=0.1. In case of GA the Max-error attains its minimum value at c=0.14 and 0.31 while the maximum value of Max-error occurs at c=0.06. For IQ the max-error attains its minimum value at c=13.3 i.e. produces greater accuracy while maximum value of Max-error occurs at c=13.3 i.e. produces less accuracy
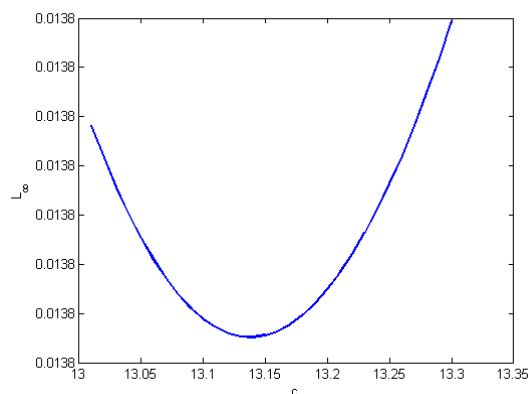
**FIGURE 4: MAX-ERROR FOR DIFFERENT VALUES OF C USING IQ**

.
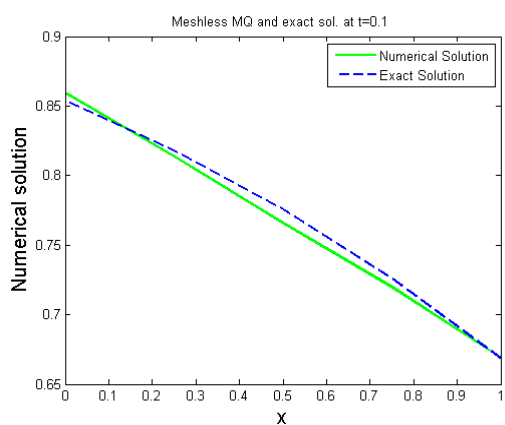


**FIGURE 5: EXACT AND NUMERICAL SOLUTION USING MQ.**
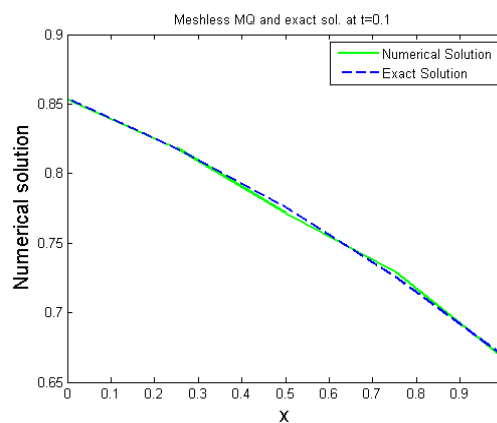


**FIGURE 6: EXACT AND NUMERICAL SOLUTION USING IMQ.**
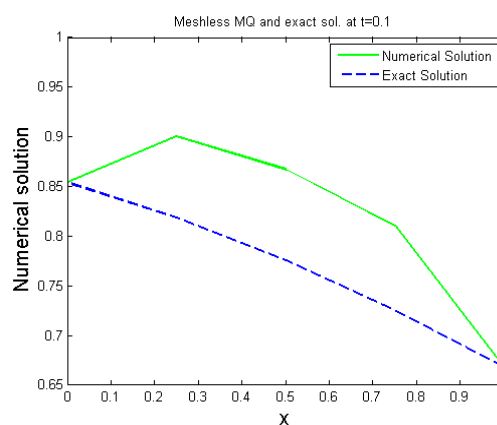


**FIGURE 7: EXACT AND NUMERICAL SOLUTION USING GA.**
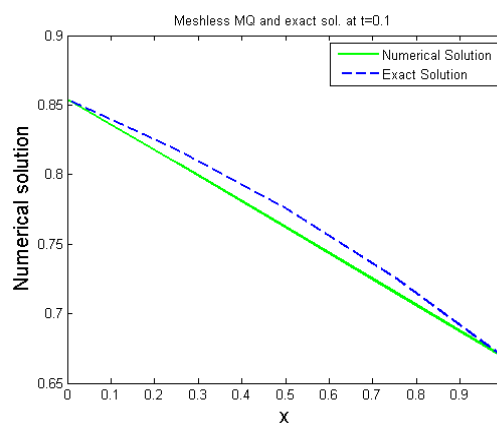


**FIGURE 8: EXACT AND NUMERICAL SOLUTION USING IQ.**

## Conclusions

In this work we have implemented Kansa' method to Fisher's equation. We have used RBFs to collocate the solution of given problem. This method is widely used because of its meshless nature. Different error norms are used to show superiority of the method. Also we have applied Brute force technique to find best values of shape parameter.

## References

1. R.A. Fisher, The wave of advance of advantageous genes, Ann. Eugenics 7 (1937) 353–369.
2. M.J. Ablowitz, A. Zeppetella, Explicit solutions of Fisher's equation for a special wave speed, Bull. Math. Biol. 41 (1979) 835–840.
3. N.F. Britton, Reaction–Diffusion Equations and their Applications to Biology, Academic Press, 1986.
4. L. Debtnath, Nonlinear Partial Differential Equations for Scientist and Engineers, Birkhauser, Boston, 1997.
5. J.D. Murray, Mathematical Biology, Springer-Verlag, 1993.
6. Z.S. Feng, Traveling wave behavior for a generalized Fisher equation, Chaos Solitons Fractals 38 (2008) 481–488.
7. B. Guo, Z. Chen, Analytic solutions of the Fisher equation, J. Phys. A: Math. Gen. 24 (1991) 645–650.
8. N.A. Kudryashov, Exact solitary waves of the Fisher equation, Phys. Lett. A 342 (2005) 99–106.
9. A.M. Wazwaz, The tanh method for traveling wave solutions of nonlinear equations, Appl. Math. Comput. 154 (2004) 713-723.
10. A.M. Wazwaz, A. Gorguis, An analytic study of Fisher's equation by using Adomian decomposition method, Appl. Math. Comput. 154 (2004) 609–620.
11. S. Braun, A. Kluwick, Blow-up and control of marginally separated boundary layers, Phil. Trans. R. Soc. A 363 (2005) 1057–1067.
12. Xin Yu, cho Xu, Jian Cha, local exponential stabilization of fisher's equation using the backstepping technique, Systems and Control Letters 74 (2014) 1-7.
13. E.J. Kansa, Multiquadrics scattered data approximation scheme with applications to computational fluid-dynamics. I. Surface approximations and partial derivative estimates, Appl. Math. Comput. 19 (1990) 127–145.
14. C.A. Micchelli, Interpolation of scattered data: distance matrix and conditionally positive definite functions, Constr. Approx. 2 (1986) 11–22.
15. W.R. Madych, S.A. Nelson, Multivariate interpolation and conditionally positive definite functions II, Math. Comput. 54 (1990) 211–230.
16. C. Franke, R. Schaback, Convergence order estimates of meshless collocation methods using radial basis functions, Adv. Comput. Math. 8 (1998) 381–399.
17. M.A. Golberg, C.S. Chen, S.R. Karur, Improved multi quadric approximation for partial differential equations, Eng. Anal. Bound. Elem. 18 (1996) 9–17.
18. Y.C. Hon, X.Z. Mao, An efficient numerical scheme for burgers equation, Appl. Math. Comput. 95 (1998) 37-50.
19. Siraj ul Haq, Siraj-ul-Islam, Marjan Uddin, A mesh-free method for the numerical solution of the KdV-Burgers equation, Applied Mathematical Modelling 33 (2009) 3442-3449.
20. R.C. Mittal, Ram Jiwari, Numerical Study of Fisher's Equation by Using Differential Quadratic Method, International General of Information And System Sciences, 5 (2009) 143-160.

# A numerical solution technique of 1D Fredholm integral equation having oscillatory kernel with stationary points

**Zaheer-ud-Din[1, 2,*], Siraj-ul-Islam[2]**

[1] Department of Basic Sciences, CECOS University of IT and Emerging Sciences, Peshawar, Pakistan
[2]Department of Basic Sciences and Islamiat, University of Engineering and Technology, Peshawar, Pakistan
*Corresponding author
Email: zaheeruddin@cecos.edu.pk

**Abstract**
In this paper, a numerical meshless solution algorithm for oscillatory Fredholm integral equation is put forward. The proposed algorithm is based on Levin's quadrature theory incorporating multi-quadric radial basis function and is specially designed to handle the case when the kernel function involves stationary point(s). The advantage of the meshless procedure is that it can be easily extended to multi-dimensional geometry. The existence of the stationary point(s) in such models has numerous applications in the field of scattering, acoustics and electromagnetic waves etc. (see [1-5]). The proposed meshless method is accurate and cost-effective and provide a trustworthy platform to solve highly oscillatory Fredholm integral equations.

**Key words**: Fredholm integral equations, ODEs, Multi-quadric radial basis functions (MQ RBF), Levin's quadrature, Radial basis function differentiation matrix.

## 1 Introduction

A boundary value problem with an oscillator can be converted to its equivalent Fredholm integral equation having oscillatory kernel and vice versa. A 1D Fredholm integral equation with oscillatory kernel model of the second kind can be articulated as given in [1, 2]:

$$s(x) = f(x) + \int_a^b h(x,y)e^{iw\,o(x,y)}s(y)dy, \; y \in [a,b], \quad (1)$$

where $f$, $h$ and $o$ are smooth functions. $o$ is an oscillator function and $w$ is the frequency of oscillator. As $w$ gets higher and higher value, the model given in the above Eq. (1) becomes highly oscillatory Fredholm integral equation.
The oscillatory integral of the Fredholm integral equation is given by:

$$I = \int_a^b h(x,y)e^{iw\,o(x,y)}s(y)dy, \quad (2)$$

where Eq. (2) may or may not have stationary point(s). If $\frac{do}{dy} = o$, at any point $\zeta \in [a,b]$, then Eq. (2) is said to have a stationary point at $\zeta$, otherwise Eq. (2) is called

integral free-of-stationary-point(s). Consequently, Eq. (1) is called Fredholm integral equation with or without stationary point(s).

The main challenge is solving Eq. (1) is how to evaluate it accurately and efficiently especially if the kernel function is highly oscillatory while incorporating stationary point(s). The literature is adequate and very few methods have been reported in the past in this scenario, (see [6-13]); the majority of authors have focussed on oscillatory integrals rather than oscillatory integral equations, where the quadrature methods fails to deliver. The literature details of the evaluation methods for the models in Eqs. (1) and (2) when the kernel function is with and without stationary point(s) are given in [1, 3] and the references therein.

In the present work, a new algorithm is proposed to solve oscillatory Fredholm integral equations. The algorithm is part and parcel of MQ-RBF differential matrix [1, 3] (a meshless differential matrix technique) and Levin's quadrature theory [1, 7]. The challenging aspect of this our algorithm is that it can accurately and efficiently handle the case when the kernel function involve stationary point(s). Furthermore, our proposed method works accurately for both uniform and non-uniform nodal points.

## 2 Proposed numerical procedure

Discretizing Eq. (1) on $\{x_j\}, j = 0,1,\ldots,M$ we have

$$s(x_j) = f(x_j) + \int_a^b h(x_j,y)e^{iw\,o(x_j,y)}s(y)dy, \; y \in [a,b], \quad (3)$$

Eq. (3) has oscillatory integrals of the form

$$I_j = \int_a^b h(x_j,y)e^{iw\,o(x_j,y)}s(y)dy, \; j = 0,1,\ldots,M \quad (4)$$

Eq. (4) with kernel function free of stationary point(s) can be easily evaluated [1, 3]. We consider here the case when Eq. (4) is having a kernel function with stationary point(s). Let $\zeta \epsilon [a,b]$ be a fixed stationary point. Choose a suitable constant $\eta > 0$ such that Eq. (4) is subdivided into the following three integrals (see [1, 3] for details) as:

$$I_j$$

$$= \int_{a}^{\zeta-\eta} h(x_j, y) e^{iw \, o(x_j,y)} s(y) dy$$

$$+ \int_{\zeta+\eta}^{\zeta-\eta} h(x_j, y) e^{iw \, o(x_j,y)} s(y) dy$$

$$+ \int_{\zeta+\eta}^{b} h(x_j, y) e^{iw \, o(x_j,y)} s(y) dy \qquad (5)$$

To evaluate Eq. (5), one has to establish connectivity between local and global nodes through barycentric interpolation [1, 3, 14]. The integrals $I_j^1, I_j^2$ and $I_j^3$ can now be evaluated through modified Levin's quadrature incorporating MQ-RBF differential matrix [1, 3], such that Eq. (5) becomes:

$$I_j$$

$$= [\sum_{q=1}^{3} \{Q_j^q (D_q + i\omega \mathbb{D}_j^q)^{-1} diag(H_i^q) M_q^l\}] \psi \qquad (6)$$

Eq. (6) in simplified form can be written as:

$$I_j = U_j \psi, \qquad (7)$$

where,

$$U_j = \sum_{q=1}^{3} \{Q_j^q (D_q + i\omega \mathbb{D}_j^q)^{-1} diag(H_i^q) M_q^l\}$$

Upon substitution of Eq. (6) into Eq. (3) we get:

$$s(x_j) = f(x_j) + U_j \psi \qquad (8)$$

The unknown function $\psi$ of order $(M+1) \times 1$ can be evaluated by considering a square mesh such that $x_j = y_j, j = 0,1, \dots, M$. Eq. (8) can then be written as:

$$\psi = F + U_j \psi, \qquad (9)$$

where, $F$ is a vector of order $(M+1) \times 1$, $U$ is a matrix of order $(M+1) \times (M+1)$.

Finally, solving (9) for $\psi$, we get the required numerical solution.

## 3 Results

In this section we test the method on a bench mark problem given in [1, 2]. The model given here is an example of oscillatory Fredholm integral equation having stationary point $\zeta = 0.3$. To check the accuracy, relative error norm has been checked against nodal points and frequencies. Consider

$$s(t) = f(t) + \int_{-1}^{1} h(t,u) e^{iw \left(\frac{t^2}{20} + (u - \frac{3}{10})\right)} s(u) du,$$

where $f(t) = 1 + \frac{\sin(5t)}{t^2 + \frac{1}{5}} - e^{-2t^3 - 6} \left( e^{iw \left(\frac{t^2}{20} + \frac{49}{100}\right)} - e^{iw \left(\frac{t^2}{20} + \frac{169}{100}\right)} \right), h(t,u) = \frac{-12u + iw(2u - \frac{3}{5})}{1 + \frac{\sin(5u)}{u^2 + \frac{1}{5}}} - e^{-2t^3 - 6u^2}$ and

the exact solution is $u(t) = 1 + \frac{\sin(5t)}{t^2 + \frac{1}{5}}$. Results are shown in the following Figures.
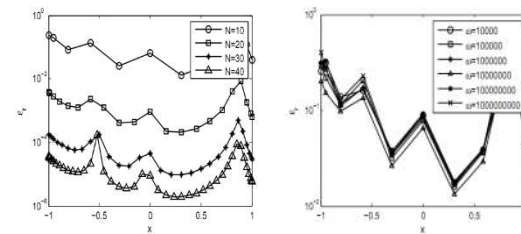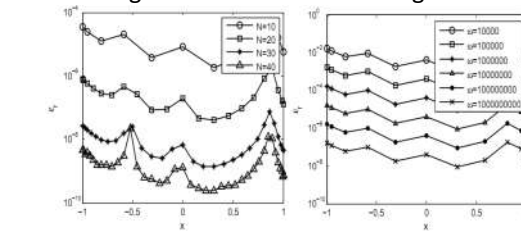


| Figure 13 | Figure 2 |



| Figure 3 | Figure 4 |

**Test Problem**: Figures 1 and 2 are results of Ref. [2], While Figures 3 and 4 shows results of new proposed method.

## 4 Conclusions

The solution of an oscillatory model of Fredholm integral equations is discussed in this paper. The kernel function of the model is having stationary points. A new numerical method is proposed to solve such type of models. In figures 1 and 3 frequency is fixed to be $10^6$; while in figures 2 and 4 nodal points are fixed to be 10. The proposed numerical method is accurate both against increasing nodal points and frequencies as shown in figures 3 and 4. It is efficient as well as it incorporate very few nodal points to get accurate results. Hence the proposed algorithm provide a reliable source for solution of the model in hand.

## 5 References

[1] Zaheer-ud-Din, Siraj-ul-Islam, Numerical solution of 1D highly oscillatory Fredholm integral equations with and without stationary points, App. Math. Comput. (2015), submitted.

[2] J. Li, X. Wang, S. Xiao, and T. Wang. A rapid solution of a kind of 1D Fredholm oscillatory integral equation, J. Comput. Appl. Math. 236 (2012) 2696–2705.

[3] Siraj-ul-Islam, I. Aziz, Zaheer-ud-Din, Meshless methods for multivariate highly oscillatory Fredholm

integral equations. Eng. Anal. Bound. Elem. 53 (2015) 100-112.

[4] O. Bruno, C. Geuzaine, J. Monro, F. Reitich, Prescribed error tolerances within fixed computational times for scattering problems of arbitrarily high frequency: the convex case, R. Soc. London. Trans. Ser. 362 (1816) (2004) 629–645.

[5] D. Huybrechs, S. Vandewalle, A sparse discretization for integral equation formulations of high frequency scattering problems, SIAM J. Sci. Comput. 29 (6) (2007) 2305–2308.

[6] F. Ursell, integral equations with a rapidly oscillating kernel, J. Lond. Math. Soc. 44 (1969) 449-459.

[7] D. Levin, Procedure for computing one and two-dimensional integrals of functions with rapid irregular oscillations, Math. Comput. 38 (1982) 531-538.

[8] K. Atkinson, The numerical solution of integral equations of the second kind, Cambridge University Press, Cambridge, 1997.

[9] A. Iserles, S. P. Norsett, Efficient quadrature of highly oscillatory integrals using derivatives, Proc. R. Soc. 461 (2005) 1388–1399.

[10] J. Li, X. Wang, T. Wang, A universal solution to one-dimensional highly oscillatory integrals, Sci. China. Ser. 51 (10) (2008) 1614– 1622.

[11] J. Li, X. Wang, T. Wang, and C. Shen, Delaminating quadrature method for multi-dimensional highly oscillatory integrals. App. Math. Comput. 209(2) (2009) 327– 338.

[12] Siraj-ul-Islam, S. Zaman, New quadrature rules for highly oscillatory integrals and the integrals with stationary points. J. Comput. Appl. Math. 278 (2015) 75-89.

[13] Siraj-ul-Islam, I. Aziz, and W. khan. Numerical integration of multi-dimensional highly oscillatory, gentle oscillatory and non-oscillatory integrands based on wavelets and radial basis functions, Eng. Anal. Bound. Elem. 36 (2012) 1284–1295.

[14] J. Berrut, L. Trefethen, Barycentric Lagrange interpolation, SIAM Review 46 (3) (2004) 501

# Meshless procedure with multiquadric radial basis function for solution of elliptic boundary value problems

**Zahid khan[1*], Siraj-ul-islam [1], Sakhi-Zaman[1]**

[1] Department of Basic Sciences, University of Engineering and Technology Peshawar, Pakistan.

*Email: zahid.na01@gmail.com

## Abstract

Due to the importance of the elliptic partial differential equations in science and engineering, one can encounter the numerical solution of these types of equations. Meshless procedure based on multiquadric radial basis function (MP) with three different strategies of selecting best value of the shape parameter is used to solve the elliptic boundary value problems (EBVPs) such as Helmholtz and Poisson equations. Comparison of the proposed method is given with some numerical methods reported in [2, 4]. Some numerical test problems are included to justify the accuracy and efficiency of the present method.

**Keywords:** Multiquadric radial basis function, Elliptic boundary value problems, Helmholtz equation, Poisson equation.

## 1 Introduction

In science and engineering EBVPs have numerous applications. It can be used in the modelling of real world problems, like the stream function, flow of air pollutants, fluid flow, temperature deflection, velocity potential and electrostatics potentials etc. The analytical solution of EBVPs is some time difficult or impossible to find out. To solve this difficulty, the researchers have developed accurate and efficient numerical methods for the solutions of EBVPs.

Several numerical methods have been developed in last few decades. These includes FDM [8], FEM [5, 6, 16], SGM [2], meshless method [11, 12, 14, 15, 18], SCM [1, 7, 10], etc. Recently, in [16], the author has used FDS based on nine-point approximation for the solution of two dimensional Helmholtz equations. Fasshauer in [11] has introduced meshless method based on RGM for the solution of EBVPs. The author combined the meshless method with FDM and FEM as well.

In [15], the authors have presented the meshless method in a new format that locally satisfy the boundary conditions using point collocation formulation and globally satisfy the boundary conditions using Galerkin formulation.

In [14], the authors proposed a new numerical scheme for two dimensional second order EBVPs. The ADSG for the solution of EBVPs is introduced in [2]. In [6], the authors developed a scheme which introduces variable coefficients for the solution of Helmholtz equation using cylindrical coordinates. The FFT technique based on separation of variables technique is used for the solution of EBVPs which strengthened the rate of convergence up to fourth order [13].

Fairweather in [10] described a numerical method based on QSCM for solving the Helmholtz boundary value problem.

The domain of calculation is taken as a unit square and non homogeneous boundary conditions such Dirichlet, Neumann, periodic and mixed boundary conditions were used. Davari in [9] used Legendre polynomials approximation for the numerical solution of second order linear PDEs. Imran Aziz et.al [3] reported a new method for the numerical solution of EBVPs using HWCM.

The general form of EBVPs is given by:

$$\delta_1 \frac{\partial^2 u}{\partial x^2} + \delta_2 \frac{\partial^2 u}{\partial y^2} + \delta_3 \frac{\partial u}{\partial x} + \delta_4 \frac{\partial u}{\partial y} + \delta_5 u = g,$$
$$\delta = \delta(x, y), \tag{1}$$

where $\delta_1, \delta_2, \delta_3, \delta_4, \delta_5$ $and$ $g$ and are functions of $x, y$ or constants. The computational domain for (1) is $[0, 1] \times [0, 1]$.

In this paper, we will use a meshless procedure based on MQ RBF for the numerical solution of Helmholtz and Poisson equations. Three different strategies will be used for the most favourable value of the shape parameter. In order to determine the accuracy of the meshless method we will compare our results with HWCM reported in [4] and ADSG method [2]. The present method is found more accurate and efficient than the HWCM and the ADSG.

The pattern of the paper is as follows. In section 2, The meshless procedure is discussed. Numerical examples and results are discussed in section 3. Finally a few remarks concluded the paper.

## 2        Meshless procedure

The univariate radial basis function $\phi(r)$ is a continuous function with $r \geq 0$. Consider a set of m-centres $(x_i{}^c, y_j{}^c)$ for $i, j = 1, 2, \ldots, m$ then the RBF interpolation can be written as:

$$S(\mathbf{x}) = \sum_{k=1}^{m} \delta_k \phi_k(\mathbf{x}), \quad \mathbf{x} \in \mathbf{R}^2. \qquad (2)$$

The unknown coefficients $\delta_k$ for $k = 1, 2, \ldots, m$ can be obtained by plugging the interpolation condition

$$S(\mathbf{x}_i) = G(\mathbf{x}_i), \qquad i = 1, 2, \ldots, n, \quad \mathbf{x}_i \in \mathbf{R}^2, \qquad (3)$$

where $G(\mathbf{x}_i), \ i = 1, 2, \ldots, n$ is the corresponding source function of the PDE. The number of centres m and the number of interpolation points are equal in this case.

Equation (3) gives a system of linear equations and can be written in matrix notation as:

$$\mathbf{H\delta = G}, \qquad (4)$$

where $\mathbf{H}$ is $m \times m$ square matrix and is called interpolation or system matrix.

The entries of H are given by

$$h_{jk} = \phi\big(||x_j{}^c, \ y_k{}^c ||_2, c\big), \qquad j, k = 1, 2, \ldots, m.$$

The unknown coefficients $\delta_k$ for k = 1, 2. . . . , m can be determined by solving the system of linear equations (3).

In this paper we have used multiquadric RBF $\phi(r)$ and. is defined as:

$$\phi(r) = \sqrt{c^2 + r^2},$$

where

$$r = \sqrt{(x - x_p{}^c)^2 + (y - y_p{}^c)^2}, \qquad p = 1, 2, \ldots, m.$$

And c is the shape parameter. The accuracy of this procedure depends on the value of c. Many algorithms have been developed for the appropriate

value of c. However, for the researchers it is still an open problem to find the optimal value of c. In this work we have used an algorithm [17] for optimal value of the c. The algorithm [17] for the shape parameter c is given as:

**Programme 1:** CostEpsilon.m

I.        $G = g(x_k); \qquad k = 1, 2, \ldots \ldots, m.$   (G is the source function)

ii.       $H = \phi_{ij}; \qquad i, j = 1, 2, \ldots \ldots, m.$ (The coefficient matrix in equation 6)

iii.      $A = inv(H);$   ( Inverse matrix of $H$)

iv.      $D = diag(A);$   ($D$ contains the diagonal element of matrix A)

v.       $\delta = A * G;$

vi.      $\kappa = \delta(:)./D;$

vii.     $c = ||\kappa||_2;$

**Algorithm 2:**

i.        Call the function $c = CostEpsilon(x_{ver}, y_{ver}, \ c, f);$

ii.       $c = fminbnd (@(c)CostEpsilon(x_{ver}, y_{ver}, c, f), mine, maxe)$

iii.      $\delta = H/G;$

iv.      $S = H * \delta.$

In this algorithm, the optimal value of c is selected in the interval [mine, maxe] using the MATLAB function fminbnd. We have taken mine $= 0$ and maxe $= 3$ in the proposed work to obtain the accurate approximate solution S($\mathbf{x}$) of the PDE.

Let $S(x) = \sum_{k=1}^{m} \delta_k \phi_k$ be an approximate solution of (1). Then (1) can be written as:

$$S''(x) + S'(x) + kS(x) = G. \qquad (5)$$

Let

$$\mathcal{L}S(x) = S''(x) + S'(x) + kS(x), \qquad (6)$$

then (5) can be expressed as:

$$\mathcal{L}S(x) = G(x). \qquad (7)$$

The unknown coefficients $\delta_k$ can be determined by the interpolation condition:

$$\mathcal{L}S(\mathbf{x}_j) = G(\mathbf{x}_j), \quad j = 1, 2, \ldots \ldots, m, \quad \mathbf{x}_j \in \mathbf{R}^2 \qquad (8).$$

Equation (8) gives a system of linear equations and can be written in matrix notation as:

$$\begin{bmatrix} L\phi_{11} & L\phi_{12} & \cdots & L\phi_{1m} \\ L\phi_{21} & L\phi_{22} & \cdots & L\phi_{2m} \\ \vdots & \cdots & \ddots & \vdots \\ L\phi_{m1} & L\phi_{m2} & \cdots & L\phi_{mm} \end{bmatrix} \begin{bmatrix} \delta_{1m} \\ \delta_{2m} \\ \vdots \\ \delta_{mm} \end{bmatrix} = \begin{bmatrix} g_{1m} \\ g_{2m} \\ \vdots \\ g_{mm} \end{bmatrix},$$

(9)

where

$$\mathcal{L}\phi_{ij}(\mathbf{x}) = \phi''_{ij}(\mathbf{x}) + \phi'_{ij}(\mathbf{x}) + k\phi_{ij}(\mathbf{x}), \quad \mathbf{x} \in \mathbf{R}^2.$$

The matrix representation of the system is given by

$$\boldsymbol{\phi}\boldsymbol{\delta} = \mathbf{G},$$

(10)

where

$$\mathbf{G} = [g_{im} \quad g_{2m} \quad g_{3m} \cdots \quad g_{mm}]^T$$

and

$$\boldsymbol{\delta} = [\delta_{1m} \quad \delta_{2m} \quad \delta_{3m} \cdots \delta_{mm}]^T.$$

Equation (10) can be written as,

$$\boldsymbol{\delta} = \boldsymbol{\phi}^{-1}\mathbf{G}.$$

(11)

Substituting (11) in (2), we can find the required approximate solution.

## 3        Numerical examples and discussions

In this section, some test problems [3, 4] are considered to verify the accuracy of the meshless procedure. The real solutions of the test problems which are not given, are obtained by using **MAPLE 15**. The results in terms of maximum error norm $L_\infty$ is obtained in each test problem which is defined as:

$$L_\infty = \max|u_{exact}(k) - u(k)|.$$

**Example 1.** Consider the Helmholtz EBVP

$$\frac{\partial^2 u}{\partial x^2} + \frac{\partial^2 u}{\partial y^2} + ku = f(x, y), \qquad 0 \leq x, \ y \geq 1,$$

where the function $f(x, y)$ is obtained from the exact solution

$$u(x, y) = \frac{1}{1+2\pi^2} Cos(\pi x)Cos(\pi y) \qquad (13)$$

The Dirichlet B.C.'s are taken from the exact solution (13). The MP is tested for the three different strategies of c. The results in terms of $L_\infty$ error norm are obtained and is shown in table 1. The CPU time (in seconds) of the MP for different strategies of c is given in table 2. In addition, we have compared the $L_\infty$ error norm and CPU time of the new MP method with HWCM [4] in table 3. We found that the results produced by the MP are more accurate and efficient than the results of HWCM. The MP reduces the error up to $O(10^{-07})$ while HWCM reduces the $L_\infty$ error norm up to O $(10^{-06})$ at N = 32 points. Also it is clear from the table 3 that the MP takes less CPU time as compared to HWCM.

Table 1:  $L_\infty$ of the MP for different values of *N* for example 1.

| N | CE | c = 0.55 | $c = \dfrac{2}{\sqrt{2m-1}}$ |
|---|---|---|---|
| 4 | $2.28e^{-04}$ | $3.16e^{-04}$ | $2.15e^{-04}$ |
| 6 | $9.55e^{-05}$ | $2.20e^{-04}$ | $1.98e^{-04}$ |
| 8 | $4.71e^{-06}$ | $9.61e^{-05}$ | $9.51e^{-05}$ |
| 16 | $6.45e^{-07}$ | $2.17e^{-06}$ | $8.68e^{-06}$ |
| 32 | $2.42e^{-07}$ | $7.61e^{-07}$ | $3.81e^{-07}$ |

Table 2:  CPU time (in seconds) of the MP for different values of  N for example 1.

| N | CE | c = 0.55 | $c = \dfrac{2}{\sqrt{2m-1}}$ |
|---|---|---|---|
| 4 | 0.2615 | 0.0851 | 0.0998 |
| 6 | 0.3387 | 0.0887 | 0.0970 |
| 8 | 0.4212 | 0.1042 | 0.0850 |
| 16 | 4.6876 | 0.1652 | 0.1413 |
| 32 | 320.73 | 1.5048 | 1.2556 |

Table 3:  $L_\infty$ comparison of the MP and HWCM method for different values of N for example 1.

| N | MP (CE) | CPU time | HWCM [4] | CPU time |
|---|---------|----------|----------|----------|
| 4 | $2.28e^{-04}$ | 0.260 | $2.34e^{-04}$ | 0.300 |
| 8 | $4.71e^{-06}$ | 0.420 | $6.09e^{-05}$ | 5.000 |
| 16 | $6.45e^{-07}$ | 4.600 | $1.54e^{-05}$ | 67.00 |
| **32** | $\mathbf{2.42e^{-07}}$ | **320.7** | $\mathbf{3.85e^{-06}}$ | **1386** |

**Example 2.** Consider the Poisson equation

$$u_{xx} + u_{yy} = f(x, y),$$

and the real solution is

$$u(x, y) = 3xye^{x+y}(1 - x)(1 - y).$$

The comparison of the $L_\infty$ error norm for different strategies of c is shown in table 4. From this table, it is shown that the results of algorithm 1 for the shape parameter c are more accurate and stable than the other two strategies. The comparison of the CPU time of the given three strategies is shown in table 5. The comparison of $L_\infty$ error norm of the MP, HWCM [4] and ADSG [2] is given in table 6. One can see from this table that the MP gives better accuracy in this case as well.

Table 4: $L_\infty$ of the MP for different values of $N$ for example 2.

| N | CE | c = 0.55 | $c = \dfrac{2}{\sqrt{2m-1}}$ |
|---|----|----------|------------------------------|
| 4 | $2.28e^{-04}$ | $1.40e^{-01}$ | $1.20e^{-01}$ |
| 6 | $9.55e^{-05}$ | $4.66e^{-02}$ | $4.08e^{-02}$ |
| 8 | $4.71e^{-06}$ | $1.61e^{-02}$ | $1.56e^{-02}$ |
| 16 | $2.00e^{-06}$ | $3.61e^{-04}$ | $1.40e^{-03}$ |
| 32 | $2.50e^{-07}$ | $1.11e^{-05}$ | $7.12e^{-05}$ |

Table 5: CPU time (in seconds) of the MP for different values of N for example 2.

| N | CE | c = 0.55 | $c = \dfrac{2}{\sqrt{2m-1}}$ |
|---|----|----------|------------------------------|
| | | | |

| 4 | 0.2554 | 0.0736 | 0.0744 |
| 6 | 0.3253 | 0.0750 | 0.0755 |
| 8 | 0.3811 | 0.0784 | 0.0771 |
| 16 | 3.9437 | 0.1271 | 0.1283 |
| 32 | 262.14 | 1.1503 | 1.1120 |

Table 6: $L_\infty$ comparison of the MP and HWCM and ADSG method for different values of N for example 2.

| N | MP (CE) | HWCM [4] | N | ADSG [2] |
|---|---------|----------|---|----------|
| 4 | $2.28e^{-04}$ | $2.25e^{-04}$ | 5 | $2.467e^{-02}$ |
| 8 | $4.71e^{-06}$ | $6.55e^{-05}$ | 9 | $4.180e^{-03}$ |
| 16 | $2.00e^{-06}$ | $4.11e^{-05}$ | 17 | $3.775e^{-04}$ |
| **32** | $\mathbf{2.50e^{-07}}$ | $\mathbf{9.33e^{-06}}$ | **33** | $\mathbf{1.163è^{-05}}$ |

**Example 3.** The Helmholtz equation for $k = 900$ is given by

$$\frac{\partial^2 u}{\partial x^2} + \frac{\partial^2 u}{\partial y^2} + ku = f(x, y), \qquad x \geq 0, \ y \geq 1,$$

The exact solution is

$$u(x, y) = e^{xy^2}.$$

The function f(x, y) can be found from the exact solution. In table 7, the comparison of $L_\infty$ error norm using three different strategies of c is given. In table 8, The CPU time comparison is given. From table 7, one can observed that the accuracy of the MP using the algorithm 1 is slightly better and stable than results of the other two strategies. It follows that in algorithm 1, a best value of c is chosen and consequently produces better accuracy.

Table 7: $L_\infty$ of the MP for different values of N for example 3.

| N | CE | c = 0.55 | $c = \dfrac{2}{\sqrt{2m-1}}$ |
|---|---|---|---|
| 4 | $7.29e^{-04}$ | $2.86e^{-04}$ | $2.86e^{-04}$ |
| 6 | $1.05e^{-04}$ | $7.70e^{-04}$ | $5.45e^{-04}$ |
| 8 | $3.90e^{-05}$ | $6.11e^{-04}$ | $5.98e^{-04}$ |
| 16 | $6.70e^{-05}$ | $1.11e^{-03}$ | $4.11e^{-03}$ |
| 32 | $2.50e^{-07}$ | $1.11e^{-05}$ | $7.12e^{-05}$ |

Table 8: CPU time (in seconds) of the MP for different values of N for example 3.

| N | CE | c = 0.55 | $c = \dfrac{2}{\sqrt{2m-1}}$ |
|---|---|---|---|
| 4 | 0.2547 | 0.0744 | 0.0774 |
| 6 | 0.3030 | 0.0782 | 0.0766 |
| 8 | 0.4003 | 0.0803 | 0.0766 |
| 32 | 269.48 | 1.1256 | 1.0686 |

## 4    Closing remarks

In this paper MP is used for numerical solution of elliptic boundary value problems. We have considered the numerical solution of Helmholtz and Poisson equations. An algorithm [17] is used for an optimal value of c for the RBF interpolation. The new MP with algorithm 1 shows better accuracy than the other strategies of c.

## References

[1] Abeer Ali Abushama and Bernard Bialecki. Modified nodal cubic spline collocation for Poisson's equation. SIAM journal on Numerical Analysis, 46(1):397-418, 2008.

[2] Nicomedes Alsono III and Kenneth L.Bowers. An alternating-direction sinc-galerkin method for elliptic problem. Journal of complexity, 25(3):237-252, 2009.

[3 Imran Aziz and Siraj-ul-Islam. An efficient modified haar wavelet collocation method for numerical solution of two-dimensional elliptic pdes. Differential equations and dynamical systems, page 1-14, 2015. .

[4] Imran Aziz, Siraj-ul-Islam and Bozidar Sarler. Wavelets collocation method for numerical solution of elliptic b.v. problems. Applied Mathematical Modelling, 37(3):676-694, 2013.

[5] Ronald F Boisvert. Families of high order accurate discretizations of some elliptic problems. SIAM Journal on Scientific and Statistical Computing, 2(3): 268-284, 1981.

[6] S Britt Semyon Tsynkov, and Eli Turkel. A compact fourth order scheme for the Helmholtz equation in polar coordinates. Journal of Scientific Computing, 45(1-3): 26-47, 2010.

[7] Christina C Christara. Quadratic spline collocation methods for elliptic partial differential equations. BIT Numerical Mathematics, 34(1): 33-61, 1994.

[8] Philippe G Ciarlet. The finite element method for elliptic problems, vol. 40 of classic in applied mathematics. Society for industrial and applied mathematics (siam), Philadelphia, PA, 2002. Reprint of the 1978 original.

[9] Ali Davari and Abozar Ahmadi. New implementation of legendre polynomials for solving partial differential equations. Applied Mathematics, 4(12): 1647, 2013.

[10] Graeme F Fairweather, Andreas Karageorghis, and Jon Maack. Compact optimal quadratic spline collocation methods for the Helmholtz equation. Journal of Computational Physics, 230(8): 2880-2895, 2011.

[11] Gregory E Fasshauer. Meshfree approximation methods with MATLAB. Volume 6, World Scientific, 2007.

[12] H.Y Hu, Z.-C. Li, and A.H.-D. Cheng. Radial basis collocation methods for elliptic boundary value problems. Computers & Mathematics with Applications, 50.1 (2005): 289-320.

[13] Andreas Karageorghis, CS Chen, and Yiorgos-Sokratis Smyrlis. A matrix decomposition rbf algorithm: approximation of functions and their derivatives. Applied numerical mathematics, 57(3):304-319, 2007.

[14] Nam Mai-Duy and Thanh Tran-Cong. A cartisian-grid discretization scheme based on local integrated rbfns two-dimensional elliptic problems. CMES: Computer Modelling in Engineering and Sciences, 51(3):213-238, 2009.

[15] Nam Mai-Duy and Thanh Tran-Cong. An integrated-rbf technique based on galerkin formulation for elliptic differential equations. Engineering analysis with boundary element, 33(2):191-199, 2009.

[16] I Singer and Eli Turkel. Sixth-order accurate finite diffence schemes for the Helmholtz equation. Journal of Computational Acoustics, 14(03):339-351, 2006.

[17] Siraj-ul-Islam, A. S. Al-Fhaid, and S. Zaman. Meshless and wavelets based complex quadrature of highly oscillatory integrals and the integrals with stationary points. . Engineering analysis with boundary element, 37:1136-1144, 2013.

[18] Q.N Yang, JJ Zheng, Y Miao, and YZ Sima. An improved hybrid boundary node method for solving steady fluid flow problems. Engineering Analysis with Boundary Elements, 35(1):18-24, 2011.

# Modified Biogeography Based Evolutionary Algorithm for Global Optimization Problems

Khug Alam[1], W.K. Mashwani[1], M.A. Jan[1], M.Asim[1] and M. Asad[2]
*[1]Kohat University of Science and Technology, KPK, Pakistan*
*[2]Bacha Khan University Charsada, KPK, Pakistan*
*[*]Email:khugkust@gmail.com*

**Abstract:** Evolutionary Computation (EC) is an emerging area of research in the last few years and so. An abundance of evolutionary algorithms (EAs) have been developed for different types of optimization and search problem. Biogeography Based Optimization (BBO) is recently newly and efficiently developed EA by using a set of uniformly and randomly generated solutions to approximate a set of optimal solutions in a single simulation unlike traditional optimization methods. BBO is mainly shares information between species of migration from one island to another island based mathematical model to perform their search process. Differential Evolution (DE) is another powerful approach in EC field. DE uses different mutation variants to perturb their population. In this paper, we have injected different mutation strategies of DE to BBO algorithm developed modified version of BBO called (BBO-DEI). The suggested BBO-DEI have efficiently solved most of the test problems of the 2005 IEEE Conference on Evolutionary Computation (CEC'05) as compared to the original BBO algorithm.

**Keywords**: Optimization Problems, Evolutionary Computation, Evolutionary Algorithms, Biogeography Based Optimization (BBO)

## 1. Introduction

Optimization is the mathematical process for finding an optimal solution to the optimization and search problem with continuous, discrete, integer or mixed of these variables. In general, optimization problem involves an objective function subject to some constraint functions described as follows:

$$Minimize\ f(x)\quad Subject\ to$$
$$g_j(x) \leq 0, j = 1, 2, \ldots u,$$
$$h_j(x) = 0, j = 1, 2, \ldots v,$$
$$(1)$$

Where $x = [x_1, x_2, \ldots, x_n]^T \in R^n$ is an $n$-dimensional vector of optimization/decision variables, u is the number of inequality constraints, and v is the number of equality constraints. Moreover, $L_i \leq x_i \leq U_i$, $i = 1, 2, \ldots n, L_i$ and $U_i$ are the lower and upper bounds of parametric space, S and the function $f(x)$ is called an objective /fitness function. A solution that optimizes this objective function well approximately is called an optimal solution of the problem (1).

Evolution is the basic strategy of the two-step process of random variation and selection. Mathematically, it could be represented as $x[t + 1] = s(v(x[t]))$, where $x[t]$ and $x[t + 1]$ are the previous and current populations obtained through the execution of selection (s) and variation (v) operators. Evolutionary algorithms (EAs) use a set of solutions, usually generated uniformly and randomly called a population. EAs employ different evolutionary operator to perturb their population for finding an approximated set of optimal solutions in a single simulation run unlike traditional optimization techniques. They are inspired by natural evolution and their successful operations are attributed to different intrinsic search operators and well configured settings of parameters.

Since the development of first evolutionary algorithms (EAs) [2], many types of EAs have been proposed in the existing literature of EC [1,3,4,5,6,7,8,9,10,11,13,14,15]. EAs do not demand for any derivative information regarding the problems at hand. They have strong ability of handling different types of optimization and real world problems. In this paper, we have employed different mutation strategies of DE in BBO [7] framework and developed modified biogeography based evolutionary algorithm denoted by BBO-DEI with aim further enhance the capabilities of the baseline BBO over test problems developed for the special session of the 2005 conference of the evolutionary computation (CEC05) [12].

The rest of the paper is organized as under. Section 2 presents basic information about the biogeography based optimization algorithm. Section 3 provides modified biogeography based evolutionary algorithm and four different differential evolution mutation strategies. Section 4 devoted to the numerical results used benchmark functions. Section 5 concludes this paper with some future work plan.

## 2. Biogeography Based Algorithm

Biogeography Based Optimization (BBO) was first introduced by D. Simon [7]. Mathematical models of biogeography describe how the species migrate from one island to another and how the species get extinct. Islands that are more suitable for species are said to have a high habitat suitability index (HSI). Those features which are affected by species such as land area, rainfall,

temperature and many other issues are called suitability index variables (SIVs). The terms of habitability are HSI which are the dependent variables and SIVs are independent variables. Islands with a high HSI have a quality to support many species and islands having low HSI can attract only a number of species. High HSI has many species which emigrate to their neighboring habitats because high HSI has the large number of populations. Emigration occurs because it is affected by a large number of species within a population. When species emigrate from an island, only a few number of representatives species emigrate. BBO simulates immigration of species between islands in a multidimensional space, where each island represents a candidate solution of the optimization problem (1). High HSI islands have a high emigration rate, but they have a low immigration rate because they support many species. Those species which migrate to a high HSI island, they die due to the competition for resources from other species. Low HSI islands have a high immigration rate because the population of that island is low. Species want to emigrate from that island because that island is an unpleasant place for living. The rate of immigration is high to these islands because there is more additional place available for new species. However, when more species arrive to the low HSI Island, the HSI of the island is increased. The pseudocode of the original BBO is outlined in the Algorithm1.

- First, define the island modification probability, mutation probability and elitism. These steps are the same as in Genetic Algorithm.
- Initialize the population size.
- The immigration rate λ and emigration rate μ are calculated for each population. The best solution has high emigration rates and low immigration rates.
- Choose the immigration population based on immigration rates. To select the emigration population use roulette wheel selection based on the emigration rates.
- Randomly select the migrated SIVs based on the selected population.
- Apply mutation based on mutation probability for each population.
- The best values are calculated for each individual population.
- If the termination criterion is not correct, then go to the previous step.

---

**Algorithm 1** BBO psoedocode without DE mutation strategy

1: generate the pop size
2: **for** $i = 1$ to pop size
3: $\mu = (\text{popsize} - i)/\text{popzize}$
4: $\lambda = 1 - \mu$
5: **If** $\text{rand} < 0.4$
6: **For** $k = 1$:popsize
7: Select $\mu$
8: Randomly select an SIV from $X_i$
9: Replace a random SIV in $X_k$
10: **end for**
11: **end if**
12: **end for**

---

## 3. Modified Biogeography Based Evolutionary Algorithm

In the proposed algorithm, BBO has been injected with different mutation strategies of differential evolution (DE) denoted by (BBO-DEI). A simple strategy of mutation such as DE/rand/1 has employed in the original framework of BBO aim to improve their search process upon test problem developed for the special session of Conference on Evolutionary Computation ( CEC'05) [1]. Modified BBO with DE Injection (BBO-DEI) Algorithm is hereby outlined in the Algorithm 2.

### 3.1 Differential Evolution (DE)

Differential Evolution (DE) is another powerful EA, which was first introduced by Rainer Storn and Kenneth Price in 1996. It came up with the idea of using vector differences for perturbing the vector population [3], [4]. Adaptation schemes are recently introduced in the framework of DE [5,6,9,10,11] to further improve their convergence properties over both complicated constrained and nonlinear optimization problems. For more details, the interested readers are referred [8]. Mutation, crossover and selection are important operators of DE framework to generate and select solutions to its next generation of population evolution. $NP$ (Population size), $F_m$ (mutation factor) and $Cr$ (crossover ratio) are their important intrinsic parameters. To maintain genetic diversity from one generation to the other is called mutation. In every generation g of DE, a mutant vector, $V_{i,g}$ of the current population, $x_{i,g,i=1,2,....,NP}$ is designed by using one of the following strategies which are often used in its literature [6].

---

**Algorithm 2: Framework of the (BBO-DEI)**

```
1:  Initialize the popsize
2:  i=1:popsize
3:  μ=(popsize-i)/popzize
4:  λ=1-μ
5:  If rand<0.4
6:  For k=1:popsize
7:  For j=1:n
8:  If rand< λ_k
9:  Select μ
10: Select H_k if (μ) < (λ)
11: If H_k is selected
12: For j=i:popsize
13: Generate different integers r_1, r_2 and r_3
14: Select emigration rate μ_j
15: H_i(SIV) = H_j(SIV)
16: Else
17: H_i(SIV) = H_{r_1}(SIV)+F.(H_{r_2}(SIV))-H_{r_3}(SIV)
18: EndIf
19: EndFor
20: EndFor
21: EndIf
22: EndIf
23: EndFor
```

24: $J_{rand}=rand(1,n)$

25: For $j=i:n$

26: If $t=rand(0,1) < CR$

27: Else

28: $U_i(j) = X_i(j)$

29: EndFor

30: EndIf

31: For $i=1$:popsize

32: Evaluate the offspring $U_i$

33: If $U_i$ is better than $P_i$

34: $P_i=U_i$

35: EndFor

36: EndIf

---

5. DE/rand/1

$$V_{i,g}=x_{r1,g} + F_m(x_{r2,g} - x_{r3,g})$$

6. DE/best/1:

$$V_{i,g}=x_{best,g} + F_m(x_{r2,g} - x_{r3,g})$$

7. DE/rand-to-best/1:

$$V_{i,g}=x_{r1,g} + x_{best,g} + F_m(x_{r2,g} - x_{r3,g})+ F_m(x_{best,g} - x_{r3,g})+$$

8. DE/current-to-best/1:
$$V_{i,g}=x_{r1,g} + x_{best,g} + F_m(x_{r2,g} - x_{r3,g})+ F_m(x_{best,g} - x_{i,g})+$$

Where $x_{r2,g} - x_{r3,g}$ is a difference variation vector with respect to corresponding to the current best and i[th] individual $x_{i,g}$, $x_{best,g}$ of the current generation and the values of the scaling factor $F_m \in (0,+1)$.

## 5 Benchmarks Functions

In the study of this paper, we have used 20 benchmark functions in order to examine the algorithmic performance of the proposed algorithm BBO-DEI. The results of these functions are listed in terms of Best, worst, Mean, standard deviation and average CPU time. The details regarding the used CEC'05 benchmark functions can be found in [12].

### 5.1 Numerical Results

Experimental results of our experiments for n=10 are given in table 1 and figure 1. Table 1 presents results in terms of best, worst, mean, Standard deviation and Average CPU time. Figure 1 shows the variation in the average function values in twenty five independent runs on each CEC'05 [12] test with search space dimension n=10. The results provided by suggested algorithm both

in numerical and graphical form for each CEC '05 test function are more promising in term of proximity.

# 6 Conclusion

In this paper, modified version of BBO in which DE has been employed as a search operator for the purpose to improve the search ability of the existing BBO algorithm. We have injected different mutation strategies of DE in BBO and developed a modified version of BBO called BBO-DEI. In this paper, we have only summarized the experimental results provided by DE/rand/1 strategy by using BBO as a global search algorithm. The provided better results indicated that our suggested algorithm have tackled most of the used test problems in the parlance of single objective optimization. In future, we intend to examine the performance of the suggested proposal over some latest test suites of the IEEE CEC series to better judge its ability and credibility.

## References

[1] [1] D. Wolpert, H. Macready, "Co evolutionary Free Lunches," IEEE Transactions on Evolutionary Computation, (2005), 9, no.6, 721- 735.

[2] D. Goldberg, ''Genetic Algorithms in Search, Optimization, and Machine Learning", Addison-Wesley, Pub. Co., (1989).

[3] R. Storn and K. Price, "Differential Evolution, A Simple and efficient Adaptive Scheme for Global Optimization over Continuous Spaces", ''International Computer Science Institute", Berkeley, (1995), Tech. Rep. TR-95-012.

[4] R. Storn and K. V. Price, "Differential evolution, A simple and efficient heuristic for Global optimization over continuous Spaces, "Journal of Global Optimization, (1997), 11, 341-359.

[5] J. Zhang and A. C. Sanderson, JADE: ''Adaptive Differential Evolution with Optional External Archive", in Proc, IEEE Congress on. Evolutionary. Computation, (2008).

[6] E. Mezura-Montes, J. Velzquez-Reyes, and C. A. Coello Coello, Comparative Study of Differential evolution variants for Global Optimization, "in the Proceeding of the Genetic Evolutionary Computation Conference (GECCO), Seattle, (2006), 485-492.

[7] D. Simon, ''Biogeography-Based Optimization", IEEE Transactions on Evolutionary Computation", (2008), 12, 702-713.

[8] Wali Khan Mashwani, Enhanced versions of Differential Evolution: State-of-the-art Survey ", International Journal Computing Sciences and Mathematics (IJCSM), 5(2), PP: 107-126, 2014.

[9] Tayyaba Shah, Muhammad Asif Jan, Wali Khan Mashwani and Hamza Wazir, "Adaptive Differential Evolution for Constrained Optimization Problems", Sci.Int.(Lahore) 28 (3), 2313-2320, 2016

[10] Hamza Wazir, Muhammad Asif Jan, Wali Khan Mashwani and Tayyaba Shah, "A Penalty Function Based Differential Evolution Algorithm for Constrained Optimization", the Nucleus Journal, Vol 53, No. 1 (2016) 155-161

[11] R.A. Khanum, Nasser Tairan, M.A. Jan, W.K. Mashwani and A. Salhi,"Reflected Adaptive Differential Evolution with Two External Archives for Large-Scale Global Optimization", International Journal of Advanced Computer Science and Applications, 7(2), 675-683, 2016

[12] P. N. Suganthan, N. Hansen, J. J. Liang, K. Deb, Y.-P. Chen, A. Auger and S. Tiwari, "Problem Definitions and Evaluation Criteria for the CEC 2005 Special Session on Real-Parameter Optimization", Technical Report, Nanyang Technological University, Singapore, May 2005 AND KanGAL Report #2005005, IIT Kanpur, India.

[13] Rashida Adeeb Khanum, Nasser Mansoor Tairan, Muhammad Asif Jan, and Wali Khan Mashwani,"Hybridization of Adaptive Differential Evolution with an Expensive Local Search Method", Journal of Optimization, Volume 2016, Article ID 3260940, 14 pages.

[14] M. Sulaiman, A. Salhi, Eric S Fraga, W.K. Mashwani and M. M Rashidi, " A Novel Plant Propagation Algorithm: Modifications and Implementation" Science International Journal, 28(1), 201-209, 2016

[15] R.A. Khanum, Islam Zari, M.A. Jan and W.K. Mashwani,"Reproductive Nelder-Mead Algorithm for Unconstrained Optimization Problems", Science International Journal, 7(2), 65-72, 2016.

Table 1. Numerical Results for the CEC'05[12] Problems with Search Space dimension n=10

| Problems | best | mean | median | st. dev. | worst | Avg CPU Time (s) |
|---|---|---|---|---|---|---|
| f01 | 0.000000 | 0.000000 | 361.013214 | 0.000000 | 0.000000 | 262.137611 |
| f02 | 0.000079 | 1.394698 | 1519.536557 | 0.001059 | 0.005634 | 272.826619 |
| f03 | 263336.798739 | 5982735.049465 | 31873830.391922 | 2697065.292528 | 15734523.933443 | 570.136425 |
| f04 | 0.000658 | 5.124856 | 1877.767715 | 0.013340 | 0.068959 | 843.323107 |
| f05 | 0.000000 | 0.000557 | 647.992035 | 0.000000 | 0.000000 | 1144.032475 |
| f06 | 3.038268 | 5.277536 | 228914540.645291 | 0.002765 | 4.742417 | 242.412855 |
| f07 | 0.000000 | 0.000000 | 0.000000 | 0.000000 | 0.000000 | 0.000000 |
| f08 | 20.210415 | 20.789490 | 20.809694 | 0.014353 | 20.987086 | 523.443369 |
| f09 | 0.000000 | 0.000000 | 0.000000 | 0.000000 | 0.000000 | 0.000000 |
| f10 | 11.417355 | 50.738798 | 56.827820 | 5.798386 | 60.406202 | 297.211704 |
| f11 | 5.604508 | 11.591520 | 11.907398 | 0.080878 | 12.980332 | 1098.352873 |
| f12 | 100.016495 | 2741.799178 | 11325.703569 | 1089.071407 | 7733.491735 | 1523.299708 |
| f13 | 0.000000 | 0.000000 | 0.000000 | 0.000000 | 0.000000 | 0.000000 |
| f14 | 2.826769 | 4.246931 | 4.259342 | 0.019029 | 4.402642 | 283.118051 |
| f15 | 0.000000 | 0.000000 | 79.244044 | 0.015802 | 58.201975 | 2069.046251 |
| f16 | 128.031967 | 211.850454 | 230.479777 | 19.927218 | 232.775737 | 3791.802968 |
| f17 | 0.000000 | 0.000000 | 0.000000 | 0.000000 | 0.000000 | 0.000000 |
| f18 | 300.000000 | 300.000026 | 468.276150 | 0.000000 | 300.000000 | 1903.238542 |
| f19 | 0.000000 | 0.000000 | 0.000000 | 0.000000 | 0.000000 | 0.000000 |
| f20 | 300.000000 | 300.000013 | 454.256166 | 0.000000 | 300.000000 | 1895.641406 |
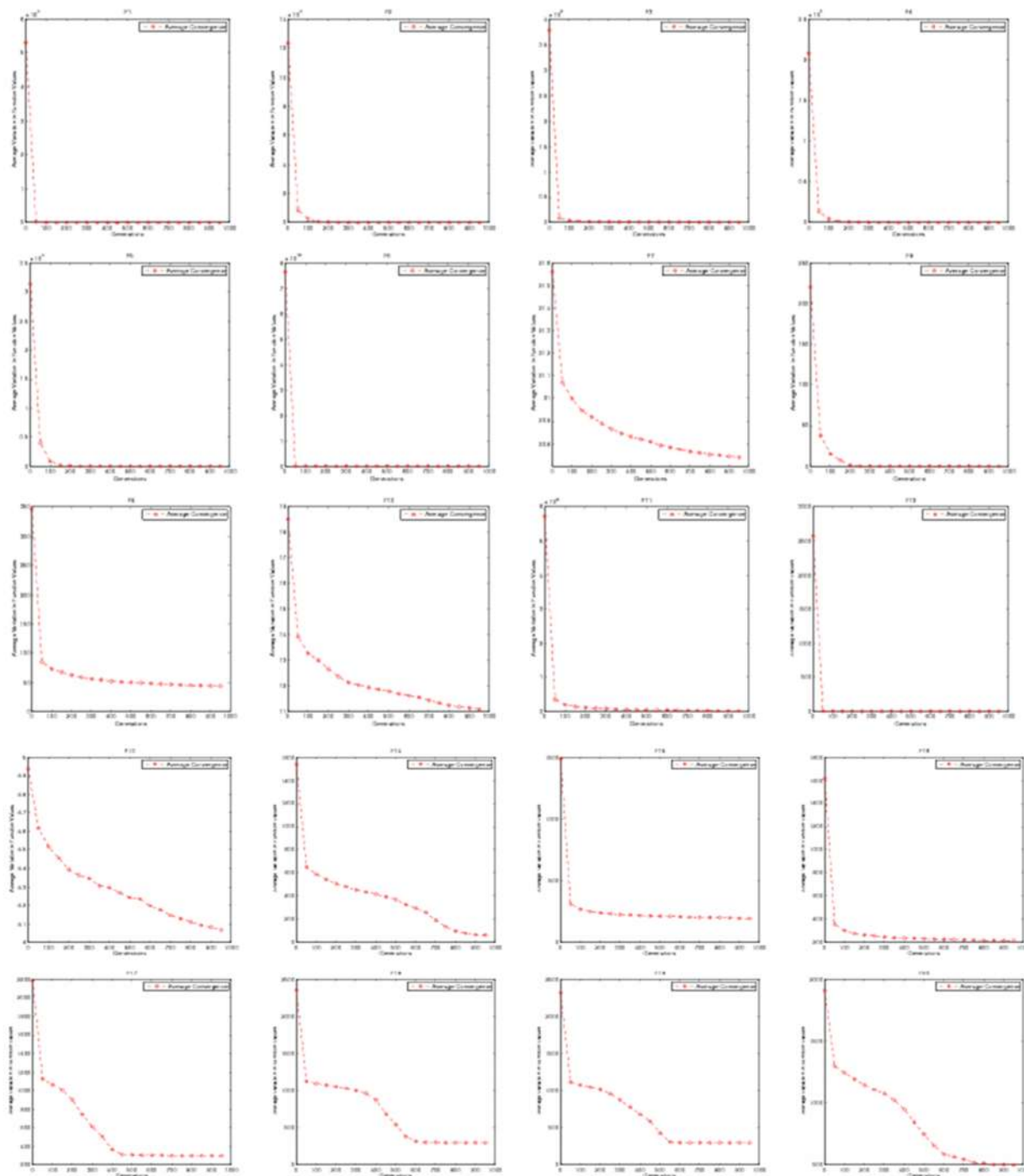
Figure 2. Convergence graphs of CEC'05 displayed by BBO-DEI with n=10 search space dimension.

# A weak formulation based meshless method with numerical integration based on Haar wavelets for boundary value problems

Abbas khan[1*] ,Siraj-ul-islam[1], wajid khan[1]

[1]*Department of basic sciences, university of science and technology Peshawar*

*Email:abbaskhanislamian@gmail.com*

**Abstract**

This paper introduces a weak meshless method combined with numerical integration based on multi-resolution Haar wavelets for the numerical solution of one-dimensional elliptic boundary value problems (EBVPs) with variable coefficients. The meshless weak formulation is the well-known Element Free Galerkin (EFG) method. The main theme presented in this research work is the implementation of the new quadrature rules introduced in [1, 2] in the EFG method and its comparison with the EFG method combined with numerical integration based on Gaussian quadrature for EBVPs in one- dimension. The numerical integration based on multi-resolution Haar wavelets has the distinguish feature of simple calculation of nodes and weights in the background of the Element Free Galerkin (EFG) method as compared to the EFG method with numerical integration based on Gaussian quadrature.

**Key words:** Element Free Galerkin method, Moving least squares, Haar wavelets, elliptic boundary value problems and Gaussian quadrature.

## 3 Introduction

The Finite Element Method (FEM) for the solution of complicated problems in science and Engineering is a well-known numerical technique. It has been used with an outstanding achievement in academic and industrial application. The domain in the FEM is presented as a collection of subdomain, and upon each subdomain the approximation of governing equation can be built on any of the traditional variational or weak formulation methods (e.g.Galerkin, Ritz, Collocation and also Least Square method). It is a strong, complete and comprehensively evolved technique, but it is not faultless and faces some shortcomings.

One of the most highlighted shortcoming in the FEM is that, the interpolation fails when element becomes excessively twisted. The second demerit of the FEM and other major methods of computational analysis like, the Boundary Element Method (BEM), the Finite Volume Method (FVM) and the Finite Differences Method (FDM) is that, these methods relied on the use of interlaced element or finite volume etc. The third problem in FEM and other mesh based methods is that, they are not convenient for the problems having discontinuities and that they don't adjust with the edges of the element.

To resolve these deficiencies of mesh based methods, a newly born category of numerical techniques were debut, named meshless methods. In meshless methods, approximation is made-up from nodes only and it depends completely on the scattered and distributed points that avoids the time and memory consuming task of mesh generation. In addition the solution of irregular and discontinuous geometries based on meshfree methods is more accurate as compared to the mesh based methods.

The Smooth Particle Hydrodynamics (SPH) method [3] is one of the first and famous meshless method. There are two groups of meshless methods. The first group of meshless methods based on collocation technique which solves the governing equations in strong form. This type of meshless methods includes the SPH, the Finite Point Method (FPM), the Diffuse Approximation Method (DAM), the meshless method of Least Square Collocation (LSC), and the RBF Collocation Method. [4, 5, 6].

The second group of meshless methods is based on Galerkin technique which solved the governing equations in weak form. This class of methods includes the Diffuse Element Method (DEM) [7], The Element Free Galerkin (EFG) scheme [8], the Petrov Galerkin meshless method [9] as well as the Radial Point interpolation technique [10].

One of the important problem in the meshless weak formulation based methods is the numerical integration of stiffness matrix and nodal force vector. The accurate solution of meshless weak formulation based methods depends on the accuracy of numerical integration of the integrals exist in weak or in variational form. Several techniques exist in engineering literature to solve the problem of numerical integration in meshless weak form methods. These techniques include the partition of unity quadrature [11], background meshless method [8] and stabilized conforming nodal integration [12] etc. However the problem of numerical integration in a meshless weak formulation based method have been not yet solved completely.

In this paper, we use a multi-resolution integration technique [1, 2] and discover their new application in the context of numerical integration in the EFG method.

## 2. Weak form of one dimensional problem

Consider the following one-dimensional equation,

$$-\frac{d}{dx}\left(p\frac{du}{dx}\right) + qu + f(x) = 0 \quad in \quad \Omega = \ (0, \ 1), \tag{1}$$

with the B.C's
$$u(0) = 1,$$

$$p\frac{du}{dx}\Big|x = 1 \ = \ 2\sinh(1), \tag{2}$$

where p, q and $f$ are known quantities of the problem.

The weak formulation of equation (1) may be written just as;

$$\int_0^1 w(x)\left[-\frac{d}{dx}\left(p\frac{du}{dx}\right) + qu + f(x)\right]dx = 0, \tag{3}$$

where $w(x)$ is the weight function also called test function.

Using Integration by parts in equation (3) and rearranging the terms leads to the following weak formulation,

$$\int_0^1 [pu'(x)w'(x)dx + pu'(1)w(0)]dx = pu'(1)w(1) - \int_0^1 qu(x)w(x) - \int_0^1 w(x)f(x)dx .\tag{4}$$

Eliminating the corresponding terms in equation (4) we have

$$\int_0^1 [pu'(x)w'(x)dx + qu(x)w(x)]dx$$
$$= pu'(1)w(1)$$
$$- \int_0^1 w(x)f(x)dx. \tag{5}$$

Typically the weight function $w(x)$ used in equation (3) and in the MLS approximation is the same, which is usually chosen either Gaussian function, quartic splines or cubic. In this paper, we use the following cubic spline weight function:

$$w(x)
= \begin{cases}
\frac{2}{3} - 4c^2 + 4c^3 & for \ c \le \frac{1}{2} \\
\frac{4}{3} - 4c - 4c^2 - \frac{4}{3}c^3 & for \ \frac{1}{2} < c \le 1 \\
0 & for \ c > 1,
\end{cases} \tag{6}$$

where $c = \frac{||x - x_I||}{d_I}$ is the normalized radius.

Supporting size of the $I^{th}$node is calculated by $d_I = k_{max}I_c$

where $d_{max}$ is the scaling parameter and in the case of uniform nodal arrangement $I_c$ shows the nodal spacing.

Thus the final system of discrete equationn is given by

$$Ku = B, \tag{7}$$

where

$$K_{i,} \qquad j= \qquad \int_0^1 (pu_i'(x)w'j(x) + qu_i(x)wj(x)dx, \tag{8}$$

$$B_{i=} \qquad \int_0^1 w_i(x)f(x) + w(1)2\sinh(1). \tag{9}$$

Where i, j = 1 …..N and N represents the number of nodal points.

## 3. Numerical Test Problems and error analysis

Considering the equation (1) with specific values of parameters p, q and f defined by

$$p(x) = 1 + x,$$
$$q(x) = 1,$$
$$f(x) = -x\cosh(x) - \sinh(x)$$

$$with \ b.c's$$

$$u(0) = 1, \quad p\frac{du}{dx}\Big|_x{=1} = 2\sinh(1).$$

In Table 1, the errors comparison of EFG method with numerical integration based on Haar wavelets (EFG-HW) and EFG method with numerical integration based on Gaussian quadrature (EFG-GQ) is given. From Table 1, one can see that the EFG-HW method produces better results as compared to EFG-GQ. The EFG-HW method produces the relative L_2 norm error

**6.8991e**$^{-005}$ using 10 nodal points and 2 quadrature points. While the EFG-GQ method produces the error **6.1252e**$^{-004}$using 10 nodal points and 2 Gaussian quadrature points. This shows that EFG-HW method gives small error as compared to the EFG-GQ

Table 1: The errors comparison of the EFG-HW and the EFG-GQ of Test Problem 1, while keeping the N fixed and changing the QP (QP presents the quadrature points).

| N | QP | EFG-HW | EFG-GQ |
|---|---|---|---|
| 10 | 2 | 6.8991e$^{-005}$ | 6.1252e$^{-004}$ |
| 10 | 4 | 6.4468e$^{-005}$ | 6.6698e$^{-005}$ |
| 10 | 6 | 6.4792e$^{-005}$ | 6.4625e$^{-005}$ |
| 10 | 8 | 6.4468e$^{-005}$ | 6.4614e$^{-005}$ |
| 10 | 10 | 6.4463e$^{-005}$ | 6.4605e$^{-005}$ |

In Table 2, the same problem is solved with different nodal points and fixed quadrature points. One can see that from Table 2 by increasing nodal points, the accuracy increases while keeping the QP fixed. Again the EFG-HW method gives better results as compared to EFG-GQ method. The EFG-HW method shows the relative L_2 norm error 1.453e$^{-006}$ $^{with}$ the 50 nodal points and 2 QP. While the EFG-GQ method gives the error **1.9647e$^{-005}$** using 50 nodal points and 2 QP.

Tabel 2 :error comparison of EFG-HW and EFG-GQ

Test problem 1 while keeping QP fixed and changing N.

| N | QP | EFG-HW | EFG-GQ |
|---|---|---|---|
| 10 | 2 | 6.8991e$^{-005}$ | 6.1252e$^{-004}$ |
| 20 | 2 | 1.2636e$^{-005}$ | 1.3202e$^{-004}$ |
| 30 | 2 | 4.7727e$^{-006}$ | 5.5709e$^{-005}$ |
| 40 | 2 | 2.4263e$^{-006}$ | 3.0777e$^{-005}$ |
| 50 | 2 | 1.4530e$^{-006}$ | 1.9647e$^{-005}$ |

.
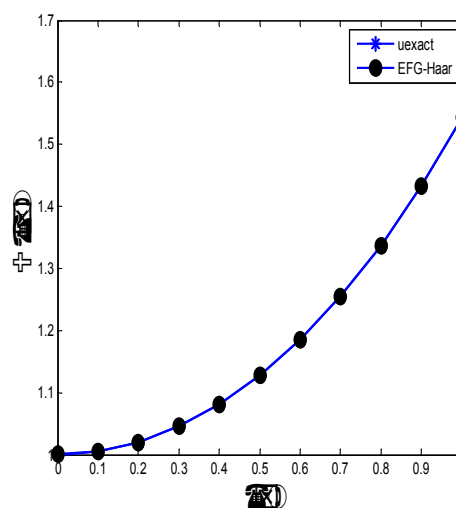


**(a)**
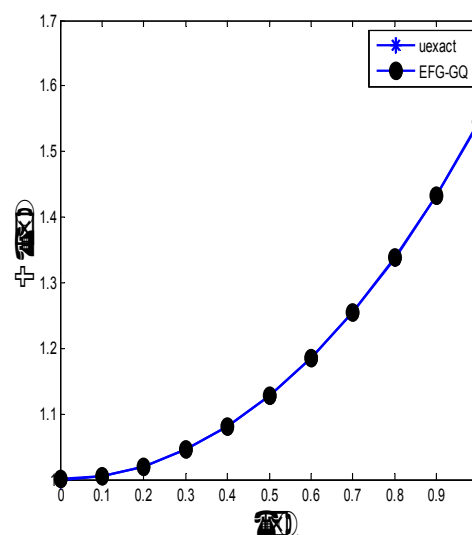


(b)

Figures 1: comparison of exact and numerical solution of X (11 nodes) obtained with (a) the EFG-HW and (b) EFG-GQ methods of test problem 1.

**Conclusions**

In this paper the weak formulation (the EFG-HW, the EFG-GQ methods) based on meshless methods, are tested for the numerical solution of 1-D elliptic boundary value problems (EBVP). For numerical integration we have used a multi resolution integration technique based on Haar wavelets [1]. Which shows that the meshless methods is less time consuming than the mesh based method because finding nodes and generating mesh is a time consuming task. To sum up in short words we can conclude from above tables and figures that the

versatility and accuracy of the EFG-HW scheme is sounder as compared to the EFG-GQ scheme.

**References**

[1] I. Aziz, Siraj-ul-Islam, and W. Khan. Quadrature rules for numerical integration based on Haar wavelets and hybrid functions. Compute. Math. Appl., 61:2770-2781, 2011.

[2] Siraj-ul-Islam, I. Aziz, and Fazal-e-Haq. A comparative study of numerical integration based on Haar wavelets and hybrid functions. Comput. Math. Appl., 59:2026-2036, 2010. [3] L.B. Lucy, A numerical approach to the testing of the fission hypothesis, Astron. J. 82 (1977) 1013–1024. [4] J. T. Chen, M. H. Chang, and K. H. Chen, and I. L. Chen, Boundary Collocation Method for Acoustic Eigen analysis of Three-Dimensional Cavities Using Radial Basis Function,Comput. Mech., vol. 29, pp. 392–408, 2002

[5] W. Chen, Symmetric Boundary Knot Method, Eng. Anal. Bound. Elem., vol. 26, pp. 489–494, 2002.

[6] W. Chen and Y. C. Hon, Numerical Convergence of Boundary Knot Method in the Analysis of Helmholtz, Modified Helmholtz, and Convection-Diffusion Problems,Comput. Meth. Appl. Mech. Eng., vol. 192, pp. 1859–1875, 2003.

[7] B. Nayroles, G. Touzot, and P. Villon. Generalizing the finite element method: diffuse Approximation and diffuse elements. Computational Mechanics, 10:307{318, 1992.

[8] J. Dolbow and T. Belytschko. Numerical integration of the Galerkin weak form in meshfree Method. Computational Mechanics, 23:219{230, 1999.

[9] S. N. Atluri and S. Shen. The Meshless Local Petrov-Galerkin method. Forsyth: Tech. Sci. Press USA, 2002.

[10] G. R. Liu and Y. T. GU. A local radial point interpolation method (LRPIM) for free vibration Analyses of 2-D solids. Sound and vibration,(246):29{46, 2001.

[11] A. Carpinteri, G. Ferro, and G. Venture. The partition of unity quadrature in meshless Methods. Int. J. Number. Methods Eng., 54:987{1006, 2002.

[12] H. Michael and J. S. Chen. An accelerated, convergent, and stable nodal integration in Galerkin meshfree methods for linear and nonlinear mechanics. Int. J. Number. Methods Eng., 2015.
.

# Physicochemical properties of agricultural biomass residues in Pakistan for future 'energy mix' potential

Salman Raza Naqvi[1, *], Abdul Hadi Chara[1], Rida Mehtab[1], Shahzeb Zafar[1], Muhammad Zubair[2]

[1]*School of Chemical & Materials Engineering, National University of Sciences & Technology, H-12 54000, Islamabad*

[5]*U.S Pakistan Centre for Advanced studies in energy, National University of Sciences & Technology, H-12 54000, Islamabad*

*\*Corresponding author*

**Email**: *salman.raza@scme.nust.edu.pk*

## Abstract

This paper characterizes various locally available agricultural residues in Pakistan to evaluate their potential as feedstock for renewable energy production and for contributing towards solving energy crisis and environmental issues. The thermo-chemical characterization has been performed in order to determine if the residues have potential to be used in biomass conversion technologies producing combined heat and power.

The characterization methods for comparing different agricultural residues include proximate and ultimate analysis, heating value, ash content, thermo gravimetric analysis (TGA) and functional group analysis (FTIR).

Widely available agricultural wastes in Pakistan were selected for the characterization i.e. bagasse, corn cob, rice husk, wheat straw and wood chip. The analysis showed that the corn cob had the highest moisture content that will result in low energy efficiency of the thermal conversion technology due to energy requirement for drying; whereas wheat straw had the lowest moisture content. Ash and volatile contents were found to be highest in rice straw and wood chip respectively.

The thermo gravimetric analysis and functional group identification showed that most of the agricultural residues can be easily decomposed and represent potential feedstock for biomass flexible combined heat and power systems through pyrolysis or gasification.

**Key words**: bioenergy, characterization, gasification, Pakistan, pyrolysis, wastes

## Introduction

### 1    Background

Agriculture is the basic sector in Pakistan. It owes to 21% of the GDP and forms 80% of the exports along with other products that are based on agriculture. [1] As per a study conducted by United Nations Food and Agriculture Organization (FAO), Pakistan produces 69 million tons of agricultural residue annually. [2] Considering how Pakistan is a developing country and faces the problem of electricity shortage, an alternate energy source in any form is a blessing. This shortage of energy is perhaps the greatest hindrance to Pakistan's development. [3] Even though Pakistan has allowed sugar mills to use bagasse to produce energy [4], most of them use it for combustion. [5] This results in environmental concerns.

The abundant biomass resources of Pakistan, o\*wing to the fact that the country is the 5th largest producer of sugar in the world, provides a rich source for gasification and liquidation of the potential fuel. [6]

### 2    Method

### a.    Initial procurement

Agricultural residues of corn cob, rice husk, wheat straw, bagasse and wood chip were used. Once harvesting is completed, these crop-based residues were attained and dried. The samples were collected and crushed. The size of each particle was kept between 100 and 150 mesh number. They were then kept in plastic bags to ensure minimum atmospheric contact to maintain original compositions.

### 2.2 Biomass Analysis

Proximate analysis of the data was carried out using D-3172 ASTM. The moisture content was determined using the weight loss of the sample by heating in an oven at 117°C. The results were recorded in Table 2.2a.

Ultimate analysis was carried out for the elemental analysis of the biomass samples. Leco CHN-600 analyzer was used to give the ultimate analysis of the dried samples. The results are shown in Table 2.2b.

To carry out structural analysis to determine the quantities of significant constituents, various methods can be used. However, the best possible

method is that of magnetic resonance. The quantities were determined and are displayed in Table 2.2c. The Higher Heating Value (HHV) was determined using the following formula:

$$HHV \left(\frac{MJ}{kg}\right) = 0.3491C + 1.1783H + 0.1005S - 0.1034O - 0.0151N - 0.0211 \, ash \, [7]$$

To carry out TGA, LECO TGA-701 TGA was used with nitrogen as the carrier gas. It determined the relationship of carrying temperature with weight loss. The temperature was increased from room temperature to 660°C with a 5°C increment per minute.

## 3    Results and Discussion

### a.    Moisture content
The moisture content present in a sample is an extremely important factor in determining an efficient way of energy conversion. The higher the moisture content, the less the energy conversion of biomass. The higher the moisture content, more energy is utilized in drying operations in order to use the conversion technology. Consequentially, the presence of moisture in biomass should not exceed 12-15%. In the sample obtained, the moisture content varies from 5% (Wheat Straw) to about 10.5% (Corn Cob). The values may differ from research previously done due to change in weather conditions, geography and the handling of the biomass.

**Table 1: Proximate Analysis (% dry wt.)**

| Sample | Moisture Contents | Ash Contents | Volatile Matter | Fixed Carbon |
|---|---|---|---|---|
| Bagasse | 8.70 ± 2.30 | 8.10 ± 2.05 | 78.89 ± 2.50 | 4.31 ± 2.33 |
| Corn Cob | 10.45 ± 1.15 | 11.67 ± 1.10 | 72.55 ± 1.31 | 5.33 ± 1.40 |
| Rice Husk | 6.55 ± 2.70 | 14.22 ± 2.45 | 58.66 ± 2.25 | 20.57 ±2.39 |
| Wheat straw | 5.22 ± 3.01 | 9.15 ± 2.90 | 66.80 ± 3.18 | 18.83 ± 2.88 |
| Wood chip | 7.10 ± 2.44 | 2.66 ± 2.98 | 86.55 ± 3.05 | 3.69 ± 2.80 |

### b.    Ash contents and volatile matter
Taken as % dry wt., the volatile contents of the residue samples range from 58.7% (rice husk) to 86.6% (wood chip). Similarly, data of this study may vary slightly from different literature due to different geographical locations and climate.

The wood chip has minimal ash contents (2.66%) whereas Rice husk and corn cob had comparatively higher amounts of ash: 14.3% and 11.7% respectively. These readings may vary with the place of findings. These inorganic compounds with a high content of ash present can, however, be used as catalysts in thermal conversion technologies such as pyrolysis [8].

### c.    Heating values and elemental composition
As listed in table 2.2b, the heating values of the residues were precisely similar to each other. Bagasse had the highest calorific value (17.24%) while rice husk gave the lowest among the samples (15.47%). The results show the potential of the agricultural waste samples to produce energy using efficient conversion technologies.

As far as elemental compositions are concerned, all samples showed almost the same values for Carbon, Hydrogen and Oxygen presence.

**Table 2: Ultimate Analysis (% dry wt.)**

| Sample | Carbon | Hydrogen | Oxygen | HHV (MJ/Kg) |
|---|---|---|---|---|
| Bagasse | 45.69 ± 1.10 | 5.81 ± 2.45 | 46.72 ± 2.11 | 17.24 ± 1.23 |
| Corn Cob | 45.62 ± 1.33 | 5.10 ± 1.89 | 47.12 ± 1.77 | 16.55 ± 1.77 |
| Rice Husk | 43.24 ± 1.88 | 5.01 ± 2.05 | 51.95 ± 1.19 | 15.47 ± 2.94 |
| Wheat straw | 47.99 ± 2.56 | 5.55 ± 1.98 | 48.80 ± 2.18 | 16.72 ± 2.13 |
| Wood chip | 48.54 ± 1.66 | 5.88 ± 2.58 | 45.93 ± 1.65 | 18.99 ± 1.88 |

### d.    Chemical compositions
These values as shown in table 2.2c will help in providing details of process models in thermal conversion technologies. Less than 50% of biomass comprises of cellulose and hemicellulose with Rice Husk having the highest percentage of cellulose present, while corn cob showing excess of hemicellulose.

Corn cob showed the lowest amounts of lignin and extractives present which makes it suitable for production of bio oil using pyrolysis, while the residues with higher amount of lignin such as Bagasse (13.38%) and wood chip (12.75%) can be used in gasification technologies.

**Table 3: Chemical Composition**

| Sample | Cellulose | Hemi-cellulose | Lignin | Extractives |
|---|---|---|---|---|
| Bagasse | 42.77 ± 2.55 | 24.77 ± 2.11 | 19.08 ± 1.43 | 13.38 ± 2.09 |
| Corn Cob | 39.22 ± 1.55 | 44.66 ± 2.44 | 7.89 ± 1.02 | 8.23 ± 1.66 |
| Rice Husk | 44.55 ± 1.13 | 25.11 ± 2.32 | 21.66 ± 1.56 | 8.68 ± 2.10 |
| Wheat straw | 36.11 ± 1.49 | 27.90 ± 2.11 | 25.66 ± 1.77 | 10.33 ± 2.55 |
| Wood chip | 41.33 ± 1.19 | 24.55 ± 2.55 | 21.37 ± 1.07 | 12.75 ± 1.61 |

### e. Thermogravimetric analysis

Thermogravimetric analysis helped determine the weight loss with respect to increase in temperature. This analysis of degradation will help find out the optimum temperature to be used in conversion technologies.
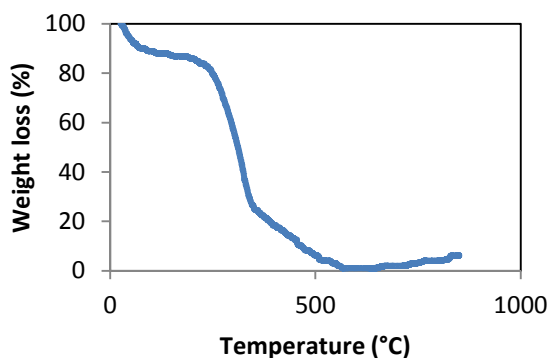


A BAGASSE
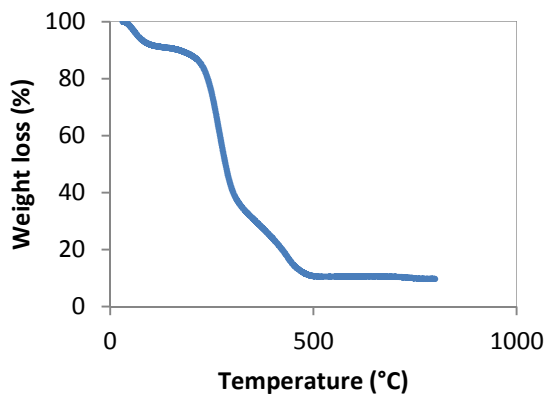


B CORN COB
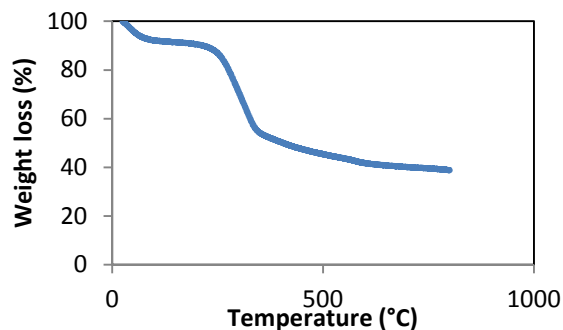


C RICE HUSK
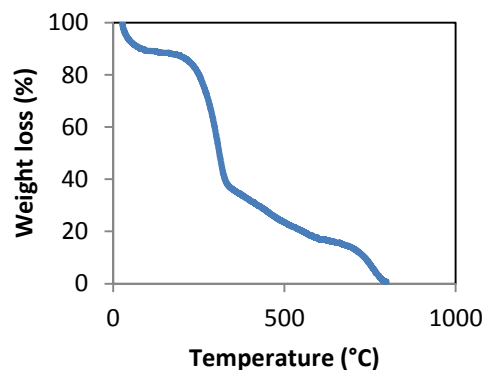


D WHEAT STRAW
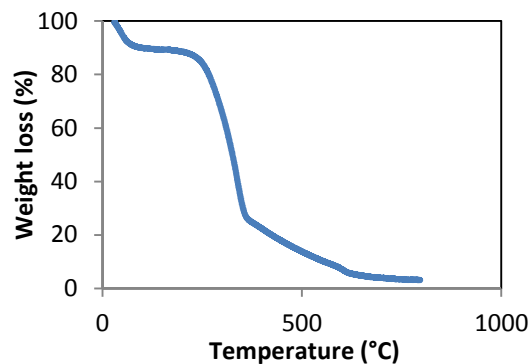


E WOOD CHIPS

**Figure 1: TGA curves of biomass samples at a heating rate of 5 °C/min**

As shown in the TGA curves, most of the sample degrades before 600°C. This easy decomposition indicates the application of biomass as ideal feedstocks for conversion technologies. [9] Around their optimum degradation temperature range, corn cob loses only 40% weight while bagasse show the maximum weight loss i.e. around 70%.

## 4    Conclusion

The research was carried out to study the chemical and physical behavior of the common biomasses in Pakistan. The agricultural residues that were used included bagasse, rice husk, wheat straw, wood chip and corn cobs. The hardest to ignite were rice husk 58% and the easiest were wood chips at 84%. This was due to the content of volatile matter in them. Corn cob and rice husk had the highest ash content while the highest heating values were of wood chip and bagasse. As per the TGA analysis, most materials lost most of their weight at around 800°C. Owing to the fact that Pakistan is in dire need of alternative energy sources, proper combustion and/or gasification can meet the needs.

## 5    References

1   G. o. t. P. Agriculture Department, "OVERVIEW | AGRI PUNJAB Agriculture Department, Government of Punjab - Pakistan," 2014. [Online]. Available: http://www.agripunjab.gov.pk/overview%20new .

2   "Bio-energy from agricultural residues - - DAWN.COM," 2009. [Online].

3   N. A. S. Shahzad Ali, "Electricity Crisis in Pakistan: Reception & Adoption of Energy Saving Campaign Messages by PEPCO," *Pakistan Journal of Social Sciences (PJSS) ,* vol. 32, no. 1, pp. 185-198, 2012.

4   N. A. a. T. M. U. K. Mirza, "An overview of biomass energy utilization in Pakistan," *Renewable and Sustainable Energy Reviews,* vol. 12, pp. 1988-96, 2008.

5   S. M. R. N. A. B. A. Qari M. K. Waheed, "Investigation of thermal behaviour and kinetic analysis of Pakistani biomass: Rice husk, sugarcane bagasse and wheat straw using thermogravimetric analysis," *IEEE,* 2015.

6   S. U. I. M. A. M. S. N. R. Waseem Raza. Hammad Saula, "Renewable Energy Resources Current Status and Barriers in their Adaptation for Pakistan," *Journal of Bioprocessing and Chemical Engineering,* vol. 3, no. 3, pp. 1-9, 2015.

7   C. a. J. L. T. A. Sheng, "Estimating the higher heating value of biomass fuels from basic analysis data," *Biomass and Bioenergy 28.5,* pp. 499-507, 2005.

8   K. L. Kenney, "Understanding biomass feedstock variability," *Biofuels 4.1 ,* pp. 111-127, 2013.

9   G. Skodras, "Pyrolysis and combustion characteristics of biomass and waste-derived feedstock," *Industrial & engineering.*

# Retrofit of Pre-Heat Train of a Crude Distillation Unit

*Yasir Zia*

*Department of Chemical Engineering, University of Engineering and Technology Peshawar, Peshawar, Pakistan.*

*Corresponding author*

*yasirchem@yahoo.com*

## Abstract

Crude oil distillation unit is the first upstream unit in the refinery complex. The unit performs initial separation of the petroleum fractions which are then further processed in the relevant process units. The crude column feed point required temperature is achieved by huge consumption of fuel in the charge heater that makes the crude distillation process energy intensive. The crude is pre-heated through a network of heat exchangers known as pre-heat train before going into the heater. The efficiency of the pre-heat train plays vital role in the overall operating cost of the crude distillation unit. The current work aims to improve efficiency of pre-heat train of Pakistan's largest oil refinery as a case study. By applying the problem table algorithm, the heat exchanger network energy targeting was carried out. The results show that the current heater duty is higher than minimum as depicted by the problem table algorithm indicating the scope of improvement, i.e. reduction in heater duty. Therefore pinch based methodology is selected and employed on the network by which heater duty got reduced by achieving higher crude upstream temperature. As a result heater fuel consumption decreased but at the cost of more heat transfer area addition to one of the heat exchangers which is crude-HVGO (heavy vacuum gas oil) heat exchanger. This capital investment payback time is 13 days only.

***Keywords:*** Crude pre-heat train, heat exchanger network, retrofit.

## Introduction

Developing energy catastrophe on the planet provoked the industrial communities to decrease the fossil fuel utilization and related natural effect because of $CO_2$ emissions. High fuel utilization in the crude charge heater makes the crude distillation process the most energy intensive in the refinery complex. The unit performs initial separation of the petroleum fractions which are then further processed in the relevant process units. There are different sections of the crude distillation unit as desalter, pre-heat train, pre-flash column, heater and crude column with side strippers. Hot product streams and circulating refluxes transfer heat to the cold crude stream in the pre-heat network reducing thermal load on heater and making crude distillation process economical. The performance of pre-heat train has direct impact on the unit energy utilization in terms of heater fuel consumption and cooling requirements of the hot products. Retrofitting the existing pre-heat train can lower the heater fuel consumption. As compared to grass root design, retrofit design is more troublesome because of constrains in the running heat exchanger network. To enhance efficiency of the heat exchanger network, there are several options like existing matches reassignment, streams repiping, increasing of additional heat transfer area and stream splitting. Heat exchanger network retrofit is an expanding research area. The most widely recognized strategies for retrofit are mathematical programming and pinch analysis.

Robin Smith et al. in 2010 [1] performed retrofit of an existing heat exchanger network taking into account the effect of temperature on thermal properties like heat capacity and the number of split divisions. Two-level pinch approach was employed in the work and the retrofit was carried out mathematically by establishing two interconnected optimization loops, one is internal loop while the other is external loop. Using the Levenberg-Marquardt algorithm, heat loads were redistributed in the inner loop while stream splits were optimized in the outer loop by SQP (successive quadratic programming) algorithm. The authors modified the network pinch approach of Zhu and Asante [3] into a two-level approach. After pinching the network for maximum heat recovery, four modifications were optimized to get cost effective design by applying the strategy of non linear programming technique using simulated annealing. The results show that the 20358 kW of hot and cold utilities consumption reduced by adding heat transfer area to the network.

Mamdouh Gadalla et al. in 2013 [2] established an advanced simulation based methodology to upgrade MIDOR (Egyptian oil refinery) crude distillation unit by dealing with both pre-heat train and crude column simultaneously. The work completed in two sections; improving top and lower pump-arounds (cold refluxes) and then upgrading pre-heat train by exploiting loops and utility paths resulting in increased inlet temperature of furnace but at the expense of additional area in the network.

N.D.K. ASANTE and X.X. ZHU [3] in 1996 worked out a scheme for retrofit of heat exchanger network by a combination of mathematical programming and pinch method. The approach consisted of two stages. The main restriction recognized in the first stage was the network pinch coming into the heat recovery potential and accordingly then different topology changes like repositioning the heat exchanger, area addition in the exchanger and stream splitting fractions were considered to remove that network pinch to gain the required heat recovery target. Then the selected topology change was optimized taking into account the trade-off between additional area and cost. The approach was employed on a case study in which the through put of the crude unit was to be increased by 10% and results show that by stream splitting and new exchanger addition helped in getting 3.9 MW more heat recovery.

H Rezaei, M Zarei, F Fazlollahi, M Sarkari, F Shahraki, and L Baxter [4] in May 2012 employed pinch methodology on crude pre-heat of a case study to achieve energy saving in the network by implementing minimum modifications.

M.A. Waheed and A.O. Oni [5] carried out revamped analysis of crude distillation unit (CDU) by performing unit process simulation, evaluation of $CO_2$ emissions and energy rate of fuel and exergy and energy analysis of the unit. Retrofit of crude pre-heat train was done by applying the pinch technology. As per problem table algorithm, network pinch point is determined and found 220.1°C while it is 224.8°C in the existing heat exchanger network because of incorrect topology of the heat exchangers network. The retrofit options then considered were; stream repiping, stream splitting and new heat exchangers addition. The retrofit analysis resulted in the cost reduction of $1.50 million but by investing capital cost of $3.68 million. The payback time is found to be 2.45 years.

Kenneth Kekpugile Dagde and Beabu Kiasira Piagbo [6] used Aspen Energy Analyzer to analyze the performance of an existing crude pre-heat train of a Nigerion oil refinery. The data used consisted of mass flow rates, streams temperatures, specific heat (calculated by formula), and density. The software explored the energy cost saving options in the given network by complete analysis of the network. By evaluating the network performance, it was observed that existing network had more number of shells and heat exchangers than target value by 92.31% and 84.62% respectively. However the energy target could be met by lower number of heat exchanger i.e. 13 with 26 shells. But in the existing network, there are almost double heat exchangers i.e. 24 with 50 shells. The network current cooling and heating duties found greater than the target by 25.14% and 71.15% respectively which is due to the improper placement of heat exchangers causing transfer of heat load of 5.52*107KJ/h across the pinch.

Ebrahim Rezaei, Sirous Shafiei [7] in 2009 developed retrofit design of heat exchanger network by mathematical programming of combining together integer linear programming (ILP) and non linear programming (NLP) strategies with genetic algorithm. The authors presented the heat exchanger network as an array of genes produced by this effective combination. In the optimization work this had resulted in the production of network feasible topologies. The approach was then applied on four cases to verify validness. The cases selected were previously retrofitted by Shenoy (1995) [8], Ciric and Floudas (1990) [9] and Briones and Kokossis (1999) [10]. The results prove that profit obtained in the current methodology is larger than previously retrofit methods.

Megan Jobson et al. [11] in June 2014 have reviewed different models regarding design philosophy and optimization techniques of heat incorporated crude distillation units. Past modeling work in this regard has been described showing three principle models classes of crude distillation systems i.e. rigorous and simplified or semi rigorous.

Pinch technology has been quite applicable to many heat exchanger networks of oil refineries across the globe and been followed by numerous researchers. Using this method, we have been able to pinpoint causes of low heat efficiency in the network by identifying the heat exchangers that are transferring heat across the pinch and also it has helped in finding the heating and cooling requirements of the process units. Retrofit by pinch technology helped in reducing the utility consumption and increasing the heat recovery potential of a heat exchanger network by adjusting or removing the cross pinch heat exchangers. But for achieving overall cost optimization relating to capital and utility, mathematical programming methods are quite precise. In mathematical programming methods, stochastic optimization methods as compared to deterministic methods are better for finding the global optimum of non-linear problems but at the expense of more time consumption. For crude-pre-heat train detailed retrofit, the application of both pinch methods and mathematical programming methods is very useful in terms of lower annualized cost and would be helpful in mitigating the energy crisis.

The present research is focused on reducing the heat duty of crude heater by enhancing the performance of crude pre-heat train. The crude heater consumes a large amount of fuels to achieve required crude column feed temperature. The pre-heat train recovers heat from hot product and pump around streams to minimize load on heater, hence indicating its crucial role in the unit economics. It is investigated that whether we can increase its output or not and then based on the result, a retrofit scheme applying the strategy of utility path exploration is employed.

## Method

The retrofit methodology adopted in the present work consists of below mentioned steps.

- Pre-heat train heat exchanger network grid diagram representation
- Problem table algorithm application
- Pre-heat train retrofit by exploring the utility path
- Pakistan's largest oil refinery has been selected as a case study. The methodology is applied on the case study crude pre-heat train of crude distillation unit for the operating scenario in which Arabian light crude is processed on 100% load of unit.

## Scope of Study

The current study is aimed at enhancing the heat recovery of the existing crude pre-heat train of crude distillation unit to maximize crude heater upstream temperature so that the crude charge heater fuel consumption can be reduced. This work deals only with the heat load adjustment within the heat exchanger network by applying the strategy of utility path exploration. If any heat exchanger in the crude pre-heat train found requiring change in its performance as a result of retrofit, that exchanger needs to be analyzed and modified in an another work. The current study is limited only to the crude preheat train of crude distillation unit (CDU) and does not cover any other process unit connected with the CDU.

## Case Study

The study sets up with the assemblage of all heat exchangers and streams properties data as shown in tables 1 and 2. Grid diagram is constructed to represent the case study heat exchanger network by mentioning all the streams data supply and target temperatures and is shown in figure 1. To determine the heating and cooling requirements and the relative pinch points in the network, problem table algorithm is applied based on which findings; retrofit of the given pre-

heat train is suggested. In this work strategy of exploring the utility path between the diesel product air cooler and crude heater is utilized by adjusting heat loads of some of the path heat exchangers keeping hold of $\Delta T_{min}$ (minimum temperature difference between hot and cold streams in the network) in range. The heat loads are adjusted based on the current available heat exchanger duty and if required, duty is increased by increasing the heat transfer area of the concerned exchanger. This has resulted in the reduced heater duty by which heater fuel consumption also reduced. Accordingly the fuel saving and additional area costs are calculated. Payback time of the additional investment of additional area is finally calculated.

## Crude Preheat Train

The main purpose of the pre-heat train is to recover heat from pump around streams and hot product streams transfer it to the crude cold stream. Eventually this mitigates the crude heater thermal load by achieving higher crude temperatures at heater inlet. The overall cost of CDU is dependent on the performance of pre-heat train by which hot and cold streams target temperature are maintained. The present crude pre-heat train consists of fourteen heat exchangers with equipment no. E19A/B, E18A/B, E17A/B, E16, E15, E14, E13, E12A/B, E11A/B, E9, E6, E4A/B, E3, and E1A/B. Crude, Desalted Crude and Flashed Crude are the three cold streams while heavy vacuum gas oil (HVGO) from VDU, VDU bottoms from VDU (vacuum distillation unit), diesel product (DP), circulating diesel (CD), circulating kerosene (CK), kerosene product (KP) and circulating naphtha (CN) are the seven hot streams.

## Collection of data

Collected data of cold and hot streams and heat exchangers is shown in the tables 1 and 2. Streams supply and target temperatures, steams average heat capacity and mass flow rates are represented by TS, TT, CPav and m respectively in the table 1.

Table 1 CDU Streams Data

Table 2 Heat Exchangers Data

| S.No | Stream | Type | Mass Flow Rate m (kg/h) | TS (ºC) | TT (ºC) | CPav (KJ/kgºC) |
|------|--------|------|------------------|---------|---------|-----------------|
| 1 | Crude | Cold | 569410 | 10 | 129.4 | 1.96 |
| 2 | Desalted Crude | Cold | 570450 | 115.6 | 193.3 | 2.34 |
| 3 | Flashed Crude | Cold | 557840 | 190.6 | 371.2 | 2.6 |
| 4 | VDU Bottoms | Hot | 132350 | 361.7 | 232.2 | 2.55 |
| 5 | HVGO | Hot | 364290 | 284.8 | 162.8 | 2.42 |
| 6 | DP | Hot | 132820 | 238.7 | 50 | 2.32 |
| 7 | CD | Hot | 332560 | 231.1 | 162.8 | 2.52 |
| 8 | CK | Hot | 322740 | 178.8 | 105.6 | 2.41 |
| 9 | KP | Hot | 80304 | 152.1 | 40 | 2.13 |
| 10 | CN | Hot | 364980 | 132.8 | 73.9 | 2.3 |

| S.No | Heat Exchang. | Service | Design Duty (MW) | Operating Duty (MW) |
|------|---------------|---------|------------------|----------------------|
| 1 | E1A/B | CN- Crude | 15.82 | 13.75 |
| 2 | E2A/B | Kerosene Trim Cooler | 1.4 | 1.09 |
| 3 | E3 | KP-Crude | 3.5 | 2.96 |
| 4 | EA1 | Kerosene Product Air Cooler | 5.72 | 5.72 |
| 5 | E4A/B | CK- Crude | 15.82 | 15.82 |
| 6 | E5 | Diesel Trim Cooler | 1.04 | 1.04 |
| 7 | E6 | CD-Crude | 3.95 | 3.95 |
| 8 | E9 | DP-Crude | 3.33 | 1.43 |
| 9 | E11A/B | HVGO-Crude | 10.68 | 10.68 |
| 10 | E12A/B | CD-Crude | 9.05 | 9.05 |
| 11 | E13 | HVGO-Crude | 4.2 | 4.2 |
| 12 | E14 | DP-Crude | 3.42 | 3.42 |
| 13 | EA2 | Diesel Product Air Cooler | 3.94 | 3.94 |
| 14 | E15 | HVGO-Crude | 5.68 | 5.68 |
| 15 | E16 | CD-Crude | 2.79 | 2.79 |
| 16 | E17A/B | VDO Bottoms-Crude | 3.23 | 3.23 |
| 17 | E18A/B | HVGO-Crude | 9.79 | 9.79 |
| 18 | E19A/B | VDO Bottoms-Crude | 9.09 | 9.09 |
| 19 | H1 | Crude Charge Heater | 61.9 | 46.98 |

Heat Exchanger Network (Pre-heat Train) Representation on Grid Diagram

Grid diagram is shown in fig. 1 to represent the crude pre-heat train.
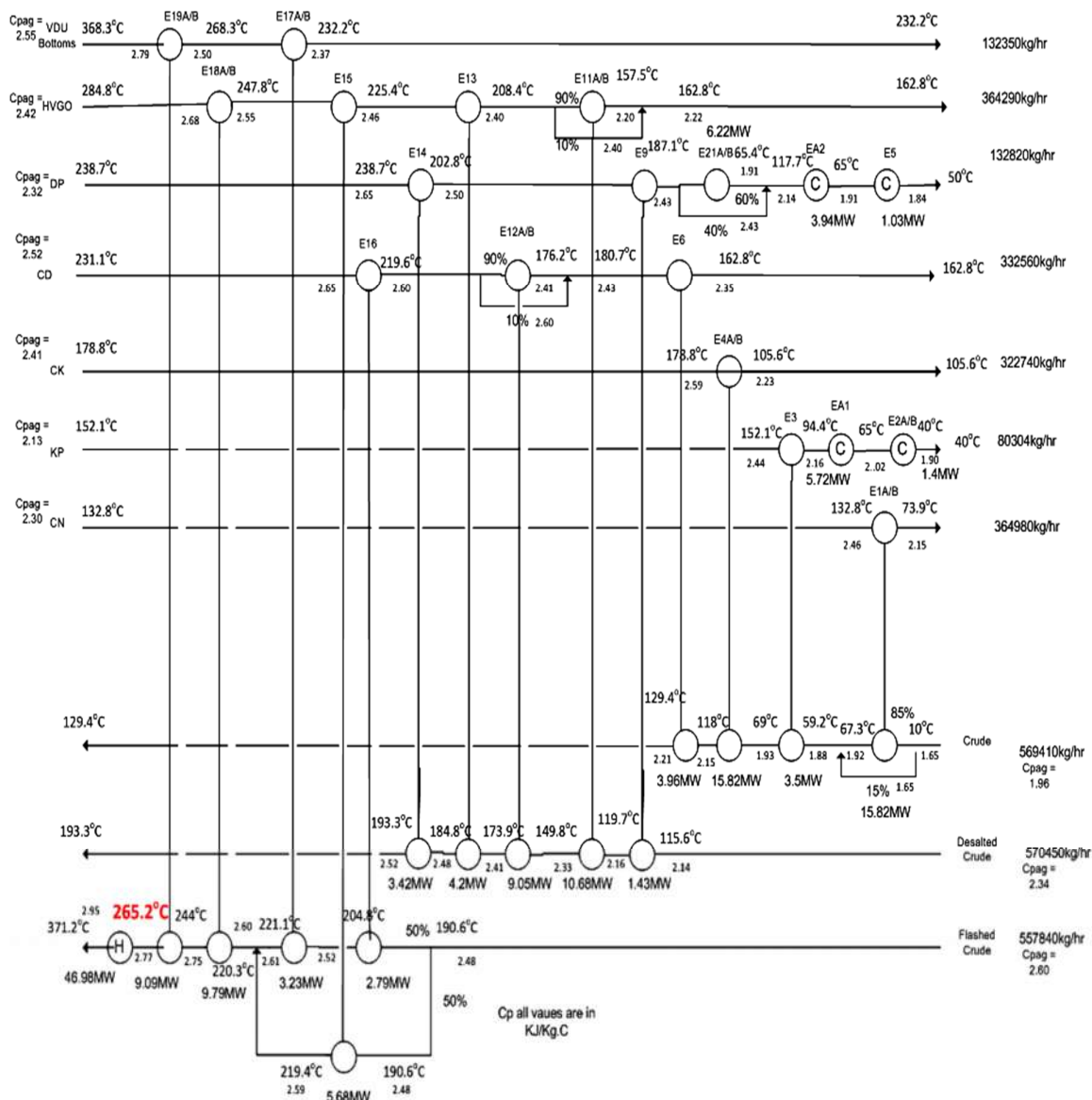


Fig. 1 Crude preheat train grid diagram

http://www.uetpeshawar.edu.pk/spi_2016

**Application of Problem Table Algorithm**

Problem table algorithm is a technique used to find out heating and cooling demands of the heat exchanger network. In this method, all streams target temperatures are shifted by a margin of $\Delta T_{min}/2$ and within each shifted interval of temperature heat balance is calculated and shown in table 3. $\Delta T_{min}$ taken for the present study is 20°C as for oil refining the typical values are 20-40°C (Linnhoff, B. and E. Hindmarsh, 1983) [13] so hot and cold stream temperatures will be shifted by 20/2 (10) in the problem table algorithm. Then cascading of heat down the temperature scale of all hot and cold streams target temperatures is done. The largest heat surplus value obtained after cascading is 38.61 is added above the top hot shifted temperature in the scale. Again the cascading is done and the temperature where heat flow equals to zero is found to be 228.7°C. This is the pinch point in the network. So hot pinch temperature actually is 228.7+10 = 238.7°C while cold pinch temperature is 228.7-10 = 218.7°C. As a result network heating and cooling demands found 38.61MW and 9.27MW respectively. But existing network heating load (i.e. heater duty) is 46.98MW and cooling load is 18.30MW both are greater than the values depicted by the algorithm. Hence scope of improvement lies in the current pre-heat train. The next section will show in detail about the retrofit analysis.

Table 3 Heat cascade within shifted temperature interval

| Interval Temperature (°C) | Stream Population | $\Delta T_{INTERVAL}$ (°C) | $\Delta H_{INTERVAL} =$ ($\Sigma CPC - \Sigma CPH$) (MW) | Surplus/ Deficit |
|---|---|---|---|---|
| 381.2 | | 29.5 | (+)11.88 | Deficit |
| 351.7 | | 76.9 | (+)23.77 | Deficit |
| 274.8 | | 46.1 | (+)2.96 | Deficit |
| 228.7 | | 6.5 | (-)0.139 | Surplus |
| 222.2 | | 1.1 | (+)0.079 | Deficit |
| 221.1 | | 17.8 | (-)2.85 | Surplus |
| 203.3 | | 2.7 | (+)0.568 | Deficit |
| 200.6 | | 31.8 | (-)6.12 | Surplus |
| 168.8 | | 16 | (-)6.54 | Surplus |
| 152.8 | | 10.7 | (+)0.739 | Deficit |
| 142.1 | | 2.7 | (+)0.058 | Deficit |
| 139.4 | | 13.8 | (+)4.54 | Deficit |
| 125.6 | | 2.8 | (-)0.116 | Surplus |
| 122.8 | | 27.2 | (-)7.47 | Surplus |
| 95.6 | | 31.7 | (-)1.86 | Surplus |
| 63.9 | | 23.9 | (+)4.17 | Deficit |
| 40 | | 10 | (+)2.6 | Deficit |
| 30 | | 10 | (+)3.07 | Deficit |
| 20 | | | | |
| | Crude | | | |

**Crude Preheat Train Retrofit**

The present heat exchanger network heating requirement can be reduced by performing a retrofit. The most suitable utility path is between the crude heater and diesel air product keeping in view the $\Delta T_{min}$ limitation which can be utilized to reduce the energy consumption in the network. As can be seen in the fig. 2 the concerned utility path is highlighted.

**Assumptions**

All Cp values for the operating case remained unchanged despite of heat duties adjusted in the utility path.

The temperature sensing instruments at all streams are working at 100% accuracy. This is being adopted to ensure that the retrofit calculations are error free.

**Constraints**

Following are the bottlenecking constraints that limit the current retrofit approach to achieve heat recovery saving up to 1MW only.

The circulating HVGO stream from vacuum distillation unit has supply temperature of 284.8°C and target temperature of 162°C. Its target temperature cannot be dropped from this value so as to avoid disturbance in vacuum distillation tower temperature profile.

The crude temperature upstream of desalter has to be maintained at around 129°C as to keep its salt removal performance at optimum level.

Currently we cannot shift a heat load of more than 1MW around the utility path as to keep $\Delta T$ equal or above 20°C.

The heat load is shifted by adjusting heat duties of following heat exchangers keeping $\Delta T_{min}$ equal to 20°C.

EA2 duty from 3.94MW to 2.94MW.

E18A/B duty from 9.79MW to 10.79MW.

E13 duty from 4.2MW to 3.2MW.

E9 duty from 1.43MW to 2.43MW.

In the current retrofit study, all heat exchangers' operating duties have been utilized. Operating (for Arabian Light Crude case) and design duties of mostly heat exchangers are same but E9 has designed duty of 3.33MW while its operating duty is 1.43MW.

The temperatures crosswise over aforementioned heat exchangers re-determined after 1MW heat load shifted using the average value of Cp at inlet and outlet of exchanger (disregarding the results of temperature change on Cp) utilizing the accompanying equation:

$$\Delta H = mCp\Delta T \qquad (1)$$

Where m is the stream mass flow rate, Cp is the constant heat capacity and $\Delta T$ is the temperature difference across heat exchanger.

**Analysis**

As E21A/B outlet has stream splitting-mixing of diesel product as can be seen in fig. 1, therefore the temperature of the mixed stream can be calculated by the accompanying equation (Muhammad Imran Ahmad et al. 2012) [14]:

$$TMXout = \frac{TMXin1 CP1 + TMXin2 CP2}{CP} \qquad (2)$$

Where TMXin1 is the temperature of stream 1, CP 1is the heat capacity flow rate (product of mass flow rate and heat capacity) of stream 1), TMXin2 is the temperature of stream 2, CP2 is the heat capacity flow rate of stream 2, $CP$ is the heat capacity flow rate of combined stream, TMXout is the temperature of mixed stream of diesel product. Stream 1 fraction is 60% while stream 2 is 40%. CP 1 and CP 2 are calculated by following equations 3 and 4:

$$CP1 = SF \times CP \qquad (3)$$

$$CP1 = (1 - SF) \times CP \qquad (4)$$

Where SF is the stream fraction.

By using equations (3) and (4) and putting the values in equation (2), the splitter mixer outlet temperature found 98°C.

Crude heater upstream temperature got increased from 265.2°C to 267.55°C as a result of shifting a heat load of 1MW over the utility path and accordingly re-finding values of temperature across the heat exchangers. Hence heater duty dropped from 46.98MW to 45.93MW indicating heat saving of 1.05MW. The grid diagram with these retrofit changes is shown in the fig 2.
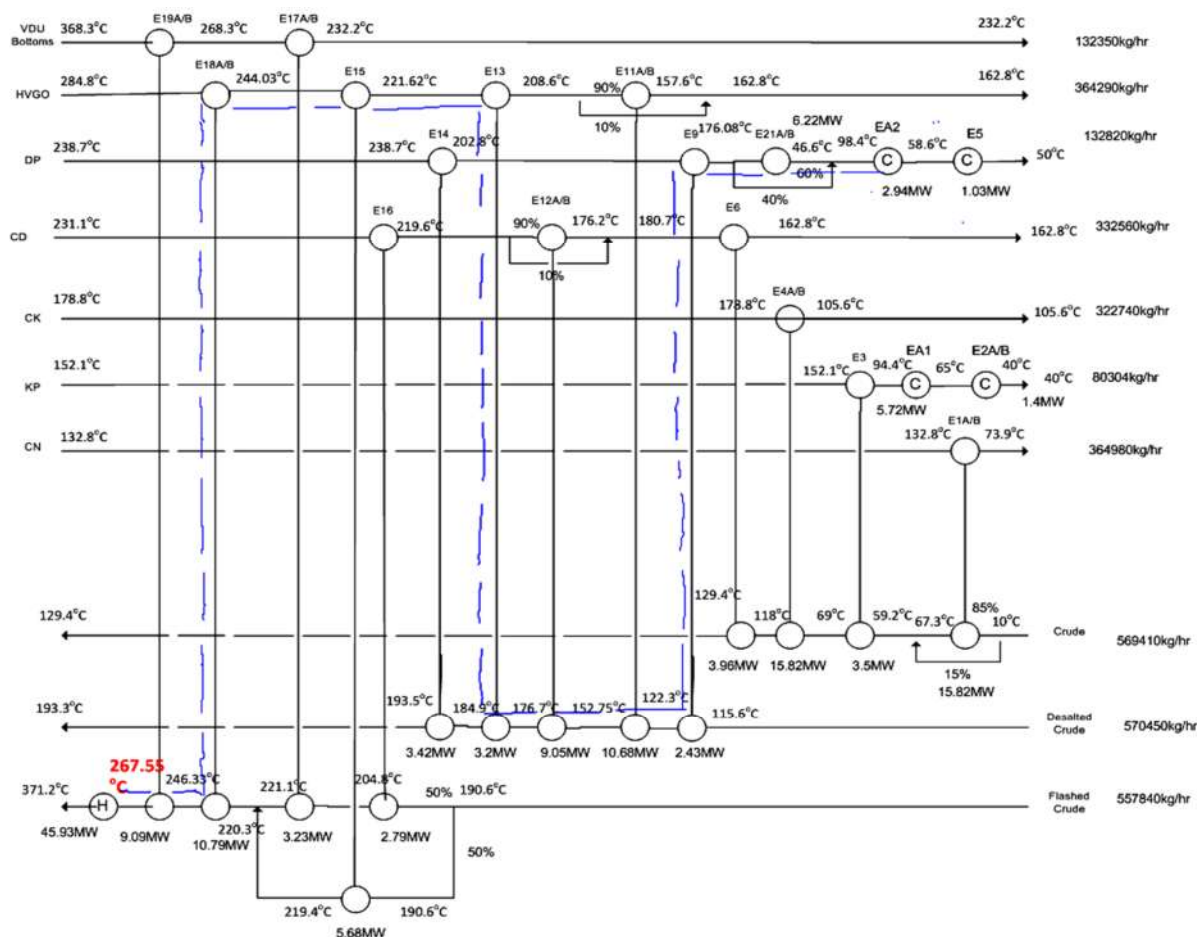
Fig.2 Crude pre-heat train after retrofit

Now E18A/B and E9 duties need to be increased for the retrofit. The design duty of E9 is already higher than its operating duty for the current case so for the retrofit its duty can be considered to 2.43MW whereas for E18A/B we have to increase its duty at the expense of adding more area to its current heat transfer area. The following section explains about the calculation of additional area required of E18A/B.

### Required Additional Area Calculation

Using the following heat transfer equation:

$$Q = UAF_T\Delta T_{lm} \qquad (5)$$

Where Q is the heat transfer rate

$F_T$ is the flow correction factor

U is the overall heat transfer coefficient

A is the heat transfer area

$\Delta T_{lm}$ is the log mean temperature difference

E18A/B data sheet shows:

U = 332 kcal/hr.m².ºC = 0.38kJ/s.m².ºC

A = 821 m²

Q = 9.79 MW

But for the increased duty Q = 9.79+1 = 10.79MW

Using the expression for $F_T$ (Ref: Robin Smith Chemical Process Design and Integration, 2005, 325-329) [15]

$$F_T = \frac{\sqrt{R^2+1}\,\ln\left[\frac{(1-P_{1-2})}{(1-RP_{1-2})}\right]}{(R-1)\ln\left\{\frac{\left[2-P_{1-2}(R+1-\sqrt{R^2+1})\right]}{\left[2-P_{1-2}(R+1+\sqrt{R^2+1})\right]}\right\}}$$

$$(6)$$

Where $\quad R = \frac{(T_{hin}-T_{hout})}{(T_{cout}-T_{cin})} = 1.56$

$$(7)$$

$$P = \frac{(T_{cout}-T_{cin})}{(T_{hin}-T_{cin})} = 0.36 \qquad (8)$$

$T_{hin}$ is the exchanger hot fluid inlet temperature, $T_{hout}$ hot fluid outlet temperature, $T_{cin}$ is the exchanger cold fluid inlet temperature and $T_{cout}$ is cold fluid outlet temperature.

R is the heat capacity flow rates ratio for current exchanger and P is the thermal effectiveness of the exchanger. Since there are two 1-2 shell in series of

E18A/B therefore value of $P_{1-2}$ for each shell will have to be determined using following equation while R value remains constant across shells [15].

$$P_{1-2} = \frac{(Z^{1/\,Nshells}-1)}{(Z^{1/\,Nshells}-R)} \qquad (9)$$

Where Z is a variable for calculation purpose and the equation for Z is mentioned as:

$$Z = \frac{(1-P_{N-2N}R)}{(1-P_{N-2N})} \qquad (10)$$

$P_{N-2N}$ = P (overall remains constant across all shells) so value putting gives Z = 0.68. So $P_{1-2}$ found 0.23.

Using the values of $P_{1-2}$ and R in equation (6) results $F_T = 0.97$

Using standard expression for $\Delta T_{lm}$ from the book by Robin Smith, Chemical Process Design and Integration 2005, 325-329, it is found 33.71.

By rearranging the equation (5) and putting the values of $F_T$ and $\Delta T_{lm}$, area for the increased duty is found 868.37m². Therefore E18A/B additional area required:

868.37- 821 = 47.37 m².

Additional Area Cost

The cost of additional heat exchanger area can be calculated by the equation given by Lu Chen (Lu Chen, 2008) [16] which is mentioned as:

Existing heat exchanger additional area = 1530$(A_{xadd})^{0.68}$ (11)

Additional area cost: 1530$(47.37)^{0.68}$ = 21087.92$

US dollar rate in Pakistani Rupees is 101.75 Rs.

Therefore cost = 21087.92$ * 101.75Rs./1$

$\qquad\qquad$ = 2.14 million Rs.

### Cost of Fuel Saving

Both fuel oil and fuel gas are being consumed in crude heater as fuels. Since the efficiency of existing crude heater is 78% as per its design so for the reduced heat duty of 45.93MW and back calculating the fuel consumption by using Microsoft Excel solver, we have found that the amount of fuel oil needed for new reduced duty is 4213.622kg/hr and fuel gas is 750.46kg/hr as compared to previous values of 4276.96 kg/hr fuel oil and 792.69 kg/hr fuel for previous duty. So amount of fuel oil saved 63.43kg/hr and fuel gas 42.23kg/hr. The annual cost of fuel saved

is calculated by incorporating fuel prices and found 59.37 million Rs. /yr.

**Payback Time**

The payback time is calculated against additional area cost by following equation:

Payback Time = Cost of Additional Area/annual Cost of Fuel saved
(12)

$$= 2.14 \text{ million Rs.}/59.37 \text{ million Rs. /yr}$$

$$= 13 \text{ days}$$

**Results and Discussion**

Retrofit methodology is applied on a case study of crude pre-heat train with base case of Arabian light crude with 100% load of crude distillation unit. The results of problem table algorithm showed that the existing pre-heat train heating and cooling duties are higher than the values obtained by the problem table algorithm. Current heating duty is 46.98 MW and cooling duty is 18.30 MW where as 39.61MW and 9.27 MW heating and cooling duties respectively are sufficient to meet the process demands by satisfying the streams target temperatures as per problem table algorithm.

By exploiting the most suitable utility path from the crude heater to diesel product air cooler, we have shifted a heat load of 1MW around the path resulting in drop of heater duty but duty of one of the exchangers (i.e. HVGO-Crude exchanger) in the path has to be increased further 1MW for which required additional area calculated and found $47.37 \text{m}^2$ to be incremented in the current heat transfer area the cost of which found is 2.14 million Rs. The required area is calculated by using the basic heat transfer equation. Due to the constraints in the existing train, heater duty could only be dropped to 45.93MW and cooling duty to 17.30MW by which heater fuel oil and fuel gas consumption dropped at the rate of 63.34kg/hr and 42.23kg/hr respectively by which annual cost saving of 59.37million Rs. achieved. The payback time of this additional capital cost found 13 days only.

**Conclusions**

In this work, retrofit case study was executed on one of the largest oil refineries in Pakistan. The study was aimed to enhance heat recovery potential of crude pre-heat train of crude distillation unit with base case

operating scenario in which Arabian light crude is processed. The problem table algorithm was employed to determine the pre-heat train minimum heating and cooling requirements and found that both were lower as compared to that of existing network. So there is a scope of improvement in the heat exchanger network.

The retrofit scheme adopted for the present study is the exploitation of utility path between the cold and hot utilities in the network. The hot utility is the crude heater and most suitable cold utility in the concerned path is the diesel product air cooler. Keeping in view all the limitations of current network, a heat load of 1MW found beneficial to be shifted around the utility path by which diesel product air cooler duty reduced from 3.94MW to 2.94MW and heater upstream temperature raised to 267.55°C from 265.2°C, resulting in drop of heater duty from 46.98MW to 45.93MW. Shifting the heat load around the concerned path has resulted in need of upgrading duty of HVGO (Heavy vacuum gas oil) - Crude exchanger. The required additional area of HVGO-Crude exchanger is then calculated for its increased duty.

The pre-heat train retrofit results in annual cost saving of 59.37miilion Rs but this requires an additional cost of 2.14 million Rs. for adding more area to the exchanger however only 13 days is the payback time for this cost. The current retrofit approach is quite easily applicable to heat exchanger network of any configuration and will result in achieving cost saving in the concerned process.

**References**

[1] Robin Smith, Megan Jobson, Lu Chen, Recent development in the retrofit of heat exchanger networks, Applied Thermal Engineering 30 (2010) 2281-2289.

[2] Mamdouh Gadalla, Dina Kamel, Fatma Ashour, Hemdan Nour El din, A New Optimisation Based Retrofit Approach for Revamping an Egyptian Crude Oil Distillation Unit, Energy Procedia 36 (2013) 454 – 464.

[3] N.D.K Asante and X.X Zhu, An automated approach for heat exchanger network retrofit featuring minimal topology modifications, Computers chem. Engng Vol. 20, Suppl., pp.(1996) $7-SI2.

[4] H Rezaei, M M Zarei, F Fazlollahi, M Sarkari, F Shahraki, & L L Baxter, Energy

saving in a crude distillation unit by a retrofit design of heat exchanger networks, Indian Journal of Chemical Technology Vol. 20, pp.(2013) 290-293.

[5] M.A. Waheed, A.O. Oni, Performance improvement of a crude oil distillation unit, Applied Thermal Engineering, 75 (2015) 315-324.

[6] Akpa, J. G. and Okoroma, J. U., Pinch Analysis of Heat Exchanger Networks in the Crude Distillation Unit of Port-Harcourt Refinery, Journal of Emerging Trends in Engineering and Applied Sciences (JETEAS) 3 (3) (2012): 475-484.

[7] Ebrahim Rezaei, Sirous Shafiei, Heat exchanger networks retrofit by coupling genetic algorithm with NLP and ILP methods, Computers and Chemical Engineering 33 (2009) 1451–1459.

[8] Shenoy, V., Heat exchanger network synthesis: Process optimization by energy and resource analysis, Gulf Publishing Company, (1995).

[9] Ciric AR, Floudas CA., A mixed integer nonlinear programming model for retrofitting heat exchanger networks, Industrial & Engineering Chemistry Research; 29(2) (1990) : 239-51.

[10] Briones, V, & Kokossis, A. C., Hypertargets: A Conceptual Programming approach for the optimization of industrial heat exchanger networks. II. Retrofit design, Chemical Engineering Science, 54 (1999), 541–561.

[11] Lluvia M. Ochoa-Estopier, Megan Jobson, Robin Smith, The use of reduced models for design and optimization of heat integrated crude oil distillation systems, Energy 75 (2014) 5-13.

[12] Ming Pan, Igor Bulatov, Robin Smith, Jin-Kuk Kim, Optimization for the retrofit of large scale heat exchanger networks with different intensified heat transfer techniques, Applied Thermal Engineering 53 (2013) 373-386.

[13] Linnhoff, B. and E. Hindmarsh, The pinch design method for heat exchanger networks, Chemical Engineering Science, 38(5) (1983): p. 745-763.

[14] Muhammad Imran Ahmad, Nan Zhang, Megan Jobson, Lu Chen, Multi-period design of heat exchanger networks", Chemical engineering research and design 90 (2012) 1883–1895.

[15] Smith, R., Chemical Process Design and Integration, Second ed. Wiley, New York, 2005.

[16] Chen, L., Heat-integrated Crude Oil Distillation System Design, The University of Manchester, Manchester, UK (Ph.D.Thesis) (2008).

# Development of Carbon Fiber Reinforced Composite Pressure Vessel and Effect of Polar Winding Pattern in Mass Saving

*Muhammad Adnan[1*], Mohammad Younas [1], Mohammad Saeed Butt[2], Sumeera Ikram [2]*
*[1]Department of Chemical Engineering University of Engineering and Technology, Peshawar*
*[2]Department of Chemistry ,Quaid-e-Azam University, Islamabad*
*[1*]Corresponding author*
*Email: madnanfaiz36@gmail.com*

**Abstract**

Experiments were performed to study the effects of increasing the aluminum liner thickness with the constant overwrapped composite thickness. An optimum thickness of aluminum liner was obtained with the help of finite element analysis. The experimental work was performed to find out the optimum composite thickness with the maximum optimal mass saving. The results obtained by using the destructive testing technique (hydro-burst test). The test results demonstrate by increasing the composite thickness value of stress decreases. The polar type helical on winding angle 20° high density pattern was introduced in the experiment results suitable for up gradation of strength of pressure vessel. Modification in process by changing the pattern a helical layer replaced by polar layer results optimum mass saving. However further improvement in the composite material properties by considering the other process parameters.

**Key words**: Helical, hoop, liner, overwrapped and pattern.

## 1    Introduction

The pressure vessels earn a lot of importance in the natural gas fuel driving system vehicles. This has been done due to increase in demand of economic fuel CNG. The pressure vessels which are using for economic fuel system are manufacturing with the material such as metal and liner-composites. Normally the metallic pressure vessels are using. These are heavy in mass and not safe. These vessels rupture on burst. On the other hand liner- composite vessels or fully composite vessels are most suitable as they are light in masses and on burst the vessel leak not rupture so it's safe. A lot of research had been done to find out the best solution to store high volume of gas with light weight and in lower cost [1].

The researchers worked to develop the pressure vessels for storage of gas in vessel of comparatively less in weight to the metallic one. There are four types of vessels used as gas storage tanks.. Type-1 is hundred percent of metal [2]. This is the heaviest in weight and normally using in the automobiles. For the manufacturing of light pressure vessels changing of material from metal to composite is required. On material change the problem is to control the porosity in composite material [3].

The metal liner with reinforced composite [4] stood the second type of vessels. The metallic liner steel and aluminum alloy used in contact with a composite. In this type composite material added on hoop/cylinder portion side. The use of metallic liner solved the porosity problem of composite material. The composite material with different type of fibers such as glass and carbon fibers are in use [5]. The third type is of aluminum alloy liner with fully wrapped of composite material [6]. The fourth type is the plastic liner with fully wrapped composite [7]. Now in this era both third and fourth types are under consideration because these types are affective on mass reduction. Furthermore the strains on hoop as well as helical portions and effect on changing on hoop material and helical material observed by different techniques [8].   Study of health safety on carbon fiber

reinforced composite pressure vessel i-e effect of temperature and mechanical response analysis of composite CNG cylinders at fire scenario [10] also included in research on the composite pressure vessel development. The study on second type in which metallic liner used where as composite wrapped on cylindrical portion i-e hoop composite wrapping is also going on the fatigue life prediction of a pressure vessel containing surface flaw on various loading and unloading crack and fatigue life calculation [11]. The light weight pressure vessels usually used in automobiles, under water and in aerospace. The designing of vessels with the layer patterns applied to develop composite pressure vessel and comparison of theoretical and practical values [12]. Composite pressure vessel with the material of carbon fiber by changing the chemistry of matrix i-e vinyl ester / epoxy combination also developed which affect the economy of composite pressure vessel development [13].

In the current research composite pressure vessel of third type is under consideration. The winding angle is calculated and it is 11°. The geometry and machine limitations allow the minimum possible angle 20°. The study on optimum composite thickness and optimum liner thickness carried out by theoretical and practical studies. The optimum values calculated with the various plots. The experiments performed with the different types of winding patterns. The polar pattern with helical combination, adopted by using wet filament winding process.

## 4  Materials and Method

The materials used in this research are :

a) Aluminum liner (cylinder with minimum thickness.

b) Carbon fiber T-300

c) Epoxy resin system (Araldite LY 564)

For the process there are two methods which are using to develop composite pressure vessels. These are as follows:

i) Wet filament winding

ii) Dry prepreg winding

The process adopted for the experimental work was wet filament winding.

#### TABLE 1 PROPERTIES OF CARBON FIBER

| Property | Value |
|---|---|
| Fiber Type | T-300(12K) |
| Tensile Strength (MPa) | 3530 |
| Tensile Modulus (GPa) | 230 |
| Elongation (%) | 1.5 |
| Density (g/cm$^3$) | 1.76 |

#### TABLE 2  PROPERTIES OF TOUGHENED EPOXY

| Property | Value |
|---|---|
| Density (g/cm$^3$) | 1.2 |
| Tensile Strength (MPa) | ≥70 |
| Young's Modulus (GPa) | 2.45 |
| Elongation at break (%) | ≥7.8 |
| Impact Strength (KJ/m) | 4.23 |

## 5  Methodology

The optimum thickness of the aluminum liner was calculated by the graph between the maximum principal stresses and the metal liner thicknesses. The values of maximum principal stresses were calculated with the help of ANSYS software. The metal thickness of 3.8mm with optimum process parameters was finalized for the experimental work.

The continuous winding took place angles of double spiral layers at the beginning of the cylindrical part [9] and at the end was coincident with the winding angles of bottoms at their equators.

Taking that into account and using Clairaut relation

$$\emptyset ai = arc\,Sin\frac{roi}{R}$$

Where Øai the winding angle at the equator of bottom (i=1,2). In the considering case a1= a2.

The winding angle along the cylindrical part as the cylinder having similar openings at both the ends can be determined [9] as

$$\text{Sin } \varphi = \frac{r}{R}$$

$$\text{Sin } \varphi = \frac{31}{164}$$

$$\varphi = 11°$$

As 11° angle is not possible to achieve in process due to process limitations so the minimum achievable winding angle is 20°.

The composite thickness, number of helical and hoop layers were calculated with the help of empirical relations.
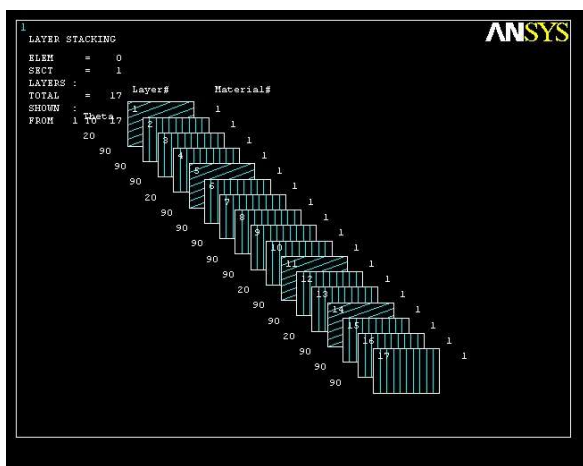


**FIGURE 14 PLY SCHEME IN ANSYS**

a.  Experimental work

Carbon fibers with the tensile strength 3530 MPa and Young's modulus of 230 GPa were used as a reinforcement. Epoxy resin (LY 564) was used as a matrix. The composite vessel consisted of an aluminum liner (3.8mm thickness) helical layers of impregnated carbon fiber with epoxy under tension at the winding angle ± 20º and hoop layers at ± 90º through the epoxy impregnation bath placed with the filament wound equipment. After the placement of fibers with the completion of number of layers mentioned in table the vessel was placed in curing oven under the temperature of 80º C for four hrs and post curing under the temperature of 120ºC for two hrs. After completion of curing cycle natural cooling of the oven started and vessel was removed when the temperature of oven down to 35ºC.

The five numbers of experiments were performed by using different plies/layers schemes with the same winding angle and same process (wet filament winding). Composite pressure vessels abbreviated as CPV (3,4,5,6&7) were developed. The process patterns and schemes mentioned in table. The polar pattern was introduced in the experiments with the helical combination. The remaining process parameters such as winding angle, fiber tension epoxy resin, type fiber and material of liner remain same with the constraint. Only polar pattern introduced for the process modification. In composite material development, weight saving is most important. The experiment work performed on the composite pressure vessels CPV-3, 4,5,6 and 7. In CPV-3&4 the same process scheme used mentioned in table. The scheme changed in CPV-5, 6 and 7. In these experiments one layer of polar winding pattern in spite of helical and another one hoop layer was added in the process. This added the mass of 300 gm to CPV-4 and shows better results to previous scheme.

**TABLE 3 DETAIL OF VESSELS AND PROCESS LAY-UP**

| ID No | Helical Layers | Polar layer | Hoop layers | Total Layers | Total thickness (mm) | Liner Weight (kg) | Total Weight (kg) |
|---|---|---|---|---|---|---|---|
| CPV-3 | 04 | - | 13 | 17 | 8.75 | 14.45 | 26.6 |
| CPV-4 | 04 | - | 14 | 18 | 9.70 | 14.45 | 27 |
| CPV-5 | 03 | 01 | 15 | 19 | 9.75 | 14.45 | 27.3 |
| CPV-6 | 03 | 01 | 15 | 19 | 9.75 | 14.45 | 27.3 |
| CPV-7 | 03 | 01 | 15 | 19 | 9.75 | 14.45 | 27.3 |

## 6  Experimental devices and procedures

The facility of destructive testing was used for vessels qualification. The vessels were fixed from both dome side ends. For hydro testing water was pumped and internal pressure developed with the rate of 10 MPa/min. The vessel during loading/pressurization the

external fiber layer was start breaking at 42 MPa in CPV-3 and 52 MPa in CPV-4 respectively. The stain gauges six in numbers were installed.
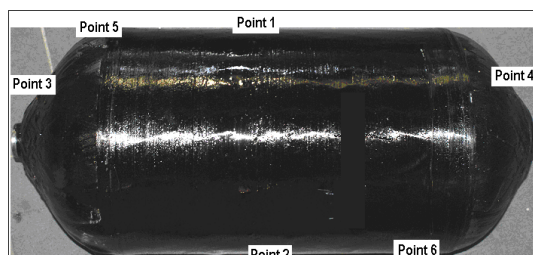


**FIGURE 15 POSITION OF STRAIN GAUGES ON VESSEL**

The distribution of strain gauges was as two of them at the cylindrical portion which monitored only hoop stresses at the cylinder. The other two gauges at the interface of cylindrical and doom portions. These gauges were monitored helical and hoop stresses at interface. The last two gauges at the dome sections which only monitored the stresses at the domes of vessels. The mentioned scheme followed in all the composite pressure vessels so that the result was comparable.

## 7    Results and discussion

The result of optimum liner thickness, composite thickness and effect of polar pattern in the winding lay-up are here detailed distinguishing. The loading of vessel with increasing internal pressure and the stresses develop in results are also under discussion.

**TABLE 4 ANALYSIS RESULT SUMMARY**

| S. N o. | Liner thick ness (mm ) | Maximu m Stresses (N/mm²) | Maxi mum Strain | Mass of Liner (Kg) | Mass of Composite Pressure vessel (Kg) |
|---|---|---|---|---|---|
| 01 . | 2.81 | 2031 | 0.020 53 | 10.33 | 22.33 |
| 02 . | 3.81 | 1987 | 0.019 88 | 14 | 26 |
| 03 . | 4.5 | 1959 | 0.019 43 | 16.5 | 28.5 |
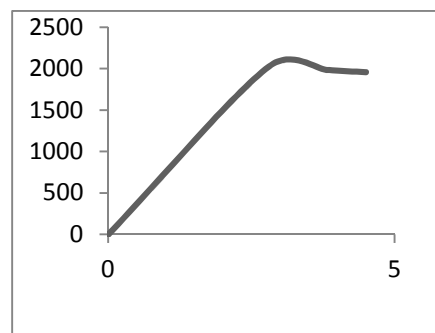


**FIGURE 16 LINER THICKNESS (MM) VS PRINCIPAL STRESS (N/SQ.MM)**

### Optimum liner thickness

The thickness of the aluminum liner is calculated by the graph plot between maximum principal stresses and the metal liner thicknesses. The metal thickness with optimum process parameters is finalized the suitable liner.

These finite element analysis results which are tabulated above and its plot give an optimum liner thickness i-e. 3.8 mm. All the plots show the liner with the thickness of 3.81 mm is in optimum position. For the experimentation liner with optimum thickness 3.81mm is suitable. Whereas the expected mass of the composite is also plotted,  this shows the optimum mass of the vessel falls on 3.81mm thickness liner.
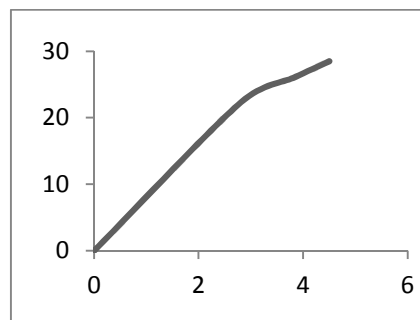


**FIGURE 17 LINER THICKNESS (MM) VS VESSEL MASS (KG)**

### Composite thickness

The composite thickness of hoop layers that is on the cylindrical portion and the helical layers throughout the

vessel which also cover the dome ends are calculated with the help of empirical relations mentioned in table.

**TABLE 5 COMPOSITE DATA CALCULATION**

| Position/Type | Values |
|---|---|
| Spiral helical layer thickness h1 | |
| $(P^{*}R) / (2\,\sigma_{+1}\,Cos^2\varphi)$ | 3.65mm |
| Circular hoop layer thickness $h_2$ | |
| $(P^{*}R) / (\sigma_{+1})$ | 6.44mm |
| Total thickness | |
| h1+h2 | 10.09mm |
| Number of helical layers | 03 |
| Number of hoop layers | 10 |

Spiral helical ($h_1$) layer thickness [8] $h_1$ and circular hoop ($h_2$) layer thickness [8] are calculated by applying the data of operating pressure i-e for the compressed natural gas cylinders is 22MPa and the factor of safety in case of composite material is 2.5. The tensile strength ($\sigma_{+1}$)of composite material with the T-300 carbon fiber is $1400 \times 10^6\,N/m^2$ is also used for finding out number of layers. This results ten hoop layers and three helical layers.

**Destructive testing**

**Table 6 Hydro burst test result**

| ID No | Total Comp. thickness (mm) | Max. Principal Stress( MPa) | Max. VON MISES Stress(MPa) | Burst Pressure (MPa) | Remarks |
|---|---|---|---|---|---|
| CPV-3 | 8.75 | 1209 | 1198 | 44 | Busted |
| CPV-4 | 9.70 | 1218 | 1202 | 55 | Busted |
| CPV-5 | 9.75 | 1044 | 1035 | 60 | Not Busted |
| CPV-6 | 9.75 | 1044 | 1035 | 60 | Not Busted |
| CPV-7 | 9.75 | 1044 | 1035 | 60 | Not Busted |

The results of experimentation destructive testing facility of hydro test are used. Principal stress data of the composite pressure vessels during hydro-burst test is shown in the table.

During the hydro testing of the pressure vessels the cyclic loading tests are performed. The CPV-3 and 4 are busted during the 2nd loading. Whereas CPV-5,6 and 7 are even not busted in thrice loading. This shows a slight decrease in stresses in second and third loading cycles. This may be due to stress relieving / rearrangement after first decompression. Minimum stresses are at point 5 of CPV-3&4 i.e. at front dome/ cylinder joint. Maximum stresses are at point 6 i.e. 60 mm from rear dome. During winding it was observed that there was a minor slippage/improper over lapping at that point due to operational and fixtures problem. These operational problems are the part of winding operation and these problem are rectified in the CPV-5,6 and 7.



**FIGURE 18 CPV-03 BUSTED IN HYDRO BURST TEST**

The hydro burst testing facility in its maximum testing range up to 600 bar or 60 MPa. Therefore, the further testing of pressure vessels which are not busted on 60 MPa is not possible yet.

The introduction of polar type helical on winding angle 20° is the high density pattern which is quite suitable for up gradation of strength of pressure vessel. This pattern also controls the composite mass of the pressure vessel. With the comparison of same capacity metallic pressure vessel i-e of 55 Kg where as the composite pressure vessel is of 27.3 Kg.

Therefore the mass saving which is the main achievement of composite material is calculated as

Mass Saving  =  [(55-27.3)/55] X 100

Mass Saving  =  50.36 %

If we use another helical layer then the mass saving will be reduced to 45 %. It means the introduction of the polar pattern saves 5% and play drastic role in improving the composite material.

## 8 Conclusion

The plots are showing the behavior of composite thickness on principal stress and burst pressure. The behavior of graphs proved that on increasing of composite thickness the vessel will be safer. On the other hand mass saving proved that the experimental work performed is quite optimal. It also concluded that with the 2.5 times safety factor the composite pressure vessels developed CPV-5,6&7 are useable as a CNG cylinders in automobiles. The requirement is 550 bar (55 MPa) pressure which is safe and CPV-5,6&7 proved above on that pressure limit which found safe. It also proved that the introduction of polar pattern which is high density pattern play important role. The pressure vessels developed with 50.36% mass saving and comparatively high pressure storage capability than that of metallic one. This also enhances its applications such as in automobiles, underwater and in aerospace and if these vessels will be tested in future in high range i-e above 70 MPa then application of the vessels way forward to hydrogen vessel.

## 7 References

1   McLaughlan,P.E Scott C.Forth Johnson Space Centre Houston, Texas .Composite Overwrapped Pressure Vessel.A Primer 2011.
2   ISO 11439:2000: Gas cylinders, High pressure cylinders for the on-board storage of natural gas as a fuel for automotive vehicles. First Edition, 2000.
3   D. Quinn. Porosity in Carbons Characterizations and applications, ed. J. W. Patrick. Halstead Press, New York. 1994.
4   L. Varga, A Nagy, A. Kovacs. Design of CNG tank Made of aluminum and reinforced plastic. Technical University of Budapest, Hungary, 1994.
5   CNG2 technical drawing data sheet, NK Co. Ltd., 2000, Korea.
6   http://www.tpub.com:content:altfuels10:desgn-5:desgn-50007.htm
7   J. M. Starbuck.Lower Cost Composite Materials for CNG Storage. Oak Ridge National Laboratory, Oak Ridge, TN 37831
8   Alexis A. Krikanov. Composite pressure vessels with higher stiffness. MATI Russian state university of Technology, Moscow, Russia.
9   Brandmaier H.E. optimum filament orientation criteria. J.Comp. materials 1970,v.4 & Outwater J.O Filament wound internal pressure vessels. Modern Plastics-.1963.vol.40 No.7,135-139.
10  Anand Kumar Agarwal & Surendra Kumar. Fatigue life prediction of a Hoop-Wrapped composite CNG cylinder containing surface flaw. International journal of Emerging Technology and Advance Engineering , Volume 4, Issue 3, March 2014.
11  K.S. Ou , J. Zheng. Heat and Mechanical Response Analysis of Composite Compressed Natural Gas Cylinders at Vehicle Fire Scenario. (2015).
12  Rao Yarrapragada K.S.S & R. Krishna Mohan. Composite Pressure Vessels. Dec 2012.
13  Yongzheng Shao, Andrea Betti. High pressure strength of carbon fiber reinforced vinyl ester and epoxy vessel. Japan.2015.

# Numerical solution of a system of reaction diffusion PDE's arising in EN Plasma

*Hajia Naseem[1], Siraj-ul-Islam[1,*], Faiq Jan[2]*

[1]Department of Basic Sciences, University of Engineering and Technology, Peshawar, Pakistan.

[2] Govt. Postgraduate college, Nowshehra,, Pakistan.

*Email:siraj-ul-islam@nwfpuet.edu.pk

## Abstract

Converting system of ODEs to PDEs to describe the diffusion of particle inside electronegative (EN) plasma is relatively new work. The resulting system of PDE's is a reaction diffusion model. For the numerical solutions of reaction diffusion PDEs arising in (EN) plasma, we have used explicit methods based on meshless procedure. In this work the dependencies of plasma parameters on gas pressure and applied power has been studied. Due to non-availability of exact solutions, the numerical results obtained are compared with the experimental results. The determination of plasma parameters and the study of diffusion of atomic oxygen inside plasma gives useful information regarding the understanding and optimization of plasma processing application.

**Keywords:** Diffusion, Finite difference method, Meshless method, Plasma parameters, Radial basis function.

## 1    Introduction

Mathematical models play a vital role in describing real world scenarios in mathematical language in the form of algebraic equations and differential equations. By creating these models we can get solutions to real world problems and predict the future behavior of the system. As the world's leading economies focus on energy and high technology, plasma has become increasingly important. For example, information and communication technologies have grown rapidly, these rely on integrated electronic circuits and mass storage devices for data and signal processing as well as storage. Plasma processing is one of the key technologies enabling the manufacture of the hardware needed in these high technology sectors.

Plasma processing has vital application in manufacturing industries. like the case of integrated circuits (ICs), which are widely used in electronics. Other applications of plasma processing include automotive, aerospace, steel, biomedical, and toxic waste management industries. The art of developing and optimizing plasma applications involves understanding how plasma properties can be controlled in order to achieve the best possible process results. Modification of surfaces by plasma is due to the particles from the plasma, so knowledge and control of their fluxes and energies is crucial.

Plasma processing usually involves (EN) gas. This is also used in numerous applications such as photo-resist ashing [1] as well as surface modification and activation [2] [3] [4]. For material processing atomic oxygen is recognized as the most reactive specie in oxygen plasma [5] [6].

In this work we are concerned with diffusion of plasma quantities and specially diffusion of atomic oxygen and the effect of power and gas pressure on plasma parameters. In the early study of electronegative plasma [7] system of equations are modeled considering seven species $O_2, O_2(^1\Delta_g), O, O^+, O^-, O_2^+,$ $e^-$ and solved numerically. Recent work is the extension of earlier work [7] to study plasma quantities more deeply by adding diffusion in the existing model.

The work given in this paper is very important in understanding and optimizing of plasma processing application. This paper is organized as follows:

Section 2 describes mathematical model without diffusion, Section 3 is about the model equations with diffusion and solution procedure, Section 4 is about numerical results and discussions, and in Section 5 a brief conclusion of the work is given

## 2 Mathematical models without diffusion

In the earlier work improved volume averaged model [7] for seven species has been presented. Using rate coefficients given in table 1, ODE model for particle balance and power balance in oxygen discharge is as follows:

$$\frac{dn_{O_2}}{dt} = \frac{Q}{V} + K_{rec}n_{O_2^+0}n_{O-0}\frac{V_{rec}}{V} + K_{det}\bar{n}_{O-}\bar{n}_O + K_{deer}n_{e0}\bar{n}_{O_2^*} + \frac{1}{2}v_On_{O0}$$
$$- (K_{iz1} + K_{att} + K_{diss} + K_{iz3} + K_{iz4} + K_{ex})n_{O_2}n_{e0} - K_{ch}\bar{n}_{O+}n_{O_2}$$
$$+ v_{O_2^+}n_{O_2^+0} + v_{O_2^*}n_{O_2^*0} - K_{pump}n_{O_2}, \tag{1}$$

$$\frac{dn_{O_2^+}}{dt} = K_{iz1}n_{O_2}n_{e0} + K_{izm}\bar{n}_{O_2^*}\bar{n}_{e0} - (K_{rec} + K_{rec2})n_{O_2^+0}n_{O-0}\frac{V_{rec}}{V} +$$
$$K_{ch}\bar{n}_{O+}n_{O_2} - K_{ei}n_{e0}\bar{n}_{O_2^+} - v_{O_2^+}n_{O_2^+0}, \tag{2}$$

$$\frac{d\bar{n}_{O+}}{dt} = K_{iz2}\bar{n}_On_{e0} + (K_{iz3} + K_{iz4})n_{O_2}n_{e0} - K_{rec3}n_{O+0}n_{O-0}\frac{V_{rec}}{V} -$$
$$K_{ch}\bar{n}_{O+}n_{O_2} - v_{O+}n_{O+0}, \tag{3}$$

$$\frac{d\bar{n}_{O-}}{dt} = (K_{att} + K_{iz3})n_{O_2}n_{e0} + K_{attm}\bar{n}_{O_2^*}n_{e0} - K_{rec3}n_{O+0}n_{O-0}\frac{V_{rec}}{V}$$
$$- (K_{rec} + K_{rec2})n_{O_2^+0}n_{O-n}\frac{V_{rec}}{V} - K_{det}\bar{n}_O\bar{n}_{O-} - K_{rec4}\bar{n}_{O-}\bar{n}_{O_2^*}, \tag{4}$$

$$\frac{d\bar{n}_O}{dt} = 2K_{ei}n_{e0}\bar{n}_{O_2^+} + (K_{rec} + 3K_{rec2})n_{O_2^+0}n_{O-0}\frac{V_{rec}}{V} + K_{ch}\bar{n}_{O+}n_{O_2} +$$
$$(2K_{diss} + K_{att} + K_{iz4})n_{O_2}n_{e0} + K_{rec4}\bar{n}_{O-}\bar{n}_{O_2^*} - K_{iz2}\bar{n}_On_{e0}$$
$$+ (K_{attm} + 2K_{dism})\bar{n}_{O_2^*}n_{e0} - K_{det}\bar{n}_O\bar{n}_{O-} + v_{O+}n_{O+0}$$
$$+ 2K_{rec3}n_{O+0}n_{O-0}\frac{V_{rec}}{V} - v_On_{O0} - K_{pump}\bar{n}_O, \tag{5}$$

$$\frac{d\bar{n}_{O_2^*}}{dt} = K_{ex}n_{O_2}n_{e0} - (K_{izm} + K_{attm} + K_{deer} + K_{dism})\bar{n}_{O_2^*}n_{e0} - v_{O_2^*}n_{O_2^*0}$$
$$- K_{rec4}\bar{n}_{O-}\bar{n}_{O_2^*} - K_{pump}n_{O_2^*}, \tag{6}$$

$$\frac{d}{dt}\left(\frac{3}{2}en_{e0}T_e\right) = \frac{P_{abs}}{V} - e(\varepsilon_{c-O_2}K_{iz1}n_{e0}n_{O_2} + \varepsilon_{c-O}K_{iz2}n_{e0}\bar{n}_O) -$$
$$e(\varepsilon_e + \varepsilon_{i-O_2^+})v_{O_2^+}n_{O_2^+0} - e(\varepsilon_e + \varepsilon_{i-O+})v_{O+}n_{O+0}. \tag{7}$$

## 3 Model equations with diffusion and solution procedure

Following the same procedure as discussed in [8] when diffusion is added the ODE model (1) is converted in to system of PDEs which is given by

The coefficients $d_1$, $d_2$, $d_3$, $d_4$, $d_5$, $d_6$ and $d_7$ are diffusion coefficients of $O_2$, $O_2^+$, $O^+$, $O^-$, $O$, $O_2(^1\Delta_g)$, and $e^-$ respectively.

$$\frac{\partial n_{O_2}}{\partial t} = \frac{Q}{V} + K_{rec}n_{O_2^+0}n_{O-0}\frac{V_{rec}}{V} + K_{det}\bar{n}_{O-}\bar{n}_O + K_{deer}n_{e0}\bar{n}_{O_2^*} + K_{rec4}\bar{n}_{O-}\bar{n}_{O_2^*} -$$
$$(K_{iz1} + K_{att} + K_{diss} + K_{iz3} + K_{iz4} + K_{ex})n_{O_2}n_{e0} - K_{ch}\bar{n}_{O+}n_{O_2}$$
$$+ v_{O_2^+}n_{O_2^+0} + v_{O_2^*}n_{O_2^*0} - \frac{1}{2}v_On_{O0} - K_{pump}n_{O_2} + d_1\frac{\partial^2 n_{O_2}}{\partial x^2}, \tag{8}$$

$$\frac{\partial \bar{n}_{O_2^+}}{\partial t} = K_{iz1}n_{O_2}n_{e0} + K_{izm}n_{O_2^*}n_{e0} + K_{ch}\bar{n}_{O+}n_{O_2} - (K_{rec} + K_{rec2})n_{O+0}n_{O-0}\frac{V_{rec}}{V} -$$
$$K_{ei}n_{e0}\bar{n}_{O_2^+} - v_{O_2^+}n_{O_2^+0} + d_2\frac{\partial^2 \bar{n}_{O_2^+}}{\partial x^2}, \tag{9}$$

$$\frac{\partial \bar{n}_{O+}}{\partial t} = K_{iz2}\bar{n}_On_{e0} + (K_{iz3} + K_{iz4})n_{O_2}n_{e0} - K_{rec3}n_{O+0}n_{O-0}\frac{V_{rec}}{V} - K_{ch}\bar{n}_{O+}n_{O_2} -$$
$$v_{O+}n_{O+0} + d_3\frac{\partial^2 \bar{n}_{O+}}{\partial x^2}. \tag{10}$$

The interval [0, $l_p$] is considered to be the domain of this system of PDE's

Table 1: **Basic reaction set for Oxygen discharge.** (Note: $T_e$ in the range 1-7 eV, $T_i$ in Kelvins.)

| Reaction | Rate coefficients($\frac{m^3}{s}$) | References |
|---|---|---|
| $e + O_2$ moment transfer | $K_{el} = 4.7E^{-14}T_e^{0.5}$ | [9] |
| $e + O_2 \rightarrow O_2^+ + 2e$ | $K_{iz1} = 2.34E^{-15}T_e^{1.03}exp(-\frac{12.29}{T_e})$ | [10] |
| $e + O_2 \rightarrow O + O^-$ | $K_{att} = 1.07E^{-15}T_e^{-1.391}exp(-\frac{6.26}{T_e})$ | [11] |
| $e + O_2 \rightarrow O + O^+ + 2e$ | $K_{iz4} = 1.88E^{-16}T_e^{1.699}exp(-\frac{16.81}{T_e})$ | [10] |
| $e + O_2 \rightarrow O^+ + O^- + e$ | $K_{iz3} = 7.1E^{-17}T_e^{0.5}exp(-\frac{17}{T_e})$ | [12] |
| $e + O_2 \rightarrow 2O + e$ | $K_{diss} = 6.86E^{-15}exp(-\frac{6.29}{T_e})$ | [9] |
| $e + O_2 \rightarrow O + O^* + e$ | $K_{diss} = 3.49E^{-14}exp(-\frac{5.92}{T_e})$ | [9] |
| $e + O \rightarrow O^+ + 2e$ | $K_{iz2} = 9.0E^{-15}T_e^{0.7}exp(-\frac{13.6}{T_e})$ | [13] |
| $e + O_2^+ \rightarrow 2O$ | $K_{ei} = 2.2E^{-14}T_e^{-0.5}$ | [14] |
| $O^- + O \rightarrow O_2 + e$ | $K_{det} = 1.6E^{-16}$ | [15] |
| $O^- + O_2^+ \rightarrow O + O_2$ | $K_{rec} = 2.6E^{-14}\frac{300}{T_i}^{0.44}$ | [14] |
| $O^- + O_2^+ \rightarrow 3O$ | $K_{rec2} = 2.6E^{-14}\frac{300}{T_i}^{0.44}$ | [14] |
| $O^- + O^+ \rightarrow 2O$ | $K_{rec3} = 4.0E^{-14}\frac{300}{T_i}^{0.43}$ | [14] |
| $O^+ + O_2 \rightarrow O + O_2^+$ | $K_{ch} = 2.0E^{-17}\frac{300}{T_i}^{0.5}$ | [16] |
| $e + O_2 \rightarrow O_2^* + e$ | $K_{ex} = 1.37E^{-15}exp^{-\frac{2.14}{T_e}}$ | [9] |
| $e + O_2^* \rightarrow e + O_2$ | $K_{deer} = 2.06E^{-15}T_e^{0.44}exp^{-\frac{2.14}{T_e}}$ | Detailed balancing |
| $e + O_2^* \rightarrow O_2^+ + 2e$ | $K_{izm} = 2.34E^{-15}T_e^{1.03}exp(-\frac{11.31}{T_e})$ | [10] |
| $e + O_2^* \rightarrow O + O^-$ | $K_{attm} = 4.19E^{-15}T_e^{-1.376}exp(-\frac{5.19}{T_e})$ | [11] |
| $e + O_2^* \rightarrow 2O + e$ | $K_{dism} = 6.86E^{-15}exp(-\frac{5.31}{T_e})$ | Threshold reduction |
| $O^- + O_2^* \rightarrow O_2 + O + e$ | $K_{rec4} = 3.3E^{-17}$ | [17] |
| $O + wall \rightarrow \frac{1}{2}O_2$ | $\gamma_O = 0.5$ for $p \leq 10mtorr$ = (0.43,0.33,0.27,0.23,0.2,0.15,0.13) for p=(15,25,35,40,50,60,70)m torr | [18] |
| $O_2^* + wall \rightarrow O_2$ | $\gamma_O = 0.007$ | [19] |

$$\frac{\partial \bar{n}_{O-}}{\partial t} = (K_{att} + K_{iz3})n_{O_2}n_{e0} + K_{attm}\bar{n}_{O_2^*}n_{e0} - (K_{rec} + K_{rec2})n_{O_2^+0}n_{O-n}\frac{V_{rec}}{V}$$
$$K_{rec3}n_{O+0}n_{O-0}\frac{V_{rec}}{V} - K_{det}\bar{n}_O\bar{n}_{O-} - K_{rec4}\bar{n}_{O-}\bar{n}_{O_2^*} + d_4\frac{\partial^2 \bar{n}_{O-}}{\partial x^2}, \tag{11}$$

$$\frac{\partial \bar{n}_O}{\partial t} = 2K_{ei}n_{e0}\bar{n}_{O_2^+} + (K_{rec} + 3K_{rec2})n_{O_2^+0}n_{O-0}\frac{V_{rec}}{V} + 2K_{rec3}n_{O+0}n_{O-0}\frac{V_{rec}}{V} +$$
$$(2K_{diss} + K_{att} + K_{iz4})n_{O_2}n_{e0} + K_{ch}\bar{n}_{O+}n_{O_2} + K_{rec4}\bar{n}_{O-}\bar{n}_{O_2^*} + (K_{attm} + 2K_{dism})\bar{n}_{O_2^*}n_{e0}$$
$$- K_{iz2}\bar{n}_On_{e0} - K_{det}\bar{n}_O\bar{n}_{O-} + v_{O+}n_{O+0} - v_On_{O0} - K_{pump}\bar{n}_O + d_5\frac{\partial^2 \bar{n}_O}{\partial x^2}, \tag{12}$$

$$\frac{\partial \bar{n}_{O_2^*}}{\partial t} = K_{ex}n_{O_2}n_{e0} - (K_{izm} + K_{attm} + K_{deer} + K_{dism})\bar{n}_{O_2^*}n_{e0} - K_{rec4}\bar{n}_{O-}\bar{n}_{O_2^*}$$
$$- v_{O_2^*}n_{O_2^*0} - K_{pump}\bar{n}_{O_2^*} + d_6\frac{\partial^2 \bar{n}_{O_2^*}}{\partial x^2}, \tag{13}$$

$$\frac{\partial}{\partial t}\left(\frac{3}{2}en_{e0}T_e\right) = \frac{P_{abs}}{V} - e(\varepsilon_{c-O_2}K_{iz1}n_{e0}n_{O_2} + \varepsilon_{c-O}K_{iz2}n_{e0}\bar{n}_O) -$$
$$e(\varepsilon_e + \varepsilon_{i-O_2^+})v_{O_2^+}n_{O_2^+0} - e(\varepsilon_e + \varepsilon_{i-O+})v_{O+}n_{O+0} + d_7\frac{\partial^2(\frac{3}{2}en_{e0}T_e)}{\partial x^2}, \tag{14}$$

### 3.1 Initial conditions

Initial conditions given in [7] are being used in present numerical simulation. These initial conditions are:

$$\bar{n}O_2{}^+{}_0 = 2E16, \qquad x \in [0, l_p],$$
$$\bar{n}O_0{}^+ = 1E16, \qquad x \in [0, l_p],$$
$$\bar{n}O_0{}^- = 3E15, \qquad x \in [0, l_p],$$
$$\bar{n}O_0 = 2E17 * (1 - \frac{x^2}{d^2}), \qquad x \in [0, l_p], \qquad (15)$$
$$\bar{n}O_2 m_0 = 0.01 * ng_0, \qquad x \in [0, l_p],$$
$$nO_2 0 = ng0 - \bar{n}O_0 - \bar{n}O_2 m_0, \qquad x \in [0, l_p],$$
$$T_e 0 = 2, \qquad x \in [0, l_p],$$
$$ne0 = \bar{n}O_2 {}_0^+ + \bar{n}O_0^+ - \bar{n}O_0^-, \qquad x \in [0, l_p],$$

### 3.2 Boundary condition

Taking boundary condition
at

$x = l_p$ is [20]

### 3.3 Numerical procedure

For the numerical solution of reaction diffusion PDE's, we used explicit method based on meshless procedure. As we have first order derivative in time and second in space. We discritized time derivative using forward difference and approximate space with MQ RBF.

## 4 Numerical results and discussion

For the numerical solution of PDEs time step $\Delta t = 2e{-}7$ and space step $\Delta x = 0.0031$, are used keeping in view Von-Neumann stability analysis. Using the above initial and boundary conditions, we get the results shown in graphs given in figure (1), figure(2) and figure (3). In the analysis of PDEs

two points has been taken from the domain (0, lp), where lp is half length of plasma reactor and 0 is the core of plasma. In this domain, pressure and power dependence of different particle densities has been observed. Pressure has been taken in the range (15 − 60 m T orr) and power (40 − 300 W).

By comparison of results taken from with diffusion model and without diffusion model, certain variation has been observed. These comparisons are shown in graphs given in figure 1 and discussed as follows:

In figure 1 density of negative ions has been shown. In the start there is greater value of negative ion density due to diffusion than without diffusion. With the passage of time this relation reverses and with diffusion results are lesser than without diffusion. This relation is due to the fact that in diffusion, dissociative attachment reaction rates increase which increase

negative ions and with the passage of time negative ion densities decreases due to lower electron density. Diffusion phenomenon increases the recombination

reaction i,e: $O^- + O^+ \rightarrow 2O,$ which decreases positive ion density and increases density of atomic oxygen. Therefore, in figure 1 with diffusion graph for positive ion is lower than without diffusion. Density of positive

ion $(nO_2{}^+)$ with diffusion is greater than without diffusion. It is due to the fact that, diffusion increases ionization rate which causes increase in positive ions. Electron density also gives greater value due to diffusion than without diffusion. This difference is due to the fact that diffusion causes inelastic collision which increases ionization rate and we get greater electron density.
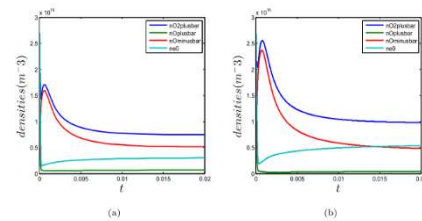


Figure 1: Without diffusion results(a) and with diffusion results(b).
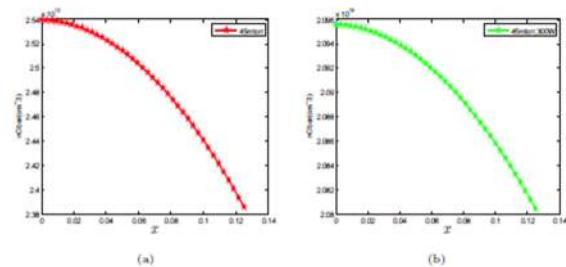


Figure 2: Atomic oxygen density with respect to space at 40 watt power (a) and 300 watt power (b).

The diffusion of atomic oxygen from the core to the wall is shown in figure 2. Figure 2 (*a*) represents diffusion at 40 *W* power and 60 *m T orr* pressure and figure 2 (*b*) shows diffusion at 300 *W* power and 60 *m T orr* pressure. Both of the figures shows a parabolic profile of oxygen density having more density at the core and lesser at the wall.

The atomic oxygen density as a function of applied power and gas pressure are shown in figure 3. The atomic oxygen density increases with the applied power and gas pressure.
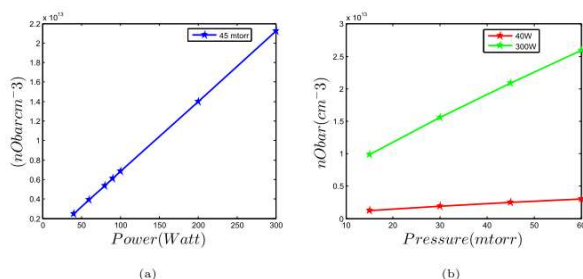
Figure 3: Pressure and power dependencies of atomic oxygen.

## 5    Conclusion

In this paper we have added a unidirectional diffusion process to the ODE model of particle densities inside plasma. The models are simulated using finite difference and meshless procedure. Simple explicit scheme are used for time integration. As a result of this numerical simulation, we study diffusion of particles inside plasma. The density of atomic oxygen from the core to the wall of plasma, gives parabolic profile. Both the temporal and spatial dynamics of particles inside plasma are studied. Particle densities are studied as a function of power and pressure. The results are useful for the general understanding of EN discharges.

## ACKNOWLEDGMENTS

## References

[1] T. H. Lin, M. Belser, and Yonhua Tzeng. Pulsed microwave plasma etching of polymers in Oxygen and Nitrogen for microelectronic applications. *Plasma Science, IEEE Transactions on*, 16(6):631–637, 1988.

[2] D. Hegemann, H. Brunner, and C. Oehr. Deposition rate and three-dimensional uniformity of RF plasma deposited SiO x films. *Surface and Coatings Technology*, 142:849–855, 2001.

[3] Norihiro Inagaki, Kazuo Narushima, and S. K. Lim. Effects of aromatic groups in polymer chains on plasma surface modification. *Journal of Applied Polymer Science*, 89(1):96–103, 2003.

[4] T. Aumann, D. Theirich, and J. Engemann. Rapid surface modification of polyethylene in microwave and rf-plasmas: comparative study. *Surface and Coatings Technology*, 142:169–174, 2001.

. [5] A. K. Srivastava and P. Sakthivel. Quartz-crystal microbalance study for characterizing atomic oxygen in plasma ash tools. *Journal of Vacuum Science & Technology A*, 19(1):97–100, 2001

[6] Hidetoshi Kumagai, Denbo Hiroki, Nobuyuki Fujii, Takaomi Kobayashi, et al. Poly (ethylene terephthalate) decomposition process in oxygen plasma; emission spectroscopic and surface analysis for oxygen-plasma reaction. *Journal of Vacuum Science & Technology A*, 22(1):1–7, 2004.

[7] Sungjin Kim, M. A. Lieberman, A. J. Lichtenberg, and J. T. Gudmundsson. Improved volume-averaged model for steady and pulsed-power electronegative discharges. *Journal of Vacuum Science & Technology A*, 24(6):2025–2040, 2006.

[8] Nadeem Haider and Siraj ul Islam. Numerical solution of compartmental models by meshless and finite difference methods. *Applied Mathematics and Computation*, 238:408–435, 2014.

[9] S A. Lawton and A. V. Phelps. Excitation of the $b^1 \Sigma_g^+$ state of $O_2$ by low energy electrons. *The Journal of Chemical Physics*, 69(3):1055–1068, 1978.

[10] E. Krishnakumar and S. K. Srivastava. Cross-sections for electron impact ionization of $O_2$. *International Journal of Mass Spectrometry and Ion Processes*, 113(1):1–12, 1992.

[11] Thomas Jaffke, Martina Meinke, Reza Hashemi, Loucas G. Christophorou, and Eugen Illenberger. Dissociative electron attachment to singlet oxygen. *Chemical Physics Letters*, 193(1-3):62–68, 1992.

[12] Michael A. Lieberman and Alan J. Lichtenberg. *Principles of plasma discharges and materials processing*. John Wiley & Sons, 2005.

[13] C. Lee, D. B. Graves, M. A. Lieberman, and D. W. Hess. Global model of plasma chemistry in a high density oxygen discharge. *Journal of the Electrochemical Society*, 141(6):1546–1555, 1994.

[14] J. T. Gudmundsson. Recombination and detachment in oxygen discharges: the role of metastable oxygen molecules. *Journal of Physics D: Applied Physics*, 37(15):2073, 2004.

[15] S. G. Belostotsky, D. J. Economou, D. V. Lopaev, and T. V. Rakhimova. Negative ion destruction by $O(^3P)$ atoms and $O_2(a^1\Delta_g)$ molecules in an oxygen plasma. *Plasma Sources Science and Technology*, 14(3):532, 2005

[16] B. Eliasson and U. Kogelshatz. Brown Boveri Konzernforschung Report. *(unpub- lished)*, KLR–11C, 1986.

[17] B. L. Upschulte, W. J. Marinelli, and B. D. Green. Reactions of oxygen ($^1\Delta_g$) with oxide and superoxide ions.

[18] S. Gomez, P. G. Steen, and W. G. Graham. Atomic oxygen surface loss coefficient measurements in a capacitive/inductive radio-frequency plasma. *Applied Physics Letters*, 81(1):19–21, 2002.

[19] R. L. Sharpless and T. G. Slanger. Surface chemistry of metastable oxygen. II. Destruction of $O_2(a^1\Delta_g)$. *The Journal of Chemical Physics*, 91(12):7947–7950, 1989.

[20] Ishfaq Ahmad Ganaie and V. K. Kukreja. Numerical solution of burgers equation by cubic hermite collocation method. *Applied Mathematics and Computation*, 237:571–581, 2014.

*The Journal of Physical Chemistry*, 98(3):837–842, 1994.

# Increase of Aluminium Particles in the Environment due to Chemtrails during the period of Autumn 2012 to Summer 2015 within Lahore, Pakistan

Humza Bin Masood[1,*], Seemal Jelani[2]

[1]*Environmental Sciences Department, FC College (A Chartered University), Lahore 54600*
[2]*Department of Chemistry, FC College (A Chartered University), Lahore 54600*
*Corresponding author*
*Email*: *15-10333@formanite.fccollege.edu.pk*

## ABSTRACT

Currently the most prevailing issue of the climate change in the world is geo-engineering and one of the most prevailing issue in this is using of Chemtrails to change the climate. These Chemtrails are left over in the sky with the help of special types of jet planes which use to spray Aluminum, Barium and Strontium is the sky to make a thick parallel lines with the help of condensation due to change of air pressure at the height. These thick parallel lines are the condense layers of Aluminum, Barium and Strontium which use to stop some rays of sunlight coming to the sky but sadly it also prevents the heat rays to go out of the earth space due to the layers formed. These sprays are causing the increase of Aluminum in the Environment as these particles can move trillions of miles and are causing different problems and diseases like Asthma in our planet earth. The analysis performed helps to know about the increase of these Aluminum particles in our planet and the studies performed shows the problem caused by the spraying to these nanoparticles in the Atmosphere.

**Keywords:** Water, Atmosphere, Sky, Seasons, Soil.

## INTRODUCTION

Engineering the climate is the Last and the Scariest option to save planet Earth (US Scientists). Many ways are there to engineering the climate like Artificial Rain, Cloud Seeding, Giant Reflectors, Using Aerosols, Haarp Project, Silver Iodide but Chemtrails is one of the cheapest sources for engineering the climate. In fact, it cost thousands of Dollars but relating to other Climate modification techniques it is the one of the cheapest sources [1]. Trillions of Nano-particles of Aluminum, Barium and Strontium are sprayed every day over our heads in our blue sky which seems like white clouds. This is done by special kind of Air Planes which have special types of engine placement by which these air planes can move to several miles in the atmosphere. Then these air planes spray Aluminum, Barium and Strontium in form of Nano-particles. These Nano-particles can move millions of miles in atmosphere (Michel J. Murphy) [2]. When Ever you see jet Chemtrails going over you are going to get Aluminum, Barium, Strontium coming down on you; and what should it be there in the soil? Yes, it should be in the soil, it was there, always being there, well should it be in the rain; absolutely not [3]. These Nano-particles are sprayed and due to change in pressure at higher altitudes they are condensed. These condense particles form a layer and they stop sunlight coming to our planet earth [4]. This causes global dimming (Why in The World are they Spraying?). Global dimming is basically a term refer when the sun rays are not able to get to the earth which may cause problems of plants to grow green. Some of the scientist says that chemtrails are nothing else but the special type of contrails which causes global dimming while those who don't support chemtrails says that this is a war technique which allows to change weather [5]. There is a debate that chemtrails are the military weapons as well as debate that it is tool for many traders to earn money. "The

growing evidence repeatedly confirms that aircraft are spraying dirty aerosols to warm the climate in Polar Regions for drilling access by BIG OIL as faux "National Security" [6]. Some Scientists believes that these techniques are also used by great traders to make a loss to other trader and make a profit out of that. Some use to change the weather of the particular area for their trades and many believes that it is use in war as a military weapon. The question that arises here is that is there any need for climate modification in wars and if so how do they help the military forces? Not only the chemtrails but there are many military projects that cause the climate to change and one of those projects is HAARP (High frequency Active Auroral Research Program) but only the one time use of HAARP cost trillions of dollars and relatively Chemtrails are less cheap but Chemtrails require some hours for weather modification but HAARP can do the same thing within the seconds [7]. These weather modification techniques are very helpful in warfare. These are used to blew snow storms on the enemy. With the help of these snow ball can be upsized easily to the size that it can break glass [8]. It is also used in places where there is soil to cause rain and it cause the soil to be muddy which is a hurdle for an enemy not only this but it also effects their health. Beside all the facts of climate modification the nano-particles of Aluminum used in this process can travel billions of miles these are causing very harmful diseases (Barb Peterson). The increase in amount of Alzheimer, Asthma, ADD, Allergy and Respiratory Orders is due to Oxides of Aluminum sprayed from chemtrails to modify the temperature of our planet earth. Beside the fact that it causes air pollution it is true that it also causes water pollution and soil pollution. So we are not going to get oxides of aluminum by inhalation through air but also from plants. Aluminum causes defects in Plants [9]. Rose Cairns explains that there is a conspiracy of contrails and chemtrails. Many big mafias who use to make profit of this use to intermix

both the terms and say that these use to disappear very soon as there are no chemtrails. Contrails are the lines caused by airplanes when going at high altitude caused under the atmospheric pressure in our blue sky which disappears hardly within 10 seconds but Chemtrails are the aerosol sprays that are used to engineer the climate. This uses to spray the nano-particles of Aluminum, Barium and Strontium in parallel lines and don't disappears within hours [10]. On Daily basis chemtrail jets is been seen in the blue sky of Lahore but public is unaware about is that what is happening. Here the study focuses on the spray of the Aluminum from the chemtrail jets in the sky and as Michael J. Murphy had explained that these nano-particles are travel trillions of miles so the rate is increasing drastically in the environment and are causing many health effects within the living organisms. The rate of Asthma is increasing drastically and now according 334 million patients of asthma around the globe [11]. About 15% of Pakistan's population suffers from asthma which includes 10% children of Pakistan [12] while the annual increase of asthma is 5% [13].

## MATERIALS AND METHODS USED
**STUDY AREA:** The study that was analyzed is Lahore city which consists of Sheikhpura district at on the North-West, on the east is India and on the district Kasur and on the North River Ravi flows. The entire city occupies the space of 404 Km2 [14]. At GPS coordinates it is located at 31.5497°N, 74.3436°E [15].



**Figure No. 1: Map of Lahore**

**SAMPLING:** Samples of Drinking Water, Surface Soil and Air was collected from different places in all the four seasons of these three years. The samples were collected from 5 different places every time. These places consist of Thokar Niaz Baig, Jallo, Kahna, Shadra and Muslim Town. Drinking water samples were collected in the sterilized bottles for Quality Assurance and reduction of error, Surface Soil was collected in sterilized jars and air is sterilized syringes. All the samples were kept air tight to eliminate the external contamination.

**ANALYSIS:** Aluminum Analysis at AAS (Atomic Absorption Spectrometer) was performed. For black samples in each case Distilled $H_2O$ was used after $CO_2$ bubbling. For Soil, each 10g sample was mixed in 100 ml Distilled $H_2O$ was used after $CO_2$ bubbling and was stirred for 1 hour each. For Air, each sample was bubbled up to 15 ml in 100ml of $CO_2$ bubbled distilled $H_2O$.

**QUALITY CONTROL AND QUALITY ASSURANCE (QC/QA):** For the quality control all the instruments were calibrated on the regular basis. For calibration of measuring instruments $CO_2$ bubbled distilled $H_2O$ was used as the weight and volume of water is always the same i.e. 1L of water is 1Kg of Water. Weight balance was also calibrated regularly with the help of mercury balance and similarly AAS was also calibrated as per-required standards. Every time strict quality control and strict procedure for calibration was used for the maximum reduction of error.

**RESULTS AND DISCUSSIONS**
The samples were collected overtime and were coded according to sample type, season, year and site of collection e.g. for Soil Sample collected from Thokar Niaz Biag in Autumn 2012 was coded as SSTNBA2 (SS: Soil Sample, TNB: Thokar Niaz Baig, A: Autumn, 2: 2012).

**RESULTS FOR AIR SAMPLES:** The results of Air Samples overtime are shown as under.
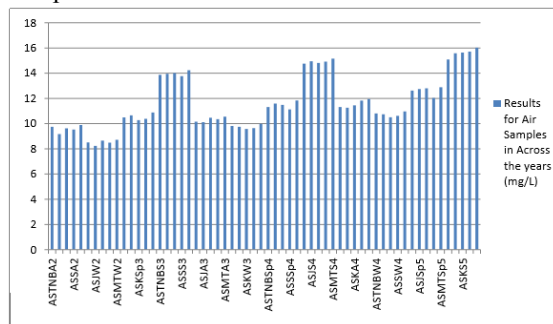


Graph 1: Aluminum Results of Air Samples across the years (mg/L)

The graph above shows the results of Aluminum in Air Samples across the three years. The graph below shows the average Amount of Aluminum detected in the samples across the seasons and years.
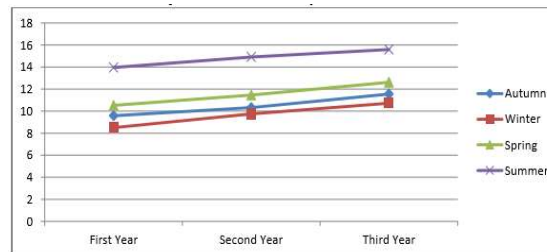


Graph 2: Average Change of Aluminum in Air Samples across the Years (mg/L)

**RESULTS OF SOIL SAMPLES:** The results of soil samples overtime are shown as under.
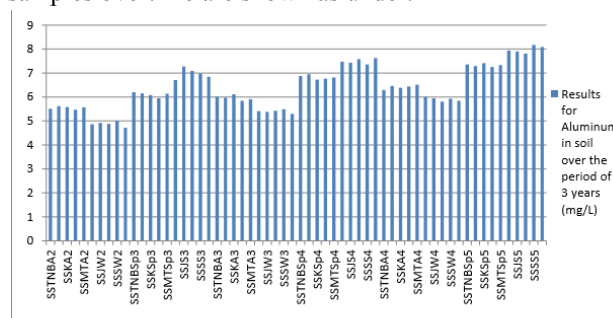


Graph 3: Results for Aluminum in soil over the period of 3 years

The graph above shows the results of Aluminum within the Soil Samples in the time span of three years while the table below shows the average Amount of Aluminum detected in the soil samples across the seasons and years.
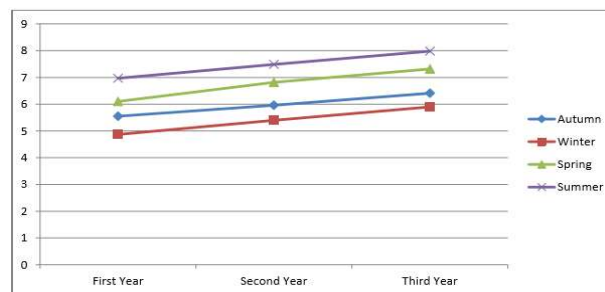


Graph 4: Average Change of Aluminum in Soil Samples across the Years (mg/L)

**RESULT OF WATER SAMPLE:**
The aluminum detection results of water samples over the period of three years are given as under.
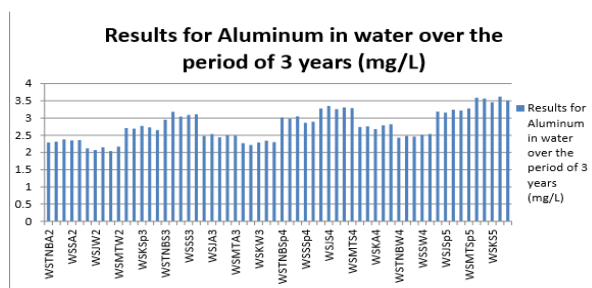
Graph 5: Results for Aluminum in water over the period of 3 years (mg/L)

The Graph Above shows the results of Aluminum in the water collected from different places from Lahore in different seasons over the period of three years. The graph below shows the average change of amount of aluminum in drinking water of Lahore over the period of three years.
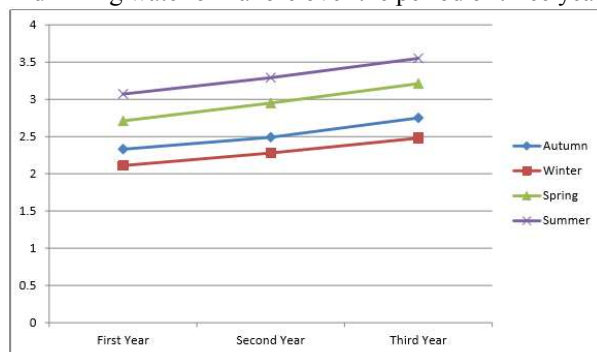


Graph 6: Average Change of Aluminum in Water Samples across the Years (mg/L)

The results above show that the amount of aluminum is increasing every year and have crossed the EPA (Environmental Protection Agency) Quality Assurance Standards of Pakistan.

**ACKNOWLEDGMENT**

Authors are thankful to Dr. Muddasir Abbas (Ex-Faculty Member, Department of Chemistry, Forman Christian College, Lahore, Pakistan) and the lab staff of Department of Chemistry, Forman Christian College, Lahore, Pakistan. Authors are also thankful to Sanwal Masood (Department of Environmental Sciences, UAAR – Rawalpindi) for sponsoring the study.

**CONCLUSION**

The amount of Asthma is increasing every year due to Chemtrails in Pakistan. On the daily basis jets are been seen in the sky spraying the chemtrails which are increasing drastically and are causing diseases like Asthma, Allergies, Skin Infection, ADD, Autism, etc. As the results shows the regular increase in aluminum in soil, water and air it is recommended that the government and related organizations should take this issue at the international level and stop the spraying of Chemtrails in the sky because these trails don't only effect the atmosphere but its nano-particles can travel trillion of miles effecting our soil, water and air.

**REFERENCES**

[1] Ten Technologies to save the planet earth by Chris Goodall; Greystone Books, D&M publisher, Vancouver/Toronto/Berkley.

[2] Michel J. Murphy, 2012, Documentary: "Why in the world are they spraying"?

[3] Franchis Mangels, 2012, Documentary: "Why in the world are they spraying"?

[4] Clark S, 2002, "Conspiracy Theories and Conspiracy Theorizing Philosophy of the Social Sciences" Vol. 32 Page. 131–150.

[5] Vapour Trail; Encyclopedia Brattian.

[6] Chemtrails Planet, May 1st 2014, (www.chemtrailsplanetuk.com)

[7] William Harris, 2010, "Can we control the weather?"

[8] Hamblin JD, 2013, "Arming Mother Nature", Oxford University Press.

[9] Barb Peterson, 2012, Documentary: "Why in the world are they spraying"?

[10] Rose Cairns, 2014, "Climates of Suspicion: 'chemtrail' conspiracy narratives and the international politics of geoengineering". Geo-engineering Governance Research.

[11] "Global Asthma Report", 2014 (www.globalasthmareport.com)

[12] "Rising Pollution escalating asthma prevalence in Pakistan", 7th of May, 2015, The News.

[13] Muhammad Qasim, "Two Million Asthma Patients in Pakistan", 1st of May, 2012, The News.

[14] Lahore Data, "Government of Punjab", (http://www.punjab.gov.pk/lahore)

[15] Google Maps.

# Environmental Terrorist: Electric Generators increasing Lead in an Environment

Humza Bin Masood[1,*], Seemal Jelani[2]

[1]*Environmental Sciences Department, FC College (A Chartered University), Lahore 54600*

[2]*Department of Chemistry, FC College (A Chartered University), Lahore 54600*

*\*Corresponding author*

*Email*: *15-10333@formanite.fccollege.edu.pk*

## ABSTRACT

Energy Crisis is a biggest challenge in developing countries like Pakistan. Many developing countries are fighting with this issue both at governmental and individual level. In Pakistan, mostly at individual levels UPS or Electric Generators are used for both offices and homes. In Electric Generators, usually methane, petrol or diesel is being used in this country. It is being promised by any petroleum organizations that petroleum provided is lead free but still there is a petroleum that is being sold in the country. The study was conducted in the capital of Punjab Province in the rich community area where the bio-accumulator of lead plants near the electric generators were studied and it was found with the help of GC-MS and flame AAS that the plants near the generators were having petroleum compounds and lead in their leaves. The study emphasizes the treatment of petroleum to make it lead free and the reduction of use of generators as they increase the lead in environment and further causes the increases the risk of diseases in plants.

**Keywords:** Electric Generators, GC-MS, flame AAS, bio-accumulator plants.

\*\*\*\*\*\*\*\*\*\*\*\*\*\*\*\*\*\*\*\*

## INTRODUCTION

Energy crisis is one of the biggest issue in the developing countries in Pakistan (Amadi H. N., 2015). The electricity consumption and its crisis is mostly at the consumer end (CEIDS, 2001). Electricity is an import element for the country and in the healthcare sector (World Bank, 2008). Due to the lack of electricity for the heating purposes many developing countries uses fuel wood which leads to many diseases and effects the public health of the country as well as social effects (Cerny M., 2013). Due to the energy crisis the use of both portable and standby electric generators had increased in Lahore which uses Methane, petrol or diesel for its operations.

Though it is being promised by many petroleum industries that the fuel provided is now lead free but still there is lead in the petroleum compounds (Busch P. O., 2014). This lead is a cause of many diseases in human and plants especially young children (Hall W., 2013) and leads to many adverse environmental effects (Newman P., 1985). This lead can be accumulated in bio-accumulating plants as *Tagestes erecta* the common name for this is marigold (Alvarado C. J., et. al., 2013).

Lead in plants leads to the adverse effects in the pollination (Xiao Y., et. al., 2016) and it effects the population of the plant. This can also effect the

chlorophyll production in plants (Yang J., et. al., 2016). Lead cause many diseases in humans as well like adverse effects in neurological development (Washam C., 2002), effecting gastrointestinal tract and blood stream (Cave M. R., et. al., 2011). The excess of lead can also lead to physiological effects (Jin Z. et. al., 2014).

Petroleum use in electric generators after burning produce many organic byproducts (Li H., et. al., 2016). These byproducts are mutagenic and can cause cancer (Voll M. J., et. al., 1977). These are released as a byproduct in form of organic aerosols and varies from season to season but it has many adverse effects on both human and plants and may be a cause of death in plants (Villegas E. R., et. al., 2013).

**MATERIALS AND METHODS USED**

**Study Area:** Capital of Punjab, Lahore, is the largest city of Punjab and second largest city of Pakistan having current population of seven million with the growth rate of 2% annually (Masood H. B., et. al., 2015) and is located at 31.5497°N and 74.3436°E with the area of 404 Km$^2$. (Masood H. B. and Jelani S., 2015). The areas of Lahore with the population of high income group were selected for the study where electric generators were under used.

**Sampling Area:** Nine leaves samples of *Tagestes erecta* were collected from DHA phase 1 to 6, Housing societies near Thokar Niaz Baig, Railway Station and Gulberg area. *Tagestes erecta* was selected as it is a common plant in Lahore and can accumulate Lead easily (Alvarado C. J., et. al., 2013) commonly known as marigold. The samples were analyzed for lead and petroleum byproducts.

**Sample Preparation and Analysis:** Leaves samples were crushed with help of mortar and pestle and were heated. Later the extractions were made in Aqua Regia (Sosa M. C., et. al., 2016). The samples were analyzed by help of flame atomic absorbance spectrophotometer for Pb analysis and GCMS was used for the petroleum compounds analysis as they are volatile and were accumulated in leaves.

**QC/QA:** For quality control and assurance the samples were packed in field so contamination may not be there. Apparatuses were washed with distilled water, autoclaved and were oven-dried so contamination may not be there. For precise analysis analytical techniques as flame AAS and GC-MS were used.

**RESULTS**

The samples were collected and were analyzed with flame AAS for Pb and with GC-MS for petroleum compounds in the leaves of *Tagestes erecta*. The studies show the lead was detected in all the samples as well as petroleum by-products were also found in all the samples. Pb standard of analytical grade of 100 mg/L was used as a standard. The following results were found with help of flame atomic absorbance spectrophotometer.

**Table No. 1: Amount of Lead in Samples**

| Sample Name | Lead (mg/L) |
|---|---|
| DHA Phase 1 | 4.975 |
| DHA Phase 2 | 4.724 |
| DHA Phase 3 | 5.024 |
| DHA Phase 4 | 4.861 |
| DHA Phase 5 | 4.924 |
| DHA Phase 6 | 4.998 |
| Housing Societies near Thokar Niaz Baig | 2.222 |
| Gulberg | 2.783 |
| Railway Station | 1.321 |

All the samples were detected for the GC-MS and the petroleum products were found in the samples which are shown in Table No. 2

**Table No. 2: Petroleum products and by-products in Samples**

| Sample Name | Petroleum Products and By-products |
|---|---|
| DHA Phase 1 | Propane, Petrol |
| DHA Phase 2 | Petrol |
| DHA Phase 3 | Propane, Diesel |
| DHA Phase 4 | Butane |
| DHA Phase 5 | Propane, Petrol |
| DHA Phase 6 | Diesel, Butane |
| Housing Societies near Thokar Niaz Baig | Propane |
| Gulberg | Butane |
| Railway Station | Propane |

**CONCLUSION**

The study shows that there is Lead and petroleum products or by-products in the sample. Though the petroleum companies are promising that the petroleum compound sold in market is now lead free but still there is lead in petroleum compounds sold in the market (Busch P. O., 2014). Busch P. O. explained the same and the current study shows that this is a same case for Lahore. This all is resulting in many environmental damages and diseases (Yang J., et. al., 2016), (Washam C., 2002), (Cave M. R., et. al., 2011), (Jin Z. et. al., 2014), (Voll M. J., et. al., 1977), (Villegas E. R., et. al., 2013). Here there is still a need for the implementation of lead free petroleum products in the market.

**REFERENCES**

[1] Alvarado C. J., et. al. 2013. Comparative Analyses of Lead and Copper in Metal Accumulating Plants with and without Mycorrhizae. *Communications in Soil Science and Plant Analysis.* 44(22)

[2] Amadi H. N. 2015. Impact of Power Outages on Developing Countries: Evidence from Rural Household in Niger Delta, Nigeria. *Journal of Energy:* Technologies and Policy. 5(3): 27-34.

[3] Busch P. O. 2014. Taming the 'tiger in the tank': Explaining the convergence of limit values of lead in petrol. *Understanding Environmental Policy Convergence.* 104-139.

[4] Cave M. R., et. al. 2011. Dealing with Contaminated Sites (From Theory Towards Practical Application). *Oral Bioavailability.*

[5] CEIDS. 2001. The cost of power disturbances to Industrial and Digital economy companies. 1-27.

[6] Cerny M. 2013. Economic and Social Cost of Power Outage: The Case of Pakistan. *Thesis: Charles University in Prague.*

[7] Hall W. 2013. Did the elimination of lead from petrol reduce crime in the USA in the 1990s? *F1000 Research.* 2:156.

[8] Jin Z., et. al. 2014. Assessment of lead bio-accessibility in soils around lead battery plants in East China. *Chemosphere.* 119: 1247-1254.

[9] Li H., et. al., 2016. A wintertime study of $PM_{2.5}$-bound polycyclic aromatic hydrocarbons in Taiyuan during 2009–2013: Assessment of pollution control strategy in a typical basin region. *Atmospheric Environment.* 140: 404-414.

[10] Newman P. 1985. Lead in Petrol: An Environmental case study. 4(1).

[11] Villegas E. R., et. al. 2013. Organic Aerosol source apportionment in London 2013 with ME-2: exploring the solution space with annual and seasonal analysis. *Atmospheric Chemistry and Physics.* 13: 1689-1712

[12] Voll M. J., et. al., 1977. Mutagenic potential of petroleum byproducts in Chesapeake waters. *Pollution collection petrochemicals.* 59(11).

[13] Washam C. 2002. Lead challenges China's children. *Environmental Health Perspective.* 110: 567-577.

[14] World Bank. 2008. World Bank Report 2008.

[15] Xiao Y., et. al. 2016. The diverse effects of habitat fragmentation on plant pollinator interactions. *Plant Ecology.* 1-12.

[16] Yang J., et. al. 2016. Interaction between Sulphur and lead in toxicity, iron plaque formation and lead accumulation in rice plant. *Ecotoxicology and Environmental Safety.* 128: 206-212.

[17] Masood H. B., Jelani S. 2015. Increase of aluminum particles in the environment due to chemtrails during the period of autumn 2012 to summer 2015 within Lahore, Pakistan. *International Journal of Engineering Research and General Science.* 3(5): 846-851.

[18] Masood H. B., et. al. 2015. Assessment and identification of quality gradients of canal water used by Lahore, Pakistan residents in summer. *International Journal of Advance Information Science and Technology.* 37(37): 9-13.

[19] Sosa M. C., et. al. 2016. Effects of Pb in Tagetes minuta L. (Asteraceae) leaves and its relationship with volatile compounds. *Industrial Crops and Products.* 82: 37-43.

# Optimal Route Guide by GIS for Fire Cases at Public Use Buildings

Humza Bin Masood[1,*] Sohail Anwar Malik[2]

[1]*Environmental Sciences Department, FC College (A Chartered University), Lahore 54600*

[2]*Operations Department, Lahore Waste Management Company, Lahore 54000*

*\*Corresponding author*

**Email**: *15-10333@formanite.fccollege.edu.pk*

## ABSTRACT

Due to the increase in population and the increase in demand of technology the cases of fire is increasing regularly which focuses on the high demand for the fire safety services to take the timely decision to cope with the fire emergencies. The study focuses on the 80 highly used public buildings with the highly risked fire catching buildings in the three areas of Lahore, Pakistan. The study shows the optimal route to decrease the time of response to these buildings in case of emergency for the better response and the timely next possible decision. The study was based on the ArcGIS considering U-turns, width, signals and traffic flow. Study highlighted the importance of the preliminary study to deal with the fire emergencies.

**Keywords:** ArcGIS, Fire Incidents, Decision making.

## INTRODUCTION

Disasters may occur naturally or due to human activities. The losses incurred can be reduced if a proper management plan is prepared beforehand and implemented with efficiency. In urban areas the risks are higher because the population is dense. The proper use of scientific tools can help prepare for such events in advance and lower the chances of loss of precious human lives. Emergency management has been defined as the field of application of science, technology, planning and management to deal with extreme events that can maim or kill populations, severely damage properties and disturb communal life by Hoetmer[1].

Urban fire is a frequent problem all over the globe[2]. Outbreaks of fire have an economic cost as well and they contribute to increasing poverty[3]. In the case of conflagrations, strategies using technology need to be made by the fire rescue service to counter challenges. Geographic information systems (GIS) have emerged as a vital technology enabling better planning and response. In the wake of a disaster, GIS is becoming integral in supporting damage assessment, rebuilding, and public education. GIS were designed to support geographical inquiry and, ultimately, spatial decision making. The value of GIS in emergency management arises directly from the benefits of integrating a technology designed to support spatial decision making into a field with a strong need to address numerous critical spatial decision[4].

A GIS is a computer based technology that links geographic information (where things are) with descriptive information (what things are like). GIS is used to collect, display and analyse data spatially. GIS combines layers of information about a place to give users a better understanding of that place. A GIS-generated map can present many layers of different information regarding a geographic space. By linking maps to databases, GIS enables users to visualize,

manipulate, analyse and display spatial data. GIS technology can create cost-effective and accurate solutions in an expanding range of applications[5].

Since a significant period of time, GIS has been aiding fire departments to reduce losses, increase efficiency and improve outcomes. GIS is a strong information system which can collect, analyse and visualise data based on location and most fire service missions are location based[3]. GIS can be used for modelling response time, incident trend and events besides the centralisation of data[6].

Response time analysis by fire departments employ attribute data attached to the layers in a GIS to perform spatial analysis. Response times for service calls are critical. They can mean the difference between life and death and between the protection of property and damage or loss. Use of GIS provides an in-depth analysis of response times. This allows fire service leadership to ensure that response targets are achieved and the provision of amendments to the strategy if they are not[3].

In Lahore, a metropolitan city of Pakistan, a large number of buildings lack any in-built fire safety features. So it is mostly the government emergency response organisation, Punjab Emergency Services - Rescue 1122, which has to deal wholly with fire emergencies. It has identified eighty buildings which lack a basic evacuation plan and are the most vulnerable in case a fire erupts in any of those buildings. The aims to devise an optimal route for those buildings using GIS through which the response time can be reduced by considering the distance from rescue stations, traffic density and optimum routes.

In performing a response time analysis, GIS builds a street network of connected lines with descriptive attribute data for all the lines and line segments[3]. Response time can be analysed using a fire station layer and a street layer (layers are sets of data). A street layer is often represented in GIS as a series of lines that intersect on the map, creating a GIS network. Each street line segment between intersections can contain the road type, distance, and travel speeds permitted in the underlying data table within GIS. This helps identify a station location, specify a travel time, and run a network analysis[6]. The ArcGIS is a GIS tool which had been used since years to deal with these issues. Ersi is another GIS software been used for mapping and optimal routes identification.

## MATERIALS AND METHODOLOGY

**Study Area:** Lahore is located at 31.5497°N and 74.3436°E on the earth map[7] and with the growing population it is the second largest city of Pakistan[8]. With the growing population the demand of fire management services is increasing regularly[9]. The study was made to calculate the time required to response the 80 highly risked public places by using ArcGIS. The study was conducted by making three highlighted Rescue Stations for the nearby buildings and the distance was calculated by using Google Earth. The three responding stations for these were Muslim Town Mor, Township and Lohari. The study buildings are expressed in table 1.

**Table 1**

| Name of Building | Address | Coordinates | | Responding Station | Distance (Km) |
|---|---|---|---|---|---|
| Eden Heights | 6- Main Gulberg Jail Road | 31°32'2.98"N | 74°20'36.74"E | Muslim Town Mor | 3.4 |
| Shalmar Tower Hotel | 2A-Main Gulberg Jail road | 31°32'2.98"N | 74°20'36.74"E | Muslim Town Mor | 2.9 |
| Land Mark Plaza | 5/6 -Jail road | 31°32'6.01"N | 74°20'48.89"E | Muslim Town Mor | 4.4 |
| Hassan Tower | 114-B, E- 1, Gulberg III | 31°30'56.00"N | 74°20'31.23"E | Muslim Town Mor | 3.1 |
| Ashrafi Towers | 19- Commercial Zone, Liberty | 31°30'40.91"N | 74°20'43.07"E | Muslim Town Mor | 3.5 |
| Jeff Heights | 77 -E1-1, Gulberg II | 31°31'0.83"N | 74°20'36.59"E | Muslim Town Mor | 3.2 |
| Lahore Centre | 77 -D Main Gulberg II | 31°30'2.54"N | 74°19'16.63"E | Muslim Town Mor | 3.4 |
| Liberty Heights | 75-A, D-1 Gulberg III | 31°30'41.51"N | 74°20'30.54"E | Muslim Town Mor | 3.1 |
| Regency Plaza | 120 P Mini Market Gulberg II | 31°31'17.29"N | 74°21'3.12"E | Muslim Town Mor | 5.5 |
| **Name of Building** | **Address** | **Coordinates** | | **Responding Station** | **Distance (Km)** |
| Kips Academy | 4-Chinab Block | 31°31'2.74"N | 74°17'37.67"E | Township | 9.1 |

| | | | | | |
|---|---|---|---|---|---|
| Hotel Liberty | 44 Commercial Zone Gulberg III | 31°30'34.97"N | 74°20'29.38"E | Muslim Town Mor | 3.5 |
| Variety Books | 1 Commercial Zone Gulberg III | 31°30'32.54"N | 74°20'43.17"E | Muslim Town Mor | 3.5 |
| Hotel Mayfair | 50 Commercial Zone, Liberty | 31°30'33.30"N | 74°20'30.78"E | Muslim Town Mor | 3.5 |
| Hamid Center | Shahalam(Plot No. 29) | 31°34'40.30"N | 74°19'4.22"E | Lohari | 0.5 |
| Hotel Gardenia | 12 Civic Centre, Garden Town | 31°30'1.76"N | 74°19'13.03"E | Township | 6.4 |
| Shan Arcade | 24 A,B,C,D Civic Centre, Garden Town | 31°30'1.18"N | 74°19'12.59"E | Township | 6.3 |
| Maisonette Hotel | 51 C II, Gulberg III | 31°30'47.54"N | 74°20'50.72"E | Muslim Town Mor | 4.2 |
| Origa (New) | 41-G Gulberg II | 31°31'29.82"N | 74°20'52.25"E | Muslim Town Mor | 3.3 |
| Al-Hafeez Centre | 74, 75 -E1, Gulberg III | 31°30'57.84"N | 74°20'34.76"E | Muslim Town Mor | 3.1 |
| Diamond Tower | 28-Commercial Zone Gulberg III | 31°30'39.30"N | 74°20'37.37"E | Muslim Town Mor | 3.5 |
| Radio Tv Centre | 57-Commercial Zone Gulberg III | 31°30'31.96"N | 74°20'33.88"E | Muslim Town Mor | 3.5 |
| Zobaida's Mall | 34-C Liberty market Gulberg III | 31°30'36.45"N | 74°20'35.88"E | Muslim Town Mor | 3.2 |
| Karim Heights | 40-C Liberty market Gulberg III | 31°30'32.93"N | 74°20'44.31"E | Muslim Town Mor | 3.5 |

| Name of Building | Address | Coordinates | | Responding Station | Distance (Km) |
|---|---|---|---|---|---|
| Blue Mall Plaza | 8-R MM Alam Road Gulberg III | 31°31'7.77"N | 74°21'6.46"E | Muslim Town Mor | 5.2 |
| Sunny flour mill | 43-N Gulberg II | 31°30'49.64"N | 74°21'30.35"E | Muslim Town Mor | 6.4 |
| Bashir & sons Fency lights | Shahalam(Plot no 10) | 31°34'36.91"N | 74°19'3.11"E | Lohari | 0.5 |
| Zartaj Building | Shahalam(Plot no 03) | 31°34'35.33"N | 74°19'3.19"E | Lohari | 0.5 |
| Aslam Center | Shahalam(Plot no 8+9) | 31°34'36.66"N | 74°19'2.98"E | Lohari | 0.5 |
| Afzal Plaza | Shahalam(Plot no 18/2) | 31°34'38.73"N | 74°19'3.56"E | Lohari | 0.6 |
| Afzal Plaza AG Traders | Shahalam(Plot no 43,44) | 31°34'42.75"N | 74°19'5.06"E | Lohari | 0.6 |
| Riaz Bulliding | Shahalam(Plot no 30) | 31°34'40.42"N | 74°19'4.21"E | Lohari | 0.6 |
| Moti House | Shahalam(Plot no 2) | 31°34'35.16"N | 74°19'3.07"E | Lohari | 0.5 |
| Qadri Market | Shahalam(Plot no 49) | 31°34'43.56"N | 74°19'5.33"E | Lohari | 0.6 |
| khyber bara market | Shahalam(Plot no E-525) | 31°34'36.29"N | 74°19'5.21"E | Lohari | 0.7 |
| Krachi Center | Shahalam(Plot no 01) | 31°34'35.04"N | 74°19'2.34"E | Lohari | 0.5 |
| **Name of Building** | **Address** | **Coordinates** | | **Responding Station** | **Distance (Km)** |
| Raheem Complex | 31-E1, Gulberg II | 31°31'25.76"N | 74°20'51.28"E | Muslim Town Mor | 3.1 |

| Zohra Heights | 19-E Main Market, Gulberg II | 31°31'29.58"N | 74°20'44.44"E | Muslim Town Mor | 2.9 |
|---|---|---|---|---|---|
| Pace Pakistan Ltd | 124-E1, Gulberg III | 31°30'55.17"N | 74°20'32.93"E | Muslim Town Mor | 3.1 |
| Prime Heights | 4 Sant Marry Park, Gulberg III | 31°30'20.36"N | 74°19'55.31"E | Muslim Town Mor | 2.4 |
| Fazal Trade Centre | 114-A, E1, Gulberg III | 31°30'56.86"N | 74°20'30.01"E | Muslim Town Mor | 2.8 |
| Ahmad Complex | 24-E Main Market, Gulberg II | 31°31'28.27"N | 74°20'47.62"E | Muslim Town Mor | 3 |
| Suleman Square | 42- F Main Market, Gulberg II | 31°31'34.35"N | 74°20'41.17"E | Muslim Town Mor | 3.1 |
| Institute of Engn. & Tech. | 97 B D 1 Liberty Market Gulberg III | 31°30'37.02"N | 74°20'33.06"E | Muslim Town Mor | 3.1 |
| Moon Plaza | 20 D 1 Liberty Market Gulberg III | 31°30'33.30"N | 74°20'44.36"E | Muslim Town Mor | 3.1 |
| HKB | 40 C Commercial Zone Gulberg III | 31°30'42.86"N | 74°20'36.88"E | Muslim Town Mor | 3.4 |
| Fazal Hospital | 90 C 2 Gulberg III, Liberty Market | 31°30'31.79"N | 74°20'44.56"E | Muslim Town Mor | 3.1 |
| Waheed Chamber | 90 A C 2 Gulberg III | 31°30'31.61"N | 74°20'50.59"E | Muslim Town Mor | 3.8 |
| Almas Tower | 3 R MM Alam Road | 31°30'51.02"N | 74°21'4.81"E | Muslim Town Mor | 4.7 |
| Azam Hostel | 12 commercial zone liberty Market | 31°30'39.46"N | 74°20'38.06"E | Muslim Town Mor | 3.5 |
| Shaheen Plaza | 14 commercial zone gulberg III | 31°30'39.91"N | 74°20'38.29"E | Muslim Town Mor | 3.5 |

| Name of Building | Address | Coordinates | | Responding Station | Distance (Km) |
|---|---|---|---|---|---|
| 17 C Commercial Zone | Gulberg III | 31°30'40.14"N | 74°20'39.05"E | Muslim Town Mor | 3.4 |
| Smart Hotel | 36 commercial zone gulberg III | 31°30'35.78"N | 74°20'35.24"E | Muslim Town Mor | 3.5 |
| Al-Hafeez View | 67 D, Liberty Market, Gulberg III | 31°30'49.48"N | 74°20'38.96"E | Muslim Town Mor | 3.6 |
| Palace Arcade | 72 D 1, Commercial Zone, Liberty | 31°30'42.00"N | 74°20'35.92"E | Muslim Town Mor | 3.5 |
| Hotel Mayfair | 51, 52 Commercial Zone, Liberty | 31°30'33.30"N | 74°20'30.78"E | Muslim Town Mor | 3.5 |
| Al-Fateh Store | 54 E Commercial Zone, Liberty | 31°30'33.26"N | 74°20'31.49"E | Muslim Town Mor | 3.5 |
| **Name of Building** | **Address** | **Coordinates** | | **Responding Station** | **Distance (Km)** |
| Mecca plaza | Shahalam(Plot no 28) | 31°34'40.52"N | 74°19'4.37"E | Lohari | 0.6 |
| Super Asia | Shahalam(Plot no 12) | 31°34'37.10"N | 74°19'3.07"E | Lohari | 0.5 |
| Kaka Building | Shahalam(plot no 07) | 31°34'36.02"N | 74°19'2.83"E | Lohari | 0.5 |
| UBL | Shahalam(Plot no 6+19) | 31°34'35.65"N | 74°19'2.67"E | Lohari | 0.5 |
| National Distrebuter | Shahalam(Plot no 8) | 31°34'36.02"N | 74°19'3.03"E | Lohari | 0.5 |
| Sulman & Garments | Shahalam(Plot no 9) | 31°34'36.39"N | 74°19'3.07"E | Lohari | 0.5 |
| 2D Singer | Shahalam(Plot no 40c/2) | 31°34'42.84"N | 74°19'3.58"E | Lohari | 0.6 |

| China Center | Shahalam(Plot no 3) | 31°34'35.33"N | 74°19'3.19"E | Lohari | 0.5 |
|---|---|---|---|---|---|
| Madina Jewler | Shahalam(Plot no 18) | 31°34'38.73"N | 74°19'3.56"E | Lohari | 0.5 |
| Hina Jewlers /BOP | Rang Mehl (Plot no 18) | 31°34'58.80"N | 74°19'6.26"E | Lohari | 1.2 |
| HBL | Shahalam(Plot no 07) | 31°34'36.02"N | 74°19'2.83"E | Lohari | 0.5 |
| UBL Bank | 115 P Gulberg II | 31°31'23.94"N | 74°20'50.98"E | Muslim Town Mor | 3.1 |
| Ahad Heights | 136 P Gulberg II | 31°31'23.02"N | 74°21'50.69"E | Muslim Town Mor | 3.1 |
| Nazar Trade Centre | 117 P Gulberg II | 31°31'23.03"N | 74°20'50.15"E | Muslim Town Mor | 3.1 |
| Zee hights | 37 civic center model town ext. | 31°28'51.43"N | 74°18'38.52"E | Township | 3.6 |
| Punjab Rural Support Program Office | 33 civic centre | 31°28'50.92"N | 74°18'37.99"E | Township | 3.6 |
| Mustafa Tower | 13 civic centre | 31°28'46.57"N | 74°18'34.60"E | Township | 3.6 |
| Sandhee Trade Centre | 19 Commercial Zone, Liberty | 31°30'40.91"N | 74°20'43.07"E | Muslim Town Mor | 3.5 |
| Akbri Store | 20-Hunza Block Iqbal Town | 31°30'52.03"N | 74°17'47.28"E | Township | 9 |
| Al hafeez plaza | Link road model town | 31°28'1.62"N | 74°18'57.66"E | Township | 2.9 |
| Tele tower # 122 | Link road model town | 31°28'8.60"N | 74°19'4.45"E | Township | 3 |

| Name of Building | Address | Coordinates | | Responding Station | Distance (Km) |
|---|---|---|---|---|---|
| Al hafiz trade center | Link road model town | 31°28'7.61"N | 74°19'4.39"E | Township | 3 |
| Wind mills tower | 189 A B- 2 Gulberg III | 31°30'27.13"N | 74°21'9.96"E | Muslim Town Mor | 4.2 |
| **Name of Building** | **Address** | **Coordinates** | | **Responding Station** | **Distance (Km)** |
| Shifa Laboratories | 39 Industrial Estate Gulberg III | 31°30'6.78"N | 74°21'26.63"E | Muslim Town Mor | 5.3 |

**Methodology Used:** To figure out the coordinates of the highly fired risked buildings the Google Earth was used[10]. Google Earth was also used to calculate the distances from the responding rescue stations to these buildings. The data for the traffic density was assumed but is calculated by City Traffic Police Lahore. City Traffic Police Lahore is a sole and a government organization to calculate and manage the traffic with in Lahore authorized by Government of Pakistan. Using the traffic density data, the required time for response of the fire vehicle was calculated by using ArcGIS[11]. The plots were designed at the ArcGIS using the traffic density data to calculate the required time.

**Materials Used:**

**ArcGIS:** ArcGIS is a GIS tool used to analyze, prepare, process the data for the maps and to manipulate is as per need to acquire the required information[12]. ArcGIS was used to make the maps and to locate the buildings to find the optimal route. It was also used to calculate the minimal time required as per calculated width, traffic flow, U-turns and Traffic Signals.

**Google Earth:** Google Earth is a GIS tool which can be used to find the distance, width, signals, turns, height as per need[13]. Google Earth was used to find the coordinates, distance, U-turns and Traffic Signals on the route.

**RESULTS**

By using network analyst tool of ARC GIS, optimal path with respect to minimum time was found with considering number of signals, U-turns, minimum distance approach and fuel efficiency as well. Keeping response time of fire services which is 7.6 mints, path defined, covered the distance of 4km with speed of 60km/hour in 4mints without having any signal on route and minimum distance to the incident site.

Three fire stations were studied and possible optimizing routes have been assessed considering number of signals, U-turns, minimum distance approach and fuel efficiency.

**ShahAlam:** Emergency station is located at the middle of the route as shown in figure 1. This a densely populated area but there is only single route so in the case of emergency no other route can be adopted even high rise buildings are very much adjacent to each other and the pathways are too narrow to access the building for rescue.

**Figure 1: Buildings and Route for ShahAlam Station**

**Township**: In case of emergency at Model Town link road fire vehicle can access the location by following the route from College Road to Maulana Shaukat Ali Road and then to Model Town Link Road. This is the best optimize route. Optimized Route map of township station is shown in Figure 2
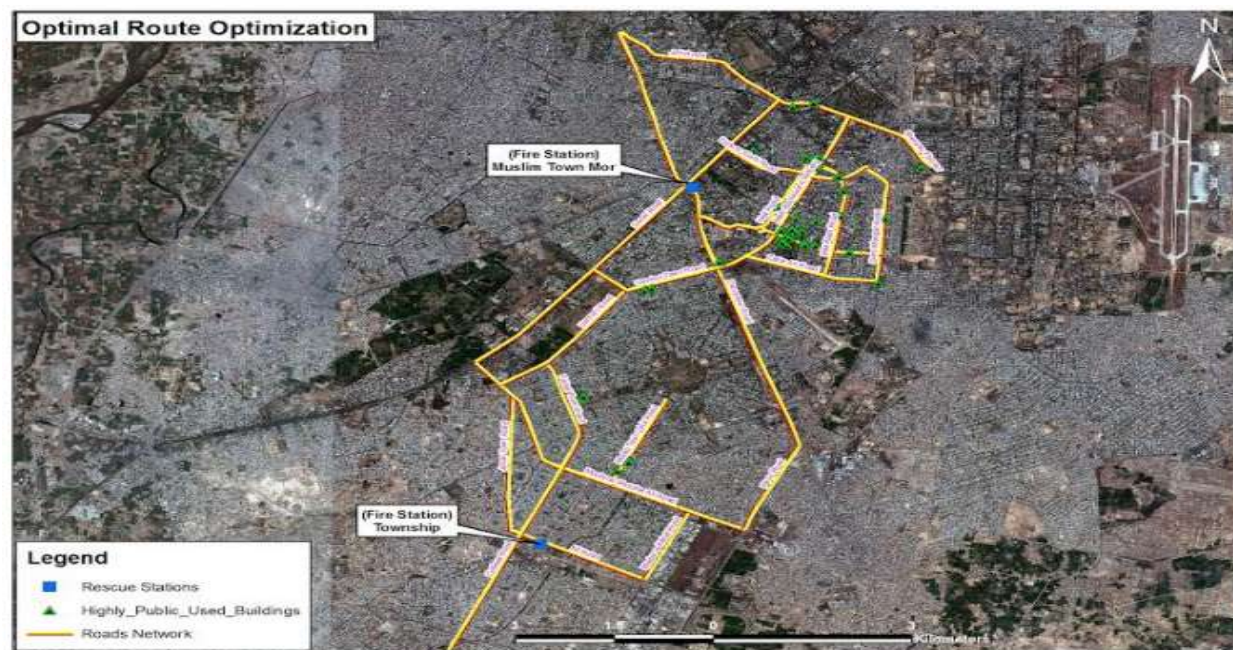


**Figure 2: Buildings and Route for Township and Muslim Town Stations**

**Muslim Town Mor:** Fire Vehicle can access the Gulberg III building by following the route from Ferozpur Road to Kalma Chowk to Liberty Roundabout from here take turn to Main Boulevard and then take left to Gulberg III Pace, Hassan Tower is at the Back side of Pace. More over for buildings near Galib Road the vehicle can also can follow the route by taking left from Ferozpur Road towards Qadafi stadium by crossing Qadafi stadium take left to Hali road and then to Galib Road. The optimal route for Muslim Town Mor Station is shown in Figure 3.



**Figure 3: Buildings, Routes and Optimal Route for Muslim Town Mor Station**

## CONCLUSION

The study highlights the utility from claiming location-allocation models which might be utilized for spotting an assortment for offices What's more services, including fire stations in Lahore. Map models dependent upon those maximal separations with the travel time are estimated. It reveals to maps and steps that were used to dissect the administration scope about fire stations inside Lahore city. The study likewise included a presentation on the utilization of ArcGIS software also its extensions, such as, spatial and network analyst data. Area choices bring a significant effect on our study to explain the strategy.

The fire administration mission may be with aid people in general in the insurance about life and property towards minimizing that effect about fire, restorative emergencies. Also possibility disasters alternately occasion that influence groups and the nature's domain. Protecting groups from regular or manmade emergencies through planning, preparedness, episode response, open education, and code requirement may be best refined through exact data imparting. GIS is a standout amongst those viable devices to analyze, define, and clarify the outcomes.

**References:**

1. Drabek, T. E., Hoetmer G J (eds) 1991 Emergency management: principles and practice for local government. Washington DC, International City Management Association

2. Nisanci, R., (2010). GIS Based Fire Analysis and Production of Fire-risk Maps: The Trabzon Experience, Scientific Research and Essays Vol. 5(9), pp. 970-977

3. Forkuo, E., Quaye-Ballard, J.A., (2013). GIS Based Fire Emergency Response System: International Journal of Remote Sensing and GIS, Vol. 2(1),pp 32-40

4. ESRI (Environmental Systems Research Institute), (2012). GIS for the Fire Service: An Esri© White Paper

5. Cova, T.J., 1999. GIS in emergency management. *Geographical information systems*, *2*, pp.845-858.

6. ESRI (Environmental Systems Research Institute), (2006). GIS Technology and Applications for the Fire Service: An Esri© White Paper

7. Masood H. B., Jelani S. Increase of aluminum particles in the environment due to chemtrails during the period of autumn 2012 to summer 2015 within Lahore, Pakistan. *International Journal of Engineering Research and General Science.* 2015;3(5): 846-851.

8. Masood H. B., Jelani S., Arshad F. K. Assessment and identification of quality gradients of canal water used by Lahore, Pakistan residents in summer. *International Journal of Advance Information Science and Technology*. 2015;37(37): 9-13.

9. Evegren F., Hertzberg T. Fire safety regulations and performance of fiber-reinforced polymer composite ship structure. *Journal of Engineering for the Maritime Environment*. 2015

10. Google Earth, 2016 www.earth.google.com

11. ArcGIS, 2016 www.arcgis.com

12. Hamdan I., Benhsinat M., Wanger. B., Sauter M. Developing a geological 3D model for the Tanour and Rasoun sprin catchment area using ArcGIS and GOCAD. *Geological Research.* 2016; 18.

13. Qi F., Zhai J. Z., Dang G. Building height estimation using Google Earth. *Energy and Buildings*. 2016; 118:123-132.

# Crime Mapping the best option for Criminology: A Review

Humza Bin Masood[1,*]

[1]*Environmental Sciences Department, FC College (A Chartered University), Lahore 54600*

*\*Corresponding author*

**Email**: *15-10333@formanite.fccollege.edu.pk*

## ABSTRACT

With the population boom the crime rate is also increasing regularly. The increase in crime rate demands the updated technology to cope with the issue of crime management operations. Crime mapping is one of the best technique which can identify the hotspots for the crimes with respect to time and date. This can be used to record the public presence in the area and helps in pre-planning for the crime control management. Street profile mapping on the basis of area, population density and vehicles provides the estimation of the nature of criminal activities that can be performed and help to calculate the required resources in case of real emergencies. Moreover, the introduction of GPS systems in police vehicles can help to reduce the response time for anti-criminal operations and can helps in motioning of the criminal activity pathway. Crime mapping can result in reduction of many criminal activities.

**Keywords:** Crime, GIS, street profile mapping.

## INTRODUCTION

Many security agencies are now preferring GIS for the crime mapping and the analysis at the current moment [1]. Maps are being used by the security agencies which highlights the important area for the intelligence and investigation as well as operation [2]. The GIS is a technology which uses hardware, software, operator and geographical data which helps to store, gather, manipulate and analyze the required information [3]. The GIS helps in the find out that where is the crime rate highest and where is the crime rate lowest, what can be the intensity of crime, which agency can deal with it, which station need to respond, which station can collaborate with the responding station, what will the response time [1]. The crime mapping helps to find the answers of these questions.

With the increased population and poverty, the crime rate is increasing day by day and one of the biggest reason for this is unemployment [4]. The terrorism activities are increasing day by day beside this the street crimes are also increasing in the developing countries like Pakistan [5]. This needs the high need of equipment, manpower and resources for the security agencies which is causing the great damage to the country economics [6]. The use of country's economy demands the upgraded techniques as per latest technology to cope with the problem of crime. Currently Punjab Police is upgrading the force by the help of anti-terrorist squad, Quick Response Force and Dolphin Force [7].

GIS is one of the latest techniques which can be used for the crime mapping and dealing with the crimes in the minimum response of time with the effective response [1]. Punjab Police can use the GIS technology to find the crime rates as per map and with the help of GPS system all the stations can be recorded and the vehicles of all the forces including patrolling, anti-terrorist squad, Quick Response Force and Dolphin Force can be monitored and can be guided to reach the crime incident place as soon as possible. Beside this the highlighted area can be monitored and the patrolling and search may be increased in this area. Moreover, the stations boundaries, locations and stations of other security agencies can be added with the required information so in case of emergencies they can be contacted and the collaboration effort can be made and to save maximum time in the case of terrorist activities [8].

The major objective of this study is to improve the patrolling ratio with the help of GPS and crime records in the different areas of Lahore. The intensity and type of crimes with the help of GIS can help to identify the particular need of patrolling in the area and in case of emergency the particular vehicle can be moved to the location using the GPS.

## LITERATURE REVIEW

Brantigham et. al. studied that the locating of the crime and the particular agency as well as reducing the

response time increases the chance of decrease in the intensity of the crime. This need to gather a lot of information and the analysis is required [9]. In many cases there is a need of the other agencies to response to the particular crime as in the case of bomb plantation information there is a need of bomb disposal squad but still the police can cordon off the area by the effective response time and mapping and can reduce the chance of life loss.

Hacin et. al. explains that the continued patrolling and the reduce in the time of response can reduce the public fear for crime and can create a friendly environment for the public in the favor of police [10]. They studied that the crime frequency varies from area to area as per intensity of crime rate in the particular area. More the crime rate in the area more will the fear. Their study further showed that the gender has no particular relation of fear for crime. They further studied that the fear of crime is more in the middle age group of 26-45 years followed by the oldest population group. They suggested that the effective response and lowering the crime rate can decrease the fear in population.

Ratnayake R. M. K. analyzed that the police division is recording the crime records manually. In this the crime location, time, factors that are directly or indirectly effected by crime is been recorded. All of the records are made manually and with time in files the records are been lost and it becomes difficult to find the location, intensity and time of the information. Moreover, the response time is not being recorded. The study used some basic GIS and GPS technique at the primary level and showed that there is a positive factor of using the GIS and GPS due to which the exact time of call, location, response time, can be recorded [11]. Further this information can be used to find the best optimum route as per time for the crime emergencies. The study showed that the open areas like Parks, Grounds, Government Institutions became more safe with record and was made easy to identify the crime making parties on time and the best decision making were done on time. The GPS records on the basis of information of crime making party can help on a single click to take the decision of resources required for the particular crime whereas the manual data may require time to find the information for the crime making party.

Ceccato V. studied the Space and Time Dynamic of crime and found that the crime rate varies from season to season. The finding shows that the crime rate use to vary with the time and season. Most of the crimes are been made in the foggy weather and at night whereas the terrorist activities are more at the day time especially at the peak hours of the particular place. The terrorist activities are least in the offices and banks on weekends but more at the recreational places. The crime rate is higher at night as per day but in days it is mostly at the time near noon [12]. So the weather conditions and time is important for criminology and should be recorded as per time and special scale. The single or two criminal activities are mostly at the place with low public whereas terrorist activities are more at the place with the more public. Moreover, crowded stations and those with alcohol selling outlets attract more criminal activities. So beside weather the time and area matters a lot for the type of crime activity and need to be recorded.

Spicer et. al. introduced the street profile for the mapping of crime on the major roads and examined it as a best solution in crime mapping. This technique helps in identification of crime at the streets. This helps in analyzing the type of crime that can take place at the particular place according to the space, previous records, etc. As the killing will not take commonly at open places until it is a target killing. This technique was applied to the major roads Burnaby, Canada by Spicer et. al. and found it useful in controlling the crime [13]. The technique can be used at small streets and institutional map as per public ration and time scales.

Adekunle et. al. advanced the vehicle tracking software. The cases of car theft are increasing on daily basis and some of them are sold without changing the chassis number. GPS which is Global Positioning System is being used to track the vehicle with the help of satellite. The Simulink design was made with the help of which the previous location of the vehicle can be studied. Previously with the help of GPS only the current location was monitored but with this the previous locations can also be studied. This will give the source code of the location from where the vehicle was theft and what other activities are being performed [14]. There can be many other crimes been placed with the vehicle before; after the theft and this can be recorded. The software can be installed in the police vehicles which can give the time to time knowledge of the tracking of crime and can be updated in vehicles so it may be easy to identify its location with respect to

previous activities been performed. It can also give an update for the upcoming criminal activity using the vehicle.

Frers et. al. studied the making of pre-crime policy with the help of public survey using the GIS. They created their own form as per need of the specified area and recorded the information in the form of GIS maps and make the pre-crime policy using the GIS on the basis of the information [15]. This help in updating the policies for the time scale patrolling and police intelligence to control the crime before it can take place.

**METHODOLOGY**

The GIS based studies for the crimes were critically analyzed for the possible step for the crime mapping for the Punjab police in their capital city, Lahore.

**Study Area:** Lahore is located at $74^o\ 1'\ 1''$ E to $74^o\ 38'\ 10''$ E longitude and from $31^o\ 15'$ to $31^o\ 44'2''$N latitude which is the second largest city of Pakistan [16]. The population of Lahore had increased to 9 million and is increasing linearly since independence [17]. The city covers the area of 1772 kilometer squares sharing the boundaries with Kasur, Raiwind and Manga as well as boundary of India with the sea levels raising from 680 to 700 feet from north east to south west with the slope gradient of 1 foot per 5-10 kilometers [16]. The population is increasing regularly as well as the crime rate and updating the technology is also required [13] which may include crime mapping.

**Data Selection:** The previous studies related to the crime mapping was analyzed for the optimal upgradation of the security measure by the help of Punjab Police in Lahore. The previous data for the crime rate was analyzed with the peak crime hours and available resources. As per division of Lahore with respect to stations it was found that Sahadra have the high crime rate while the lowest crime rate was recorded at Sarwar Road police station. The figure below explains the crime recorded at different police stations of Lahore. The per week crime rate for Shahdara is 68, 59 in Baghpanpura, 59 in North Cantonment, 55 for Chung while it was 53 for Factory Area and Raiwind City. The stations of these areas records at least 10 to 20 crime incidents per day in these areas. Whereas the crime rate recorded in the area of Sarwar Road, Mochi Gate, Model Town, Lohari Gate, Mustafa Town and Lower Mall are up to

10 per day. The reported crimes at Sarwar Road Station were 3, Mochi Gate 4, 5 in Model Town, 6 in Lahorai Gate, Mustafa Town 6 and 7 in Lower Mall Station in the week of February [18].

Now the Lahore Police have a crime mapping technology in which they can record the information for the calls and can identify the hotspots. This leads to the planning for Patrolling. This is being done for 24 hours with 3 hours shift on daily basis. The peak hours recorded for the emergency response calls are from 4 pm to 11 pm. In the peak hours the armed patrolling is increased in the city. There are 21233 policemen working in operations wing, 3968 in Investigation Wing and 1253 in security division. Now the organization had equipped the policemen with the android phones on which a software is installed for the checking of the vehicles and if the registration copy is not available with the owner it is cross-verified with the stolen vehicles report and helps in finding the stolen vehicles [18].

**Analysis:** The studies shows that the security agencies across the world are upgrading the system to control the crime with the help of GIS. They use to identify the hotspots with the help of crime mapping and make a pre-crime plan to control the crime rate. With the help of analysis and the collaboration of different agencies the appropriate measures can be taken before time to stop many criminal activities both at the major and minor scale including terrorism.

The GPS system was introduced in the police vehicles helps in tracking the police vehicle and can be moved to the area of incident. With the collaboration of Tracking Organizations different public vehicles can also be monitored and the unusual activities for these vehicles can be monitored resulting in decrease of crime rate including the vehicles especially the stolen vehicles.

Punjab Police for Lahore is now recording the calls make on the emergency numbers and is recording the information in the form of maps. The crime mapping is currently helping out to identify the peak hours of the crime with the response time, responding stations and hotspots. Still there are some incidents that are happening and are not informed at the emergency numbers and is recorded in manual form instead of GIS maps. These manually recorded reports are those that are reported directly by the victim or the relative in the police stations.

The introduction of the street profile mapping can help to identify the hotspot and areas can be measured for the possible criminal activities taking place with the help of experts of the field and hotspot as per time and space can be identified on the streets as well as major roads of the city. The street profiles may explain as the major terrorist activities can take place at major road but might not take place in the streets while the minor crimes may be more in streets.

The addition of the police stations on the map with the optimal routes study with respect to time and day can help in the upgrading of the collaborations. These online maps can involve the stations of the other securities agencies or emergency agencies like FIA, Pakistan Army, Bomb Disposal Unit, Anti-Terrorist Force, Rescue 1122 and Edhi services with their response time. This actually help the operator at the control room to take the best timely decision in case of real emergency. In some cases, as of killing there is a need of urgent first aid but the security clearance need to make as well so in these cases the crime activities may also be recorded with time graph in GIS maps and can be used further as per needs for the investigation of the crime cases.

## RESULTS AND DISCUSSION

The studies show that the crime rate for Lahore is been recorded but not at the required level. There is a use of crime mapping but not as per the demand of the system. There is an upgrading but it is slow as per need to cope with the crime rate. Crime rates is increasing at much faster rate as per compared to the policy making and planning to cope with these crimes. The figure below shows the detail result of the Lahore city for the crimes at current situation.

The risk of crime need to be mapped and on this the strategy can be made to take the particular decision. In this instead of the criminals the focus should be made at the areas where there are more crime rate and the factors behind the high crime rate need to be studied. This may be due to poverty or might be the group of gangs. The nature of crime at that area, the way of making a crime need to be monitored. The crime by the use of mobile phones and the crimes including the theft of mobile phones is now becoming common in Pakistan with the theft of vehicles but many of them are not even reported in the police stations by the public and are not recorded in both digitalized or manual way. This mostly with the cases of mobile phones.

The corruption is one of the reason of lacking behind the developed countries for many of the developing countries. The recording of the crimes for the theft is free and to provide the services to find the item been theft is actually provided free of cost for the citizen but the policemen use to demand some cost of recording the theft report and also charge a separate cost for finding these items. Moreover, they are also found rude to the public and their response time for the real emergencies are really very high due to which they don't have a good image in common public due to which they feel it better to not to report the crime of theft. This gives a chance to criminals to increase the activities of theft as they are poorly managed and recorded.

The police department is not equipped with the latest weapons for security and the safety jackets for the policemen are really in less amount. In many cases they have to provide the record for every bullet that have been used. Though beside all they are human beings and everyone prefer to save their lives first before dealing with the criminals. Moreover, many of the criminal activities are made by help of latest weapons and the Police of Lahore operating under Punjab Police can't cope with the situation due to which they usually have to seek help from the other security agencies especially Rangers or Army which have updated weapons, technology, hot-spot studies, possible injuries, possible intensity and policy making on the basis of crime mapping of the real time graphs. This is because they have updated technology. In some major criminal activity especially for the terrorist attacks the information is been recorded in the images with the help of some monitoring helicopters or drones.

GIS is very important in the field of criminology especially the crime mapping. This is also being done now by the help of smart phone apps by the Lahore Police in which they can record many theft incidents and other criminal activities. This uses to give the minor maps at the software which gives the information of the location of incident with time and been collaborated with the relative police stations. This smart phone app has different options to record the nature of the crime but it is not being recorded in a group data for the complete Lahore to make the particular data. This is making the locations and

number of incidents been made with the time for the crimes.

Patrolling is being made for the certain areas and there is an introduction of new patrolling force named as dolphin force by the police of Lahore. The patrolling is being made by help of the previous experiences but still there is no patrolling plan based on the GIS maps as there is no proper collection of data at the certain place. Tough the information is recorded at different places for the respective police stations but the network need to expand to all police stations for the proper human resource management as per stations with respect to peak times can be managed.

The GPS system need to be introduced in the police vehicles. Many of the new vehicles have been introduced for the patrolling purposes. With the help of GPS in the case of call for emergency the vehicle near to the emergency can be directed to deal with the crime and can save the response time. The nearby stations can be added and can be contacted directly for the emergency. Rescue 1122 with the help of collaboration of PTA have an updated system which with the graphical location of the call being made with the name and residential address of the person making a call. This helps in finding the location of the emergency and saves the time in emergency. This need to be introduced in this system as well. Moreover, the optimal routes with respect to time also need to studied for the areas.

**CONCLUSION**

The continual upgrading of the technology for the crime control is the demand of the time. The crime rate is increasing which demands for the upgrading in the crime mapping. Several Techniques are being introduced in the crime mapping by different countries and one of the best techniques is the street profile mapping. This uses the area of the roads and streets of the area and provides the information of the chances for the criminal activity in the area and at which extent it can be done. Beside this it also provides the information to the security agencies for coping with criminal activity by taking the response decision as per area. This records the peak public and vehicle hours of the streets and roads. This provides the information of how much human resources are required to cope with the issue with other technical skills. Mostly to deal with the criminal activities it requires the 1:6 ratios to

deal with it. It explains that if there is one criminal then there is a need of 6 personal from the security agency for the safe operations but it is not true in all cases. In the case of Rajanpur Operations against the Chotu Mazari gang same information was reviled later by the Army for the successful operations and approximately 2000, armed army men were there in operations against the 60 criminals with the latest technology which is basically a ratio of 1:33 which was because some of the policemen were inside. So this technique beside the streets and the major roads can help in mapping the area and location with the criminal numbers to make decision for successful and safe operations.

Beside this the next best possible technique is to introduce the GPS system in the patrolling vehicles and been recorded with the current and previous locations. This will help in managing the emergencies by moving the nearest police patrolling vehicle to the place of incident and by taking in collaboration of the other required agencies to cope with the situation for safe operations. The previous GPS records can help in finding the optimal routes with respect to time and the betterment can be made by the help of the information recorded in the form of maps.

Combining the both techniques can make a better and up to date crime mapping system for Lahore police. There are the trained personal available for 24/7 to record the information digitally by help of emergency calls and GIS experts but there is still a need of upgrading the system for the crime mapping. Beside this there are no complete computerized records for criminal activities as more of them are recorded manually and need to be make available at the map for the study of crime with help of crime mapping resulting in better management.

**REFERENCES:**

[1] Argun U., Daglar M. Crime Mapping and Geographical Information Systems in Crime Analysis. 2016. *International Journal of Human Sciences*. 13(1): 2208-2221

[2] Block, C.R., M. Dabdoub., S. Fregly (eds). Crime Analysis through Computer Mapping. 1995. *Police Executive Research Forum Washington DC*. pp. 15-32.

[3] Heikkila, E. J. GIS is dead; long live GIS! 1998. *Journal of the American Planning Association*, 64(3), 350.

[4]   Liesenfeld R., Richard J. F., Vogler J. Likelihood based inference and prediction in spatio-temporal panel count models for urban crimes. 2015. *Social Science Research Network*. Electronic Paper

[5]   Ali G., Li Z. Role of Economic Factors in terrorism in Pakistan. 2015. *Quality and Quantity*. 1(13)

[6]   Xiong H. Conclusions and Future. 2016. *Urban Crime and Social Disorganization in China*. pp 131-138

[7]   Press Release, Punjab Police. http://punjabpolice.gov.pk/press_releases_2015

[8]   Griffith D. A., Smith G. M. Real-time planning/re-planning of ongoing operations in a crisis situation. 1997. *Proceedings of SPIE.*

[9]   Brantingham P. J., Brantingham P. L. Environmental Criminology. 1991. *Prospect Heights.* Waveland Press.

[10]  Hacin R., Eman K. Study of the Fear of Crime in the Municipality of Trbovlje Using Crime Mapping Tools. 2014. *Revija za kriminalistiko in kriminologijo*. 65(4):299-315

[11]  Ratnayake R. M. K. Distribution Pattern of Urban Crimes in Sri Lanka; with Special Reference to Mirihana Police Division. 2015. *International Journal of Multidisciplinary Research and Development*. 2(8): 441-453

[12]  Ceccato V. Space-Time Dynamics of crime in Transport Nodes. 2014. *Annals of Association of American Geographers.* 104(1): 131-150

[13]  Spicer V., Justin S., Patricia L. B., Andrew P., Martin A. A. Street Profile Analysis: A new method for mapping crime on major roadways. 2016. *Applied Geology.*

[14]  Adekunle A. A., Adejuyigbe S. B., Julius O. B., Oluwole A. H., Folajimi A. Development of Software for Car tracking device. 2015. *American Journal of science and Technology.* 2(6): 283-297

[15]  Frers L., Krasmann S., Wehrheim J. Geo-policing and crime-mapping. Police Vision. 2013. *Kriminologisches Journal.* 45(3): 166-179

[16]  Riaz O., Ghaffar A., Butt I. Modelling Land Use Patterns of Lahore (Pakistan) using Remote Sensing and GIS. 2014. *Global Journal of Science Frontier Research: Environment and Earth Science.* 14(1).

[17]  Riaz, O. Impact of Population growth on Urban Expansion in Lahore, 1951-1998. 2011. Unpublished PhD thesis, University of the Punjab, Lahore.

[18]  Shahdara has Highest, Sarwar Road area lowest crime rate. February 24, 2016. *The Nation.*

# Study of Chemically Synthesized Rare-earth Terbium Substituted BaM Hexagonal ferrites

**M. Imran Asgha\*r[a], M. Younas[a], Ihsan Ali[b], M. U. Islam[b], M. S. Awan[c], M. Ahmad[c],**

[a]Departmment of Chemical Engineering, University of Engineering and Technology, Peshawar.
[b]Department of Physics, Bahauddin Zakariya University, Multan 60800, Pakistan.
[c]Center for Micro and Nano Devices, Department of Physics, COMSATS Institute of Information Technology, Islamabad, Pakistan.
\*Corresponding author
Email: imran1097@yahoo.com

## ABSTRACT

Barium based rare-earth terbium ($Tb^{3}+$) substituted M-type hexagonal ferrite materials with nominal composition $BaTbxFe_{12-x}O_{19}$ (x=0.0, 0.1, 0.2, 0.3) synthesized using chemical technique namely "Sol-gel Auto-combustion". The rare-earth terbium ($Tb^{3}+$) element has been substituted at Fe3+ site to investigate its effect on chemical, electrical and magnetic parameters. The synthesized materials were characterized by various characterization techniques namely DSC -Differential Scanning Calorimetry, (XRD) - X-ray diffraction,(SEM)- scanning electron microscopy (SEM), (EDX)-energy dispersive X-ray spectroscopy. EDX spectra confirm the presence of Ba, Tb, and Fe elements in the synthesized materials. XRD analysis confirms the successfully formation of single phase rare-earth terbium ($Tb^{3}+$) substituted M-type hexagonal ferrites. The ratio 'c/a' fall in the expected range 3.945-3.952 for M-type hexagonal ferrites. The particle size is found to be from 65.15-37.35 nm, that is suitable to achieve the suitable signal of noise for high density recording media. Scanning electron microscopy (SEM) laboratory analysis exhibits the geometry of grains in hexagonal shape. X-ray density improves from 8.084-8.359 $g/cm^3$ and the bulk density enhances from 5.78-5.93 $g/cm^3$. The values of coercivity (Hc) fall in the range 174-5529 Gauss. DC electrical resistivity of synthesized materials enhances with the rise of rare-earth element $Tb^{3}+$ concentration. The values of DC resistivity found to be lie in the range 3.6x109 to 6.82x109 ohm-cm. The investigated materials may be potential candidates for a new developing technology perpendicular magnetic recording media, permanent magnets, for high frequency applications

**Keywords:** Hexagonal ferrites; Rare-earth; Sol-Gel Auto-combustion

## INTRODUCTION

**Terbium** It is element which atomic weight is 65 & symbol is Tb. It belongs to rare earth family in periodic table. It looks like silver- white metal combination. It is ductile & hard naturally. A Swedish chemist discovered it in mid of nineteen century. Its physical state is solid with atomic weight 158.9254; the values of melting and boiling point are very high above 1000C & 3000 C respectively. Its stability is better than element like lanthanide when put it openly in air. The behaviour of Terbium is a ferromagnetic under the temperature of 219 K. After increasing the temperature more than 219K it behaves a state of ant ferromagnetic. Some of chemical properties are as follow.

a. It reacts with oxygen to produce Terbium oxide.

b. It also react with water to produce Terbium hydro oxide.

c. It reacts with halogen group elements to form tri-halides.

It dissolves in $H_2SO_4$ to produce different solutions. It reacts with many others components like carbon, boron, silica & nitrogen to produce different compound of these elements.

Naturally it is found in the form of rocks in which different other rare earths are mixed in different fractions. As discussed earlier the terbium belongs to the family of rare earth in periodic table with location of group 3 & periods of 6th & 7th. It consists of two series. My work is here to study of chemically synthesized rare earth terbium substituting the Ba M-Type hexagonal ferrites[1].

## EXPERIMENTAL

Rare-earth terbium substituted M-type Ba-hexagonal ferrites with nominal compositions $BaTb_xFe_{12-x}O_{19}$ (x=0.00, 0.10, 0.20, 0.30) was prepared using sgac technique. Following are the chemicals used for the making of the samples $Ba(NO_3)_2$ (99%, Sigma Aldrich), $Fe(NO_3)_3 \cdot 9H_2O$ (99%, Sigma Aldrich) and $Tb_2O_3$ (99%, Sigma Aldrich). The solution of each chemical in distilled water was made in a 100 ml beaker by applying stoichiometric amounts of the concerned metal salts and stirred them for 15 minutes. This solutions of specific concentrations were mixed in a Pyrex beaker of 100ml and heated a temperature range of 100 °C keep stirring continuously by using hot plate along with magnetic stirrer. Citric acid was mixed to the solution for keeping molar ratio 1:1.5 in metal and citric acid. To keep the pH value at about 7.0 ammonia solution is used. This solution then evaporated at 100 °C slowly until a viscous gel is produced. The temperature range of the hot plate magnetic stirrer improved up to value 300 °C for the explosion of the gel. This dried gel burnt in self-propagating combustion way until it was fully burnt

out with brown coloured powders. This gel was then heated at temperature range of 500 °C about 3- 4 hours to decompose the organic precursor. Digitally controlled microwave oven was used for this procedure. Cold Iso static Pressing (CIP) technique was used to make pellets of powders of size 12 mm dia. The pellets were sintered at 1000 °C for about 4-5 hours. A furnace "Hobersal model HD-230" was used to change it into single phase. Following fig shows all the main steps involved in SLAC technique.

## Synthesis of M-Type Rare-earth Terbium (Tb$^{3+}$) Substituted Barium

### Hexagonal Ferrites using Chemical Method

Rare-earth terbium ($Tb^{3+}$) substituted barium based M-type hexagonal ferrite samples with nominal composition $BaTb_xFe_{12-x}O_{19}$ (x=0.00, 0.10, 0.20, 0.30) were synthesized using a chemical method. This synthesis of sole phase M-type hexagonal ferrite is a challenge for many researchers and engineers due to their complicated crystal structure.

### Requirement of Chemicals

The chemicals of high purity were purchased from well-known suppliers to synthesize the M-type hexagonal ferrite BaTbxFe12-xO19 (x=0.00, 0.10, 0.20, 0.30). Following are the chemicals which we have utilized for the synthesis of samples.

**Table :** Chemical formulas, formula weight, purity and supplier of chemicals utilize for the synthesis process of ferrite $BaTb_xFe_{12-x}O_{19}$ (x=0.00-0.30) samples.

| Composition | BaTb$_x$Fe$_{12-x}$O$_{19}$ (x=0.00, 0.10, 0.20, 0.30) | | | | |
|---|---|---|---|---|---|
| **Name of Chemicals** | **Chemical Formulas** | **Molecular weights (g/mol)** | **Purity %** | **Suppliers/ Company name** | |
| Barium nitrate | Ba(NO$_3$)$_2$ | 261.35 | 99+ | Sigma Aldrich | |
| Iron nitrate | Fe( NO$_3$)$_3$·9H$_2$O | 162.20 | >97 | Same | |
| Terbiu(III) Oxide | Tb$_2$O$_3$ | 207 | 99.99 | Same | |
| Citric Acid. | C$_3$H$_4$OH(COOH)$_3$ | 210.14 | 99.9 | Fisher Scientific. United Kingdom | |
| Ammonia solution | NH$_4$OH | 17.03 | 33 | Riedel Dehaen | |
| Nitric Acid | HNO$_3$ | 63.01 | 65 | Labscan Asia co Ltd | |

**Synthesis Techniques for Ferrite Materials**

A lots of procedures have been established to synthesize the BaTb$_x$Fe$_{12-x}$O$_{19}$ (x=0.00, 0.10, 0.20, 0.30). There are mainly two methods to synthesize ferrite materials, namely conventional method (or dry method) and non-conventional methods (or wet methods/chemical methods).

1) Dry method- Conventional method
➤ Standard Ceramic technique [1]
2) Chemical method/wet methods- Non-conventional
a. Hydro-thermal precipitation technique[2]
b. **Sol gel combustion technique (SGAC)** [3]
c. Aerosol pyrolysis technique[4].
d. Chemical co-precipitation technique[5].
e. The low temperature combustion synthesis (LCS) technique [6] .
f. Glass crystallization technique  [7].
g. Mechanical alloying technique [8].

There are different drawbacks of conventional ceramic methods i.e time-consuming and can introduce of impurities in the prepared components. Stearic-acid is used as gel for synthesize the ultrafine ferrite powders, that is a easy route but have a few drawbacks. Several synthesis methods i.e. co precipitation, and sol-gel auto combustion established in recent times. Co-precipitation is also simple method to synthesize fine particles of hexagonal ferrites, but there is probability of agglomeration of particles and extra milling is needed[9].

**Sol-Gel Auto combustion Technique (SGAC)**

In this research task, the sol-gel auto combustion technique was utilized for the synthesis of  BaTb$_x$Fe$_{12-x}$O$_{19}$ (x=0.00, 0.10, 0.20, 0.30) samples due to its many advantages. This S-L technique is a wet-chemical technique which is in practice in the fields of materials science and ceramic engineering. This type of techniques are used for the manufacturing of components (like a metal oxide).

**Advantages of SLAC Technique (SGAC)**

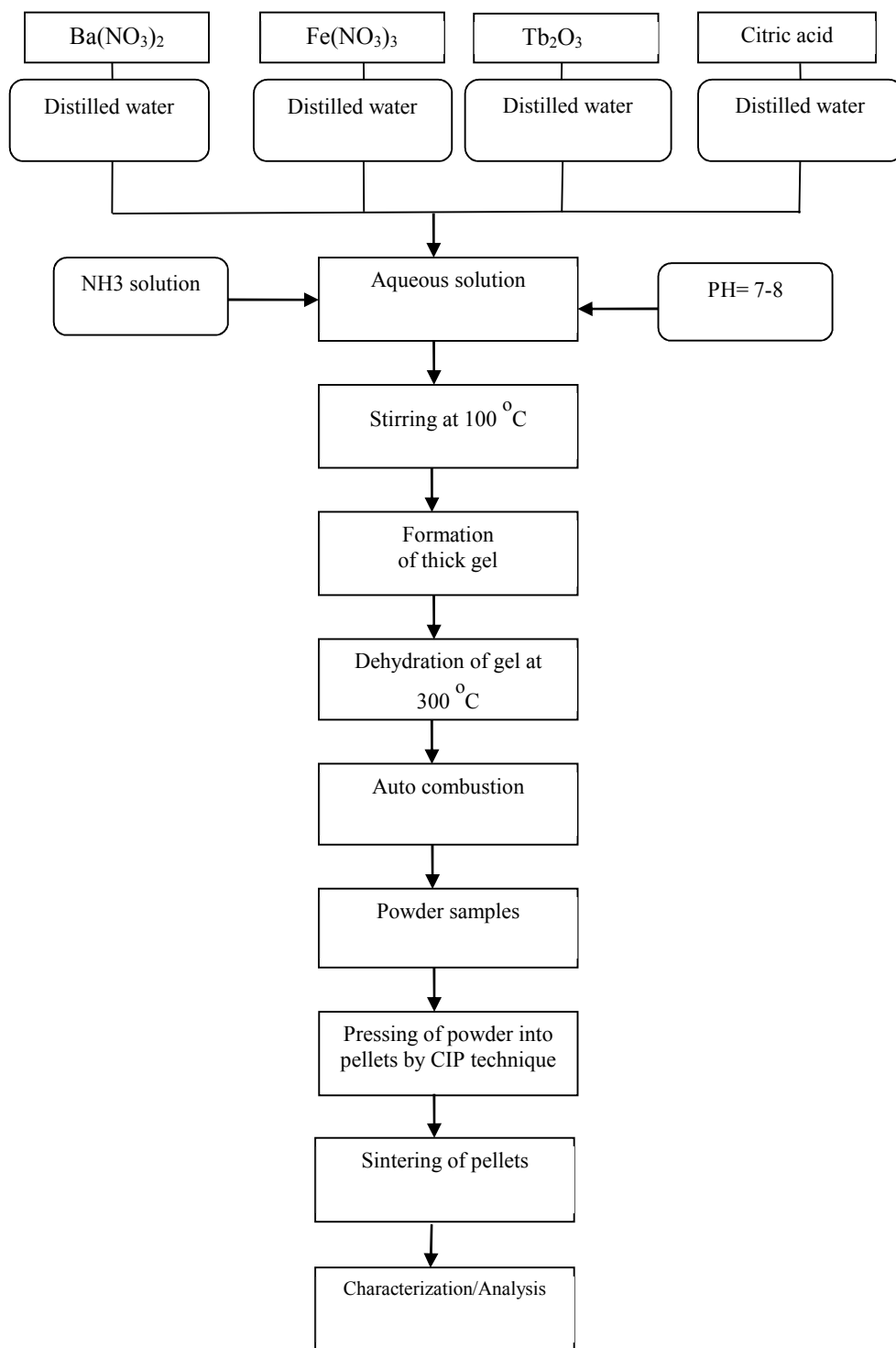Some main advantage of SLAC technique are written below.

a. Energy economical

b. Low reaction rate

c. Very fine powder with very small size

d. Simple in operation e. Low range of Anneal and Calcine temperature

f. Good particle size distribution

g. brilliant chemical homogeneity

## CONCLUSIONS

❖ Rare-earth terbium ($Tb^{3+}$) substituted M-type hexagonal ferrite materials $BaTb_xFe_{12-x}O_{19}$ (x=0.0, 0.1, 0.2, 0.3) have been synthesized using economical and simple chemical method namely "sol-gel auto-combustion technique".

❖ The sintering temperature 1000 °C was estimated from the DSC-TGA analyses for the formation of single phase M-type hexagonal ferrites.

❖ Chemical analysis (EDX) confirms the presence of elements Ba, Tb, and Fe in the synthesized compounds of M-type hexagonal ferrites. EDX also shows the replacement of rare-earth terbium ($Tb^{3+}$) ions with that of $Fe^{3+}$ ions.

❖ XRD analysis confirms the successfully formation of single phase rare-earth terbium ($Tb^{3+}$) substituted M-type hexagonal ferrite

materials. The lattice parameters ratio 'c/a' lies in the expected range 3.945-3.952 for M-type hexagonal ferrites phase. The crystallite size fall in the range 65.15-37.35 nm, which is suitable enough to obtain the suitable signal to noise ratio in the high density magnetic recording media.

❖ X-ray density enhances from 8.084-8.359 $g/cm^3$ and the bulk density lie in the range 5.78-5.93 $g/cm^3$. The porosity of the substituted samples is lower than that of the un substituted BaM hexagonal ferrite materials.

❖ The magnetic properties saturation magnetization ($M_s$), remanance ($M_r$) and coercivity ($H_c$) were determined from the MH-loops. The values of squareness ratio ($M_r/M_s$) lie in the range from 0.556 to 0.093. The values of coercivity ($H_c$) fall in the range 174-5529 Gauss.

❖ DC electrical resistivity of synthesized materials enhances with the increase of rare-earth element $Tb^{3+}$ contents. The values of DC resistivity found to be lie in the range $3.6x10^9$ to $6.82x10^9$ ohm-cm.

```
┌──────────────┐  ┌──────────────┐  ┌──────────────┐  ┌──────────────┐
│  Ba(NO₃)₂    │  │  Fe(NO₃)₃    │  │    Tb₂O₃     │  │  Citric acid │
└──────────────┘  └──────────────┘  └──────────────┘  └──────────────┘

┌──────────────┐  ┌──────────────┐  ┌──────────────┐  ┌──────────────┐
│Distilled water│ │Distilled water│ │Distilled water│ │Distilled water│
└──────────────┘  └──────────────┘  └──────────────┘  └──────────────┘
```

$Ba(NO_3)_2$ → Distilled water

$Fe(NO_3)_3$ → Distilled water

$Tb_2O_3$ → Distilled water

Citric acid → Distilled water

NH3 solution → Aqueous solution ← PH= 7-8

Stirring at 100 $^o$C

Formation of thick gel

Dehydration of gel at 300 $^o$C

Auto combustion

Powder samples

Pressing of powder into pellets by CIP technique

Sintering of pellets

Characterization/Analysis

Flowchart for the synthesis of ferrite $BaTb_xFe_{12-x}O_{19}$ (x=0.00, 0.10, 0.20, 0.30) by SGAC Technique.

The investigated materials may be potential candidates for a new developing technology perpendicular magnetic recording media, permanent magnets, for high frequency applications, and to reduce the electromagnetic interference (EMI).

**References**

[1]  A. M. El-Rifae, Egypt. J. Sol., 23 (2000) 93.

[2]  M.L. Wang, Z.W. Shih, J. Crystal Growth 114 (1991) 435.

[3]  O. Kubo, T. Ido, H. Yokoyama, IEEE Trans. Magn. Magn.18 (1982) 1122.

[4] W. Zhong, W.P. Ding, N. Zhang, J.M. Hong, Q.J. Yan, Y.W. Du, J. Magn. Magn.Mater. 168 (1997) 196. (1994).

[5] W. Roos, J. Am. Ceram. Soc. 63 (1980) 601.

[6] A. Chakraborty, P.S. Devi, H.S. Maiti, J. Mater. Res. 10 (4) (1995) 918.

[7] E. Lucchini, S. Meriani, G. Slokar, J. Mater. Sci. 18 (1983) 1331.

[8] J. Ding, D. Maurice, W.F. Miao, P.G. McCormick, and R. Street, J. Magn.Magn.

[9] X.H Wang, T.L. Ren, L.Y. Li, L.S. Zhang, J. Magn. Magn.Mater.184 (1998) 95.

# Exploration Framework for the Sustainable Development of Dimension Stone Industry: A Case Study of Buner

*Abdur Rahman¹\*, Safi Ur Rehman¹*

¹*Department of Mining Engineering, UET Peshawar, 25120*

*abdurrahman0614@gmail.com*

## Abstract

Mining operations are an integral component in dimension stone process industry's value chain. Scientific exploration of dimension stone deposits is a pre-requisite for planning and design of these mining operations. Therefore, an exploration framework is necessary for the sustainable development of the industry. This research focuses on formulating exploration framework and its application to dimension stone mineral industry cluster in district buner. The proposed framework is based on modern ways of exploration, technologies and methods for the effective characterization of dimension stone deposits. The results of the application of framework on a case study of district buner revealed that, despite the use of modern mining techniques, projects became technically and economically unsustainable due to inadequate and insufficient exploration. Therefore, an exploration framework is required for sustainable development of dimension stone mineral industry cluster.

**Keywords:** pre-requisite, characterization, developmental planned

## Introduction

Dimension stone can be defined as a natural rock that fit on certain qualitative aspects i.e. homogeneity in color, texture and discontinuities and therefore economically extracted and processed to different dimensions for use in the construction, building and monumental industries. The term include raw stone or block but excludes crushed or powdered material which is used in aggregate or to form artificial stone [7]. The most common types of these stones are granite, limestone, marble, sandstone, quartzite and slate [4].

The dimension stone industry is not widely appreciated within the mainstream mining industry. While the fact is that the industry has grown at an average of 7% per annum since the industry has grown at an average of 7% per annum since 1980, and it is estimated that the global turnover is more than US$ 60 Billion per annum [1]. Rapid changes in technology during the past 70-80 years improved production and processing of dimension stone throughout the world, commercially classified dimension stone are given in Figure 1. Due to the high labour cost and environmental impacts the world is shifting towards technology. Which is more environmental friendly and reduced the cost to optimum if efficiently utilized. At the same time to use these technologies proficiently detailed developmental and extraction plans are required.

Planning of dimension stone quarry is an important part of mining operations but it is neglected or mostly evaluate by the non-professional prospectors which are unable to formerly plan or investigate the deposit prior to opening quarries [3, 5]. These are mainly used in construction industry and extensively available in nature at low depth, therefore they are not the objects of huge exploration investment, despite of the high development in exploitation technology [4]. There are different perception for the technical evaluation of dimension stones. According to Carvalho et al [4] the criteria for the dimension stone evaluation is the color, texture and presence or absence of discontinuity. Loudes et al [6, 7] identified slightly a different criteria which consist upon the appearance (color homogeneity), soundness and market demand. But in exploration phase during the geological survey color, texture and discontinuities are more relevant, therefore Carvalho et al [4] have proposed the following decision criteria for the exploration of dimension stone (Table 1).

The criteria in Table 1 can be evaluated through basic geological tools mapping and discontinuities survey with support from structure geology and diamond core drilling. For dimensioning and homogeneity detail data of close core drills will be required which will effect dimension stone blocks and if the distance is given between drill holes some of the important data may be skipped because dimension stone properties change through small distance [1].

## Exploration Framework for Dimension Stone Deposits:

The framework is design to characterize different properties of dimension stone and to figure out multiple procedures for the exploration. The framework can be split into two parts, criteria matrix and procedure model. In the earlier, different parameter are considered to develop a criteria matrix for the characterization of dimension stone deposits. While the later describe the procedure and methods for the determination or description of decision parameters.

## 1. Aesthetic Aspects:

A variety of colors and textures provide ready options in the aesthetic choices among dimension stones. The appearance of stone decide the market value. Also the importance of colour vary from culture/fashion to culture/fashion. Texture can be measured through XRD, SEM, neutron diffraction etc [12]. Crystal size, shape, position and orientation can be quantified. The grain size of granite range from 2 to 3 mm upto 25 mm or above. Marble of large grain size with equigranular texture has more polishing and weather resistant surface than small grains.

**Table 1: Decision criteria for the exploration of dimension stone [4]**

| Dimensioning | Homogeneity | Fracturing |
|---|---|---|
| • Thickness of the productive units (sedimentary beds, metamorphic facies etc)<br>• Volume of the deposit<br>• Spatial Disposition | • Color<br>• Texture<br>• Discontinuities | • Preferential Directions<br>• Frequency<br>• Density<br>• Intensity<br>• Type and Morphology |
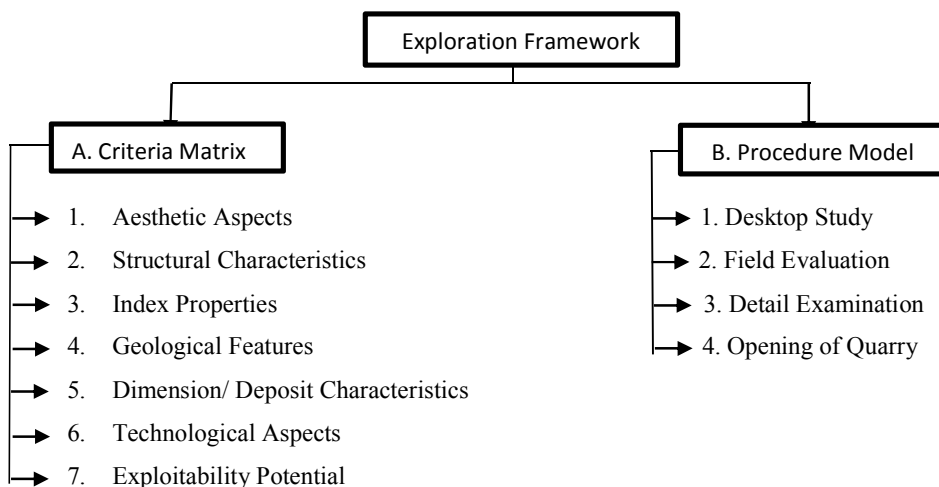


Role of Homogeneity in Exploration of dimension stone is important because it is the identification of variability or continuity in colour, texture and discontinuity. Both blockability and market demand critically depend upon the homogeneity of deposit appearance and discontinuities.

## 2. Structural Characteristics:

The most important discontinuities in dimension stone deposits are joints which leads to the formation of blocks of different sizes in the rock mass [8]. In folding permanent deformation occur in plate surfaces of bent or curved shape. It presence rarely effect quality and extraction of dimension stone deposits. Joints mostly occur in well consolidated, lithified and highly competent rocks i.e. sandstone, limestone, quartzite and granite. If there is joint set with parallel orientation and spacing then conditions are favourable. Main

aspects of fractures are its preferential direction, frequency, density and intensity. Range for low, medium and high density fractures are 1.33-3.30, 0.67-1.33 and 0.18-0.67 respectively. Joint orientation is with respect to the face of extraction, if jointing is irregular than orientation does not matter, orientation of regular joints should be measured.

## 3. Index Properties:

Water absorption is the proportion of water to be absorbed by stone under specific immersion conditions. A stone with higher water absorption and porosity, and lower density, tends to be less durable and less stain resistant and more susceptible to frost attack [10]. Other index properties have also a huge impact on the properties of dimension stones i.e. flexural strength is critically important when used in buildings particularly as a flooring material.

**Table 2: Criteria Matrix for dimension stones with properties**

1. **Aesthetic Aspects**
   - Color
   - Texture
   - Homogeneity

2. **Structural Characteristics**
   - Folds
   - Joints
   - Fractures
   - Joints Orientation

3. **Index Properties**
   - Density
   - Absorption
   - Modulus of Rupture
   - Compressive Strength
   - Hardness
   - Thermal Expansion
   - Flexural Strength

4. **Geological Features**
   - Topography
   - Composition
   - Bedding
   - Fault
   - Dip & Strike

5. **Dimensioning/ Deposit Characteristics**
   - Volume
   - Thickness
   - Shape
   - Spatial Disposition

6. **Technological Aspects**
   - Cutting
   - Polishing

7. **Exploitability Potential**
   - Reserves
   - Legislation
   - Labour Availability
   - Market Demand
   - Environmental Impact
   - Storage
   - Access

**Table 3: Index Properties of different dimension stones [9, 10]**

| Stone type | Density (g/cm³) | Absorption (wt%) | Modulus of rupture, Mpa | Compressive strength, Mpa | Hardness | Flexural strength, Mpa | Thermal Expansion, $10^{-6}$/°C |
|---|---|---|---|---|---|---|---|
| Granite | 2.6-2.7 | 0.1-3.0 | 10.34 | 80-310 | 5-7 | 8-18 | 5-11 |
| Black Granite | 2.8-2.9 | 0.1-1.8 | 10.34 | 110-300 | 5-6.5 | 15-28 | 4-7 |
| Marble | 2.6-2.7 | 0.1-1.5 | 7 | 40-190 | 2-4 | 7-19 | 3-7 |
| Limestone | 2.2-2.6 | 0.3-20.0 | 2.9-6.9 | 20-230 | 2-3 | 4-20 | 2-6 |
| Sandstone | 2.0-2.6 | 2.0-25.0 | 2.4-6.9 | 20-240 | 2-7 | 4-12 | 2-12 |
| Quartzite | 2.6-2.7 | 0.1-1.5 | 6.9-13.9 | 110-350 | 5-7 | 10-25 | 8-16 |
| Slate | 2.6-2.7 | 0.1-2.5 | 37.9-62.1 | 50-300 | 3-5 | 35-55 | 3-9 |

## 4. Geological Features:

Topography has a relation with sheeting fracture zones, general soundness and elevation of the rock. Areas with uneven surface, hilly terrain and undeveloped sheets indicate broken and jointed rock surface. Common dimension stone are marble (calcite, dolomite), granite (quartz, feldspar), limestone (calcite, chert, silt, and clay), sandstone (feldspar & quartz) and slate (quartz, mica, and chlorite). Bedding orientation is quite important in determination of stength. The strength acting parallel to bedding plane may be very low than perpendicular to it. The presence of fault has negative effect on the stone extration and quality. Also spacing and intrusion in fault line effect quality and blockability of dimension stone. Strike and dip mainly refer to the orientation and attitude of geological features. Strike represent a line of intersection between a feature and horizontal surface while dip is the steepest angle of a feature relative to horizontal plane.

## 5. Dimensioning/Deposit Characteristics:

Dimension stone deposits often exist as huge deposit, usually in hundreds of meters. But the stone to be extracted economically does not rely on the extent or volume of the deposit, though it is necessary to identify the size and shape of deposit because that's how an explorer can limit has exploration area or extending it. Finding out the shape and thickness of deposit is important in planning the quarry direction or in extracting the blocks in favourable environment. Spatial disposition of the deposit is also important when there are multiple quarries to be established and getting maximum work or profit from minimum machinery. The profitable spatial characteristic is central disposition, in which all of the facilities are group together in central part in spatial structure and develop the quarries around it. The other disposition can be linear, which exist in dimension stones, the direction of quarry development is in single line. The last one is scattered or dislocated disposition, in which multiple quarries are operated independently in a single deposit. This is because of the different physical and economic conditions which restrict one from operating multiple quarries from single point or position.

## 6. Technological Aspects:

Different technologies are used for the cutting and polishing of dimension stone deposits. The selection of these technologies depend upon the characteristics of deposit i.e. quality of color, texture, hardness, density and orientation of discontinuities, thickness of deposit and other geological and environmental aspects. The common cutting techniques are flame channelling, diamond wire sawing, drilling and blasting, chain sawing,

plugs and feathers etc. Each of them may be efficient with particular scenario individually or in combination [13]. After cutting and extraction, blocks transported to the processing units are further cut and polish to slabs or market size product with the help of gang saw, stationary wire saw, circular diamond saw and polishing lines. Common polishing agents are oxalic acid, tin oxide and aluminium oxide. Automated bevelling and edge polishing machines are finding use in industry [13].

## 7. Exploitability Potential:

Resources are calculated using various data and field evaluation techniques, such as core drilling, trenches and pits and regular sampling [6]. Stone exploration and extraction is controlled by the local legislation of the country, therefore detailed exploration, extraction and reclamation plans are often required. Skilled, efficient and chiefly available workforce reduce overall cost of mining operation. Market demand vary with variety and quality of stone and also location of deposit. Other factors are fashion and culture of stone, extraction methods, natural factors etc. Most of the time mining has environmental impacts with noise and vibration produced by blasting operation, degradation of land and deforestation with production of waste. Storage for the extracted blocks or low grade blocks, and also for waste material extracted during exploitation. Simple topography with no complex terrains make the developmental plan easier and cost effective and non-favourable topography make the plan complex and sometime stone of good quality cannot be extracted.

## 8. Procedure Model:

The procedures are proposed by scientists for the exploration of dimension stones, but scientific research as compared to metals and non-metal on exploration methodologies are scarce [4]. One of the method proposed by Richter 1985, starting from hand sampling and mapping simultaneously followed by test polishing, petrographic evaluation, fabric & colour and jointing pattern, small test blocks, ASTM testing, large test quarry, core drilling and test quarrying [13]. Exploration sequence proposed by louden et al consist of desktop study, field mapping, detailed mapping, geo-radar survey, core drilling, reserve assessment, test quarrying, test processing and quarry planning [1]. I. Ashmole squeezed the above method into seven stages namely desktop study, field evaluation, detailed mapping, geophysical method, drilling, bulk sampling and test quarrying. We thus recommend the following exploration procedure to

figure out the suitability of deposit to be extracted or abandoned.

## 1. Desktop Study:

Desktop study is comprise of gathering the existing information about the geology, geophysics, topography, infrastructure and environmental aspects on the area of interest [7]. Utilizing the available literature about the geological evaluation and geological mapping, geophysical analysis,

Modern tools including satellite imagery and aerial photographs with GIS (Geographical Information System) and Google Earth mapping are helpful in regional evaluation and resource identification. GIS facilitate the desktop study by generating topographical and geological maps while mapping of Google Earth is a tool with capability of simulated three dimensional view [1].

Preliminary economic analysis with data gathered about infrastructure and environment i.e. topography, access, water and skill labour availability, market demand, local legislation, security issues and environmental impacts which later will affect the profitability of the project should be evaluate at this stage. For example, if there is no market demand than a stone with acceptable aesthetic characteristics and soundness cannot be extract economically because it is one of the requirement for dimension stone [4]. Most of these information can be collected with precision by using the online sources i.e. google maps, official sites of government legislative bodies, security issues etc.

## 2. Field Evaluation:

Targeted areas identified by the analysis of existing data are further evaluate in the field. After acquiring the legal rights, samples are collected and mapping is done on general level and on natural outcrop. Mostly, dimension stone deposits are exposed on the surface if not overburden is removed to exposed the surface of deposit. At the start general soundness and appearance of the stones are defined. Few samples from fresh surface are collected for aesthetic evaluation and mineralogical analysis of the stone, if acceptable than further evaluation is carried out otherwise the project is to be discarded at this stage. Sometime samples of acceptable colour show variation after cutting and polishing, therefore sample should be collected for cut and polish.

After sample collection the outcrop of the deposit should be evaluate to ascertain the possibility of producing the blocks of commercial value. Dimension stone deposits are most of the time expose to the surface and joint can be readily determined. Where the solid outcrop is not available the boulders give the indication

review and analysis of the topography and natural terrain with infrastructure conditions and collecting the reports on rock type and old works carried out in the targeted area. The target is to build an exploration plane about the specific areas and identify the favourable conditions i.e. when looking for marble, belts of regionally metamorphosed sedimentary rocks or beds of thermally metamorphosed carbonate rocks are suitable, it will maximize the possibility of finding dimension stone [14].

of producing blocks, large boulders are normally of widely spaced joints in the underlying deposit. The important thing about the joints are orientation, length, continuity and spacing. In ideal situation mapping of joint system should be performed on quarry vertical wall according to the methods suggested by International Society for Rock Mechanics (ISRM), with window sampling or scanline sampling technique [4, 15].

Different test should be performed on the samples collected after the acceptance of aesthetic aspects and structural characteristics of the stone. Standardization systems for dimension stone evaluation are ASTM (American Standard for Testing Material), DIN (Deutsche Industrie Norm), CSIRO (Australian standard), CEN (European Committee for Standardization), ISRM (International Society of Rock Mechanics) etc. The ASTM standard is more prevail as compared to other methods, therefore common ASTM standard for dimension stone identification are granite C616, marble C503, limestone C568, sandstone and quartzite C616 and slate C629. Index properties of dimension stone are determined on the following ASTM standard test: water absorption (ASTM C 97), modulus of rupture (ASTM C 99), compressive strength (ASTM C170), abrasion resistance (ASTM C 241) and flexural resistance (ASTM C 880).

## 3. Detailed Examination:

Field evaluation indicate the possibility of economically viable resources, there detailed mapping, geophysical analysis and drill core sampling is to be done for further examination of the deposit. Special attention should be given to the composition, colour, texture and discontinuities during detailed mapping of the targeted area [4]. For this purpose detailed sampling should be done mainly consist of large size boulders, to ascertain the homogeneity in colour, texture, composition and discontinuities. Structure and geological maps are constructed for further evaluation and assistant of the physical and geological characteristics of the deposit. This type of maps gives indication of future reserves and helpful identifying regional discontinuities i.e. fault, folds, fractures, veins etc. Testing the cutting and polishing capability of the stone is next phase of

examination. Samples are tested to be cut and polish, and their ability to sustain the polish surface under varying condition of weathering, temperature and pressure. After successful testing the samples are compared to the existing product on the market and distributed to obtain feedback from the customers as to ascertain the demand and price for the material. These results will also be helpful in economic evaluation of the deposit. The above mapping and experimentation gives the information about the surface or outcrop of the deposit while for the successful evaluation of dimension stone deposits, the detail information about the discontinuous and varying geological features in three dimension must be clearly understood [16]. For this purpose geophysical methodologies are important to imply for detail research of subsurface fracturing pattern. These methods are very low frequency electromagnetic/radio frequency electromagnetic (VLF-EM/RF-EM) and the ground-penetrating radar (GPR). All methods have corresponding advantages and disadvantages regarding execution speed, type and detail of the information gathered and cost [1, 4]. The VLF-EM/RF-EM is based on the propagation of low to very low-frequency radio waves that generate a secondary electromagnetic field dependant on lithology which allows the acquisition of data about the propagation environment and its heterogeneities; clay-filled fractures, karst, lateral facies variation, etc. This method has limitation of low investigation depth but can be quickly carried out with very low cost, allowing the acquisition of data about major structure [4]. GPR is electromagnetic method that uses high frequency (10MHz- 2.5GHz) radio waves for shallow upto 10-25m, high resolution and subsurface investigation of the earth. The operating principle of geo-radar is based on an electromagnetic wave sent to the ground which reflect from horizontal fracture and rock boundaries [7]. The method is effective homogenous rock type than heterogeneous, also horizontal and sub horizontal appears clearly in geo-radar profiles while vertical and sub vertical are difficult to interpret [1, 4, 7]. Despite of limitation, it is least expensive method to evaluate homogenous rock types and also evaluate whether to proceed or not to drilling which is very much expensive in above type of rock. The next phase of examination is to drill the formation in order to evaluate the deposit as well as to provide information on the vertical extent of the formation and observed variation in colour, minerology and fractures in depth of prospect by producing drill core. Diamond core drilling is preferable because a completer information about the colour variation, minerology, joints, veins, texture, formation and extent of deposit can be interpret from it. Percussion drilling is cheaper than diamond core drilling but only chips can be collected which are only indicative of

variation in colour. The correct placing and spacing of inclined or vertical drill holes is very important and depend on the amount of geological information acquired during the preceding steps of the exploration phases.

## 4. Opening of Quarry:

After acceptable results from drilling the next phase is to open the quarry, extract preliminary blocks of commercial size to test the feedback of market demand before the full evaluation and establishment of quarry. Fruitful results from the market will lead towards the establishment of quarry on small scale to test the blockability/drillability of the stone. The extracted material is then processed into final product to determine their sawability, honability and polishing ability. To establish a full scale quarry and start actual mining developmental plan is made with geostatistical and economical evaluation of production and cost. The blockability and recovery is determine which is to be made realistic with actual extraction.

**Case Study of Buner:**

Buner is located in the north Khyber Pakhtunkhwa (KPK), bordering Swat in the north, Malakand agency in the west, Mardan-Swabi districts in south and Hazara in the east. The area of the district is 1760 square kilometres lies between 34°9' and 34°43' N latitudes and 72°10' and 72°47' E longitudes. The marble in buner is present in Kashala formation of Alpurai Group and Nikanai Ghar formation of Palaeozoic-Mesozoic age [17]. It is the major cluster of marble having the largest deposits with variety of shades and colours commonly white, grey and black marble. The best quality marble is bampokha white in bampokha and jet black in torwarsak area. The target area is shown in Figure 1.
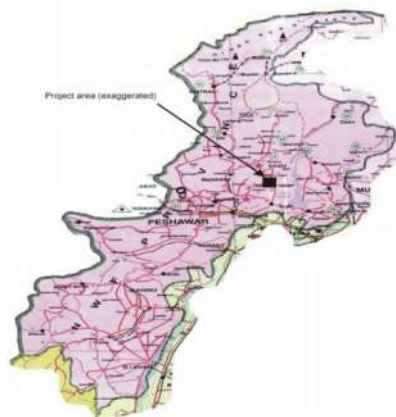


Figure 1: Map of KPK (Khyber Pakhtunkhwa) province showing the study area

**Aesthetic Aspects:**

The potential marble deposits in buner are located in Bampokha, Bazargai, Torwarsak, Mirdara, Yakhdara, Nanser, Matwanai and Daggar. The common colour of the marble is white, grey and black while marketed name are bampokha no.1, bampokha white, carrara white, sunny white, sunny grey, jet black, silky black etc. Aesthetic aspects are shown in Table 5.

**Structural and Geological Features:**

The study area lies in the Main Mantle Thrust (MMT) and is extensively deformed. The deformation style is a combination of folding, directed thrusting and regional metamorphism. Indicators associated with regional scale folding and regional faulting are available while the rocks of lower Swat-Buner group are part of huge recumbent fold making a nape structure [18]. Swat-Buner group have same metamorphic history, but the intensity of metamorphism decrease towards south of Rustam. This area have been found to undergo multiple deformations with at least four periods of folding during a single Palaeogene metamorphism [17]. The significance of regional metamorphism is realised as it has fruitful effects on the index properties of dimension stones.

There are two faults in the study area, Main Mantle Thrust (MMT) fault and the Nikanai Ghar fault as shown in area, in which most are formed in schistose portion while others developed in thin bedded deposits [19]. **Fold axes** are oriented towards northeast direction and are gently plunge towards northeast, which is either symmetric or asymmetric, no tight or overturned fold were observed in the study area. Different types of **fractures** observed in the study area, the bedding-parallel fractures are normally parallel to the bedding planes or foliation and making acute angle of 2° to 10°. **Bedding** inclination is steep in Buner therefore associated fractures also dipping steeply. Vein fractures are also present in which some are open which are filled with secondary clay deposits as in Figure 6 and weathered material from the country rock which can be observed on the fresh surface. Plumose fractures are developed when the rock is homogeneous, several small fractures of this type observed in the study area, which suggest that on local scale the rock is homogeneous.

**Index Properties:**

Index properties are given in Table 4.

**Table 4**

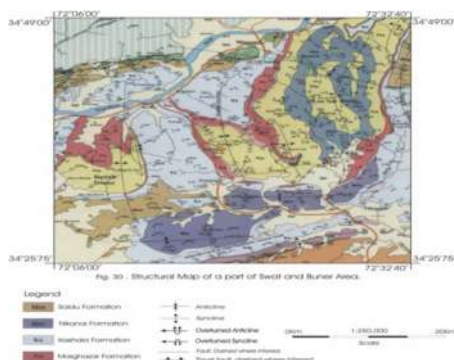| Sample No. | Absorption test ASTMC-97 | Density test ASTMC-97 | Compression test ASTMC-179 (psi) | Hardness test ASTMC-241 |
|---|---|---|---|---|
| Bazargai-1 | 0.15 | 2.798 | 11326 | 4 |
| Bampokha-1 | 0.14 | 2.686 | 3538 | 3.5 |
| Mariamay-1 | 0.14 | 2.807 | 8183 | 4 |
| Barikot-1 | 0.06 | 2.673 | 10626 | 3.5 |



**Figure 2: Structure map of Swat-Buner area, showing the different formation with folding and faulting [19]**

**Table 5: Different marble deposits of Buner with colour, texture and composition [1]**

| S.No | Marble Deposits | Colour | Texture | Composition |
|------|-----------------|--------|---------|-------------|
| 1 | Bampokha | Creamy white, grey | Calcite, traces | Calcite, dolomite |
| 2 | Yakhdara | White to milky white on fresh surface to dirty grey on weathered surface | Fine to medium grain, subhedral | Calcite, dolomite, quartz |
| 3 | Mirdara | Yellowish brown on weathered surface to light grey on fresh surface | Medium grain, rhombohedral | Calcite, quartz |
| 4 | Nanser | Reddish brown on weathered to dark gray on fresh surface | Fine to medium grain, subhedral to anhedral | Calcite, hematite, quartz, muscovite |
| 5 | Bazargai | Yellowish brown on weathered to greyish white on fresh surface | Medium to coarse grain, crystalline | Calcite, dolomite, muscovite |
| 6 | Torwarsak | Grey and black | Fine to medium grain, anhedral, foliation | Calcite, pyrite |
| 7 | Matwanai | White to greyish | Coarse grain, subhedral, equigranular | Calcite, quartz |
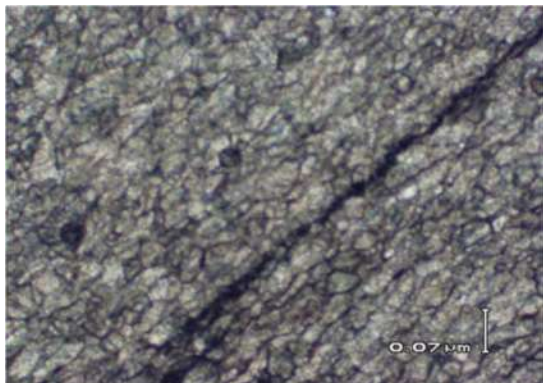
**Figure 3: Photomicrograph of torwarsak marble to Showing foliation and fracture filled.**



**Figure 4: Photomicrograph of cryptocrystalline Micritic calcite grains.**
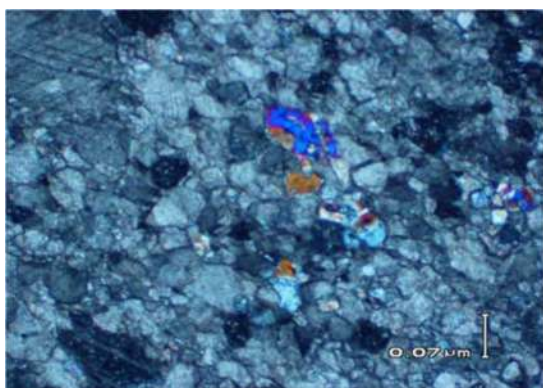


**Figure 5: Fractures filled with clay in Bampokha Marble, abandoned quarry of PASDEC**



**Figure 6: Fractures in Bazargai marble, now abandoned by PASDEC, (photo 2009)**

**Technology and Exploitability**

The common mining technique in Buner is drilling and blasting, in which horizontal holes are drilled in the vertical face, charge with high explosive and blasted. But this method produce blasting induce cracks in blocks which cannot be exported, therefore sold to the local market with much of reduction in cost. The mechanized technique of cutting i.e. wire saw and chain saw was applied by PASDEC (Pakistan Stone Development Corporation) but fail due to multiple reasons, some of the quarries are shown in Figures 8, 9 and10. Some of the reasons observed in the abandoned quarries are lack of proper exploration, improper selection of quarries location, market demand and low blockability due to excessive fracturing.

The statistics reflect machine configuration in the target cluster, the investment culture within the cluster and market demand justifies machinery being preferred by entrepreneurs. In Buner, most companies are using vertical cutters for stripes and 18" section machines for sizing.

The Buner district has a good **infrastructure**, roads are in good condition which results safe transportation of blocks, but in mines the roads are in bad condition which stop supply of raw material to processing units in the rainy

season. Telephone and mobile network facility is available. Regular power is the key influential factor to mechanized mining and processing industry. This facility is available, but prolonged load shedding and irregular power supply affect the processing units and bringing the attention of investors into the cluster. **Market demand** of Buner varies largely from international to local market, but almost 98% of the marble is consumed in local and national market. The only export quality marble is Bampokha super white with existing market price of Rs.12000-20000 per ton. Roughly estimated that Buner is consumed 50% in local market, 28% in national market and 2% international market. These figures can be improved if the trend is shifted towards mechanized mining technique.

The topographical location of the quarries and their transportation cost greatly affect the productiveness of quarry and actual cost of operation at the given place. The extracted blocks are of irregular shape and sometime make problems in loading and hauling to processing units or to the stock yard.

## Results and Conclusions

The ultimate goal is, to develop an exploration framework which bring sustainability in dimension stone industry and to provide a criteria for decision making of opening a quarry or abandoned the site. For this purpose, the criteria matrix and procedure model is develop to determine the aesthetic aspects, structural characteristics, index properties, geological feature, dimensioning, technological aspects and exploitability potential of dimension stone deposit. There should be a proper procedure or method to evaluate all these characteristic and aspects of dimension stone in early stage of prospecting and exploration of deposits.

The best results can be obtained if the study start from the desk, collecting the information and identifying the targeted area and dividing the area into smaller units of high, medium and low potential. Careful and thorough investigation is required at this stage to identify the potential area at that early stage. The aesthetic aspects and structural characteristics are the most important criteria in field evaluation, small overburden can be problem at this stage but fresh surface is expose by removing it. However, weathered surface and clay filled fractures can still produce problems in identifying the prospect. At this stage, scanline method for the identification and determination of fractures is preferred. The quality and durability of the prospect can be assessed through detailed examination of the prospect by using some of the latest methods and technology. The work is narrow down at this stage, detailed structure and geological maps are produced after sampling and investigation. Density and type of discontinuities, orientation of bedding, dip & strike of deposit with other multiple factors can spoil the soundness and blockability. As alone outcrop is not the indicator of what inside the earth, therefore GPR and core drilling must also be the part of detail examination. In the studied area the deposits are either exposed on the surface or being exposed due to active mining or abandoned quarries. Therefore the discontinuities and colour variation can be observed on the naked eye as shown in Figures 3, 4, 5, and 6. So the area is evaluated on the outcrop or freshly exposed surface due to mining activities. Commonly the outcrop surface is effected by intensive fracturing and weathering, therefore the first layer in the bedded rock is useless and may be diminishes.

After the evaluation of abandoned quarries it can be clearly stated that appearance, soundness and market demand of the stone are the key factors to be determined before opening of quarry and it will lead towards the successful mining operation. The subsurface method of GPS and core drilling are not implied to this study, as the prospect is either exposed or quarries are in operation.

The paper concluded that without proper exploration the mining and processing operation cannot be sustainable because it will lead towards the deficiency of blockability and higher waste production due to high density of fractures and uncertainties. As discussed in case study Figure 8, 9 and 10, due to improper exploration quarries are abandoned due to excessive fracture and low market demand after high developmental and exploitation cost. To be on the safe side, the preliminary exploration study is necessary. Most characteristics and features are described subjectively in dimension stone exploration therefore single objective results cannot be displayed.

## References

[1] I. Ashmole, M. Motloung "Dimension stone: The latest trends in exploration and production technology", *the South African institute of mining and metallurgy, 2008.*

[2] Marco Cosi "The dimension stone sector: new perspectives on the global market and on the reporting of international mining standards", *European geologist 39 | may 2015.*

[3] M. Diehl, "Exploration of natural stone deposits with special regard to Southern Africa", *Paper presented at the African Stone Indaba, Johannesburg; 10-12 March 1996.*

[4] J. F. Carvalho et al "Decision Criteria for the exploration of ornamental-stone deposits: Application to the marbles of Portuguese Estremoz Anticline", *International journal of rock mechanics & mining sciences 45 (2008) 1306-1319.*

[5] M. Mutluturk, "Determining the amount of marketable blocks of dimension stone before actual extraction", *Journal of mining sciences, Vol. 43, No. 1, 2007.* [6] Venkat

Reddy, D "Evaluation of Natural Defects in Commercial Decorative Rock Deposits in Karnataka, India" *Gondwana Research (Gondwana Newsletter Section) Vol 5, No 2, pp. 557-560, 2000.*

[7] O. Selonen et al "Exploration for dimensional stone, implications and examples from the Precambrian of Southern Finland", *Engineering Geology 56, 275-291, 2000.*

[8] Reza Yarahmadi et al "How to determine the appropriate methods to identify the geometry of in situ rock blocks in dimension stones", *Environ Earth Sci (2015) 74:6779–6790.*

[9] M. R. Smith "Stone, Building Stone, Rock Fill and Armourstone in Construction", *the Geological Society, London, UK, 1999.*

[10] Geoff Quick "selective guide to the specification of dimension stone", *CSIRO Building, Construction and Engineering, Highett, Victoria, Australia, 3190.*

[11] "Standard Guide for Selection of Dimension Stone" *ASTM International, Designation: 10.1520/C1528-2015*

[12] Standard Guide for Petrographic Examination of Dimension Stone" *ASTM International, Designation: C1528- 2015.* [13] C. Papertzian & D. Farrow "Dimension Stone: A guide to prospecting and developing; Ontario Geological Survey, Open File Report 5920, 82p, 1995.

[13] C. Papertzian & D. Farrow "Dimension Stone: A guide to prospecting and developing; Ontario Geological Survey, Open File Report 5920, 82p, 1995

[14] Hora, Z.D, 'Dimension Stone "Marble" RO4", in Selected British Columbia Mineral Deposit, Profiles, *British Columbia Geological Survey, Victoria, B.C., Canada, 2007.*

[15] S. Mosch et al, "Optimised extraction of dimension stone blocks", *Environ Earth Sci 62:1911-1924 (2011).*

[16] H. Loudes et al, "Evaluation of dimension stone in gneissic rocks – a case history from southern Finland", *Engineering Geology Volume 58, Issue 2, pp 209-223, November 2000.*

[17] J.A DiPietro, and R.D. Lawrence, "Himalayan structure and metamorphism south of the Main Mantle Thrust, lower Swat, Pakistan", *Journal of Metamorphic Geology, vol. 9, p. 481-495, 1991.*

[18] I. Ahmad, "Geology of Jowar area, Karakar Pass, Swat District, NWFP, Pakistan. *Unpublished M.Phil. Thesis, University of Peshawar, 144p, 1986.*

[19] Cluster Mapping of Pakistan's Marble Sector (NWFP), *a project of PFSSRP, PAK/AIDCO/2002/0382/0/*

## A fuzzy based active contour model for image segmentation using Gaussian distribution

*Ali Ahmad[1*], Noor Badshah [1]*

[1]Department of Basic sciences & Islamiat, UET Peshawar

[1*]Corresponding author

Email: aliahmadmath@gmail.com

**Abstract**

In this paper, we propose a new fuzzy variational model for image segmentation based on generalized averages. Generalized averages are usually very effective in images having minimum, maximum or average intensity background. Therefore, our proposed model works well in images having such properties. Pseudo zero level set (fuzzy membership) is regularized using Gaussian smoothing filter instead. This model is independent of initial contour. It is also observed from experiments that the proposed model works well in images having noise and outliers.

**Key words**: Active contour, Fuzzy logic, Gaussian smoothing filter, Pseudo level set, Segmentation.

## 1 Introduction

Image segmentation is an important and fundamental problem in image analysis and computer vision. The main aim of image segmentation is to partition a gray or color image into different sub-regions of homogeneous intensities such as texture, color etc. The main challenge of this problem is how to construct effective algorithms and methods to solve such problems. A number of image segmentation techniques is developed over the years, among those, active contour models got great attention since the proposal of first active contour model by Kass et al. [1]. Active contour models are mainly organized into two groups: edge-based [1, 2] and region-based [3-5]. Edge-based models depend on edge information to stop the curve evolution. Edge-based models are good in images having strong object boundaries. However, these models have some drawbacks such as: high dependence on initial position of the curve and are sensitive to noise and outliers. Whereas , region-based models [3-7], use region information such as texture, color, intensity etc. Region-based models have no dependence on the initial position of the curve, less sensitive to noise and outliers and works well in images having weak object boundaries. Chan-Vese (CV) model [5] derived from the well-known Mumford-Shah (MS) functional [7] is a popular region-based model. They solved their energy functional in the level set formulation [8].

Fuzzy set theory[9] which is widely used in data clustering and image segmentation is first introduced to the active contour frame work by Krinidis and Chatzis, who developed the fuzzy energy based active contour (FEBAC) model [10], which is fast, free of its initial position and takes very few iteration to converge.

In this work, with novel generalized averages a fuzzy segmentation model using Gaussian distribution is proposed. Our proposed model works well not only in general images, but also performs well in images having maximum, minimum and average background. The role of "$\alpha$" in the generalized averages is very important. For $\alpha \geq 0$, the contour will move towards object boundary having maximum intensity (black), On the other hand, for $\alpha < 0$, the contour will segment object with minimum intensity (white). Gaussian smoothing filter is used to regularize the pseudo zero level set (fuzzy membership).

## 2 Previous works

### 2.1 Chan-Vese (CV) model

Chan and Vese [5] proposed energy functional, which is a special case of the Mumford and Shah (MS) model [7]. Let $I_0(\varkappa, \ell)$ be a gray image such that $I_0: \Omega \to R$, where $\Omega \subset R^2$ is an image domain. The energy functional of their proposed model is given by:

$$\mathcal{F}^{cv}(c_1^\otimes, c_2^\otimes, \mathsf{C}) = \mu \, Length(\mathsf{C}) + \lambda_1 \int_{inside \, (\mathsf{C})}(I_0(\varkappa, \ell) - c_1^\otimes)^2 d\varkappa d\ell + \lambda_2 \int_{outside(\mathsf{C})}(I_0(\varkappa, \ell) - c_2^\otimes)^2 d\varkappa d\ell.$$

$$(1)$$

Where $\lambda_1$, $\lambda_2$ and $\mu$ are real constants, $\mathsf{C}$ represent active curve. Two constants $c_1^\otimes$ and $c_2^\otimes$ approximate image intensities inside and outside ($\mathsf{C}$) respectively. This model not only show less sensitivity to the initial contour position, but also works well in images having blur object boundaries. But if the intensities inside and outside ($\mathsf{C}$) are non-homogenous then $c_1^\otimes$ and $c_2^\otimes$ are different from the image data and flops to segment images with intensity non-homogeneity. To solve the energy functional in Eq. (1), the active curve $\mathsf{C}$ is replaced by level set function $\phi^o$ and re-write the energy functional as:

$$\mathcal{F}^{cv}(c_1^\otimes, c_2^\otimes, \phi^o) = \mu \int_\Omega \delta(\phi^o(\varkappa, \ell))|\nabla(\phi^o(\varkappa, \ell))| + \lambda_1 \int_\Omega (I_0(\varkappa, \ell) - c_1^\otimes)^2 H(\phi^o(\varkappa, \ell)) d\varkappa d\ell + \lambda_2 \int_\Omega (I_0(\varkappa, \ell) - c_2^\otimes)^2 (1 - H(\phi^o(\varkappa, \ell))) d\varkappa d\ell \qquad (2)$$

where $H(.)$ is Heaviside and $\delta(.)$ is the Dirac delta function, is defined by:

$$H(\chi) = \begin{cases} 0, & \chi < 0 \\ 1, & \chi \geq 0 \end{cases} \quad , \quad \delta(\chi) = \frac{d}{dx}H(\chi).$$

The gradient descent flow for the energy functional defined in Eq. (2) is

$$\frac{\partial \phi^o}{\partial t} = \delta(\phi^o(\varkappa,\ell))\left[\mu div\left(\frac{\nabla(\phi^o(\varkappa,\ell))}{|\nabla(\phi^o(\varkappa,\ell))|}\right) - \lambda_1(I_0(\varkappa,\ell) - c_1^{\otimes})^2 + \lambda_2(I_0(\varkappa,\ell) - c_2^{\otimes})^2\right]. \tag{3}$$

The constants $c_1^{\otimes}$ and $c_2^{\otimes}$ are updated with the help of

$$c_1^{\otimes} = \frac{\int_\Omega I_0(\varkappa,\ell)H(\phi^o(\varkappa,\ell))d\varkappa d\ell}{\int_\Omega H(\phi^o(\varkappa,\ell))d\varkappa d\ell} \tag{4}$$

$$c_2^{\otimes} = \frac{\int_\Omega I_0(\varkappa,\ell)(1-H(\phi^o(\varkappa,\ell)))d\varkappa d\ell}{\int_\Omega(1-H(\phi^o(\varkappa,\ell)))d\varkappa d\ell}. \tag{5}$$

To maintain the evolution of the active curve stable, re-initialization is assumed which is a time consuming stage.

## 2.2 Fuzzy energy based active contour (FEBAC) Model

The FEBAC model [10] is the first fuzzy model which combines fuzzy set theoretic approach with active contour methodology aims to segment images into two regions of interest. The energy functional of FEBAC model is given by:

$$\mathcal{F}_{facm}(c_1^\circ, c_2^\circ, v, C) = \lambda_1 \int_{inside(C)}(I_0(\varkappa,\ell) - c_1^\circ)^2(v(\varkappa,\ell))^m d\varkappa d\ell + \lambda_2 \int_{outside(C)}(I_0(\varkappa,\ell) - c_2^\circ)^2(1 - v((\varkappa,\ell))^m d\varkappa d\ell + \mu\, length(C). \tag{6}$$

Where $\lambda_1$, $\lambda_2$ and $\mu$ are positive constants. $v(\varkappa,\ell)$ and $(1 - v(\varkappa,\ell))$ are two fuzzy membership functions such that $v(\varkappa,\ell) \in [0,1]$ show the degree of membership of $I_0(\varkappa,\ell)$ to $inside$ and $outside(C)$ respectively. $m = 2$, is a weighting exponent on each fuzzy membership function. Similar to level set method [8], a pseudo level set formulation based on fuzzy membership $v(\varkappa,\ell)$ is used. The active curve $C \subset \Omega$ is represented by the pseudo zero level set of Lipschitz similar function (LSF) $v: I_0 \to R$

$$\begin{cases} C = \{(\varkappa,\ell) \in I_0 : v(\varkappa,\ell) = 0.5\}, \\ outside(C) = \{(\varkappa,\ell) \in I_0 : v(\varkappa,\ell) < 0.5\}, \\ inside(C) = \{(\varkappa,\ell) \in I_0 : v(\varkappa,\ell) > 0.5\}. \end{cases} \tag{7}$$

The two average prototypes $c_1^\circ$ and $c_2^\circ$ in Eq. (6) is updated with the help of

$$c_1^\circ = \frac{\int_\Omega I_0(\varkappa,\ell)(v(\varkappa,\ell))^m d\varkappa d\ell}{\int_\Omega(v(\varkappa,\ell))^m d\varkappa d\ell} \tag{8}$$

$$c_2^\circ = \frac{\int_\Omega I_0(\varkappa,\ell)(1-v(\varkappa,\ell))^m d\varkappa d\ell}{\int_\Omega(1-v(\varkappa,\ell))^m d\varkappa d\ell} \tag{9}$$

and the fuzzy membership is updated with the help of

$$v(\varkappa,\ell) = \frac{1}{1+[\frac{\lambda_1(I_0(\varkappa,\ell)-c_1^\circ)^2}{\lambda_2(I_0(\varkappa,\ell)-c_2^\circ)^2}]^{\frac{1}{m-1}}}. \tag{10}$$

Instead of Euler-Lagrange a fast algorithm proposed by Song et al. [11] is used for the minimization of their energy functional. The computational speed of this model is very fast and can achieve convergence after very few iterations.

## 3. Proposed Model

The energy functional of our proposed model is given by:

$$\mathcal{F}_{FGD} = \lambda_1 \int_\Omega -log p_{1,(\varkappa,\ell)}(v(\varkappa,\ell))^m d\varkappa d\ell + \lambda_2 \int_\Omega -log p_{2,(\varkappa,\ell)}(1 - v(\varkappa,\ell))^m d\varkappa d\ell \tag{11}$$

where $\lambda_1$ and $\lambda_2$ are positive parameters, $\Omega$ an image domain and $p_{i,(\varkappa,\ell)}$ $i = 1,2$ defined by:

$$p_{i,(\varkappa,\ell)} = \frac{1}{\sqrt{2\pi}\sigma_i(\varkappa,\ell)}\exp\left(-\frac{(I_0(\varkappa,\ell)-c_i^*)^2}{2\sigma_i^2(\varkappa,\ell)}\right)\ where\ i = 1,2$$

$c_i^*$, $\sigma_i(\varkappa,\ell)$, $i = 1,2$ are generalized averages and standard deviation respectively. Also

$$-log p_{i,(\varkappa,\ell)} = log\sqrt{2\pi} + log\sigma_i(\varkappa,\ell) + \frac{(I_0(\varkappa,\ell)-c_i^*)^2}{2\sigma_i^2(\varkappa,\ell)},\ i = 1,2 \tag{12}$$

$v(\varkappa,\ell)$, is the degree of membership such that $v(\varkappa,\ell) \in [0,1]$. $m$ is a weighting exponent on membership function usually set to 2. Instead of length term a Gaussian smoothing filter (GSF) is used for the regularization of pseudo zero level set function $v(\varkappa,\ell)$ (fuzzy membership) defined by

$$GSF = \frac{1}{2\pi\sigma^2}\exp\left(-\frac{\varkappa^2+\ell^2}{2\sigma^2}\right).$$

Minimize the energy functional in Eq. (11), w.r.t the fuzzy membership $v(\varkappa,\ell)$ and keeping $c_i^*, \sigma_i^2$, $i = 1,2$ constant. We get the updated fuzzy membership as follows:

$$v(\varkappa,\ell) = \frac{1}{1+\left[\frac{\lambda_1\left(log\sqrt{2\pi}+log\sigma_1(\varkappa,\ell)+\frac{(I_0(\varkappa,\ell)-c_1^*)^2}{2\sigma_1^2(\varkappa,\ell)}\right)}{\lambda_2\left(log\sqrt{2\pi}+log\sigma_2(\varkappa,\ell)+\frac{(I_0(\varkappa,\ell)-c_2^*)^2}{2\sigma_2^2(\varkappa,\ell)}\right)}\right]^{\frac{1}{m-1}}} \tag{13}$$

again minimizing the energy functional in Eq. (11), w.r.t $c_i^*, \sigma_i^2$, $i = 1,2$. we get:

$$\sigma_1^2 = \frac{\int_\Omega(I_0(\varkappa,\ell)-c_1^*)^2(v(\varkappa,\ell))^m d\varkappa d\ell}{\int_\Omega(v(\varkappa,\ell))^m d\varkappa d\ell} \tag{14}$$

$$\sigma_2^2 = \frac{\int_\Omega(I_0(\varkappa,\ell)-c_2^*)^2(1-v(\varkappa,\ell))^m d\varkappa d\ell}{\int_\Omega(1-v(\varkappa,\ell))^m d\varkappa d\ell} \tag{15}$$

$$c_1^* = \frac{\int_\Omega I_0(\varkappa,\ell)(v(\varkappa,\ell))^m d\varkappa d\ell}{\int_\Omega(v(\varkappa,\ell))^m d\varkappa d\ell} \tag{16}$$

$$c_2^* = \frac{\int_\Omega I_0(\varkappa,\ell)(1-v(\varkappa,\ell))^m d\varkappa d\ell}{\int_\Omega(1-v(\varkappa,\ell))^m d\varkappa d\ell}. \tag{17}$$

Instead we are using generalized averages given by:

$$c_1^* = \frac{\int_\Omega I_0^\alpha(\varkappa,\ell)(v((\varkappa,\ell))^m d\varkappa d\ell}{\int_\Omega I_0^{\alpha-1}(\varkappa,\ell)(v(\varkappa,\ell))^m d\varkappa d\ell} \tag{18}$$

$$c_2^* = \frac{\int_\Omega I_0^\alpha(\varkappa,\ell)(1-v((\varkappa,\ell))^m d\varkappa d\ell}{\int_\Omega I_0^{\alpha-1}(\varkappa,\ell)(1-v(\varkappa,\ell))^m d\varkappa d\ell} \tag{19}$$

where $\alpha \in R$, and will be set according to the images.

To get Euler-Lagrange equation (evolution equation) we minimize the energy functional in Eq. (11), w.r.t $v$ and keeping $c_i^*, \sigma_i^2$, $i = 1,2$ constant, for expressing the fuzzy membership

function $v(\varkappa, \ell)$ defined in Eq.(13) as the pseudo level set function, we get the following partial differential equation.

$$\frac{\partial v}{\partial t} = -\lambda_1 \left[ log\sqrt{2\pi} + log\sigma_1(\varkappa, \ell) + \frac{(I_0(\varkappa,\ell)-c_1^*)^2}{2\sigma_1^2(\varkappa,\ell)} \right] v(\varkappa, \ell) +$$
$$\lambda_2 \left[ log\sqrt{2\pi} + log\sigma_2(\varkappa, \ell) + \frac{(I_0(\varkappa,\ell)-c_2^*)^2}{2\sigma_2^2(\varkappa,\ell)} \right] (1 - v(\varkappa, \ell)).$$
$$(20)$$

A conditionally stable simple explicit scheme for the solution of the above partial differential equation is used. Other technique may also be applied. Solution of the above Eq. (20), gives pseudo level set function which will then be used for the updating of fuzzy membership defined in Eq. (13), and $c_i^*, \sigma_i^2$, $i = 1,2$.

### 3.1 Experimental Results

In this subsection, our model is compared with other two well-known models, CV [5] and FEBAC model [10]. While performing experiments we set the time step $\Delta t = 0.01, \lambda_1 = \lambda_2 = 1$, $\sigma = 1$, window of size $= 5 \times 5$, for CV model $\lambda_1 = \lambda_2 = 1$. For FEBAC $\mu = 1$, unless otherwise specified.

In   Figure 1, the segmentation result of a skin lesion image is shown. First row show segmentation result of the proposed model, whereas, second and third row show segmentation result of FEBAC and CV model.    The efficacy of our model is clear from the result.

In Figure (2, 3), the proposed model (first row) outperforms other two models (FEBAC (second), CV (third)) in images having average and maximum (black) background respectively.

In Figure 4, an infrared image with white foreground is shown. A Gaussian noise of variance 0.15 and mean zero is added. The performance of our model is shown in the first row, whereas, performance of FEBAC and CV model is shown in the third row. Our proposed model as compared to other two models works well in Gaussian noise too.
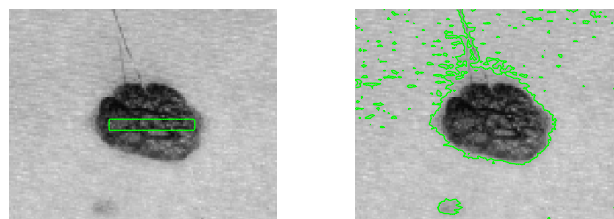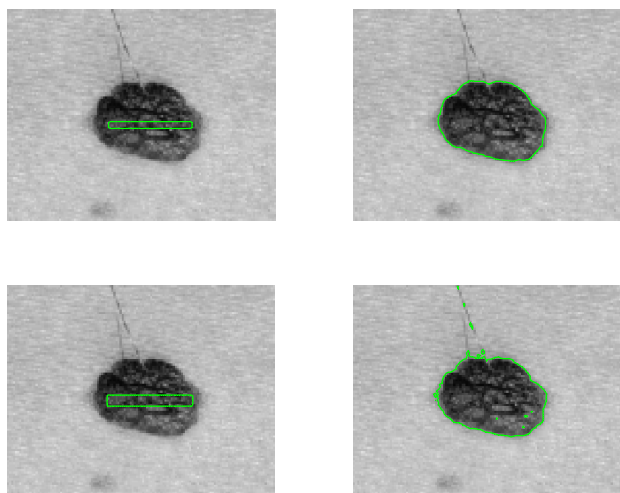


FIGURE 1: FIRST ROW SHOW SEGMENTATION RESULT OF THE PROPOSED MODEL. SETTING $= 1$, $\textbf{\textit{image size}} = \mathbf{131 \times 94}$ . SECOND AND THIRD ROW SHOW SEGMENTATION RESULTS OF FEBAC AND CV MODEL. $\boldsymbol{\lambda_1 = 0.00009}$, $\boldsymbol{\lambda_2 = 0.0009}$ $\textbf{\textit{for FEBAC and}}$ $\boldsymbol{\mu = 0.00005 \times 255.^2}$ $\textbf{\textit{for CV model}}$.



FIGURE 2: FIRST ROW SHOW SEGMENTATION RESULTS OF THE PROPOSED MODEL. SETTING $\boldsymbol{\alpha = 09}$, $\textbf{\textit{image size}} = \mathbf{125 \times 192}$. SECOND AND THIRD ROW SHOW SEGMENTATION RESULT OF FEBAC AND CV MODEL. $\boldsymbol{\lambda_1 = 0.000008}$, $\boldsymbol{\lambda_2 = 0.0008}$ $\textbf{\textit{for FEBAC and}}$ $\boldsymbol{\mu = 0.00000009 \times 255.^2}$, $\textbf{\textit{for CV model}}$.

FIGURE 3: FIRST ROW SHOW SEGMENTATION RESULT OF THE PROPOSED MODEL. SETTING $\lambda_1 = 8$, $\lambda_2 = 1$, $\alpha = 2.5$, $image\ size = 129 \times 114$. SECOND AND THIRD ROW SHOW SEGMENTATION RESULTS OF FEBAC AND CV MODEL. $\lambda_1 = 0.000006$, $\lambda_2 = 0.0009\ for\ FEBAC\ and\ \mu = 0.000025 \times 255.^2$, $for\ CV\ model$.
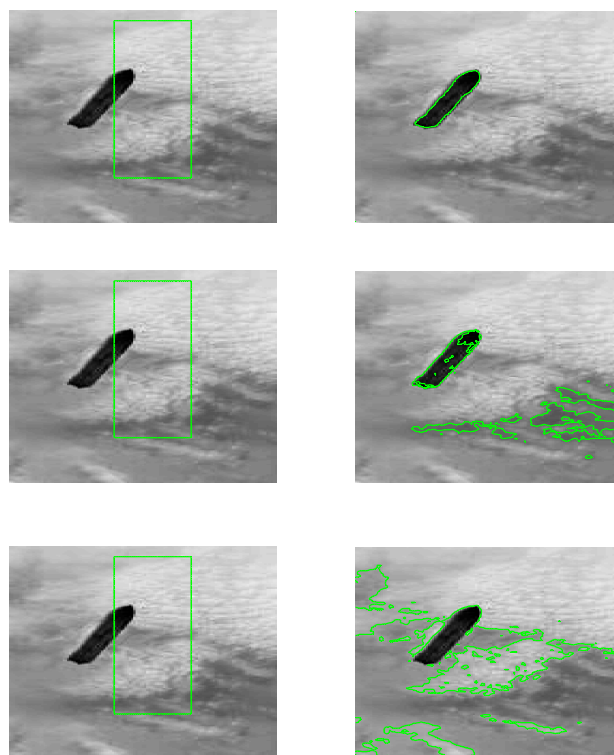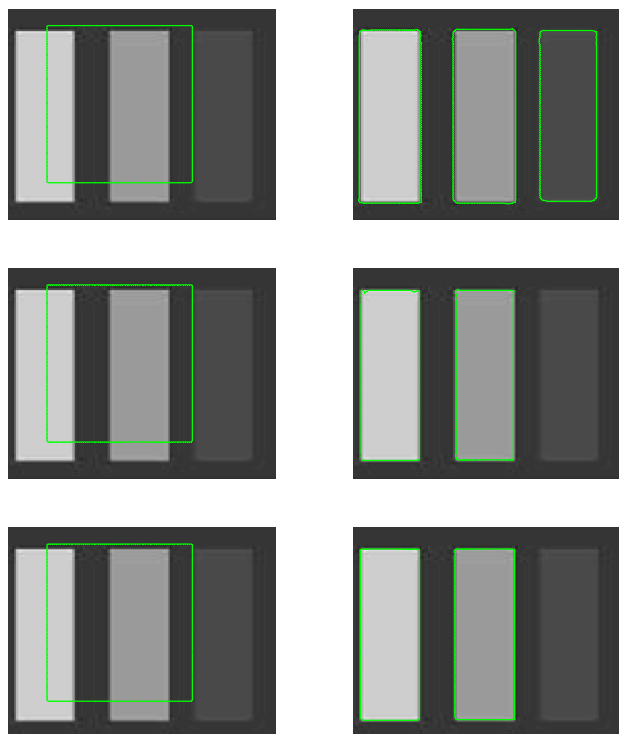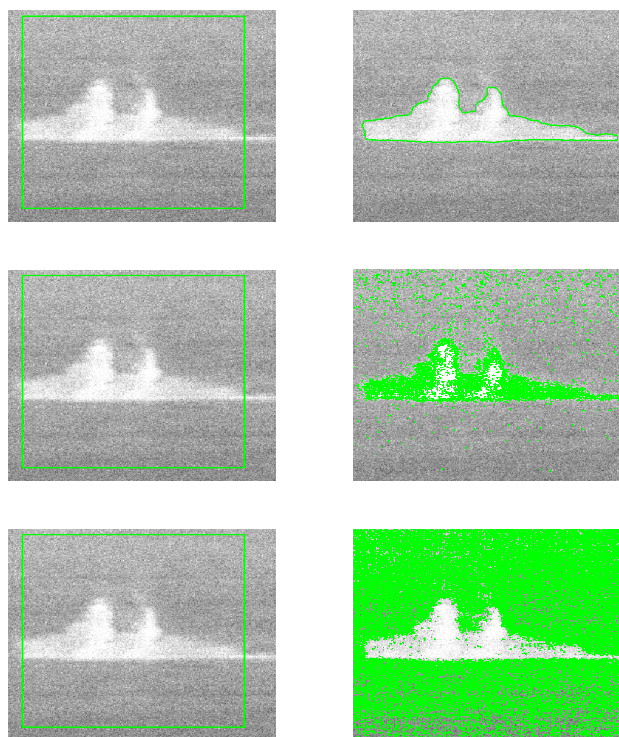


FIGURE 4: FIRST ROW SHOW SEGMENTATION RESULT OF THE PROPOSED MODEL ADDING GAUSSIAN NOISE OF VARIANCE =0.15 AND MEAN=0. SETTING, $= -25$, $\sigma = 15$, $and\ window\ of\ size = 10 \times 10$, $image\ size = 347 \times 332$. SECOND AND THIRD ROW SHOW SEGMENTATION RESULTS OF FEBAC AND CV MODEL. SETTING $\lambda_1 = 0.00009$, $\lambda_2 = 0.000001\ for\ FEBAC\ and\ \mu = 0.0000001 \times 255.^2$, $for\ CV\ model$.

### 4    Conclusion

In this work, a fuzzy region based segmentation model with generalized averages using Gaussian distribution is proposed. The generalized averages usually work well in images having minimum, maximum and average background. The proposed model is robust against noise and outliers, especially works well against Gaussian noise. In future we are looking to add local image information to the proposed model, due to which the model will be able to work well in images having intensity inhomogeneity.

### 5  References

[1] V. Caselles, R. Kimmel, and G. Sapiro, Geodesic active contours, *International Journal of Computer Vision*, 22 (1997) 61–79.

[2] M. Kass, A. Witkin, and D. Terzopoulos, Snakes: Active contour models International *Journal of Computer Vision*, 1 (1988) 321–331.

[3] X. Wang, J. Shan, Y. Niu, L. Tan, S. Zhang, Enhanced distance regularization for re-initialization free level set evolution with application to image segmentation, Neuro computing , 141 (2014) 223–235.

[4] K. Zhang, L. Zhang, H. Song, W. Zhou, Active contours with selective local or global segmentation: a new formulation and level set method, Image Vision Computing, 28 (2010) 668–676.

[5] T. Chan and L. Vese, Active contours without edges, *IEEE Transactions on Image Processing*, 10 (2001) 266–277.

[6] L. Wang, L. He, A. Mishra, C. Li, Active contours driven by local Gaussian distribution fitting energy. Signal Process, 89 (2009) 2435–47.

[7] D. Mumford, J. Shah, Optimal approximations by piecewise smooth functions and associated variational problems. Communication on Pure and Applied Math, 42 (1989) 577–685.

[8] S. Osher and J. A. Sethian, Fronts propagating with curvature dependent speed: Algorithms based on hamilton-jacobi formulation, *Journal of Computational Physics*, 79 (1988) 12–49.

[9] L. Zadeh, Fuzzy sets, Information and control, 8 (1965) 338-353.

[10] S. Krinidis, V. Chatzis, Fuzzy energy-based active contours, IEEE Transactions on Image Processing, 18 (2009) 2747–2755.

[11] B. Song, T. Chan, A Fast Algorithm for Level Set based Optimization, UCLA Cam Report, 2 (2002) 68.

# Simulation and Optimization of Membrane-Thermal Concentration Process for Concentration of Thin Sugar Juice

**Farhan[1], Saeed Gul[2]**

*Chemical Engineering Department, University of Engineering & Technology Peshawar Pakistan*

*\*Corresponding Author: farhaan.ppl@gmail.com*

## Abstract

Due to lofty latent heat of water, aqueous solutions demand elevated energy input for water removal. Investigators have made tons of attempts to separate water by alternate methods, for example concentration of solutions through membranes. In the last two decades scientists put efforts to improve membrane thermal concentration (MTC) process for water extraction from aqueous solutions, which adopts the conception to concentrate a solution with membranes prior to feed it into multiple effect evaporators (MEE). Hence steam consumption in MEE would decrease. In the present work, reduction in steam consumption was evaluated after integration of membranes into conventional MEE using ASPEN HYSYS. For present research a specific traditional MEE process was analyzed, it incorporated of six effects to enhance thin sugar juice concentration from 16.95 wt% to 74 wt%. In MTC process, the membranes attain concentration of 50 wt% and final 74 wt% concentration is achieved in MEE. In this research work, ASPEN HYSYS was used to develop two separate simulation models for concentration of thin sugar juice. First model was created for the genuine traditional evaporator process of six effects whereas second model for MTC process with six effects. The product concentration of 74 w% was achieved by each model. Comparison of both the models concluded that steam consumption is reduced by 85.12 % using membrane for pre-concentration without having any significant changes to the actual effects of process.

*Keywords: HYSYS, process simulation, sugar concentration process*

## 1.    Introduction

An optimum temperature of about 70-73 °C is required for isolation of sucrose from beet in the sugar industries. During liming and carbonation (purification section) for removal of non-sugars, enough heat is given to the juice to raise its temperature up to 80-90 °C which is then called thin sugar juice having 16.95 °B sucrose [1]. Thin juice is further concentrated in MEE up to 74 °B. In sugar industry most of the energy is consumed during evaporation process, having two major shortcomings. It drags a remarkable quantity of heat because of lofty latent heat of water and decomposition of sugar molecules may occur resulting in low quality and dark colored sugar [2, 3, 4]. Compared to any other separation process, membrane technology consumes less energybecause it's capableof water removal from aqueous solutions without phase change. Nanofiltration and/or Reverse Osmosis (RO) membranes can be utilized for pre-concentration of thin juice to save energy and lessen the thermal burden on evaporators. Gul and Harasek saved 85 % energy by introducing a multistage membrane separation processes for concentration of thin sugar juice from primary feed concentration of 16.95 °B to 50 °B with modest trans-membrane pressure and temperature of 32 Barg and 80 degree Celsius respectively. 70 w% of water was separated from the solution in membranes without change in phase. The pre-concentrated solution was next fed to MEE for final concentration of 74 °B [5]. In present work the proposed hybrid model for thin sugar juice concentration by Gul and Harasek was simulated in ASPEN HYSYS to find reduction in steam consumption compared to the initial conventional model.

Membranes can concentrate a sugar solution up to 50 wt%, in other words about 85% of the total water to be removed

can be obtained by membranes. Rest of the water can then be removed in evaporators. Hence in MTC process less amount of water need to be evaporated compared to conventional sugar production process which means steam consumption must be lower in MTC process. Solution is pumped with high pressure through membranes hence energy consumed by pump must be calculated for net reduction in energy due to MTC process. HYSYS can calculate power required for the pump if parameters for suction and discharge of pump are known, which for the current study are known, hence pump power can be calculated. For this study sufficient data is available so that steam consumption for the MTC process can be calculated. Hence net energy conservation by the proposed MTC process can be calculated as;

*Net energy conserved = (Energy consumption for conventional sugar production process) – (Energy consumption for MTC process + Energy consumption by pump)*

## 2.      Materials

A process simulation software ASPEN HYSYS was selected as an optimization tool because it offers simulation of any combination of various unit operations, it's widely used in process industries and it is user friendly. HYSYS has no

evaporator and the results were validated with real data [6, 7]. Margules fluid package was used and calculations were performed on the basis of mass balance [8]. Components used are Sucrose and Water.

### 2.1      Simulation of conventional MEE

An actual conventional MEE process was simulated using ASPEN HYSYS, having six evaporator effects to augment thin sugar juice concentration from 16.95 wt% to 74 wt%. Data of the real process was obtained from research carried out by Gul and Harasek [5]. The simulated model was compared on each effect with the real process to ensure validity of parameters.

### 2.2      Simulation and optimization of MTC process with six evaporator effects

Another model was created for MTC process in ASPEN HYSYS in which concentration from 16.95 wt % to 50 wt% was increased by membranes while the end 74 wt% concentration was achieved by six effects MEE. Steam flow rate for first effect of new model was calculated using modeling techniques in HYSYS and the results showed it decreased from 114640 kg/hr (for conventional MEE) to 17050 kg/hr (for MTC process). Heat transfer area was also calculated and it is certain
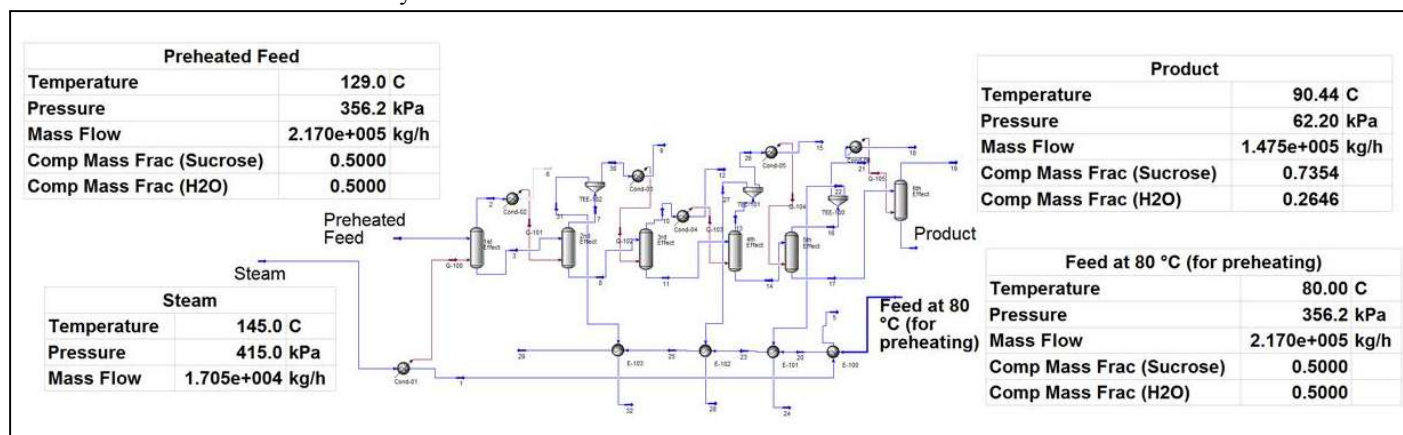


| Preheated Feed | |
| --- | --- |
| Temperature | 129.0 C |
| Pressure | 356.2 kPa |
| Mass Flow | 2.170e+005 kg/h |
| Comp Mass Frac (Sucrose) | 0.5000 |
| Comp Mass Frac (H2O) | 0.5000 |

| Steam | |
| --- | --- |
| Temperature | 145.0 C |
| Pressure | 415.0 kPa |
| Mass Flow | 1.705e+004 kg/h |

| Product | |
| --- | --- |
| Temperature | 90.44 C |
| Pressure | 62.20 kPa |
| Mass Flow | 1.475e+005 kg/h |
| Comp Mass Frac (Sucrose) | 0.7354 |
| Comp Mass Frac (H2O) | 0.2646 |

| Feed at 80 °C (for preheating) | |
| --- | --- |
| Temperature | 80.00 C |
| Pressure | 356.2 kPa |
| Mass Flow | 2.170e+005 kg/h |
| Comp Mass Frac (Sucrose) | 0.5000 |
| Comp Mass Frac (H2O) | 0.5000 |

*Figure 1: MTC process with six effects for MEE*

specific module for evaporator, alternative models were sought from the existing modules of process simulator. Flash separator with energy stream and a condenser for vapors was used as an

that the MTC process requires less heat transfer area compared to conventional evaporation process. Vapor bleed was optimized as well whose streams were taken from second, fourth and fifth effects.

| Parameters | Conventional MEE with 6 Effects | 6 effects MTC process |
|---|---|---|
| Feed Concentration (wt%) | 16.95 | 50 |
| Feed Temperature (°C) | 129 | 129 |
| Feed Pressure (kPa) | 356.2 | 356.2 |
| Feed Flow (kg/hr) | 640000 | 217000 |
| Product Concentration | 73.4 | 73.54 |
| Product Temperature (°C) | 88 | 90.44 |
| Product Pressure (kPa) | 57 | 62.2 |
| Product Flow (kg/hr) | 1.48E+05 | 1.48E+05 |
| Steam Flow (kg/hr) | 1.15E+05 | 1.71E+04 |
| Decrease in steam consumption(kg/hr) | | 9.76E+04 |
| % Decrease in steam flow | | 85.12% |

*Table 1: Comparison conventional MEE process and MT process for thin sugar juice concentration*

### 3.     Results

Table-1 shows actual data which was simulated in ASPEN HYSYS. Comparison of simulated models of both conventional MEE and MTC process shows that steam consumption is curtailed by 85.12 % when the solution is pre-concentrated with membrane prior to enter into evaporators. An incredible saving in operating cost can be obtained using membranes as pre-concentrators as it can save 85.12% of steam consumption. Analysis through simulation software reduced

reliance on pilot plant experiments for evaluating the performance of MTC Processes.

### 4.     Conclusions

At present energy conservation of already established process like MEE process is focused round the world. Performing experiments through pilot plants is time consuming, require remarkable resources and is laborious. In this work evaluation of a new process for sugar juice concentration called membrane thermal concentration was carried out through simulation. Simulation results showed that steam consumption can be curtailed by 85.12% in the new process compared to conventional process. New process is more economical as operating cost for steam production is lowered tremendously.

### 5.     References

[1]    E. Hugot, Handbook of cane sugar engineering, 1986.
[2]    Madaeni S.S, Tahmasebi K., and Kerendi S. H., Sugar syrup concentration using reverse osmosis membranes, Eng. Life Sci, 4, 2004, 187-190.
[3]    R. Rautenbach, R. Knauf, A. Struck, J. Vier, Simulation and design of membrane plants with ASPENPLUS, 19, 1996, 391-397.
[4]    Carl L. Yaws, Thermophysical properties of chemicals and hydrocarbons, 2008.
[5]    S. Gul, M. Harasek, Energy saving in sugar manufacturing through the integration of environmental friendly new membrane processes for thin juice pre-concentration, Applied Thermal Engineering, 43, 2012, 128–133.
[6]    Chawankul, N. Chuaprasert, S. Douglas, P. Luewisutthichat, Simulation of an agitated thin film evaporator for concentrating orange juice using aspen plus, food engineering, 47, 2001, 247–253.
[7]    L.M.M. Jorge, A.R. Righetto, P.A. Polli, O.A.A. Santos, R. Maciel Filho, Simulation and analysis of a sugarcane juice evaporation system, food engineering, 90, 2010, 351-359.
[8]    A.E. Lewis, F. Khodabocus, V. Dhokun, M. Khalife, Thermodynamic simulation and evaluation of sugar refinery evaporators using a steady state modeling approach, Applied thermal engineering, 30, 2010, 2180-2186.

# Numerical Solution of an Integro-Differential Equation Model for the Spread of Alcohol Abuse using RBF

*Hazrat Bilal, Marjan Uddin*
*Department of Basic Sciences and Islamiat, University of*
*Engineering and Technology Peshawar, Pakistan.*
*bilalrajjarms@yahoo.com*

**Abstract**

The study of alcohol abuse level is an important issue in public health sector. Many factors exist in population that may effect the spread of alcohol abuse. For example peer influence. The aim of this study is to understand mathematically the effect of peer influence on the spread of alcohol abuse in a population. The phenomena may be model by an integro-differential equation. The solution of such mathematical model is a difficult task. In the present study, we will approximate the given model using the radial basis function and to analyze the model solution behavior especially in terms of travelling wave.

**Key words**: Traveling wave solution, Radial basis function, Alcohol abuse, Integro-differential equation.

## 1 Introduction

Alcohol abuse is one the most important problem in our society these days. Many factors maximize the spread of alcohol abuse in our neighborhood. One of those factors is a Peer influence (i.e., personal contacts in drinking environment). In the present work our aim would be to understand mathematically the role of peer influence on the spread of alcohol abuse. In the works of the authors [1, 2] a discrete network model was used to study the spread and treatment of alcohol abuse. More recently Sanchez et.al [3] proposed mathematical model of three ODEs for spread of alcohol abuse. They divided their work in three phases, (S) moderate drinkers, (D) problem drinkers

and (R) recovered alcoholics and transition between these groups happens due to peer influence. More recently the authors of work in [4]

Proposed an integro-differential equation model which represents the peer influence. These authors used perturbation analysis and phase plane techniques in finding travelling wave-types solution. In the present work, we study the problem of spread of alcohol abuse by considering the integro-differential equation. As the IDE solution is difficult to obtain, so the IDE is converted into partial differential equation. We approximated the solution of corresponding partial differential equation by using radial basis functions.

.

## 2 Mathematical model

Most of the dynamics of the physical events can be model with integro-differential equations. For example the authors in [5] develop the integro-differential equation for the study of spread of disease between infectious persons. Here use the following IDE to study spread of alcohol abuse due to peer influence.

$$(1.0.1) \quad \frac{\partial u}{\partial t} = \upsilon u_{xx} + \lambda u \, (1 - u) \, (m - r),$$

$$u(x, 0) \ = \ u_0$$

Where $u(x, t)$ denotes the level of alcohol abuse at position $x$ in given neighborhood at given time t. For the individual to be sober $u \approx 0$, while alcoholic

if $u \approx 1,\ 0 < \upsilon \ll 1$ and $\lambda > 0$. Peer influence at position $x$ on individuals by other individuals at position $y$ may represent as convolution integral

(1.02)

$$m(x,t) = \int_{-\infty}^{\infty} w(x - y)\, u(y,t)\, dy$$

Where $w$ is a weight function, denotes the personal contact between the individual. The weight function must satisfy

(1.0.3) $$\int_{-\infty}^{\infty} w(z)\, dz = 1,\ w(z) > 0.$$

The level of personal resilience $r(x)$ which is the tendency of a person to become alcoholic. An individual have an alcoholic problem if $r(x) \approx 0$, while resilient if $r(x) \approx 1$. The nonlinear factor $u(1 - u)$ have not much effect when the individuals are almost sober or alcoholic. In our study, we choose the weight function $w(z) = \dfrac{1}{2c}$ in $[-c, c]$. The weight function is used to show a tie between neighbors. So equation (1.0.2) becomes as

(1.0.4) $$m(x,t) = \frac{1}{2c} \int_{-c}^{c} u(t, z + x)\, dz.$$

We use Taylor series expansion on $u(t, z + x)$ around $x$ and ignoring $O(c^3)$ and higher order terms, we get

(1.0.5) $$m(x,t) \cong u(x,t) + \frac{c^2}{6}\, u_{xx}.$$

So our IDE reduces to a PDE of the form $(1.0.6)$

$$u_t - \left(\upsilon + \frac{\lambda c^2}{6}\, u(1 - u)\right) u_{xx}$$
$$= \lambda u(r - u)(u - 1).$$

We solve this model using RBF-PS method. In applied method we approximate the derivative by RBF methods and for time integration we use the RK4 method.

**3 RBF-PS Technique**

A function defined by

$$\psi(x,y) = \phi(\|x - y\|) = \phi(r)$$

is called radial basis function centered at $y$. For example $\phi(r) = \sqrt{(1 + (\varepsilon r)^2)}$ is a multiquadric radial basis function,

$\phi(r) = e^{-(\varepsilon r)^2}$ is a Gaussian radial basis function etc. Assume a set of scattered points $x_1, x_2, x_3, ..., x_N \in R^d$, then

(2.0.7) $$u(x) = \sum_{j=1}^{N} b_j \phi(\|x - x_j\|)$$

The $N \times N$ linear system in matrix form is given as

(2.0.8) $$Ab = \mathbf{u}$$

The entries of matrix $A$ are

(2.0.9) $$a_{ij} = \phi(\|x_i - x_j\|)\quad i,j = 1,...,N$$

Consider time dependent boundary value problem.

(2.0.10) $$u_t = \pounds u \text{ in } \Omega$$

(2.0.11) $$Bu = g(x) \text{ in } \partial\Omega$$

RBF collocation method apply to the operator £ then the RBF interpolate of equation as

(2.0.12) $£ u(x_i) =$

$$\sum_{j-1}^{N} b_j £\phi(\|x_i - x_j\|) \quad i=1,...,N_I$$

Where $N_I$ interior center and boundary operator $B$ are applied, so

(2.0.13)

$$Bu(x_i) = \sum_{j=1}^{N} b_j B\phi(\|x_i - x_j\|) \quad i=N_I +1,...,N$$

The matrix $H$ is the evaluation matrix that discretizes the PDE's into two slabs.

(2.0.14)
$$H = \begin{bmatrix} £\phi \\ B\phi \end{bmatrix}$$

So from the interpolation problem, we have $b = A^{-1} u$ and $A$ is the system matrix. Thus PDE problem that discretize matrix in a space is known as Differentiation matrix.

(2.0.15)
$$D = H A^{-1}$$

For time dependent PDE's we have

(2.0.16)
$$u_t = £ u \approx Du$$

Wherever D is a $N \times N$ is differentiation matrix. Later on for the space discretization by RBF methods, we have the following system of ODE's

(2.017)
$$u_t = F(u),$$

In our case $F(u) = D u$ in the time integration is done by RK4 methods.

## 4. Computational results

To approximate our solution, we use RBF-PS methods discussed in the above section. In our numerical approximation we use the Multiquadrics radial basis functions. We choose N = 140 points in the domain [-2, 2]. The other parameters used in our computation are $\upsilon =0.005, c = 0.1, \varepsilon = 10, \lambda =10.$ and final time T = 7 and initial solution $u_0 =(1/2)(1 + \tanh(x))$. Here we discussed two cases when $r>0.5$ and $r < 0.5$. If $r >0.5$ the traveling wave will moves from left to right show that the individual becomes sober. On the other hand when $r <0.5$ the traveling wave moves from right to left, which implies that the individuals are alcoholic. These solution profiles are shown in Figure (1.0.1), and Figure (1.0.2) respectively.
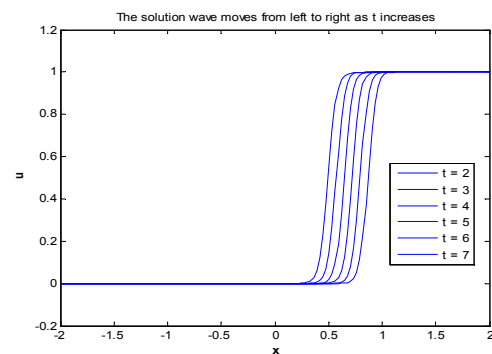


**Figure 1. Traveling wave: N = 140, $\varepsilon$ = 10, L = 2, $\upsilon$ = 0.005, $\lambda$ = 10, $c$ = 0.1 and $r$ = 0.7**
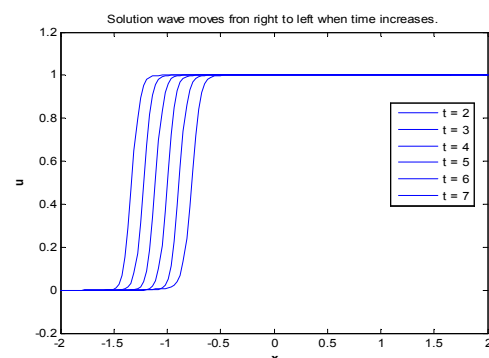
**Figure 2. . Traveling wave: N = 140, $\varepsilon$ = 10, L = 2, $\upsilon$ = 0.005, $\lambda$ = 10, $c$ = 0.1 and $r$ = 0.2**

## 5. Conclusions

In the present work, we approximate the integro-differential equation which is a model for the spread of alcoholic abuse. First we converted the given integro-differential equation into a partial differential equation. Then approximate the resultant PDE using RBF-PS methods. We discussed various aspect related to spread of alcoholic abuse mathematically for different types of parameters. This work may be extended to study the spread of obesity by social ties and similar other related problems.

## 6. References

1. R. J. Braun and .al.et, Application of small world network Theory in alcohol epidemiology, Alcohol study 67(2006)591— 699.
2. R.A. Wilson and al.et, A network model of alcoholism and Alcohol policy, Proc. Math. Problems in Industry Workshop 67 (2004).
3. F. Sanchez and al.et, drinking as an epidemic – a simple Mathematical model with recovery and relapse, Therapists Guide to the Evidence-Based Relapse Prevention (2007).
4. D.A.French and al.et, an integro-differential equation Model for the spread of alcohol abuse, The Journal of Integro-differential equation and Applications 22(2010), No.3, 434—464.
5. Medlock and M.Kot, Spreading disease; integro-differentia Equations old and new, Math.Bio.Science 184 (2003),202—222.

# Cost effective approach to prevent corrosion by using geopolymer coating

*Fawad Khan[1,*], Amir Naveed[1], Noor-ul- Amin[2], Saeed Gul[1]*

*[1]Department of Chemical Engineering, University of Engineering & Technology Peshawar*

*[2]Department of Chemistry, Abdul Wali Khan University Mardan*

*\*Corresponding author*

engr.fawad.chemical@gmail.com

## Abstract

This article presents research into durability of Geopolymer coating material (Geospray) made from using class-F fly ash (alumino silicate source material) with Si/Al ratio 1.80 and alkaline activator using sodium hydroxide and sodium silicate solution, exposed to acidic medium. The concentration of acidic solution was taken 10% in water. The parameters studied were composition and x-ray diffraction (XRD) of fly ash and scanning electron microscopy (SEM) of geospray applied to metallic plates. SEM analysis of metallic plate However, the aim of this research is to make Geospray having good resistance to chemical corrosion. Comparative analysis was made between coated and uncoated metallic plates exposed to acid medium at the age of 56 days. Non coated metallic plate was severely corroded by the acid environment while no significant deterioration was observed for coated plate.

Key Words: Chemical attack, Fly ash, Geopolymer coating material, surface analysis.

## 2.  Introduction

Geopolymerization technology has been used for making geopolymeric materials which belongs to an inorganic materials class and it can be produced by activation of aluminosilicate source materials through alkaline liquids at room temperature. Mechanical, thermal and chemical properties of the geopolymeric materials are basically rely upon the raw materials from which they are produced [1]. Such raw materials are e-g, metakaolin, slag and fly ash. Since the last decades of the 20th century, Class-F fly ash having low calcium content, based geopolymers are having a lot of significance due to their characteristics such as low shrinkage, high compressive strength and very good and high resistance to acidic nature as well as sulphate medium and having low creep as well[2,3]. Also fly-

ash based Geopolymer concrete is about 10–30% cheaper than that of ordinary Portland cement OPC) concrete [2]. It has also been investigated that class-F fly ash geopolymer can be used to manufacture structural elements such as railway sleepers [4] and concrete columns [3] and have confirmed their applicability as structural material.

It is also been found that geopolymer material is able to prevent deterioration from acid where such attack may occur in the harsh environment of mining, sewers, mineral processing, acid rain and acid ground-water [5, 6].

Davidovits [7] reported that geopolymer has very low mass losses when immersed in 5% $H_2SO_4$ solutions for four weeks. Song et al [8] investigated experimental data based on the response of Alkaline liquid fly ash base Geopolymer (AAFG) concrete immersed in 10% sulphuric acid solutions for up to 56 days, in terms of mass loss, visual analysis, alkalinity and residual compressive strength. Deng et al [9] reported the strength of alkali-activated slag cement and Portland cement pastes in 5% sodium hydroxide and other corrosive solutions. The reference samples were

immersed in water. It was found that the strength of OPC pastes decreases significantly after immersion in the sodium hydroxide and the other corrosive solutions, but alkali-activated slag cement pastes, after immersion in the sodium hydroxide and the other corrosive solutions, showed basically the same strength when immersed in water.

In the present work, geopolymer coating has been synthesized from fly ash and applied on mild steel plates to investigate the resistance against harsh environments

## 2. Experimental methods

### 2.1. Materials

Fly ash was taken from matrix company Karachi. It's chemical and mineral composition are shown in table.1 and figure.1, respectively. This is mainly amorphous with some crystalline quartz, mullite and hematite. Sodium silicate solution was taken from Peshawar chemicals, hayatabad while sodium hydroxide was purchased from Haq chemicals Peshawar. Sodium hydroxide and sodium silicate are being used to activate fly ash.

Fly ash was activated by sodium hydroxide and sodium silicate taking ratio of sodium silicate to sodium hydroxide 2.5 and then fly ash to alkaline activator 3.0. water was added such that water to cement (w/b) ratio becomes 0.34. The paste was properly mixed for 10-15 minutes. The metallic plates of 1×1 cm dimensions were dipped in the pastes and then were cured at room temperature for 48 hours. Samples were then immersed for tests in various solutions.

The resistance of Geopolymer coating material was studied by being immersed in acidic medium. The concentration of the solutions was taken 10%. The metallic plate without coating was put in the solution

separately for the same time as coating plates. The time was 56 days to analyze the surface morphology being corroded by the acidic solutions.

The deterioration was studied by Scanning electron microscopy. For the analysis the samples (coating and uncoating) were taken for micro structural observations of the fracture surfaces.

### 2.2. Mix design for experimental work

Fly ash was taken as an aluminosilicate source and combination of sodium hydroxide and sodium silicate was used as alkaline activator. Ratio of silica to alumina was 2.08 in fly ash. Based on Mustafa et al research work [10] ratio of sodium silicate to sodium hydroxide for making alkaline activator was taken 2.5 and fly ash to alkaline activator 3.0, also sodium hydroxide concentration 12 M. Water to binder ratio was taken 0.35 according to Temuujin work [11]. All the parameters used for making Geopolymer coating materials are given in table 1.

**Table 1: Geospray Mix Design**

| Materials | Mass Ratios |
|---|---|
| Ratio of fly ash to alkaline activator | 3.0 |
| Ratio of $Na_2SiO_3$/NaOH | 2.5 |
| Mass of fly ash(g) | 3790 |
| Mass of NaOH(g) | 361 |
| Mass of $Na_2SiO_3$ | 902.5 |

## 3. Results

**3.1.** Geopolymer coating material typically offer strong resistance against harsh environment like acids. a very small deterioration in the surface structure after immersion in harsh medium (acidic) for about two months has been observed. In all the experiments the concentration of acid was kept 10 %.

### 3.2. XRF analysis of Fly Ash

X-Ray Fluorescence analysis has been done to determine the composition of various compounds in percentage. It is required to find the presence of main raw source i-e silica and alumina. Hence the XRF analysis shows that silica and alumina both are present in greater amount which is suitable to make geopolymer. XRF analysis also confirms that the flyash is of class-F for which the calcium content must be less than 15 % or in some context class-F fly ash is when the sum of alumina, silica and iron oxide is greater than 70 % while in this fly ash, the sum is about 80%.

### 3.3. X-ray Diffraction

Fig. 1 shows XRD pattern of fly ash having mainly amorphous structure, which is the desired phase to take part in the phenomenon of geopolymerization process. The XRD pattern also shows the peaks of exposed to high temperature. This crystalline phase doesn't take part in the reaction that is why XRD must be done to see phase composition of material

quartz, mullite and hematite of the crystalline phase and which are having geometrical structure due to whether suitable for the reaction or not. The XRD results shows that alumino silicate material is mainly amorphous which took part in the Geopolymerization reaction while crystalline phase doesn't take part in the reaction.

Table.2 Composition of Fly ash by XRF analysis

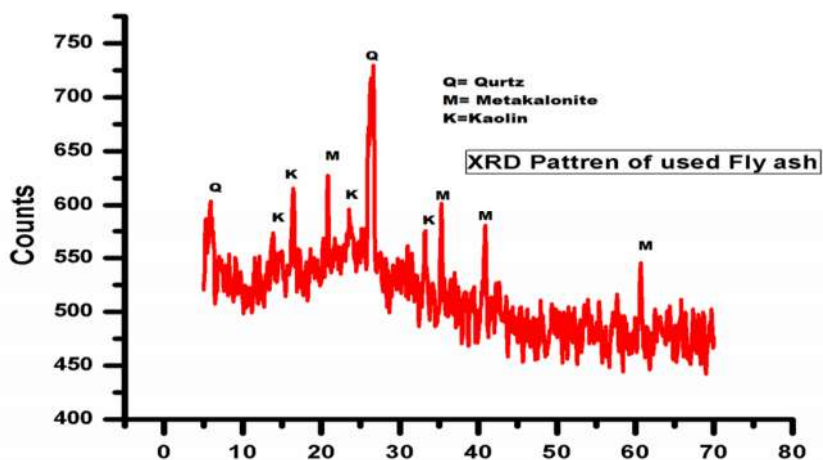| Oxides | Percentage |
|---|---|
| $SiO_2$ | 50.0 |
| $Al_2O_3$ | 28.0 |
| $Fe_2O_3$ | 12.0 |
| CaO | 3.0 |
| MgO | 1.3 |
| $Na_2O$ | 0.2 |
| $TiO_2$ | 3.2 |
| $P_2O_5$ | 0.42 |
| MnO | 0.03 |
| $SO_3$ | 0.12 |
| LOI | 0.53 |

**Figure1. XRD pattern of Fly Ash**

### 3.4. Scanning Electron Microscopy (SEM)

SEM analysis is used for micro structural study of geopolymers universally. Figures 2 show SEM analysis as well as comparison between coated and uncoated surfaces in acid which is hydrochloric acid. Figure 2(a-d) shows SEM analysis of various surfaces. Image (a) is the uncoated metallic surface before dipping or exposed to acid showing no fracture compared to image (c) which is showing clearly many fractures on the surface exposed to acid for 56 days. Figure 2- (b) is shows geopolymer coating surface applied to metal plate before exposure while figure 2-(d) is being exposed to acid for 56 days while there is no significant difference in the samples of before and after exposure.



a)



b)
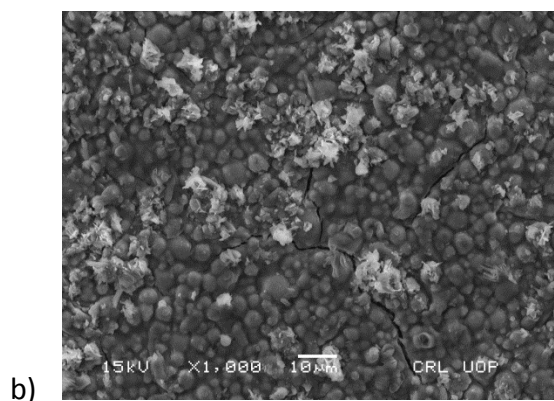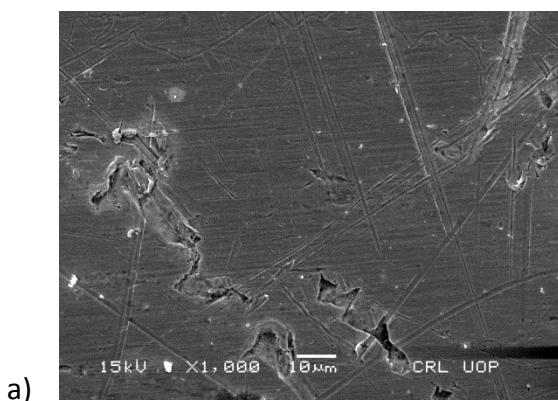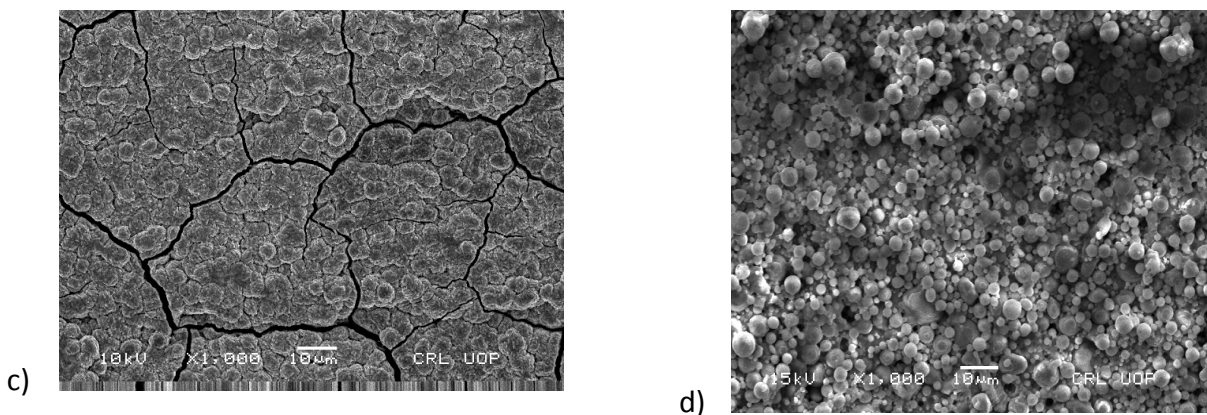
**Figure 2. SEM analysis various of surfaces in 10% HCL solution a) uncoated metal surface before exposure, b) geopolymer coated surface before exposure, c) uncoated metal surface exposed for 56 days, and d) geopolymer coated surface exposed for 56 days**

## 4.  Conclusion

Geopolymer coating material was prepared using Class-F fly ash activated by sodium hydroxide and sodium silicate. The coating was applied on mild steel metallic plate and was exposed to acidic medium for 56 days. The cracks were found on the uncoated surface exposed to harsh acidic medium while the prevention has been seen for the coated surface applied to metallic plates. Therefore, geospray can be used to coat metallic surfaces to prevent chemical attacks and chemical corrosions.

## 5.  References

[1]  P. Duxson , A. Fernandez-Jimenez , J. L. Provis , G. C. Lukey , A. Palomo ,J. S. J. van Deventer, Geopolymer technology: the current state of the art: J Mater Sci (2007) 42:2917–2933

[2]  B. V Rangan, Low-calciumfly-ash based geopolymer concrete, editor. Concrete construction engineering handbook. New York: CRC Press; 2008.

[3]  D. Hardjito, B.V Rangan, Development and properties of low-calcium fly ash based geopolymer concrete: Research report GC1, Faculty of Engineering, Curtin University of Technology, Perth, Australia; 2005.

[4]  Johnson G. Geopolymer railway sleepers. CSRP annual geopolymer meeting, Perth, Australia; 21–22 April 2008.

[5]  T. Bakharev, Resistance of geopolymer materials to acid attack: J.Cement and Concrete Research (2005);35:658–70.

[6]  A. Allahverdi , F. Skvara, Sulfuric acid attack on hardened paste of Geopolymer cements – Part 1. Mechanism of corrosion at relatively high concentrations: Ceram-Silik (2005);49:225–9.

[7]  J. Davidovits, D. Comrie, J. Paterson, and D. Ritcey, 1990, Geopolmeric concretes for environmental protection: *ACI Concrete International*, 1990, 12, 30-40.

[8]  J. Songa, M. Marosszekya, M. Brungsb, R. Munna, Durability of fly ash basedGeopolymer concrete against sulphuric acid attack: (2005)

[9]  Y. Deng, X.Wu, and M.Tang, M., , High strength alkali-slag cement: Journal of Nanjing Institute of Chemical Technology (in Chinese), P.R. China, (1989) 11(2), 1–7.

[10]  A. Mustafa Al Bakri, J. Liyana, H. Kamarudin, M. Binhussain, C.M. Ruzaidi, A.M. Izzat,. Fly Ash Porous Material using Geopolymerization Process for High Temperature Exposure: International Journal of Molecular Science, (2012) 13: 4388-4395.

[11]  J. Temuujin, A. Minjigmaa, W. Rickard and A. van Riessen,. Thermal Properties of Spray-Coated Geopolymer – Type Compositions: Journal Thermal Analysis Calorimetry, (2012) 107:

# Feasibility and Potential of Parabolic Trough Solar Thermal Power Plants in Pakistan

**Asad Riaz[*], Muhammad Zubair**

*U.S.-Pakistan Centre for Advanced Studies in Energy, NUST, Sector H-12, Islamabad 44400*
***Email**: asadriaz2999@yahoo.com*

## Abstract

Pakistan is currently facing severe energy crises due to its growing population and expansion in industrial and agricultural sector. Addressing the energy crises by installing fossil fuel based power plants has severe adverse effects on environment and also will result in depletion of fossil fuel resources. Pakistan lies on a sunny belt that receives Direct Normal Irradiance (DNI) of 4.45 to 5.83 kWh/m$^2$/day as compared to the world average DNI of 3.61 kWh/m$^2$/day. Thus solar energy emerged as the most promising candidate to fulfill the electricity and heating requirements even for rural communities as roughly 35 % of population in Pakistan is off-grid. Solar energy has potential of generating around 2.9 million MW of electricity. Harnessing of this huge amount of energy will not only reduce the $CO_2$ emissions but will also save the conventional energy resources. It is generally assumed that solar thermal power plants are feasible for areas where DNI is greater than 5 kWh/m$^2$/day. In Pakistan many such locations exist where installation of solar thermal power plants is most feasible.

This paper aims to give the feasibly study and the associated levelized electricity cost (LEC) at different suitable locations of Pakistan using TRNSYS software. It was found that LEC of the power plants is comparable to conventional fossils fuel power plant provided that DNI at the location is high. By installing solar thermal power plants will not only address environmental problems but cost effective energy solution.

**Key Words:** Direct Normal Irradiance, Levelized Electricity Cost, TRNSYS.

## 1.      Introduction

Solar energy is the biggest and unending source of energy which is available for free and has got more attention now-a-days [1]. It is free from pollutants and thus more beneficial to our society. Solar energy can be utilized in many ways to get electricity. One method is concentrating solar power (CSP). There are three existing technologies which uses CSP namely: parabolic trough, Dish and tower technology. Among these, parabolic trough technology is proven and several parabolic trough power plant are already working worldwide successfully [2][3]. Parabolic trough uses a mirror in parabolic shape which reflects and concentrate sun light on its focal line where absorber tube is present in which heat transfer fluid (HTF) is passing. The heated HTF passes through steam generator where steam is formed which is then passes through steam turbine and hence electricity is generated [2]. In comparison with other CSP technologies, Parabolic trough technology involve low technical and financial risk. In this paper feasibility and potential of Solar Parabolic Trough Power Plant (SPTPP) is evaluated at major cities of Pakistan where DNI is high and its weather data is available in TRNYS data base. Multan, Lahore and Peshawar are taken and its technical and economic feasibility has been investigated.

### 1.1      Development of SPTPP in Pakistan

For development of PTSTP Plant, some key parameters must be considered which affects the performance and successful operation of the plant. First is the climate conditions of the locations. It is general believed that SPTPP is efficient and economical where daily average radiations are greater than 5 kWh/m$^2$. The second most important parameter is price and sufficient amount of lend for overall slop of less than 3% [4]. Moreover, accessibility to grid and availability of sufficient amount of water is the next key parameters.

### 1.1.1      Direct Normal Irradiance

Pakistan lies on a sunny belt and most of its land receives high solar insolation which is depicted from figure 1 [5].
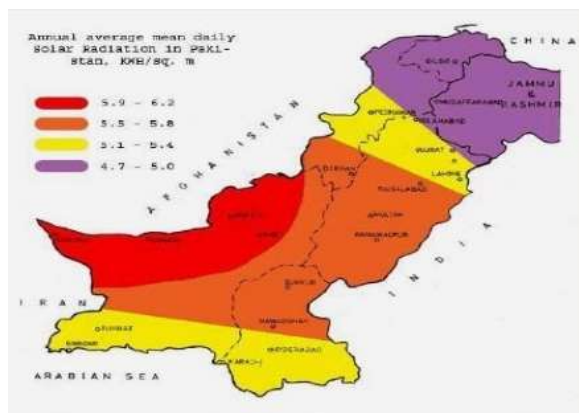
Fig. 1. Annual Average mean daily radiations in Pakistan

In TRNSYS we have only the weather data of Multan, Lahore and Peshawar where annual average daily radiations are greater than 5.5 kWh/m$^2$. We have more locations where DNI value is high but due to unavailability of solar radiations data of that locations we cannot perform our simulations at those locations. It is obvious that greater is the DNI value, greater will be the power density and lower will be the cost.

### 1.1.2 Land Topography

Beside high level of DNI, larger quantity of land would also be required and the land which is unsuitable for residential and agricultural purpose will be the ideal one. In USA several SPTPP are installed in the Mojave Desert of California and produces hundreds of MW of electricity [3].

### 1.1.3 Water Availability

One of the most influencing key perimeter is the water availability. Water is manually used for cooling of SPTPP. Abundant amount of water resources are present in Multan, Lahore and Peshawar.

### 1.1.4 Power Grid Availability

Several electricity grids are there in Multan, Lahore and Peshawar and thus the generated power could be easily transmitted to national grid.

### 2 Methodology

A 100 MW SPTPP is created in TRNSYS simulation environment using STEC library [4]. The weather data is taken from Meteonorm data base present in TRNSYS. Therminol vp-1 is used as a HTF and steam as a working fluid. When sun radiations fall on the solar field, it heats up the HTF and when the temperature reached to 400 C$^0$, It will start flowing through steam generator and steam will be formed which will run the Rankine cycle. The flow rate of both HTF and condensed water is adjusted such as to give the set point temperatures else the system is auto shut down. The electricity per annum is calculated hour by hour taking into account the instant solar radiations. The TRNSYS model of 100 MW SPTPP is shown in figure 2.
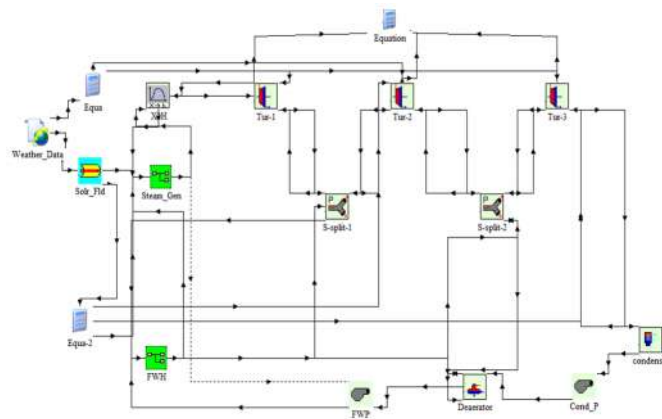


Fig. 2. TRNSYS model of 100 MW SPTPP

The LEC is calculated from Eqs. (1) and (2) according to the simplified IEA method [5].

$$LEC = \frac{a.CC + O\ \&\ M + F}{P}$$

(1)

Where

a: annuity factor $= \frac{K\ (1+k)}{[(1+k)^n] - 1} + K\ insurance = 7.76\%$

(2)

K : Interest rate = 6%
K $_{Insurance}$ : Annual Insurance rate = 0.5 %
n : Depreciation period in years (30 years)
CC : Capital cost
O&M : Operation and maintenance cost
P : Yearly electricity production (kWh)
F : Fuel consumption (solar only made F=0)

### 3. Results
### 3.1 Technical Feasibility

The required solar field area is 1 km$^2$ while Luz System (LS-3) parabolic trough collector has been used of which characteristics are shown in table 1 [7].

Table1. List of Characteristics of LS-3 parabolic trough collector

| Characteristics | Value |
|---|---|
| Aperture width | 5.76 m |
| Collector length | 150 m |
| Focal length | 1.71 m |
| Distance between Rows | 16-17 m |
| Diameter of absorber tube | 0.07 m |
| Concentration ratio | 82 |
| Reflectivity of mirror | 0.93 |
| Coefficient of absorption of absorber tube | 0.96 |
| Coefficient of emission of absorber tube | 0.17 |
| Coefficient of transmission of mirror | 0.98 |
| Coefficient of transmission of glass tube | 0.96 |
| Collector peak efficiency | 68% |

Table2. List of losses of solar field

| Losses | Value |
|---|---|
| Clean reflectivity | 0.94 |
| Broken mirror fraction | 0.98 |
| Tank heat losses at 400 C$^0$ | 257 kW |
| Piping heat losses | 20 W/m$^2$ |
| Field tracking Parasitics | 0.86 |
| Cleanliness of solar field | 0.95 |
| Ground reflectiveness-no snow | 0.2 |
| Ground reflectiveness snow | 0.7 |

The temperature of solar field is kept fix at 400 C$^0$ while mass flaw rate of HTF is allowed to change. In Winter, when DNI is lower, then mass flow rate passing through solar field is also lower so as to attain the set point temperature and when it became Summer, DNI increases and thus the mass flow rate of HTF also increases in order keep the temperature at constant value of 400 C$^0$. When DNI becomes too much low so that it could not give the output temperature of 400 C$^0$ or when it is non-sun shine hours then flow of HTF will stop and the power plant will automatically shut down. The mass flow rate of condensed water is so adjusted that it gives

the steam output temperature of 350 C$^0$. The following losses are considered while taking the solar field model of Solar Thermal Electric Component (STEC) library of TRNSYS.

Meteonorm weather data for location of Multan, Lahore and Peshawar is used with two axis tracking from east to west and north to south. While the turbines properties are given in table 3.

Table3. Turbine properties

| Property | Turbine-1 | Turbine-2 | Turbine-3 |
|---|---|---|---|
| Inlet pressure (Bar) | 100 | 20 | 5 |
| Outlet pressure (Bar) | 20 | 5 | 0.05 |
| Flow rate (kg/S) | Depends on DNI | Depends on DNI | Depends on DNI |
| Steam quality | 1 | 1 | 1 |

As we can see when DNI varies, it alters the flow rate of HTF, condensed and Colling water required for condenser while temperature and enthalpies remain the same for the whole year. It implies that the only parameter which change with DNI is the mass flow rate which causes change in power output. The annual power output is show in figure 3 for the aforementioned cities.



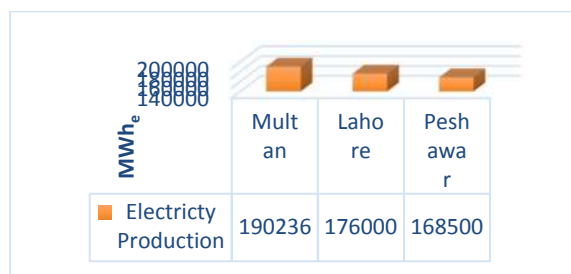| | Multan | Lahore | Peshawar |
|---|---|---|---|
| Electricty Production | 190236 | 176000 | 168500 |

Fig. 3. Annual power output

### 3.2 Economic Feasibility

Economic feasibility is most important for installation of any kind of a power plant. For comparison with other power plants, LEC is calculated which is a measuring stick that tells how much a power plant is economical. It tells the per unit cost of electricity while its formula incorporates capital cost, annuity factor, maintenance and operational cost along with project life and interest rate [8]. The LEC is calculate from Eqs. (1) and (2) by taking the operation and maintenance cost equal to 3% of the capital cost while capital cost itself is about

300800 PKR/kWe. The LEC of the selected sites are given in figure 4.
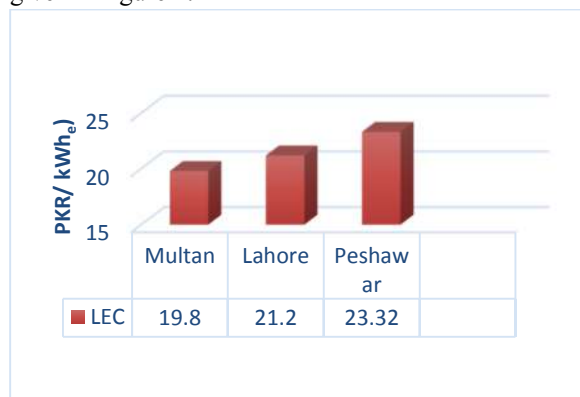


Fig. 4. LEC of selected sites

## 4.    Conclusion

From the technical and economic analysis, it is obvious that SPTPP is much feasible in locations where DNI is high and large land area is available. Due to higher DNI valve, Multan is the most favorable location while Peshawar the least. Moreover, the LEC is higher than conventional fossil fuel power plant but it is a clean and renewable energy source lasting forever.

## 5. References

[1] Michael Geyer, "International market introduction of concentrated solar power-policies and benefits", ISES Solar World Congress 2007, vol.1, 2007, pp.75–82.

[2] Qu Hang and Zhao Jun, "Feasibility and potential of concentrating solar power in China", ISES Solar World Congress 2007, vol.4, 2007, pp.1724–1728.

[3] H. Price, "Reducing the cost of energy from parabolic trough solar power plant", National Renewable Energy Laboratory, 2003.

[4] Jones, S. A., Pitz-Paal, R., Schwarzboezl, P., Blair, N., and Cable, R., 2001, "TRNSYS Model of the SEGS VI Parabolic Trough Solar Electricity Generating System," Proc. of Solar Forum 2001: Solar Energy: The Power to Choose, Washington, DC, April 21–25, ASME, New York

[5] Roy, A., Meinecke, W., and Blanco Muriel, M., ed., 1997, "Introductory Guidelines for Preparing Reports on Solar Thermal Power Systems," SolarPACES Report No. III-3/97.

[6] Qu Hang and Zhao Jun, "Prospect of concentrating solar power in China—the sustainable future", Renewable and sustainable energy reviews, vol.12, 2008, pp.2506–2514.

[7] A. Khalid and H. Junaidi, "Study of economic viability of photovoltaic electric power for Quetta-Pakistan",
Renewable Energy, Vol. 50, Feb 2013, pp. 253-258.

[8] Zaaraoui, Abdelkader, Mohamed Lamine Yousfi, and Noureddine Said. "Technical and economical performance of parabolic trough collector power plant under Algerian climate." *Procedia Engineering* 33 (2012): 78-91.

[9] Yang, Bin, et al. "Feasibility and potential of parabolic trough solar thermal power plants in Tibet of China." *2010 Asia-Pacific Power and Energy Engineering Conference*. IEEE, 2010.